



Méthodes expérimentales instationnaires et leurs applications en mécanique des fluides

Thierry M. Faure

► To cite this version:

Thierry M. Faure. Méthodes expérimentales instationnaires et leurs applications en mécanique des fluides. Sciences de l'ingénieur [physics]. Université Pierre et Marie Curie - Paris VI, 2009. tel-00911074v2

HAL Id: tel-00911074

<https://theses.hal.science/tel-00911074v2>

Submitted on 27 Apr 2018

HAL is a multi-disciplinary open access archive for the deposit and dissemination of scientific research documents, whether they are published or not. The documents may come from teaching and research institutions in France or abroad, or from public or private research centers.

L'archive ouverte pluridisciplinaire **HAL**, est destinée au dépôt et à la diffusion de documents scientifiques de niveau recherche, publiés ou non, émanant des établissements d'enseignement et de recherche français ou étrangers, des laboratoires publics ou privés.

HABILITATION À DIRIGER DES RECHERCHES

présentée devant l'Université Pierre et Marie Curie – Paris VI

par

Thierry M. FAURE

MÉTHODES EXPÉRIMENTALES INSTATIONNAIRES ET LEURS APPLICATIONS EN MÉCANIQUE DES FLUIDES

Soutenue le 9 décembre 2009 devant la Commission d'Examen

JURY

G. BOIS	ENSAM Lille (rapporteur)
J. BORÉE	ENSMA Futuroscope (rapporteur)
J. N. GENCE	Université Claude Bernard Lyon I (président)
B. LECORDIER	CORIA Rouen
P. LE QUÉRÉ	LIMSI Orsay (invité)
F. LUSSEYRAN	LIMSI Orsay
M. RIETHMULLER	Institut Von Kármán Rhode St Genèse (rapporteur)
P. SAGAUT	Université Pierre et Marie Curie Paris VI

Résumé

Cette synthèse porte sur plusieurs thématiques de mécanique des fluides et s'articule autour d'une approche par des méthodes expérimentales instationnaires. Les domaines successivement abordés sont la turbulence, l'aérodynamique compressible, les machines tournantes, l'hydrodynamique et les instabilités, tandis que les techniques expérimentales mises en œuvre comprennent les sondes directionnelles de pression, l'anémométrie fil/film chaud, la vélocimétrie laser Doppler, la visualisation par injection de traceur et la vélocimétrie par images de particules. Dans la plupart des cas, on développe des techniques multi-composantes, afin d'obtenir les trois composantes du champ de vitesse. Lorsqu'un phénomène périodique est présent dans l'écoulement, des traitements par moyennes de phase permettent de reconstruire, à partir d'un maillage de mesures ponctuelles, une information globale dans un plan ou dans un volume, et son évolution temporelle moyenne. Il est aussi possible de reconstituer une dynamique en fonction du temps à partir d'une mesure dans un plan, non résolue en temps, synchronisée avec une mesure ponctuelle, résolue en temps. L'ensemble des configurations étudiées par ces méthodes expérimentales constitue des bases de données, utiles notamment pour une comparaison avec des résultats de simulations numériques.

Abstract

This synthesis is about different topics in fluid mechanics, linked by an approach with unsteady experimental methods. The following domains are successively considered: turbulence, compressible aerodynamics, rotating machinery, hydrodynamics and instabilities. The experimental techniques used include directional pressure probes, hot wire/film anemometry, laser Doppler velocimetry, flow visualization by tracer injection and particle image velocimetry. Most of the time, multi-component techniques are developed to get the three components of the velocity field. If a periodic phenomenon exists in the flow, phase-average analysis allows building, from a mesh of measurement points, global information within a plane or a volume, and its averaged time development. The establishment of the time dynamics is also possible from non time-resolved plane measurements, synchronized with a time-resolved measurement acquired at one position. All the cases considered in the report and their experimental approaches are data bases, useful, for instance, for comparison with numerical simulations results.

Remerciements

Je tiens à exprimer ma gratitude à l'ensemble des membres du jury, Gérard Bois, Jacques Borée, Jean-Noël Gence, Bertrand Lecordier, Patrick Le Quéré, François Lusseyran, Michel Riethmuller et Pierre Sagaut.

Ma reconnaissance s'adresse également à l'ensemble des collègues avec lesquels j'ai eu l'opportunité de participer à de nombreux échanges scientifiques au cours de ces années, dans différents laboratoires.

Enfin, ce travail n'aurait pas pu se faire sans la contribution de tous les étudiants que j'ai encadrés, qu'ils en soient ici remerciés.

Table des matières

A. RAPPORT D'ACTIVITE	1
I CURRICULUM VITAE	3
<i>I-1 Formation.....</i>	3
<i>I-2 Expérience professionnelle.....</i>	3
II LISTE DES TRAVAUX.....	5
<i>II-1 Publications.....</i>	5
II-1-1 Mémoires.....	5
II-1-2 Livre	5
II-1-3 Articles dans des revues à comité de lecture.....	5
<i>II-2 Communications.....</i>	6
II-2-1 Congrès avec comité de lecture et actes publiés	6
II-2-2 Communication comme invité à une conférence	8
II-2-3 Congrès divers et séminaires	8
II-2-4 Supports de cours	9
<i>II-3 Rapports de contrats</i>	9
III ENSEIGNEMENT ET RESPONSABILITES SCIENTIFIQUES	11
<i>III-1 Enseignement</i>	11
<i>III-2 Direction de recherches</i>	12
III-2-1 Stages de 2 ^{ème} cycle.....	12
III-2-2 Thèse de doctorat et stages de DEA (3 ^{ème} cycle).....	13
III-2-3 Programme de formation permanente	13
<i>III-3 Responsabilités administratives et scientifiques</i>	13
<i>III-4 Collaborations extérieures.....</i>	14
IV RESUME DES TRAVAUX DE RECHERCHE	17
V PROJET DE RECHERCHES A QUATRE ANS.....	19
B. SYNTHESE SCIENTIFIQUE	21
NOMENCLATURE.....	23
INTRODUCTION	25
I APERÇU SUR LES METHODES DE MESURE INSTATIONNAIRES EN MECANIQUE DES FLUIDES	27
<i>I-1 Mesure de la vitesse.....</i>	27
<i>I-2 Domaines d'application.....</i>	28
<i>I-3 Références.....</i>	29
II ÉTUDE DU SILLAGE TURBULENT D'UN CORPS A SYMETRIE DE REVOLUTION AUTOPROPULSE PAR HELICE.....	31
<i>II-1 Introduction.....</i>	31
<i>II-2 Dispositif expérimental.....</i>	31
II-2-1 Banc expérimental	31
II-2-2 Instrumentation.....	33
<i>II-3 Principaux résultats</i>	35
II-3-1 Affinité du sillage lointain	35
II-3-2 Bilans d'énergie cinétique turbulente et de tensions de Reynolds	36
II-3-3 Analyse spectrale	37
II-3-4 Moyennes de phase.....	38
<i>II-4 Conclusion.....</i>	38
<i>II-5 Références</i>	39
III DEVELOPPEMENT DE L'ANEMOMETRIE FIL CHAUD A TENSION CONSTANTE ET APPLICATION A UNE COUCHE LIMITE SUPERSONIQUE	41
<i>III-1 Introduction.....</i>	41
<i>III-2 Dispositif expérimental</i>	41
III-2-1 Soufflerie expérimentale	41
III-2-2 Instrumentation	41
<i>III-3 Principaux résultats</i>	42
III-3-1 Constante de temps	42
III-3-2 Comparaison des spectres mesurés par CCA, CTA et CVA	44
III-3-3 Caractérisation de la couche limite turbulente.....	45
<i>III-4 Conclusion</i>	46
<i>III-5 Références</i>	46
IV ANALYSE DE L'ÉCOULEMENT DANS UN MODELE DE TURBOPOMPTE CENTRIFUGE.....	49
<i>IV-1 Introduction.....</i>	49

<i>IV-2 Dispositif expérimental</i>	49
IV-2-1 Banc d'essais.....	49
IV-2-2 Instrumentation	49
<i>IV-3 Principaux résultats</i>	50
IV-3-1 Recirculation amont	50
IV-3-2 Moyennes de phase	51
<i>IV-4 Conclusion</i>	52
<i>IV-5 Références</i>	52
V ANALYSE DE L'ÉCOULEMENT DANS UN ETAGE DE COMPRESSEUR AXIAL	53
<i>V-1 Introduction</i>	53
<i>V-2 Dispositif expérimental</i>	53
V-2-1 Banc d'essais.....	53
V-2-2 Instrumentation	53
<i>V-3 Principaux résultats.....</i>	54
V-3-1 Champ de vitesse dans le rotor.....	54
V-3-2 Vitesse instationnaire dans un canal inter-aubes stator.....	55
V-3-3 Interaction rotor-stator.....	56
V-3-4 LDV trois composantes en coïncidence	57
V-3-5 Évaluation du tenseur de Reynolds par LDV trois composantes non coïncidente	57
<i>V-4 Conclusion.....</i>	59
<i>V-5 Références</i>	60
VI ÉCOULEMENT DANS UN MODELE D'ECHANGEUR THERMIQUE	61
<i>VI-1 Introduction.....</i>	61
<i>VI-2 Dispositif expérimental</i>	61
VI-2-1 Banc d'essais.....	61
VI-2-2 Instrumentation	62
VI-2-3 Algorithme PIV.....	62
<i>VI-3 Principaux résultats</i>	63
VI-3-1 Champ moyen de vitesse.....	63
VI-3-2 Comparaison mesure / simulation numérique	64
VI-3-3 Moments d'ordre 2 des fluctuations de vitesse	65
<i>VI-4 Conclusion</i>	66
<i>VI-5 Références</i>	67
VII ÉCOULEMENT CISAILLE AU-DESSUS D'UNE CAVITE PARALLELEPIPEDIQUE OUVERTE	69
<i>VII-1 Introduction</i>	69
<i>VII-2 Dispositif expérimental</i>	69
VII-2-1 Banc d'essais	69
VII-2-2 Instrumentation	70
VII-2-3 Algorithme PIV	71
<i>VII-3 Principaux résultats</i>	72
VII-3-1 Morphologie de l'écoulement	72
VII-3-2 Instabilité de la couche de cisaillement.....	73
VII-3-3 Instabilités centrifuges	75
VII-3-4 Champ moyen en phase par rapport à l'instabilité de Kelvin-Helmholtz	80
VII-3-5 PIV stéréoscopique	81
<i>VII-4 Conclusion</i>	82
<i>VII-5 Références</i>	83
CONCLUSION	85
PERSPECTIVES.....	87
C. PUBLICATIONS	91

A. Rapport d'activité

I Curriculum vitae

I-1 Formation

- 1995** **Doctorat spécialité Acoustique**, mention très honorable
École Centrale de Lyon
- 1991** **Diplôme d'Études Approfondies d'Acoustique**, mention très bien
École Centrale de Lyon et Université Claude Bernard Lyon I
Diplôme Universitaire de Post-Maîtrise de Mécanique
Université Claude Bernard Lyon I
- 1990** **Maîtrise de Mécanique**, mention assez bien
Université Claude Bernard Lyon I
- 1989** **Licence de Mécanique**, mention assez bien
Université Claude Bernard Lyon I
- 1988** **DEUG A - Mathématiques, Mécanique et Physique**
Université Claude Bernard Lyon I
- 1986** **Baccalauréat C**, mention assez bien
Académie de Grenoble

I-2 Expérience professionnelle

- depuis septembre 1997** **Maître de Conférences à l'Université Pierre et Marie Curie Paris VI**
Laboratoire d'Informatique pour la Mécanique et les Sciences de l'Ingénieur
- depuis septembre 2002* *Laboratoire d'Énergétique et de Mécanique des Fluides Interne*
- septembre 1997-août 2002* *Laboratoire d'Énergétique et de Mécanique des Fluides Interne*
- septembre 1996 / août 1997** **Ingénieur**
Société METRAFLU
- septembre 1994 / août 1996** **Attaché Temporaire d'Enseignement et de Recherche à l'École Centrale de Lyon et à l'Université Lyon I (IUT B)**
Laboratoire de Mécanique des Fluides et d'Acoustique
- septembre 1991 / août 1994** **Allocataire de Recherche DRET / DGA**
Laboratoire de Mécanique des Fluides et d'Acoustique
- avril / août 1991** **Stage de DEA réalisé à l'École Centrale de Lyon**
Laboratoire de Mécanique des Fluides et d'Acoustique

II Liste des travaux

II-1 Publications

II-1-1 Mémoires

- FAURE, Th. M.** (1995) *Étude expérimentale du sillage turbulent d'un corps à symétrie de révolution autopropulsé par hélice*, Thèse de doctorat, École Centrale de Lyon, n°95-01
FAURE, Th. M. (1991) *Automatisation d'une technique de mesure par anémométrie à films chauds croisés*, Rapport de DEA, École Centrale de Lyon

II-1-2 Livre

- FAURE, Th.** (2008) *Dynamique des fluides appliquée, Applications à l'aérodynamique*, Dunod, Paris, 304 pages

II-1-3 Articles dans des revues à comité de lecture

- FAURE, Th. M., PASTUR, L. R., LUSSEYRAN, F., FRAIGNEAU, Y., BISCH, D** (2009) Three-dimensional centrifugal instabilities development inside a parallelepipedic open cavity of various shape, *Experiments in Fluids*, Vol. 47, No. 3, pp. 395–410
- PASTUR, L. R., LUSSEYRAN, F., FAURE, Th. M., FRAIGNEAU, Y., PETHIEU, R., DEBESSE, Ph.** (2008) Quantifying the non-linear mode competition in the flow over an open cavity at medium Reynolds number, *Experiments in Fluids*, Vol. 44, No. 4, pp. 597–608
- FAURE, Th. M., ADRIANOS, P., LUSSEYRAN, F., PASTUR, L. R.** (2007) Visualizations of the flow inside an open cavity at medium range Reynolds numbers, *Experiments in Fluids*, Vol. 42, No. 2, pp. 169–184
- FAURE, Th. M., LUSSEYRAN, F., GOUGAT, P., LAUNAY, F.** (2006) Experimental investigation of the flow distribution inside a tubular heat exchanger, *Journal of Fluids Engineering*, Vol. 128, No. 6, pp. 1218–1227
- FAURE, Th. M., MITON, H., VASSILIEFF, N.** (2004) A laser Doppler anemometry technique for Reynolds stresses measurement, *Experiments in Fluids*, Vol. 37, No. 3, pp. 465–467
- BARIO, F., FAURE, Th. M., JONDEAU, E., NORMAND, J. L., N'GUYEN DUC J. M.** (2003) Analysis of inducer recirculating flow, *Journal of Propulsion and Power*, Vol. 19, No. 4, pp. 521–528
- FAURE, Th. M., MICHON, G. J., MITON, H., VASSILIEFF, N.** (2001) Laser Doppler anemometry measurements in an axial compressor stage, *Journal of Propulsion and Power*, Vol. 17, No. 3, pp. 481–491
- SHARMA, V. C., FAURE, Th. M.** (2000) Indian launchers aim at commercial market, *Aerospace America*, January 2000, pp. 14–19
- SARMA, G. R., COMTE-BELLOT, G., FAURE, Th. M.** (1998) Software corrected hot wire thermal lag for the constant voltage anemometer featuring a constant bandwidth at the selected compensation setting, *Review of Scientific Instruments*, Vol. 69, No. 9, pp. 3223–3231
- FAURE, Th. M.** (1997) The Reynolds stress transport equations in a momentumless wake: experiments and models, *AIAA Journal*, Vol. 35, No. 2, pp. 281–287
- FAURE, Th. M., ROBERT, G.** (1997) Spectral analysis of the turbulent structure in the momentumless wake of a propeller-driven body, *European Journal of Mechanics / B Fluids*, Vol. 16, No. 2, pp. 211–226
- FAURE, Th. M., ROBERT, G.** (1996) Turbulent kinetic energy balance in the wake of a self-propelled body, *Experiments in Fluids*, Vol. 21, No. 4, pp. 268–274

FAURE, Th. M., ROBERT, G. (1995) Bilan des tensions de Reynolds dans un sillage de traînée et dans un sillage de corps autopropulsé par une hélice, *Comptes-Rendus de l'Académie des Sciences, Paris*, série II b, tome 321, n°11, pp. 455–461

II-2 Communications

II-2-1 Congrès avec comité de lecture et actes publiés

FAURE, Th. M., LEFÈVRE, G., PASTUR, L. R., LUSSEYRAN, F. (2009) Identification de structures tourbillonnaires par PIV dans un écoulement de cavité, *13^{ème} Colloque de Visualisation et de Traitement d'Images en Mécanique des Fluides*, Reims (France), 16-20 Novembre 2009

LUSSEYRAN, F., PASTUR, L. R., DEBESSE, Ph., BALTEAN, D., FAURE, Th. M. (2009) Self referenced phase averaging and flow complexity, *14th International Conference on Fluid Flow Technologies*, Budapest (Hungary), September 9-12, 2009

PASTUR, L. R., LUSSEYRAN, F., FAURE, Th. M., LETELLIER, Ch. (2009) Investigating a mode-switching regime in an oscillating flow by means of symbolic dynamics, *14th International Conference on Fluid Flow Technologies*, Budapest (Hungary), September 9-12, 2009

BASLEY, J., PASTUR, L. R., LUSSEYRAN, F., FAURE, Th. M., DELPRAT, N. (2009) Investigation of the spatial organization of spectral dynamics in an uncompressible cavity flow using time-resolved high-speed PIV, *8th International Symposium on Particle Image Velocimetry*, Melbourne (Australia), August 25-28 2009

FAURE, Th. M., LEFÈVRE, G., PASTUR, L. R., LUSSEYRAN, F. (2009) Critères d'apparition d'instabilités centrifuges dans une cavité ouverte, *19^{ème} Congrès Français de Mécanique*, Marseille (France), 24-28 Août 2009, article n°131-S09

PASTUR, L. R., LUSSEYRAN, F., FAURE, Th. M., LETELLIER, Ch. (2009) Intermittent regime in flow oscillations investigated by means of symbolic dynamics, *3rd International Conference on Complex Systems and Applications*, Le Havre (France), 29 June-2 July 2009

FAURE, Th. M., DEFRAZNE, A., LUSSEYRAN, F., PASTUR, L. R., FRAIGNEAU, Y. (2008) Structure 3D d'un écoulement de cavité ouverte de forme variable, *11^{ème} Congrès Francophone de Techniques Laser*, Futuroscope (France), 15-19 Septembre 2008, pp. 433–440

LUSSEYRAN, F., PASTUR, L. R., FAURE, Th. M., LETELLIER Ch. (2008) Poincaré section analysis of an experimental frequency intermittency in an open cavity flow, *22nd International Congress of Theoretical and Applied Mechanics*, Adelaide (Australia), August 25-29, 2008, paper ID 11329

FAURE, Th. M., DEFRAZNE, A., LUSSEYRAN, F., PASTUR, L. R. (2008) Flow instabilities development inside an open cavity, *13th International Symposium on Flow Visualization*, Nice (France), July 1-4 2008, paper ID 81

PASTUR, L. R., LUSSEYRAN, F., FAURE, Th. M., PODVIN, B., FRAIGNEAU, Y. (2008) POD-based technique for 3D flow reconstruction using 2D data set, *13th International Symposium on Flow Visualization*, Nice (France), July 1-4 2008, paper ID 223

PASTUR, L. R., LUSSEYRAN, F., FAURE, Th. M., LETELLIER, Ch. (2008) Analyse déterministe de la compétition non-linéaire de modes dans un écoulement en cavité, *11^{ème} Rencontre du Non-Linéaire*, Paris (France), 25-27 Mars 2008, pp. 137–142

FAURE, Th. M., PECHLIVANIAN, N., LUSSEYRAN, F., PASTUR, L. R. (2007) Apparition de structures tourbillonnaires de type Görtler dans une cavité parallélépipédique ouverte de forme variable, *Actes du 18^{ème} Congrès Français de Mécanique*, Grenoble (France), 27-31 Août 2007, CFM2007-0008

- LUSSEYRAN, F., PASTUR, L. R., FAURE, Th. M., PETHIEU, R.** (2007) Structures tourbillonnaires cohérentes et intermittence des modes fréquentiels dans un écoulement en cavité ouverte, *Actes du 18^{ème} Congrès Français de Mécanique*, Grenoble (France), 27-31 Août 2007, CFM2007-1197
- PETHIEU, R., PASTUR, L. R., LUSSEYRAN, F., DEBESSE, Ph., FAURE, Th. M.** (2007) Caractérisation expérimentale de la compétition non-linéaire de modes de Kelvin-Helmholtz dans un écoulement en cavité, *10^{ème} Rencontre du Non-Linéaire*, Paris (France), 14-16 Mars 2007, pp. 143–148
- FAURE, Th. M., LUSSEYRAN, F., PASTUR, L. R., PETHIEU, R., DEBESSE, Ph.** (2006) Développement d'instabilités dans un écoulement subsonique se développant au-dessus d'une cavité : mesures synchronisées PIV-LDV, *10^{ème} Congrès Francophone de Techniques Laser*, Toulouse (France), 19-22 Septembre 2006, pp. 577–584
- LUSSEYRAN, F., PASTUR, L. R., DEBESSE, Ph., FAURE, Th. M.** (2005) Dynamique locale de l'écoulement dans une cavité ouverte, *5^{ème} Colloque de Chaos Temporel et de Chaos Spatio-temporel*, Le Havre (France), 12-13 Décembre 2005, pp. 63–68
- LAUNAY, F., FAURE, Th. M., LUSSEYRAN, F., GOUGAT, P.** (2005) Investigations expérimentales et numériques d'un écoulement tridimensionnel dans une structure d'échangeur thermique pour le RQF d'IPHI, *Journées Accélérateurs de la SFP*, Roscoff (France), 10-12 Octobre 2005
- QUÉNOT, G. M., FAURE, Th. M., LUSSEYRAN, F.** (2005) Synchronous orthogonal dynamic programming for 3C vector field evaluation, *Worldwide PIV Challenge 2005*, Pasadena (USA), September 19-20, 2005
- PASTUR, L. R., LUSSEYRAN, F., FAURE, Th. M., FRAIGNEAU, Y., GOUGAT, P.** (2005) Dynamical reduction of a subsonic flow over a cavity with an aim of control, *6th SIAM Conference on Control and its Applications*, New Orleans (USA), July 11-14, 2005
- FAURE, Th. M., DEBESSE, Ph., LUSSEYRAN, F., GOUGAT, P.** (2005) Structures tourbillonnaires engendrées par l'interaction entre une couche limite laminaire et une cavité, *11^{ème} Colloque de Visualisation et de Traitement d'Images en Mécanique des Fluides*, Lyon (France), 6-9 Juin 2005
- FAURE, Th. M., LUSSEYRAN, F., GOUGAT, P., LAUNAY, F.** (2004) Exploration de l'écoulement dans un échangeur de chaleur tubulaire par vélocimétrie par images de particules, *9^{ème} Congrès Francophone de Vélocimétrie Laser*, Bruxelles (Belgique), 14-17 Septembre 2004, pp. K.4.1-K.4.8
- LUSSEYRAN, F., FAURE, Th. M., ESCHENBRENNER, C., FRAIGNEAU, Y.** (2004) Shear layer instability and frequency modes inside an open cavity, *21st International Congress of Theoretical and Applied Mechanics*, Warsaw (Poland), August 15-21, 2004, FM13S_10188
- FAURE, Th. M., MITON, H., VASSILIEFF, N.** (2002) Applications de la vélocimétrie laser Doppler tridimensionnelle aux machines tournantes, *8^{ème} Congrès Francophone de Vélocimétrie Laser*, Orsay (France), 17-20 septembre 2002, pp. 369–372
- COMTE-BELLOT, G., SARMA, G. R., FAURE, Th. M., DUSSAUGE, J. P., DUPONT, P., DEBIÈVE, J. F.** (1999) Performance studies of the constant voltage anemometer in a Mach 2.3 boundary layer, *18th International Congress on Instrumentation in Aerospace Simulation Facilities*, Toulouse (France), June 14-17 1999, pp. 40.1–40.9
- BÉRA, J. C., CASSAM-SULLIMAN, Y. S., FAURE, Th. M., NICOT, C., SUNYACH, M.** (1997) Contrôle par un jet synthétique pariétal de l'échappement tourbillonnaire derrière un cylindre, *Actes du 13^{ème} Congrès Français de Mécanique*, Mini-Colloque Mécanique des Fluides Active, Poitiers (France), 4 septembre 1997, pp. 56–59

FAURE, Th. M. (1996) The Reynolds stress transport equations in a momentumless wake: experiments and models, *27th AIAA Fluid Dynamics Conference*, New Orleans (USA), June 17-20 1996, AIAA paper 96-2037

FAURE, Th. M. (1996) The boundary layer approximation: an application to energy transport in wakes, in *Advances in Turbulence VI*, Eds. S. Gavrilakis, L. Machiels & P. A. Monkewitz, Lausanne (Switzerland), July 2-5 1996, pp. 517–518

FAURE, Th. M. (1995) Analyse des structures cohérentes dans un sillage de corps autopropulsé par hélice, *Actes du 12^{ème} Congrès Français de Mécanique*, Strasbourg (France), 4-8 septembre 1995, vol. 3, pp. 357–360

FAURE, Th. M., ROBERT, G. (1993) Étude expérimentale des lois de similitude dans un sillage autopropulsé par hélice, *Actes du 11^{ème} Congrès Français de Mécanique*, Lille-Villeneuve d'Ascq (France), 6-10 septembre 1993, vol. 2, pp. 273–276

II-2-2 Communication comme invité à une conférence

FAURE, Th. M., LUSSEYRAN, F., PASTUR, L. R., FRAIGNEAU, Y. (2008) Détection de structures tourbillonnaires dans un écoulement de cavité, *24^{ème} Journée Thématique de l'AFVL*, Meudon (France), 20 Novembre 2008

II-2-3 Congrès divers et séminaires

FAURE, Th. M. (2008) Développement et identification de structures tourbillonnaires dans un écoulement de cavité, *Séminaire groupe Aérodynamique Instationnaire*, LIMSI, Orsay (France), 12 Décembre 2008

TRAN, T., SICOT, Ch., BORÉE, J., ALT, J., PASTUR, L., LUSSEYRAN, F., FAURE, Th. M. (2008) Développement de méthodes lagrangiennes pour l'analyse d'écoulements instationnaires, *Séminaire GdR Bruit des Transports*, Paris (France), 6 Novembre 2008

LUSSEYRAN, F., PASTUR, L. R., FAURE, Th. M., DEBESSE, Ph., BALTEAN, D., FRANÇOIS, M. X. (2006) Mesure synchronisée PIV – grandeur scalaire locale : la moyenne de phase et ses possibles évolutions, *20^{ème} Journée Thématique de l'Association Francophone de Vélocimétrie Laser*, Meudon (France), 14 Décembre 2006

FAURE, Th. M., ADRIANOS, P., DEBESSE, Ph., LUSSEYRAN, F., PASTUR, L. R. (2005) Dynamique tourbillonnaire 3D dans une cavité ouverte de rapport de forme variable, *6^{ème} Journée de Dynamique des Fluides sur le Plateau*, Université Paris XI, Orsay (France), 14 Novembre 2005

FAURE, Th. M., ADRIANOS, P., DEBESSE, Ph., LUSSEYRAN, F., PASTUR, L. R. (2005) Structures tourbillonnaires engendrées par l'interaction d'une couche limite laminaire avec une cavité ouverte, *Séminaire*, Laboratoire d'Informatique pour la Mécanique et les Sciences de l'Ingénieur, UPR 3251, Orsay (France), 20 Octobre 2005

LAUNAY, F., FAURE, Th. M., LUSSEYRAN, F., GOUGAT, P. (2004) Écoulement tridimensionnel dans une structure d'échangeur – Collaboration IPN-LIMSI, *Séminaire Division Accélérateurs*, Institut de Physique Nucléaire d'Orsay, UMR CNRS 8608, Orsay (France), 16 Novembre 2004

FAURE, Th. M., LUSSEYRAN, F., GOUGAT, P., ESCHENBRENNER, C. (2004) PIV par flot optique : applications à l'étude d'une couche de mélange et à l'écoulement dans un échangeur thermique, *Séminaire*, Laboratoire de Mécanique des Fluides et d'Acoustique, UMR CNRS 5509, Lyon (France), 27 Février 2004

FAURE, Th. M., LUSSEYRAN, F., QUÉNOT, G. (2003) Vélocimétrie par images de particules : flot optique par programmation dynamique, *Journées du Département Mécanique-Energétique*, Laboratoire d'Informatique pour la Mécanique et les Sciences de l'Ingénieur, UPR CNRS 3251, Orsay (France), 20-21 Novembre 2003

- LUSSEYRAN, F., GOUGAT, P., FAURE, Th. M., FRAIGNEAU, Y., PODVIN, B.** (2003) Structures spatiales et modes de Fourier dans une cavité en interaction avec une couche limite, *5^{ème} Journée de Dynamique des Fluides sur le Plateau*, Université Paris XI, Orsay (France), 24 Avril 2003
- FAURE, Th. M.** (2001) Vélocimétrie laser Doppler 3-D : application aux écoulements internes, *Séminaire*, Laboratoire Fluides Automatique et Systèmes Thermiques, UMR CNRS 7608, Orsay (France), 10 Octobre 2001
- FAURE, Th. M.** (1997) Anémométrie à films chauds triples : application à un sillage de corps autopropulsé, *Séminaire*, Laboratoire d'Énergétique et de Mécanique des Fluides Interne, URA CNRS 1504, Orsay (France), 10 Juin 1997
- FAURE, Th. M.** (1996) Étude expérimentale d'un sillage de corps autopropulsé, *Séminaire*, Laboratoire d'Études Aérodynamiques, URA CNRS 191, Poitiers (France), 22 Avril 1996
- FAURE, Th. M.** (1992) Mesures du champ cinématique à l'aval d'un corps autopropulsé par hélice, *1^{er} Colloque des Jeunes Chercheurs de l'Intergroupe des Écoles Centrales*, Nantes (France), 25-26 Novembre 1992

II-2-4 Supports de cours

- FAURE, Th. M.** (2004) *Aérodynamique appliquée*, cours de Master Sciences de l'Ingénieur 1^e année, parcours Mécanique et Ingénierie des Systèmes, Université Pierre et Marie Curie et ENS Cachan (204 pages)
- FAURE, Th. M.** (1999) *Méthodes expérimentales et méthodes de visualisation en mécanique des fluides*, cours de DEA de Conversion de l'Énergie et de DESS de Propulsion Aéronautique et Terrestre, Université Pierre et Marie Curie (80 pages)

II-3 Rapports de contrats

Coll. (2008) *Développement d'outils quantitatifs pour l'analyse couplée pression-vitesse en aérodynamique instationnaire. Phénomènes acoustiques associés*, D.I.B., Rapport à 6 mois, Projet A.N.R.-07-BLAN-0177-03, Juin 2008

HONORÉ, D., LECORDIER, B., TRINITÉ, M., LUSSEYRAN, F., FAURE, Th. M., SUSSET, A., QUÉNOT, G. (2005) *PLIV : Particle Large Image Velocimetry – Développement de méthodes de traitement avancées adaptées à la réalisation de mesures PIV grand champ*, Rapport final, contrat CNRT / 2004 / 061, Juillet 2005

LAUNAY, F., FAURE, Th. M., LUSSEYRAN, F., GOUGAT, P. (2004) *Écoulement 3D dans une structure d'échangeur – Confrontation mesures simulations*, Rapport de synthèse, contrat IPNO-04-02, Collaboration Laboratoire d'Informatique pour la Mécanique et les Sciences de l'Ingénieur - Institut de Physique Nucléaire d'Orsay

FAURE, Th. M., LUSSEYRAN, F. (2004) *PLIV : Particle Large Image Velocimetry – Développement de méthodes de traitement avancées adaptées à la réalisation de mesures PIV grand champ*, Rapport intermédiaire, contrat CNRT / 2004 / 061, Laboratoire d'Informatique pour la Mécanique et les Sciences de l'Ingénieur, Juin 2004

FAURE, Th. M. (2004) *Caractérisation par PIV de l'écoulement dans un échangeur thermique – mesures PIV dans chacun des tubes de l'échangeur*, Rapport d'essais, contrat IPNO-04-02, Collaboration Laboratoire d'Informatique pour la Mécanique et les Sciences de l'Ingénieur - Institut de Physique Nucléaire d'Orsay, Avril 2004

FAURE, Th. M. (2004) *Caractérisation par PIV de l'écoulement dans un échangeur thermique – mesures de pression et mesures PIV sur un tube isolé*, Rapport d'essais, contrat IPNO-04-02, Collaboration Laboratoire d'Informatique pour la Mécanique et les Sciences de l'Ingénieur - Institut de Physique Nucléaire d'Orsay, Janvier 2004

FAURE, Th. M., SATO, M., LECOCQ, Y. (2003) *Mesures PIV par flot optique dans deux types d'écoulements turbulents*, Rapport interne LIMSI-CNRS 2003-17

- FAURE, Th. M., MICHON, G. J., MITON, H., VASSILIEFF, N.** (2000) *Convention spécifique au projet CME-2 : banque expérimentale de données pour la validation de codes de calcul*, Rapport d'avancement, contrat Consortium Industrie Recherche en Turbomachines
- FAURE, Th. M., GEROLYMONS, G. A., HANISCH, C., MICHON, G. J., MITON, H., VALLET, I., VASSILIEFF, N.** (1998) *Création et validation de codes d'écoulements instationnaires en turbomachines*, Rapport de synthèse Université Pierre et Marie Curie, contrat SNECMA-TM-EDF 764 488 Rc
- FAURE, Th. M., BARIO, F.** (1997) *Analyse de l'écoulement dans un modèle à l'air de turbopompe centrifuge : Influence du calage inducteur-roue centrifuge*, Rapport de synthèse METRAFLU, contrat SEP 865.586
- FAURE, Th. M., BARIO, F.** (1997) *Analyse de l'écoulement dans un modèle à l'air de turbopompe centrifuge : Bilan et étude comparative de calages*, Rapport d'essais METRAFLU, contrat SEP 865.586
- FAURE, Th. M., BARIO, F., BOIS, G.** (1997) *Analyse de l'écoulement dans un modèle à l'air de turbopompe centrifuge : Caractérisation stationnaire de l'écoulement*, Rapport de synthèse METRAFLU, contrat SEP 865.586
- FAURE, Th. M., BARIO, F., BOIS, G.** (1997) *Analyse de l'écoulement dans un modèle à l'air de turbopompe centrifuge : Caractérisation globale du BCA à différentes vitesses de rotation et sondages à calages imposés*, Rapport d'essais METRAFLU, contrat SEP 865.586
- FAURE, Th. M., ROBERT, G., BENARROUS, E.** (1995) *Mesure de sillage turbulent en soufflerie aérodynamique / Rapport final de synthèse*, Rapport METRAFLU, contrat DRET 92 524
- ROBERT, G., FAURE, Th. M.** (1994) *Analyse spectrale et structures cohérentes dans un sillage autopropulsé par hélice*, Rapport d'étude METRAFLU, contrat DRET 92 524
- ROBERT, G., FAURE, Th. M.** (1994) *Évaluations radiales et axiales des caractéristiques cinématiques moyennes et turbulentes d'un sillage autopropulsé par hélice*, Rapport d'étude METRAFLU, contrat DRET 92 524
- ROBERT, G., FAURE, Th. M., BENARROUS, E.** (1992) *Mesure de sillage turbulent / Rapport final de synthèse*, Rapport METRAFLU, contrat DRET 89 537
- FAURE, Th. M., BENARROUS, E., ROBERT, G., ROLAND, P.** (1992) *Étude de sillage turbulent de corps autopropulsé / Caractérisation de l'écoulement turbulent et du champ acoustique*, Rapport d'étude METRAFLU, contrat DRET 89 537

III Enseignement et responsabilités scientifiques

III-1 Enseignement

depuis 1997 Maître de Conférences à l'Université Pierre et Marie Curie, Paris VI
Chargé de Cours à l'École Normale Supérieure de Cachan

1^{er} cycle

- **2009–présent : Cours et Travaux Dirigés** d'Initiation aux Techniques Expérimentales, Licence d'Ingénierie Mécanique, 2^e année (Université Paris VI)

2^{ème} cycle

- **1997–2009 : Cours et Travaux Dirigés** d'Aérodynamique Appliquée du **Master Sciences de l'Ingénieur**, parcours Mécanique et Ingénierie des Systèmes, 1^e année (ENS Cachan)
- **2008–2009 : Cours et Travaux Dirigés** d'Aérodynamique Externe du **Master Sciences de l'Ingénieur**, parcours Mécanique des Fluides et Énergétique (Université Paris VI)
- **2009– présent : Cours et Travaux Dirigés** d'Aérodynamique et Aéronautique du **Master Sciences de l'Ingénieur**, parcours Mécanique des Fluides Fondamentale et Appliquée, 1^e année (Université Paris VI)
- **1997–2002 : Travaux Dirigés** de Bases de la Mécanique de **Licence de Mécanique**, parcours Mécanique et Technologies (Université Paris VI / ENS Cachan)
- **2009–présent : Travaux Pratiques** d'Aérodynamique et Aéronautique du **Master Sciences de l'Ingénieur**, parcours Mécanique des Fluides Fondamentale et Appliquée, 1^e année (Université Paris VI) : *écoulement autour d'une aile, tuyère de Laval*
- **1997–2009 : Travaux Pratiques** d'Aérodynamique Appliquée du **Master Sciences de l'Ingénieur**, parcours Mécanique et Ingénierie des Systèmes (ENS Cachan) : *étude de l'écoulement autour d'une maquette d'automobile, calcul de l'écoulement autour d'un profil par la méthode des panneaux, écoulement autour d'une aile*
- **1997–présent : Travaux Pratiques** de Modélisation des Structures et des Écoulements de **Licence de Mécanique**, parcours Mécanique et Technologies (Université Paris VI / ENS Cachan) : *écoulement laminaire, écoulement turbulent, mesures de débits, rhéologie, réaction d'un jet*
- **1997–2003 : Travaux Pratiques** d'Écoulements Compressibles de **Licence de Mécanique**, parcours Mécanique et Technologies (Université Paris VI / ENS Cachan) : *tuyère de Laval, écoulement autour d'un cylindre*
- **2001–présent : Travaux Pratiques** de Mécanique des Milieux Continus de **Licence de Mécanique**, parcours Mécanique et Modélisation (Université Paris VI) : *écoulement laminaire, écoulement autour d'un cylindre, rhéologie, réaction d'un jet*
- **Tutorat de stages** du **Master Sciences de l'Ingénieur** (ENS Cachan) : encadrement pédagogique d'étudiants de la formation en stage en entreprise

3^{ème} cycle

- **1997–2001 : Cours de Méthodes Expérimentales et Méthodes de Visualisation en Mécanique des Fluides du DEA de Conversion de l'Énergie et du DESS de Propulsion Aéronautique et Terrestre** (Université Paris VI)

1995-1996 Attaché Temporaire d'Enseignement et de Recherche à l'École Centrale de Lyon

2^{ème} cycle

- **1995–1996 : Travaux Pratiques** d'Ordre et Chaos de **3^e année** cycle ingénieur (ECL) : *étude du pendule de Moon*

- **1995–1996** : **Encadrement de projets de 1^e année** cycle ingénieur (ECL) : *étude d'un jet plan turbulent, caractérisation expérimentale des transferts énergétiques turbulents dans un jet plan*

3^{ème} cycle

- **1995–1996** : **Travaux Pratiques** de Turbulence du **DEA** de Mécanique (ECL) : *étalonnage d'une sonde à fil chaud, mesure de corrélations spatiales dans un jet libre*

- **1995–1996** : **Travaux Pratiques** et **Bureaux d'Études** d'Acoustique du **DEA** d'Acoustique (ECL) : *propagation acoustique dans les conduits en présence de singularité, puissance d'une source, mesure de temps de réverbération, propagation acoustique en présence d'un gradient de célérité*

- **1995–1996** : **Travaux Pratiques** d'Acoustique du **DESS** Techniques et Applications de la Physique (Université Joseph Fourier Grenoble I) : *intensimétrie acoustique, mesure de coefficients d'absorption*

1994-1995 Attaché Temporaire d'Enseignement et de Recherche à l'Université Claude Bernard Lyon I, IUT B

1^{er} cycle

- **1994–1995** : **Travaux Dirigés** de Mécanique de **1^e année** du département de Maintenance Industrielle : *cinématique, dynamique et cinétique des systèmes de solides*

- **1994–1995** : **Travaux Pratiques** de Mécanique de **2^e année** du département de Génie Mécanique et Productique : *pertes de charge dans une conduite, utilisation d'un tube de Venturi, équilibrage d'un système en rotation, pendule de torsion, étude du gyroscope, oscillations forcées d'une poutre rigide*

1992-1994 Vacations d'enseignement à l'École Centrale de Lyon

3^{ème} cycle

- **1992–1994** : **Travaux Pratiques** de Turbulence du **DEA** de Mécanique (ECL, Université Claude Bernard, Lyon I) : *étalonnage d'une sonde à fil chaud, mesure de corrélations spatiales dans un jet libre*

III-2 Direction de recherches

III-2-1 Stages de 2^{ème} cycle

THACH, H. (2009) *Analyse de stabilité d'un écoulement confiné à partir de mesures PIV résolues en temps*, Rapport de Master de Mécanique Physique 1^e année, Université Paris-Sud XI

MOCHKI, S. (2009) *PIV stéréoscopique et application à un écoulement confiné*, Rapport de Master de Sciences de l'Ingénieur, parcours Mécanique des Fluides et Énergétique, 1^e année, Université Pierre et Marie Curie Paris VI

LEFÈVRE, G. (2009) *Traitement et analyse des caractéristiques d'un écoulement de cavité à partir de mesures PIV*, Rapport de Licence de Physique Mécanique 3^e année, Université Paris-Sud XI

HABABOU, S. (2008) *Analyse de mesures PIV : détermination d'épaisseur de couche limite*, Rapport de Licence de Physique Mécanique 3^e année, Université Paris-Sud XI

DEFRASNE, A. (2007) *Évolution du champ de vitesse dans une allée de tourbillons de type Görtler prenant naissance dans une cavité ouverte*, Rapport de Master de Mécanique Physique 1^e année, Université Paris-Sud XI

PECHLIVANIAN, N. (2006) *Détermination des seuils d'apparition d'instabilités aérodynamiques en fonction de la géométrie d'une cavité rectangulaire affleurant un*

- écoulement*, Rapport de Master de Mécanique Physique 1^e année, Université Paris-Sud XI
SATO, M. (2003) *Étude de l'écoulement par PIV dans un tube d'échangeur thermique*, Rapport de Maîtrise de Technologie Mécanique, Université Pierre et Marie Curie, Paris VI
LECOCQ, Y. (2003) *Étude par PIV de l'interaction d'un écoulement avec une cavité*, Rapport de Maîtrise de Technologie Mécanique, Université Pierre et Marie Curie, Paris VI
RAZAFY, N. (1999) *Étude et analyse de systèmes éoliens*, Rapport de Maîtrise de Technologie Mécanique, Université Pierre et Marie Curie, Paris VI
KASIERSKI, T. (1996) *Étude expérimentale d'un nouveau type d'anémomètre à fil chaud*, Rapport de Fin d'Études, Institut Polytechnique de Lodz (Pologne)
COUVE, P., GRENOUILLET, R., MARQUET, F., MARTY, L., MASFRAND, V. (1995) *Caractérisation expérimentale des transferts énergétiques turbulents dans un jet plan*, Projet de 1^e année d'Ingénieur, Département Acoustique, École Centrale de Lyon
GAIRE, J., GUYOT, X., MASSON, C., SUTTER, P., VAUTHERIN, N. (1994) *Étude d'un jet plan turbulent*, Projet de 1^e année d'Ingénieur, Département Acoustique, École Centrale de Lyon

III-2-2 Thèse de doctorat et stages de DEA (3^{ème} cycle)

- ADRIANOS, P.** (2005) *Interaction d'un écoulement avec une cavité ouverte : étude spatio-temporelle*, Rapport de Master de Sciences de l'Ingénieur (DEA) 2^e année, spécialité Mécanique des Fluides et Énergétique, Université Pierre et Marie Curie, Paris VI
DEBESSE, Ph. (2004) *Étude de l'intermittence d'une couche de cisaillement générée par un écoulement affleurant une cavité*, Rapport de DEA de Dynamique des Fluides et Transferts, Université Paris-Sud XI
VASSILIEFF, N. (2001) *Analyse de l'écoulement dans un compresseur axial par vélocimétrie laser tridimensionnelle*, Thèse de Doctorat de Mécanique de l'Université Pierre et Marie Curie, Paris VI (en collaboration avec H. MITON)
BARTHET, S. (1997) *Contribution à la compréhension et à la connaissance de l'écoulement au sein d'une turbopompe de type cryogénique*, Rapport de DEA de Thermique et Énergétique, École Centrale de Lyon (en collaboration avec F. BARIO)

III-2-3 Programme de formation permanente

- BLASZCZAK, J.** (1993) *Technique de mesure avec une sonde à films chauds triples*, Rapport de Stage de Formation Permanente, Institut Polytechnique de Lodz (Pologne)

III-3 Responsabilités administratives et scientifiques

- 1993-1996** **Représentant élu** dans le collège Chercheurs et Assimilés au Conseil de Département Acoustique de l'École Centrale de Lyon.
- 2000-2002** **Représentant élu** dans le collège Chercheurs au Conseil de Laboratoire du Laboratoire d'Énergétique et de Mécanique des Fluides Interne de l'Université Paris VI.
- Depuis 2004** **Représentant nommé** à l'Équipe de Formation Universitaire de la Licence de Mécanique de l'Université Paris VI.
- Depuis 1998** **Responsable du module Aérodynamique Appliquée** du Master Sciences de l'Ingénieur, parcours Mécanique et Ingénierie des Systèmes (Université Paris VI et ENS Cachan).
- 2002-2004** **Président du jury et responsable de la Licence de Technologie Mécanique**, formation commune à l'Université Paris VI et l'ENS Cachan.
- Depuis 2002** **Responsable de la plate-forme de Travaux Pratiques Fluides**, gestion d'un parc de vingt installations de TP, de dix postes informatiques et organisation des enseignements pratiques en Mécanique des Fluides effectués par les étudiants de Licence et Master de Mécanique (Université Paris VI) de Licence

et Master de Mécanique-Physique (Université Paris XI), de Licence de Mécanique et Technologies et de Master de Mécanique et Ingénierie des Systèmes (Université Paris VI et ENS Cachan), et de Licence de Physique et Applications (Université Paris XI).

2007 **Membre du jury** du concours de recrutement de personnels Ingénieurs Techniques, Administratifs de Recherche et de Formation de Technicien d'expérimentation et d'exploitation en techniques expérimentales, Branche d'Activité Professionnelle C (10 postes au concours).

Participation à l'organisation de congrès :

1993 13^{ème} Colloque d'Aéro et Hydroacoustique organisé par la Société Française d'Acoustique et l'École Centrale de Lyon, 9-11 juin 1993.

1994 Flows Acoustics: A Technology Audit, École Centrale de Lyon, 11-13 July 1994.

1996 7th International Symposium on Long Range Sound Propagation, École Centrale de Lyon, 24-26 July 1996.

Organisation de congrès :

2009 25^{ème} Journée Thématique de l'AFVL en partenariat avec FLUVISU : « Techniques d'Imagerie à la visualisation 3D d'écoulements », LIMSI, Orsay, 9 avril 2009.

Selecteur d'articles pour des revues scientifiques à comité de lecture :

1997 AIAA Journal

1997 Comptes-Rendus à l'Académie des Sciences, Paris, Série II-b

2004 The European Physical Journal – Applied Physics

2007 Journal of Fluids Engineering, ASME

2008 Experiments in Fluids

2009 Comptes-Rendus de Mécanique, Académie des Sciences, Paris

2009 Comptes-Rendus de Mécanique, Académie des Sciences, Paris

Membre de sociétés savantes :

American Institute of Aeronautics and Astronautics (AIAA)

Association Francophone de Vélocimétrie Laser (AFVL)

Association Française de Mécanique (AFM)

Association Aéronautique et Astronautique de France (AAAF)

III-4 Collaborations extérieures

1991-1994 Dans le cadre de ma thèse portant sur les sillage de corps autopropulsés, deux contrats de recherche de la Direction Générale de l'Armement ont été menés en collaboration avec J. P. Borleteau de la société SIREHNA (Nantes).

1996-1997 L'étude d'une nouvelle version de turbopompe à hydrogène liquide équipant le lanceur Ariane V, dans le cadre de partenariats avec la Société Européenne de Propulsion et le Centre National d'Études Spatiales, avec J. L. Normand et J. M. Nguyen Duc.

1996-1999 La validation expérimentale en écoulement supersonique de l'anémométrie fil chaud à tension constante, a fait l'objet d'une collaboration avec G. R. Sarma et S. M. Mangalam de la société Tao Systems Inc. (Williamsburg, Va, USA).

1997-2001 Le projet Turbo-3D pour le développement de la LDV 2 composantes et l'étude du compresseur CME-2 dans le cadre d'un soutien par la SNECMA, Turboméca, EDF et le CNRS.

1998-2001 Le Consortium Industrie Recherche en Turbomachine pour l'extension de la LDV à 3 composantes et l'étude du compresseur CME-2 dans le cadre de la thèse de N. Vassilieff.

- 2003** Le développement de la PIV par flot optique utilisant une programmation dynamique fait l'objet d'une collaboration avec G. Quénod du laboratoire CLIPS-IMAG (Grenoble).
- 2003-2004** L'étude par PIV du champ de vitesse dans un modèle d'échangeur de chaleur fut l'objet d'une collaboration avec F. Launay de l'Institut de Physique Nucléaire d'Orsay.
- 2004-2005** Le développement de la PIV Grand Champ dans le cadre du CNRT Aérodynamique, Aéroacoustique des Véhicules Terrestres a fait l'objet d'une collaboration avec D. Honoré, B. Lecordier et M. Trinité du CORIA (Rouen) ainsi qu'avec A. Susset de la société R&D Vision (Paris).
- 2007-2010** ANR blanche Dynamique-Instationnarité-Bruit (DIB) associant le LEA (Poitiers), le LIMSI (Orsay) et PSA (Vélizy).
- 2008-2011** ANR blanche Contrôle Optimal et Robuste par Modèles d'Ordre Réduits d'Écoulements Décollés (CORMORED) associant le LEA (Poitiers), l'IMFT (Toulouse), le LIMSI et le laboratoire SIMUNEF (ENSAM Paris).

IV Résumé des travaux de recherche

Dans le cadre de mes activités de recherche, la vitesse a toujours été la quantité fondamentale pour la caractérisation expérimentale des écoulements. Pour mesurer cette quantité, j'ai été amené à employer les techniques suivantes. L'enregistrement d'une différence de pression avec une sonde directionnelle à cinq trous est la méthode la plus simple et s'avère utile pour la caractérisation du champ moyen. L'anémométrie fil / film chaud permet d'accéder aux fluctuations jusqu'à des fréquences de plusieurs dizaines de kilohertz et reste donc adaptée à l'étude des écoulements turbulents. La velocimétrie laser Doppler (LDV), permet également la caractérisation d'un écoulement à des fréquences élevées mais présente l'avantage de ne pas avoir à introduire de sonde dans le milieu. Il en est de même de la visualisation par émission de fumée, pour les écoulements basse vitesse, qui ne fournit qu'une information qualitative dans un plan, mais présente un intérêt pour la caractérisation de zones décollées ou l'identification de structures tourbillonnaires. La visualisation par images de particules (PIV) est une technique de visualisation quantitative qui fournit la répartition de vitesse dans un plan. Malgré la faible résolution en fréquence des premiers systèmes, l'évolution des lasers pulsés vers de hautes cadences, couplée à l'utilisation de caméras rapides, permet désormais de mettre en œuvre une PIV résolue en temps.

J'ai été conduit, au cours de ma carrière, à aborder différentes thématiques qui couvrent l'aérodynamique compressible et incompressible, l'aérodynamique interne des machines tournantes et l'hydraulique. L'étude du sillage turbulent d'un corps autopropulsé par hélice, par anémométrie à films chauds triples, a permis de caractériser l'écoulement et les échanges énergétiques à travers des bilans de tensions de Reynolds. Un autre axe d'étude a consisté à mettre en place un nouveau type d'anémomètre à fil chaud à tension constante, dans une couche limite supersonique, qui montre une fréquence de coupure plus élevée par rapport aux anémomètres à température constante et courant constant. Un troisième domaine d'application concerne l'aérodynamique interne des machines tournantes. L'utilisation de l'anémométrie fil chaud sur un nouveau modèle expérimental de turbopompe centrifuge m'a permis de reconstruire une mesure dans un plan, en effectuant des moyennes en phase avec la rotation. Ces données ont caractérisé les performances du modèle d'essais et les zones décollées, pour différents points de fonctionnement. Une autre application aux machines tournantes a consisté à développer une LDV tridimensionnelle, pour explorer l'écoulement dans un étage de compresseur axial à partir d'un maillage volumique de points de mesure et en effectuant un traitement en phase avec la rotation du rotor. Ces résultats ont permis d'appréhender la dynamique instationnaire de l'écoulement et notamment le tourbillon de jeu, créé par le gradient de pression sur les pales du rotor. Une application à l'hydraulique a eu pour objet la mise en place d'une PIV sur un modèle d'échangeur thermique composé de cinq canaux parallèles. L'étude a permis de connaître la répartition de débit et d'intensité de turbulence, afin de constituer une base de données en vue d'une confrontation à une simulation numérique. Enfin, un algorithme avancé de PIV par flot optique a été mis en œuvre pour caractériser un écoulement de cavité ouverte, pour une gamme de nombre de Reynolds modérés. L'analyse de la morphologie de l'écoulement, en fonction des paramètres géométriques et du nombre de Reynolds, a permis de caractériser différentes structures et dynamiques tourbillonnaires. En particulier, il a été possible d'établir le domaine d'existence d'instabilités centrifuges créées par la recirculation. L'origine des instabilités centrifuges a été analysée et a mis en évidence un seuil unique d'apparition de ces instabilités. La comparaison entre un entraînement par un cisaillement avec l'extérieur, ou par un couvercle mobile, a montré que l'écoulement dans la cavité est plus instable en présence d'une couche de cisaillement.

V Projet de recherches à quatre ans

Les bases de mon projet de recherche à quatre ans ont été posées par les études conduites jusqu'à présent sur l'écoulement de cavité, dans le cadre de deux ANR blanches débutées récemment.

Dans un premier temps, la mise en place de la PIV stéréoscopique par flot optique devra être poursuivie pour obtenir les trois composantes de vitesse en fonction des paramètres géométriques de la cavité et du nombre de Reynolds. L'analyse de mesures PIV résolues en temps, par moyennes en phase par rapport au passage d'un tourbillon de la couche de cisaillement, devrait permettre de mieux comprendre les interactions entre l'instabilité de Kelvin-Helmholtz et les instabilités centrifuges, internes à la cavité. Des mesures synchronisées entre la PIV et un capteur de pression, permettront d'étudier le couplage entre vitesse et pression afin d'identifier des critères sur la dynamique de l'écoulement à partir d'une mesure localisée. Une signature propre des instabilités sera recherchée dans le signal de pression. L'objectif de ces mesures à plus long terme, sera la mise en place d'un contrôle en boucle fermée. Des méthodes d'identification de structures tourbillonnaires seront développées et évaluées dans ce cadre. Ce projet s'inscrit dans l'ANR DIB.

Un deuxième axe de recherche portera sur le développement de méthodes expérimentales utilisant l'algorithme de PIV par flot optique. Il consistera à mettre en place une ébauche de PIV stéréoscopique tomographique, éventuellement résolue en temps, qui est une voie vers une mesure spatiale instationnaire. Un système de deux nappes lasers perpendiculaires entre elles et utilisant deux lasers YAG en polarisation croisée, pour caractériser le plan de la recirculation et le plan des instabilités centrifuges, pourra être détecté par 2×2 caméras, chaque caméra possédant un filtre passe-bande en longueur d'onde. Ce montage permettra d'obtenir des champs de vitesse corrélés dans les deux plans pour améliorer la compréhension du couplage dynamique entre les structures de la couche de cisaillement et les instabilités centrifuges. Par ailleurs, ces données fourniront davantage d'information pour la mise en place de modèles réduits, et rendre le contrôle plus pertinent.

Enfin, la perspective à plus long terme de ce projet est le développement du contrôle en boucle fermée, qui s'inscrit dans le cadre de l'ANR CORMORED. Une série de capteurs de pression seront placés en aval de la cavité, tandis qu'un système d'actionneurs, fixé en amont, permettra de transmettre l'action définie en temps réel par le modèle de contrôle, modèle développé au sein de l'équipe Aérodynamique du LIMSI. Le contrôle envisagé aura pour but la diminution ou l'augmentation des instabilités selon l'objectif recherché, afin de piloter l'échange entre la cavité et l'écoulement extérieur. Ce projet diffère par ce point de la plupart des projets de contrôle qui s'attachent au rayonnement acoustique de la cavité. Le montage au LIMSI d'un second dispositif expérimental, à savoir un canal en eau, viendra en renfort à la soufflerie basse vitesse actuelle, pour une implantation de différents types d'actionneurs et de capteurs. Ce canal hydraulique permettra de mesurer la pression sur une plage dynamique plus grande, et d'identifier plus facilement un signal d'activation du contrôle. De plus, des moyens électrolytiques pourront être mis en œuvre en eau et permettront une évaluation quantitative du transfert d'un scalaire.

B. Synthèse scientifique

Nomenclature

A_S	base, matrice orthogonale	T_c	constante de temps appliquée au CVA
a_w	coeffcient de surchauffe du fil ou du film	U	vitesse
B_S	base, matrice orthogonale	u	fluctuation de vitesse
C	capacité électrique	U_c	vitesse de convection
C	paramètre de contrôle	U_e	vitesse extérieure à la couche limite
c_r	corde en pied de pale	U_q	vitesse débitante
D	diamètre	U_t	vitesse périphérique
d_i	distance instable de l'écoulement	V_m	vitesse méridienne
D_S	matrice des valeurs singulières	W	vitesse relative
E	tension	X	matrice de l'espace des phases
E	spectre unidimensionnel de la turbulence	x	coordonnée cartésienne
e	fluctuation de tension	y	coordonnée cartésienne
f	fréquence	z	coordonnée cartésienne
F_P	force de poussée	δ	différence
F_T	force de traînée	δ	épaisseur de couche limite
H	hauteur de veine	ε	incertitude sur l'écart-type des fluctuations de vitesse
H	hauteur de la cavité	$\bar{\varepsilon}$	dissipation
\mathcal{H}	hélicité	η	incertitude sur la vitesse moyenne
I	matrice identité	η	discriminant de Rayleigh
L	longueur de la cavité	Θ	température
M_w	constante de temps mesurée	θ	fluctuation de température
N	vitesse de rotation en $\text{tr}\cdot\text{min}^{-1}$	θ	coordonnée cylindrique
P	pression	ϑ	angle de tangage
p	fluctuation de pression	ν	viscosité cinématique
Q_n	débit nominal	ρ	masse volumique
R	rayon de la maquette	τ_w	cisaillement pariétal
r	coordonnée cylindrique	ϕ	angle de roulis
r^*	rayon du sillage	χ	demi-angle entre les têtes laser
R_c	rayon de courbure	ψ	angle de lacet
R_c	résistance du fil ou du film à froid	Ω	vitesse de rotation en $\text{rad}\cdot\text{s}^{-1}$
R_w	résistance du fil ou du film chaud	$\bar{\Omega}$	vorticité
r_h	rayon moyeu		
r_t	rayon en tête		
Re	nombre de Reynolds		Indices
S	section	b	composante laser bleue
S	envergure de la cavité	cor	corrigé
S	matrice des retards	e	extérieur
$S_{\rho u}$	coefficient de sensibilité au flux de masse	j	composante laser verte-jaune
$S_{\theta,t}$	coefficient de sensibilité à la température totale	m	maximum
T	période	mes	mesuré
t	temps	t	total
		v	composante laser verte

Introduction

Cette synthèse de mes activités porte sur les différentes thématiques de recherche que j'ai traitées, en mécanique des fluides, et s'articule autour de la mise en œuvre de méthodes expérimentales instationnaires. Les applications sont essentiellement liées à l'exploration du champ de vitesse en aérodynamique.

Après un aperçu des méthodes de mesures de la vitesse utilisées dans ces travaux, chacun des chapitres de cette thèse fait l'objet d'une application sur un thème particulier, où, après une présentation des techniques mises en œuvre, l'exposé s'oriente vers l'analyse des résultats et la physique des phénomènes.

L'ensemble de ces travaux est réalisé dans le cadre d'actions contractuelles en partenariat industriel ou de programmes de recherche (CNRT, ANR blanches, ...) et font l'objet de publications dans des revues internationales à comité de lecture.

I Aperçu sur les méthodes de mesure instationnaires en mécanique des fluides

I-1 Mesure de la vitesse

La connaissance de la vitesse dans un domaine fluide est fondamentale pour caractériser un écoulement. Le vecteur vitesse présente trois composantes dans l'espace à trois dimensions, et dépend du temps. Sa mesure peut être réalisée à partir de plusieurs techniques fournissant tout ou partie de ces informations. Il est ainsi possible de classifier les renseignements fournis par ces techniques selon les critères suivants :

- mesure qualitative (lignes d'émission, décollements, ...) ou quantitative ;
- mesure de la composante moyenne ou mesure de la composante fluctuante au cours du temps ;
- mesure d'une composante, de deux composantes, ou de trois composantes de vitesse ;
- mesure ponctuelle, mesure globale ;
- mesure invasive (introduction d'une sonde dans le milieu sans modifier sensiblement l'écoulement) ou mesure non invasive (essentiellement optique).

On peut donc citer les techniques de mesure de vitesse suivantes, qui ont été utilisées dans le cadre de ces travaux, selon leur apparition historique et leur degré de complexité, ainsi que leurs possibles développements futurs (Figure 1) :

- Le tube de Pitot (une composante) et la sonde clinométrique à cinq trous (trois composantes) où la vitesse s'obtient à partir d'une différence de pressions (Pitot, 1732).
- La visualisation des lignes d'émission par émission de fumée convectée par l'écoulement (Marey, 1901).
- L'anémométrie fil / film chaud (une à trois composantes) où la mesure de la vitesse se déduit de transferts thermiques (King, 1914).
- La velocimétrie laser Doppler (LDV), méthode optique où la grandeur mesurée est le décalage Doppler d'une lumière monochromatique (Yeh & Cummins, 1964, Rolfe & Huffaker, 1967).
- La velocimétrie par images de particules, méthode optique qui est la technique la plus intuitive dans son principe puisqu'elle mesure le déplacement de particules pendant un intervalle de temps (Dudderar & Simpkins, 1977, Adrian, 1984). Son application pratique aux écoulements bénéficie des développements de l'informatique et des méthodes de traitement d'images.

Pour les techniques optiques (visualisations, LDV, PIV), le choix des traceurs et leur moyen d'introduction dans l'écoulement sont prépondérants. En effet, l'ensemencement doit présenter les propriétés suivantes :

- il doit suivre parfaitement l'écoulement sans le perturber ;
- il ne doit pas sédimerter ;
- il doit avoir de bonnes propriétés de réflexion de la lumière ;
- son introduction doit être uniforme dans tout le volume fluide d'étude ;
- l'enrassement des parois de la veine d'essais en cours d'expérience doit être résolu.

D'autres techniques expérimentales n'ont pas été mises en œuvre dans le cadre de mes activités de recherche. On peut citer, à titre d'exemples, parmi les méthodes qualitatives, l'ombroscopie, la strioscopie, l'interférométrie, qui mesurent respectivement la dérivée seconde, la dérivée première de l'indice de réfraction ou directement l'indice de réfraction du milieu. Ces méthodes sont particulièrement adaptées aux écoulements présentant des gradients de masse volumique (écoulements compressibles, combustion, ...). Comme

méthodes quantitatives, on peut mentionner la vélocimétrie Doppler globale (DGV) et l'holographie double exposition laser qui nécessitent souvent de lourds montages expérimentaux.

L'évolution actuelle des capacités de stockage d'information, de traitement et de représentation spatiale des données conduit au développement de techniques de mesure tridimensionnelles et résolues en temps (vélocimétrie par images de particules tomographique résolue en temps, holographie cinématographique, ...) qui relèvent encore du domaine de la recherche et d'applications limitées à certains types d'écoulements. Cependant, on verra dans la suite qu'il est possible de reconstruire une information 2D ou 3D à partir de mesures ponctuelles (sonde de pression, fil chaud, LDV) en effectuant un maillage spatial du domaine, dans le cas d'un écoulement ergodique (Figure 10), ou à partir de moyennes en phase par rapport à un phénomène périodique de l'écoulement (Figure 15, Figure 25, Figure 26, Figure 30).

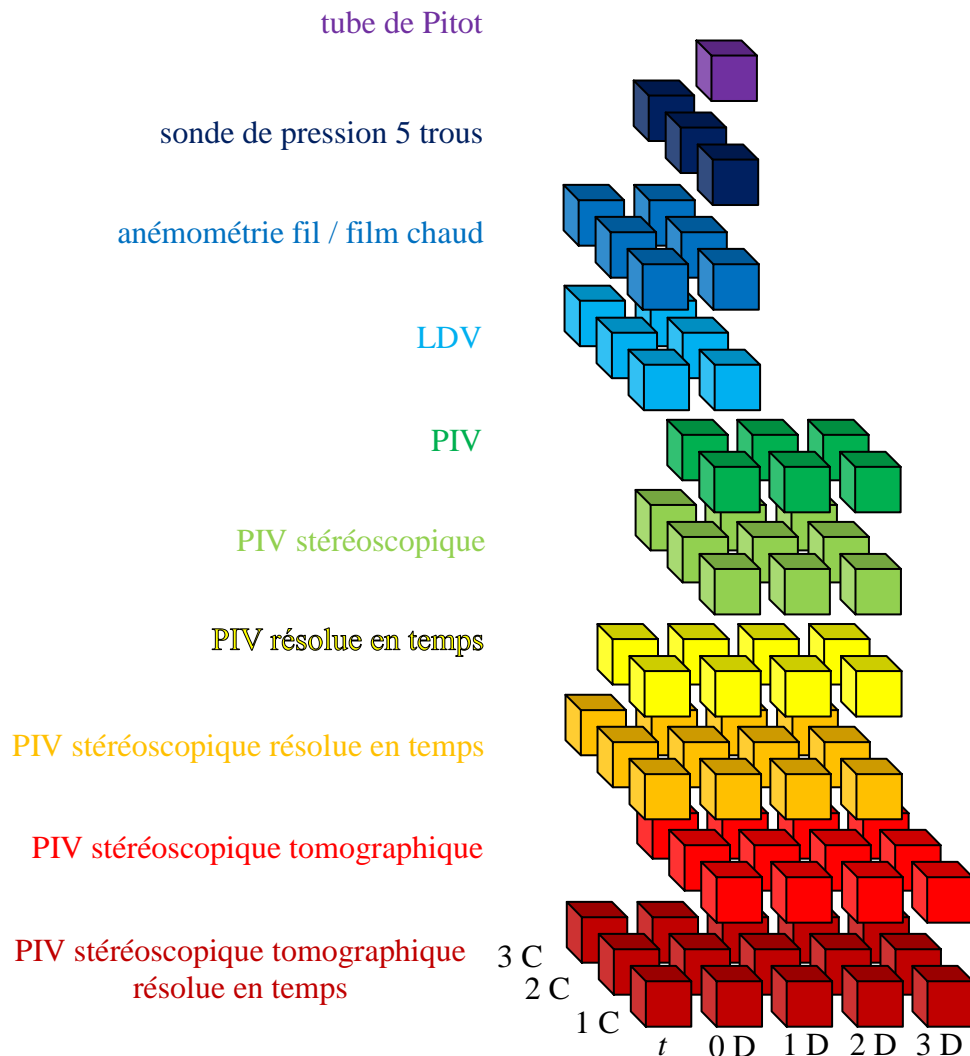


Figure 1 : Différentes techniques de mesure de la vitesse.

I-2 Domaines d'application

Dans le cadre des travaux présentés par la suite, on abordera différents domaines de la mécanique des fluides. L'aérodynamique instationnaire est le cadre de la plupart de ces études. La turbulence est l'objet des deux chapitres suivants, à travers respectivement l'étude d'un sillage de corps autopropulsé et la caractérisation d'une couche limite supersonique.

L'aérodynamique interne des machines tournantes est l'objet des chapitres IV et V qui traitent successivement de l'étude d'une turbopompe centrifuge et du couplage rotor-stator dans un étage de compresseur axial. L'hydraulique est abordée par une application à la thermique et l'étude de l'écoulement dans un échangeur de chaleur. Enfin, la thématique des instabilités est développée dans le dernier chapitre qui traite de l'écoulement de cavité engendré par une couche de cisaillement qui présente une instabilité de Kelvin-Helmholtz et, dans certaines configurations, des instabilités centrifuges.

I-3 Références

- ADRIAN, R. J.** (1984) Scattering particle characteristics and their effects on pulsed laser measurements of fluid flow: speckle velocimetry versus particle image velocimetry, *Appl. Opt.*, Vol. 23, pp. 1690–1691
- DUDDERAR, T. D., SIMPKINS, P. G.** (1977) Laser speckle photography in a fluid medium, *Nature*, No. 270, pp. 45–47
- KING, L. V.** (1914) On the convection of heat from small cylinders in a stream of fluid: determination of the convective constants of small platinum wires with applications to hot-wire anemometry, *Proc. Roy. Soc.*, Vol. 214 A, No. 14, pp. 373–432
- MAREY, É. J.** (1901) Les mouvements de l'air étudiés par la chronophotographie, *La Nature – Revue des Sciences*, 2nd semestre, p. 232
- PITOT, H.** (1732) Description d'une machine pour mesurer la vitesse des eaux courantes et le sillage des vaisseaux, *Mémoires de l'Académie Royale des Sciences*, pp. 363–376
- ROLFE, E., HUFFAKER, R. M.** (1967) Laser Doppler velocity instrument for wind tunnel turbulence and velocity measurements, *NASA Report N68-18099*
- YEH, Y., CUMMINS, H. Z.** (1964) Localized fluid flow measurements with an He-Ne laser spectrometer, *Appl Phys. Lett.*, Vol. 4, pp. 176–178

II Étude du sillage turbulent d'un corps à symétrie de révolution autopropulsé par hélice

II-1 Introduction

Ce thème de recherche constitue mon sujet de thèse de doctorat (Faure, 1995), proposé par la Direction Générale de l'Armement, et a pour objectif de caractériser et de comprendre les phénomènes physiques présents dans le sillage turbulent d'un corps autopropulsé par hélice. L'intérêt de cette configuration résulte du possible développement d'une méthode de détection passive d'un sillage lointain de sous-marin en immersion profonde, où la forte pression rencontrée empêche l'apparition de la cavitation. En parallèle à la thèse, ce sujet de recherche fait l'objet de deux contrats de la Direction Générale de l'Armement (DRET 89 537 et DRET 92 524) et d'une collaboration avec la société SIREHNA (contrat DRET 92 522).

Une expérience est mise en place dans la grande soufflerie anéchoïde de l'École Centrale de Lyon, dans des conditions de similitude de Reynolds. Une maquette motorisée permet de générer un sillage autopropulsé à quantité de mouvement nulle. La même maquette, sans système de propulsion, est étudiée pour avoir en référence le sillage à déficit de quantité de mouvement. Un système d'anémométrie à films chauds triples, entièrement automatisé, a été spécialement développé afin d'explorer différentes sections du sillage.

L'analyse porte d'abord sur la caractérisation statistique du champ de vitesse et la recherche d'une affinité en sillage lointain. Le sillage autopropulsé est comparé au sillage à déficit de quantité de mouvement, au niveau des transferts énergétiques, par des bilans d'énergie cinétique turbulente et de tensions de Reynolds. En particulier, on montre par l'analyse dimensionnelle du problème, que le terme de production est négligeable dans le cas autopropulsé. Différents modèles des termes de corrélation pression/déformations sont également confrontés aux résultats expérimentaux. Une analyse spectrale du champ de vitesse met en évidence une composante large bande, avec des raies spectrales dans la zone de sillage proche où les structures organisées de l'écoulement sont caractérisées par des moyennes en phase par rapport à la rotation de l'hélice.

II-2 Dispositif expérimental

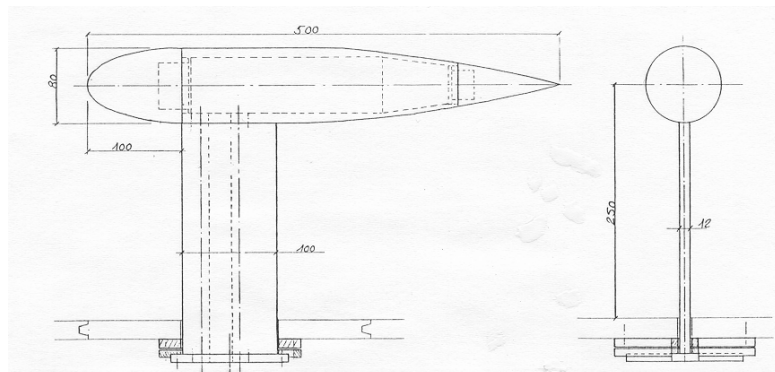
II-2-1 Banc expérimental

La veine d'essais, de six mètres de longueur et de section carrée $0,5 \times 0,5 \text{ m}^2$, comporte des parois supérieures et inférieures modulables qui permettent son instrumentation et son exploration axiale (Figure 2). Pour les conditions d'essais, l'uniformité de la vitesse dans une section est de $\pm 2\%$ en début de veine et $\pm 3\%$ en fin de veine, avec une intensité de turbulence résiduelle maximale de 0,7% pratiquement constante de l'amont à l'aval.

La maquette à symétrie axiale, de 50 cm de longueur et de diamètre maximum $D = 8 \text{ cm}$, comporte une partie amont ellipsoïdale, une partie centrale cylindrique de section constante, et une partie aval profilée (Figure 3-a). Pour l'étude du sillage autopropulsé, on utilise une partie terminale contenant un moteur électrique à courant continu sans collecteur (Minimotor SA type 3556 K BL 1) d'alimentation variable de 12 à 56 V, qui entraîne une hélice tripale de 4 cm de diamètre à $15\,000 \text{ tr}\cdot\text{min}^{-1}$ (Figure 3-b). Une carte de commande (Minimotor SA type BLD 568) implantée dans le boîtier d'alimentation permet une régulation de la rotation. Un capteur à effet Hall intégré génère à chaque tour un signal carré de 5 V de tension de sortie. Le refroidissement du moteur, rendu nécessaire par l'endommagement du câblage électrique pour des températures supérieures à 80°C , est réalisé par la convection forcée de l'écoulement intérieur à la maquette au moyen d'un ventilateur. Pour améliorer l'échange thermique entre la maquette et l'extérieur, celle-ci a été réalisée en aluminium.



Figure 2 : Dispositif expérimental : veine d'essais avec la maquette (configuration de sillage à déficit de quantité de mouvement) et le système de déplacement de la sonde à films chauds triples.



a)



b)

Figure 3 : Maquette d'essais : a) vues latérale et de face, b) parties terminales avec et sans propulseur.

L'expression de la différence entre le coefficient de poussée F_P et le coefficient de traînée F_T s'obtient par un bilan de quantité de mouvement, sur un volume de contrôle entourant la maquette (Figure 4) :

$$F_P - F_T = \rho \int_{\Sigma_2} \bar{U}_x^2 dS - \rho U_e^2 S + \int_{\Sigma_2} \bar{P} dS - P_e S$$

Les deux paramètres qui peuvent varier pour annuler l'équation précédente sont la vitesse de rotation de l'hélice N et la vitesse de l'écoulement extérieur U_e . Pour obtenir un rapport signal sur bruit optimum, nous avons fixé la vitesse de rotation à sa valeur maximum et fait varier la vitesse de l'écoulement. Tous les termes de l'équation sont mesurés à l'aide d'une sonde à cinq prises de pression. La configuration de sillage de corps autopropulsé est obtenue lorsque la différence entre la poussée et la traînée est nulle (Figure 5). On retient finalement comme paramètres pour l'autopropulsion, une vitesse d'écoulement $U_e = 11,6 \pm 0,25 \text{ m}\cdot\text{s}^{-1}$ et une vitesse de rotation du propulseur $N = 15\,000 \text{ tr}\cdot\text{min}^{-1}$.

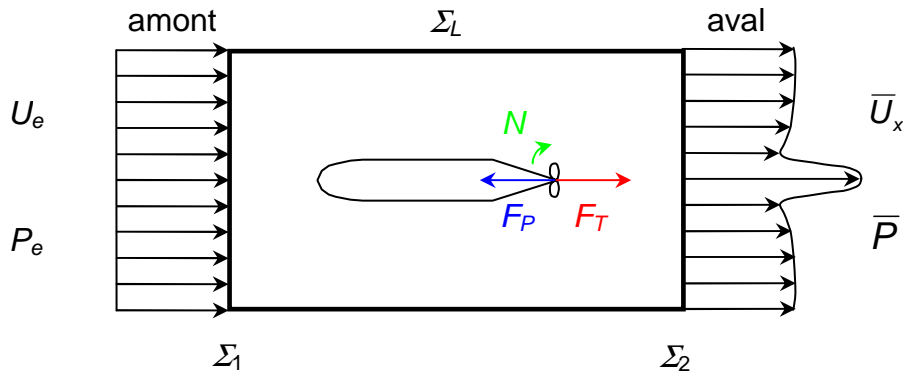


Figure 4 : Volume de contrôle autour d'un corps autopropulsé par hélice pour le calcul d'un bilan de quantité de mouvement.

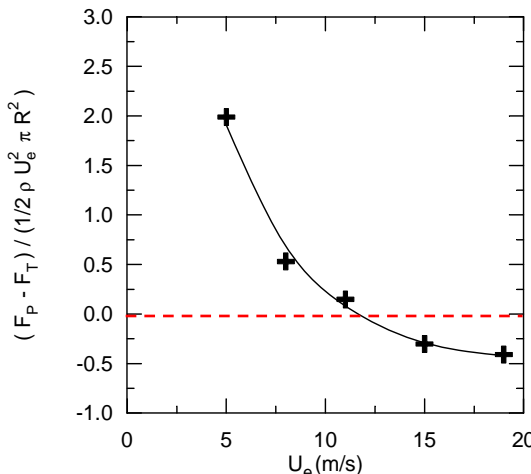


Figure 5 : Différence entre le coefficient de poussée et le coefficient de traînée, mesurée par un bilan de quantité de mouvement, en fonction de la vitesse de l'écoulement extérieur U_e , pour $N = 15\,000 \text{ tr}\cdot\text{min}^{-1}$.

II-2-2 Instrumentation

La sonde utilisée est une sonde triple à films chauds orthogonaux DANTEC 55R91. Chaque capteur est constitué d'un cylindre de quartz de $70 \mu\text{m}$ de diamètre et de $1,25 \text{ mm}$ de long sur lequel est déposé un film de nickel, l'ensemble est protégé par un revêtement de quartz de $0,5 \mu\text{m}$ d'épaisseur. Les trois capteurs sont perpendiculaires entre eux et contenus dans une sphère de 3 mm de diamètre (Figure 6). La gamme de vitesse de la sonde, d'après le constructeur, est $0,2 - 350 \text{ m}\cdot\text{s}^{-1}$ dans l'air, et sa limite de réponse en fréquence est 175 kHz . La résistance des capteurs est d'environ 6Ω et ils sont utilisés dans un montage d'anémométrie à température constante (CTA) avec un coefficient de surchauffe défini par $a_w = (R_w - R_c) / R_c = 0,7$ (Figure 7). L'étalonnage de la sonde consiste à établir trois lois de

King (1914) pour chacun des capteurs. La sonde est ensuite ajustée avec soin par rapport à l'écoulement afin d'utiliser les relations de projection géométrique de Jorgensen (1971).

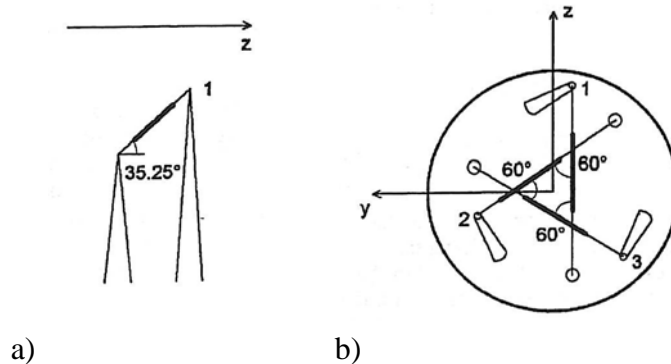


Figure 6 : Géométrie de la sonde triple à films chauds : a) vue latérale d'un film, b) vue de face.

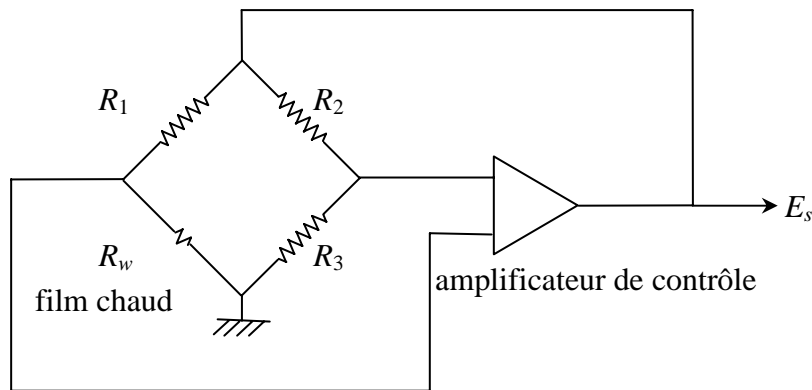


Figure 7 : Schéma de principe de l'anémomètre à température constante (CTA).

Par ailleurs, les conditions d'utilisation d'une sonde à films chauds peuvent varier au cours d'une campagne de mesure de plusieurs heures, principalement du fait de la variation de la température ambiante. Afin de s'affranchir de cette contrainte, un recalage des signaux en température est réalisé en cours d'acquisition dans l'écoulement extérieur (Figure 8).

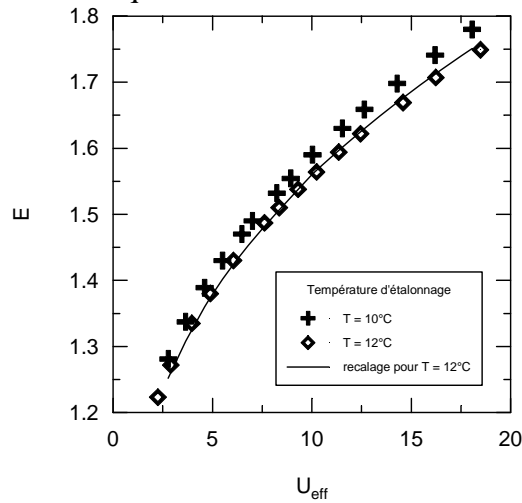


Figure 8 : Étalonnage d'un film chaud et recalage en température pour une dérive de $2^\circ C$.

La chaîne de mesure complète comprend :

- la sonde triple à films chauds DANTEC 55R91 décrite précédemment ;
 - l'anémomètre TSI IFA 100 à 3 voies, chaque voie est constituée par un module anémomètre 150 et par un module conditionneur de signal 157 ;
 - une carte d'acquisition 12 bits 8 voies 200 kHz ;
 - un chariot de déplacement deux axes et rotation associé à un boîtier de commande Dynapar.

La précision des déplacements est de $\pm 0,1$ mm. L'ensemble de ces composants est piloté à partir d'un micro-ordinateur 80 386 16 MHz par liaisons RS 232 (Figure 9).

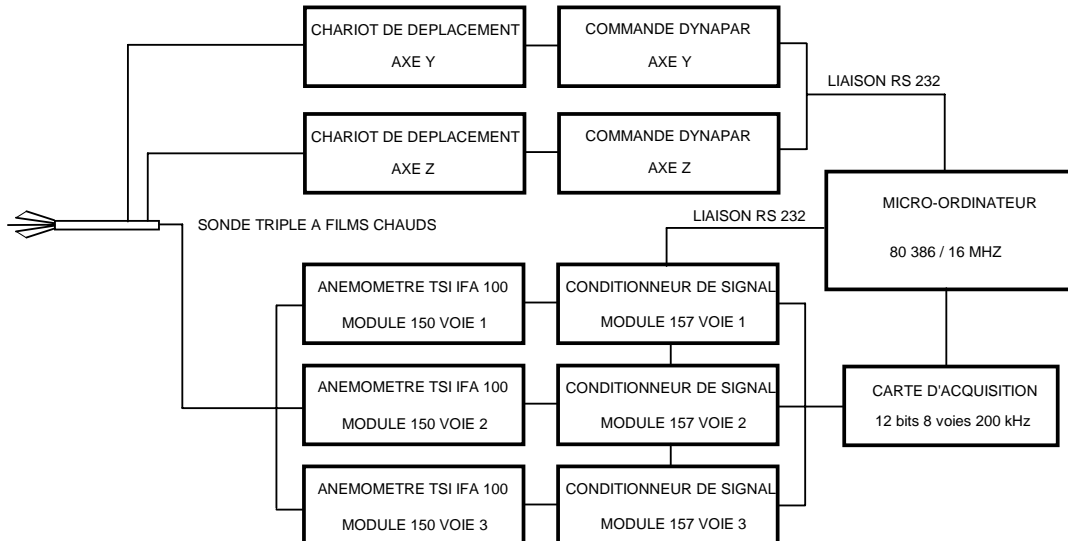


Figure 9 : Système de mesure, déplacement et acquisition.

Trois types d'acquisition sont effectués pour chaque configuration de sillage et chaque distance d'exploration :

- une acquisition dans une section complète de la veine d'essais (400 points, $f_{acq} = 4$ kHz, $t_{acq} = 5$ s), afin d'obtenir les vitesses moyennes et quadratiques moyennes ;
 - une acquisition « basse fréquence » selon un rayon à partir de l'axe du sillage (30 points, $f_{acq} = 7,5$ kHz, $t_{acq} = 20$ s), pour assurer la convergence des moments de vitesse d'ordre 3 et le calcul de spectres de vitesse « basse fréquence » ;
 - une acquisition « haute fréquence » selon le même rayon que précédemment (30 points, $f_{acq} = 50$ kHz, $t_{acq} = 3$ s), pour recueillir un signal échantillonné très finement et réaliser un traitement périodique du signal calé sur la rotation de l'hélice. De plus, cette acquisition permet le calcul de spectres de vitesse « haute fréquence ».

Avec ces paramètres, l'incertitude de mesure est estimée :

- pour les valeurs moyennes (moments d'ordre 1) à 0,43% ;
 - pour les moments d'ordre 2 à 1,4% ;
 - pour les moments d'ordre 3 à 2,7%.

II-3 Principaux résultats

II-3-1 Affinité du sillage lointain

On explore différentes positions axiales dans le sillage (Figure 10). L'ensemble des résultats obtenus constitue une base de données originale, compte tenu du faible nombre de publications sur ce sujet (Naudascher 1965, Schetz & Jakubowski 1975, Cimbala & Park 1990 et Park & Cimbala 1991). Un résultat de cette étude est la mise en évidence de l'affinité des vitesses moyennes et des écarts-types des fluctuations, observé à partir de $x / D = 17,5$, pour le sillage lointain de corps autopropulsé (Faure 1995, Figure 11). La vitesse moyenne

mesurée correspond au profil de similitude déterminé analytiquement pour $x / D = 17,5$, mais la similitude n'est pas observée plus en aval du fait de la croissance du rapport signal sur bruit de l'écoulement dans la soufflerie. Cependant, les lois d'évolution fournies par l'analyse des équations du mouvement et reposant sur la distinction entre deux régimes extrêmes d'écoulement (Ferry & Piquet 1987) ne paraissent pas justifiées expérimentalement.

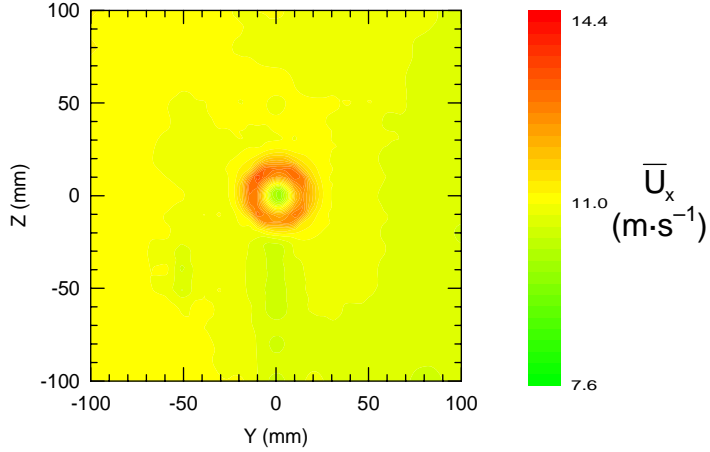


Figure 10 : Champ de vitesse moyenne axiale pour $x/D = 1$.

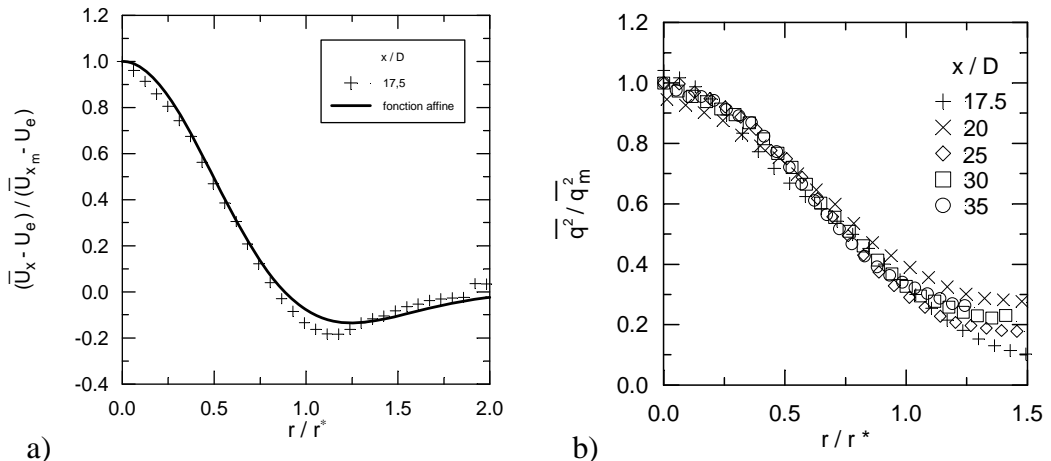


Figure 11 : Affinité du champ de vitesse en sillage autopropulsé lointain : a) vitesse moyenne axiale, b) énergie cinétique turbulente.

II-3-2 Bilans d'énergie cinétique turbulente et de tensions de Reynolds

Tous les termes de l'équation d'énergie cinétique turbulente accessibles à la mesure ont été déterminés (Faure & Robert 1995, Faure & Robert 1996). Cette équation peut se réduire à l'expression suivante, pour un sillage à symétrie de révolution axiale, dans le cadre de l'approximation de « couche limite » valable en sillage lointain :

$$\overline{U}_x \frac{\partial \overline{q^2}}{\partial x} = -\overline{u_x u_r} \frac{\partial \overline{U}_x}{\partial r} - \overline{u_r u_\theta} \left(\frac{\partial \overline{U}_\theta}{\partial r} - \frac{\overline{U}_\theta}{r} \right) - \frac{1}{r} \frac{\partial}{\partial r} \left(r \overline{q^2 u_r} \right) - \frac{1}{\rho r} \frac{\partial}{\partial r} \left(r \overline{p u_r} \right) - \bar{\epsilon}$$

On montre l'affinité des échanges turbulents en champ lointain (Figure 12). Il faut remarquer que le terme de production est négligeable par rapport aux autres types de transfert, ce qui n'est pas le cas du sillage à déficit de quantité de mouvement.

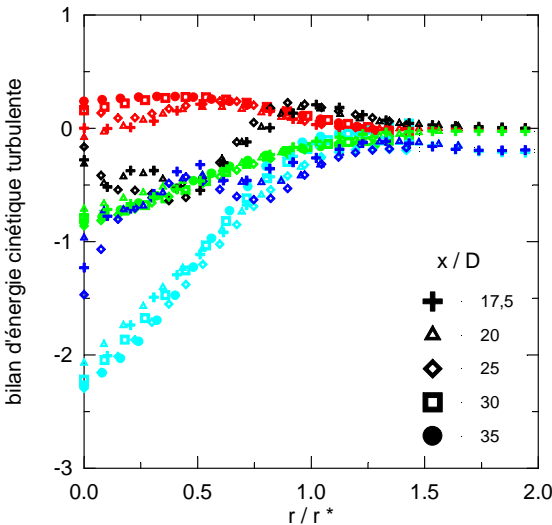


Figure 12 : Évolution affine de chacun des termes du bilan d'énergie cinétique turbulente en sillage autopropulsé pour 5 distances en aval de la maquette (bleu clair : convection, rouge : production, noir : transfert cinétique, vert : transfert pression, bleu foncé : dissipation isotrope).

Une détermination expérimentale de chacun des termes des équations de transport des tensions de Reynolds est également effectuée (Faure 1997). De tels bilans ont un intérêt certain car ils sont pris en compte par les codes numériques dans l'utilisation de fermetures au second ordre. Ainsi, il est possible de comparer plusieurs modèles du terme pression-déformations (Launder *et al.* 1975 modèles d'isotropisation de la production IP et quasi-isotope QI, Gibson & Younis 1986, Fu *et al.* 1987) avec les évolutions fournies par les mesures (Figure 13). Le modèle de Fu *et al.* 1987, calibré pour un jet tournant avec recirculation, donne des évolutions assez proches des évolutions mesurées.

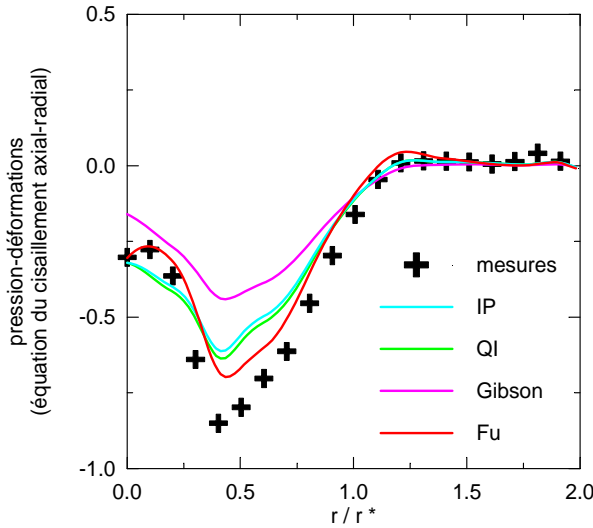


Figure 13 : Comparaisons entre le terme pression-déformations mesuré et modélisé pour l'équation du cisaillement axial-radial.

II-3-3 Analyse spectrale

Une analyse spectrale est également menée (Faure & Robert 1997, Figure 14). Les raies spectrales associées à la rotation de l'hélice ainsi qu'au passage périodique des pales sont identifiées. On remarque que la seconde raie présente un niveau plus élevé que la première dans une zone initiale ; cependant, elle disparaît rapidement et seule la raie caractéristique de

la rotation du propulseur persiste jusqu'à 10 diamètres d'hélice en aval du bord de fuite de la maquette. Les propriétés d'affinité des densités spectrales de puissance sont établies dans une zone lointaine du sillage. En particulier, on note sur la partie large bande du spectre de vitesse radiale, un maximum à la frontière du sillage, que l'on peut associer à l'émission de grosses structures turbulentées.

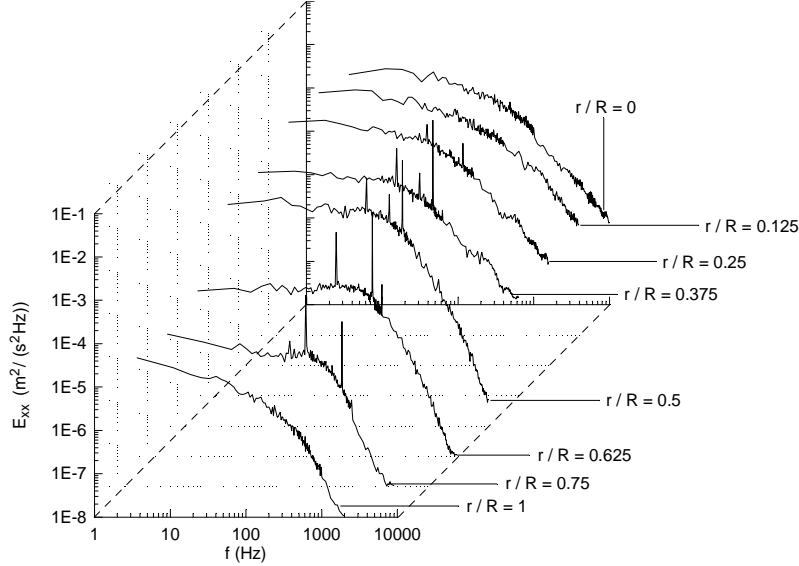


Figure 14 : Évolution radiale de la densité spectrale de puissance des fluctuations de vitesse axiale pour $x / D = 1$.

II-3-4 Moyennes de phase

Un traitement conditionnel des signaux permet de mettre en évidence les structures organisées de l'écoulement, par rapport à la rotation de l'hélice, jusqu'à une distance de 4 diamètres d'hélice en aval de celle-ci (Figure 15). Les processus d'émission et d'aspiration de fluide au passage des pales sont clairement identifiés. Il faut aussi noter, sur la composante axiale moyenne de la vorticité, les tourbillons de bout de pale contrarotatifs.

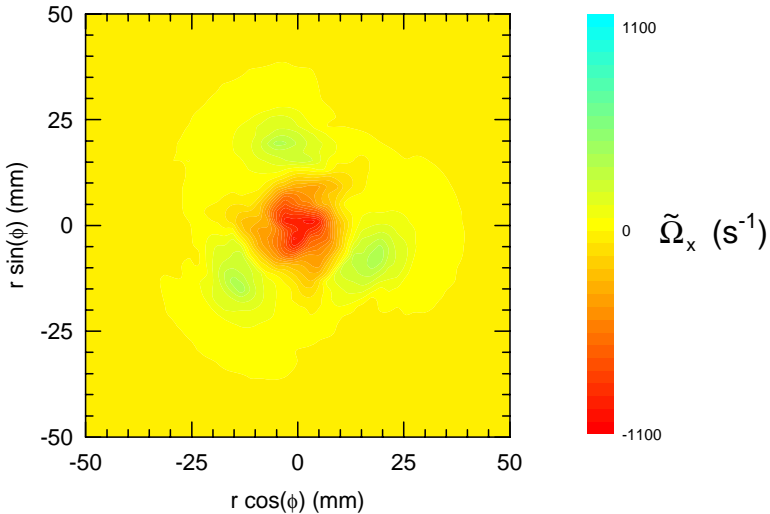


Figure 15 : Moyenne de la vorticité axiale en phase avec la rotation de l'hélice pour $x / D = 0,4$.

II-4 Conclusion

Un système automatisé en déplacement et acquisition, utilisant l'anémométrie films chauds à trois composantes, permet l'exploration d'un sillage autopropulsé de son origine

jusqu'à une distance aval de 50 diamètres du corps. Cette technique expérimentale, faiblement invasive, est bien adaptée à l'étude de cet écoulement libre turbulent tridimensionnel. La configuration de sillage à déficit de quantité de mouvement permet de retrouver les résultats classiques concernant l'affinité des profils de vitesse ainsi que les lois axiales d'évolution prédictes par l'analyse des équations du problème. Ces mesures sont également en accord avec les quelques expériences disponibles sur le sujet. La configuration de sillage autopropulsé par hélice, à quantité de mouvement nulle, montre un certain nombre de résultats originaux. Différentes zones d'évolution axiale sont identifiées :

- le sillage proche pour $x / D < 5$, marqué par la signature spectrale de l'hélice ;
- une région intermédiaire d'établissement pour $5 < x / D < 20$;
- le sillage lointain pour $x / D > 20$, qui présente des propriétés d'affinité des champs moyens, turbulents et des échanges énergétiques.

La mesure de tous les termes de l'équation d'énergie cinétique turbulente met en évidence que la production est négligeable dans la zone affine, pour le sillage autopropulsé, ce qui est différent par rapport à un sillage à déficit de quantité de mouvement. Les lois d'évolution axiales d'un sillage de corps autopropulsé, reposant sur une séparation entre un régime axial dominant, dans le cas d'une propulsion par jet, et un régime de rotation dominante, pour une propulsion par hélice, ne sont pas validées expérimentalement. Une fermeture du problème pourrait être envisagée en prenant en compte le fait que la production d'énergie cinétique turbulente est négligeable.

II-5 Références

- CIMBALA, J. M., PARK, W. J.** (1990) An experimental investigation of the turbulent structure in a two-dimensional momentumless wake, *Journal of Fluid Mechanics*, Vol. 213, pp. 479–509
- FAURE, Th. M.** (1995) *Étude expérimentale du sillage turbulent d'un corps à symétrie de révolution autopropulsé par hélice*, Thèse de doctorat, École Centrale de Lyon, n°95-01
- FAURE, Th. M., ROBERT, G.** (1995) Bilan des tensions de Reynolds dans un sillage de trainée et dans un sillage de corps autopropulsé par une hélice, *Comptes-Rendus de l'Académie des Sciences, Paris*, série II b, tome 321, n°11, pp. 455–461
- FAURE, Th. M., ROBERT, G.** (1996) Turbulent kinetic energy balance in the wake of a self-propelled body, *Experiments in Fluids*, Vol. 21, No. 4, pp. 268–274
- FAURE, Th. M., ROBERT, G.** (1997) Spectral analysis of the turbulent structure in the momentumless wake of a propeller-driven body, *European Journal of Mechanics / B Fluids*, Vol. 16, No. 2, pp. 211–226
- FAURE, Th. M.** (1997) The Reynolds stress transport equations in a momentumless wake: experiments and models, *AIAA Journal*, Vol. 35, No. 2, pp. 281–287
- FERRY, M., PIQUET, J.** (1987) *Sillage visqueux lointain d'un corps sous-marin autopropulsé*, Rapport d'étude SIREHNA, contrat DRET 86 1201
- FU, S., LAUNDER, B. E., LESCHZINER, M. A.** (1987) Modelling strongly recirculating jet flow with Reynolds-stress transport closures, *Proceedings of the 6th Symposium on Turbulent Shear Flows*, Toulouse, France
- GIBSON, M. M., YOUNIS, B. A.** (1986) Calculation of swirling jets with a Reynolds stress closure, *Physics of Fluids*, Vol. 29, No. 1, pp. 38–48
- JORGENSEN, F. E.** (1971) Directional sensitivity of wire and fiber film probes, *DISA Information*, No. 11, pp. 31–37
- LAUNDER, B. E., REECE, G. J., RODI, W.** (1975) Progress in the development of Reynolds-stress turbulence closure, *Journal of Fluid Mechanics*, Vol. 68, No. 3, pp. 537–566

- KING, L. V.** (1914) On the convection of heat from small cylinders in a stream of fluid: determination of the convective constants of small platinum wires with applications to hot-wire anemometry, *Proc. Roy. Soc.*, Vol. 214 A, No. 14, pp. 373–432
- NAUDASCHER, E.** (1965) Flow in the wake of self-propelled bodies and related sources of turbulence, *Journal of Fluid Mechanics*, Vol. 22, Part 4, pp. 625–656
- PARK, W. J., CIMBALA, J. M.** (1991) The effect of jet injection geometry on two-dimensional momentumless wakes, *Journal of Fluid Mechanics*, Vol. 224, pp. 29–47
- SCHETZ, J. A., JAKUBOWSKI, A. K.** (1975) Experimental studies of the turbulent wake behind self-propelled slender bodies, *AIAA Journal*, Vol. 13, No. 12, pp. 1568–1575

III Développement de l'anémométrie fil chaud à tension constante et application à une couche limite supersonique

III-1 Introduction

Cette étude est menée dans le cadre du développement de l'anémomètre à tension constante (CVA, constant voltage anemometry, Sarma, 1991) en collaboration avec la société Tao Systems Incorporated et fait l'objet d'un partenariat avec le LEA (CEAT) à Poitiers et l'IRPHE à Marseille pour l'utilisation de souffleries supersoniques. L'analyse préliminaire de l'utilisation du CVA est le sujet du stage de fin d'étude de Tomasz Kasierski (1996). La mesure prenant en compte la compensation du circuit électronique avec la constante de temps mesurée dans l'écoulement, ou la mesure avec une constante de temps arbitraire et une correction a posteriori de la constante de temps, sont deux possibilités d'utilisation du CVA. Une comparaison avec les montages classiques d'anémométrie fil chaud termine l'analyse (anémomètre à courant constant, CCA et anémomètre à température constante, CTA).

III-2 Dispositif expérimental

III-2-1 Soufflerie expérimentale

La soufflerie à rafale du CEAT présente une section d'essais de $150 \text{ mm} \times 150 \text{ mm}$. Les conditions à l'extérieur de la couche limite sont une température de 158 K et une pression de $0,122 \cdot 10^5 \text{ Pa}$. Le nombre de Mach extérieur à la couche limite est de 2 . L'épaisseur de la couche limite à l'abscisse de mesure est $\delta = 15,7 \text{ mm}$. Deux fils chauds en tungstène de diamètres respectifs $2,5 \mu\text{m}$ et $5 \mu\text{m}$ sont placés à deux positions relatives $y / \delta = 0,32$ et $0,64$ de la paroi.

La soufflerie continue de l'IRPHE permet l'étude d'une couche limite sans gradient de pression extérieure de nombre de Mach $2,3$. Elle est utilisée pour trois pressions de $0,163 \cdot 10^5 \text{ Pa}$, $0,492 \cdot 10^5 \text{ Pa}$ et $0,746 \cdot 10^5 \text{ Pa}$. La position de mesure est située à $0,75 \text{ m}$ en aval du col de la soufflerie, où la couche limite présente une épaisseur $\delta = 15 \text{ mm}$. Un fil chaud en tungstène avec un plaquage de platine de $2,5 \mu\text{m}$ de diamètre est placé à $y / \delta = 0,27$. Les essais sont réalisés pour différentes valeurs du coefficient de surchauffe $a_w = (R_w - R_c) / R_c$.

III-2-2 Instrumentation

Le CVA (Figure 16) peut être utilisé de deux manières : soit en effectuant la compensation du circuit électronique avec la constante de temps mesurée pour les conditions d'essais, soit avec une compensation thermique arbitraire, la correction par la vraie valeur de la constante de temps s'effectuant a posteriori. Ce second processus opératoire permet une plus grande productivité dans les mesures. La compensation thermique du circuit est réalisée par la combinaison des résistances et de la capacité (R_a , R_b , R_d , C). Les signaux sont enregistrés à une fréquence d'acquisition de 1 MHz par un système LeCroy 8007 sous la forme de 127 segments de 4096 échantillons.

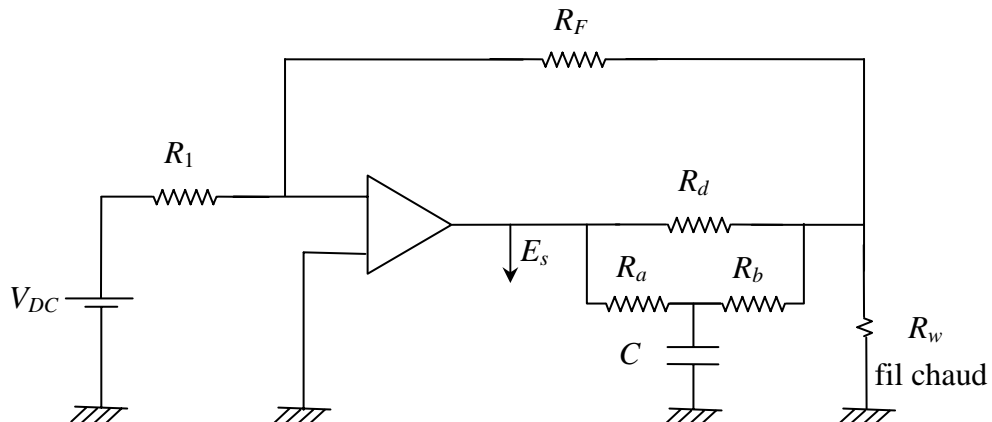


Figure 16 : Schéma de principe de l'anémomètre à tension constante (CVA)

III-3 Principaux résultats

III-3-1 Constante de temps

La mesure de la constante de temps M_w est réalisée par l'injection d'un signal carré de 20 Hz à la jonction entre les résistances R_1 et R_F (Figure 16). La réponse de l'anémomètre est présentée sur la Figure 17 (Sarma *et al.*, 1998). La constante de temps mesurée M_w correspond au temps nécessaire pour une décroissance en amplitude de 63 %, elle est ici de 0,1 ms.

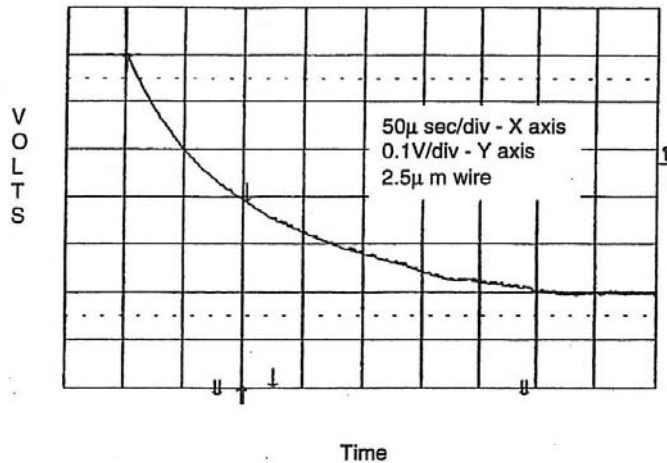


Figure 17 : Réponse moyenne d'un fil chaud de 2,5 μm dans un montage CVA pour une surchauffe $a_w = 0,5$ et $Re = 19$.

La comparaison entre les constantes de temps mesurées par CVA et CCA est présentée sur la Figure 18. Pour le CVA, la constante de temps décroît avec la surchauffe et reste inférieure à la constante de temps du CCA. Ces résultats sont en accord avec l'approximation (Comte-Bellot, 1998) :

$$M_{w,CVA} = \frac{M_{w,CCA}}{1 + 2a_w}$$

Les petites valeurs de $M_{w,CVA}$ permettent une correction plus aisée de la compensation thermique de l'anémomètre par un post-traitement, avec un bruit de fond plus faible et une plus grande bande-passante du circuit électrique, par rapport à une compensation thermique effectuée avant la mesure.

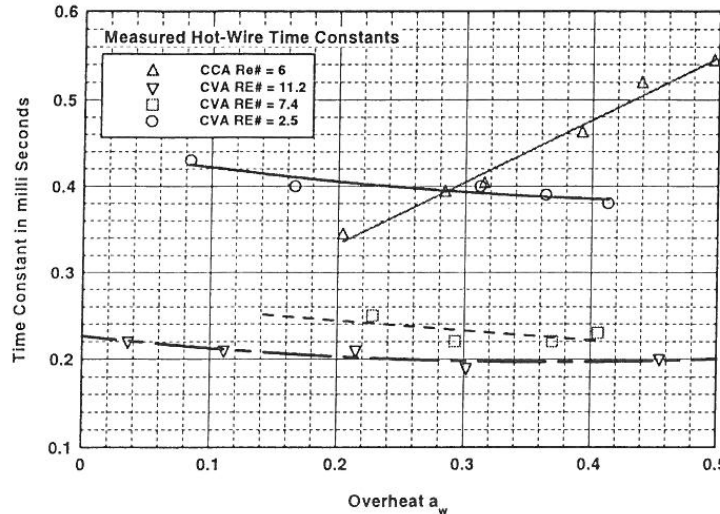


Figure 18 : Constantes de temps M_w en fonction de la surchauffe a_w mesurées pour le CVA et le CCA autour d'un fil de 2,5 μm pour différents nombres de Reynolds.

La compensation thermique par post-traitement du signal est réalisée par l'équation (Sarma, 1998) :

$$e_{cor} + T_c \frac{de_{cor}}{dt} = e_{mes} + M_{w,CVA} \frac{de_{mes}}{dt}$$

où e_{mes} est la tension mesurée, e_{cor} la tension corrigée par post-traitement, T_c la constante de temps arbitrairement imposée au circuit électronique avant la mesure et $M_{w,CVA}$ la constante de temps du circuit mesurée dans l'écoulement. Au-delà de 10 kHz, la relation précédent se réduit asymptotiquement à :

$$e_{cor} = \frac{M_{w,CVA}}{T_c} e_{mes}$$

Le comportement du circuit électronique est parfaitement défini et n'est pas modifié par les effets de capacitance des câbles de connexion au fil chaud. Les spectres des fluctuations de vitesse sont présentés Figure 19 pour une position dans la couche limite $y / \delta = 0,27$ et deux coefficients de surchauffe $a_w = 0,15$ et $a_w = 0,59$. La représentation $f E(f)$ permet d'identifier la gamme de fréquences qui contribue le plus à la turbulence puisque l'énergie du signal est :

$$\overline{e^2} = \int_0^{\infty} E(f) df = \int_0^{\infty} f E(f) d(\ln f)$$

On observe, sur les trois séries de spectres, un plateau particulièrement identifiable pour les grandes surchauffes et la présence de raies vers 150 kHz et 250 kHz, interprétées comme les vibrations des broches de soudure du fil (Dussauge *et al.*, 1996). Pour le circuit électronique compensé par la constante de temps mesurée (Figure 19-a), le plateau s'étend jusqu'à environ 100 kHz du fait de la bande passante réduite du CVA dans ce cas. Les spectres bruts (Figure 19-b) montrent un plateau bien plus long, mais avec une amplitude trop faible. Les spectres corrigés par post-traitement (Figure 19-c) retrouvent le niveau du spectre obtenu avec le circuit compensé, mais avec une plage en fréquence supérieure s'étendant jusqu'à 300 kHz. Ce dernier mode opératoire est donc préféré pour obtenir la bande-passante la plus étendue.

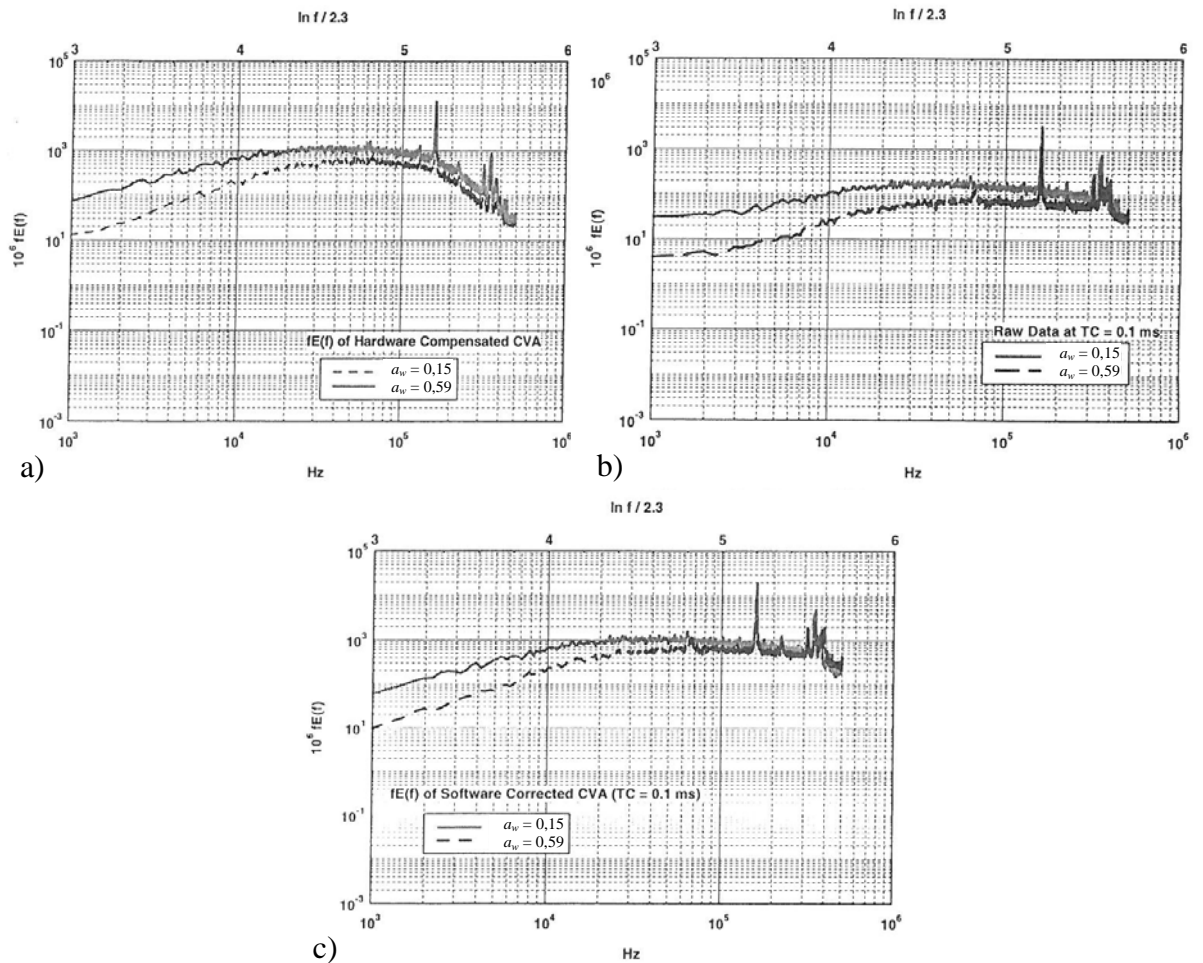


Figure 19 : Spectre $f E(f)$ en fonction de $\ln f$ pour deux surchauffes $a_w = 0,15$ (trait plein) et $a_w = 0,60$ (tirets) avec a) compensation du circuit du CVA, b) mesure avec une compensation de 0,1 ms, c) correction par post-traitement du spectre mesuré avec $M_{w,CVA} = 0,25$ ms pour $a_w = 0,15$ et $M_{w,CVA} = 0,20$ ms pour $a_w = 0,60$.

III-3-2 Comparaison des spectres mesurés par CCA, CTA et CVA

La comparaison entre les trois types de circuit d'anémométrie fil chaud, CCA, CTA et CVA, est réalisée au même point de mesure dans la couche limite avec un fil de $2,5 \mu\text{m}$ (Comte-Bellot *et al.*, 1999). Le CCA est un DISA 56C02, la compensation thermique de son circuit électrique est réalisée avant la mesure en deux étapes à travers un préamplificateur puis un conditionneur. Le coefficient de surchauffe du fil est $a_w = 0,5$. Le CTA est un DANTEC Streamline 90C10 qui fonctionne avec un pont symétrique et un coefficient de surchauffe $a_w = 0,6$. Le CVA opère avec une surchauffe $a_w = 0,6$ et une compensation du circuit électrique à $T_c = 0,1$ ms corrigée par post-traitement avec la valeur mesurée $M_{w,CVA} = 0,2$ ms. Les spectres sont présentés Figure 20 et mettent en évidence une fréquence de coupure vers 70 kHz pour le CTA, 200 kHz pour le CCA et 300 kHz pour le CVA. La réponse en fréquence du CCA est limitée par la valeur élevée de la constante de temps et la présence d'un filtre passe-bas à 400 kHz. Le CTA sous-estime les hautes fréquences par la présence du filtre passe-bas introduit dans son circuit pour assurer la stabilité de la boucle de rétroaction. Seul le CVA, utilisé avec correction de la constante de temps lors du post-traitement, est capable de reproduire le plateau qui s'étend jusqu'à 300 kHz.

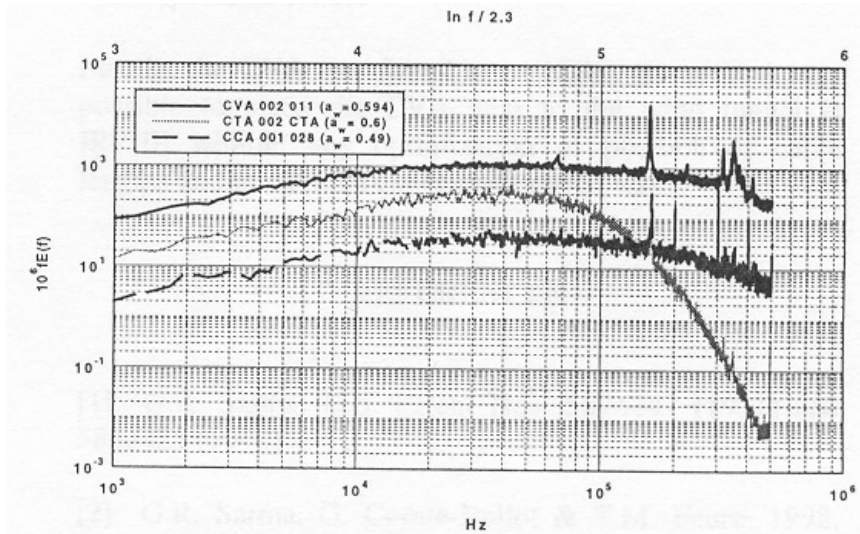


Figure 20 : Comparaison entre les spectres mesurés par CVA, CTA et CCA dans une couche limite supersonique de nombre de Mach extérieur 2 avec un fil chaud de $2,5 \mu\text{m}$ placé à 0,27 épaisseur de couche limite (les trois spectres sont arbitrairement décalés pour identifier leur fréquence de coupure respective).

III-3-3 Caractérisation de la couche limite turbulente

La réponse d'un fil chaud dépend à la fois des fluctuations de flux de masse et de température totale et peut s'écrire (Sarma *et al.*, 1998) :

$$\frac{\overline{e}}{\overline{E}} = S_{\rho u, CVA} \frac{\rho u}{\bar{\rho} \bar{U}} + S_{\theta_t, CVA} \frac{\theta_t}{\bar{\Theta}_t}$$

L'expression des coefficients de sensibilité étant (Comte-Bellot, 1998) :

$$S_{\rho u, CVA} = S_{\rho u, CTA} \frac{2a_w}{1+2a_w} \quad S_{\rho u, CTA} \approx 0,25$$

$$S_{\theta_t, CVA} = -S_{\theta_t, CTA} \frac{1}{1+2a_w} \quad S_{\theta_t, CTA} \approx 1$$

on obtient :

$$\frac{\overline{e}^2}{\overline{E}^2} = (S_{\rho u, CVA})^2 \frac{\overline{(\rho u)^2}}{\overline{\rho}^2 \overline{U}^2} + 2 S_{\rho u, CVA} S_{\theta_t, CVA} \frac{\overline{(\rho u) \theta_t}}{\overline{\rho} \overline{U} \overline{\Theta}_t} + (S_{\theta_t, CVA})^2 \frac{\overline{\theta_t^2}}{\overline{\Theta}_t^2}$$

L'application de cette équation à trois inconnues, pour trois coefficients de surchauffe différents ($a_w = 0,30, 0,45$ et $0,62$) conduit à un système que l'on peut résoudre (point noté CVA 3 Eq. Figure 21). En négligeant les fluctuations de température, on obtient alors la forme simplifiée (utilisée pour les autres positions de mesure, Figure 21) :

$$\frac{\overline{e}^2}{\overline{E}^2} = (S_{\rho u, CVA})^2 \frac{\overline{(\rho u)^2}}{\overline{\rho}^2 \overline{U}^2}$$

Le CVA permet de retrouver le flux de masse, rapporté à la contrainte de cisaillement à la paroi, pour $y/\delta = 0,3$ et $0,6$ (Figure 21). Ces résultats présentent un bon accord avec les précédentes mesures (Smits *et al.*, 1983).

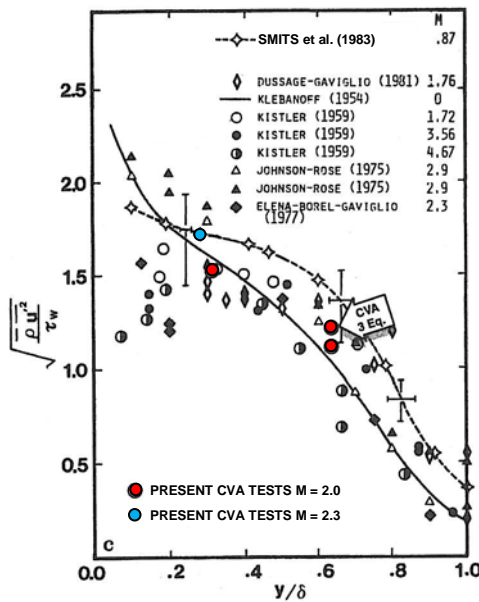


Figure 21 : Flux de masse rapporté à la contrainte de cisaillement à la paroi dans une couche limite en écoulement supersonique (en rouge mesures CEAT, en bleu mesure IRPHE).

III-4 Conclusion

La mise en œuvre du CVA dans une couche limite supersonique, avec une constante de temps du circuit électronique différente de celle mesurée in situ, suivie de la correction du signal lors d'un post-traitement, permet d'obtenir une réponse en fréquence supérieure à celle donnée par le circuit électronique compensé par la constante de temps effectivement mesurée avant l'enregistrement du signal. Cette correction est possible du fait de la fonction de transfert de l'anémomètre qui est parfaitement définie. De plus, il n'est pas nécessaire de modifier la constante de temps avant chaque acquisition, ce qui assure une meilleure productivité des mesures. La comparaison, dans les mêmes conditions d'essais, de la réponse en fréquence du CCA, du CTA et du CVA, montre que ce dernier possède la fréquence de coupure la plus élevée. L'utilisation de trois coefficients de surchauffe du fil permet de discriminer les variances des fluctuations de flux de masse et de température totale. Le flux de masse ainsi mesuré, pour plusieurs positions dans la couche limite supersonique, présente un bon accord avec de précédentes réalisations.

III-5 Références

- COMTE-BELLOT, G.** (1998) Hot-wire anemometry, in *The Handbook of Fluid Dynamics*, Edited by R. W. Johnson, CRC Press, Boca Raton, pp. 34-1–34-29
- COMTE-BELLOT, G., SARMA, G. R., FAURE, Th. M., DUSSAUGE, J. P., DUPONT, P., DEBIÈVE, J. F.** (1999) Performance studies of the constant voltage anemometer in a Mach 2.3 boundary layer, *18th International Congress on Instrumentation in Aerospace Simulation Facilities*, Toulouse (France), June 14-17 1999, pp. 40.1–40.9
- DUSSAUGE, J. P., SMITH, R. W., SMITS, A. J., FERNHOLZ, H., FINLEY, P. J., SPINA, E. F.** (1996) *Turbulent boundary layers in subsonic and supersonic flows*, Edited by W. S. Saric, AGARDograph 335
- KASIERSKI, T.** (1996) *Étude expérimentale d'un nouveau type d'anémomètre à fil chaud*, Travail de Fin d'Études, Institut Polytechnique de Lodz (Pologne)
- SARMA, G. R.** (1991) *Flow rate measuring apparatus*, U.S. Patent No. 5074147

- SARMA, G. R.** (1998) Transfer function analysis of the constant voltage anemometer, *Review of Scientific Instruments*, Vol 69, No. 6, pp. 2385–2391
- SARMA, G. R., COMTE-BELLOT, G., FAURE, Th. M.** (1998) Software corrected hot wire thermal lag for the constant voltage anemometer featuring a constant bandwidth at the selected compensation setting, *Review of Scientific Instruments*, Vol. 69, No. 9, pp. 3223–3231
- SMITS, A. J., HAYAKAWA, K., MUCK, K. C.** (1983) Constant temperature hot-wire anemometer practice in supersonic flows, *Experiments in Fluids*, Vol. 1, pp. 83– 92

IV Analyse de l'écoulement dans un modèle de turbopompe centrifuge

IV-1 Introduction

Cette étude a pour objectif de caractériser l'écoulement dans une évolution technologique, à un seul étage, de la turbopompe d'alimentation en hydrogène liquide du moteur Vulcain, équipant le lanceur Ariane V. Elle fait l'objet d'une action contractuelle avec la Société Européenne de Propulsion (contrat SEP 865.586) et le Centre National d'Études Spatiales. Un modèle à l'air de la turbopompe à l'échelle 1 est caractérisé par plusieurs techniques de mesures stationnaires (sonde cinq trous, capteurs de pression pariétale) et instationnaires (anémométrie à fils chauds croisés, capteurs de pression instationnaire). Ce projet constitue le sujet de stage de DEA de Sylvain Barthet (1997).

L'objectif de cette campagne est double. Dans un premier temps, il s'agit de valider le concept de ce nouveau type de turbopompe. Dans une seconde phase, il s'agit d'affiner la compréhension des phénomènes physiques mis en jeu, en particulier en ce qui concerne l'écoulement en amont de l'inducteur.

IV-2 Dispositif expérimental

IV-2-1 Banc d'essais

Le modèle, nommé Boîtier Composant à l'Air (BCA), est constitué d'une conduite circulaire d'entrée, d'un inducteur axial à 4 aubes, d'une roue centrifuge, comprenant 8 aubes principales et 8 aubes intercalaires, et d'un diffuseur à 11 aubes (Figure 22-a). Le rôle de l'inducteur, utilisé en entrée de pompe, est de protéger les étages haute-pression de l'instationnarité due à la cavitation (Lakshminarayana, 1982). Le BCA est intégré à un banc d'essais en circuit ouvert (Figure 22-b). Une roue dentée est montée sur l'arbre, couplée à un codeur optique, elle fournit un signal carré de 0–5 V d'une période par tour, qui sert à la synchronisation des mesures avec la rotation. L'étude porte principalement sur le débit nominal Q_n , un débit réduit 0,7 Q_n et un sur-débit 1,3 Q_n .

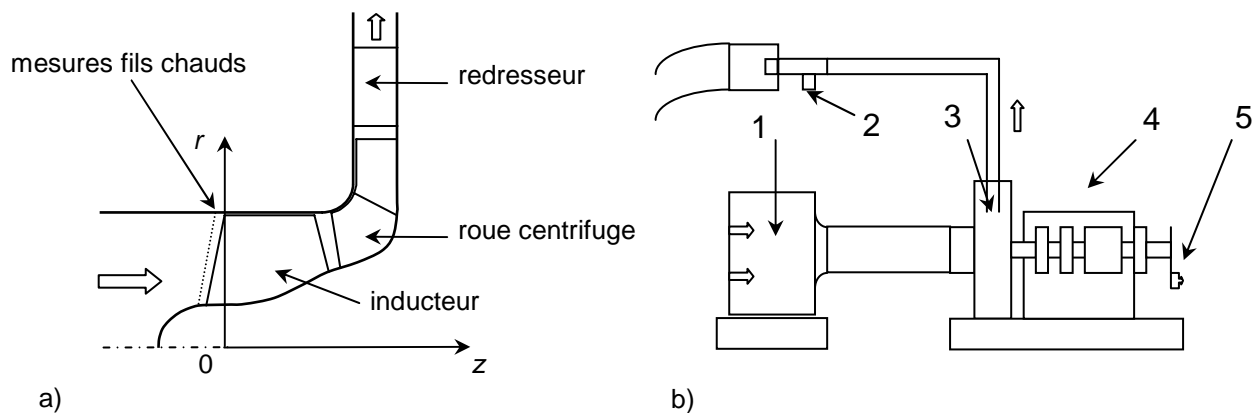


Figure 22 : Banc expérimental : a) composants du BCA et position de mesure par anémométrie à fils chauds croisés, b) vue d'ensemble : 1 - caisson de tranquillisation, 2 - sortie et tube de Venturi, 3 - BCA, 4 - moteur d' entraînement, couple-mètre, arbre et paliers, 5 - système de synchronisation par codeur optique.

IV-2-2 Instrumentation

Une sonde directionnelle à cinq trous, de 1 mm de diamètre, permet d'explorer les trois composantes du champ moyen de vitesse. Elle est commandée en translation et en

rotation autour de son axe par un système de déplacement. Les pressions sont mesurées par des capteurs de pression différentielle de 10 Pa de précision. Sept positions axiales sont prévues pour l'exploration de l'écoulement en amont de l'inducteur. Une sonde à fils chauds croisés permet d'obtenir deux composantes de vitesse instantanée pour une position en amont du bord d'attaque de l'inducteur. Cette sonde est étalonnée angulairement et en amplitude (Browne *et al.*, 1989) et produit une erreur maximum de 0,5% sur la vitesse.

IV-3 Principaux résultats

IV-3-1 Recirculation amont

La pression totale relative pour le débit réduit $0,7 Q_n$ est présentée sur la Figure 23 en amont de l'inducteur, en fonction de la hauteur de veine $H = (r - r_h) / (r_t - r_h)$. Pour les positions les plus en amont, la pression totale est presque constante selon la direction radiale, et légèrement négative, du fait des pertes causées par la chambre de tranquillisation. Plus près de l'inducteur ($z / D \geq -1,5$), on observe une zone de pression totale négative vers 50% de hauteur de veine, due aux pertes générées en amont de l'inducteur et qui sont causées par un décollement de forte énergie. Cette recirculation présente de fortes vitesses axiales et tangentielles au voisinage du carter, elle fait barrage à l'écoulement incident et induit le décollement côté moyeu. La région de transition, entre la zone de basse pression totale et la zone d'écoulement de retour, correspond à un écoulement provenant de l'inducteur et y retournant, sous l'effet de l'écoulement principal (Yokota *et al.* 1999). L'origine de cet écoulement de retour est un tourbillon non-visqueux qui provient de l'inducteur. Ce tourbillon n'est pas lié à un tourbillon de jeu d'extrémité de pale. Cette explication purement potentielle est validée par un calcul d'Euler tridimensionnel (El Ghazzani *et al.* 1992). Cet effet tridimensionnel est fortement couplé à un effet d'incidence le long de l'envergure du bord d'attaque des pales de l'inducteur.

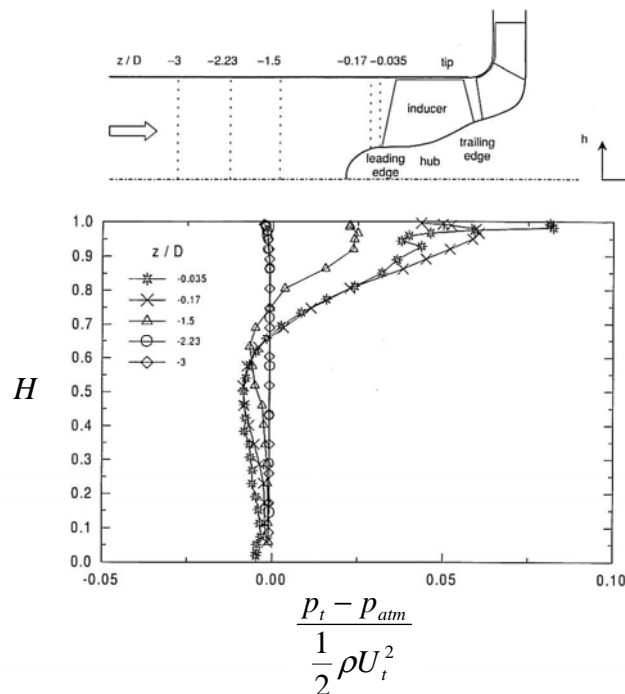


Figure 23 : Répartition de pression totale relative selon la hauteur de veine en amont de l'inducteur pour un débit réduit $0,7 Q_n$.

La limite de la zone de recirculation correspond à la position axiale où la vitesse axiale s'annule pour la première fois à partir du carter (Figure 24). La limite de pré-rotation

correspond à la position où une vitesse tangentielle, sans vitesse axiale négative, est mesurée pour la première fois près du carter. Pour $0,7 Q_n$, la zone de pré-rotation s'étend jusqu'à 1,85 diamètre en amont de l'inducteur. Par extrapolation des mesures, on peut estimer que la zone de pré-rotation atteint 4 à 5 diamètres en amont de l'inducteur pour $0,4 Q_n$. Très près de l'inducteur, il faut également remarquer la présence d'une zone de recirculation jusqu'à $1,2 Q_n$.

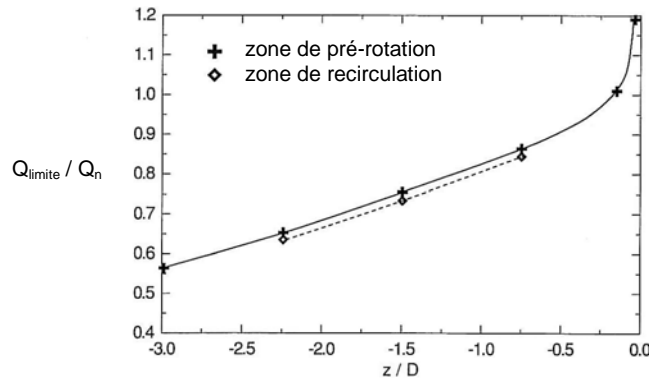


Figure 24 : Longueur axiale de la zone de recirculation en fonction du débit.

IV-3-2 Moyennes de phase

L'exploration, à l'aide d'une sonde à fils chauds croisés, d'une direction radiale juste en amont de l'inducteur, permet de reconstituer le champ de vitesse en effectuant des moyennes en phase avec le signal de synchronisation délivré par le codeur optique (Figure 25 et Figure 26). Pour $1,3 Q_n$ (Figure 25-c), il n'y a pas de vitesse méridienne négative et les quatre aubes de l'inducteur sont clairement identifiées par un déficit de vitesse. La vitesse relative est uniforme (Figure 26-c), les gradients azimuthaux de vitesse méridienne étant corrélés aux angles relatifs β (Bario *et al.*, 2003). Il n'y a donc pas de blocage en termes de vitesse relative. Pour le débit nominal Q_n (Figure 25-b), la vitesse méridienne présente une région quasi-annulaire de vitesse négative au voisinage du carter, la recirculation atteint entre 8% et 10% de la hauteur de veine selon l'azimut. Le débit réduit $0,7 Q_n$ (Figure 25-a) présente un fort gradient de vitesse méridienne selon la direction circonférentielle. La recirculation atteint alors entre 8% et 20% de la hauteur de veine selon l'azimut. Les variances des fluctuations de vitesse tangentielle sont plus fortes que les variances des fluctuations de vitesse méridienne et les plus forts niveaux sont relevés près de la tête des aubes (Bario *et al.*, 2003). De même, la tension de cisaillement est très élevée à la frontière de la zone de recirculation. Cette zone correspond au point de cavitation dans un inducteur d'une pompe à liquide.

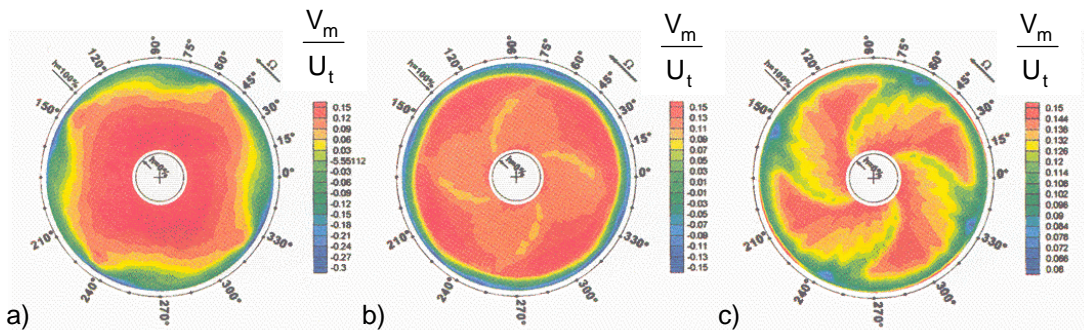


Figure 25 : Vitesse méridienne adimensionnée mesurée en amont du rotor pour 3 débits : a) $0,7 Q_n$, b) Q_n , c) $1,3 Q_n$.

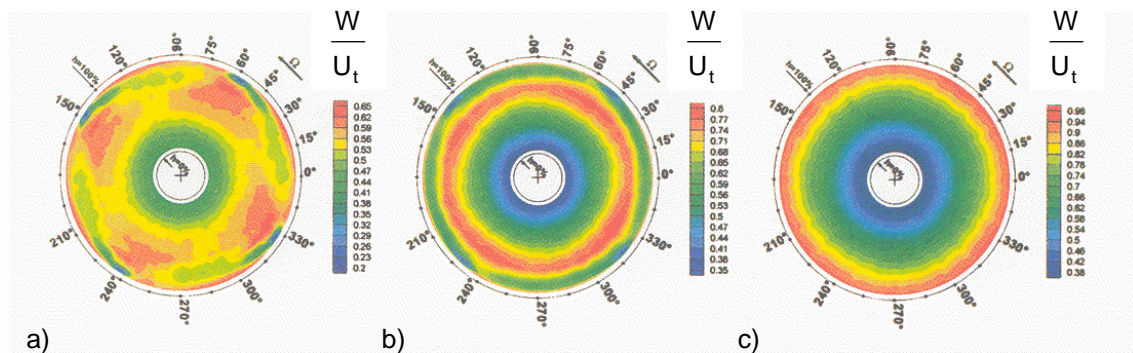


Figure 26 : Vitesse azimutale adimensionnée mesurée en amont du rotor pour 3 débits : a) $0,7 Q_n$, b) Q_n , c) $1,3 Q_n$.

IV-4 Conclusion

L'utilisation de sondes directionnelles, stationnaires ou instationnaires, permet de comprendre les phénomènes physiques qui ont lieu en amont de l'inducteur, et de valider ce nouveau modèle de turbopompe. Un écoulement de retour, marqué par de fortes vitesses tangentielles, affecte la zone proche du carter et agit comme un obstacle à l'écoulement axial incident. Une zone de pré-rotation de l'écoulement est aussi présente en amont de l'inducteur, et sa longueur est supérieure à celle de la recirculation. Cette dernière n'est pas due à un écoulement de jeu de pale, mais trouve son origine dans sa nature tridimensionnelle couplée à un effet d'incidence le long de l'envergure du bord d'attaque des pales de l'inducteur. Il n'y a pas d'effet de blocage en termes de réduction de la vitesse relative. Les écarts-types des fluctuations de vitesse azimutale sont supérieurs à ceux de vitesse méridienne, particulièrement au voisinage du carter. Il semble également qu'une remontée de l'information aval, provenant du rouet ou du diffuseur de sortie, affecte la vitesse tangentielle au débit $1,3 Q_n$.

IV-5 Références

- BARIO, F., FAURE, Th. M., JONDEAU, E., NORMAND, J. L., N'GUYEN DUC J. M.** (2003) Analysis of inducer recirculating flow, *Journal of Propulsion and Power*, Vol. 19, No. 4, pp. 521–528
- BARTHET, S.** (1997) *Contribution à la compréhension et à la connaissance de l'écoulement au sein d'une turbopompe de type cryogénique*, Rapport de DEA de Thermique et Énergétique, École Centrale de Lyon
- BROWNE, L. W. B., ANTONIA, R. A., CHUA, L. P.** (1989) Calibrating of X-probes for turbulent flow measurements, *Experiments in Fluids*, Vol. 7, No. 3, pp. 201–208
- EL GHAZZANI, E. M., BOIS, G., GEAI, P., LEBŒUF, F.** (1992) Three-dimensional inviscid flow computations in a spatial turbopump inducer using a distributed loss model, *37th International Gas Turbine and Aeroengine Congress and Exposition*, Cologne, Germany, June 1-4, 1992, ASME Paper 92GT65, 9 p.
- LAKSHMINARAYANA, B.** (1982) Fluid dynamics of inducers—A review, *Journal of Fluids Engineering*, Vol. 104, No. 4, pp. 411–427
- YOKOTA, K., KURAHARA, K., KATAOKA, D., TSUJIMOTO, Y., ACOSTA, A. J.** (1999) A study of swirling backflow and vortex structure at the inlet of an inducer, *Japanese Society of Mechanical Engineers International Journal, Series B*, Vol. 42, No. 3, pp. 451–459

V Analyse de l'écoulement dans un étage de compresseur axial

V-1 Introduction

L'objectif de cette étude est d'obtenir des données expérimentales de l'écoulement dans une configuration de référence d'étage de compresseur axial, afin d'améliorer la compréhension des phénomènes physiques mis en jeu. L'exploration est d'abord menée avec un vélocimètre laser Doppler (LDV) bi-composantes. L'extension du système à une troisième composante est réalisée dans un second temps pour permettre des mesures coïncidentes. Une méthode permettant l'estimation du tenseur de Reynolds à partir de mesures non coïncidentes est développée dans le cadre de ce projet.

Cette étude est menée dans le cadre du Consortium Industrie Recherche en Turbomachines (CIRT) et la thèse de Nicolas Vassilieff (2001) ainsi que du contrat SNECMA-TM-EDF 764 488 Rc.

V-2 Dispositif expérimental

V-2-1 Banc d'essais

Le compresseur axial mono-étage (CME2) est constitué d'un rotor de 30 aubes et d'un stator de 40 aubes. La vitesse de rotation du rotor est de $6\ 330 \pm 14 \text{ tr} \cdot \text{min}^{-1}$ et le débit nominal du compresseur est de $10,5 \pm 0,1 \text{ kg} \cdot \text{s}^{-1}$, il fournit un rapport de pression totale $p_{t,2} / p_{t,1} = 1,15$. Les différents éléments du banc d'essais sont présentés sur la Figure 27. La position d'une aube est obtenue au moyen d'un codeur optique placé sur l'arbre de rotation, qui délivre un signal périodique d'amplitude comprise entre 0 et 5 V.

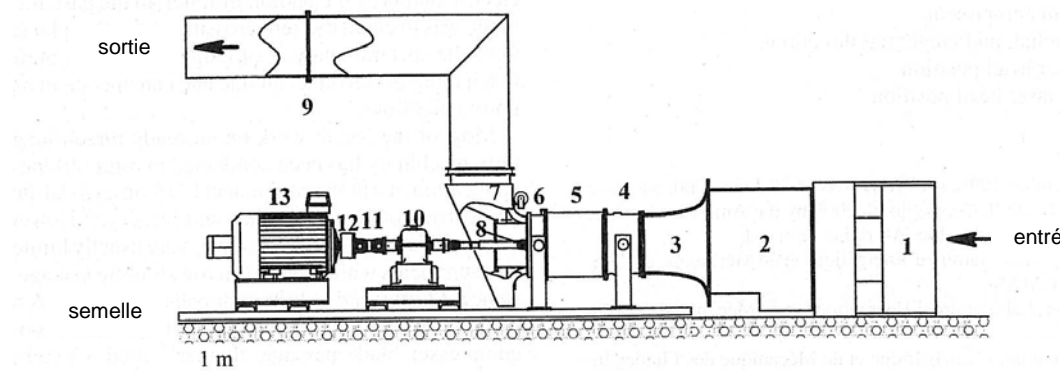


Figure 27 : Banc d'essais : 1 - filtres d'entrée, 2 - chambre de tranquillisation, 3 - convergent, 4 - palier amont, 5 - étage de compresseur, 6 - palier aval, 7 - vanne de réglage du débit, 8 - cardan haute-vitesse, 9 - diaphragme, 10 - multiplicateur, 11 - cardan basse vitesse, 12 - limiteur de couple, 13 - moteur d'entraînement (180 kW).

V-2-2 Instrumentation

Un vélocimètre laser Doppler à deux composantes utilise les longueurs d'onde bleue (488 nm) et verte (514,5 nm) d'un laser argon-ion Spectra Physics Innova 300 de 5 W de puissance. Il fonctionne en rétrodiffusion. Pour chaque composante couleur, un faisceau est décalé en fréquence à 40 MHz, le demi-angle au sommet formé par chaque paire de faisceaux est de $6,77^\circ$ et le volume de mesure a une longueur de 0,8 mm et un diamètre et de 0,1 mm. Afin d'explorer un canal inter-aubes, la tête laser est placée sur un bras robotisé Staübli à 6 degrés de liberté, qui permet d'atteindre n'importe quel point dans le compresseur (Figure

28). Les limitations imposées par le masquage de certains points de mesure par les aubages sont résolues en adaptant l'orientation de la tête laser. L'ensemencement s'effectue dans le caisson de tranquillisation 20 cm en amont du convergent, avec un générateur de fumée qui produit des gouttelettes de diamètre moyen 1,068 μm . Deux mesures successives, suivant deux orientations différentes de la tête laser, permettent de reconstruire les trois composantes du champ de vitesse (Faure *et al.*, 2001). Les signaux laser sont échantillonnés par une carte 14 bits jusqu'à une fréquence de 10 000 bursts par seconde, l'analyse de la fréquence Doppler s'effectuant avec des analyseurs à transformée de Fourier rapide (burst signal analyzer, BSA). Les deux composantes de vitesse ne sont pas enregistrées en filtre de coïncidence et le nombre de données validées est de 3 000, ce qui donne une erreur de mesure relative de 0,72% sur le champ moyen (Strazisar, 1986). L'enregistrement synchronisé du signal de rotation permet d'identifier la phase de chaque mesure.

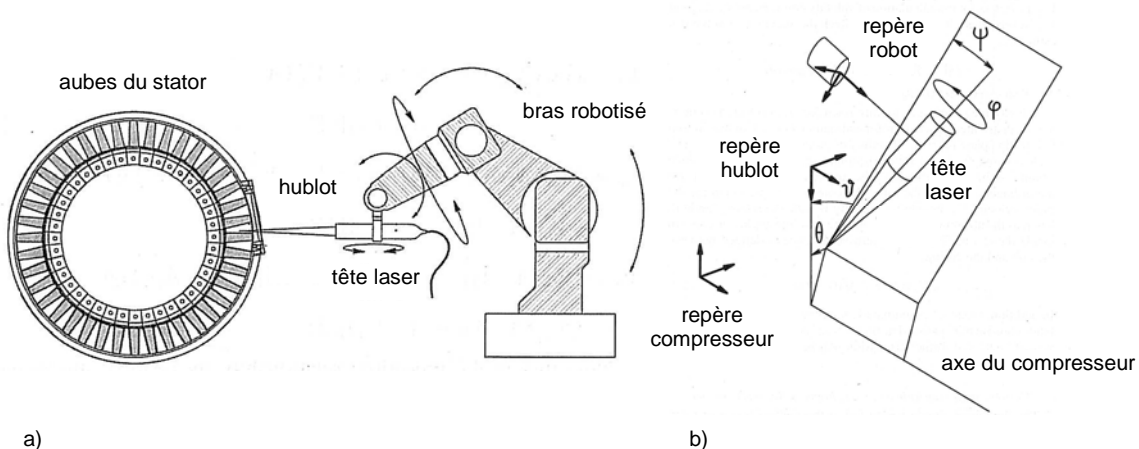


Figure 28 : Orientation du laser : a) montage du bras robotisé sur le banc d'essais,
b) repérage de la tête laser par rapport au repère compresseur.

V-3 Principaux résultats

V-3-1 Champ de vitesse dans le rotor

Le champ de vitesse est complètement accessible à l'intérieur du rotor, du fait de la forte vitesse de rotation et l'utilisation de BSA, qui n'engendrent pas de détection de vitesses erronées. En effet, l'éclairage dû au passage des pales est rejeté par les analyseurs. Le champ moyen de vitesse relative, en phase avec la rotation du rotor, est présenté sur la Figure 29 dans un canal inter-aubes, pour différentes hauteurs de veine H . On observe le blocage potentiel des pales du rotor à $x / c_r = -0,059$ ainsi qu'une augmentation régulière de la vitesse avec l'envergure, causée par l'augmentation de la vitesse d'entraînement selon la hauteur de pale. À l'intérieur du rotor, à $x / c_r = 0,12$, la vitesse relative W augmente linéairement entre l'intrados et l'extrados. La vitesse devient pratiquement linéaire entre l'intrados et l'extrados pour $x / c_r = 0,63$ et on observe le sillage des pales en sortie du rotor à $x / c_r = 0,80$. Le plus large sillage observé, pour $H = 0,90$, est probablement dû à la présence d'un tourbillon de jeu, créé côté extrados par le gradient de pression et convecté en aval. Une analyse similaire de l'écoulement dans un repère fixe à l'intérieur du stator met en évidence la décélération entre l'entrée et la sortie (Faure *et al.*, 2001).

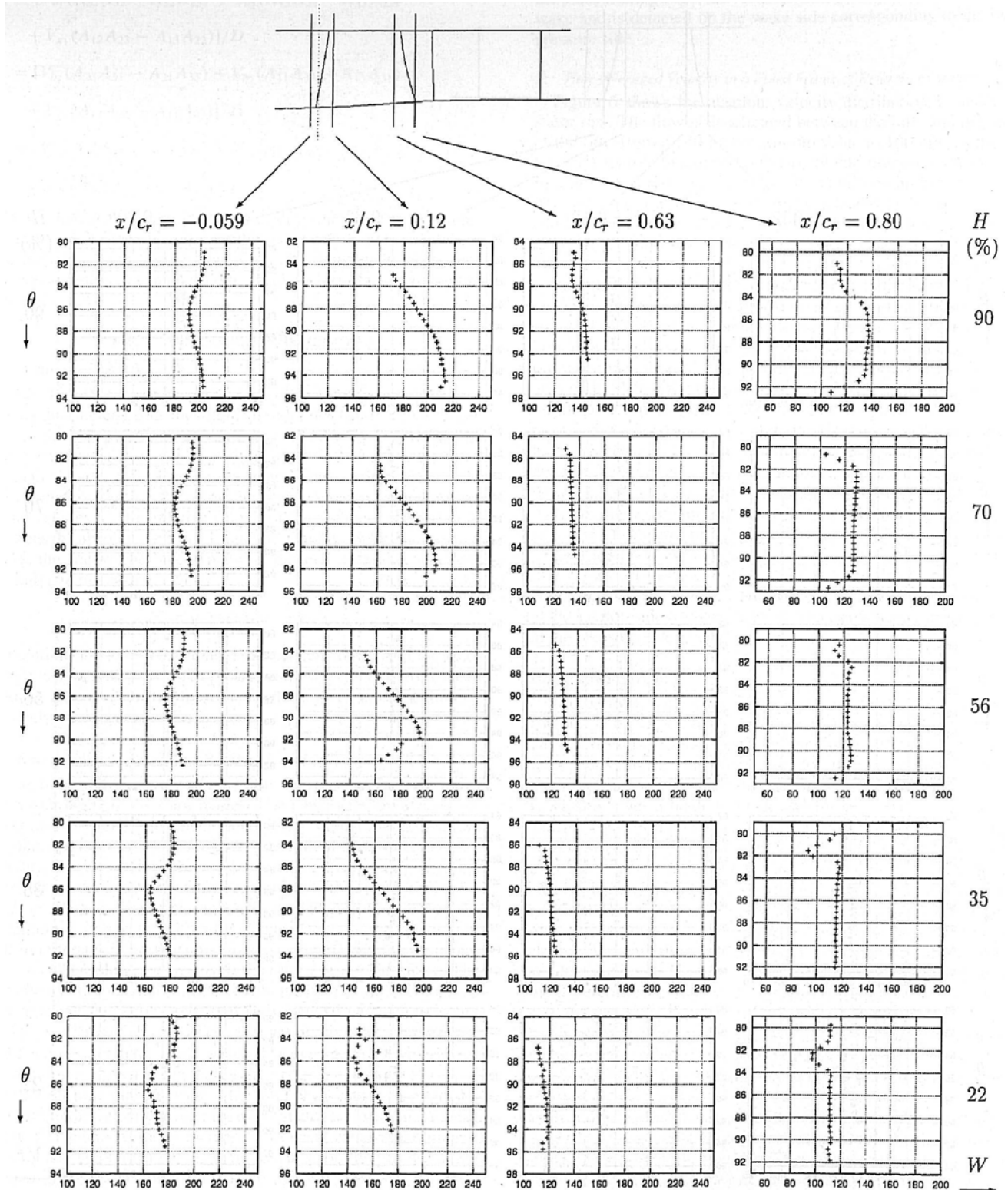


Figure 29 : Répartition tangentielle (en degrés) de la vitesse relative W dans un repère tournant, pour quatre positions axiales dans le rotor et cinq positions selon l'envergure.

V-3-2 Vitesse instationnaire dans un canal inter-aubes stator

Afin de quantifier l'instationnarité globale de l'écoulement, le canal inter-aubes du rotor est décomposé en 24 phases successives, ce qui fournit un intervalle de temps de $1,32 \cdot 10^{-5}$ s et une précision angulaire de $0,5^\circ$. Afin de visualiser les aspects tridimensionnels

de l'écoulement, trois plans sont définis dans l'étage de compression (Figure 30) : un plan A qui s'étend du moyeu au carter et de l'entrée du rotor à la sortie du stator en suivant la cambrure du stator, un plan B entre le rotor et le stator à $x / c_r = 0,87$ et couvrant un passage aube à aube du stator, et un plan C situé à 0,31 hauteur de veine. Six phases successives permettent l'observation de l'évolution temporelle de la vitesse axiale lors du passage d'un canal inter-aubes du rotor. La région bleue dans le plan A du stator correspond à l'accélération de l'écoulement côté extrados. On observe dans le plan B l'évolution du sillage d'une aube du rotor, correspondant à un déficit de vitesse à $35 \text{ m}\cdot\text{s}^{-1}$ ainsi que la dynamique du tourbillon de passage en tête du rotor. Il y a une forte interaction entre ce tourbillon et le sillage d'une aube du rotor.

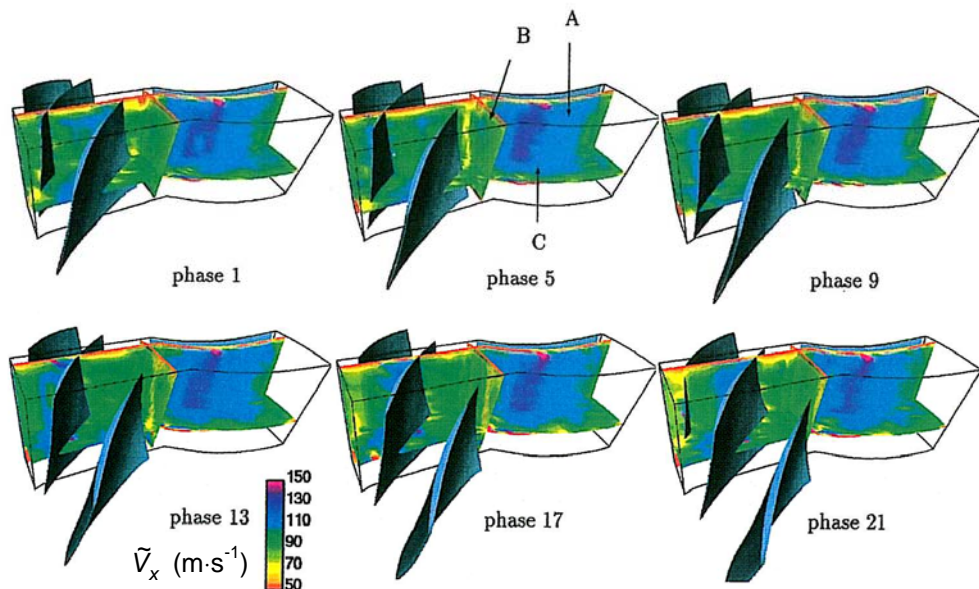


Figure 30 : Répartition de la vitesse axiale absolue pour six phases différentes de passage d'un canal inter-aubes du rotor.

V-3-3 Interaction rotor-stator

Les sillages des aubes du rotor sont convectés par l'écoulement et hachés par les aubes du stator. Ils demeurent cependant visibles jusqu'à la sortie du stator. On observe, dans un plan aube à aube du stator situé à 50% de hauteur de veine, trois sillages pour chaque phase (Figure 31, flèches 1, 2 et 3 pour la phase 5). Leur interaction avec les couches limites des aubes du stator créent de fortes structures instationnaires dans l'écoulement, qui entraînent des déphasages entre les sillages du rotor et la sortie du stator, et une variation périodique de la charge aérodynamique du stator. La zone orange de vitesse négative correspond à un décollement quasi-stationnaire côté extrados au voisinage du bord de fuite.

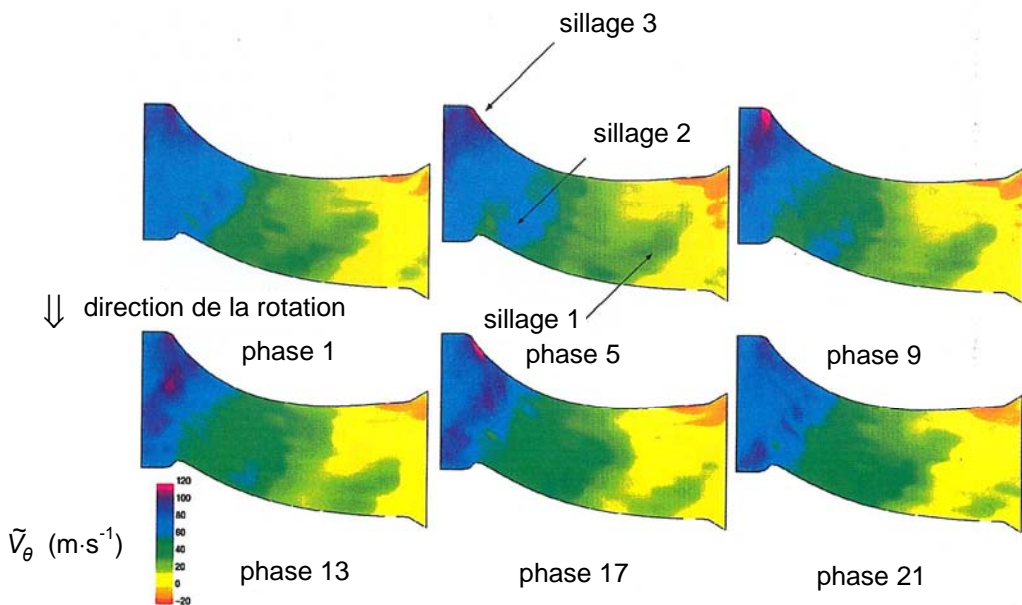


Figure 31 : Répartition de la vitesse azimutale en phase avec la rotation du rotor à l'intérieur du stator dans un plan situé à $H = 0,50$ pour six phases différentes.

V-3-4 LDV trois composantes en coïncidence

L'intégration d'une seconde tête, utilisant la longueur d'onde jaune-verte (532 nm) d'un laser YAG continu Coherent Millenia de puissance 5 W, constitue un système LDV à trois composantes. Les deux têtes sont montées sur un bras robotisé, l'angle formé entre leurs axes optiques $2\chi = 30^\circ$ (Figure 32) permet d'obtenir une bonne résolution de la vitesse radiale pour les applications aux turbomachines (Ristic *et al.*, 1999). La superposition du volume de mesure de cette troisième composante, aux volumes de mesure des deux composantes du laser argon-ion, permet l'acquisition de données coïncidentes. Cependant, ce réglage et particulièrement délicat et le taux de validation des données chute rapidement. Certaines parties de l'écoulement deviennent complètement inaccessibles à la mesure et il est pratiquement impossible d'explorer le rotor. Dans le stator, les résultats obtenus par une unique mesure coïncidente sont en accord avec ceux obtenus par la LDV deux composantes avec deux orientations de la tête laser (Vassilieff, 2001).

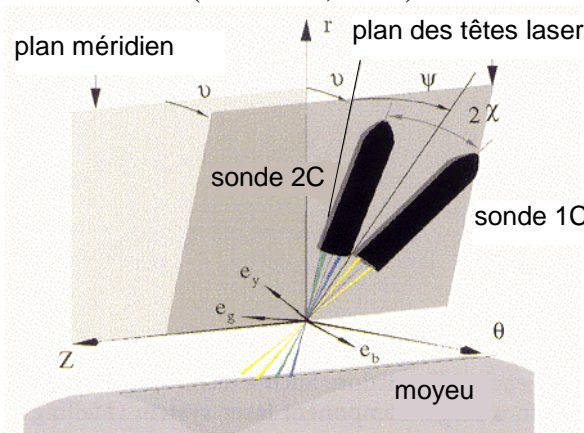


Figure 32 : Montage de vélocimétrie laser Doppler à 3 composantes

V-3-5 Évaluation du tenseur de Reynolds par LDV trois composantes non coïncidente

La confrontation de résultats expérimentaux à des codes de simulation numérique turbulents repose sur la comparaison du champ moyen et des six composantes du tenseur de

Reynolds. Du point de vu des applications expérimentales en turbomachines, comme nous l'avons observé précédemment, il est souvent difficile d'obtenir des mesures coïncidentes sur les trois composantes de vitesse dans toute la veine. C'est pour cela qu'une méthode d'évaluation de ce tenseur reposant sur quatre mesures tridimensionnelles non-coïncidente est spécialement développée dans le cadre de cette étude (Faure *et al.* 2004). Les quatre positions de la tête laser sont :

- position 1 : $\vartheta = 0$ $\psi = -\chi$ $\varphi = 0$
- position 2 : $\vartheta = 0$ $\psi = \chi$ $\varphi = 0$
- position 3 : $\vartheta = -\chi$ $\psi = -\chi$ $\varphi = 0$
- position 4 : $\vartheta = \chi$ $\psi = -\chi$ $\varphi = 0$

Comme les axes des composantes couleurs ne sont pas des axes orthogonaux entre eux, les orientations successives fournissent une résolution angulaire maximum dans le positionnement de la sonde, et une erreur minimale dans l'estimation de la vitesse. Si l'on décompose la vitesse en une valeur moyenne (stationnaire ou en phase avec la rotation du rotor) et une valeur fluctuante, il est alors possible d'écrire les composantes du tenseur de Reynolds en fonction des variances des fluctuations dans le repère couleur. Chaque position de mesure fournit les trois composantes de la vitesse moyenne. Néanmoins, pour minimiser l'incertitude, les composantes moyennes n'utilisent que les deux premières positions de la sonde laser :

$$\bar{U}_z = \frac{\bar{U}_{v,1} + \bar{U}_{j,2}}{2} \quad \bar{U}_\theta = \frac{\bar{U}_{b,1} + \bar{U}_{b,2}}{2} \quad \bar{U}_r = \frac{\bar{U}_{v,2} + \bar{U}_{j,1}}{2 \sin 2\chi}$$

Les composantes du tenseur de Reynolds sont alors :

$$\begin{aligned} \overline{u_z^2} &= \frac{\overline{u_{v,1}^2} + \overline{u_{j,1}^2}}{2} & \overline{u_\theta^2} &= \frac{\overline{u_{b,1}^2} + \overline{u_{b,2}^2}}{2} & \overline{u_r^2} &= \frac{\overline{u_{j,1}^2} + \overline{u_{v,2}^2} - \cos^2 2\chi (\overline{u_{v,1}^2} + \overline{u_{j,2}^2})}{2 \sin^2 2\chi} \\ \overline{u_z u_r} &= \frac{\overline{u_{v,2}^2} - \overline{u_{j,1}^2}}{4 \sin 2\chi \cos 2\chi} & \overline{u_r u_\theta} &= \frac{\overline{u_{b,4}^2} - \overline{u_{b,3}^2}}{4 \sin \chi \cos \chi} & \overline{u_\theta u_z} &= \frac{\overline{u_{j,4}^2} - \overline{u_{j,3}^2} + 4 \cos^2 \chi \sin^2 \chi (\overline{u_{b,4}^2} - \overline{u_{b,3}^2})}{8 \cos \chi \sin^2 \chi (\cos^2 \chi - \sin^2 \chi)} \end{aligned}$$

Si l'incertitude de mesure sur la vitesse moyenne des composantes couleurs est constante et vaut η , et que l'incertitude de la variance des composantes couleurs vaut ϵ^2 , alors il est possible de calculer l'erreur de mesure absolue (Tableau 1).

Tableau 1 : Erreurs de mesure absolues des composantes de la vitesse moyenne et du tenseur de Reynolds.

quantité	\bar{U}_z	\bar{U}_θ	\bar{U}_r	$\overline{u_z^2}$	$\overline{u_\theta^2}$	$\overline{u_r^2}$	$\overline{u_z u_r}$	$\overline{u_r u_\theta}$	$\overline{u_\theta u_z}$
erreur	η	η	2η	ϵ^2	ϵ^2	$7\epsilon^2$	$1,15\epsilon^2$	$2\epsilon^2$	$5,58\epsilon^2$

La comparaison de la vitesse axiale moyenne et des variances des fluctuations de vitesse axiale est présentée Figure 33 et Figure 34.

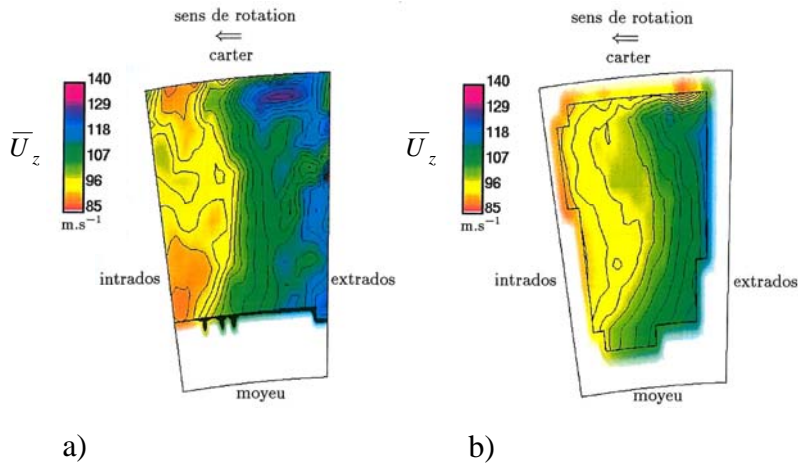


Figure 33 : Comparaison de la vitesse axiale moyenne obtenue sans filtre de coïncidence par a) une double mesure 2D et b) une quadruple mesure 3D.

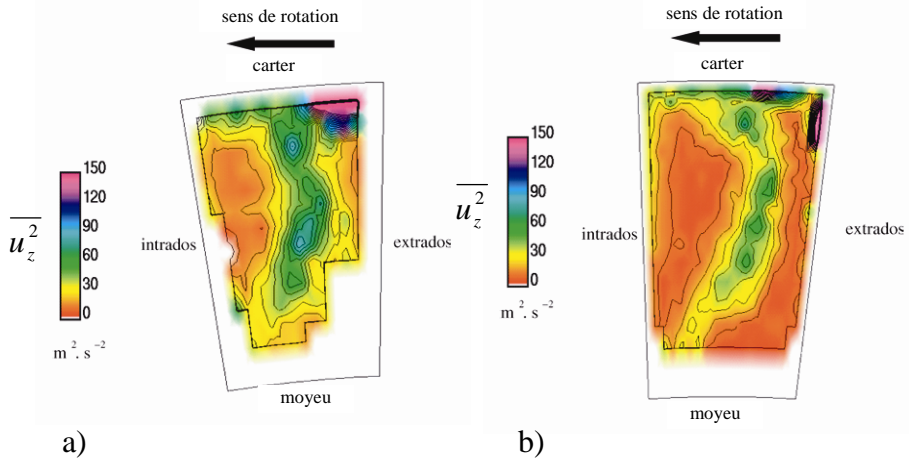


Figure 34 : Comparaison de la variance des fluctuations de vitesse axiale obtenue par a) une quadruple mesure sans filtre de coïncidence et b) une mesure avec filtre de coïncidence.

V-4 Conclusion

Un système LDV deux composantes, implanté sur un bras robotisé à six degrés de liberté, permet, par une double acquisition selon deux directions, la mesure des trois composantes de vitesse dans l'étage de compresseur, en limitant les contraintes du masquage des aubes. L'utilisation des BSA est intéressante dans le sens où il n'est pas nécessaire de couper les faisceaux laser pendant le passage des pales. L'extension de la LDV à une troisième composante fournit, en une seule mesure, les trois composantes de vitesse et le tenseur de Reynolds lors de l'acquisition des bursts Doppler en filtre de coïncidence. La réalisation de mesures coïncidentes étant souvent difficiles en environnement turbomachine, une méthode est développée pour obtenir les mêmes quantités sans filtre de coïncidence, mais en effectuant quatre mesures successives selon quatre angles différents.

Ces résultats permettent d'appréhender la dynamique instationnaire de l'écoulement en phase avec la rotation du rotor. Les couches limites du carter sont observées dans tout l'étage. Le tourbillon de jeu créé par le gradient de pression sur les pales du rotor est défléchi et interagit avec les sillages des aubes. Ces sillages sont convectés par l'écoulement à l'intérieur du stator. Pour une phase donnée, trois sillages sont identifiés dans le canal inter-

aubes du stator et leur interaction avec les parois engendre des variations périodiques de la charge aérodynamique du stator. La vélocimétrie laser Doppler à trois composantes reste donc une méthode de mesure performante pour les applications en turbomachine.

V-5 Références

- FAURE, Th. M., MICHON, G. J., MITON, H., VASSILIEFF, N.** (2001) Laser Doppler anemometry measurements in an axial compressor stage, *Journal of Propulsion and Power*, Vol. 17, No .3, pp. 481–491
- FAURE, Th. M., MITON, H., VASSILIEFF, N.** (2004) A laser Doppler anemometry technique for Reynolds stresses measurement, *Experiments in Fluids*, Vol. 37, No. 3, pp. 465–467
- STRAZISAR, A. J.** (1986) Laser fringe anemometry for aero engine components, *Advanced Instrumentation for Aero Engine Components*, CP-399, AGARD, pp. 6.1–6.32
- RISTIC, D., LAKSHMINARAYANA, B., CHU, S.** (1999) Three-dimensional flowfield downstream of an axial-flow turbine rotor, *Journal of Propulsion and Power*, Vol. 15, pp. 334–344
- VASSILIEFF, N.** (2001) *Analyse de l'écoulement dans un compresseur axial par vélocimétrie laser tridimensionnelle*, Thèse de Doctorat de Mécanique de l'Université Pierre et Marie Curie, Paris VI

VI Écoulement dans un modèle d'échangeur thermique

VI-1 Introduction

L'objectif général de cette étude, menée en collaboration avec l'Institut de Physique Nucléaire d'Orsay (IPNO), porte sur les problèmes de comportement thermomécanique des structures soumises à des flux de puissance élevés. Elle a pour cadre la caractérisation de l'écoulement tridimensionnel dans un nouveau concept de composant d'échangeur thermique, conçu pour le développement du Radio Frequency Quadrupole (RFQ) de l'Injecteur de Protons à Haute Intensité (IPHI). L'échangeur doit évacuer une puissance totale de 1 MW. Ce projet est également le thème du stage de maîtrise de Magali Sato (2003).

VI-2 Dispositif expérimental

VI-2-1 Banc d'essais

Le modèle d'échangeur présente une géométrie tridimensionnelle (Figure 35-a) avec un conduit d'entrée, un collecteur d'entrée permettant l'alimentation de six canaux parallèles de 44 mm de longueur, un collecteur de sortie et un conduit de sortie. Le diamètre intérieur des canaux parallèles est de 4 mm et celui des conduits et des collecteurs est de 8 mm. Les canaux et les collecteurs sont dans un même plan, tandis que le conduit d'entrée forme un angle de 25° et le conduit de sortie un angle de 155° par rapport à ce plan. Une maquette à l'échelle 1 est réalisée afin d'explorer chacun des canaux et de déterminer la répartition de débit et les caractéristiques turbulentes (Figure 35-b). L'écoulement dans l'échangeur correspond à un nombre de Reynolds, construit sur la vitesse débitante et le diamètre d'entrée, compris entre 7 960 et 39 790. La structure de la maquette est en aluminium et les canaux sont réalisés en verre de 1 mm d'épaisseur pour permettre un accès optique aisément. Un canal supplémentaire contient une mire pour l'étalonnage de la caméra et le calcul de son grandissement (Figure 35-b, à gauche). Un second canal isolé (Figure 35-b, à droite) permet d'effectuer les réglages préliminaires du circuit hydraulique et de tester l'ensemencement (Sato, 2003). La maquette est alimentée par une pompe radiale mono-étage de vitesse de rotation nominale de $2\,850 \text{ tr}\cdot\text{min}^{-1}$ permettant d'obtenir un débit maximum de $15 \text{ l}\cdot\text{min}^{-1}$. Deux rotamètres permettent de régler le débit d'alimentation.

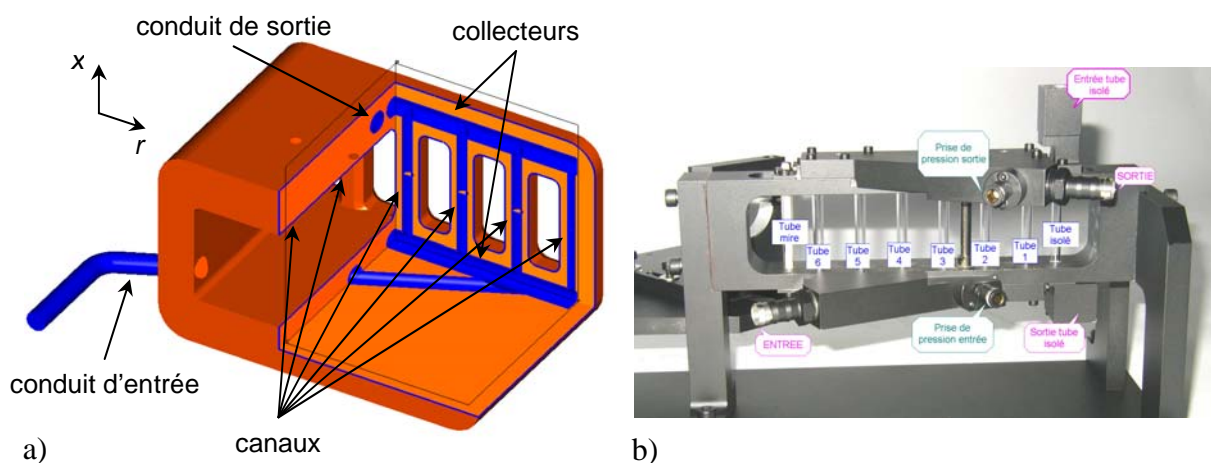


Figure 35 : a) Écorché du modèle de composant d'échangeur thermique (la veine fluide est en bleu), b) vue de la maquette permettant l'exploration des six canaux par PIV.

VI-2-2 Instrumentation

Un laser YAG Quantel Twins Ultra à deux sources, qui émettent des éclairs d'une durée de 6 ns à 532 nm et de 30 mJ par impulsion, génère une nappe laser de 0,25 mm d'épaisseur. L'enregistrement des images s'effectue avec une caméra 8 bits de résolution 768×484 pixels et de distance focale 25 mm. L'ensemble est monté sur une platine de déplacement et permet l'exploration successive des six canaux, en maintenant la nappe laser perpendiculaire au plan d'observation, avec une précision de 1 μm dans le déplacement axial (Figure 36). Ce plan laser forme un angle de 45° par rapport au plan de six canaux. La synchronisation entre l'émission laser et l'enregistrement des images de la caméra s'effectue par un boîtier Quantel DPS 01 qui permet de gérer l'intervalle de temps Δt entre les deux impulsions laser. L'ensemencement de l'écoulement est réalisé avec des sphères de verre creuses argentées de 10 μm de diamètre.

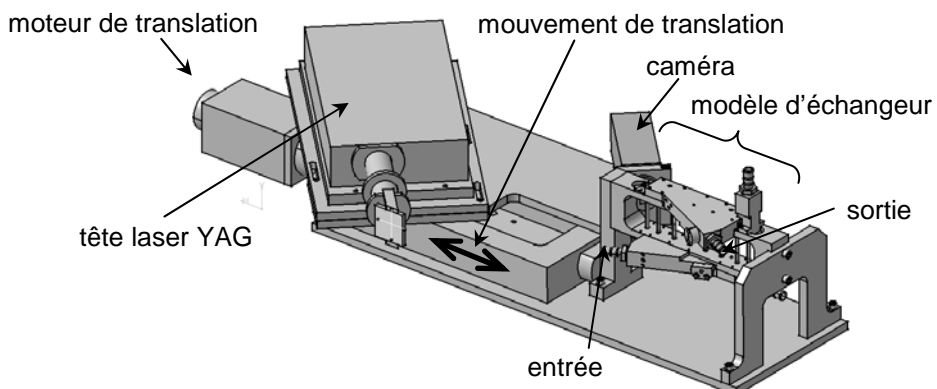


Figure 36 : Montage du laser YAG et de la caméra sur la platine de déplacement de la maquette d'essais.

VI-2-3 Algorithme PIV

Une attention particulière est portée à la qualité des images utilisées pour le traitement par l'algorithme de PIV. On applique ainsi, un prétraitement des images qui permet d'éliminer toute réflexion parasite sur la paroi ou liée au dépôt de particules. Différentes méthodes de soustraction d'une image de référence sont testées (Faure *et al.*, 2003, Figure 37). Par ailleurs, la présence d'un double dioptrre entre, d'une part l'air et le verre, puis entre le verre et l'eau, induit une distorsion des distances et des déplacements de particules selon la direction radiale, qui est corrigée lors du post-traitement des données (Sato, 2003).

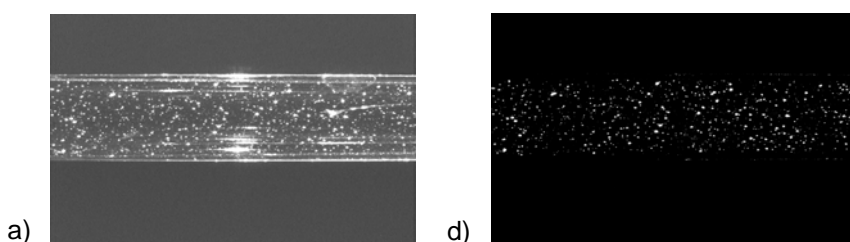


Figure 37 : Prétraitement des images : a) image brute et b) image après soustraction d'une image de référence.

Le traitement PIV des images utilise un algorithme avancé, le flot optique par programmation dynamique orthogonal (Quénod, 1992, Quénod *et al.*, 1998). Cette méthode est fondée sur la recherche itérative d'un alignement global d'images sous contraintes de régularités et de continuités (minimisation d'une norme de Minkowski). Pour cela, le

problème est ramené à un problème monodimensionnel et ne considère le déplacement que selon une direction dans une bande d'analyse. La solution en deux dimensions s'effectue par résolution successive et itérative dans des bandes d'analyse orthogonales de plus en plus petites. Les principaux avantages de cette méthode précise et robuste sont les suivants :

- elle peut être utilisée sur des séquences de deux ou plusieurs images ;
- elle permet d'obtenir un champ de déplacement dense avec une résolution d'un vecteur par pixel d'image ;
- elle fournit un champ de vitesse continu et différentiable spatialement, particulièrement adapté aux écoulements qui présentent de forts gradients ;
- elle peut être généralisée à la PIV stéréoscopique à trois composantes.

Ses inconvénients principaux sont :

- compte-tenu de la densité d'information, le temps de calcul et la capacité de stockage des données ;
- le nombre important de paramètres à ajuster en fonction du type de configuration.

Afin d'optimiser les mesures PIV, on choisit un déplacement moyen de 10 pixels entre deux images, ce qui correspond, selon les débits, à des intervalles de temps entre deux éclairages laser compris entre 84 et 422 μs . Le choix des paramètres retenus, dans l'algorithme de flot optique par programmation dynamique orthogonale, conduit à une interrogation sub-pixel et une incertitude sur les déplacements de $1/32^{\circ}$ de pixel, soit une erreur relative en vitesse de 0,31%. Les résultats expérimentaux sont obtenus à partir de l'enregistrement de 600 images qui fournissent 300 champs de vitesse dans chacun des canaux. La précision sur le champ moyen de vitesse est alors de $0,1 \text{ m}\cdot\text{s}^{-1}$ ce qui correspond à un maximum d'erreur relative de 2,5%. Pour les moments statistiques d'ordre 2, la précision est estimée à $0,015 \text{ m}^2\cdot\text{s}^{-2}$ et correspond à un maximum d'erreur relative de 5%.

VI-3 Principaux résultats

VI-3-1 Champ moyen de vitesse

La caméra permet l'observation de la partie centrale de chaque canal (21 mm). Dans les figures suivantes l'origine de l'axe des abscisses est donc fixée à 11 mm en aval du raccordement entre le collecteur d'entrée et chacun des canaux, l'origine radiale étant fixée au centre de ceux-ci. Compte-tenu de la géométrie tridimensionnelle de l'échangeur, la répartition de vitesse axiale n'est pas uniforme et présente une forte asymétrie radiale entre les six canaux (Figure 38). Les plus grandes vitesses sont mesurées dans le canal 2, situé en face du conduit d'entrée, et les plus faibles dans le canal 3. On note une augmentation relative de la vitesse dans le canal 5, situé face au conduit de sortie. Le fort gradient de vitesse axial dans le canal 2 montre que l'écoulement n'est pas établi (Faure *et al.*, 2006). Comme le coefficient de transfert thermique est proportionnel au gradient de vitesse axial en paroi, et comme par ailleurs la vitesse est nulle à la paroi, au plus la vitesse est forte, au plus son gradient est important. Par conséquent le canal 2 présente le plus fort transfert thermique.

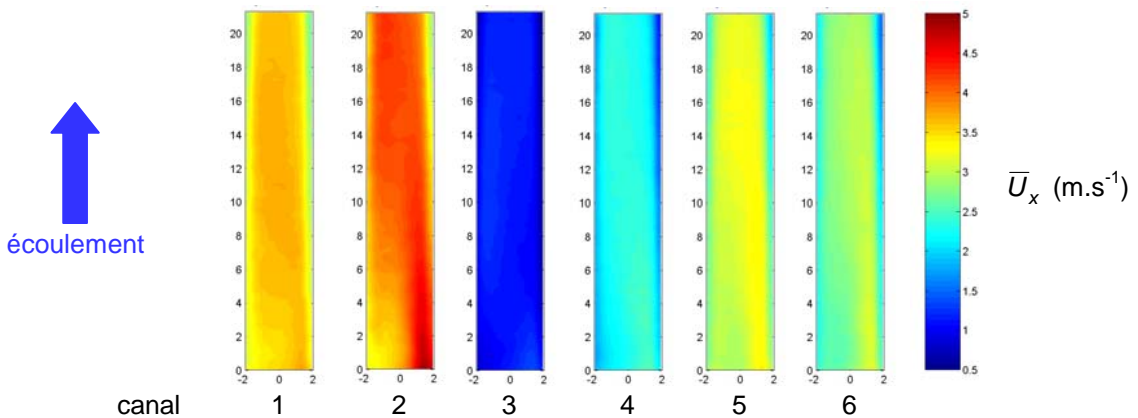


Figure 38 : Vitesse moyenne axiale mesurée par PIV dans chacun des canaux pour un débit de $12 \text{ l}\cdot\text{min}^{-1}$ ($Re = 31\,830$).

VI-3-2 Comparaison mesure / simulation numérique

L'un des objectifs de l'étude expérimentale est de comparer les résultats des mesures aux calculs issus du logiciel du commerce I-DEAS (Launay *et al.*, 2004). L'ensemble du volume de l'échangeur, du canal d'entrée au canal de sortie, est maillé avec 123 571 éléments tétraédriques du premier ordre, les surfaces extérieures enveloppant les volumes étant maillées avec des éléments triangulaires. Les calculs sont de type linéaire, réalisés en régime établi. Pour les cas présentés, le solveur d'écoulement utilise le modèle de longueur de mélange avec un schéma d'advection du deuxième ordre. Une comparaison entre mesure et simulation est présentée Figure 39 pour la vitesse moyenne axiale dans le plan laser pour le canal 2 et un débit de $12 \text{ l}\cdot\text{min}^{-1}$ ($Re = 31\,830$). La comparaison montre un accord global même si la simulation sous-estime la vitesse dans la partie gauche du plan de mesure du canal. De façon générale, les écarts relatifs entre mesure et simulation sont compris dans une plage de 17%. De plus, la résolution spatiale du modèle numérique n'atteint pas l'échelle de résolution de la mesure PIV.

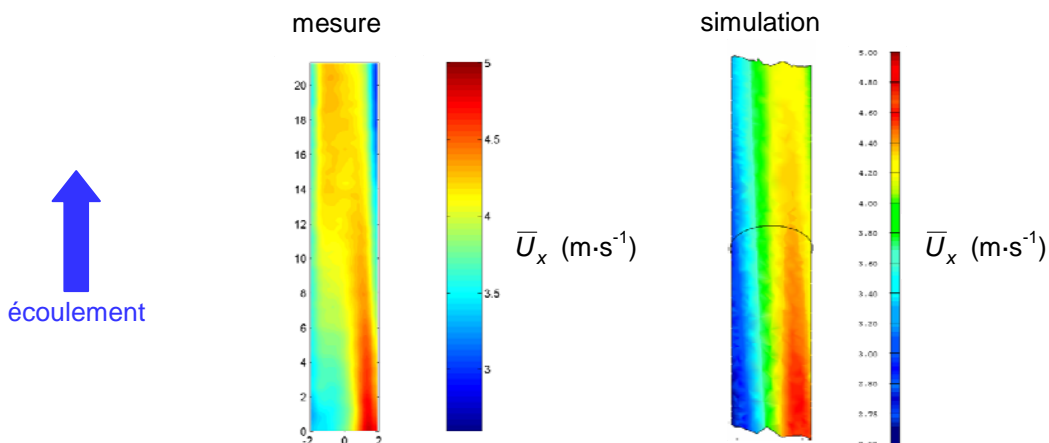


Figure 39 : Comparaison de la vitesse moyenne axiale issue de la mesure et de la simulation pour le canal 2 et un débit de $12 \text{ l}\cdot\text{min}^{-1}$ ($Re = 31\,830$).

La comparaison de la répartition de vitesse débitante U_q entre chacun des canaux montre un bon accord entre expérience et simulation (Figure 40). On retrouve par intégration de U_q entre les six canaux, une valeur proche de la vitesse débitante en entrée de l'échangeur, mesurée par rotamètre. Quelque soit le débit d'alimentation de l'échangeur, on observe un

maximum dans le canal 2, situé face au conduit d'entrée, un minimum dans le canal 3 et un maximum local dans le canal 5, situé face au conduit de sortie.

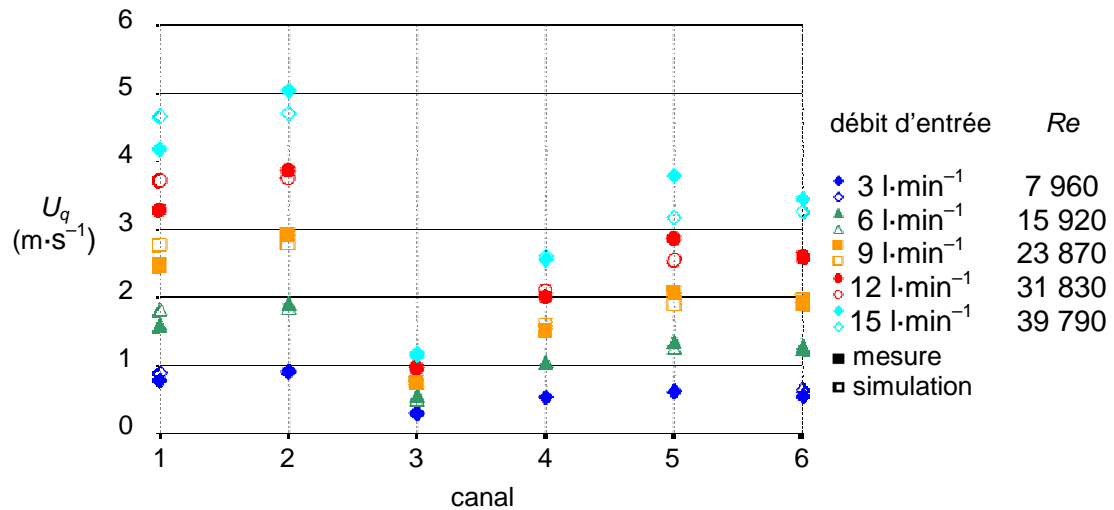


Figure 40 : Répartition de la vitesse débitante mesurée dans chacun des six canaux pour cinq débits d'entrée.

VI-3-3 Moments d'ordre 2 des fluctuations de vitesse

Les variances de fluctuations de vitesse axiale présentent des valeurs élevées au début de la zone de mesure, où l'écoulement est plus fortement inhomogène, et dans les canaux où la vitesse moyenne axiale est la plus forte (Figure 41). Une forte dissymétrie est observée dans le canal 2, preuve d'une recirculation importante en aval du raccordement entre le collecteur d'entrée et ce canal. La variance des fluctuations de vitesse radiale présente une plus grande symétrie dans le canal 2 (Figure 42). Une forte anisotropie est observée dans le canal 2 à travers la covariance des fluctuations de vitesse axiale et radiale qui montre une zone centrale négative caractéristique d'une recirculation en amont de la zone de mesure (Figure 43).

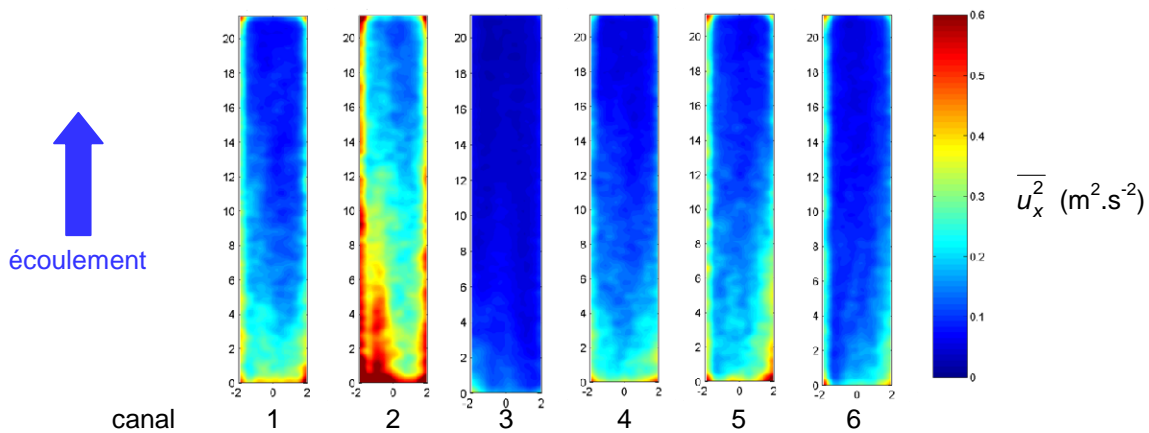


Figure 41 : Variance des fluctuations de vitesse axiale mesurée par PIV dans chacun des canaux pour un débit de $12 \text{ l} \cdot \text{min}^{-1}$ ($Re = 31 830$).

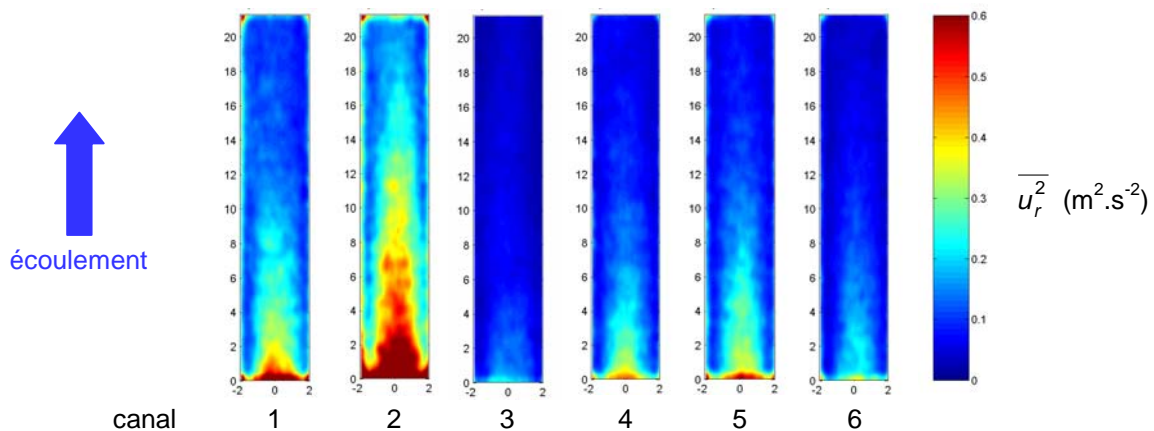


Figure 42 : Variance des fluctuations de vitesse radiale mesurée par PIV dans chacun des canaux pour un débit de $12 \text{ l}\cdot\text{min}^{-1}$ ($Re = 31\,830$).

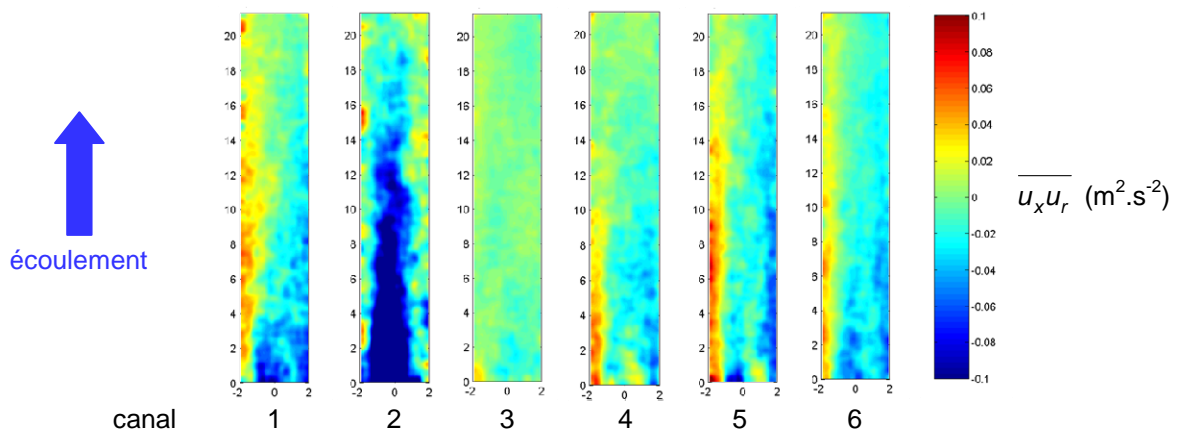


Figure 43 : Covariance des fluctuations de vitesse axiale et radiale mesurée par PIV dans chacun des canaux pour un débit de $12 \text{ l}\cdot\text{min}^{-1}$ ($Re = 31\,830$).

VI-4 Conclusion

Une PIV est mise en place sur une maquette d'échangeur thermique présentant une géométrie tridimensionnelle, à l'intérieur de laquelle se développe un écoulement inhomogène avec plusieurs zones décollées. Les corrections des réflexions lumineuses sur les parois de chacun des canaux sont effectuées par soustraction d'une image de référence. Les réfractions induites par la présence d'un double dioptrre courbe sont également prises en compte dans le calcul des positions radiales et des déplacements de particules. La mise en œuvre d'un algorithme avancé de PIV, le flot optique utilisant une programmation dynamique orthogonale, offre une grande résolution spatiale et permet de caractériser les gradients de vitesse à l'intérieur de chacun des canaux.

L'analyse des mesures montre que la forme de la répartition de vitesse entre les différents canaux est indépendante du débit d'entrée, le canal 2 étant toujours marqué par les plus fortes vitesses axiales. La confrontation de ces résultats à une simulation utilisant un code commercial permet de valider le calcul numérique. Les moments d'ordre 2 des fluctuations de vitesse corroborent l'analyse du champ moyen et mettent en évidence une forte anisotropie de l'écoulement et la présence de décollements au niveau des raccordements entre le collecteur amont et chacun des canaux. Enfin, cette étude montre que le canal 2 est celui où le transfert thermique entre le fluide et la paroi est le plus important.

VI-5 Références

- FAURE, Th. M., LUSSEYRAN, F., GOUGAT, P., LAUNAY, F.** (2006) Experimental investigation of the flow distribution inside a tubular heat exchanger, *Journal of Fluids Engineering*, Vol. 128, No. 6, pp. 1218–1227
- FAURE, Th. M., SATO, M., LECOCQ, Y.** (2003) *Mesures PIV par flot optique dans deux types d'écoulements turbulents*, Rapport interne LIMSI-CNRS 2003-17
- LAUNAY, F., FAURE, Th. M., LUSSEYRAN, F., GOUGAT, P.** (2004) *Écoulement 3D dans une structure d'échangeur – Confrontation mesures simulations*, Rapport de synthèse, contrat IPNO-04-02, Collaboration Laboratoire d'Informatique pour la Mécanique et les Sciences de l'Ingénieur - Institut de Physique Nucléaire d'Orsay
- QUÉNOT, G. M.** (1992) The orthogonal algorithm for optical flow detection using dynamic programming, *Proceedings IEEE*, Vol. III, pp. 249–252
- QUÉNOT, G. M., PAKLEZA, J., KOWALEWSKI, T. A.** (1998) Particle image velocimetry with optical flow, *Experiments in Fluids*, Vol. 25, No. 3, pp. 177–189
- SATO, M.** (2003) *Étude de l'écoulement par PIV dans un tube d'échangeur thermique*, Stage de Maîtrise de Technologie Mécanique, Université Pierre et Marie Curie, Paris VI

VII Écoulement cisaillé au-dessus d'une cavité parallélépipèdique ouverte

VII-1 Introduction

Les écoulements de cavité se rencontrent dans de nombreuses applications industrielles (transport aérien de polluants, refroidissement de composants électroniques, césures de portières automobiles, système hypersustentateurs et riblets en aéronautiques, anévrisme sanguin, paliers hydrodynamiques, ...). L'objectif de cette étude est de fournir une configuration de référence d'écoulement de cavité engendré par une couche de cisaillement, pour une gamme de nombre de Reynolds modérés. Les objectifs suivants seront exposés :

- la description générale de l'écoulement selon la géométrie de la cavité et le nombre de Reynolds ;
- la caractérisation de la couche de cisaillement et du développement de l'instabilité de Kelvin-Helmholtz ;
- la caractérisation de l'écoulement dans la cavité et du développement d'instabilités centrifuges.

Les activités menées dans ce cadre font l'objet de plusieurs actions de recherche :

- le CNRT Aéroacoustique et Aérodynamique des Véhicules ;
- l'ANR Dynamique Instationnarité Bruit (DIB) ;
- l'ANR Contrôle Optimal et Robuste par Modèles d'Ordre Réduits d'Écoulements Décollés (CORMORED).

Cette configuration expérimentale fait aussi l'objet de plusieurs stages de licence (Gaëlle Lefèvre, 2009), maîtrise ou master 1 (Yannick Lecocq, 2003, Nicolas Pechlivanian, 2006, Sépass Mochki, 2009, Hélène Thach, 2009) et de DEA ou master 2 (Philippe Debesse, 2004, Panayotis Adrianos, 2005).

VII-2 Dispositif expérimental

VII-2-1 Banc d'essais

L'écoulement est engendré par une soufflerie basse vitesse en circuit ouvert (Figure 44-a). La section d'essais est entièrement réalisée en verre antireflet de 2 mm d'épaisseur, ce qui rend possible son exploration par des méthodes optiques. Les extrémités de la cavité, selon son envergure $S = 300$ mm, sont les parois latérales fixes de la soufflerie (Figure 44-b). La cavité est modulaire, sa longueur L et sa hauteur H sont variables ce qui permet de considérer plusieurs rapports de forme L / H entre 0,25 et 2,5 et plusieurs rapports d'envergure S / H entre 2 et 12. L'origine du repère (x,y,z) est fixée au bord amont de la cavité à mi-envergure. La vitesse caractéristique de l'écoulement est la vitesse extérieure à la couche limite amont U_e . Le nombre de Reynolds $Re_L = U_e L / \nu$ est compris entre 860 et 37 000.

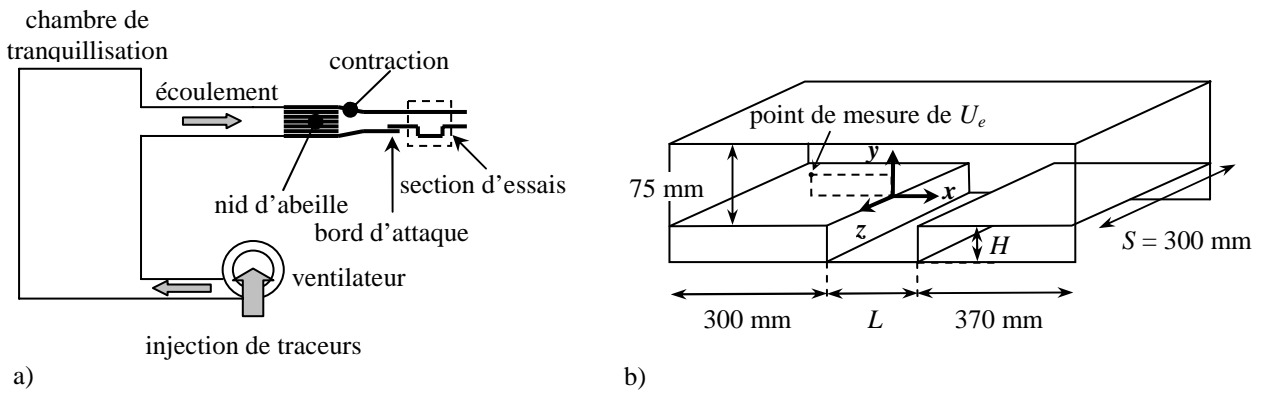


Figure 44 : Dispositif expérimental : a) soufflerie basse vitesse, b) section d'essais.

VII-2-2 Instrumentation

Les visualisations sont obtenues à l'aide d'un laser argon-ion Aerometrics de 5 W dont on utilise les longueurs d'onde bleue (488 nm) et verte (514,5 nm). Chaque faisceau est conduit par fibre optique jusqu'à une lentille cylindrique et fournit une nappe lumineuse de 0,25 mm d'épaisseur. Un enregistrement synchronisé de l'écoulement dans deux plans est obtenu en utilisant ces deux nappes lumineuses, en plaçant sur chacune des caméras un filtre passe-bande qui correspond à la longueur d'onde souhaitée. La composante bleue du laser est également employée pour la LDV. L'ensemencement est réalisé par de la fumée de spectacle faible densité, injectée en amont du caisson de tranquillisation de la soufflerie. Les lignes d'émission qui proviennent du développement de la couche de cisaillement, permettent de visualiser les structures dynamiques de l'écoulement dans la cavité.

Les mesures PIV sont effectuées avec deux paires de sources lasers YAG pulsés, d'énergie respectives 30 mJ ou 200 mJ par impulsion, qui émettent à 532 nm une nappe lumineuse de 0,25 mm d'épaisseur maximum. L'ensemencement est réalisé par des gouttelettes de DEHS (di-éthyl-hexyl-sébacate). Leur taille moyenne est d'environ 1 μm , elles sont nébulisées en amont de la soufflerie par air comprimé. Pour les mesures synchronisées PIV/LDV, la LDV utilise la longueur d'onde bleue (488 nm) du laser continu Argon-ion et fonctionne en mode de diffusion avant. Elle permet d'acquérir la composante axiale de vitesse à une fréquence d'environ 1 500 Hz. Afin de s'affranchir de la longueur d'onde 488 nm sur les images PIV, un filtre passe-bande, centré sur la longueur d'onde du YAG et d'une largeur de bande de 10 nm, est monté sur l'objectif de la caméra. Les séquences d'images sont enregistrées par une caméra 10 bits de résolution 1 032×778 pixels à une fréquence de 20 Hz.

Deux plans d'observation sont utilisés pour les visualisations et les mesures PIV : un plan (x,y), pour appréhender la morphologie de l'écoulement principal, et un plan (x,z), pour décrire le développement des instabilités qui se superposent à cet écoulement (Figure 45). Dans chaque cas, la caméra a une vue complète de la cavité, selon sa longueur ou son envergure. Dans le premier cas, le plan (x,y) est placé à mi-envergure de la cavité. Dans le second cas, le plan (x,z) est placé à une position verticale relative $y / H < 0$.

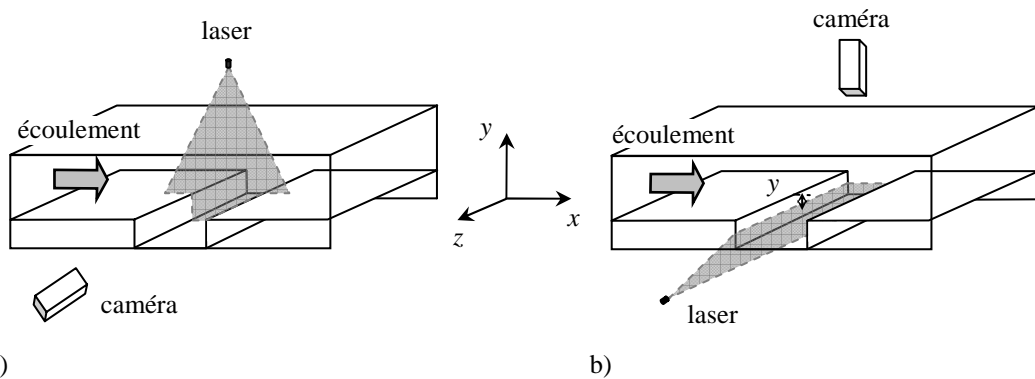


Figure 45 : Plans d’observation : a) plan (x,y), b) plan (x,z).

VII-2-3 Algorithme PIV

Compte-tenu de la présence des parois de la cavité, de nombreuses réflexions sont présentes sur les images. Un prétraitement consiste à retrancher une image de bruit de fond, enregistrée avec la nappe laser à la même puissance que lors des mesures mais en l’absence d’ensemencement. Un masque correspondant aux parties qui ne sont pas situées dans l’écoulement est aussi appliqué. Enfin, le contraste des particules entre les différentes régions de l’image peut être amélioré grâce à une renormalisation locale de la dynamique de l’image, en effectuant un filtrage passe-haut (Quénnot *et al.*, 1998, Figure 46). Le calcul PIV des champs de vitesse utilise un algorithme de flot optique par programmation dynamique orthogonale (Quénnot, 1992, cf. VI-2-3).

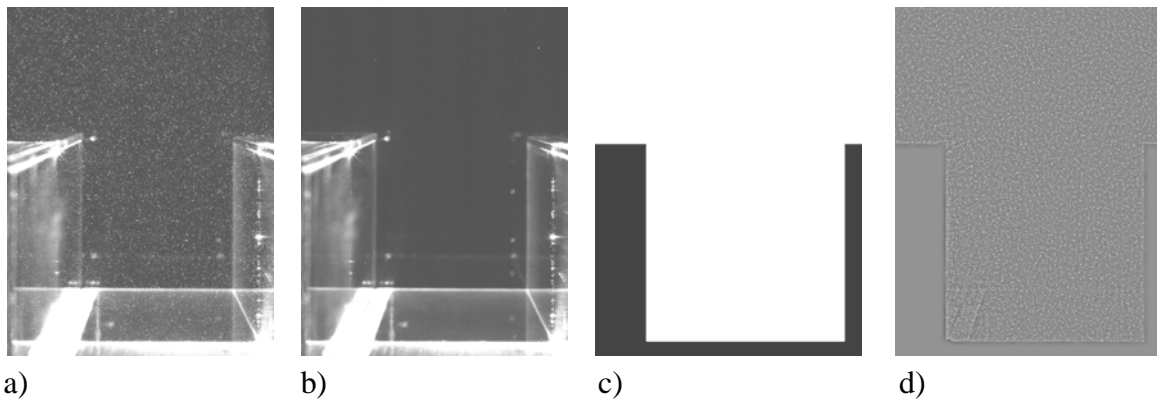


Figure 46 : Prétraitement des images avant application de l’algorithme de PIV : a) image brute, b) image de bruit de fond, c) masque de la cavité, c) image filtrée après renormalisation dynamique.

Afin d’optimiser les mesures PIV, on choisit un déplacement moyen de 10 pixels entre deux images pour les mesures dans le plan (x,y), ce qui correspond, selon la vitesse de l’écoulement extérieur, à des intervalles de temps entre deux éclairements laser compris entre 1 461 et 7 812 μ s (Adrianos, 2005). Pour obtenir une meilleure résolution à l’intérieur de la cavité, certaines séries de mesures considèrent un déplacement moyen de 10 pixels dans la cavité, ce qui donne des intervalles de temps compris entre 2 198 et 14 244 μ s (Defrasne, 2007). Pour les mesures PIV dans le plan (x,z), et compte-tenu des très faibles vitesses dans ce plan, l’intervalle de temps en deux éclairages est fixé à la cadence d’acquisition de la caméra, soit 50 000 μ s. Le choix des paramètres retenus dans l’algorithme de flot optique par programmation dynamique orthogonale, conduit à une interrogation sub-pixel et une incertitude sur les déplacements de 1/32^e de pixel, soit une erreur relative en vitesse de 0,15%. Les résultats expérimentaux sont obtenus à partir de l’enregistrement de 2 200 images qui

fournissent 1 100 champs de vitesse. Une étude de la convergence statistique pour le plus grand nombre de Reynolds, montre que l'acquisition de 200 champs assure une convergence inférieure à 1% d'erreur pour le champ moyen et que 600 champs fournissent la même précision pour les moments d'ordre 2.

VII-3 Principaux résultats

VII-3-1 Morphologie de l'écoulement

La morphologie de l'écoulement en fonction du rapport de forme L / H (Faure *et al.*, 2007) met en évidence la présence d'un tourbillon principal d'axe transverse qui est le moteur du mouvement au cœur de la recirculation, et dont la dimension est fixée par la hauteur H de la cavité (Figure 47). Ce tourbillon principal se situe vers la paroi aval pour $L / H = 2$, avec un tourbillon contrarotatif secondaire dans la partie amont. Pour $L / H = 1,5$, ce tourbillon secondaire tend à diminuer et il est réduit à un tourbillon de coin pour $L / H = 1$. Dans ce cas, le tourbillon principal s'inscrit parfaitement dans la cavité. Pour une cavité profonde, par exemple pour $L / H = 0,5$, le tourbillon principal s'inscrit dans la partie supérieure, son diamètre est imposé par la longueur de la cavité. L'analyse temporelle des visualisations dans deux plans parallèles met en évidence que l'écoulement dans la cavité est tridimensionnel mais que cette nature tridimensionnelle n'est pas due aux instabilités secondaires de la couche de cisaillement, cette dernière se présente en effet comme un phénomène essentiellement bidimensionnel (Figure 48). On remarque également que l'instationnarité de l'écoulement dans la cavité augmente avec le nombre de Reynolds mais aussi avec le rapport de forme L / H .

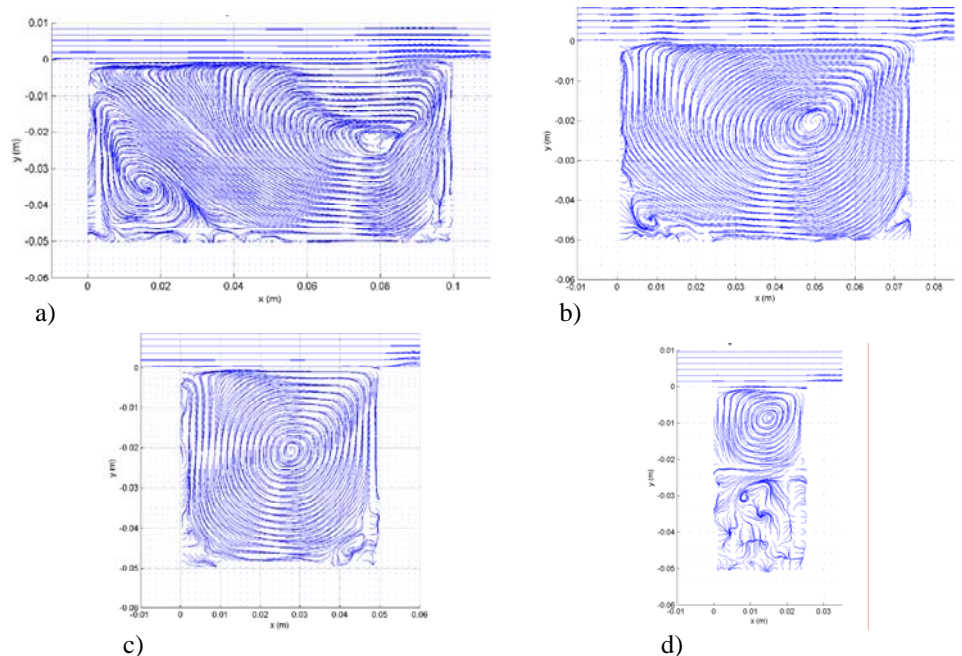


Figure 47 : Lignes de courant moyennes pour un rapport d'envergure $S / H = 6$, $Re_H = 4230$ et a) $L / H = 2$, b) $L / H = 1,5$, c) $L / H = 1$ and d) $L / H = 0,5$.

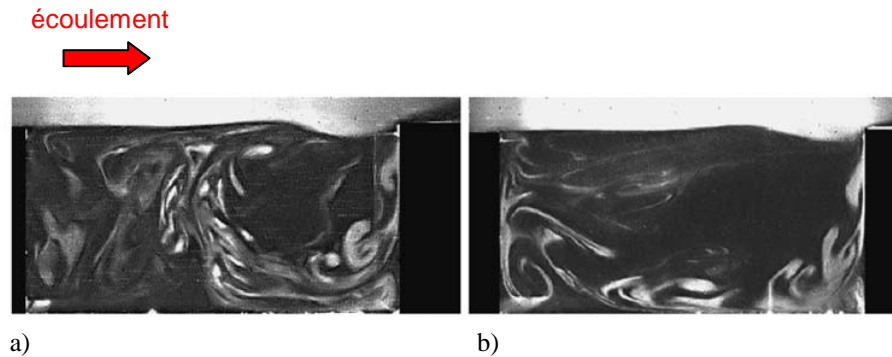


Figure 48 : Visualisation dans deux plans parallèles au même instant pour $S / H = 6$, $Re_H = 4230$, $L / H = 2$ a) $z / H = 0$ (longueur d'onde 514,5 nm), b) $z / H = 0,6$ (longueur d'onde 488 nm).

VII-3-2 Instabilité de la couche de cisaillement

Des mesures LDV, effectuées en aval de la couche de cisaillement à $x / L = 1,15$ et $y / H = 0,3$, permettent de caractériser les différents modes de l'instabilité de la couche de cisaillement en fonction de la vitesse de l'écoulement incident et de la géométrie (Figure 49). Si, pour certaines vitesses, on n'observe qu'un seul mode associé à l'instabilité, certains cas présentent deux fréquences non-harmoniques. Afin de mesurer l'évolution temporelle de chacune de ces fréquences au cours du temps, on opte pour une représentation par spectrogramme, qui met clairement en évidence l'intermittence de chaque mode (Figure 50). Une étude de l'évolution des oscillations de la couche de cisaillement montre qu'elle est essentiellement dominée par un basculement de mode (Pastur *et al.*, 2008). Le changement du nombre de Reynolds, construit sur la longueur de la cavité Re_L , modifie les fréquences d'excitation de la couche de cisaillement, l'amplitude relative de leur densité spectrale de puissance ainsi que leur taux d'existence et de co-existence (Faure *et al.*, 2005). La structure spatiale de l'écoulement étant imposée par la géométrie de la cavité, on suspecte que les parois latérales selon l'envergure jouent un rôle dans la compétition non-linéaire de modes, mais une étude complémentaire est nécessaire pour confirmer cette interprétation.

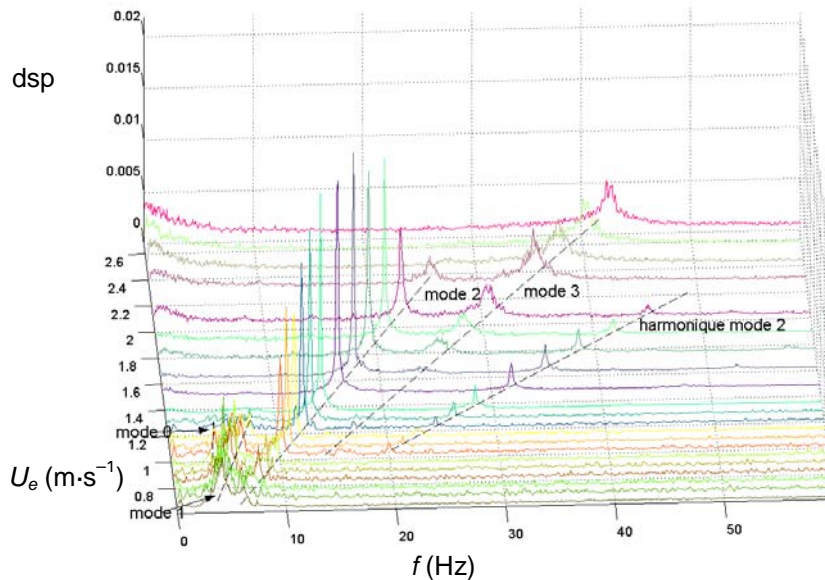


Figure 49 : Densités spectrales de puissance de la vitesse axiale mesurée en aval de la couche de cisaillement en fonction de la vitesse U_e pour $L / H = 2$.

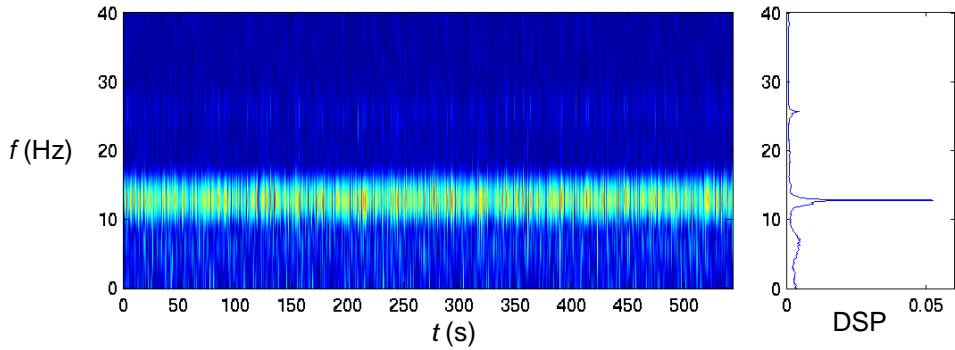


Figure 50 : Spectrogramme de la vitesse axiale mesurée en aval de la couche de cisaillement pour $L / H = 2$ et $Re_L = 8\,470$ (à droite la densité spectrale de puissance correspondante).

À partir des mesures synchronisées PIV/LDV, la moyenne par phase des champs spatiaux PIV, non résolus en temps, est effectuée par rapport au signal ponctuel LDV, résolu en temps (Faure *et al.*, 2006, Pastur *et al.*, 2008). Cette analyse est réalisée à partir du portrait de phase du signal LDV obtenu par une décomposition en valeurs singulières (SVD). Le signal LDV $U_x(t)$ est tout d'abord ré-échantillonné à une fréquence multiple de la fréquence des champs PIV. Il est ensuite filtré au moyen d'un filtre passe-bande, de largeur de bande 1 Hz autour de la fréquence correspondant au mode caractéristique de la couche de cisaillement. Ce signal sert à la construction de la matrice des retards S définie, pour N échantillons temporels, par :

$$S = \begin{pmatrix} U_x(t_1) & U_x(t_2) & \cdots & U_x(t_m) \\ U_x(t_2) & U_x(t_3) & \cdots & U_x(t_{m+1}) \\ \vdots & \vdots & & \vdots \\ U_x(t_{N-m+1}) & U_x(t_{N-m+2}) & \cdots & U_x(t_N) \end{pmatrix}$$

La décomposition aux valeurs singulières consiste alors à écrire cette matrice sous la forme :

$$S = A_S \cdot D_S \cdot B_S^T$$

où D_S est la matrice des valeurs singulières, rangées de la plus grande à la plus petite. La matrice des retards est projetée sur sa base B_S , qui est une matrice orthogonale, telle que :

$$B_S^T \cdot S \cdot B_S = I$$

avec I la matrice identité et la base A_S , telle que :

$$S \cdot B_S = A_S \cdot D_S$$

L'espace des phases est alors déterminé par les colonnes de la matrice X définie par :

$$X = A_S \cdot D_S$$

Les deux premières colonnes de cette matrice X constituent le portrait de phase (X_1, X_2), chaque point de mesure pouvant être aussi repéré par son rayon r et sa phase ϕ (Figure 51). On effectue la moyenne des champs PIV correspondants, par secteurs en 16 phases de résolution angulaire $22,5^\circ$ (Figure 52). Ce traitement permet de reconstituer les oscillations de la couche de cisaillement au-dessus de la cavité à travers la composante U_y , qui présente une alternance de zones positives (injections) et négatives (éjections) évoluant au cours d'un cycle. Le même traitement est appliqué aux cas présentant deux modes caractéristiques, en choisissant d'effectuer la moyenne par rapport au premier ou au second mode.

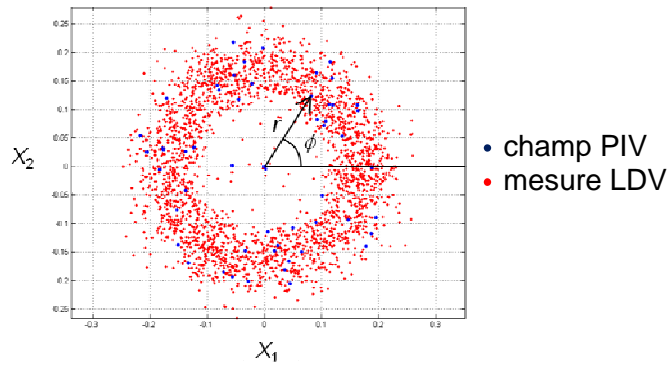


Figure 51 : Portrait de phase du signal LDV pour $L / H = 2$ et $Re_L = 13\,930$.

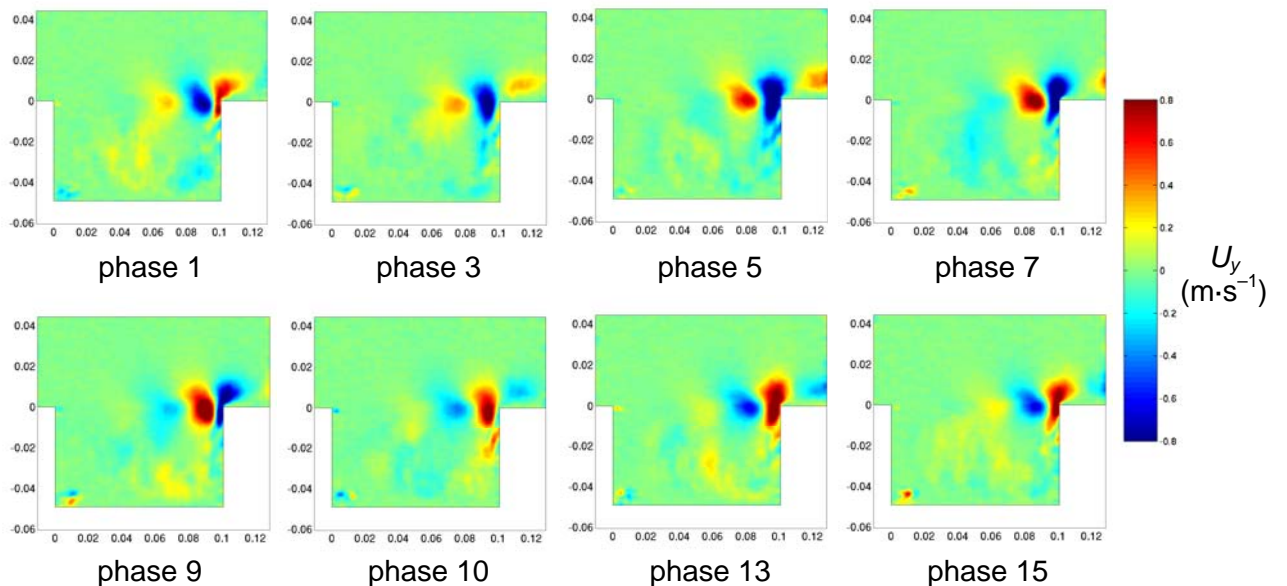


Figure 52 : Composante verticale de vitesse mesurée par PIV en phase avec le signal LDV pour $L / H = 2$ et $Re_L = 8\,470$.

VII-3-3 Instabilités centrifuges

L’écoulement à l’intérieur de la cavité est dominé par un tourbillon principal d’axe transverse, et le confinement entre le fond de la cavité et la couche de cisaillement. Un autre nombre de Reynolds Re_H , construit sur la hauteur H de la cavité, est alors plus adapté pour décrire l’écoulement interne (Brès & Colonius, 2008). La recirculation peut engendrer, selon les paramètres, l’absence d’instabilité (Figure 53-a), l’apparition d’instabilités centrifuges selon l’envergure (Figure 53-b) ou la présence d’instabilités isolées (Figure 53-c, Faure *et al.*, 2009).

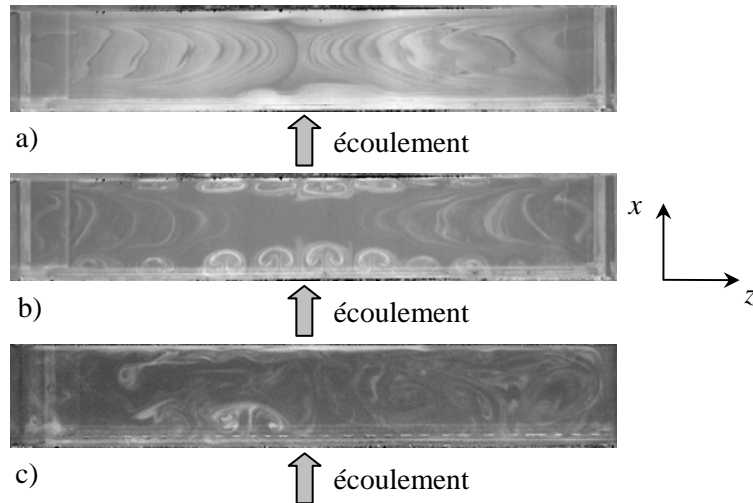


Figure 53 : Visualisation dans un plan horizontal situé à $y / H = -0,3$ pour : a) $L / H = 1, S / H = 6$ et $Re_H = 2\,970$, b) $L / H = 1, S / H = 6$ et $Re_H = 4\,230$, c) $L / H = 0,5, S / H = 3$ et $Re_H = 15\,000$.

Une simulation numérique directe (DNS) instationnaire est réalisée pour $S / H = 6$, $L / H = 1$ et $Re_H = 4\,230$, à l'aide d'un code Olorin volumes finis, comportant un maillage de $256 \times 128 \times 128$ nœuds et un resserrement des points à proximité des parois et dans la couche de cisaillement (Faure *et al.*, 2009). Des conditions aux limites de parois rigides sont également imposées selon les parois latérales. La simulation correspond à 40 s après la convergence statistique du calcul, à une fréquence d'enregistrement de 30 Hz. La Figure 54 présente l'hélicité du champ de vitesse définie par :

$$\mathcal{H} = \vec{V} \cdot \vec{\Omega}$$

où \vec{V} est le vecteur vitesse et $\vec{\Omega} = \overrightarrow{\text{rot}} \vec{V}$ la vorticité. On observe, tout comme sur les visualisations (Figure 53-b), la nature quasi-annulaire des paires d'instabilités centrifuges qui se répartissent, selon l'envergure de la cavité, en zones d'iso-hélicité négatives (bleues) et positives (jaunes).

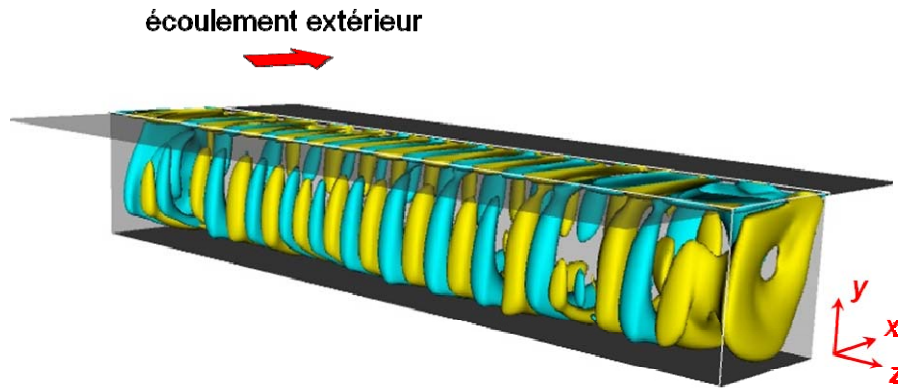


Figure 54 : Représentation de l'hélicité obtenue par DNS pour $S / H = 6, L / H = 1$ et $Re_H = 4\,230$.

Le domaine d'existence des instabilités centrifuges montre la présence d'un seuil d'apparition et d'un seuil de transition vers la turbulence, indépendant du rapport d'envergure pour $S / H \geq 3$ (Figure 55).

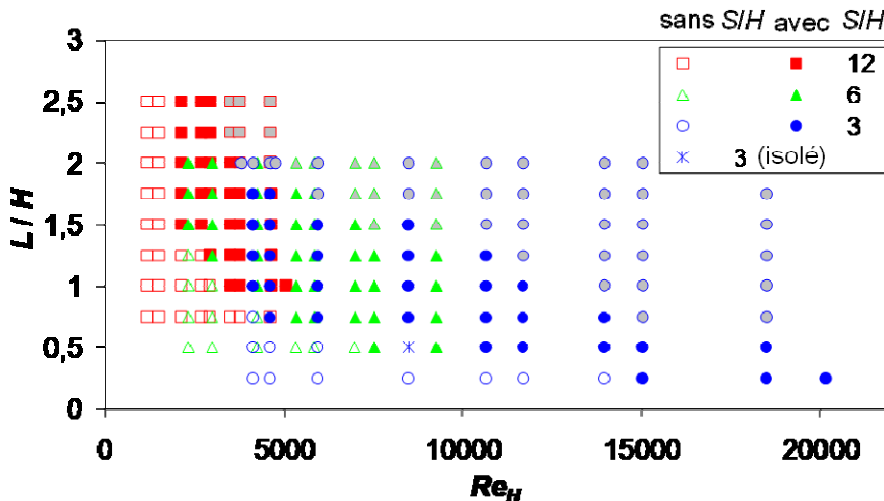


Figure 55 : Diagramme d'existence d'instabilités centrifuges en fonction du rapport L / H et du nombre de Reynolds Re_H pour $S / H = 12, 6$, et 3 : symboles creux : absence, symboles pleins : présence, symboles gris : écoulement transitionnel et croix : instabilité isolée.

Pour identifier les structures tourbillonnaires, à partir de mesures PIV dans un plan (x,z) , où le bruit de mesure est important compte-tenu de la forte composante de vitesse transverse, on utilise le critère Γ_2 (Graftieaux *et al.*, 2001) défini par :

$$\Gamma_2(\vec{x}) = \frac{1}{S} \int_{\vec{x}' \in S} \frac{(\vec{x}' - \vec{x}) \wedge [\vec{U}(\vec{x}') - \vec{U}(\vec{x})]}{\|\vec{x}' - \vec{x}\| \|\vec{U}(\vec{x}') - \vec{U}(\vec{x})\|} d\vec{x}'$$

Il s'agit d'un moment cinétique normalisé pour le mouvement relatif autour d'une particule fluide donnée, qui est donc compris entre -1 et 1 , ces deux bornes correspondant à la présence d'un tourbillon. On observe ainsi l'allée de paires de tourbillons contra-rotatifs au bord amont de la cavité sur la visualisation (Figure 56-a) et sur le critère Γ_2 appliqué aux mesures PIV (Figure 56-b). Il est alors possible d'extraire une ligne passant par l'allée d'instabilités (lignes blanches, Figure 56) et de construire un diagramme spatio-temporel en empilant ces différentes lignes au cours du temps (Faure *et al.*, 2007). On observe alors la migration des paires de tourbillons vers les parois latérales de la cavité, à une vitesse correspondant à la pente des motifs du diagramme (Figure 57).

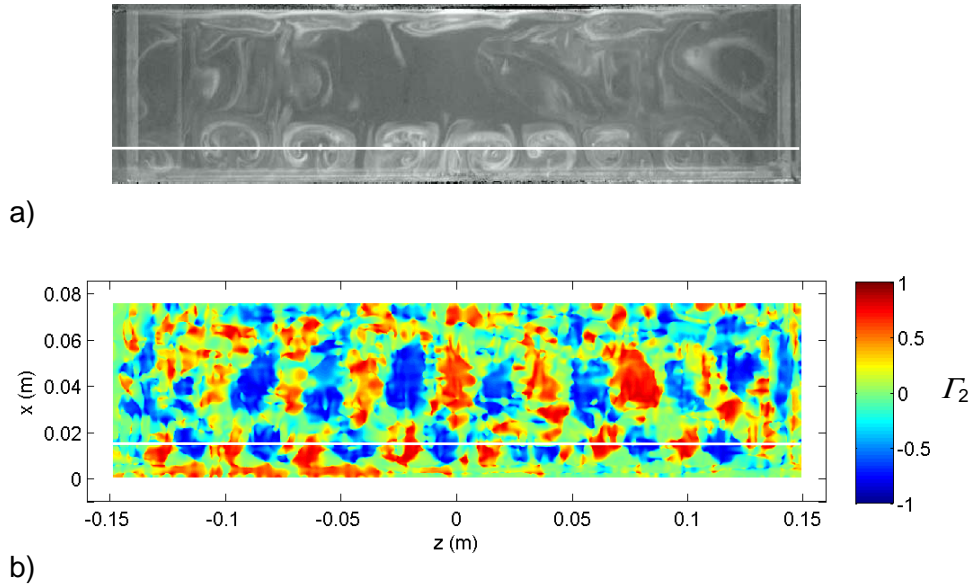


Figure 56 : Identification des instabilités centrifuges dans un plan horizontal situé à $y / H = -0,3$ pour $L / H = 1,5$, $S / H = 6$ et $Re_H = 2\ 300$: a) visualisation, b) mesures PIV et critère Γ_2 .

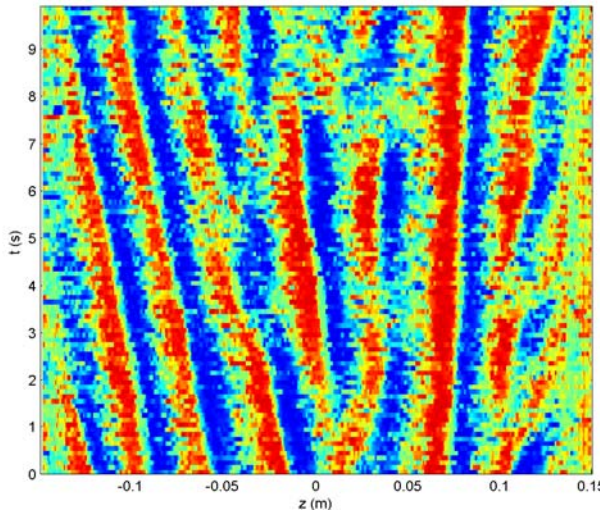


Figure 57 : Diagramme espace-temps du critère Γ_2 pour $L / H = 1,5$, $S / H = 6$ et $Re_H = 2\ 300$.

Afin d'analyser l'origine des instabilités centrifuges, on utilise le discriminant de Rayleigh (1916) :

$$\eta(x, y) = -\frac{\partial \|\vec{r}(x, y) \wedge \bar{\vec{U}}(x, y)\|^2}{\partial r}$$

L'écoulement est stable si $\eta < 0$ et potentiellement instable si $\eta > 0$. Comme l'analyse concerne la stabilité d'un état de base, on calcule ce discriminant à partir des champs PIV moyens. On observe, pour un nombre de Reynolds donné, que l'étendue et l'intensité de la zone potentiellement instable augmente avec le rapport L / H de la cavité (Figure 58). La confrontation de la valeur maximale de η , mesurée pour chaque configuration, aux visualisations correspondantes, montre que le seuil d'apparition des instabilités centrifuges est lié à la dimension du tourbillon principal d'axe transverse. Pour prendre en considération les effets stabilisants de la viscosité, on définit un paramètre de contrôle (Migeon, 2000) :

$$C = \frac{\text{temps de stabilisation}}{\text{temps de déstabilisation}} = \frac{\frac{d_i^2}{v}}{\sqrt{d_i R_c}} = \frac{U_c d_i}{v} \sqrt{\frac{d_i}{R_c}}$$

où d_i est la distance instable de l'écoulement, R_c le rayon de courbure et U_c la vitesse de convection dans la recirculation. La comparaison de l'évolution de ce paramètre de contrôle C selon l'azimut θ de l'écoulement dans la cavité, montre un comportement différent entre l'entraînement du fluide par une couche de cisaillement et par un couvercle mobile (Figure 59, Migeon, 2002). La confrontation des visualisations et des mesures PIV met en évidence les seuils d'apparition des instabilités centrifuges :

- pour une recirculation induite par une couche de cisaillement, $C \sim 30$;
- pour une recirculation induite par une paroi mobile, $C > 80$.

L'entraînement par couche de cisaillement présente donc un caractère plus instable que l'entraînement par une paroi mobile, et facilite l'apparition d'instabilités centrifuges.

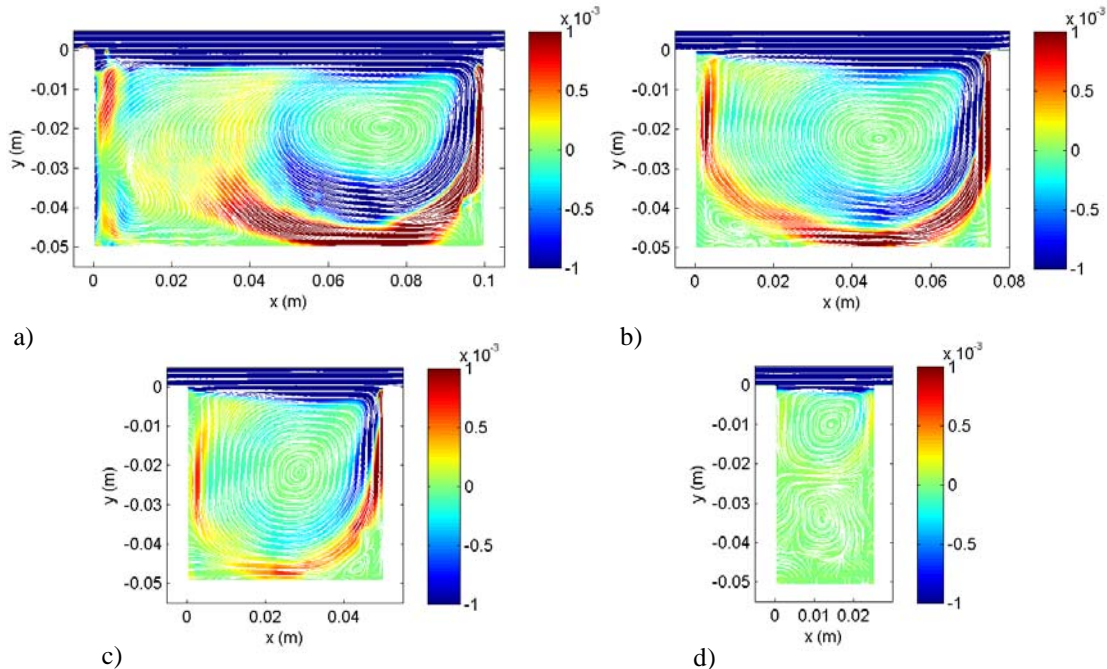


Figure 58 : Discriminant de Rayleigh η pour un rapport d'envergure $S / H = 6$, $Re_H = 4230$ et a) $L / H = 2$, b) $L / H = 1,5$, c) $L / H = 1$ et d) $L / H = 0,5$.

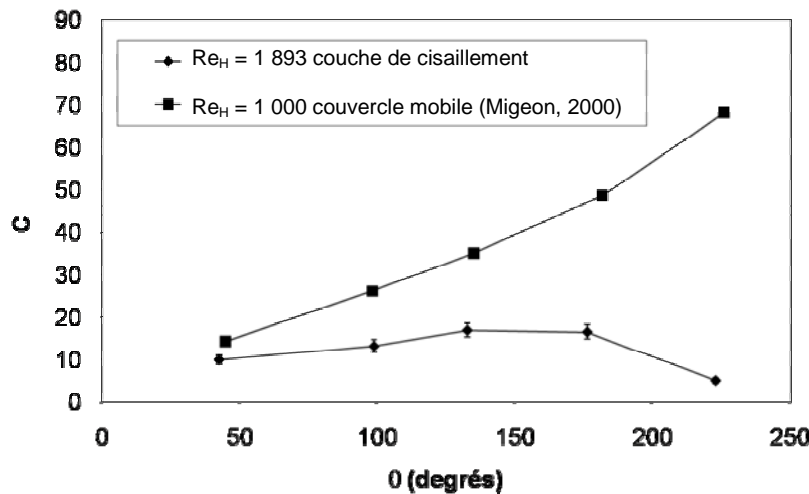


Figure 59 : Paramètre de contrôle C dans la recirculation pour $S / H = 6$ et $L / H = 1$: comparaison entre un entraînement par une couche de cisaillement et par un couvercle mobile.

VII-3-4 Champ moyen en phase par rapport à l'instabilité de Kelvin-Helmholtz

Des mesures PIV résolues en temps sont effectuées dans un plan (x,y) situé à $z / S = 0,07$ à l'aide d'une caméra Fastcam-APX RS de résolution 1024×1024 pixels et de fréquence d'acquisition 500 Hz (Basley *et al.*, 2009). Ces données permettent donc de résoudre directement les oscillations de la couche de cisaillement, dont les modes caractéristiques sont à quelques dizaines de Hertz. Les 4 096 champs de vitesse calculés permettent de construire l'histogramme des périodes d'oscillation à partir du passage d'un petit tourbillon de la couche de cisaillement en une position donnée ($x / L = 0,9$, Thach, 2009) qui montre que la période la plus probable est de 0,05 s (Figure 60). L'analyse du critère de Rayleigh pour chacune des 12 phases d'un cycle met en évidence que les zones stables et potentiellement instables dans la recirculation ne sont pas affectées par l'instabilité de Kelvin-Helmholtz. Le caractère instable de l'écoulement au sein de la recirculation est donc global, est ne dépend pas de la phase des oscillations.

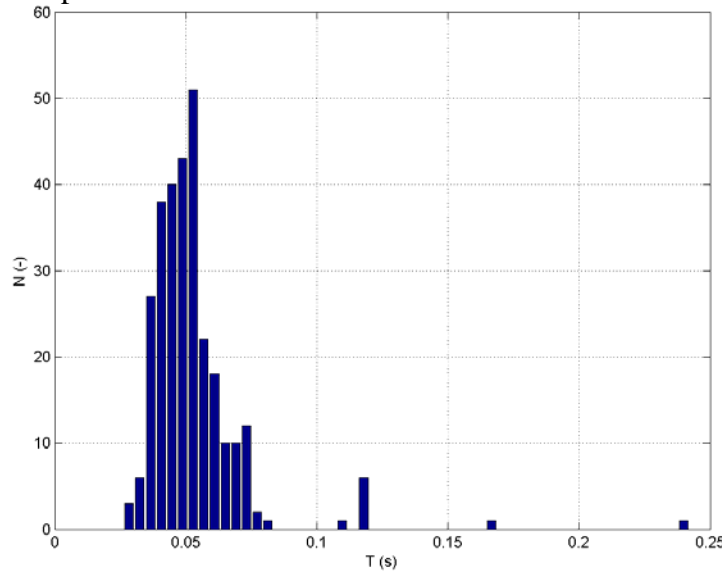


Figure 60 : Histogramme de la période de la couche de cisaillement pour $L / H = 2$ et $Re_L = 10\,630$.

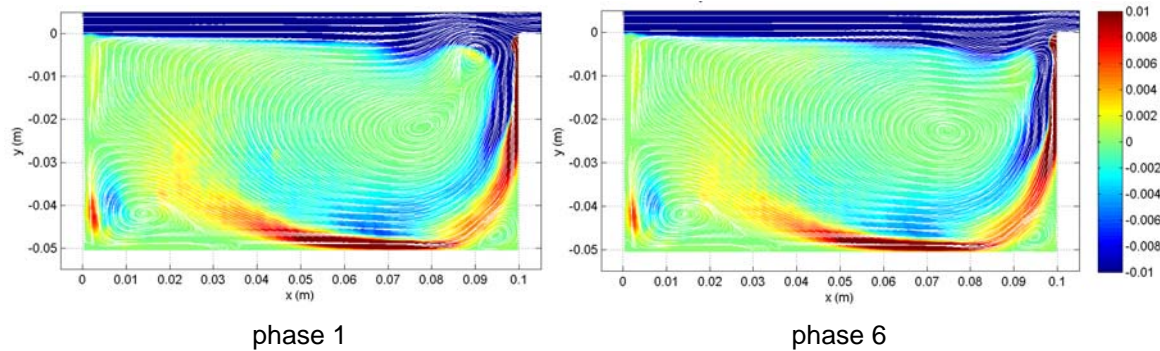


Figure 61 : Critère de Rayleigh η calculé à partir de la vitesse moyenne pour les phases 1 et 6, pour $L / H = 2$ et $Re_L = 10\,630$.

VII-3-5 PIV stéréoscopique

Une PIV stéréoscopique par flot optique utilisant une programmation dynamique orthogonale est mise en place (Mochki, 2009). L'avantage de cet algorithme est qu'il inclut un étalonnage de la position de chacune des caméras, par rapport à une mire positionnée dans le plan de mesure. Pour la caractérisation du plan (x, y), une première caméra est placée selon l'axe de la cavité, et permet une confrontation du résultat avec l'algorithme de PIV-2C, tandis que la seconde caméra est placée au-dessus et forme un angle d'environ 20° par rapport à la première. La comparaison des deux composantes de vitesse instantanée mesurées avec les deux méthodes, montre un excellent accord dans la cavité (Figure 62).

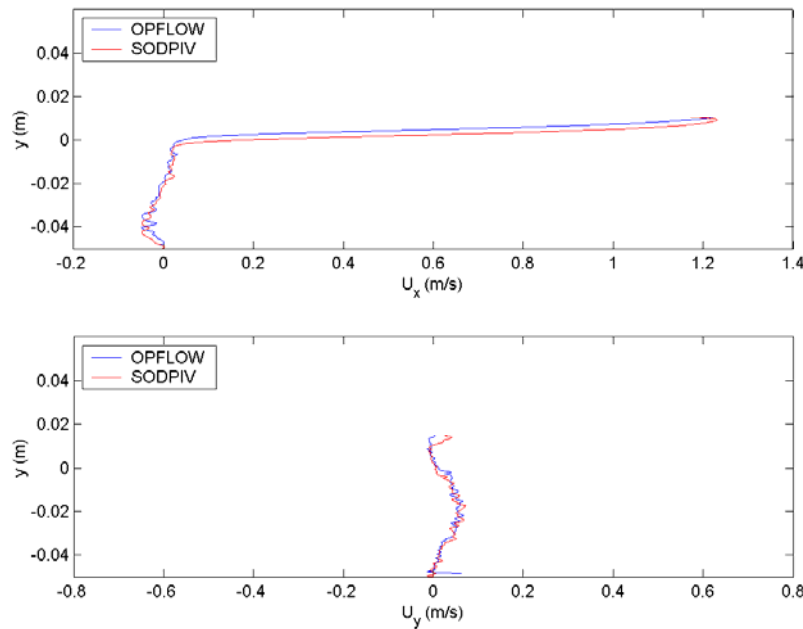


Figure 62 : Profils de vitesse U_x et U_y selon le diamètre du tourbillon principal d'axe transverse pour $L/H = 1$ et $Re_L = 4\,230$: comparaison entre la PIV-2C (OPFLOW) et la PIV-3C stéréoscopique (SODPIV).

La caractérisation dans un plan (z, x) situé à l'intérieur de la cavité met en évidence, dans une même mesure, les lignes de courant associées aux instabilités centrifuges et le mouvement du tourbillon principal d'axe transverse (Figure 63). Ce dernier est identifié par des vitesses positives au bord amont de la cavité (remonté de l'écoulement) et des vitesses négatives au bord aval (descente de l'écoulement).

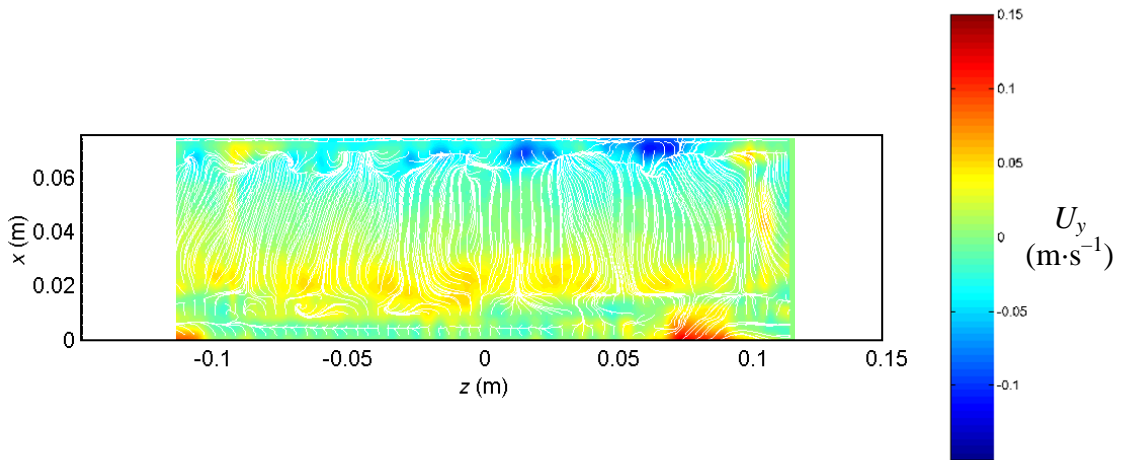


Figure 63 : Lignes de courant (U_x , U_z) et vitesse verticale U_y mesurées par PIV stéréoscopique pour $L/H = 1,5$, $Re_L = 4\,450$ dans un plan situé à $y/H = -0,3$.

VII-4 Conclusion

Une expérience de référence est mise en place pour l'étude d'un écoulement de cavité entraîné par une couche de cisaillement. La géométrie de la cavité est modulable et l'étude, qui concerne une gamme de nombres de Reynolds moyens (entre 860 et 37 000), est effectuée au moyen de techniques expérimentales optiques (visualisation, LDV, PIV).

La description de la morphologie de l'écoulement en fonction de la géométrie de la cavité et de nombre de Reynolds, met en évidence que la recirculation est marquée par un tourbillon principal d'axe transverse et des tourbillons secondaires. Par ailleurs, l'écoulement dans la cavité est de nature tridimensionnelle alors que la couche de cisaillement reste essentiellement bidimensionnelle.

Cette couche de cisaillement est le siège, pour certains rapports d'envergure L / H , du développement d'une instabilité de Kelvin-Helmholtz, dont la dynamique est décrite par un nombre de Reynolds Re_L , construit sur la longueur de la cavité. Un ou plusieurs modes fondamentaux sont observés en fonction de Re_L . Lorsque deux modes sont présents, chacun montre un caractère intermittent. Une décomposition en valeurs singulières des mesures synchronisées PIV / LDV permet la réalisation de moyennes en phase par rapport à un mode d'oscillation.

Le développement de l'écoulement à l'intérieur de la cavité met en évidence des instabilités centrifuges pour certains paramètres expérimentaux. La dynamique de ces dernières est décrite par un nombre de Reynolds Re_H construit sur la hauteur du tourbillon d'axe transverse, c'est-à-dire la hauteur H de la cavité. Le domaine d'existence de ces instabilités est établi, il présente un seuil d'apparition et d'évolution vers un écoulement transitionnel. Ce diagramme est indépendant du rapport d'envergure dès que $S / H > 2$. Les caractéristiques de ces instabilités, notamment leur nombre, leur longueur d'onde et leur vitesse de dérive transverse vers les parois latérales, sont mesurées à partir de diagrammes spatio-temporels, issus des visualisations ou du critère Γ_2 calculé à partir des mesures PIV. L'origine des instabilités centrifuges est analysée avec le discriminant de Rayleigh, et met en évidence une valeur seuil unique pour une taille de tourbillon principal donnée. Afin d'étudier l'effet stabilisant de la viscosité, un paramètre de contrôle est mesuré au cours du mouvement au sein de la recirculation. La confrontation de ces résultats à ceux obtenus pour une cavité entraînée par un couvercle mobile indique que le développement de la couche de cisaillement a un effet déstabilisant sur l'écoulement à l'intérieur de la cavité.

Les perspectives de cette étude s'orientent selon deux directions. Tout d'abord, l'analyse de mesures PIV résolues en temps, pour réaliser directement des moyennes en phase par rapport aux oscillations de la couche de cisaillement et l'étude du couplage entre l'instabilité de Kelvin-Helmholtz et les instabilités centrifuges. Ensuite la mise en œuvre de la PIV stéréoscopique par flot optique par programmation dynamique orthogonale, pour obtenir les trois composantes de vitesse instantanée dans un plan de mesure. Pour chacun de ces points, l'analyse doit être poursuivie de façon systématique pour tous les paramètres expérimentaux (rapports de géométrie, nombre de Reynolds).

VII-5 Références

- ADRIANOS, P.** (2005) *Interaction d'un écoulement avec une cavité ouverte : étude spatio-temporelle*, Stage de Master de Sciences de l'Ingénieur (DEA) 2^e année, spécialité Mécanique des Fluides et Énergétique, Université Pierre et Marie Curie, Paris VI
- BASLEY, J., PASTUR, L. R., LUSSEYRAN, F., FAURE, Th. M., DELPRAT, N.** (2009) Investigation of the spatial organization of spectral dynamics in an uncompressible cavity flow using time-resolved high-speed PIV, *8th International Symposium on Particle Image Velocimetry*, Melbourne (Australia), August 25-28 2009
- BRÈS, G. A., COLONIUS, T.** (2008) Three-dimensional instabilities in compressible flow over open cavities, *Journal of Fluid Mechanics*, Vol. 599, pp. 309–339
- DEBESSE, Ph.** (2004) *Étude de l'intermittence d'une couche de cisaillement générée par un écoulement affleurant une cavité*, Stage de DEA de Dynamique des Fluides et Transferts, Université Paris-Sud XI
- DEFRASNE, A.** (2007) *Évolution du champ de vitesse dans une allée de tourbillons de type Görtler prenant naissance dans une cavité ouverte*, Stage de Master de Mécanique Physique 1^e année, Université Paris-Sud XI
- FAURE, Th. M., ADRIANOS, P., LUSSEYRAN, F., PASTUR, L. R.** (2007) Visualizations of the flow inside an open cavity at medium range Reynolds numbers, *Experiments in Fluids*, Vol. 42, No. 2, pp. 169–184
- FAURE, Th. M., DEBESSE, Ph., LUSSEYRAN, F., GOUGAT, P.** (2005) Structures tourbillonnaires engendrées par l'interaction entre une couche limite laminaire et une cavité, *11^{ème} Colloque de Visualisation et de Traitement d'Images en Mécanique des Fluides*, Lyon (France), 6-9 Juin 2005
- FAURE, Th. M., LUSSEYRAN, F., PASTUR, L. R., PETHIEU, R., DEBESSE, Ph.** (2006) Développement d'instabilités dans un écoulement subsonique se développant au-dessus d'une cavité : mesures synchronisées PIV-LDV, *10^{ème} Congrès Francophone de Techniques Laser*, Toulouse (France), 19-22 Septembre 2006, pp. 577–584
- FAURE, Th. M., PASTUR, L. R., LUSSEYRAN, F., FRAIGNEAU, Y., BISCH, D** (2009) Three-dimensional centrifugal instabilities development inside a parallelepipedic open cavity of various shape, *Experiments in Fluids*, Vol. 47, No. 3, pp. 395–410
- GRAFTIEAUX, L., MICHAUD, M., GROSJEAN, N.** (2001) Combining PIV, POD and vortex identification algorithms for the study of unsteady turbulent swirling flows. *Measurement Science and Technology*, Vol. 12, pp. 1422–1429
- LECOQC, Y.** (2003) *Étude par PIV de l'interaction d'un écoulement avec une cavité*, Stage de Maîtrise de Technologie Mécanique, Université Pierre et Marie Curie, Paris VI
- LEFEVRE, G.** (2009) *Traitement et analyse des caractéristiques d'un écoulement de cavité à partir de mesures PIV*, Stage de Licence de Physique Mécanique 3^e année, Université Paris-Sud XI
- MIGEON, Ch.** (2000) *Contribution à l'analyse de l'écoulement tridimensionnel instable s'établissant à l'intérieur de cavités cylindriques*, Thèse de Doctorat, Université de Poitiers

- MIGEON, Ch.** (2002) Details on the start-up development of the Taylor-Görtler-like vortices inside a square-section lid-driven cavity for $1,000 \leq \text{Re} \leq 3,200$, *Experiments in Fluids*, Vol. 33, pp. 594–602
- MOCHKI, S.** (2009) *PIV stéréoscopique et application à un écoulement confiné*, Stage de Master de Sciences de l'Ingénieur, parcours Mécanique des Fluides et Énergétique, 1^e année, Université Pierre et Marie Curie Paris VI
- PASTUR, L. R., LUSSEYRAN, F., FAURE, Th. M., FRAIGNEAU, Y., PETHIEU, R., DEBESSE, Ph.** (2008) Quantifying the non-linear mode competition in the flow over an open cavity at medium Reynolds number, *Experiments in Fluids*, Vol. 44, No. 4, pp. 597–608
- PECHLIVANIAN, N.** (2006) *Détermination des seuils d'apparition d'instabilités aérodynamiques en fonction de la géométrie d'une cavité rectangulaire affleurant un écoulement*, Stage de Master de Mécanique Physique 1^e année, Université Paris-Sud XI
- QUÉNOT, G. M.** (1992) The orthogonal algorithm for optical flow detection using dynamic programming, *Proceedings IEEE*, Vol. III, pp. 249–252
- QUÉNOT, G. M., PAKLEZA, J., KOWALEWSKI, T. A.** (1998) Particle image velocimetry with optical flow, *Experiments in Fluids*, Vol. 25, No. 3, pp. 177–189
- RAYLEIGH, J. S.** (1916) On the dynamics of evolving fluids, *Scientific papers*, Vol. 6, pp. 447–453.
- THACH, H.** (2009) *Analyse de stabilité d'un écoulement confiné à partir de mesures PIV résolues en temps*, Stage de Master de Mécanique Physique 1^e année, Université Paris-Sud XI

Conclusion

L'ensemble de mes activités de recherche porte sur plusieurs thématiques en mécanique des fluides, qui reposent sur la mesure du champ de vitesse, à travers différentes techniques, le plus souvent multi-composantes et instationnaires.

L'anémométrie à films chauds triples à température constante (CTA) a permis de caractériser le sillage turbulent d'un corps autopropulsé par hélice. Les résultats ont montré l'affinité du champ de vitesse mais aussi des échanges énergétiques turbulents. Une analyse spectrale et des moyennes en phase avec la rotation du propulseur, ont permis d'identifier les zones marquées par des structures organisées de l'écoulement.

Le développement de l'anémométrie fil chaud à tension constante (CVA) a démontré ses performances pour l'étude d'une couche limite supersonique. Cette technique présente une fréquence de coupure du signal plus élevée par rapport aux montages à température constante (CTA) et à courant constant (CCA). L'utilisation de trois coefficients de surchauffe du fil a aussi permis de discriminer les variances des fluctuations de flux de masse et de température totale.

L'anémométrie fil chaud a également été employée pour l'exploration de l'écoulement à l'intérieur d'un nouveau concept de turbopompe centrifuge. Une recirculation et une zone de pré-rotation ont été identifiées en amont de l'inducteur, cette dernière trouvant son origine dans sa nature tridimensionnelle couplée à un effet d'incidence le long de l'envergure du bord d'attaque des pales de l'inducteur.

Une autre application aux machines tournantes a permis de mettre en place un système de vélocimétrie laser Doppler à trois composantes sur un étage de compresseur axial. Cette technique de mesure permet d'appréhender la dynamique instationnaire de l'écoulement en phase avec la rotation du rotor. En particulier, on a observé le couplage fluide-structure entre les sillages des aubes du rotor et les parois du stator, qui est alors soumis à des variations périodiques de charge aérodynamique.

Une PIV par flot optique a caractérisé l'écoulement à l'intérieur d'un échangeur de chaleur constitué de canaux parallèles. La répartition du débit entre ces différents canaux et la présence de zones décollées ont constitué une base de validation pour une simulation numérique.

L'étude de l'écoulement dans une cavité ouverte, pour des nombres de Reynolds modérés, a également été réalisée par cette technique PIV couplée à la LDV et des visualisations. L'étude des modes associés au développement de la couche de cisaillement, a révélé leur nature intermittente. L'écoulement présente, pour certains paramètres, des instabilités centrifuges, engendrées par la recirculation de la cavité, dont le domaine d'existence a été établi. La comparaison d'un écoulement entraîné par une couche de cisaillement, aux résultats obtenus pour une cavité entraînée par un couvercle mobile, a montré que cette dernière configuration est beaucoup plus stable et ne permet généralement pas l'apparition d'instabilités centrifuges.

Au cours de ces travaux de recherche, la mise en œuvre d'outils de reconstruction a permis de générer une information globale à partir d'une mesure localisée. Ainsi, il est possible de reconstruire le champ de vitesse dans un volume en effectuant un maillage de points expérimentaux, lorsqu'un phénomène ergodique ou périodique est considéré. De même, on peut obtenir une périodicité temporelle du champ de vitesse lorsqu'on dispose d'un signal de synchronisation périodique en effectuant des moyennes de phase, ou lorsque l'on sélectionne un mode propre à l'écoulement. Ce mode peut être issu d'un signal de vitesse local résolu en temps, synchronisé avec une PIV non résolue en temps, au moyen d'une décomposition en valeurs singulières. On peut également traiter directement des mesures PIV résolues en temps, en prenant comme critère de détection une structure caractéristique de

l'écoulement, comme le passage d'un tourbillon à une position donnée. Les développements futurs des techniques expérimentales s'orientent vers une mesure volumique des trois composantes de la vitesse, si possible résolue en temps, à travers des méthodes du type de la PIV stéréoscopique tomographique.

Perspectives

Mes perspectives de recherche s'articulent autour de quatre axes principaux :

- la poursuite de la caractérisation phénoménologique de l'écoulement de cavité, selon la géométrie, et du couplage entre couche de cisaillement et instabilités centrifuges ;
- le développement d'une PIV stéréoscopique tomographique fondée sur un algorithme de flot optique ;
- le développement de méthodes d'identification de frontières et de structures de l'écoulement ;
- le contrôle en boucle fermée de l'écoulement.

La caractérisation physique de la dynamique de l'écoulement dans la cavité et du couplage entre couche de cisaillement et instabilités centrifuges, pourra faire l'objet de l'encadrement d'une thèse. Si la morphologie de la recirculation de l'écoulement en fonction du rapport de forme L/H et le domaine d'existence des instabilités centrifuges ont été établis à partir de visualisations, des mesures complémentaires quantitatives sont néanmoins nécessaires pour comprendre complètement l'effet du rapport d'envergure S/H . Des informations supplémentaires pourront être apportées sur la déstabilisation de l'écoulement en fonction du rapport d'envergure S/H et du confinement des parois latérales de la cavité. En effet, le comportement du domaine d'existence des instabilités centrifuges diffère fortement pour $S/H = 2$ par rapport aux autres rapports d'envergure. Cette différence a été interprétée par le rôle prépondérant du confinement dans ce cas, mais cette question ne peut être définitivement tranchée que par une analyse de stabilité. De même, l'étude de la sensibilité de l'écoulement aux conditions limites devra être réalisée, comme cela a été le cas pour une cavité entraînée par un couvercle mobile (Migeon, 2000), où l'ajout de rugosités en paroi pilote l'apparition des instabilités centrifuges. Dans le cas présent de l'entraînement par un écoulement extérieur, on doit analyser la déstabilisation de la rangée des tourbillons centrifuges et l'oscillation périodique de leur amplitude, qui est observée seulement pour $S/H = 12$ et définie comme une instabilité secondaire (Faure *et al.*, 2009). Des données quantitatives et résolues en temps du champ de vitesse permettraient d'évaluer les mécanismes de déstabilisation de l'écoulement dans ce cas. La synergie entre expérimentation et DNS s'est bien développée dans notre groupe. L'analyse conjointe des données expérimentales et numériques restera un des leviers nous permettant d'accéder au développement spatio-temporel des structures tourbillonnaires.

Le deuxième axe de recherche est le développement de la PIV par flot optique vers une PIV stéréoscopique tomographique, éventuellement résolue en temps. L'objectif est l'obtention de bases de données expérimentales des trois composantes de vitesse dans un volume, pouvant faire écho aux résultats de simulations numériques, qui fournissent les trois composantes de vitesse dans l'espace au cours du temps. L'intérêt de ces mesures et leur représentation a été exposé lors de la 25^e Journée Thématische de l'AFVL, en partenariat avec FLUVISU, et intitulé « Des techniques d'imagerie à la visualisation 3D d'écoulements » que j'ai organisée le 9 avril 2009 à Orsay. Une telle densité d'information permettrait non seulement une confrontation complète aux résultats issus de simulations numériques, mais ces données pourraient être représentées à travers l'environnement de réalité virtuel immersif développé au LIMSI. Cet environnement devrait contribuer à surmonter l'obstacle de représentation que constitue la richesse de l'information des trois composantes d'un champ volumique instationnaire, à travers le couplage entre le visuel, le son et l'haptique (retour d'effort, sens du toucher). Il est une aide à la compréhension des structures de l'écoulement et à leur suivi temporel. Afin de s'orienter vers cette voie et constituer une base de données expérimentales, une ébauche de PIV stéréoscopique tomographique pourrait être réalisée dans un premier temps. Ce système consisterait à mettre en place deux nappes perpendiculaires

entre elles et utilisant deux lasers YAG en polarisation croisée, chaque plan étant couplé à 2×2 caméras, chacune possédant un filtre polarisant adapté. Du point de vue de la compréhension phénoménologique, ces informations permettraient de caractériser le plan de la recirculation et le plan des instabilités centrifuges de la cavité, afin d'obtenir des informations corrélées dans les deux plans et d'améliorer la compréhension du couplage dynamique entre les structures de la couche de cisaillement et les instabilités centrifuges. À plus long terme, l'avancée des technologies laser et du traitement informatique des données permettra de considérer un système réellement volumique. Un tel système de vélocimétrie volumétrique à trois composantes est déjà commercialisé et utilise la PIV numérique défocalisée (Pan *et al.*, 2008). L'apport de l'algorithme du flot optique par programmation dynamique orthogonale sur de tels champs expérimentaux, quoique nécessitant des temps de calcul élevés et fournissant une base de données extrêmement dense, mériterait une évaluation.

Le troisième point vise à apporter des progrès significatifs dans la compréhension de la structuration spatio-temporelle de l'écoulement, et s'inscrit dans le cadre de l'ANR DIB. Pour cela, des outils d'analyse quantitatifs d'identification de structures tourbillonnaires seront mis en œuvre sur des champs de vitesse résolus en temps. Des critères eulériens seront appliqués aux champs de vitesse de la cavité (vorticité, critères Q , λ_2 , Γ_2 , suivi de points critiques de l'écoulement ou Feature Flow Fields, …). Des techniques de suivi de frontières matérielles au cours du temps, fondées sur une analyse lagrangienne (structures cohérentes lagagiennes, ou LCS, extraites des champs d'exposants de Lyapunov aux temps finis ou FTLE, ou à distance finie ou FSLE, …) seront développées et adaptées. L'objectif sera d'extraire et de corrélérer la dynamique du champ de vitesse, à travers sa topologie, au champ de pression. Le cas échéant, on espère pouvoir mettre en évidence une dynamique basse fréquence, éventuellement présente dans les structures de l'écoulement. Il est en effet possible que ces basses fréquences se dissimulent dans un signal de pression ou dans des mesures LDV réalisées dans la couche de cisaillement. La mise en œuvre de ces méthodes d'identification et de suivi s'effectuera à partir d'une base de données de mesures couplées pression/vitesse établie sur la cavité. L'objectif sera de pouvoir remonter à une structure spatiale de l'écoulement à partir d'une information locale. Après validation, l'extension de l'application de ces moyens à des classes plus larges d'écoulements pourra être envisagée.

Enfin, une perspective à plus long terme sera le développement du contrôle en boucle fermée de l'écoulement de cavité, et s'inscrit dans le cadre de l'ANR CORMORED. Son application pratique concerne notamment la problématique environnementale du transport d'un polluant et des échanges de quantité de mouvement avec l'extérieur, dans un milieu partiellement confiné, comme une rue bordée d'immeubles. Le contrôle envisagé ici a pour but la suppression, ou au contraire l'augmentation, des instabilités afin de piloter l'échange entre la cavité et l'écoulement extérieur. Ce projet diffère par ce point de la plupart des projets de contrôle développé actuellement et qui s'attachent principalement au rayonnement acoustique engendré. Une série de capteurs de pression sera implanté en aval de la cavité, tandis qu'un système d'actionneurs, placé en amont, permettra d'agir sur l'écoulement en temps réel, via le modèle de contrôle. Ce modèle sera développé au sein de l'équipe Aérodynamique du LIMSI (Lionel Mathelin, Luc Pastur). À nombre de Reynolds modéré, les applications concernent le transport d'un scalaire dans et à l'extérieur de la cavité. À la suite de la thèse de Jérémie Basley, actuellement en cours, qui porte sur l'implantation d'un premier système, un sujet de thèse pourra être proposé afin de mettre en œuvre pratiquement ce contrôle et caractériser systématiquement son impact selon les paramètres de l'écoulement (nombre de Reynolds, géométrie de la cavité) et le type d'action souhaitée (diminution ou augmentation des instabilités). Dans ce contexte, le montage au LIMSI d'un second dispositif expérimental, à savoir un canal en eau, pourra compléter la soufflerie basse vitesse actuelle.

Ce canal hydraulique donnera accès à une meilleure dynamique de pression, permettant d'identifier plus facilement un signal d'activation du contrôle. De plus, des moyens électrolytiques pourront être utilisés en eau et permettront une évaluation quantitative du transfert d'un scalaire. Dans ce cadre, les outils d'identification, de suivi et d'analyse des structures de l'écoulement développées dans le troisième point de ces perspectives, seront mis en pratique et devraient constituer des éléments déterminants pour la compréhension de la dynamique et des effets du modèle de contrôle retenu.

L'utilisation de la PIV multi-plans, d'outils d'identification de structures d'écoulement et le savoir-faire acquis en contrôle actif, qui constituent les trois dernières perspectives de mon projet, pourront également permettre une ouverture vers des applications plus larges que le cadre des écoulements de cavité. La mise en œuvre de ce savoir-faire pourra concerter tout écoulement présentant une recirculation. Une première application touche au domaine automobile, où la caractérisation et le contrôle de l'écoulement de culot sont des préoccupations majeures en vue d'une réduction de la traînée. On pourrait ainsi envisager une étude expérimentale sur une maquette typique d'un arrière-corps de véhicule (corps d'Ahmed). Un autre domaine d'application serait celui des énergies renouvelables, à travers les hydroliennes et les éoliennes. Le couplage fluide-structure résultant de l'interaction entre un tourbillon d'extrémité et la pale qui le suit, pourrait être envisagé à travers une étude en grille d'aubes.

Références

- FAURE, Th. M., PASTUR, L. R., LUSSEYRAN, F., FRAIGNEAU, Y., BISCH, D** (2009) Three-dimensional centrifugal instabilities development inside a parallelepipedic open cavity of various shape, *Experiments in Fluids*, Vol. 47, No. 3, pp. 395–410
- MIGEON, Ch.** (2000) *Contribution à l'analyse de l'écoulement tridimensionnel instable s'établissant à l'intérieur de cavités cylindriques*, Thèse de Doctorat, Université de Poitiers
- PAN, G., MENON, R., ZHANG, H., LAI, W., GRAFF, E., GHARIB, M.** (2008) Quantitative 3D flow visualization using volumetric 3-component velocimetry, *13th International Symposium on Flow Visualization*, Nice (France), July 1-4 2008, paper ID 286

C. Publications

Turbulence/Turbulence

Bilans de tension de Reynolds dans un sillage de traînée et dans un sillage de corps autopropulsé par une hélice

Thierry FAURE et Gilles ROBERT

Résumé – Chaque terme des bilans de tension de Reynolds est déterminé expérimentalement pour un sillage avec traînée et pour le sillage d'un corps autopropulsé par une hélice. La nature fondamentalement différente de ces deux types d'écoulement est clairement mise en évidence à travers l'analyse des bilans de la tension de Reynolds axiale, du cisaillement axial-radial et du cisaillement radial-tangential.

Reynolds stress balances in a wake with drag and in the wake of a self-propelled, propeller-driven body

Abstract – All the terms in the Reynolds stress balances are experimentally evaluated in a wake with drag and in the wake of a self-propelled, propeller-driven body. The fundamental difference between these two kinds of flow is particularly evident in the analysis of the axial Reynolds stress, the axial-radial shear and the radial-tangential shear balances.

Abridged English Version – Reynolds stress equations are important for understanding and modelling physical phenomena in a flow. However, for the subject flow, very few experimental data are available, except for axisymmetric jets (Panchapakesan, 1993; Hussein, 1994, etc.) and a two-dimensional wake (Aronson, 1994). We present measurements of these balances for two different kinds of axisymmetric wakes tested in a wind tunnel: a wake with drag and the wake of a self-propelled, propeller-driven body. The model used to generate the wake is a streamlined body of 50 cm in length with a diameter $D = 8$ cm immersed in an air flow of 11 m/s (fig. 1). Self-propulsion is produced by means of a propeller, rotating at a velocity of 15,000 rpm. For that wake, the flow is characterized by a mean azimuthal velocity, a component that does not exist in the case of a jet-driven body (Naudascher, 1965; Cimbala, 1990 and Park, 1991). All the measurements are taken with a triple hot-film anemometric probe, in the self-preservation zone ($x/D > 15$).

We consider a simplified expression for each Reynolds stress equation, using boundary layer approximation that is based on an analysis of the order of magnitude for each term (Corrsin, 1963). Then, each equation can be written as the balance:

$$\text{convection} = \text{production} + \text{kinetic transfer} + \text{pressure transfer} + \text{dissipation}$$

The method used to experimentally determined the terms of this balance is the same as the one used by Browne (1989). All the terms are measured except the pressure transfer, which is deduced from the balance. Dissipation is determined by the means of an isotropic formulation, and vanishes in the shear stress equations. An analysis of the dissipation spectrum validates the use of the isotropic formulation (fig. 2).

Results of the axial Reynolds stress, the axial-radial shear and the radial-tangential shear are presented for both experimental configurations. From equation (1), we note that our measurements are in good agreement with those of Aronson (fig. 3). Whereas for the wake with drag all the transfers are taking part in the balance (fig. 4), the self-propelled wake is mainly dominated by convection (fig. 5), which proves that the turbulence generated by the propeller

Note présentée par Geneviève COMTE-BELLOT.

is carried downstream in the far wake. For the axial-radial shear equation (2), given for the wake with drag (*fig. 6*), an equilibrium between production and pressure transfer is established away from the wake axis (*fig. 7*) in the self-propelled case. The balance (3) demonstrates that for the wake of a propeller-driven body, radial-tangential shear is produced by the mean azimuthal velocity gradient (*fig. 8*).

1. INTRODUCTION. — Les équations des tensions de Reynolds donnent des renseignements sur les évolutions des propriétés statistiques d'ordre deux associées aux fluctuations de vitesse en un point. Si ces équations sont fondamentales dans la compréhension de la modélisation des phénomènes physiques intervenant dans un écoulement, il faut noter que très peu de données expérimentales relatives aux sillages sont disponibles dans la littérature. La plupart du temps, on se contente de donner le bilan d'énergie cinétique turbulente, qui correspond aux échanges turbulents selon les trois directions de l'espace. De tels résultats ont été publiés pour un jet cylindrique (Wygnanski, 1969), un sillage de barreau (Browne, 1987) et un sillage à symétrie de révolution axiale, avec traînée ou propulsé par une hélice (Faure, 1995). Les seules données disponibles, de chacun des bilans des variances des fluctuations de vitesse \bar{u}_i^2 , concernent les jets (Panchapakesan, 1993 ; Hussein, 1994, ...) et le sillage bidimensionnel d'un cylindre (Aronson, 1994). On s'intéresse ici à la mesure des bilans complets des tensions de Reynolds pour deux types de sillages à symétrie de révolution axiale.

2. CONFIGURATIONS EXPÉRIMENTALES. — Les essais sont effectués dans une veine aérodynamique où est implantée une maquette profilée à symétrie de révolution axiale, de diamètre $D=8$ cm et de 50 cm de long (*fig. 1*). Deux configurations expérimentales sont étudiées :

— un sillage de traînée, créé simplement par un écoulement uniforme incident sur l'obstacle ;

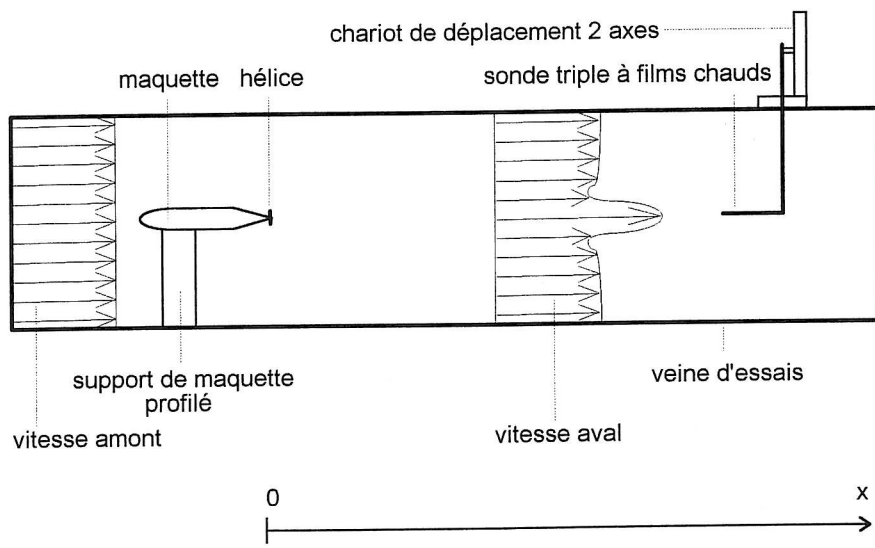


Fig. 1. — Dispositif expérimental.

Fig. 1. — Experimental set-up.

– un sillage de corps autopropulsé par hélice, pour lequel la force de traînée due à l'écoulement incident est exactement compensée par une force de poussée générée par le système de propulsion, qui est en l'occurrence une hélice de 4 cm de diamètre entraînée par un moteur électrique et montée au bord de fuite de la maquette.

La vitesse de l'écoulement amont est de 11 m/s et la vitesse de rotation de l'hélice correspondant à la configuration autopropulsée est fixée à 15 000 tr/mn. La particularité de l'autopropulsion par hélice est la présence d'une composante moyenne de vitesse tangentielle, qui n'existe pas pour les sillages propulsés par jet (Naudascher, 1965 ; Cimbala, 1990 et Park, 1991). L'ensemble des mesures est réalisé à l'aide d'une sonde anémométrique triple à films chauds permettant la détermination complète du vecteur vitesse instantané (Müller, 1992). Les trois capteurs sont orthogonaux entre eux et inclus dans une sphère de 3 mm de diamètre, qui correspond à l'échelle de Taylor des plus petites structures rencontrées dans l'écoulement. Dans les deux cas, les résultats présentés proviennent de la zone où il y a l'affinité des échanges turbulents ($x/D > 15$).

3. LES ÉQUATIONS DES TENSIONS DE REYNOLDS. – Ces équations sont très compliquées car elles comportent de nombreux termes ; il est donc intéressant d'en rechercher des formes simplifiées valables dans une région de l'écoulement située loin de l'obstacle générateur du sillage. Des expressions simplifiées s'obtiennent en réalisant une approximation dite de la « couche limite », qui consiste à effectuer une analyse en ordre de grandeur de chacun de leurs termes et à ne conserver que ceux d'un ordre suffisamment grand (Corrsin, 1963). Chacune des six équations des tensions de Reynolds se présente alors sous la forme suivante :

$$\text{convection} = \text{production} + \text{transfert cinétique} + \text{transfert pression} + \text{dissipation}$$

La méthode utilisée pour déterminer expérimentalement les différents types de transport des tensions de Reynolds est semblable à celle employée par Browne (1987). Tous les termes sont mesurés à l'exception du transfert par interaction pression-vitesse qui est obtenu par différence du bilan. Les termes de convection où apparaît une dérivée axiale, sont déterminés en considérant chaque grandeur physique à dériver comme étant le produit d'une fonction d'échelle ne dépendant que de x/D et d'une fonction de forme dépendant de r/r^* , où r^* est le rayon du sillage qui dépend de la distance axiale x/D . Par exemple, pour la variance des fluctuations de vitesse axiale, on a la décomposition :

$$\overline{u_x^2} = \overline{u_{x_m}^2}(x/D) f(r/r^*)$$

Un lissage des données par une méthode des moindres carrés est effectué avant leur dérivation. Les moments d'ordre 3 qui apparaissent dans les termes de transfert cinétique sont mesurés directement grâce à la sonde triple, en choisissant un temps d'acquisition suffisamment grand pour que soit assurée la convergence statistique de ces quantités. Les termes de dissipation sont évalués à l'aide d'une hypothèse de turbulence isotrope. De ce fait, ces termes dissipatifs n'apparaissent pas dans les équations des tensions de cisaillement $\overline{u_x u_r}$ et $\overline{u_r u_\theta}$. L'utilisation de cette formulation isotrope sous-estime la dissipation réelle d'environ 20 à 30 % dans le cas d'un sillage de barreau (Browne, 1987 ; Aronson, 1994). Cependant, une analyse des spectres unidimensionnels montre que dans la zone où il y a le maximum de dissipation, le spectre des fluctuations de vitesse radiale E_{rr} estimé à l'aide de la formule isotrope, à partir du spectre axial, ne diffère que très peu du spectre radial mesuré (fig. 2).

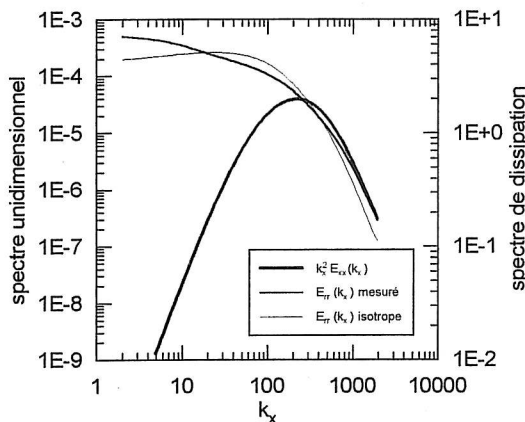


Fig. 2. – Comparaison entre le spectre de dissipation et les spectres unidimensionnels de vitesse radiale mesuré et isotrope, pour le sillage de corps autopropulsé.

Fig. 2. – Comparison between the dissipative spectrum and the measured and isotropic radial one-dimensional spectra, for the wake of a self-propelled body.

4. RÉSULTATS EXPÉRIMENTAUX. – On présente successivement pour chaque configuration étudiée (sillage de traînée et sillage de corps autopropulsé) les évolutions radiales des bilans de la tension de Reynolds axiale, du cisaillement axial-radial, et dans le second cas, le bilan du cisaillement radial-tangential. La direction radiale est représentée sous forme relative par rapport au rayon du sillage r^* .

L'équation de la tension de Reynolds axiale s'écrit en coordonnées cylindriques, pour un écoulement à symétrie de révolution axiale :

$$(1) \quad \underbrace{\bar{U}_x \frac{\partial \bar{u}_x^2}{\partial x}}_{\text{convection}} = \underbrace{-2 \bar{u}_x \bar{u}_r \frac{\partial \bar{U}_x}{\partial r}}_{\text{production}} - \underbrace{\frac{\partial \bar{u}_x^2 \bar{u}_r}{\partial r} - \frac{\bar{u}_x^2 \bar{u}_r}{r}}_{\text{transfert cinétique}} + \underbrace{\frac{2}{\rho} \bar{p} \frac{\partial \bar{u}_x}{\partial x}}_{\text{transfert pression}} - \underbrace{\bar{\varepsilon}_{xx}}_{\text{dissipation}}$$

Les résultats de notre étude (sillage de traînée à symétrie de révolution axiale) sont comparés avec ceux obtenus par Aronson et Löfdahl dans le cas du sillage bidimensionnel d'un barreau circulaire (fig. 3). Les mêmes formes pour chacun des transports sont observées pour ces deux types de sillages lointains. Notons que les termes sont représentés

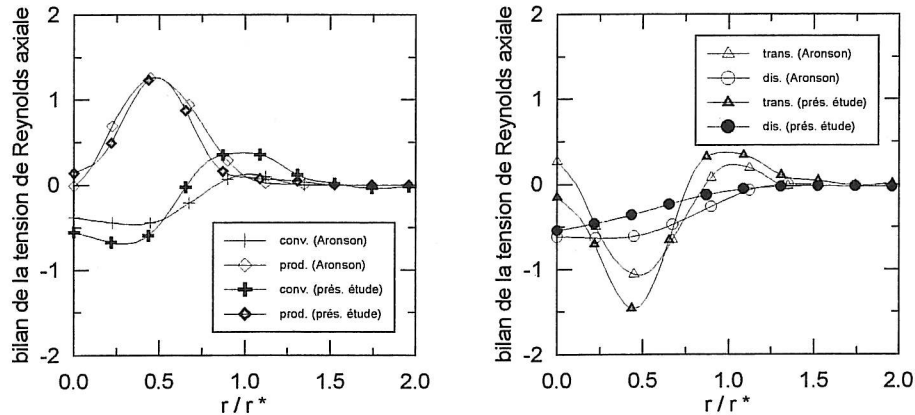


Fig. 3. – Comparaison du bilan de la tension de Reynolds axiale dans un sillage de traînée bidimensionnel (Aronson) et un sillage de traînée à symétrie cylindrique (présente étude).

Fig. 3. – Comparison of the axial Reynolds stress balance for a two-dimensional wake with drag (Aronson) and for an axisymmetric wake with drag (present study).

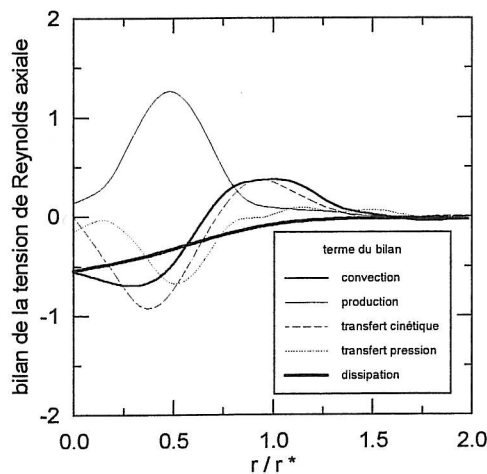


Fig. 4. – Bilan de la tension de Reynolds axiale (sans dimension) dans un sillage de traînée.

Fig. 4. – Axial Reynolds stress balance (dimensionless) in a wake with drag.

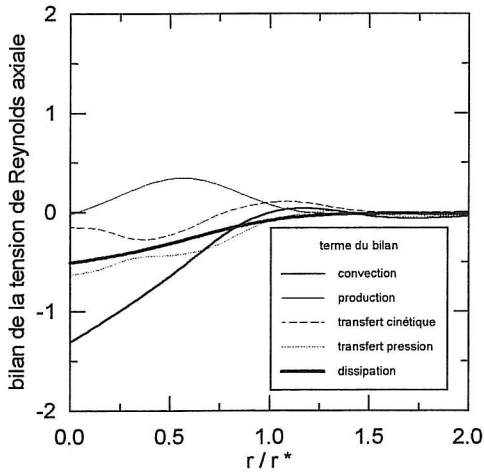


Fig. 5.

Fig. 5. – Bilan de la tension de Reynolds axiale (sans dimension) dans le sillage d'un corps autopropulsé.

Fig. 5. – Axial Reynolds stress balance (dimensionless) in the wake of a self-propelled body.

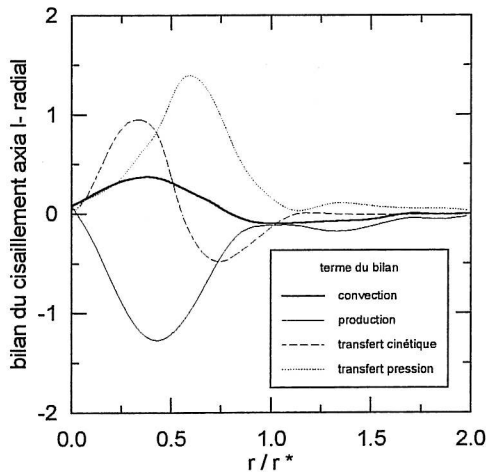


Fig. 6.

Fig. 6. – Bilan du cisaillement axial-radial (sans dimension) dans un sillage de traînée.

Fig. 6. – Axial-radial shear balance (dimensionless) in a wake with drag.

sur deux graphes différents pour une meilleure lisibilité. Si on trace tous ces échanges sur la même figure, pour le sillage de traînée (fig. 4), tous les types de transport interviennent dans le bilan. Par contre, les résultats originaux concernant le sillage de corps autopropulsé montrent que l'écoulement est dominé par le terme de convection, les autres transferts n'intervenant que dans un moindre proportion (fig. 5). Cela indique, dans ce second cas, que l'agitation turbulente générée par l'hélice est massivement transportée par l'écoulement moyen et qu'il n'y a que très peu de production où de diffusion radiale dans le sillage lointain. Les mêmes commentaires peuvent être effectués pour les équations des tensions de Reynolds $\overline{u_r^2}$ et $\overline{u_\theta^2}$ qui ne sont pas présentées ici.

Les bilans des tensions de cisaillement constituent des résultats originaux, pour le sillage de traînée comme pour le sillage de corps autopropulsé par hélice. L'équation du cisaillement axial-radial est donnée par l'expression :

$$(2) \quad \underbrace{\bar{U}_x \frac{\partial \bar{u}_x u_r}{\partial x} - \frac{2}{r} \bar{U}_\theta \bar{u}_x u_\theta}_{\text{convection}} = \underbrace{-\bar{u}_r^2 \frac{\partial \bar{U}_x}{\partial x} - \frac{\partial \bar{u}_x \bar{u}_r^2}{\partial r} - \frac{\bar{u}_x \bar{u}_r^2}{r} + \frac{\bar{u}_x \bar{u}_\theta^2}{r}}_{\text{production}} + \underbrace{-\frac{1}{\rho} \frac{\partial p \bar{u}_x}{\partial r} + \frac{p}{\rho} \frac{\partial \bar{u}_x}{\partial r}}_{\text{transfert pression}}$$

Pour le sillage de traînée (*fig. 6*), il faut remarquer que les termes de transfert cinétique, de transfert par interaction pression-vitesse et de production sont prépondérants par rapport à la convection : l'agitation turbulente contribue donc à la création du cisaillement et à son transport selon la direction radiale. Par contre, dans le cas de l'autopropulsion (*fig. 7*), il y a équilibre uniquement entre la production et le transfert par interaction pression-vitesse, en dehors de l'axe du sillage. La turbulence intervient dans une moindre proportion dans la diffusion radiale de cette composant de cisaillement. Il faut également remarquer que la contribution du terme de production est négative pour le sillage de traînée, et positive dans le cas du sillage de corps autopropulsé.

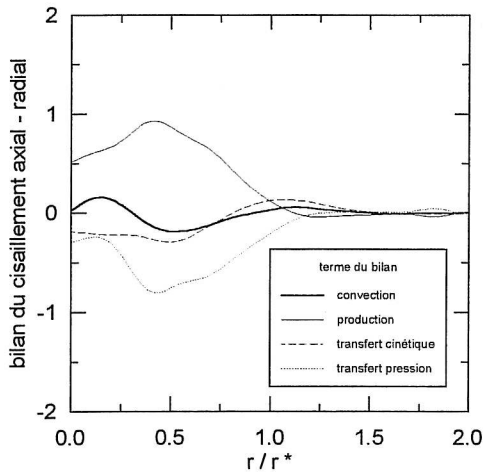


Fig. 7.

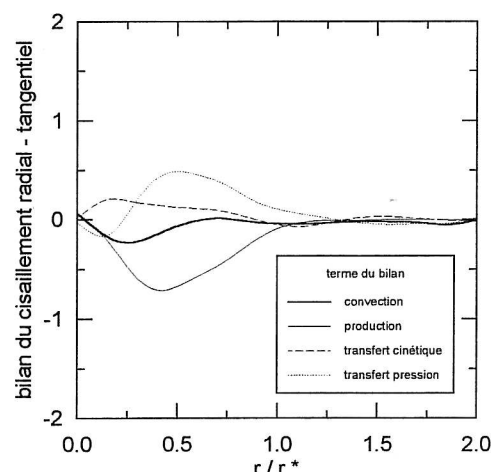


Fig. 8.

Fig. 7. – Bilan du cisaillement axial-radial (sans dimension) dans le sillage d'un corps autopropulsé.

Fig. 7. – Axial-radial shear balance (dimensionless) in the wake of a self-propelled body.

Fig. 8. – Bilan du cisaillement radial-tangential (sans dimension) dans le sillage d'un corps autopropulsé.

Fig. 8. – Radial-tangential shear balance (dimensionless) in the wake of a self-propelled body.

Le bilan de la tension de cisaillement $\bar{u}_x \bar{u}_\theta$ n'est pas significatif dans les deux configurations étudiées du fait de la symétrie de révolution axiale des écoulements. Par contre, la présence d'une composante de vitesse moyenne tangentielle, propre

à l'autopropulsion par hélice, conduit à s'intéresser à l'équation du bilan du cisaillement radial-tangential dans ce cas :

$$(3) \quad \underbrace{\overline{U}_x \frac{\partial \overline{u}_r u_\theta}{\partial x} - \frac{\overline{U}_\theta}{r} (\overline{u}_r^2 - \overline{u}_\theta^2)}_{\text{convection}} = \underbrace{-\overline{u}_r^2 \frac{\partial \overline{U}_\theta}{\partial r} + \overline{u}_\theta^2 \frac{\overline{U}_\theta}{r}}_{\text{production}} - \underbrace{\frac{\partial \overline{u}_r^2 u_\theta}{\partial r} - 2 \frac{\overline{u}_r^2 \overline{u}_\theta}{r} + \frac{\overline{u}_\theta^3}{r}}_{\text{transfert cinétique}} - \underbrace{\frac{1}{\rho} \frac{\partial p \overline{u}_\theta}{\partial r} + \frac{1}{\rho r} p \frac{\partial \overline{u}_r}{\partial \theta} + \frac{1}{\rho} p \frac{\partial \overline{u}_\theta}{\partial r}}_{\text{transfert pression}}$$

Le bilan de l'équation (3) pour le sillage de corps autopropulsé (fig. 8) met clairement en évidence le fait que le cisaillement radial-tangential est globalement produit par le gradient de vitesse moyenne tangentielle.

Les principales différences entre les phénomènes d'échanges turbulents des tensions de Reynolds pour un sillage avec traînée et un sillage de corps autopropulsé par une hélice sont mises en évidence. L'ensemble de ces résultats expérimentaux permet une meilleure compréhension des processus énergétiques intervenant dans ces deux types d'écoulement. En particulier, une confrontation avec les modèles de prédiction du terme de transfert par les fluctuations de pression pourra être envisagée.

Note remise le 20 juillet 1995, acceptée le 11 octobre 1995.

RÉFÉRENCES BIBLIOGRAPHIQUES

- D. ARONSON et L. LÖFDAHL, The plane wake of a cylinder: an estimate of the pressure-strain rate tensor, *Physics of Fluids*, 6, (8), 1994, p. 2716-2721.
 L. W. B. BROWNE, R. A. ANTONIA et D. A. SHAH, Turbulent energy dissipation in a wake, *Journal of Fluid Mechanics*, 179, 1987, p. 307-326.
 J. M. CIMBALA et W. J. PARK, An experimental investigation of the turbulent structure in a two-dimensional momentumless wake, *Journal of Fluid Mechanics*, 213, 1990, p. 479-509.
 S. CORRSIN, Turbulence: experimental methods, *Handbuch Der Physik*, VIII/2, Springer-Verlag, Berlin, 1963, p. 524-590.
 T. FAURE, Étude expérimentale du sillage turbulent d'un corps à symétrie de révolution autopropulsé par hélice, *Thèse de doctorat*, École Centrale de Lyon, n° d'ordre 95-01, 1995.
 H. J. HUSSEIN, S. P. CAPP et W. K. GEORGE, Velocity measurements in a high-Reynolds-number, momentum-conserving, axisymmetric, turbulent jet, *Journal of Fluid Mechanics*, 258, 1994, p. 31-75.
 U. R. MÜLLER, Comparison of turbulence measurements with single, X and triple hot-wire probes, *Experiments in Fluids*, 13, 1992, p. 208-216.
 E. NAUDASCHER, Flow in the wake of self-propelled bodies and related sources of turbulence, *Journal of Fluid Mechanics*, 22, (4), 1965, p. 625-656.
 N. R. PANCHAPAKESAN et J. L. LUMLEY, Turbulence measurements in axisymmetric jets of air and helium. Part. 1. Air Jet, Part 2. Helium Jet, *Journal of Fluid Mechanics*, 246, 1993, p. 197-247.
 W. J. PARK et J. M. CIMBALA, The effect of jet injection geometry on two-dimensional momentumless wakes, *Journal of Fluid Mechanics*, 224, 1991, p. 29-47.
 I. WYGNANSKI et H. FIEDLER, Some measurements in the self-preserving jet, *Journal of Fluid Mechanics*, 38, (3), 1969, p. 577-612.

Turbulent kinetic energy balance in the wake of a self-propelled body

T. Faure, G. Robert

268

Abstract An experimental study of the turbulent wake of a self-propelled body in a wind tunnel is reported. A significant difference is formed between the turbulent kinetic energy balance in a wake with drag and in the wake of a self-propelled body: the production term is very small in comparison with the other terms of the turbulent kinetic energy balance, and this result seems to be typical of self-propulsion. The axial evolution of the wake radius and turbulent kinetic energy profiles are described. Sufficiently far downstream from the body, a self-similar profile is found. Particular attention is devoted to the turbulent kinetic energy balance; all the terms in the energy balance are evaluated experimentally.

List of symbols

D	diameter of the body
L	axial length scale
l	radial length scale
R	radius of the body
r	radial coordinate
r^*	radius of the wake
U	mean axial velocity scale
\hat{U}	defect velocity
U_e	freestream velocity
u	fluctuating velocity scale
x	axial coordinate
ε	dissipation rate
$\eta = r/r^*$	radial relative direction
θ	azimuthal coordinate
ν	kinematic viscosity
ρ	density

1

Introduction

Although wakes that spread behind different kinds of bodies have been studied many times (Carmody 1965, Chevray 1968), the development of a turbulent wake behind a self-propelled body is the subject of few publications. In this configuration,

the drag of the body is cancelled by a thrust, so that the momentum integral, which expresses the difference between thrust and drag, is equal to zero and a self-propelled wake is a momentumless one.

Two-dimensional self-propelled wakes have been studied experimentally by Cimbala and Park (1990) and Park and Cimbala (1991) where a momentumless configuration was obtained using jet injection. These authors found self-similarity of the axial and transverse turbulence intensities. The behaviour of turbulence was quite different from that of plane wakes with drag or jets but rather similar to grid turbulence. The type of injection (central or peripheral jet) was found to be an important parameter for the rate of decay of mean velocity and for spreading, however it had no influence on axial turbulence intensity.

Axisymmetric momentumless wakes were first investigated by Schooley and Stewart (1963) in a stratified medium; they observed slower entrainment in the vertical than in the horizontal direction but did not give data for the velocity field inside the wake. The benchmark experimentation for a self-propelled body is that of Naudascher (1965): a circular disk with a coaxial jet at its centre was placed in a wind tunnel at a Reynolds number based on the diameter of the disk of $Re_D = 5.5 \times 10^4$. He pointed out that, whereas the self-similar profiles for simple jets and wakes require only a single amplitude and width scaling, those for the momentumless wake depend on a number of additional normalising scales. The measurement of some of the terms of the turbulent kinetic energy balance led to the conclusion that the production term was very small in comparison with the convection term.

The problem was examined in a more theoretical way by Finson (1975). He used Naudascher's results to show that the far wake behaviour does not become independent of the initial conditions and that there is no natural length scale with which to characterise this region.

A comparison between a propeller-driven slender body and a peripheral-jet model was carried out by Swanson et al. (1974), Chieng et al. (1974) and Schetz and Jakubowski (1975). The Reynolds number was $Re_D = 6 \times 10^5$ and they observed that the wake development of a blunt body driven by a central jet to yield a zero momentum wake was different from the wake of a body driven by a peripheral jet.

Another noteworthy experiment is the investigation in the momentumless wake of an axisymmetric jet-propelled body, by Higuchi and Kubota (1990). They tested the influence of injection and showed that the relaxation zone depended on the turbulence in the initial wake.

Received: 25 May 1995/Accepted: 27 March 1996

T. Faure, G. Robert
Laboratoire de Mécanique des Fluides et d'Acoustique,
URA CNRS 263 École Centrale de Lyon, F-69131 Écully Cedex, France

Correspondence to: T. Faure

The authors wish to express their gratitude to Pr. J. N. Gence and Pr. J. Scott for their attention to this work. This experimental program was sponsored by the Direction des Recherches Études et Techniques.

The near region of the wake of a momentumless, propeller-driven body was compared with the wake generated by a body with a rotating hub without blades by Hyun and Patel (1992). The Reynolds number was $Re_D = 1.53 \times 10^5$. They processed the velocity measurements in phase with the propeller rotation and observed structures induced by each blade in a region that extended to two diameters downstream of the body.

We now turn our attention to theoretical approaches to the self-propelled wake flow problem. Tennekes and Lumley (1972) discussed the solution analytically far downstream for a two-dimensional momentumless wake. A similar approach was used by Ferry and Piquet (1987) in the axisymmetric case for a propeller-driven body. The problem is more complex than for the jet-driven body because of a tangential mean velocity component that appears in the turbulent kinetic energy equation.

Turbulent kinetic energy balances are available for jets and simple wakes. Wygnanski and Fiedler (1969) experimentally determined all the terms of the balance for an axisymmetric jet. Dissipation was evaluated using a semi-isotropic formulation and pressure transfer was deduced from the balance. Recently, balances of turbulent kinetic energy and Reynolds stresses were produced in axisymmetric jets (Panchapakesan and Lumley 1993, Hussein et al. 1994). A two-dimensional cylinder wake was studied by Browne et al. (1987); they measured all the terms of the balance (except the pressure transfer term) and paid great attention to the dissipation. The nine major terms that make up the total dissipation were measured in the self-preserving region and compared with an isotropic dissipation formulation: the result indicated that the isotropic relation underpredicted the total dissipation by about 30%. These authors found self-similarity for every transport term in the far wake region.

The objective of the present investigation is to provide experimental data for a momentumless, propeller-driven, axisymmetric wake. An experiment was carried out in a wind tunnel and a complete characterisation from the near to the far region obtained. An analysis of the turbulent kinetic energy balance is carried out and we observe that the production term is an order of magnitude smaller than the other terms. In the self-similar zone, all the terms of the turbulent kinetic energy balance are evaluated.

2 Analysis

We consider the wake that develops far downstream from the body. The classical definition of this zone is based on a small velocity defect criterion. Let \hat{U} be the characteristic defect velocity, that is the maximum difference between the free-stream velocity U_e and the axial mean velocity. The small defect

$$\frac{\partial \bar{q}^2}{\partial x} = -\bar{u}_x \bar{u}_r \frac{\partial \bar{U}_x}{\partial r} - \bar{u}_r \bar{u}_\theta \left(\frac{\partial \bar{U}_\theta}{\partial r} - \frac{\bar{U}_\theta}{r} \right) - \frac{1}{r} \frac{\partial}{\partial r} (r \bar{q}^2 \bar{u}_r) - \frac{1}{\rho r} \frac{\partial}{\partial r} (r \bar{p} \bar{u}_r) - \varepsilon$$

$$\underbrace{\left(\frac{U}{u} \frac{l}{L} \right) \frac{u^3}{l}}_{\text{convection}} \quad \underbrace{\left(\frac{u}{U} \frac{L}{l} \right) \frac{u^3}{l}}_{\text{production}} \quad \underbrace{\left(\frac{u}{U} \frac{L}{l} \right) \frac{u^3}{l}}_{\text{kinetic transfer}} \quad \underbrace{\frac{u^3}{l}}_{\text{pressure transfer}} \quad \underbrace{\frac{u^3}{l}}_{\text{dissipation}}$$
(2)

criterion is

$$\frac{\hat{U}}{U_e} \ll 1$$

This definition of the far wake is difficult to quantify experimentally because we do not know, a priori, how small the above velocity ratio should be. A more useful working definition of the far region is where there is self-similarity of velocity profiles.

We now turn our attention to the behaviour of turbulence in this self-similar region. The average turbulent kinetic energy is defined as

$$\bar{q}^2 = (\bar{u}_x^2 + \bar{u}_r^2 + \bar{u}_\theta^2)/2$$

which satisfies the following equation in cylindrical coordinates for an axisymmetric mean flow with weak swirl:

$$\begin{aligned} \bar{U}_x \frac{\partial \bar{q}^2}{\partial x} + \bar{U}_r \frac{\partial \bar{q}^2}{\partial r} &= -\bar{u}_x^2 \frac{\partial \bar{U}_x}{\partial x} - \bar{u}_x \bar{u}_r \frac{\partial \bar{U}_r}{\partial x} - \bar{u}_x \bar{u}_\theta \frac{\partial \bar{U}_\theta}{\partial x} \\ &\quad - \bar{u}_x \bar{u}_r \frac{\partial \bar{U}_x}{\partial r} - \bar{u}_r^2 \frac{\partial \bar{U}_r}{\partial r} - \bar{u}_\theta^2 \frac{\bar{U}_r}{r} \\ &\quad - \bar{u}_r \bar{u}_\theta \frac{\partial \bar{U}_\theta}{\partial r} + \bar{u}_r \bar{u}_\theta \frac{\bar{U}_\theta}{r} \\ &\quad - \frac{\partial \bar{q}^2 \bar{u}_x}{\partial x} - \frac{\partial \bar{q}^2 \bar{u}_r}{\partial r} - \frac{\bar{q}^2 \bar{u}_r}{r} \\ &\quad - \frac{1}{\rho} \frac{\partial \bar{p} \bar{u}_x}{\partial x} - \frac{1}{\rho} \frac{\partial \bar{p} \bar{u}_r}{\partial r} - \frac{\bar{p} \bar{u}_r}{\rho r} \\ &\quad + \nu \left(\frac{\partial^2 \bar{q}^2}{\partial x^2} + \frac{\partial^2 \bar{q}^2}{\partial r^2} + \frac{1}{r} \frac{\partial \bar{q}^2}{\partial r} \right) - \varepsilon \end{aligned} \quad (1)$$

A simplified form can be obtained using the boundary layer approximation, which is based on an analysis of the order of magnitude of each term of the above equation (Corrsin 1963). Characteristic length and velocity scales are chosen and order of magnitude relations between these scales deduced from the continuity and momentum equations. In our problem, all terms in the equations of motion can be estimated using four independent scales:

- L the axial length scale ($\sim x$)
- l the radial length scale ($\sim r^*$, the wake width)
- U the mean axial velocity scale ($\sim U_e$)
- u the fluctuating velocity scale

In the far wake, we have $l/L \ll 1$ and $u/U \ll 1$ with both these ratios going to zero as x tends to infinity. This leads to the following dominant terms in the turbulent kinetic energy equation:

The order of magnitude of each term retained in the balance is noted in equation (2). Since, a priori, the relative magnitudes of the small quantities $l/L \ll 1$ and $u/U \ll 1$ are unknown, those terms which contains factors of their ratio,

$$K = \frac{u}{U} \frac{L}{l} \quad (3)$$

have been retained. For a drag wake, it is known that K tends to a constant value in the far wake. For a momentumless wake, we can argue that K ought also to tend towards a constant value as x tends to infinity, by appeal to the principle of the least degeneracy from the theory of asymptotics. Of course, this is not an argument that can be proved because the latter principle is only a rule of thumb. Nonetheless, a constant value of K is formed experimentally in the far wake. If we accept this, then all terms in (2) would appear to be necessary. In fact, we shall see, the numerical value of K turns out to be small and the term on the left of (2) dominates over the first two terms on the right.

For a drag wake, we can use conservation of momentum in the far wake to show that

$$\int_0^\infty r U_e (U_e - \bar{U}_x) dr = \text{const} \quad (4)$$

and this relation allows derivation of the overall properties of self-similarity. However, for the momentumless wake the constant is zero and Eq. (4) yields no useful result. To resolve this difficulty, a less obvious relation was established by Tennekes and Lumley (1974) in the plane case and by Ferry and Piquet (1987) for an axisymmetric flow. These authors use the equation for the axial mean velocity to show that

$$\int_0^\infty r^3 U_e (U_e - \bar{U}_x) dr = \text{const} \quad (5)$$

for a momentumless far wake. The order of magnitude relation for mean velocity defect is

$$\hat{U} = \frac{u^2}{U} \frac{L}{l} \quad (6)$$

which follows from the order of magnitude analysis of the equations of motion mentioned before Eq. (2). Then, Eq. (5) leads to the relation:

$$l^3 u^2 L = \text{const} \quad (7)$$

which, with (3) gives

$$u = \text{const} \times \left(\frac{U^3 K^3}{L^4} \right)^{1/5} \quad (8)$$

and

$$l = \text{const} \times \left(\frac{L}{U^2 K^2} \right)^{1/5} \quad (9)$$

If we now use constancy of K , $U = U_e$, $L = x$, and $l = r^*$, we have

$$u \sim x^{-4/5}, \quad r^* \sim x^{1/5} \quad \hat{U} \sim x^{-4/5} \quad (10)$$

These results are well known in the existing literature (Tennekes and Lumley 1974).

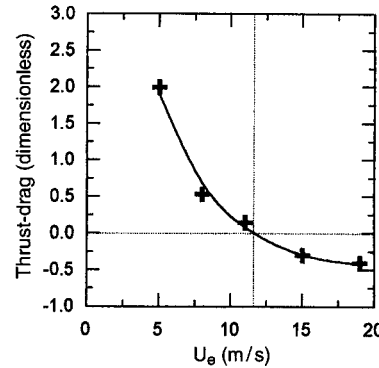


Fig. 1. Variation of the thrust-drag balance (dimensionless) with the freestream velocity

3

Experimental arrangements

The wake is generated by an axisymmetric, streamlined body, mounted in the working section of a wind tunnel (500 mm \times 500 mm, 6 m long). The experimental freestream velocity can vary from 5 to 80 m/s with a uniformity of $\pm 2\%$ and a maximum turbulence intensity of 0.7%. The model has a diameter $D = 8$ cm and a length of 50 cm. It has an elliptical nose, a cylindrical middle section and a conical stern. The propulsion system consists of a three-blade marine type propeller with a diameter of 4 cm. The inside of the body is hollow and contains the motor (Minimotor SA BLD 568 type, 15 000 rpm maximum speed) which drives the propeller. An electronic system is available to control the rotation speed. A support having a symmetrical NACA 66,012 profile with a chord of 10 cm and a maximum width of 1.2 cm was chosen to minimise aerodynamic perturbations around the body. Electrical wires for power supply and speed regulation are mounted inside this support. An alignment system allows the model to be oriented with the freestream flow. Once this adjustment is made, the angle between the wake axis and the tunnel axis was found to be less than 0.3° .

For a self-propelled body, the drag generated by the model equals the thrust created by the propulsion system. To bring about this state a momentum balance was established for the model. To this effect, we have two parameters which can vary, the freestream velocity and the propeller rotation speed. The momentum balance need the measurement of velocity and pressure, and these quantities were determined with a five-hole pressure probe. Note in Fig. 1 that the thrust-drag balance is normalized by the upstream momentum flux. The propeller rotation was fixed at its maximum value and the freestream velocity was varied to make the drag equal to the thrust. Self-propulsion was realised with a freestream velocity of 11 m/s.

The measurements are made in a closed wind tunnel and wakes are easily influenced by pressure gradients. Nevertheless, this pressure effect is small, as it is shown in Fig. 2; the momentum flux, plotted with the same scale as in Fig. 1 for comparison, is constant with axial distance.

The flow is three-dimensional and turbulent; it is therefore necessary to use a directional probe that can measure both the mean and the fluctuating parts of the velocity. An automated

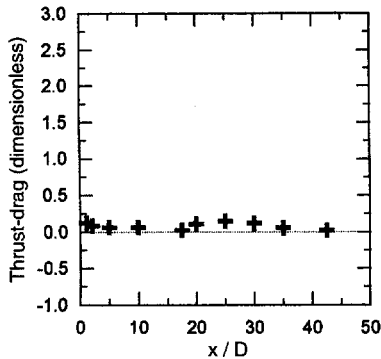


Fig. 2. Variation of the momentum flux (dimensionless) with the axial distance

triple hot-film anemometry system was developed that gives all three components of instantaneous total velocity. The probe is a Dantec 55R91 type, with an active length of 0.8 mm. It has a nickel film deposited on a quartz cylinder, 70 μm in diameter. The three film supports are orthogonal and inserted into a sphere of 2 mm diameter. Calibration of each sensor was performed in the unperturbed freestream. Periodic verification was carried out during the acquisition procedure: the probe was placed in the freestream from time to time and a calibration point obtained for each film. As part of the signal processing, such points were used to update the calibration curve. This procedure is used to avoid any change in the ambient temperature.

The films were operated as constant temperature anemometers at an overheat ratio of 0.7. Output voltages from the anemometers were passed through offset and gain circuits, before low-pass filtering with a cut-off frequency of 2 kHz. They were then digitised at a sampling frequency of 4 kHz per channel using a 12 bit A-D converter. The data were stored on the hard disk of a 80 386 PC computer for later processing. Sample of at least 20 s was necessary to obtain convergence of the averages for third order moments of fluctuating velocity.

A complete investigation in a plane perpendicular to the wake axis was performed for several axial distances from the near to the far wake. The Reynolds number based on the diameter of the body and the freestream velocity was $Re_D = 5.8 \times 10^4$.

4

Experimental determination of the turbulent kinetic energy balance

The method used to experimentally determine the turbulent kinetic energy balance is similar to the one described by Browne et al. (1987). Measurements were made of all the terms of Eq. (2) except for the pressure transfer term which was determined from the overall balance. The axial turbulent kinetic energy gradient, appearing on the left of Eq. (2), is defined from the self-similar form:

$$\overline{q^2} = \overline{q_m^2}(x/D) h(\eta) \quad (11)$$

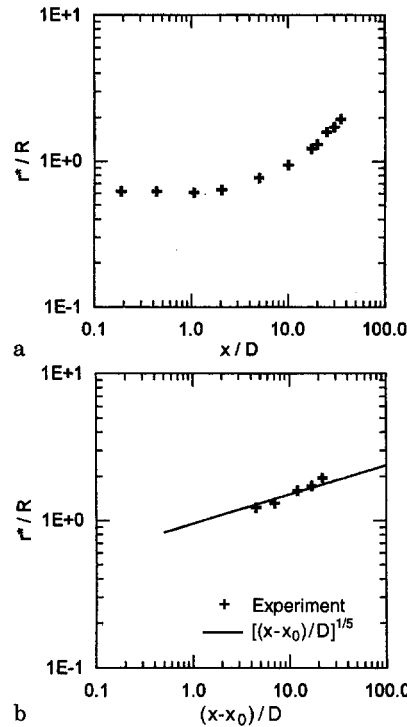


Fig. 3. a Axial variation of the radius of the wake from the trailing edge of the body; b axial variation of the radius of the wake from its virtual origin

where $\overline{q_m^2}$ is the maximum value of $\overline{q^2}$ at station x and $\eta = r/r^*(x/D)$ the radial similarity variable. Thus,

$$\frac{\partial \overline{q^2}}{\partial x} = \left[\frac{d\overline{q_m^2}}{dx}(x/D) h(\eta) - \overline{q_m^2}(x/D) \frac{\eta}{r^*} \frac{dr^*}{dx}(x/D) \frac{dh}{d\eta}(\eta) \right] / D \quad (12)$$

A least-square spline fit was first applied to the data on $h(\eta)$ before numerical differentiation yielding to $d h/d \eta$. The radial derivatives of $\overline{U_x}$, $\overline{U_\theta}$ and $r \overline{q^2 u_r}$ were obtained in a similar way. The three third order moments of the $\overline{q^2 u_r}$ term could be measured directly, thanks to the triple hot film probe. The dissipation term was evaluated using the classical isotropic formulation:

$$\varepsilon = 15 \nu \left(\frac{\partial \overline{u_x}}{\partial x} \right)^2 \quad (13)$$

in which the axial gradient term was evaluated using Taylor's hypothesis and the time derivative of the velocity fluctuation:

$$\varepsilon = \frac{15}{\overline{U_x^2}} \nu \left(\frac{\partial \overline{u_x}}{\partial t} \right)^2 \quad (14)$$

5

Results

The measurements were carried out over a wide range of axial positions ($0.19 \leq x/D \leq 50$, $x=0$ being at the trailing edge of the body). The radius of the wake r^* was defined as the location at which the axial turbulence intensity had fallen to half of its maximum value. Its axial evolution is plotted in Fig. 3a and

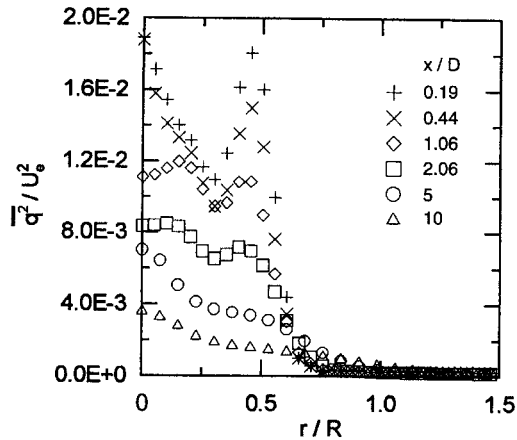


Fig. 4. Radial variation of the turbulent kinetic energy for $x/D \leq 10$

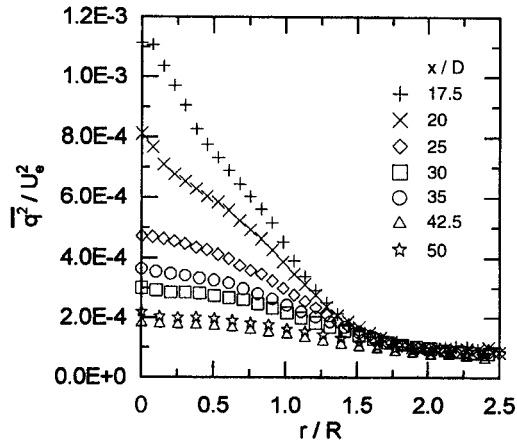


Fig. 5. Radial variation of the turbulent kinetic energy for $x/D \geq 17.5$

shows three different regions: the near wake where r^* is nearly constant, the establishment zone between $2 < x/D < 10$, and the far wake in which the behaviour has the asymptotic power law form. The virtual origin of the wake was determined by fitting the maximum turbulent kinetic energy to a self-similar power law in $x - x_0$. A least-squares method was used, leading to the virtual origin $x_0/D = 13$. With this correction, the asymptotic law for an axisymmetric, self-propelled body, with r^* proportional to $(x - x_0)^{1/5}$ is found (Fig. 3b).

Turbulent kinetic energy profiles are plotted for different axial positions in Figs. 4 and 5. We observe that the overall level decreases with axial distance in the wake. For this reason, it has been necessary to represent the evolution using two plots with a different scale. The turbulent kinetic energy shows two peaks in the near wake region, associated with the hub ($r/R \sim 0.15$) and the tip ($r/R = 0.5$) of the propeller blades. The higher level of turbulence is due to the emission of a horseshoe vortex on the hub and a tip vortex for each blade. The secondary peak vanishes for $x/D > 5$ and the primary one becomes a central maximum.

In Fig. 6, the turbulent kinetic energy has been scaled by its local maximum value and the radial coordinate scaled on the radius of the wake. It will be noticed that the form is the same

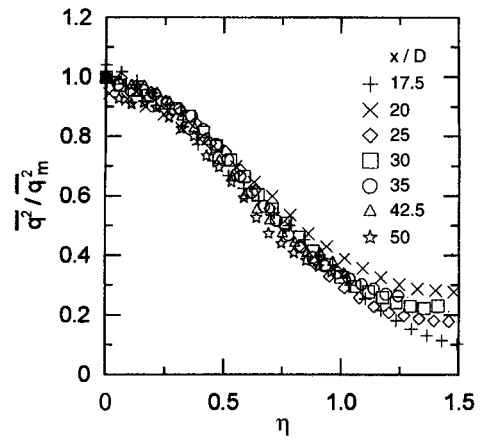


Fig. 6. Self-similar profile for the turbulent kinetic energy

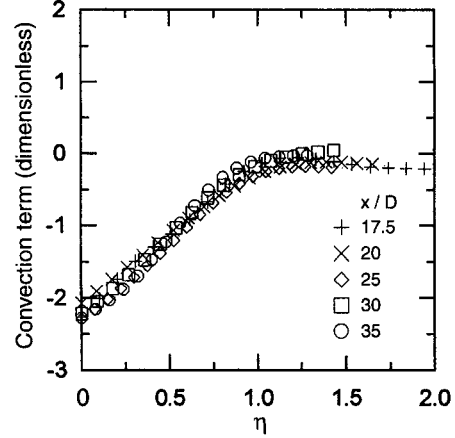


Fig. 7. Self-similar form of the convection term (dimensionless)

for any axial position, illustrating self-similarity of turbulent kinetic energy.

We can obtain a more precise definition of the constant K if we take $U = U_e$, $L = x$, and $l = r^*$ as the scales in Eq. (3). It is then found experimentally that $K \approx 0.05$, which is small and leads to negligible values for the first two terms on the right hand side of Eq. (2), which both contain factors of K in their order of magnitude estimates. Thus, to a good approximation, the energy balance in the momentumless far wake is described by:

$$\overline{U_x} \frac{\partial \overline{q_x^2}}{\partial x} = -\frac{1}{r} \frac{\partial}{\partial r} (r \overline{q^2 u_r}) - \frac{1}{\rho r} \frac{\partial}{\partial r} (r \overline{p u_r}) - \varepsilon \quad (15)$$

This equation expresses the fact that, in contrast with the case of a drag wake, the production terms are small and can be neglected.

The convection term, normalised by $\overline{q^2}^{3/2}/r^*$, is plotted in Fig. 7 for the far wake. Self-similarity is evident since the same curve is found for any axial distance $x/D \geq 17.5$. The same result is found for the other terms of the turbulent kinetic energy equation.

All the terms in (2) are given for the self-similar momentumless wake with weak swirl in Fig. 8. Note that in this

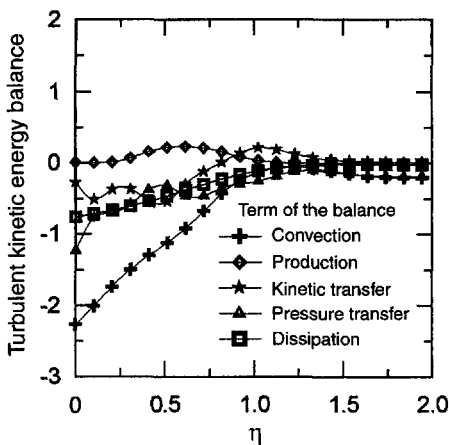


Fig. 8. Self-similar form of the turbulent kinetic energy balance (dimensionless) in the momentumless far wake

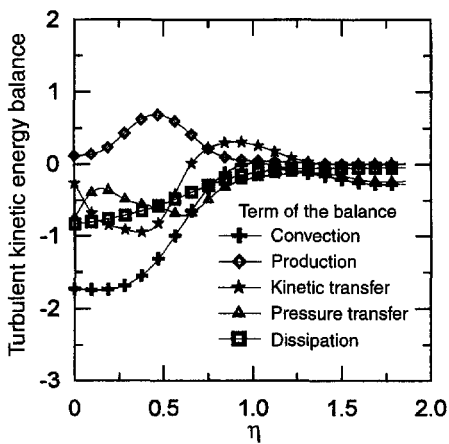


Fig. 9. Self-similar form of the turbulent kinetic energy balance (dimensionless) in the far wake of the same body without propeller

equation, the balance is written as an equilibrium between convection on the left hand side, and other transfers on the right hand side. As a result, a convection input of energy appears as a negative contribution in the balance, unlike the other terms. If one looks more closely at the radial variation of the overall turbulent kinetic energy balance, on the centreline of the wake, energy input is due to convection, while losses result from dissipation and kinetic and pressure transfers. As distance from the centreline increases, the magnitude of convection tends to decrease but remains the largest term in the balance. The kinetic transfer becomes positive in the outer part of the wake, where it represents an input of kinetic energy due to radial transport. The measurement of the production term validates the previous analysis that brings to (15). Although a wake is a decaying turbulent flow, and as a consequence, all the transfers are decreasing in magnitude with axial distance, the relative part of these transfers in the turbulent kinetic energy balance remains the same. This is provided with the dimensionless self-similar form. The observation that the production term is negligible in comparison with other

transfers could not be related to a decaying turbulence but to the momentumless relation (5). This result, previously observed for axisymmetric or two-dimensional jet-driven wakes, seems to be typical of the self-propelled bodies. In fact, for a drag-body wake, production is not small as shown in Fig. 9 (Faure 1995), but is the same order in magnitude as dissipation (see also Browne et al. 1987 for the two-dimensional case).

6 Conclusion

The turbulent far wake of a self-propelled body behaves in a different way than a drag wake. A velocity excess is characteristic of this kind of flow and the propeller-driven configuration considered here has a swirl component (in θ) that is not present for a jet-driven body. Self-similarity of the turbulent kinetic energy profile is found for any axial distance $x/D \geq 17.5$. All the terms of the turbulent kinetic energy equation are measured in this flow, which is an original set of data provided from this study. A main result of this investigation is that self-similarity of the turbulent kinetic energy balance is found experimentally in the far wake, by measurement of all the terms appearing in the balance. An important conclusion is that production of turbulent energy is negligible in comparison to the other transfer terms, a result which is typical of self-propulsion. This fact was previously established for a jet-driven two dimensional body wake (Cimbala and Park 1990) and for a jet-driven axisymmetric body wake (Naudascher 1965). In a drag wake, production and dissipation are of the same order of magnitude. In a momentumless wake the simple balance between production and dissipation no longer exists and this is a reason why turbulence models fail to predict this flow correctly. This result has been suggested by order of magnitude analysis of the energy equation based on the boundary layer approximation in the case of self-propulsion with limited experimental input, and confirmed by the detailed measurements.

References

- Browne LWB; Antonia RA; Shah DA (1987) Turbulent energy dissipation in a wake. *J Fluid Mech* 179: 307–326
- Corrsin S (1963) Turbulence: experimental methods. In: *Handbuch der Physik*. Vol. 8, Part 2 pp 524–590, Berlin: Springer-Verlag
- Carmody T (1964) Establishment of the wake behind a disk. *Trans ASME D J Basic Engng* 87: 869–882
- Cimbala JM; Park WJ (1990) An experimental investigation of the turbulent structure in a two-dimensional momentumless wake. *J Fluid Mech* 213: 479–509
- Chevray R (1968) The turbulent wake of a body of revolution. *Trans ASME D J Basic Engng* 90: 275–284
- Chieng CC; Jakubowski AK; Schetz JA (1974) Investigation of the turbulent properties of the wake behind self-propelled, axisymmetric bodies: Office of Naval Research, VPI-Aero-025, Sept. 1974, available through NTIS
- Faure T (1995) Étude expérimentale du sillage turbulent d'un corps à symétrie de révolution autopropulsé par hélice. PhD Thesis, No 95-01, École Centrale de Lyon
- Ferry M; Piquet J (1987) Sillage visqueux lointain d'un corps sous-marin autopropulsé. Report DRET 86 1201, SIREHNA
- Finson ML (1975) Similarity behaviour of momentumless turbulent wakes. *J Fluid Mech* 71 (3): 465–479
- Higuchi H; Kubota T (1990) Axisymmetric wakes behind a slender body including zero-momentum configurations. *Phys Fluids A* 2 (9): 1615–1623

- Hussein HJ; Capp SP; George WK** (1994) Velocity measurements in a high-Reynolds-number, momentum-conserving, axisymmetric, turbulent jet. *J Fluid Mech* 258: 31–75
- Hyun BS; Patel VC** (1991) Measurements in the flow around a marine propeller at the stern of an axisymmetric body. Part 1: Circumferentially-averaged flow, Part 2: Phase-averaged flow. *Exp Fluids* 11: 33–44 105–117
- Naudascher E** (1965) Flow in the wake of self-propelled bodies and related sources of turbulence. *J Fluid Mech* 22 (4): 625–656
- Panchapakesan NR; Lumley JL** (1993) Turbulence measurements in axisymmetric jets of air and helium. Part 1. Air jet, Part 2. Helium jet. *J Fluid Mech* 246: 197–247
- Park WJ; Cimbala JM** (1991) The effect of jet injection geometry on two-dimensional momentumless wakes. *J Fluid Mech* 224: 29–47
- Schetz JA; Jakubowski AK** (1975) Experimental studies of the turbulent wake behind self-propelled slender bodies. *AIAA J* 13 (12): 1568–1575
- Schooley AH; Stewart RW** (1963) Experiments with a self-propelled body submerged in a fluid with a vertical density gradient. *J Fluid Mech* 15 (1): 83–99
- Swanson Jr RC; Schetz JA; Jakubowski AK** (1974) Turbulent wake behind slender bodies including self-propelled configurations. Office of Naval Research, VPI-Aero-024, Sept. 1974, available through NTIS
- Tennekes H; Lumley JL** (1974) A first course in turbulence. Cambridge, MA: MIT Press
- Wygnanski I; Fiedler H** (1969) Some measurements in the self-preserving jet. *J Fluid Mech* 38: 577–612

Spectral analysis of the turbulent structure in the momentumless wake of a propeller-driven body

T. FAURE and G. ROBERT *

ABSTRACT. – Wind tunnel measurements of the velocity spectra behind a propeller-driven model with a momentumless wake are described. Immediately behind the body the spectra display marked peaks associated with the propeller rotation. These peaks become less marked downstream, the periodic effect becoming negligible beyond five body diameters behind the model, and they are concentrated in a limited zone directly affected by the rotor. The wide-band part of the radial velocity spectrum indicates a maximum near the normalised frequency $\beta \sim 4$, possibly associated with large turbulent structures near the wake boundary. In the far-wake the spectra tend to become self-similar.

1. Introduction

The investigation of the turbulent structure in the momentumless wake of a propeller-driven body is of interest because of its direct applicability to naval and aeronautical devices. In this configuration, the drag of the body is cancelled by a thrust, so that the momentum integral, which expresses the difference between thrust and drag, is equal to zero. It is of interest to investigate the effect of this initial condition on the development of the turbulent flow although, particularly with respect to spectral analysis, there are relatively few published studies.

Axisymmetric momentumless wakes were first investigated by Schooley and Stewart (1963) in a stratified fluid at a Reynolds number based on the diameter of the body $Re_D = 9900$; they observed slower entrainment in the vertical than in the horizontal direction but did not give data for the velocity field inside the wake. The benchmark experimentation for a self-propelled body is that of Naudascher (1965): a circular disk with a coaxial jet at its centre was placed in a wind tunnel at a Reynolds number based on the diameter of the disk $Re_D = 5.5 \times 10^4$. He pointed out that, whereas the self-similar profiles for simple jets and wakes require only a single amplitude and width scaling, those for the momentumless wake depend on a number of additional normalising scales. The measurement of some of the terms of the turbulent kinetic energy balance led to the conclusion that the production term was very small in comparison with the convection term.

* Laboratoire de Mécanique des Fluides et d'Acoustique, UMR CNRS 5509, École Centrale de Lyon, 69131 Écully Cedex, France.

A comparison between a propeller-driven slender body and a peripheral-jet model was carried out by Swanson *et al.* (1974), Chieng *et al.* (1974) and Schetz and Jakubowski (1975). The Reynolds number was $Re_D = 6 \times 10^5$ and they observed that the wake development of a blunt body driven by a central jet to yield a zero momentum wake was quite different from the wake of a body driven by a peripheral jet.

Another noteworthy experiment is the investigation in the momentumless wake of an axisymmetric jet-propelled body, by Higuchi and Kubota (1990). They tested the influence of injection and showed that the relaxation zone depended on the turbulence in the initial wake.

The near region of the wake of a momentumless, propeller-driven body was compared with the wake generated by a body with a rotating hub without blades by Hyun and Patel (1991). The Reynolds number was $Re_D = 1.53 \times 10^5$. They processed the velocity measurements in phase with the propeller rotation and observed structures induced by each blade in a region that extended to two diameters downstream of the body.

Two-dimensional self-propelled wakes have been studied experimentally by Cimbala and Park (1990) and Park and Cimbala (1991) where a momentumless configuration was obtained using jet injection at Reynolds number $Re_D = 5400$. These authors found self-similarity of the axial and transverse turbulence intensities. The behaviour of turbulence was quite different from that of plane wakes with drag or jets but rather similar to grid turbulence. The type of injection (central or peripheral jet) was found to be an important parameter for the rate of decay of mean velocity and for spreading, however it had no influence on the axial turbulence intensity. The first of these two studies is the only one where spectral analysis is carried out in a momentumless wake, a two-dimensional, jet-driven case. While a Kármán vortex shedding frequency and its harmonics are present for a wake with drag, there are no such identifiable peaks when self-propulsion is established. Noteworthy in the radial spectra is the maximum that occurs at the edge of the wake, which indicates that there exists a quasi-periodic vertical motion caused by some sort of large turbulent structure near the wake boundary.

Some spectral data are available for wakes with drag, where there is vortex shedding; we mention in a non-exhaustive list the experiments of Cimbala *et al.* (1988), Jones *et al.* (1988) and Cimbala and Krein (1990) for two-dimensional circular cylinder wakes. The experiment of Peterson and Hama (1978) performed in the axisymmetric wake of a slender body of revolution at $Re_D = 3600$ leads to the conclusion that the far-wake is the region in which non-linear interactions appear to predominate. Finally, self-preservation of spectra was shown in the far-wake of a two-dimensional cylinder by Wygnanski *et al.* (1986).

The objective of the present investigation is to provide spectral data for the axisymmetric momentumless wake of a propeller-driven body. An experiment is performed in a wind tunnel and a complete characterisation from the near to the far region is obtained. The analysis of the power spectral density functions will lead to the observation, in the near region of the wake, of spectral peaks associated with the propeller rotation and the periodic blade passage. The study of the turbulent structures will be conducted in the outer part of the wake. Then, the evolution of the wide-band part of the

spectra to self-similar behaviour will be shown for the far-wake. The similarity of the spectra in this region to homogeneous isotropic turbulence will suggest that turbulence in the momentumless far-wake may be treated as isotropic. The difficulties of measuring the dissipation function will be discussed.

2. Experimental arrangements and signal processing

The wake is generated by an axisymmetric, streamlined body mounted in the working section of a wind tunnel (500 mm × 500 mm, 6 m long). The experimental freestream velocity can vary from 5 m/s to 80 m/s with a uniformity of $\pm 2\%$ and a maximum turbulence intensity of 0.7%. The model diameter D is 8 cm and the length is 50 cm. It has an elliptical nose, a cylindrical middle section and a conical stern. The propulsion system consists of a three-blade marine type propeller with a diameter of 4 cm. The inside of the body is hollow and contains the motor (15,000 rpm maximum speed) which drives the propeller. An electronic system is available to control the rotation speed. A support having a symmetrical NACA 66₁ 012 profile with a chord of 10 cm and a maximum width of 1.2 cm was chosen to minimise aerodynamic perturbations around the body. Electrical wires for power supply and speed regulation are carried through this support. Provision was made for adjustment of the model with the freestream. Once this adjustment was made, the angle between the wake axis and the tunnel axis was found to be less than 0.3°. In the text, all the axial distances are measured from the trailing edge of the body and scaled on its diameter D .

For a self-propelled body, the drag generated by the model equals the thrust created by the propulsion system. To bring about this state a momentum balance was established for the model. To this effect, we have two parameters which can vary, the freestream velocity and the propeller rotation speed. The propeller rotation was fixed at its maximum value and the freestream velocity was varied to make the drag equal to the thrust (*Fig. 1*). Self-propulsion was established with a freestream velocity $U_e = 11.6$ m/s. The corresponding Reynolds number based on the diameter of the body was $Re_D = 5.8 \times 10^4$.

The flow is three-dimensional and turbulent; it is therefore necessary to use a directional probe that can measure both the mean and the fluctuating parts of the velocity. An automated triple hot-film anemometry system was developed that gives all three components of instantaneous total velocity. The probe is a Dantec 55R91 type, with the active lengths of the three sensors included into a sphere of diameter $d = 1.2$ mm. Each sensor is a nickel film deposited on a quartz cylinder, 70 μm in diameter. The three film supports are orthogonal and inserted into a sphere of 3 mm diameter. This dimension corresponds to the Taylor scale of the structures encountered in the flow. The smallest Kolmogorov microscale is $\eta = 0.4$ mm, which may be compared with the measurement volume according to the criterion $d \leq 3 - 4\eta$ given by Wyngaard and Pao (1971). Calibration of each sensor is performed in the unperturbed freestream. Periodic verification is carried out during the acquisition procedure: the probe is placed in the freestream from time to time and a calibration point obtained for each film. As part of the signal processing, such points are used to update the calibration curve. This procedure

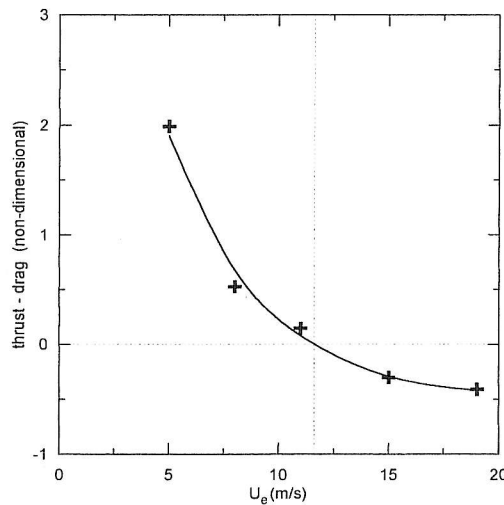


Fig. 1. – Variation of the thrust-drag balance (non-dimensional) with the freestream velocity.

avoids the influence of any change in the ambient temperature. The films are operated as constant temperature anemometers at an overheat ratio of 0.8. Output voltages from the anemometers are passed through offset and gain circuits. The signal is then analog filtered with a low-pass filter at a cut-off frequency that is half the sampling frequency, before being digitised with a 12 bit A-D converter. The data are stored on the hard disk of a 80386 PC computer for later processing. The various error sources throughout the acquisition procedure are carefully identified (Faure, 1995). Finally, the maximum global measurement errors are estimated to be 1.7% for mean velocity, 1.4% for second moments and 2.7% for triple moments.

When measuring spectra, an accurate bandwidth for low frequencies and a wide range of frequencies are needed. Thus, in order to obtain a single spectrum, two data acquisitions are carried out:

- a low-frequency-acquisition with a sampling frequency $f_{\text{samp}} = 7.5$ kHz and an acquisition time $t_{\text{samp}} = 20$ s;
- a high-frequency-acquisition with a sampling frequency $f_{\text{samp}} = 50$ kHz and an acquisition time $t_{\text{samp}} = 3$ s.

In each case 150,000 samples are taken for every point of measurement. Once these two spectra are measured, they are connected at a frequency of 1 kHz below which there is 95% of the turbulent energy. The mean-squared value of the error e is given according to Bendat and Piersol (1986) by:

$$e \approx \frac{1}{\sqrt{2\Delta f T}}$$

where T denotes the integration time and Δf is the frequency resolution. In the present study, an error of 8.3% is found.

3. The near-wake and the intermediate region

The radial evolution of the power spectral density function for the axial velocity fluctuations E_{xx} is plotted for different radial positions in Figure 2. The axial location in the momentumless wake is $x/D = 1$ and the radial coordinate is normalised with the radius of the model R . All the profiles for $0.25 \leq r/R \leq 0.75$ show peaks at the frequencies $f_0 = 250$ Hz and $3f_0$, that are associated respectively with the propeller rotation rate and the blade passing frequency. Harmonics of the first, $2f_0$ and $4f_0$, are also present but they are smaller in magnitude. Note that there is no peak in the inner part of the wake ($r/R \leq 0.25$). This region is associated with the wake of the propeller hub, and there is no influence of the periodic motion. Furthermore, for $r/R > 0.75$, there is again no peak in the spectrum. As a consequence, the rotation is restricted to a wake core while the outer region remains without swirl influence. The confinement of the rotation shows a behaviour quite different from isolated swirling motions. This effect may be typical of a momentumless rotor-driven wake. In fact, in any momentumless wake, there is a peripheral velocity deficit in the mean axial velocity profile, resulting from the drag effects. So, the isolation of the swirling motion in a central region may be due to these confinement effects. It is also noticeable in this figure that the wide-band part is decreasing from the centre to the freestream. A rapid change in the slope of spectra, in the high-frequency domain, appears from $r/R \sim 0.5$. This corresponds to a greater rate of decrease for the small turbulent structures. For the low frequencies, which contain most of the turbulent energy, the level falls rapidly at the wake boundary where $r/R = 0.625$. This means that turbulence is lower at the edge and in the freestream than in the core of the wake, and this transition is strongly marked. Therefore the turbulence intensity would be a good criterion to indicate the wake boundary.

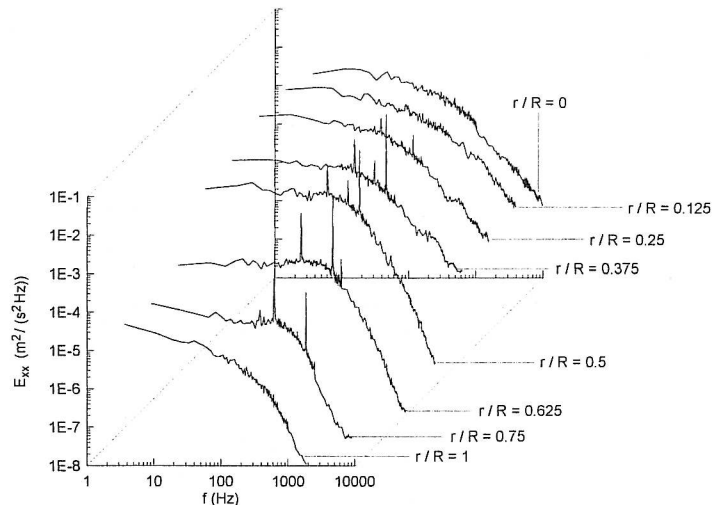


Fig. 2. – Radial evolution of the power spectral density function of the axial velocity fluctuations for the axial location $x/D = 1$.

The radius of the wake r^* is defined as the radial location where the axial turbulence intensity has fallen to half of its maximum value. An important position in the flow is the edge of the wake, corresponding to $r/R = 0.625$ in Figure 2 or $r/r^* = 1$. If we look at the axial evolution of spectral density functions for this particular location (Fig. 3), it is interesting to see that the wide-band level of turbulent structures is increasing with the axial distance, and that the spectral peaks for frequencies f_0 and $3f_0$ are always present. The harmonics $2f_0$ and $4f_0$ remain in the spectrum up to $x/D = 1$. For greater distances (Fig. 4) the wide-band part of the spectra is characterised by a decreasing level. The spectral peaks vanish, when $x/D > 2$ for $3f_0$ and when $x/D > 5$ for f_0 . Downstream of this location, the wake is not marked by any forced periodic motion. This evolution may be compared with the axial evolution of the maximum turbulence intensity (Fig. 5). For $x/D < 2$ this level remains approximately constant and it starts to decrease from this distance. In the near wake, the turbulent energy is concentrated in spectral peaks due to the periodic motion, and transferred to the turbulence (the peaks feed the wide-band); the turbulence levels remains constant (Fig. 5) while the wide-band spectrum is increasing. In the intermediate region, for $2 < x/D < 10$, the spectral peaks vanish, and there is no more transfer from the periodic motion to turbulence. Consequently, the maximum turbulence intensity is decreasing, as is shown in Figure 5. For further axial locations, the change in the slope leads to another turbulent behaviour in the far-wake which will be discussed below.

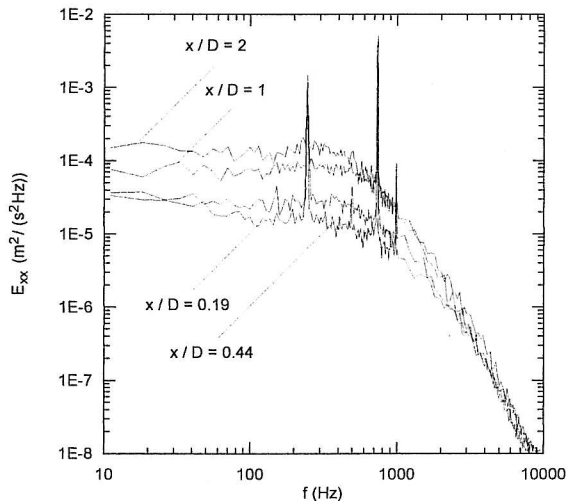


Fig. 3. – Axial evolution for $x/D \leq 2$ of the power spectral density function of the axial velocity fluctuations for the radial location $r/r^* = 1$.

The axial evolution of the peak level for the characteristic frequencies f_0 and $3f_0$ is presented for axial, radial and azimuthal power spectral density functions, at the boundary of the wake, in Figures 6-8. In every plot, the peak value is compared with the wide-band spectral level around the corresponding frequency, and of course when there is no more peak in the spectrum the two curves are identical. Generally, note that peak levels for the axial and radial spectra are quite close, while the levels for the

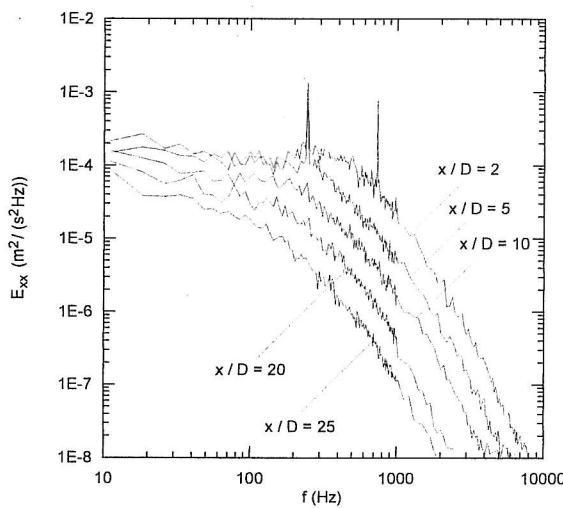


Fig. 4. – Axial evolution for $x/D \geq 2$ of the power spectral density function of the axial velocity fluctuations for the radial location $r/r^* = 1$.

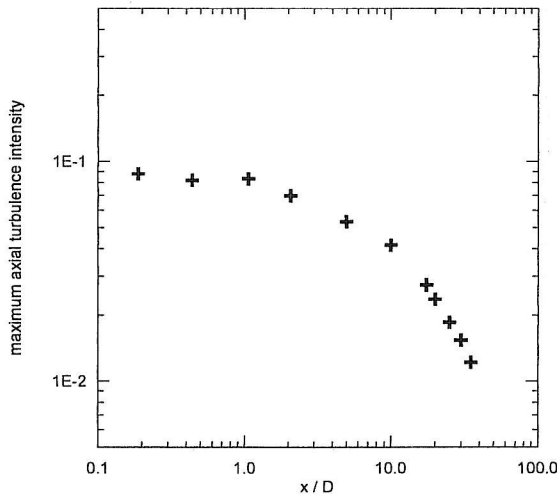


Fig. 5. – Axial evolution of the maximum axial turbulence intensity.

azimuthal spectra are somewhat different, even if the general evolution is the same. For the spectra of the axial velocity, in the region $x/D \leq 1$, the blade passing frequency $3f_0$ takes the highest level, which means that the coherent structures induced by the blade contain more energy than the global rotation motion. It is worth noticing that in this zone, the peak levels are constant and the wide-band level is increasing; there is creation of turbulent energy. For $x/D = 2$, there is a change in the dominating frequency, the level at frequency f_0 becomes higher than the level at frequency $3f_0$. Then, the spectral peak at $3f_0$ vanishes rapidly around $x/D = 5$ whereas the peak at f_0 remains up to $x/D = 10$. Throughout this region, there is a transfer of energy between the peak and the wide-band spectrum. Regarding the azimuthal spectrum the change in the dominant

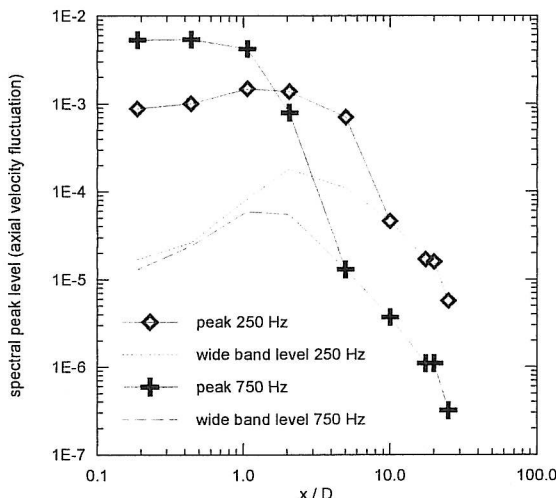


Fig. 6. – Axial evolution of the spectral peaks for frequencies $f_0 = 250$ Hz and $3f_0 = 750$ Hz (axial velocity fluctuations).

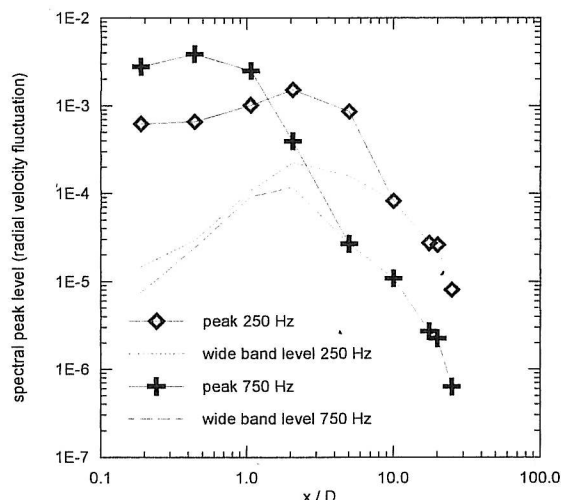


Fig. 7. – Axial evolution of the spectral peaks for frequencies $f_0 = 250$ Hz and $3f_0 = 750$ Hz (radial velocity fluctuations).

peak occurs further downstream, for $x/D > 2$. For $x/D \geq 10$, all spectral peaks have vanished and turbulence levels fall as a result of dissipation.

If we turn our mind to the power spectral density functions of the radial velocity fluctuations, at the radial location where $r/r^* = 1$, the spectra display a marked maximum at relatively low frequencies. In order to enhance this phenomenon and to remove the effects of the periodic motion, the signal is filtered for $f < 50$ Hz and spectral peaks at frequencies f_0 and $3f_0$ are removed when they are present. Then all the curves are

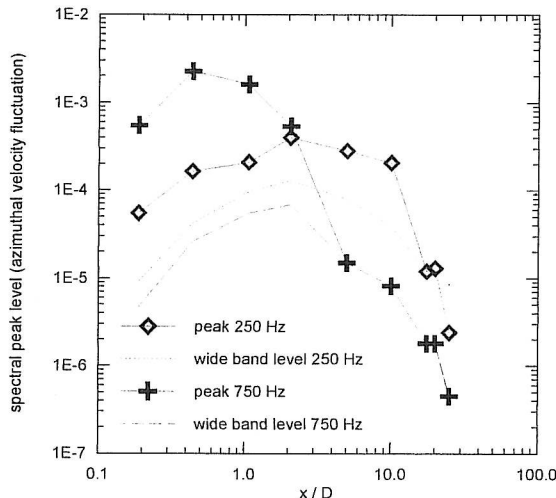


Fig. 8. – Axial evolution of the spectral peaks for frequencies $f_0 = 250$ Hz and $3f_0 = 750$ Hz (azimuthal velocity fluctuations).

smoothed and normalised by their maximum value. The frequency is normalised in the usual manner:

$$\beta = \frac{2\pi r^* f}{U_e}$$

The resulting amplitude spectra are plotted in Figures 9 and 10. All the profiles have a maximum at about the same non-dimensional frequency $\beta \sim 4$ for $x/D > 2$. This behaviour was mentioned previously by Cimbala and Park (1990) who found a peak around $\beta \sim 3$ in the two-dimensional jet-propelled momentumless wake. This indicates that there exists a quasi-periodic radial motion caused by some sort of large turbulent structure near the edge of the wake. It can be understood as the ejection of large eddies at the boundary, leading to the intermittent character of the flow. For the small values of x/D , this maximum amplitude occurs for a slightly lower frequency, as was found by Cimbala and Park (1990). Moreover, unlike jet propulsion, the propeller-driven momentumless wake is characterised by a periodic fluid motion, which adds peaks to the spectra, in the initial development region.

4. The far-wake

After the near-wake, which is strongly marked by spectral peaks and the intermediate region, where turbulence is decreasing and the peaks vanish, a third region appears in Figure 5, with a second change in the slope of the maximum turbulence intensity. In Figure 11, the turbulent kinetic energy profile \bar{q}^2 has been scaled by its local maximum value \bar{q}_{lm}^2 for several axial positions in this zone. It will be noticed that the form is the same for any axial position, illustrating self-similarity of turbulent kinetic energy for $x/D \geq 17.5$ (Faure and Robert, 1996). This result suggests that there might be a self-similar behaviour of the power spectral density functions, as was found in the

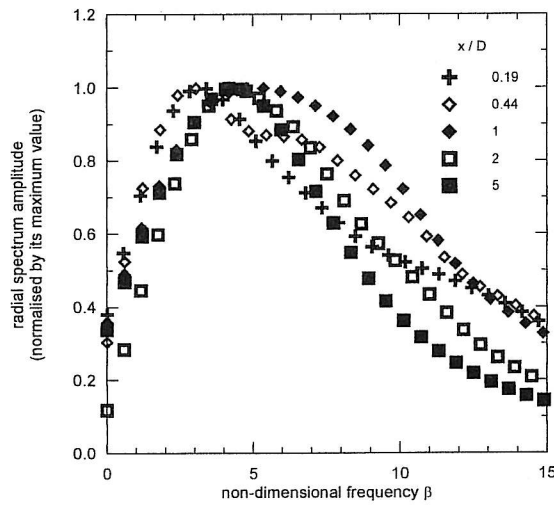


Fig. 9. – Axial evolution of the relative power spectral density function of the radial velocity fluctuations for $x/D \leq 5$.

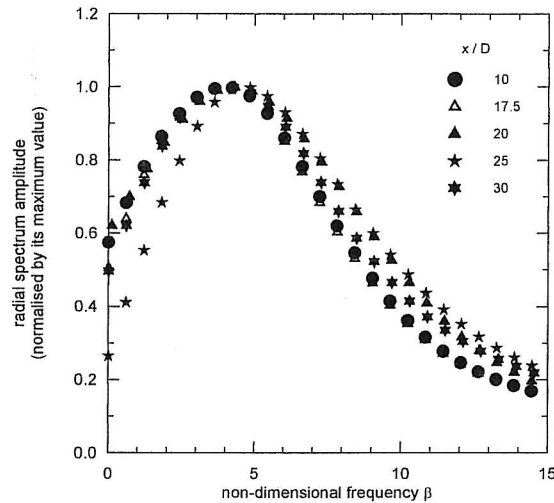


Fig. 10. – Axial evolution of the relative power spectral density function of the radial velocity fluctuations for $x/D \geq 10$.

two-dimensional wake by Wygnanski *et al.* (1986). In Figures 12 and 13 we plot the power spectral density functions of the axial velocity normalised with its zero value, as a function of the non-dimensional frequency β . In Figure 12, the spectra measured on the centreline are plotted for different axial positions in the wake; a self-similar behaviour is found since the discrepancy between the curves is not greater than the measurement error. Furthermore, spectra for an axial location where self-similarity is attained are plotted for different radial positions in Figure 13. The spectra are very close for any radial position inside the wake, leading to an equilibrium between the different

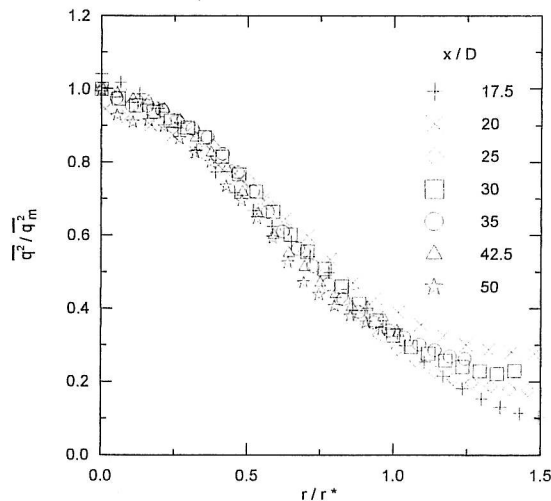


Fig. 11. – Self-similarity of the turbulent kinetic energy profiles in the far wake.

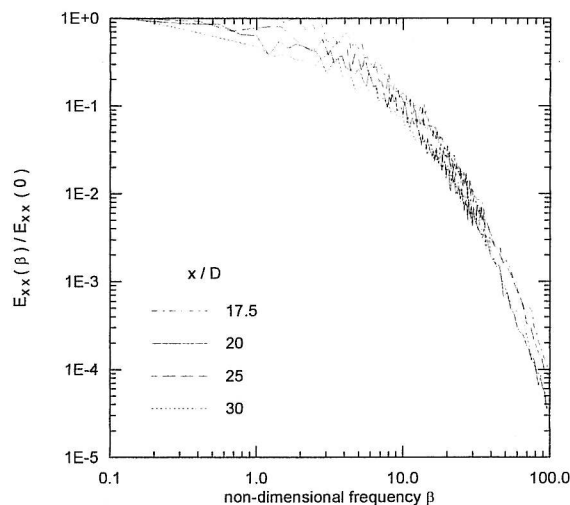


Fig. 12. – Axial evolution for $r/r^* = 0$ of the relative power spectral density function of the axial velocity fluctuations.

turbulent scales. Then, in the far-wake, the turbulent transfer from the large to the small structures is qualitatively the same in the radial and in the axial directions. In addition, the comparison with the spectrum measured in the freestream indicates that this behaviour is not very far from that of grid turbulence. This remark confirms the conclusion of Naudascher (1965) and Cimbala and Park (1990) for jet-propelled momentumless wake. Finally, for a far-momentumless-wake with or without swirl, the behaviour is relatively close to decaying homogeneous turbulence.

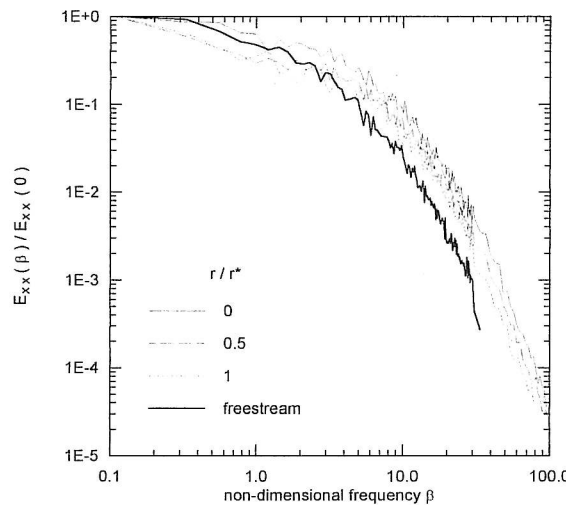


Fig. 13. – Radial evolution for $x/D = 20$ of the relative power spectral density function of the axial velocity fluctuations.

5. Isotropy of turbulence

In this last part, the closeness of the far-wake to decaying homogeneous turbulence is discussed in the context of isotropy. There are few real turbulent flows in which the turbulence can be assumed to be isotropic. However, in high-Reynolds-number flows, the energy is mostly dissipated at the smallest scales of motion which do not receive energy directly from the mean flow, but through an energy transfer from large to small scales. This transfer process removes the directional information of the energy-containing eddies so that the small scales could be considered to be locally isotropic. For such locally isotropic flows, only the statistical properties of the smallest scales of motion would be expected to satisfy the isotropic relations, and there are some implications for the evaluation of the dissipation function. The way to determine this function correctly is to measure all the second-order moments of the derivatives of velocity fluctuations. This was done by Browne *et al.* (1987) who determined with care the nine terms that make up the total dissipation in the self-similar region of a cylinder wake. But this method is difficult and requires special arrangements of multiple miniature X-wire probes. Another approach, used more often, is to determine the function from isotropic turbulence and Taylor's hypothesis; thus, dissipation requires only the measurement of the second-order moment of the time derivatives of the axial velocity fluctuations (Taylor, 1935):

$$\varepsilon = 15\nu \overline{\left(\frac{\partial u_x}{\partial x} \right)^2} \approx \frac{15}{\bar{U}_x^2} \nu \overline{\left(\frac{\partial u_x}{\partial t} \right)^2}$$

However, it was shown by Browne *et al.* (1987) that this estimate gives about 20% of the real dissipation on the cylinder wake centreline, where the Reynolds number

based on the Taylor microscale λ , and the root mean squared value of the axial velocity fluctuation, was $Re_\lambda = 40$. An argument for the appropriate use of the isotropic estimate of dissipation is a large value of Re_λ . In the present investigation, $Re_\lambda = 140$ on the centreline of the far-wake. However, there is more evidence to suggest how isotropic are the structures which have a significant contribution to the dissipation function. The one-dimensional wavenumber spectrum E_{xx} is scaled by $\varepsilon^{1/4}\nu^{5/4}$, where ν is the kinematic viscosity, and plotted for this location and compared with other experiments in Figure 14. On the abscissa axis the wavenumber k_r multiplied with the Kolmogorov scale η is non-dimensional. This compilation of data is from McComb (1990) and Saddoughi and Veeravalli (1994). We note that the spectrum fits with the other curves, and for the momentumless wake the $-5/3$ Kolmogorov law is validated for $0.03 \leq k_r \eta \leq 0.1$, where the upper limit corresponds to the boundary between inertial and dissipation effects. For greater wavenumbers, in the dissipative region, the experimental spectrum is in good agreement with the universal function. This figure however can not provide a definite indication of how nearly the dissipation corresponds to the isotropic case.

Knowledge of the axial, radial and azimuthal spectral allows a determination of the ratios K_1 and K_2 defined as:

$$K_1 = 2 \left(\overline{\left(\frac{\partial u_x}{\partial x} \right)^2} \right) / \left(\overline{\left(\frac{\partial u_r}{\partial x} \right)^2} \right) \quad K_2 = 2 \left(\overline{\left(\frac{\partial u_r}{\partial x} \right)^2} \right) / \left(\overline{\left(\frac{\partial u_\theta}{\partial x} \right)^2} \right)$$

Note that the expected value for isotropic turbulence is one; nevertheless, this is never the case in experiments. The radial evolution of these ratios in the far-wake is given in Figure 15. They are both smaller than one; this result is surprising, if you compare it with the compilations given by Browne *et al.* (1987) and completed by George and Hussein (1991), because K_1 and K_2 are generally greater than one. While constant values for K_1 and K_2 cannot be rigorously assumed, the hill and valley behaviour of these two ratios is similar to that obtained by Browne *et al.* (1987). These variations are probably due to the uncertainties involved in evaluating experimental derivatives.

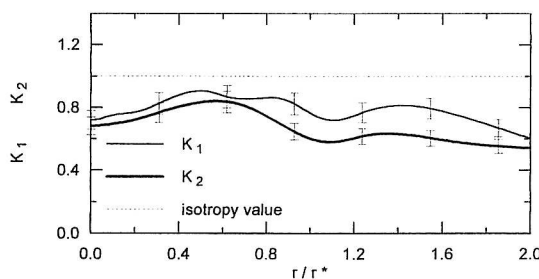


Fig. 15. – Radial evolution of the ratios K_1 and K_2 in the self-similar wake.

6. Concluding remarks

A velocity spectrum investigation was carried out in the turbulent wake of a rotor-driven body, providing new data about this momentumless flow. The near-wake is

strongly marked by spectral peaks related to the propeller rotational frequency f_0 and the blade passing frequency $3f_0$. The latter is dominant at the beginning of the wake but vanishes more rapidly around $x/D \sim 2$, whereas the peak at f_0 remains to $x/D \sim 5$. These peaks contain a large amount of energy which is transferred to the turbulent motion. Another noteworthy result which is valid for any axial position is the wide-band part of the spectrum for the radial velocity fluctuation; it shows a maximum for a radial location corresponding to the edge of the wake. This maximum can be associated with a large scale turbulent motion near the wake boundary and is similar to that found in a jet-propelled momentumless wake. Furthermore, spectra evolve to self-similarity in the far-wake, and are not very far from homogeneous turbulence, as was assumed in previous studies. Finally, the closeness of the flow to decaying homogeneous turbulence suggests

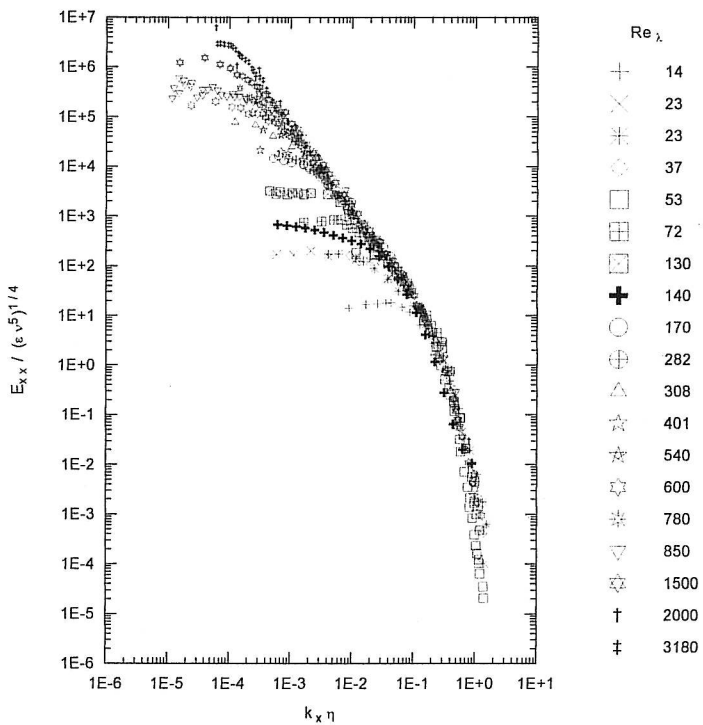


Fig. 14. – Kolmogorov's universal scaling for one-dimensional longitudinal power spectra. This compilation of data is from McComb (1990) and Saddoughi and Veeravalli (1994). The various symbols are associated with different Reynolds numbers referring to the following investigations: 14 grid turbulence (Stewart and Townsend, 1951); 23 wake behind cylinder (Uberoi and Freymuth, 1969); 23 boundary layer (Tielman, 1967); 37 grid turbulence (Comte-Bellot and Corrsin, 1971); 53 channel centreline (DNS Kim and Antonia, 1991); 72 grid turbulence (Comte-Bellot and Corrsin, 1971); 130 homogeneous shear flow (Champagne *et al.*, 1970); 140 momentumless wake (present investigation); 170 pipe flow (Laufer, 1954); 282 boundary layer (Tielman, 1967); 308 wake behind cylinder (Uberoi and Freymuth, 1969); 401 boundary layer (Sandborn and Marshall, 1965); 540 grid turbulence (Kistler and Vrebalovich, 1966); 600 boundary layer (Saddoughi and Veeravalli, 1994); 780 round jet (Gibson, 1963); 850 boundary layer (Coantic and Favre, 1974); 1500 boundary layer (Saddoughi and Veeravalli, 1994); 2000 tidal channel (Grant *et al.*, 1961); 3180 return channel (CAHI Moscow, 1991).

a comparison of the far-momentumless-wake with isotropic turbulence. Measurements of the ratios K_1 and K_2 were carried out.

Acknowledgements

We wish to thank Professor J. N. Gence and Dr L. Le Penven for valuable discussions during the course of this work.

REFERENCES

- BENDAT J. S., PIERSOL A. G., 1986, *Random Data: Analysis and Measurement Procedures*, John Wiley & Sons.
- BROWNE L. W. B., ANTONIA R. A., SHAH D. A., 1987, Turbulent energy dissipation in a wake, *J. Fluid Mech.*, **179**, 307-326.
- CHAMPAGNE F. H., HARRIS V. G., CORRSIN S., 1970, Experiments on nearly homogeneous turbulent shear flow, *J. Fluid Mech.*, **41**, 81-139.
- CHIENG C. C., JAKUBOWSKI A. K., SCHETZ J. A., 1974, *Investigation of the Turbulent Properties of the Wake Behind Self-propelled, Axisymmetric Bodies*, Office of Naval Research, VPI-Aero-025.
- CIMBALA J. M., KREIN M. V., 1990, Effect of freestream conditions on the far wake of a circular cylinder, *AIAA J.*, **28**, 1369-1373.
- CIMBALA J. M., NAGIB H. M., ROSHKO A., 1988, Large structure in the far wakes of two-dimensional bluff bodies, *J. Fluid Mech.*, **190**, 265-298.
- CIMBALA J. M., PARK W. J., 1990, An experimental investigation of the turbulent structure in a two-dimensional momentumless wake, *J. Fluid Mech.*, **213**, 479-509.
- COANTIC M., FAVRE A., 1974, Activities in, and preliminary results of, air-sea interactions research at I.M.S.T., *Advances in Geophysics*, **18A**, 391-405.
- COMTE-BELLOT G., CORRSIN S., 1971, Simple Eulerian time correlation of full and narrow-band velocity signals in grid-generated "isotropic" turbulence, *J. Fluid Mech.*, **48**, 273-337.
- FAURE T., 1995, *Étude expérimentale du sillage turbulent d'un corps à symétrie de révolution autopropulsé par hélice*, Ph.D. Thesis, École Centrale de Lyon, n° 95-01.
- FAURE T., ROBERT G., 1996, Turbulent kinetic energy balance in the wake of a self-propelled body, *Exp. Fluids*, **21**, 268-274.
- GEORGE W. K., HUSSEIN H. J., 1991, Locally axisymmetric turbulence, *J. Fluid Mech.*, **233**, 1-23.
- GIBSON M. M., 1963, Spectra of turbulence in a round jet, *J. Fluid Mech.*, **15**, 161-173.
- GRANT H. L., STEWART R. W., MOILLIET A., 1961, Turbulence spectra from a tidal channel, *J. Fluid Mech.*, **12**, 241-268.
- HIGUCHI H., KUBOTA T., 1990, Axisymmetric wakes behind a slender body including zero-momentum configurations, *Phys. Fluids A*, **2**, 1615-1623.
- HYUN B. S., PATEL V. C., 1991, Measurements in the flow around a marine propeller at the stern of an axisymmetric body/Part 1: Circumferentially-averaged flow, *Exp. Fluids*, **11**, 33-44, Part 2: Phase-averaged flow, *Exp. Fluids*, **11**, 105-117.
- JONES F. L., RITZ C. P., MIKSAD R. W., POWERS E. J., SOLIS R. S., 1988, Measurement of the local wavenumber and frequency spectrum in a plane wake, *Exp. Fluids*, **6**, 365-372.
- KISTLER A. L., VREBALOVICH T., 1966, Grid turbulence at large Reynolds numbers, *J. Fluid Mech.*, **26**, 37-47.
- LAUFER J., 1954, *The Structure of Turbulence in Fully Developed Pipe Flow*, NACA Report 1174.
- MC COMB W. D., 1990, *The Physics of Fluid Turbulence*, Oxford Science Publications.
- NAUDASCHER E., 1965, Flow in the wake of self-propelled bodies and related sources of turbulence, *J. Fluid Mech.*, **22**, 625-656.
- PARK W. J., CIMBALA J. M., 1991, The effect of jet injection geometry on two-dimensional momentumless wakes, *J. Fluid Mech.*, **224**, 29-47.
- PETERSON L. F., HAMA F. R., 1978, Instability and transition of the axisymmetric wake of a slender body of revolution, *J. Fluid Mech.*, **88**, 71-96.

- SADDOUNGH S. S., VEERAVALLI S. V., 1994, Local isotropy in turbulent boundary layers at high Reynolds number, *J. Fluid Mech.*, **268**, 333-372.
- SANDBORN V. A., MARSHALL R. D., 1965, *Local Isotropy in Wind Tunnel Turbulence*, Colorado State University Report CER 65 UAS-RDM71.
- SCHETZ J. A., JAKUBOWSKI A. K., 1975, Experimental studies of the turbulent wake behind self-propelled slender bodies, *AIAA J.*, **13**, 1568-1575.
- SCHOOLEY A. H., STEWART R. W., 1963, Experiments with a self-propelled body submerged in a fluid with a vertical density gradient, *J. Fluid Mech.*, **15**, 83-99.
- STEWART R. W., TOWNSEND A. A., 1951, Similarity and self-preservation in isotropic turbulence, *Phil. Trans. Roy. Soc. London A*, **243**, 359-386.
- SWANSON Jr. R. C., SCHETZ J. A., JAKUBOWSKI A. K., 1974, *Turbulent Wake Behind Slender Bodies Including Self-Propelled Configurations*, Office of Naval Research, VPI-Aero-024.
- TAYLOR G. I., 1935, Statistical theory of turbulence, *Proc. Roy. Soc. London A*, **151**, 421-478.
- TIELMAN H. W., 1967, *Viscous Region of Turbulent Boundary Layer*, Colorado State University Report CER 67-68 HWT21.
- UBEROI M. S., FREYMUTH P., 1969, Spectra of turbulence in wakes behind circular cylinders, *Phys. Fluids A*, **12**, 1359-1363.
- WYGNANSKI I., CHAMPAGNE F., MARASLI B., 1986, On the large-scale structures in two-dimensional, small-deficit, turbulent wakes, *J. Fluid Mech.*, **168**, 31-71.
- WYNGAARD J. C., PAO Y. H., 1971, Some measurements of the fine structure of large Reynolds number turbulence, *Statistical Models and Turbulence*, edited by M. Rosenblatt and C. Van Atta, Springer-Verlag, Berlin, 384-401.

(Manuscript received February 15, 1996;
revised September 3, 1996;
accepted October 14, 1996.)

Reynolds Stress Transport Equations in a Momentumless Wake: Experiments and Models

Thierry M. Faure*
École Centrale de Lyon, 69 131 Écully, France

The determination of the transfer terms in the Reynolds stress transport equations is an important issue in the improvement of closure models in turbulence. A part of these efforts is to provide accurate experimental information on each term of these equations and, particularly, on the pressure-strain term. The self-similar region of the momentumless wake of an axisymmetric, propeller-driven body is studied to enable the required balances of the Reynolds stress transport equations. The axial and azimuthal balances show that the flow is mainly dominated by convection. For the shear equations, there is a quasiequilibrium between production and pressure strain, except in the center of the wake. Comparisons are made between the experimentally determined distributions of pressure-strain terms and the corresponding distributions predicted by second-order closure models. The quasi-isotropic model and the isotropic production model do not predict well the amplitude of the pressure-strain term. Fu's model, calibrated for a strongly swirling recirculating jet, gives the best results in comparison with experimental data.

I. Introduction

REYNOLDS stress transport equations are important for understanding physical phenomena in a flow, mainly because of the wide use of second-order closure models in turbulent numerical codes. The aim of the present study is to investigate the momentumless axisymmetric wake of a propeller-driven body, where the drag of the body is completely canceled by the thrust created by the propulsion system. For this kind of flow, however, very few experimental data are available, and no Reynolds stress balances have been published. Note that these results are available for wall-bounded flows such as a manipulated boundary layer,¹ a wing/body junction,² and the flow around a surface mounted cube.³ However, for nonbounded flows, these budgets are given only for plane jets,⁴ axisymmetric jets,^{5,6} and two-dimensional wakes.⁷ We provide measurements of the balances for the self-similar region of a momentumless wake tested in a wind tunnel. For that wake, the flow is characterized by a mean azimuthal velocity, a component that does not exist in the case of a jet-driven body.^{8,9} The experimental determination of these balances permits the radial evolution of the pressure-strain term to be obtained. A comparison between this term and the one given by classical second-order closure models is presented. Different expressions for this term, determined for shear flow with swirl^{10,11} or without swirl¹² are tested.

II. Experimental Arrangements

The wake is generated by an axisymmetric, streamlined body, mounted in the working section of a wind tunnel (500 × 500 mm, 6 m long). The experimental freestream velocity can vary from 5 to 80 m/s with a uniformity of ±2% and a maximum turbulence intensity of 0.7%. The model has a diameter of 8 cm and a length of 50 cm (Fig. 1). It has an elliptical nose, a cylindrical middle section and a conical stern. The propulsion system consists of a three-blade marine type propeller with a diameter of 4 cm. The inside of the body is hollow and contains the motor (15,000-rpm maximum speed), which drives the propeller. An electronic system is available to control the rotation speed. A supporting device having a symmetrical NACA 66, 012 profile with a chord of 10 cm and a maximum width of 1.2 cm was chosen to minimize aerodynamic

perturbations around the body. Electrical wires for power supply and speed regulation are mounted inside this support. An alignment system permits the model to fit with the freestream flow. Once this adjustment is made, the angle between the wake axis and the tunnel axis was found to be less than 0.3 deg.

For a self-propelled body, the drag generated by the model equals the thrust created by the propulsion system. These quantities could be obtained by the measurement of the support force on the body. Unfortunately, a direct determination of this force was not available in this study. Thus, to bring about self-propulsion, a momentum balance was established for the model. To this effect, we had two parameters that were able to vary, the freestream velocity and the propeller rotation speed. The propeller rotation was fixed at its maximum value, and the freestream velocity was varied to make the drag equal to the thrust. In Fig. 2, the thrust minus drag balance is normalized by the upstream momentum flux and plotted vs the freestream velocity. The different quantities of this balance were measured with a five-hole pressure probe, which gave the mean velocity and pressure. Note that the probe generates a nonlinear averaging function in the estimate of pressure in a turbulent flow. As a consequence, it produces an uncertainty in the determination of the balance. Mean velocities have been checked

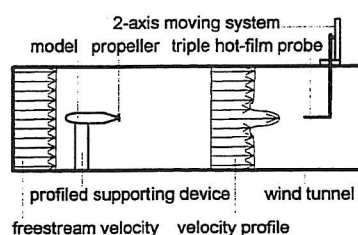


Fig. 1 Experimental setup.

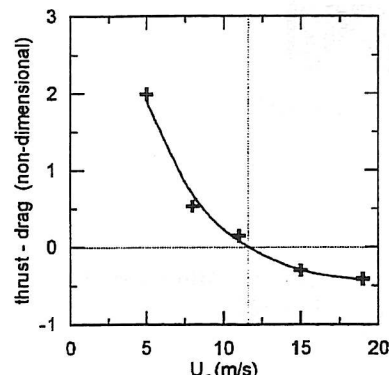


Fig. 2 Variation of the thrust-drag balance with the freestream velocity.

Received March 19, 1996; presented as Paper 96-2037 at the AIAA 27th Fluid Dynamics Conference, New Orleans, LA, June 17–20, 1996; revision received Sept. 16, 1996; accepted for publication Oct. 20, 1996; also published in *AIAA Journal on Disc*, Volume 2, Number 2. Copyright © 1996 by the American Institute of Aeronautics and Astronautics, Inc. All rights reserved.

*Postdoctoral Research Assistant, Laboratoire de Mécanique des Fluides et d'Acoustique, Unité Mixte de Recherche 5509, Centre National de la Recherche Scientifique. Member AIAA.

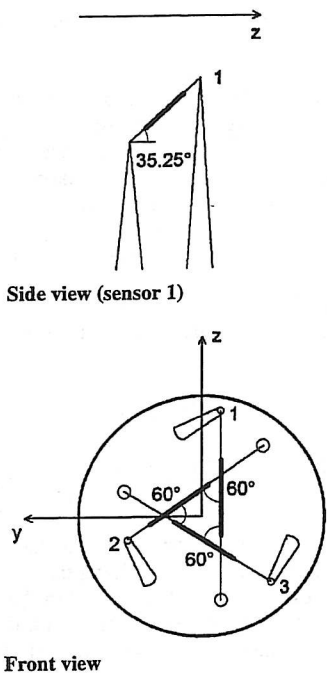


Fig. 3 Triple-sensor probe geometry.

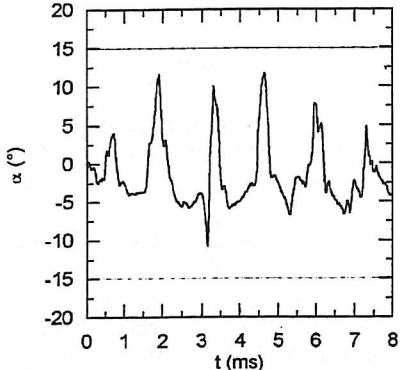


Fig. 4 Time sample of the angle $\alpha = \arctan(V/U)$ for the maximum turbulence intensity point ($x/D = 0.44$, $r/r^* = 0.6$).

with the hot-film measurements. Self-propulsion was realized with a freestream velocity of 11.6 ± 0.25 m/s; the uncertainty is due to the pressure estimate and the freestream velocity deviation. The corresponding Reynolds number based on the diameter of the body was $Re = 5.8 \times 10^4$.

The flow is three dimensional and turbulent; it is, therefore, necessary to use a directional probe that can measure both the mean and the fluctuating parts of the velocity. An automated triple hot-film anemometry system, which has been developed in the laboratory, gives all three components of instantaneous velocity. The probe is a Dantec 55R91 type, with the active lengths of the three sensors included into a sphere of diameter $d = 1.2$ mm. The smallest Kolmogorov microscale is $\eta = 0.4$ mm, which is in comparison with the measurement volume according to the relation $d \leq 3-4\eta$ given by Wyngaard and Pao.¹³ Each sensor is a nickel film deposited on a quartz cylinder, 70 μm in diameter. The three film supports are orthogonal and inserted into a sphere of 3 mm diameter (Fig. 3). This dimension corresponds to the Taylor scale of the structures encountered in the flow. Calibration of each sensor is performed in the unperturbed freestream. From calibration data, three King's laws are determined for each film. Then, the probe is carefully adjusted with the flow to use Jorgensen's geometric relations.

Figure 4 shows a time sample of the angle α between the radial and axial velocity components for the location in the wake where the flow is strongly marked by the blade passage influence and where the maximum turbulence intensity is measured. For this position, α

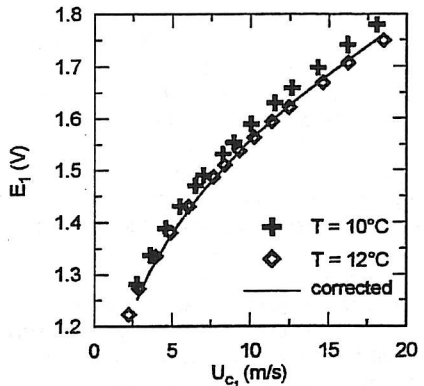


Fig. 5 Temperature drift effect on the calibration curve and its correction for hot-film number 1.

reaches its maximum value. Note the peaks in the sample, distributed every 1.3 ms and linked with the periodic blade passage, which generates a rapid change in the velocity direction. Nevertheless, this angle remains inside the 15-deg acceptance cone, which is the limit for unambiguous velocity determination with a triple sensor probe.

When an experiment is performed, a long time is necessary to move the probe after data acquisition at each point of measurement, leading to a long experimental time (typically, 4 h). As a consequence, the ambient temperature during measurements may change and can affect the data processing because the calibration curves can be modified with the temperature. Film aging or contamination problems may introduce similar effects in these curves. Thus, periodic verification is carried out during the acquisition procedure: the probe is placed in the freestream from time to time and a calibration point obtained for each film. As part of the signal processing, such points are used to update the calibration curve. Figure 5 shows two calibration curves (output voltage vs cooling velocity) for sensor 1 plotted for two ambient temperatures with a 2°C temperature drift. The solid line is the corrected curve for the calibration achieved for $T = 10^\circ\text{C}$ when it is used to process data acquired at temperature $T = 12^\circ\text{C}$. The agreement between the corrected curve and the calibration curve performed at 12°C is very good because a deviation smaller than 0.94% is found. The films are operated as constant temperature anemometers at an overheat ratio of 0.8. The anemometer is a 3-channel TSI IFA 100 type including a conditioner unit for each channel. Output voltages from the anemometer are passed through buck and gain circuits. To avoid aliasing, the signal should be low-pass filtered at a cutoff frequency that is half the sampling frequency. The low-pass filters, which are identical for each conditioner unit, are third-order, -18-dB per octave, Sallen-Key type. The phase shifts introduced are identical; the cross spectra between the measured voltages delivered by each channel were checked that no phase deviation was detected. Then, the data are digitized with a 12-bit A/D converter. Three types of acquisition were necessary for a single point of measurement, to determine correctly the desired quantities: 1) a sampling frequency of 4 kHz, to measure the mean and the second-order moments of velocity components; 2) a sampling frequency of 7.5 kHz with a sample of at least 20 s to obtain the convergence of third-order moments; and 3) a sampling frequency of 50 kHz for a good estimate of spectra E_{ij} and an accurate evaluation of the dissipation function.

The data are stored on the hard disk of a 80386 PC computer for later processing. The various error sources all along the acquisition procedure are carefully identified (see Ref. 14). They are as follows.

1) The conditioning error is due to the buck and gain process of signal before treatment. In this study, the values delivered by the signal conditioning unit were checked, and do not generate any voltage deviation.

2) The digital error is due to signal sampling. This error is maximized in the case of no previous signal conditioning (gain = 1, buck = 0). In the present study, where the voltages were optimized before sampling, this error is found to be less than 0.04% and can be neglected.

3) The thermal response variation of the sensor is a potential error source in the processed velocity. Here, a temperature variation is corrected in the previously mentioned way, leading to a maximum deviation of 0.94%. If this procedure is not carried out, a variation of 2°C between the calibration temperature and the measurement temperature can induce errors of 12.5% in the mean velocity.

4) The signal treatment error is due to the inversion of the voltages delivered by the anemometer, into the velocity components. From the range of velocity processed in this study, the corresponding error is 0.33%.

5) The statistical treatment error is related to the moment of velocity measured. The average time has to be adjusted with the desired moment. Note that for velocity moments greater than one, this is the only important error source. In this work we found statistical errors of 0.43% for mean velocity, 1.4% for second moments, and 2.7% for triple moments.

Finally, the maximum global measurement errors were found to be 1.7% for mean velocity, 1.4% for second-order moments, and 2.7% for third-order moments.

III. Reynolds Stress Transport Equations

We consider a simplified expression for each Reynolds stress transport equation, using a boundary-layer approximation¹⁵ that is based on an analysis of the order of magnitude for each term. This is justified because measurements are carried out in the self-similar part of the wake.¹⁶ In Fig. 6, the turbulent kinetic energy $q^2 = 1/2(u^2 + v^2 + w^2)$, where u , v , and w are, respectively, the velocity fluctuations for the axial, radial, and azimuthal directions, is normalized by its local maximum value $q_{\max}^2(x/D)$. The radial coordinate is scaled with the radius of the wake r^* defined as the location at which the axial turbulence intensity had fallen to half of its maximum value. The same profile is found for any axial position, illustrating self-similarity of the turbulent flow in the far wake. Then, each Reynolds stress transport equation can be written as the balance,

$$C_{ij} = P_{ij} + T_{ij}^1 + T_{ij}^2 + \Pi_{ij} - \varepsilon_{ij} \quad (1)$$

where the terms denote convection C_{ij} , production P_{ij} , turbulent transfer T_{ij}^1 , pressure transfer T_{ij}^2 , pressure-strain Π_{ij} , and dissipation $-\varepsilon_{ij}$, respectively. Their general expressions in Cartesian coordinates are

$$\begin{aligned} C_{ij} &= \bar{U}_k \frac{\partial \bar{u}_i \bar{u}_j}{\partial x_k} & P_{ij} &= -\bar{u}_i \bar{u}_k \frac{\partial \bar{U}_j}{\partial x_k} - \bar{u}_j \bar{u}_k \frac{\partial \bar{U}_i}{\partial x_k} \\ T_{ij}^1 &= -\frac{\partial \bar{u}_i \bar{u}_j \bar{u}_k}{\partial x_k} & T_{ij}^2 &= -\frac{\partial}{\partial x_k} \left(\frac{\rho \bar{u}_i}{\rho} \delta_{jk} + \frac{\rho \bar{u}_j}{\rho} \delta_{ik} \right) \\ \Pi_{ij} &= \frac{p}{\rho} \left(\frac{\partial u_i}{\partial x_j} + \frac{\partial u_j}{\partial x_i} \right) & \varepsilon_{ij} &= 2\nu \frac{\partial u_i}{\partial x_k} \frac{\partial u_i}{\partial x_k} \end{aligned}$$

where δ_{ij} is the Kronecker symbol. The subscripts denote the axes. Repeated dummy indices in a multiplication denote summation. In

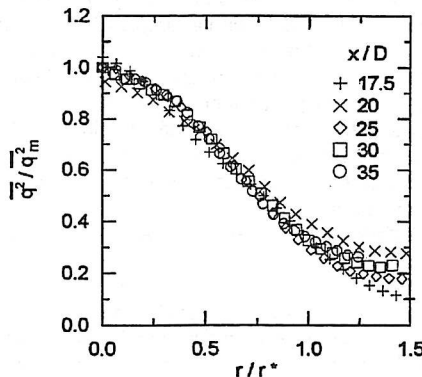


Fig. 6 Self-similar turbulent kinetic energy profile.

a wake, the molecular diffusion is neglected because there are no wall effects.

The method used to experimentally determine the Reynolds stress transport balances is similar to the one described by Browne et al.¹⁷ Each term of the equation is measured except for the pressure transfer and pressure-strain terms, which are determined from the overall balance. The axial gradient, appearing on the convection term, is defined from the self-similar form

$$\overline{u_i u_j} = \overline{u_i u_{j,m}}(x/D) h_{ij}(r/r^*)$$

where $\overline{u_i u_{j,m}}$ is the maximum value of $\overline{u_i u_j}$ at station x/D and $r/r^*(x/D)$ is the radial similarity variable. Thus,

$$\begin{aligned} \frac{\partial \overline{u_i u_j}}{\partial x} &= \left[\frac{d \overline{u_i u_{j,m}}}{dx} \left(\frac{x}{D} \right) h_{ij} \left(\frac{r}{r^*} \right) \right. \\ &\quad \left. - \overline{u_i u_{j,m}} \left(\frac{x}{D} \right) \frac{r}{r^{*2}} \frac{dr^*}{dx} \left(\frac{x}{D} \right) \frac{dh_{ij}}{d(r/r^*)} \left(\frac{r}{r^*} \right) \right] / D \end{aligned}$$

A least-square spline fit is first applied to the data on $h_{ij}(r/r^*)$ before numerical differentiation yielding $dh_{ij}/d(r/r^*)$. The radial derivatives of these quantities that appear in the production terms are obtained in a similar way. The three third-order moments of the turbulent transfer terms can be measured directly, thanks to the triple hot-film probe.

Dissipation of turbulent kinetic energy ε is determined by means of an isotropic formulation,

$$\varepsilon = 15\nu \left(\frac{\partial u}{\partial x} \right)^2$$

The integration of the dissipation spectrum is preferred to avoid the influence of the energetic part of the spectrum in the estimate of the dissipation function

$$\varepsilon = 15\nu \int_0^\infty k_1^2 E_{11}(k_1) dk_1$$

The reliability of this expression is good because the Reynolds number, based on the turbulent velocity and the Taylor scale, is around 140. In addition, Fig. 7 shows the comparison between the dissipation spectrum $k_1^2 E_{11}(k_1)$ and two spectra of the radial velocity determined in different ways: the first one is the measured spectrum $E_{22}(k_1)$ and the second one is calculated with the isotropic formulation from measurements of the spectrum of the axial velocity $E_{11}(k_1)$ (Ref. 18). We note that in the range of wave numbers where dissipation reaches its maximum, the agreement between the two spectra is good. The dissipation of the Reynolds stress transport equations ε_{ij} is determined from the dissipation of turbulent kinetic energy ε ,

$$\varepsilon_{ij} = \frac{2}{3} \varepsilon \delta_{ij}$$

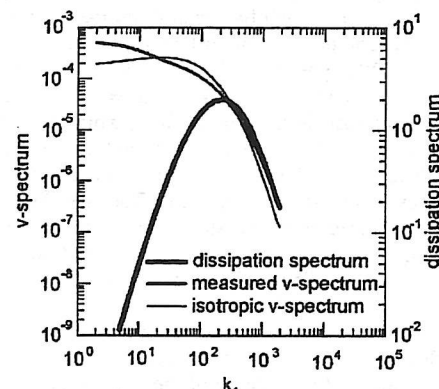


Fig. 7 Comparison between the dissipation spectrum and the measured and isotropic v spectra.

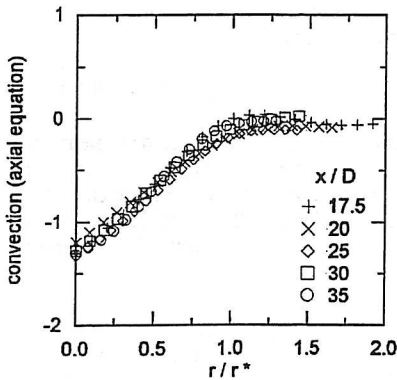


Fig. 8 Self-similar profile of convection for the axial Reynolds stress equation.

For the axial, radial, and tangential equations this term exists, and it vanishes in the shear stress equations.

All of the results presented are carried out in the self-similar far momentumless wake, for axial distances from the trailing edge of the propeller $x/D \geq 17.5$. Note that the balances are nondimensional and normalized by

$$\overline{q^2}^{1/2}/r^*$$

Self-similarity is pointed out in the convection term for the axial Reynolds stress equation (Fig. 8), where the different symbols are associated to different axial locations in the wake. This self-similar behavior is also checked for the other terms and other equations.

The distributions of the axial, radial, and tangential Reynolds stress transport equations and the axial–radial and radial–tangential shear transport equations are given. For the axial and tangential equations, the pressure transfer vanishes and the pressure strain is determined from the balance. For the radial Reynolds stress equation and the shear stress equations, both of these terms exist; the pressure transfer term is determined with the relation given by Lumley¹⁹ for homogeneous and nonisotropic turbulent structures that are the most important for transfer:

$$\overline{pu_i}/\rho \approx -\frac{1}{5}\overline{q^2}u_i \quad (2)$$

Note that this term is very small in comparison with pressure strain. However, this result was expected. The large-eddy simulations of Shao et al.²⁰ of a shearless turbulent mixing layer shows that the constant $\frac{1}{5}$ is an overestimation, and pressure transfer can be easily neglected.

Then, the pressure strain is determined from the balance. The residual errors of the various measured transport terms are the pressure-strain error, because it is balanced from the other terms. This error is estimated around 20% in the inner part of the wake, and decreases to 5% in the outer region.

The axial, radial, and tangential Reynolds stress equations in cylindrical coordinates for an axisymmetric flow, after the boundary-layer approximation, are given by

$$\bar{U} \frac{\partial \bar{u}^2}{\partial x} = -2\bar{uv} \frac{\partial \bar{U}}{\partial r} - \frac{\partial \bar{u}^2 v}{\partial r} - \frac{\bar{u}^2 v}{r} + \frac{2}{\rho} p \frac{\partial \bar{u}}{\partial x} - \frac{2}{3} \varepsilon \quad (3)$$

$$\begin{aligned} \bar{U} \frac{\partial \bar{v}^2}{\partial x} - \frac{2}{r} \bar{W} \bar{vw} &= \frac{2}{r} \bar{W} \bar{vw} - \frac{\partial \bar{v}^3}{\partial r} - \frac{\bar{v}^3}{r} + \frac{2}{r} \bar{vw}^2 \\ &- \frac{2}{\rho} \frac{\partial \bar{p} \bar{v}}{\partial r} + \frac{2}{\rho} p \frac{\partial \bar{v}}{\partial r} - \frac{2}{3} \varepsilon \end{aligned} \quad (4)$$

$$\begin{aligned} \bar{U} \frac{\partial \bar{w}^2}{\partial x} + \frac{2}{r} \bar{W} \bar{vw} &= -2\bar{vw} \frac{\partial \bar{W}}{\partial r} - \frac{\partial \bar{vw}^2}{\partial r} \\ &- \frac{3\bar{vw}^2}{r} + \frac{2}{\rho r} p \frac{\partial \bar{w}}{\partial \theta} - \frac{2}{3} \varepsilon \end{aligned} \quad (5)$$

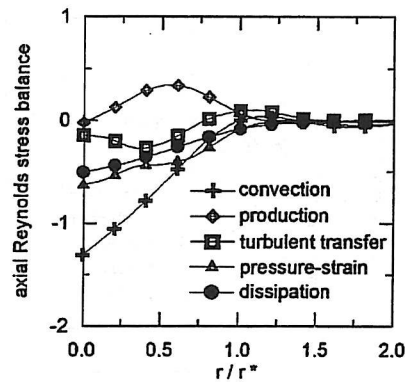


Fig. 9 Axial Reynolds stress balance.

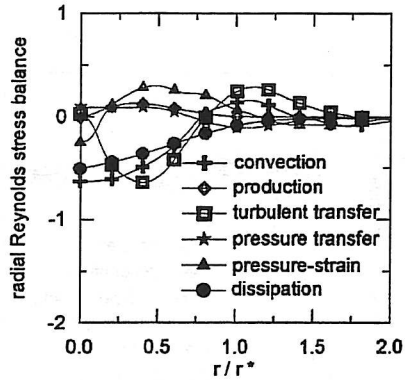


Fig. 10 Radial Reynolds stress balance.

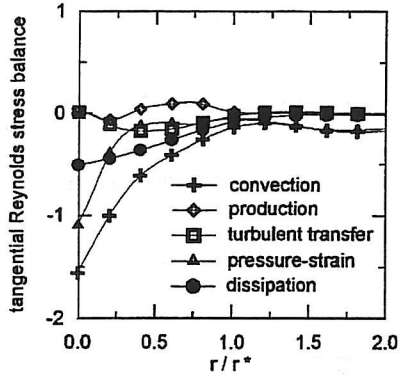


Fig. 11 Tangential Reynolds stress balance.

where U , V , and W are the velocity components for the axial, radial, and azimuthal directions, respectively. Note that there is no pressure transfer term in Eqs. (3) and (5).

Afterward, all of the terms for each Reynolds stress transport equation are plotted with their signs. All of the balances are dimensionless, and the radial direction is normalized with the radius of the wake r^* . We can observe from the balance of the axial equation (Fig. 9) that this flow is mainly dominated by convection, which indicates that the turbulence generated by the propeller is carried downstream in the far wake. Dissipation is continuously decreasing in amplitude from the center to zero in the freestream, while production reaches a maximum around $r/r^* \approx 0.6$. The balance of the radial equation (4) shows a convection that is not more important than other transfers (Fig. 10). Turbulent transfer reaches a minimum around $r/r^* \approx 0.4$ and a maximum at the boundary of the wake ($r/r^* \approx 1.1$) that indicates a change in the energy redistribution between these regions. Other information can be obtained from the balance of Eq. (5), which points out an important amplitude for the convection term, due to the propeller rotation influence (Fig. 11). This term almost equilibrates the sum of pressure strain

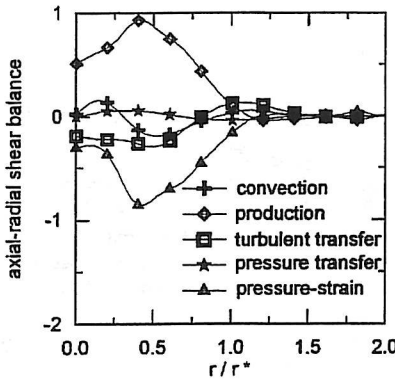


Fig. 12 Axial-radial shear balance.

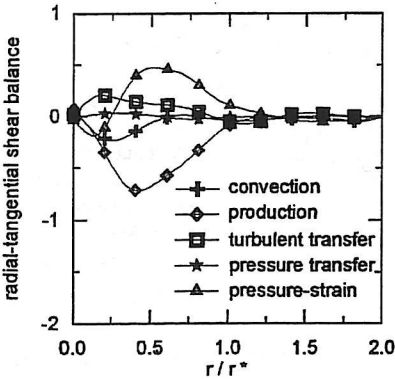


Fig. 13 Radial-tangential shear balance.

and dissipation. A contraction of Eqs. (3–5) brings the kinetic energy balance, in which no pressure-strain term occurs due to continuity (see Refs. 14 and 16).

Similar results are presented for the axial–radial shear equation

$$\bar{U} \frac{\partial \bar{u}\bar{v}}{\partial x} - \frac{2}{r} \bar{W} \bar{u}\bar{w} = -\bar{v}^2 \frac{\partial \bar{U}}{\partial r} - \frac{\partial \bar{u}\bar{v}^2}{\partial r} - \frac{\bar{u}\bar{v}^2}{r} + \frac{\bar{u}\bar{w}^2}{r} - \frac{1}{\rho} \frac{\partial \bar{p}\bar{u}}{\partial r} + \frac{1}{\rho} \bar{p} \frac{\partial \bar{u}}{\partial r} \quad (6)$$

In that case (Fig. 12), an equilibrium between production and pressure strain is established away from the wake axis while convection makes up for turbulent transfer. The axial–tangential shear balance is not significant because of the axisymmetry of the flow.

The distribution for the radial–tangential shear equation is given in Fig. 13:

$$\bar{U} \frac{\partial \bar{v}\bar{w}}{\partial x} + \frac{\bar{W}}{r} (\bar{v}^2 - \bar{w}^2) = -\bar{v}^2 \frac{\partial \bar{W}}{\partial r} + \frac{\bar{w}^2 \bar{W}}{r} - 2 \frac{\bar{v}^2 \bar{w}}{r} + \frac{\bar{w}^3}{r} - \frac{\partial \bar{v}^2 \bar{w}}{\partial r} - \frac{1}{\rho} \frac{\partial \bar{p}\bar{w}}{\partial r} + \frac{1}{\rho} \bar{p} \frac{\partial \bar{v}}{\partial r} + \frac{1}{\rho} \bar{p} \frac{\partial \bar{w}}{\partial r} \quad (7)$$

Production is dominant and generated by the mean azimuthal velocity gradient. As for the previous equation, we note an equilibrium between production and pressure strain for $r/r^* > 0.3$.

IV. Pressure-Strain Term

We present results of the comparison between the pressure-strain term balanced from the measurements and the corresponding

distributions given by classical models. The pressure strain may be divided into three parts:

$$\Pi_{ij} = \Pi_{ij}^r + \Pi_{ij}^s + \Pi_{ij}^w \quad (8)$$

where the first term is denoted the rapid or linear part, the second one is the slow or nonlinear part, and the third one is associated to the wall effects and will be zero in the present case. Afterwards, several models for the rapid part will be tested, together with a single model for the slow part proposed by Rotta.²¹ Its expression in Cartesian coordinates is

$$\Pi_{ij}^s = -c_1 \varepsilon \left(\frac{\bar{u}_i \bar{u}_j}{q^2} - \frac{2}{3} \delta_{ij} \right) \quad (9)$$

Different values for the constant c_1 are set according to the model used for the rapid part.

Two models, given by Launder et al.,¹² are tested for the rapid part of the pressure strain. The first one is the quasi-isotropic (QI) model

$$\Pi_{ij}^r = -\gamma (P_{ij} - \frac{2}{3} P \delta_{ij}) \quad (10)$$

The second one is the isotropic production (IP) model

$$\begin{aligned} \Pi_{ij}^r = & -\frac{c_2 + 8}{11} \left(P_{ij} - \frac{2}{3} P \delta_{ij} \right) - \frac{8c_2 - 2}{11} \left(D_{ij} - \frac{2}{3} P \delta_{ij} \right) \\ & - \frac{30c_2 - 2}{55} \left(\frac{\partial \bar{U}_i}{\partial x_j} + \frac{\partial \bar{U}_j}{\partial x_i} \right) \bar{q}^2 \end{aligned} \quad (11)$$

with

$$P = \frac{P_{kk}}{2} \quad \text{and} \quad D_{ij} = -\left(\bar{u}_i \bar{u}_k \frac{\partial \bar{U}_k}{\partial x_j} + \bar{u}_j \bar{u}_k \frac{\partial \bar{U}_k}{\partial x_i} \right)$$

For an axisymmetric flow, the expressions are available in Ref. 22.

For the QI model, the single set $c_1 = 1.5, c_2 = 0.4$ is used. Three sets of values are tested for the IP model, $c_1 = 1.5, \gamma = 0.6$ (denoted IP 1), which are the first values published in Launder et al.¹²; $c_1 = 1.8, \gamma = 0.6$ (denoted IP 2), which were later adjusted by Launder,²³ where the relation $(1 - \gamma)/c_1 = 0.23$ is validated; and $c_1 = 3, \gamma = 0.3$ (denoted IP 3), which were adjusted for a swirling jet by Gibson and Younis.¹⁰ The last model tested is proposed by Fu et al.¹¹ for a strongly swirling, recirculating flow. In that expression, the rapid part of pressure strain is calculated not only from production but also from convection:

$$\Pi_{ij}^r = -\gamma (P_{ij} - \frac{2}{3} P \delta_{ij} - C_{ij} + \frac{1}{3} C \delta_{ij}) \quad (12)$$

with $C = C_{kk}$. The constants c_1 and γ keep the same values as for the IP 1 model. Afterwards, the evolution of the pressure strain given by the several models for the rapid part, in relation with Rotta's model for the slow part, is determined from the measurements of first- and second-order moments of velocity. The gradients that appear in these expressions are calculated in the same way as for the production terms.

We note in Fig. 14, for the pressure-strain term of the axial Reynolds stress equation, that the IP and QI models give the shape of the measured term for $r/r^* > 0.5$, but with a lower level than the measured one. There is very little difference between the predictions of IP 1, IP 2, IP 3, and QI. Fu's model is the best one, predicting well the amplitude and the shape of the measured distribution. The pressure-strain term for Eq. (5) is compared with the distributions given by the same models in Fig. 15. It is clear that Fu's model is the only one that is able to predict the evolution of the term in the center of the wake, even if there is a difference of about 45% on the amplitude.

The results for the axial–radial shear are shown in Fig. 16. It can be seen that the pressure-strain term predicted by Fu's model is in very good agreement with data, only the peak level around $r/r^* = 0.4$ is slightly underestimated. The IP 1, IP 2, and QI models give similar results, with a lower level than Fu's model, but do not predict well the

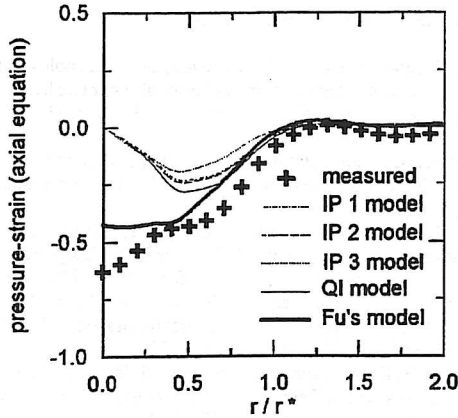


Fig. 14 Comparison between measured and calculated pressure strain for the axial equation.

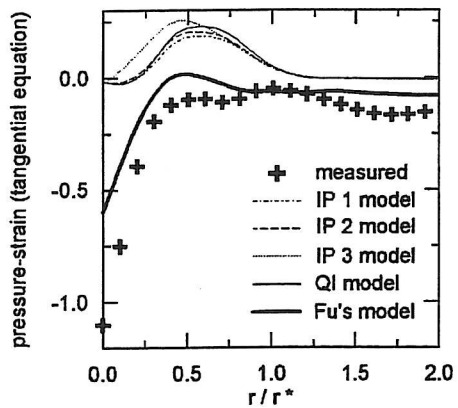


Fig. 15 Comparison between measured and calculated pressure strain for the tangential equation.

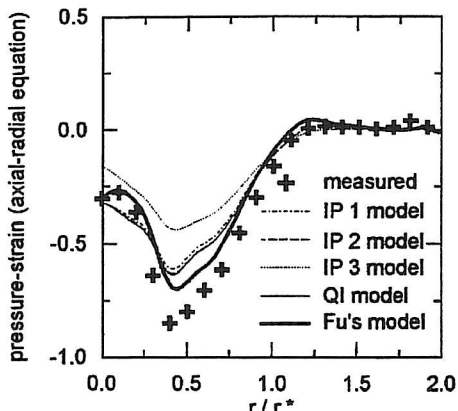


Fig. 16 Comparison between measured and calculated pressure strain for the axial-radial equation.

evolution near the center. The IP 3 model brings the worst behavior, with a peak level about 50% of the experimental value.

The same comments are valid for the radial-tangential shear equation (Fig. 17), where IP 1, IP 2, and QI estimate the measured maximum within about 60% and Fu's model is about 80% of this value, whereas the IP 3 model is almost zero. This surprising difference for this last model calibrated for a swirling jet may lie in the weakness of the swirl and the simple configuration (established jet), whereas Fu's model, calibrated for a strongly swirling recirculating jet, could be applied to many other swirling flows.

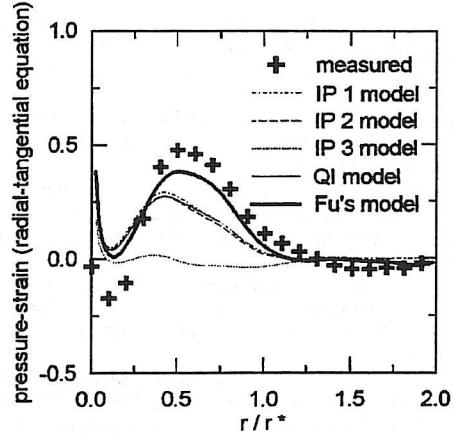


Fig. 17 Comparison between measured and calculated pressure strain for the radial-tangential equation.

V. Conclusion

The different terms of the Reynolds stress transport equations are measured or deduced from the balance, in the momentumless wake of a propeller-driven body. The importance of the convection term in the axial and tangential equations is shown. For the shear equations, a quasiequilibrium between production and pressure strain is established away from the axis of the wake.

Comparisons are made between the experimentally determined evolution of the pressure-strain terms and the corresponding predictions of classical closure models. For any equation, we notice that Fu's model, given for a strongly swirling flow, is very close to the measured terms in the present study. The IP and QI models give a prediction of the shape for pressure strain, away from the center, but underestimate the amplitude. Gibson's model gives an awkward prediction of pressure-strain terms and should not be appropriate for this momentumless rotating wake. This result shows that convection must be an important parameter in the modeling of a momentumless swirling flow.

Acknowledgments

The author wishes to thank G. Comte-Bellot, J. N. Gence, and L. Le Penven for valuable discussions during the course of this work.

References

- ¹Lemay, J., Bonnet, J. P., and Delville, J., "Experimental Testing of Diffusion Models in a Manipulated Turbulent Boundary Layer," *AIAA Journal*, Vol. 33, No. 9, 1995, pp. 1597-1603.
- ²Ölçmen, M. S., and Simpson, R. L., "Experimental Transport-Rate Budgets in Complex 3-D Turbulent Flow Near a Wing/Body Junction," AIAA Paper 96-2035, June 1996.
- ³Hussein, H. J., and Martinuzzi, R. J., "Energy Balance for Turbulent Flow Around a Surface Mounted Cube Placed in a Channel," *Physics of Fluids*, Vol. 8, No. 3, 1996, pp. 764-780.
- ⁴Everitt, K. W., and Robins, A. G., "The Development and Structure of Turbulent Plane Jets," *Journal of Fluid Mechanics*, Vol. 88, Pt. 3, 1978, pp. 563-583.
- ⁵Panchapakesan, N. R., and Lumley, J. L., "Turbulence Measurements in Axisymmetric Jets of Air and Helium. Part 1. Air Jet, Part 2. Helium Jet," *Journal of Fluid Mechanics*, Vol. 246, 1993, pp. 197-247.
- ⁶Hussein, J. H., Capp, S. P., and George, W. K., "Velocity Measurements in a High-Reynolds-Number, Momentum-Conserving, Axisymmetric, Turbulent Jet," *Journal of Fluid Mechanics*, Vol. 258, 1994, pp. 31-75.
- ⁷Aronson, D., and Löfdahl, L., "The Plane Wake of a Cylinder: An Estimate of the Pressure-Strain Rate Tensor," *Physics of Fluids*, Vol. 6, No. 8, 1994, pp. 2716-2721.
- ⁸Naudascher, E., "Flow in the Wake of Self-Propelled Bodies and Related Sources of Turbulence," *Journal of Fluid Mechanics*, Vol. 22, Pt. 4, 1965, pp. 625-656.
- ⁹Schetz, J. A., and Jakubowski, A. K., "Experimental Studies of the Turbulent Wake Behind Self-Propelled Slender Bodies," *AIAA Journal*, Vol. 13, No. 12, 1975, pp. 1568-1575.
- ¹⁰Gibson, M. M., and Younis, B. A., "Calculation of Swirling Jets with a Reynolds Stress Closure," *Physics of Fluids*, Vol. 29, No. 1, 1986, pp. 38-48.

- ¹¹Fu, S., Launder, B. E., and Leschziner, M. A., "Modelling Strongly Recirculating Jet Flow with Reynolds-Stress Transport Closures," *Proceedings of the 6th Symposium on Turbulent Shear Flows*, Toulouse, France, 1987.
- ¹²Launder, B. E., Reece, G. J., and Rodi, W., "Progress in the Development of a Reynolds-Stress Turbulence Closure," *Journal of Fluid Mechanics*, Vol. 68, No. 3, 1975, pp. 537-566.
- ¹³Wyngaard, J. C., and Pao, Y. H., "Some Measurements of the Fine Structure of Large Reynolds Number Turbulence," *Statistical Models and Turbulence*, edited by M. Rosenblatt and C. Van Atta, Springer-Verlag, Berlin, 1971, pp. 384-401.
- ¹⁴Faure, T., "Étude expérimentale du sillage turbulent d'un corps à symétrie de révolution autopropulsé par hélice," Ph.D. Thesis, No. 95-01, Laboratoire de Mécanique des Fluides et d'Acoustique, École Centrale de Lyon, Écully, France, Jan. 1995.
- ¹⁵Corrsin, S., "Turbulence: Experimental Methods," *Handbuch der Physik*, Vol. 8, Pt. 2, Springer-Verlag, Berlin, 1963, pp. 524-590.
- ¹⁶Faure, T., and Robert, G., "Turbulent Kinetic Energy Balance in the Wake of a Self-Propelled Body," *Experiments in Fluids*, Vol. 21, No. 4, 1996, pp. 268-274.
- ¹⁷Browne, L. W. B., Antonia, R. A., and Shah, D. A., "Turbulent Energy Dissipation in a Wake," *Journal of Fluid Mechanics*, Vol. 179, 1987, pp. 307-326.
- ¹⁸Faure, T., and Robert, G., "Bilans de tension de Reynolds dans un sillage de traînée et dans un sillage de corps autopropulsé par une hélice," *Comptes-Rendus de l'Académie des Sciences*, Paris, Vol. 321, No. 11, Série II b, 1995, pp. 455-461.
- ¹⁹Lumley, J. L., "Computational Modeling of Turbulent Flows," *Advances in Applied Mechanics*, edited by C. S. Yih, Vol. 18, Academic, New York, 1978, pp. 123-174.
- ²⁰Shao, L., Le Penven, L., and Bertoglio, J. P., "Study of the Modelling of the Transport Terms in One-Point Closures Using Large Eddy Simulation of Turbulence," *Engineering Turbulence Modelling and Experiments*, edited by W. Rodi and E. N. Ganic, Elsevier Science, New York, 1990, pp. 83-92.
- ²¹Rotta, J. C., "Statistische Theorie nichthomogener Turbulenz," *Zeitschrift für Physik*, Vol. 129, 1951, pp. 547-572.
- ²²Launder, B. E., and Morse, A., "Numerical Prediction of Axisymmetric Free Shear Flows with a Reynolds Stress Closure," *Turbulent Shear Flows I*, Springer-Verlag, Berlin, 1979, pp. 279-294.
- ²³Launder, B. E., "Second-Moment Closure and its Use in Modelling Turbulent Industrial Flows," *International Journal for Numerical Methods in Fluids*, Vol. 9, 1989, pp. 963-985.

Software corrected hot wire thermal lag for the constant voltage anemometer featuring a constant bandwidth at the selected compensation setting

Garimella R. Sarma^{a)}

Tao Systems, Inc. Williamsburg, Virginia 23185

Genevieve Comte-Bellot^{b)}

LMFA, Ecole Centrale Lyon, Ecully Cedex, France

Thierry M. Faure^{c)}

LEMF, Universite P. et M. Curie, Paris 6, Orsay Cedex, France

(Received 2 June 1998; accepted for publication 29 June 1998)

Software compensation correction for thermal lag of a hot wire in the application of a constant voltage anemometer (CVA) for turbulence measurements in the boundary layer of a supersonic wind tunnel has been demonstrated. The CVA was used with a fixed compensation setting while measuring the *in situ* thermal lag (time constant) of the hot wire. Using the measured time constant, corrections are applied to the fixed compensation output of the CVA in postprocessing of the data. To demonstrate the flexibility of the approach it was used for two compensation settings at a test point to obtain the same results from both settings. A unique advantage of this approach is shown to be that for a given compensation setting in the CVA the bandwidth of the measurements for the test remains constant for all of the different test conditions and yields higher productivity. The results of the turbulence levels measured with this method agree with earlier research using other anemometers. Spectral plots of the mass flux and temperature and the measured *in situ* time constant responses under different conditions of the hot wire have been presented. © 1998 American Institute of Physics. [S0034-6748(98)05209-5]

I. INTRODUCTION

The constant temperature anemometer (CTA) and the constant current anemometer (CCA) have been traditionally used with hot wires for the study of turbulent flows. Several studies have been successfully conducted with them making important contributions in the understanding of turbulent flows. In recent years the patented¹ constant voltage anemometer (CVA) is also emerging as a good alternative tool for applications in fluid dynamics. Several experimental studies have been conducted with the CVA in boundary layer transition in hypersonic flows^{2–4} at NASA Langley Research Center. A very good comparative study of the CTA and CVA was also carried out with experiments in a probe calibration wind tunnel.⁵ The frequency response of the CVA and CTA were also studied using laser radiative heating of the hot wire in an air jet.⁶ Analysis relating the sensitivity coefficients of the three anemometers (CTA, CCA, and CVA) and the time constants relationship of the CVA and CCA was recently presented by Comte-Bellot.⁷ In addition, the CVA was successfully used with hot films to detect the incidence of the transonic shock in flight on an F-15B aircraft.⁸ CVA had also been used in under water application with hot films to detect transition and flow bifurcation regions on a hydrofoil.⁹ Some of the features noticed in these

studies are lower electromagnetic interference noise in CVA compared to the other anemometers, very small variation of the bandwidth from changes with the hot wire overheat and Reynolds number, and tolerance of larger cable lengths without affecting the bandwidth. One of the most important aspects of the CVA operation is the appropriate compensation for the thermal inertia of the hot wire (which manifests as a first-order time constant) to extend the bandwidth of the CVA. It is shown in the present article that with the CVA it is possible to set a fixed hardware compensation for the time constant (TC), measure the *in situ* time constant of the wire, and apply the necessary correction to the fixed compensation setting for the actual measured time constant (through software processing) to obtain accurate results. This approach is possible with the CVA because of its well-defined circuit behavior without any influence of the external hot wire cable capacitance. Productivity of the measurements is also enhanced with this method. In the following sections the application of this method for turbulence measurements in the boundary layer of a supersonic wind tunnel is presented.

The CVA circuit was analyzed by Sarma in terms of its transfer function in Ref. 10 where a method of measuring the *in situ* TC of the hot wire under constant voltage (CV) operation was also described. To demonstrate the versatility of the method, two fixed compensation settings (0.2 and 0.4 ms) were used for taking data at the same point in addition to three overheat settings. The output voltage at each test point was then corrected through software in the postprocessing of

^{a)}Electronic mail: sarma@taosystem.com

^{b)}Electronic mail: gcb@selene.mecaflu.ec-lyon.fr

^{c)}Electronic mail: faure@iris6.lemfi.u-psud.fr

the data with the *in situ* measured TC of the hot wire. In the experiments reported here TC was measured with quick manual adjustments on a digital scope and data was postprocessed to calculate the TC. This adjustment has since been fully automated in the CVA, thus eliminating all manual adjustments during the entire experimental process, a feature particularly useful for blow-down tunnels. It is also shown that this procedure assures a constant bandwidth for all the tests with a particular hardware compensation setting. The processed voltage perturbations from the CVA were converted to mass flux and temperature components using the sensitivity expressions derived by Comte-Bellot in Ref. 7.

II. HARDWARE DESIGN

A. Hot wire time constant

The dynamic behavior of the hot wire can be described through a differential equation:

$$M_{CVA} \frac{dr}{dt} + r = ai + bu, \quad (1)$$

where M_{CVA} is the TC of the hot wire under CV operation, r is the perturbation in the hot wire resistance, i and u are the perturbations in the hot wire current and flow velocity, respectively, and a and b are calibration constants. With $u = 0$, M_{CVA} can be determined from the first-order response due to a step change in the hot wire current. Typical averaged responses from the measurement of the TC in the supersonic tunnel for a 2.5 and 5 μm hot wires are shown in Figs. 1(a) and 1(b), respectively. Numerical values of the M_{CVA} with various V_w values obtained at $y/\delta=1.5$ at $Ma_{ext}=2$ are shown in Fig. 2. Values of the time constants M_{CCA} under constant current (CC) operation measured by Arzoumanian and Debieve¹¹ ($Ma_{ext}=2.3$) are also presented for quick comparison. It can be seen that while the hot wire TC increases with overheat under CC operation, it has quite the opposite effect under CV operation, just as predicted by Freymuth¹² and in Ref. 7. The convergence of the TC values at higher overheats is apparent in Fig. 2. Also in Fig. 2, experimental data from the TC measurements in a low-speed tunnel on a 5 μm hot wire with variations in hot wire overheat and its Reynolds number are shown. Figure 2 shows that the TC under the CV operation also converges to a constant value with higher Reynolds (Re) numbers of the wire. Such a convergence to a constant value with the Reynolds number has been shown to be theoretically possible in an earlier study.¹³ The convergence of the TC to a constant value with higher Reynolds numbers and also with overheats (unlike CCA) of the wire will offer an immediate advantage of the CVA. There may be certain engineering applications in fluid mechanics involving measurements only above certain hot wire Reynolds numbers and overheat values, where it will thus be possible to use only a fixed compensation for the TC with a judicious *a priori* choice of the value. Thus, adjustments for each test point are eliminated for that application. The reduction of the hot wire TC under CV operation relative to the CC operation makes the CVA operate with a smaller ac gain from the compensation circuit than the CCA for the same bandwidth.

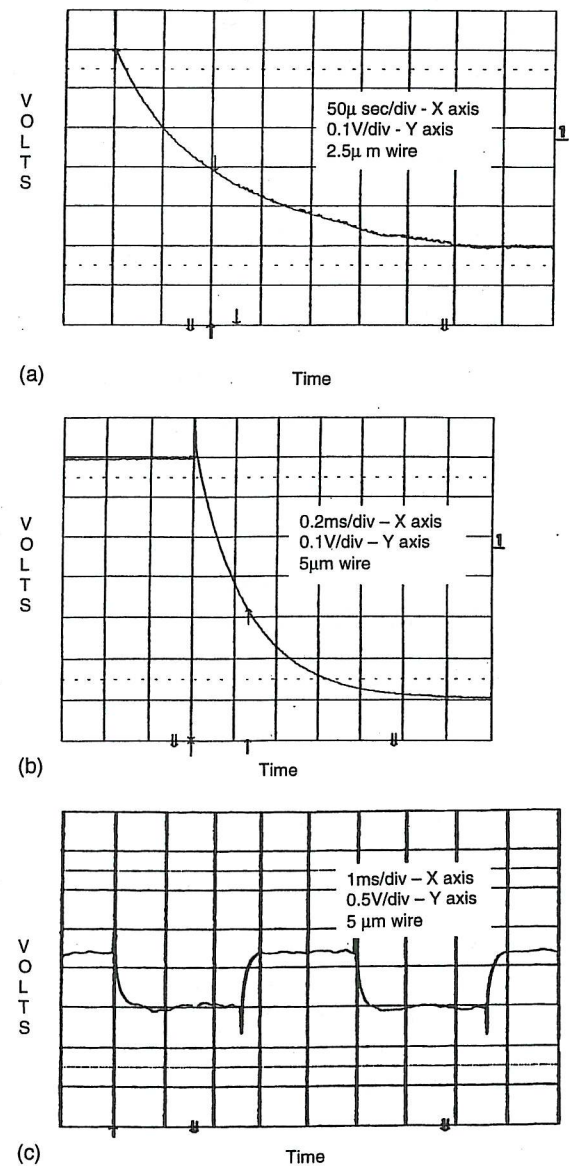


FIG. 1. (a) Averaged step response of a 2.5 μm hot wire with overheat $\alpha_w=0.5$ at $y/\delta=1.5$ at $Ma_{ext}=2.0$. (b) Averaged step response of a 5 μm hot wire with overheat $\alpha_w=0.6$ at $y/\delta=1.5$ at $Ma_{ext}=2.0$. (c) Typical output from TC measurement unit of the CVA with a 5 μm wire with an overheat $\alpha_w=0.5$ at $y/\delta=1.5$ at $Ma_{ext}=2.0$.

B. Compensated CVA

A compensated CVA circuit is shown in Fig. 3. The transfer function of the circuit as derived by Sarma in Ref. 10 is repeated below:

$$\frac{e_{CVA}}{u}(s) = \frac{(R_2/R_w)I_w}{\frac{s^2}{\omega_n^2} + \frac{(1/T_c + R_w/R_D 2\pi f_t)}{\omega_n^2} s + 1} \frac{(1+T_c s)}{(1+M_{CVA}s)} b', \quad (2)$$

where e_{CVA} and u are the perturbations in CVA output and input velocity, respectively. $R_2=R_a+R_b$, and R_D are components shown in Fig. 3 and R_w is the hot wire resistance. I_w is the mean hot wire current at the operating point that sets

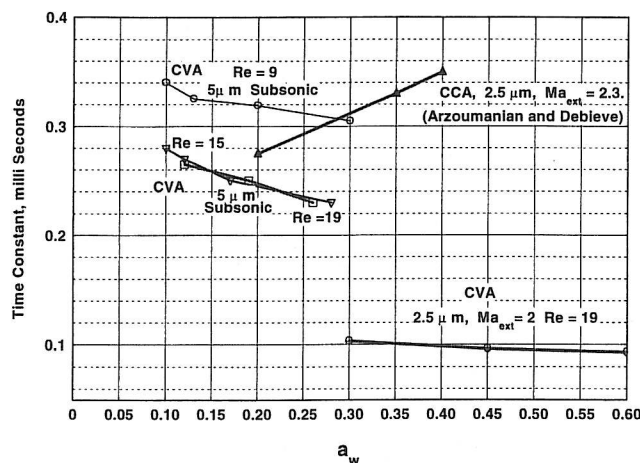


FIG. 2. Measured time constants of the hot wires at different overheating values (a_w).

the overheating of the hot wire and s is the Laplace operator. f_t is the gain bandwidth product of the operational amplifier used in the CVA and b' is the calibration constant of the CVA and the hot wire. The other constant related to the circuit is T_c , the hardware time constant compensation setting, given by

$$T_c = \frac{CR_a R_b}{R_2}. \quad (3)$$

ω_n and ζ are defined in the next section.

The prototype CVA used in the present experiment is equipped with a variable compensation setting in 72 overlapping ranges covering a TC range of 0.1–0.6 ms, and one way to conduct the test is to measure *in situ* M_{CVA} and select the matching T_c in the CVA, thus canceling the pole with the zero in Eq. (2). However, the procedure for such a cancellation involves taking the hot wire M_{CVA} data, calculating the M_{CVA} at that point from the averaged data samples and manually setting the matching T_c in the CVA. This process will impede the productivity of the test. With the complete postprocessing approach described in the next section, high productivity particularly attractive for blow-down tunnels can be assured with the CVA.

A possible test sequence with the CVA for higher productivity testing is formulated with the following steps:

- (1) Position the hot wire in the desired location in the wind tunnel.
- (2) Turn on the flow.

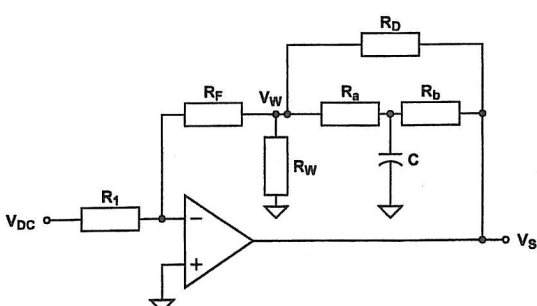


FIG. 3. Compensated CVA circuit.

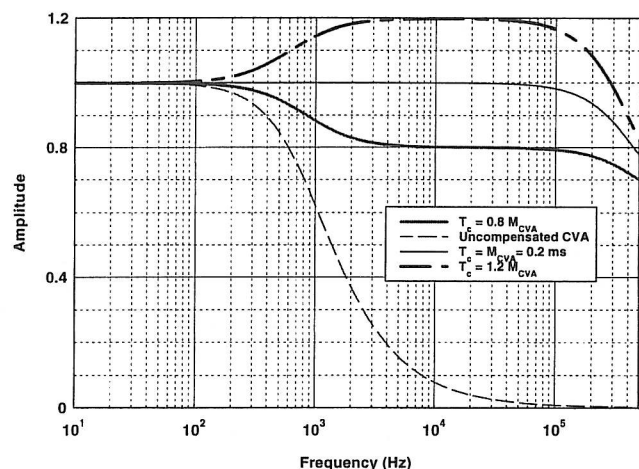


FIG. 4. Response curves due to the mismatch of the time constants.

- (3) Adjust the desired overheating (remote adjustment and monitoring of the overheating is possible with the CVA).
- (4) With the hot wire in the TC measurement mode of the CVA, obtain the M_{CVA} data for about 3 s.
- (5) Switch the hot wire to the turbulence measurement mode in the CVA (with a fixed compensation) from the TC measurement mode and take data for the desired duration.

III. POSTPROCESSING

A. Time constant calculation

The data obtained under step (4) in the previous section will be a series of first-order response pulses similar to those shown in Fig. 1(c). The average of such a series of pulses are shown in Figs. 1(a) and 1(b) for a 2.5 and 5 μm hot wires, respectively. The M_{CVA} of the hot wire is calculated as the time it takes the amplitude to reach 63% of the final value from the initial value. Measured values of the time constants (M_{CVA}) in the present experiment are shown in Fig. 2.

B. Software correction and constant bandwidth operation

The data from CVA could be collected by using a fixed T_c setting, while also collecting the M_{CVA} data at each test point without actually matching them at the time of the test. Figure 4 shows typical outputs that would arise due to mismatch of the T_c and M_{CVA} . In postprocessing, M_{CVA} is computed from the acquired TC measurement data and correction can be applied to the set T_c . The CVA output voltage is modified by the following equation:

$$e_c = e_{\text{CVA}} \left[\frac{1 + M_{\text{CVA}} s}{1 + T_c s} \right], \quad (4)$$

where, e_{CVA} is the acquired CVA output and e_c is the corrected output of the CVA. It is seen that Eq. (4) cancels the fixed compensation setting T_c used in the CVA and applies the correct compensation value from the measured M_{CVA} , thereby canceling the denominator term with the numerator term in Eq. (2). The bracketed expression in Eq. (4) is implemented with software and applied to the sampled analog

voltages from the CVA output. The CVA without any hardware compensation (full software compensation) is not a good approach since the signal levels from such a system would be low, even though its bandwidth could be several times larger than a hardware compensated CVA. The limiting case for the bracketed expression in Eq. (4) is (M_{CVA}/T_c) , and is independent of frequency.

When the pole due to the hot wire time constant is canceled by the zero due to the compensating circuit ($M_{\text{CVA}} = T_c$) the transfer function in Eq. (2) shows that the CVA will now be a simple second-order system as given below:

$$\frac{v_s}{u}(s) = \frac{(R_2/R_w)I_w}{s^2/\omega_n^2 + [(1/T_c + R_w/R_D 2\pi f_t)/\omega_n^2] s + 1} b'. \quad (5)$$

In Ref. 10, it was shown that the natural frequency ω_n and the damping ratio ζ of the above transfer function are given by

$$\omega_n = \sqrt{\frac{R_w}{R_2} \frac{2\pi f_t}{T_c} \left(1 + \frac{R_2}{R_D}\right)} \quad (6)$$

and

$$\zeta = \frac{1}{2} \frac{\left(\frac{1}{T_c} + 2\pi f_t \frac{R_w}{R_D}\right)}{\sqrt{\frac{R_w}{R_2} \frac{2\pi f_t}{T_c} \left(1 + \frac{R_2}{R_D}\right)}}, \quad (7)$$

where R_w , R_2 are as shown in Fig. 3. The bandwidth (BW) of such a system can be estimated from the following equation:

$$\text{BW} = \omega_n \sqrt{(1 - 2\zeta^2) + \sqrt{4\zeta^4 - 4\zeta^2 + 2}}. \quad (8)$$

In the above equations [Eqs. (6), (7) and (8)], for a given design, the only variables that could influence the BW are R_w and T_c and the BW is independent of the cable capacitance. Even so, with the software compensation approach, T_c is also held constant, leaving only one variable R_w that may have any effect on the BW at all. Variable R_w means variable overheat. In Ref. 5 it was experimentally established that in the CVA, the BW does not change with overheat, which was theoretically substantiated in Ref. 10. As shown in Ref. 10, an increase in R_w increases both ω_n and ζ to make Eq. (8) fairly constant. A lower T_c would, of course, give a larger BW. In the present experiments, two compensation settings at 0.2 and 0.4 ms were used, giving 230 and 120 kHz bandwidths, respectively. It may appear attractive to select a lower compensation setting for T_c to increase the bandwidth, but unless it is warranted by the test requirements such a selection of a larger bandwidth may also increase the system noise. The biggest advantage with this method is, therefore, that the bandwidth remains constant for the test with higher productivity.

IV. WIND TUNNEL TESTING AND DATA PROCESSING

Turbulence measurements were made in the Mach 2 blow-down tunnel of the CEAT in Poitiers (France). The conditions at the upstream of the sonic throat are typically

285 K and 9.5×10^4 Pa. The turbulent boundary layer on the flat floor of the 150 mm \times 150 mm test section was used for the test. At the downstream location of the measurements the boundary layer thickness δ was 15.7 mm, and the mean and turbulence characteristics have been fully documented by Dury.¹⁴ In the present study, most of the turbulence measurements were made at a wall distance y corresponding to $y/\delta = 0.64$. A few additional measurements were also taken at $y/\delta = 0.32$. A 0.5 mm length, 2.5 μm diam tungsten hot wire with a cold resistance $R_a = 6 \Omega$ was used. The cable resistance was $\approx 0.9 \Omega$ and this value was taken into account to obtain R_{ca} (cold resistance of the wire placed in the flow), R_w (heated wire resistance), and the associated overheat ratio $a_w = (R_w - R_{ca})/R_{ca}$. Three overheat ratios, i.e., 0.30, 0.45, and 0.62 were generally used. All the turbulence signals were recorded with a sampling rate of 10^6 samples/s for about 0.25 s using a 16 bit analog-to-digital converter and stored in binary format in a workstation. They were later converted to ASCII format for analysis. Data were processed in terms of 4096 points and 29 such samples were averaged for the final results. The M_{CVA} values were measured *in situ* outside the boundary layer at $y/\delta = 1.5$ where the free stream turbulence was about 1%. The time constant values remained fairly constant throughout the external part of the boundary layer because the wire Re remained fairly large for $y/\delta = 0.32$ to 1.5 with the wire Re in the range 13.5–19, respectively. The measured M_{CVA} values in this tunnel at three overheats (\bar{a}_w) have been already shown in Fig. 2. They range from 0.103 ms at an overheat of 0.30–0.096 ms at an overheat of 0.45 and 0.093 ms at an overheat of 0.62. Spurious low-frequency unsteady flow was inherent in the supersonic flow in the wind tunnel generated by a downstream ejector powered by a 110–160 bar air supply. These low-frequency signals were filtered out by using a high-pass (hp) filter with a 3 kHz cutoff. This hp filtering was also implemented by Dury¹⁴ who has extensively studied the tunnel performance and found that the filtering did not affect the turbulence levels. As a check, the integral length scales L were calculated from the spectra and are found to be within the correct range $L/\delta = 0.2–0.3$, agreeing with previous data, e.g., Smits and Dussauge.¹⁵ Unless otherwise identified, the data collected with $T_c = 0.2$ ms for which that prototype CVA had a 230 kHz bandwidth, were filtered with a low-pass (lp) filter with a cutoff at 120 kHz, making it equal to the bandwidth obtained with the $T_c = 0.4$ ms setting of the CVA. (The CVA has since been improved to have over 300 kHz at $T_c = 0.2$ ms.) This low-pass filtering also brought the CVA bandwidth closer to the CTA bandwidth used for comparison at the point at $y/\delta = 0.32$.

V. RESULTS

A. Effect of a small change in M_{CVA} at a compensation setting T_c

With the CVA compensation TC set at $T_c = 0.2$ ms, the power spectral density (psd) plots were calculated for $M_{\text{CVA}} = 0.095$, 0.100, and 0.105 ms, a 5% change on either side of a nominal value 0.100 ms at an overheat of 0.62. The 5% change in M_{CVA} is larger than the $\pm 2\%$ estimated maxi-

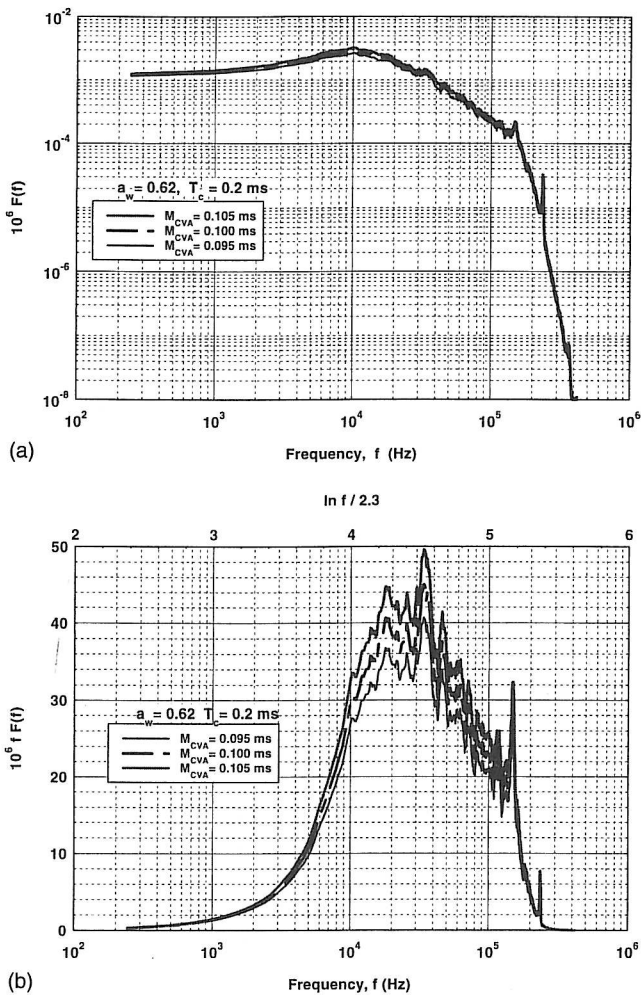


FIG. 5. (a) Response changes in $F(f)$ due to variations in M_{CVA} . (b) Response changes in $fF(f)$ due to variations in M_{CVA} .

mum error in the TC measurement process. The (e'/E) psd curves so obtained are plotted as $F(f)$ in Fig. 5(a). It can be seen that all three curves are close to each other with an error of $\pm 4\%$ in the rms values of the fluctuating voltage. A more physically meaningful and more stringent comparison would be to invoke the definition:

$$\frac{e'^2}{E^2} = \int_0^\infty F(f) df, \quad (9)$$

from which we can obtain:

$$\frac{e'^2}{E^2} = \int_0^\infty fF(f) \frac{df}{f} = \int_0^\infty fF(f) d(\ln f). \quad (10)$$

Hence, if we plot $fF(f)$ on the Y axis and $\ln f$ on the X axis, we can have linear scales for both. This plot is shown in Fig. 5(b). By simple visual inspection alone, significant features of the signals will be apparent, like the most energetic frequency range of the turbulent signal and the absolute differences in different spectra.

B. Comparison of two compensation settings

One important consideration for the software correction should be its adaptability to apply to any reasonable compen-

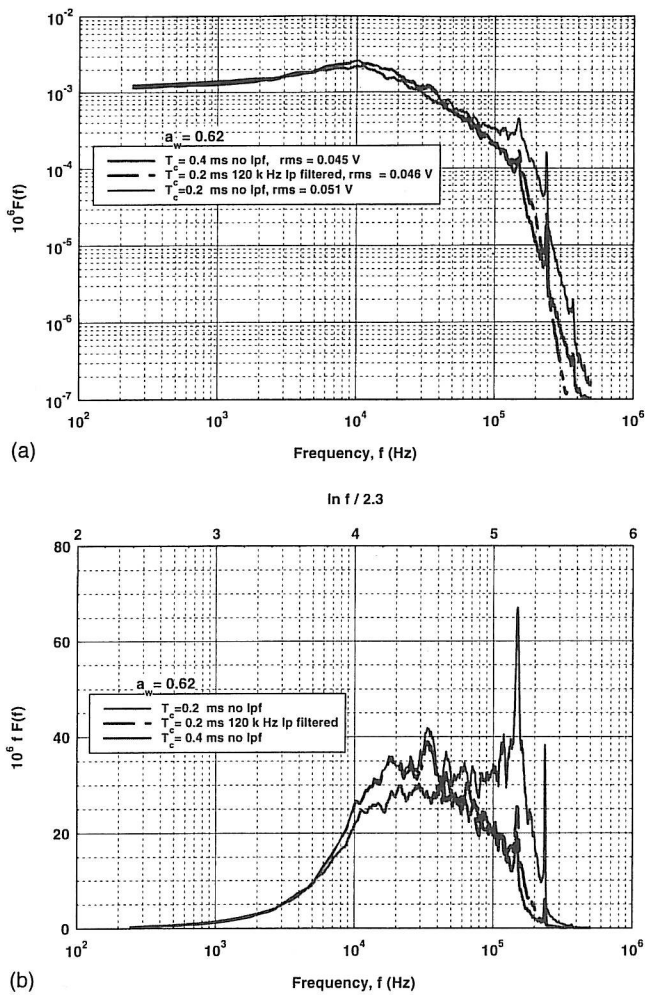


FIG. 6. (a) Response from two compensation settings in $F(f)$ at $a_w = 0.62$. (b) Response from two compensation settings in $fF(f)$ at $a_w = 0.62$.

sation setting. That is, if a CVA with only one fixed compensation setting (T_c) can be used for a wide range of measurements, then the hardware design becomes simple and a specified bandwidth can be assured. To study such a case, data from two T_c settings (0.2 and 0.4 ms) at an overheat of 0.62 was processed for psd with the software correction of the actual measured $M_{CVA}=0.093$ ms. For the 0.2 ms setting, a 120 kHz lp filter (lpf) was again used. The corresponding plots are shown in Figs. 6(a) and 6(b). From the legend on the graph and the plots, it can be seen that there is good agreement between the two data sets (T_c), indicating that indeed the software correction is accurate. The peaks around 150 and 250 kHz are due to strain gauging of the hot wire similar to that explained by Smits and Dussauge.¹⁵ Due to the bandwidth limit of the 0.4 ms setting, the strain gauge peaks are less visible for that case. The 120 kHz lp filter used with the 0.2 ms setting to take its bandwidth closer to the 0.4 ms setting, also leads to a reduction in the strain gauging peaks in the former setting. This filtering does not affect the kinetic-energy content of the turbulence. Kistler¹⁶ has shown that supersonic turbulence spectra encompass energetic eddy sizes down to one-fourth of the boundary layer thickness, $(f_{max}\delta/4)/U=1$. In the present case, the above condition

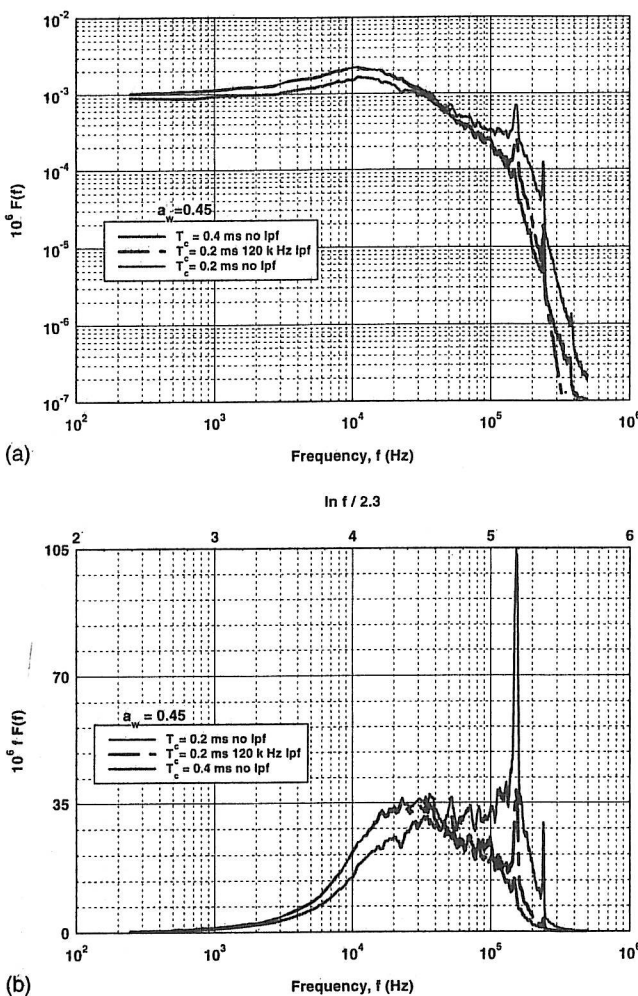


FIG. 7. (a) Response changes in $F(f)$ due to T_c changes at $a_w = 0.45$. (b) Response changes in $fF(f)$ due to T_c changes at $a_w = 0.45$.

gives a $f_{\max} = 100$ kHz, so that the 120 kHz lp filter of the data should be acceptable. Again, the agreement between the two compensation settings shown in Figs. 6(a) and 6(b) is an indication of the versatility of the CVA setup and software compensation method. Figures 7(a) and 7(b) show results similar to Fig. 6, except now it is with an overheat of 0.45.

C. Comparison of CVA and CTA spectra

A Dantec CTA (M5012) was used to collect the turbulence data with the frequency response adjusted with a gain setting of 4, high-pass filter 2. The maximum bandwidth with such a setting was specified as 100 kHz. The data were collected with the wire located at $y/\delta = 0.32$ with an overheat of

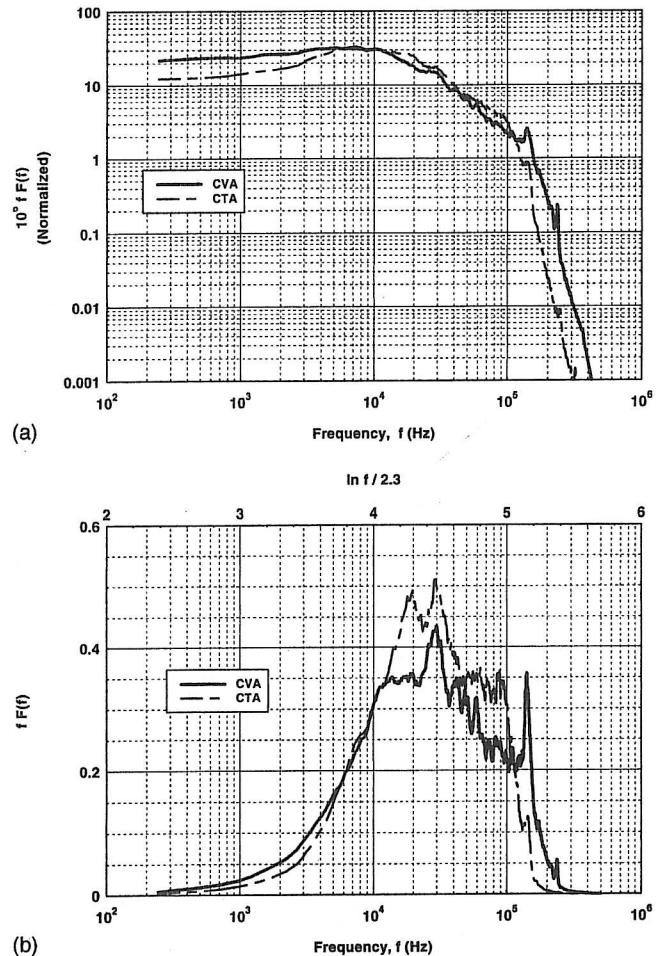


FIG. 8. (a) $F(f)$ Spectra of CVA and CTA normalized with their mean-square output voltages. (b) $fF(f)$ responses in CVA and CTA normalized with their mean-square output voltages.

0.60. The mean and rms voltages of the CTA are 2.21 and 0.065 V, respectively. With the same overheat setting, data were also collected at the same point with the CVA with $T_c = 0.2$ ms, cf. Table I. Psd plots from both are shown in Figs. 8(a) and 8(b). The anemometer psds were normalized with their respective mean-square outputs. Very distinct peaks at 150 and 250 kHz due to the aforementioned strain gauging effect are observed in the CVA but not as much in the CTA. Figure 8(b) shows broader energy levels in the CVA than the CTA because of the larger bandwidth in the CVA even with the lp filter. From Fig. 8(b) it can be seen that energy contributions below 5 kHz are insignificant. In the most energetic part of the spectrum (5–100 kHz) the

TABLE I. Summary of CVA test conditions and results.

y/δ	a_w	T_c ms	M_{CVA} ms	E V	Rms e' V (^a no lpf)	S Skewness	T Flatness	I Intermittency
0.64	0.30	0.20	0.103	3.28	0.0346	-0.64	4.19	0.847
	0.45	0.20	0.096	4.29	0.0420	-0.44	4.09	0.88
	0.45	0.40	0.096	4.29	0.0389 ^a	-0.59	3.92	0.91
	0.62	0.20	0.093	4.66	0.0463	-0.43	3.73	0.899
	0.62	0.40	0.093	4.66	0.0450 ^a	-0.426	3.14	0.94
0.32	0.60	0.20	0.093	4.08	0.0540	0.218	8.9	0.92

response from both the anemometers is very similar. The differences below 5 kHz are attributed to remnants of wind tunnel unsteadiness.

D. Skewness, flatness, and intermittency factors from CVA

Table I summarizes the various test points using the CVA in the present experiments in the supersonic tunnel. It also presents the rms output voltage, the skewness, the flatness factors, and the intermittency factors at each test run. Results show that the majority of cases have a negative skewness factor around -0.4, which agrees with the results obtained by Dury¹⁴ in the same tunnel. The negative skewness suggests negative spikes in the turbulent signal. The intermittency factor with a 10 mV threshold is between 0.84 and 0.94.

E. Mass flux and temperature characteristics of the turbulence

A hot wire responds to both mass flux and total temperature fluctuations in the turbulence with relative sensitivity depending upon the overheat of the wire, cf. Kovasznay.¹⁷ For small perturbations in mass flux ρu and temperature θ_t , we can write the wire response using the wire sensitivity coefficients $S_{\rho u}^{\text{CVA}}$ and $S_{\theta_t}^{\text{CVA}}$ as

$$\frac{e'}{E} = S_{\rho u}^{\text{CVA}} \frac{(\rho u)'}{\bar{\rho} U} + S_{\theta_t}^{\text{CVA}} \frac{\theta_t'}{\Theta_t}. \quad (11)$$

In principle, values of the sensitivity coefficients could be evaluated through the calibration of the hot wire. Fortunately, however, because of knowledge of the CCA and CTA systems, the sensitivity coefficients of the CVA can be evaluated knowing the CVA setup fairly well, cf. Comte-Bellot.⁷ These can be expressed as (from Ref. 7):

$$S_{\rho u}^{\text{CVA}} = S_{\rho u}^{\text{CTA}} \left[\frac{2a_w}{(1+2a_w)} \right] \quad \text{with } S_{\rho u}^{\text{CTA}} = 0.25 \quad (12)$$

and

$$S_{\theta_t}^{\text{CVA}} = -S_{\theta_t}^{\text{CCA}} \left[\frac{1}{(1+2a_w)} \right] \quad \text{with } S_{\theta_t}^{\text{CCA}} \approx 1. \quad (13)$$

In the above expressions for the CVA, the advantage that $S_{\rho u}^{\text{CTA}}$ and $S_{\theta_t}^{\text{CCA}}$ are nearly constant with a_w is utilized. Squaring and averaging Eq. (11) gives

$$\begin{aligned} \frac{e'^2}{E^2} &= [S_{\rho u}^{\text{CVA}}]^2 \frac{(\rho u)'^2}{\bar{\rho}^2 U^2} + 2[S_{\rho u}^{\text{CVA}} S_{\theta_t}^{\text{CVA}}] \frac{(\rho u)' \theta_t'}{\bar{\rho} U \Theta_t} \\ &\quad + [S_{\theta_t}^{\text{CVA}}]^2 \frac{\theta_t'^2}{\Theta_t^2}. \end{aligned} \quad (14)$$

Equation (14) is valid for a fixed overheat ratio and has to be solved for the three unknowns $(\rho u)'^2/\bar{\rho}^2 U^2$, $(\rho u)' \theta_t'/\bar{\rho} U \Theta_t$, and $\theta_t'^2/\Theta_t^2$. To solve for the three unknowns, we need to obtain data at three overheat values at the test point. To accomplish this, the present experiment was conducted with the three overheat values of 0.30, 0.45, and 0.62 with $T_c = 0.2$ ms and 120 kHz lpf, at $y/\delta = 0.64$. The $S_{\rho u}^{\text{CTA}}$ value

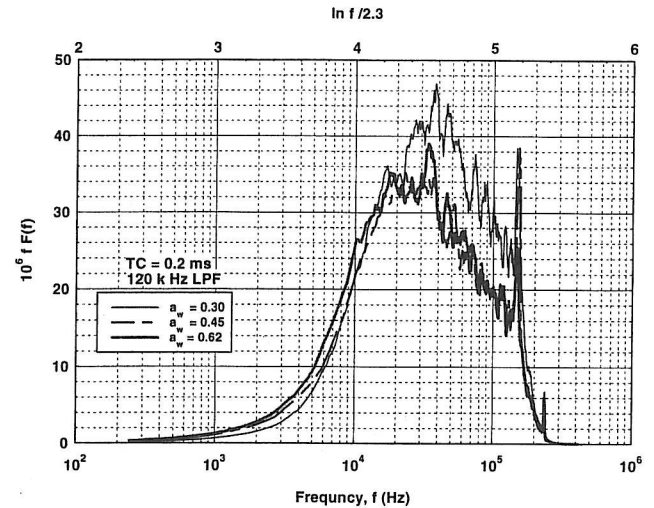


FIG. 9. CVA response of $fF(f)$ at three overheats.

was more like 0.22 instead of 0.25 according to Dury's work.¹⁴ Using the rms values listed in Table I, the components in the turbulence are calculated to be

$$\frac{\sqrt{(\rho u)'^2}}{\bar{\rho} U} = 8.87\%, \quad \frac{\sqrt{\theta_t'^2}}{\Theta_t} = 1.93\%,$$

and

$$R = \frac{\overline{(\rho u)' \theta_t'}}{\sqrt{(\rho u)'^2} \sqrt{\theta_t'^2}} = 0.49. \quad (15)$$

The same technique could be applied to the power spectral density calculations as well. Figure 9 shows the plots of the e'/E spectra at $T_c = 0.2$ ms with 120 kHz lpf solved from the three overheats 0.30, 0.45, and 0.62. The $fF(f)$ versus $\ln(f)$ shown in Fig. 9 gives a clear glimpse of the most energetic part of the turbulent signals. The three responses are different, as they should be at different overheats. Using the three data arrays for the three overheats, the matrix solution of the spectra is obtained for $G_{\rho u}(f) = \text{psd}(\rho u)'$, defined by $(\rho u)^{1/2}/\bar{\rho}^2 U^2 = \int_0^\infty G_{\rho u}(f) df$ and $G_{\theta_t}(f) = \text{psd}(\theta_t)'$ defined by $\theta_t'^{1/2}/\Theta_t^2 = \int_0^\infty G_{\theta_t}(f) df$, and the cross-correlation spectra is denoted by $G_{\rho u \theta_t}$. These spectra are shown in Fig. 10(a). As can be expected¹⁵ the total temperature fluctuation component is small. The psd of the correlation coefficient $R(f)$ is shown in Fig. 10(b). The numerical value of the $R(f)$ computed with this method is smaller than 1, except in the vicinity of the strain gauging peaks, which are difficult to analyze anyway. The above results demonstrate that it is possible to use the CVA also with different overheats and resolve the turbulence components.

F. Comparison with earlier research

An exhaustive chart of previously measured turbulence intensities by different researchers was presented by Smits, Hayakawa, and Muck.¹⁸ In order to put the present CVA data into that chart, we need to transform the $(\rho u)^{1/2}/\bar{\rho}^2 U^2$ results into $\bar{\rho} u'^{1/2}/\tau_*$, where u' is the velocity fluctuation, $\bar{\rho}$ is the

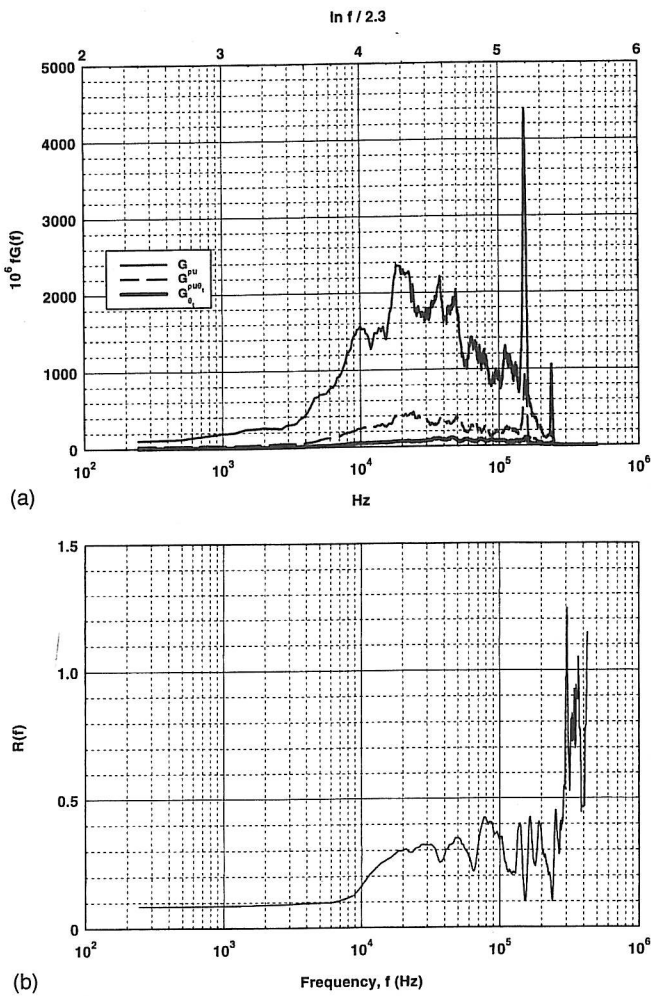


FIG. 10. (a) Resolved components of turbulence obtained by solving three simultaneous equations with three overheat. (b) Spectra of the correlation coefficient $R(f)$ for CVA.

mean local density, and τ_* is the wall stress such that $\tau_* = \rho_* u_*^2$ where ρ_* is the density at the wall and u_* is the friction velocity. Several of the characteristics of the supersonic tunnel needed to convert the CVA output into $\bar{\rho}u'^{1/2}/\tau_*$ for comparison with earlier research are available from Dury's work¹⁴ in the same tunnel: $u_* = 20$ m/s, $\rho_* = 0.1455$ kg/m³, $Ma_{ext} = 2$, $U_{ext} = 505$ m/s, $\rho_{ext} = 0.2682$ kg/m³, and $Re_{ext} = 19$. Profiles of the local wire Reynolds number Re and the flow Mach number Ma across the boundary layer were also available, from which, at $y/\delta = 0.64$, $Re = 17$ and $Ma = 1.8$.

The first step in the computations is to transform the relative change $(\rho u')/\bar{\rho}U$ into

$$\frac{(\rho u')'}{\bar{\rho}U} = \frac{\rho'}{\bar{\rho}} + \frac{u'}{U}. \quad (16)$$

It is assumed that the static pressure across the boundary layer and stagnation temperature are constants. It was also assumed that the strong Reynolds analogy (SRA) is valid for the test, cf. Gaviglio¹⁹ and Barre, Dupont, and Dussauge²⁰ so that:

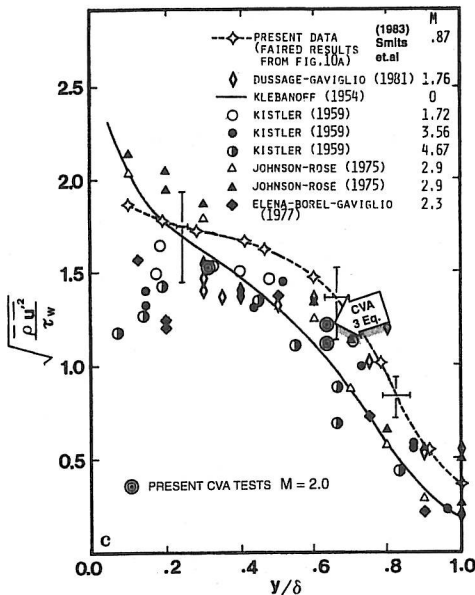


FIG. 11. CVA test results superimposed with earlier research results.

$$(\gamma - 1)Ma^2 \frac{(\overline{u'^2})^{1/2}}{U} = \frac{(\overline{\rho'^2})^{1/2}}{\bar{\rho}} \quad \text{with } \gamma = 1.4, \quad (17)$$

and

$$\overline{\rho' u'} = 0.80(\overline{u'^2})^{1/2}(\overline{\rho'^2})^{1/2}. \quad (18)$$

From Eqs. (16)–(18), we can obtain

$$\frac{\overline{u'^2}}{U^2} \approx \frac{(\rho u')'^2}{\bar{\rho}^2 U^2} [1 + (\gamma - 1)^2 M_a^4 + 1.6(\gamma - 1)M_a^2]^{-1}. \quad (19)$$

From the assumption of constant static pressure and constant stagnation temperature across the boundary layer we have

$$\frac{\bar{\rho}}{\rho_{ext}} \approx \frac{Re^2}{Re_{ext}^2} \frac{Ma_{ext}^2}{Ma^2} \quad \text{and} \quad \frac{\bar{U}}{U_{ext}} \approx \frac{Ma^2}{Ma_{ext}^2} \frac{Re_{ext}}{Re}. \quad (20)$$

We can now write the explicit expression for $\bar{\rho}u'^{1/2}/\tau_*$ as

$$\frac{\bar{\rho}u'^{1/2}}{\tau_*} = \frac{\bar{\rho}}{\rho_*} \frac{\overline{u'^2}}{u_*^2} = \frac{1}{\rho_* u_*^2} \frac{\bar{\rho}}{\rho_{ext}} \frac{\overline{u'^2}}{U^2} \frac{U^2}{U_{ext}^2} \rho_{ext} U_{ext}^2, \quad (21)$$

and using Eqs. (20) and (21) and the data listed above for the boundary layer, we obtain

$$\frac{\bar{\rho}u'^{1/2}}{\tau_*} = 186 \frac{(\rho u')'^2}{\bar{\rho}^2 U^2} \quad \text{at } y/\delta = 0.64 \quad (22)$$

and

$$\frac{\bar{\rho}u'^{1/2}}{\tau_*} = 190 \frac{(\rho u')'^2}{\bar{\rho}^2 U^2} \quad \text{at } y/\delta = 0.32. \quad (23)$$

The CVA results for $\bar{\rho}u'^{1/2}/\tau_*$ calculated with the above expressions are shown in Fig. 11 superimposing the results of other earlier research. A total of three data points are shown in Fig. 11 that were obtained with the present CVA tests. One point is obtained by solving the three simultaneous overheat (0.30, 0.45, and 0.62) equations at $y/\delta = 0.64$. This value is shown to be 1.21 on the y axis in the graph. The two other points shown in Fig. 11 for the $\bar{\rho}u'^{1/2}/\tau_*$ that were

computed from the CVA results at the two boundary layer points $y/\delta=0.64$ (at $a_w=0.62$) and $y/\delta=0.32$ (at $a_w=0.60$) are 1.11 and 1.52, respectively. They were computed using the following approximate relationship neglecting the total temperature effect:

$$\frac{e'^2}{E^2} = [S_{\rho u}^{\text{CVA}}]^2 \frac{(\rho u)^{1/2}}{\bar{\rho}^2 U^2}. \quad (24)$$

From Fig. 11, it is very clear that the CVA results agree quite well with several other experiments, indicating that the CVA with an *in situ* measured time constant and software corrected thermal lag is indeed a viable option for quantitative measurements.

ACKNOWLEDGMENTS

The authors are indebted to Dr. Jean-Paul Bonnet, Head of the LEA-CEAT, Poitiers (France) for permitting the use of their supersonic tunnel facility and Dr. Stéphane Barre, Dr. Gérard Dury, Marie Christine Guégan, Philippe Szeger, and Serge Sapin who helped them in running the facility and data acquisition systems.

¹G. R. Sarma, U.S. Patent No. 5074147 (1991).

²J. T. Lachowicz, N. Chokani, and S. P. Wilkinson, AIAA J. **34**, 2496 (1996).

- ³A. E. Blanchard, J. T. Lachowicz, and S. P. Wilkinson, AIAA J. **35**, 23 (1997).
- ⁴G. P. Doggett, N. Chokani, and S. P. Wilkinson, AIAA 35th Aerospace Sciences Meeting and Exhibit, Reno, Nevada, January, 1997, AIAA Paper No. 97-0557.
- ⁵M. A. Kegerise and E. F. Spina, ASME 3rd International Symposium on Thermal Anemometry, San Diego, California, July, 1996. (ASME-FED, 239).
- ⁶M. A. Kegerise and E. F. Spina, AIAA Fluid Dynamic Conference, Snowmass, Colorado, July, 1997, AIAA Paper No. 97-1955.
- ⁷G. Comte-Bellot, in *Handbook of Fluid Dynamics*, edited by R. W. Johnson (CRC Boca Raton, FL, 1998), Chap. 34.
- ⁸T. Moes, G. R. Sarma, and S. M. Mangalam, NASA TM-4806 (1997).
- ⁹S. M. Mangalam, G. R. Sarma, R. A. Pfouts, T. S. Kwa, J. H. Casper, M. A. Wallace, and R. Nigon, Report TS9801, Tao Systems, 1998.
- ¹⁰G. R. Sarma, Rev. Sci. Instrum. **69**, 2385 (1998).
- ¹¹E. Arzoumanian and J. F. Debieve, L'Onde Electrique **70**, 55 (1990).
- ¹²P. Freymuth, DLR FB 66-03 (1966).
- ¹³S. Kuppa, G. R. Sarma, and S. M. Mangalam, ASME Fluid Measurement Instrumentation Forum FED **61**, 67 (1993).
- ¹⁴G. Dury, Ph.D. dissertation, University of Poitiers, 1997.
- ¹⁵A. J. Smits and J. P. Dussauge, *Turbulent Shear Layer in Supersonic Flows* (AIP, New York, 1996).
- ¹⁶A. L. Kistler, Phys Fluids **2**, 290 (1959).
- ¹⁷L. S. G. Kovasznay, J. Aeronaut. Sci. **20**, 657 (1953).
- ¹⁸A. J. Smits, K. Hayakawa, and K. C. Muck, Exp. Fluids **1**, 83 (1983).
- ¹⁹J. Gaviglio, J. Mécanique Appliquée **2**, 449 (1978).
- ²⁰S. Barre, P. Dupont, and J. P. Dussauge, Eur. J. Mech. B/Fluids **11**, 439 (1992).

Indian launchers aim at commercial market

India's space program has passed important milestones with the recent launch of INSAT-2E, a new generation of telecommunications satellites, and PSLV, the indigenous polar satellite launch vehicle.

The PSLV launch of Oceansat-1 plus German and South Korean minisats was the fifth for this vehicle and the first launch of a foreign payload by an Indian rocket. It is spearheading India's efforts to get into the commercial launcher business. The next steps will be the lofting of INSAT-3B and the geostationary satellite launch vehicle (GSLV). If successful, GSLV will enable the Indians to launch 2.5-tonne payloads to GEO and will also inaugurate India's use of cryogenic technologies.

First steps

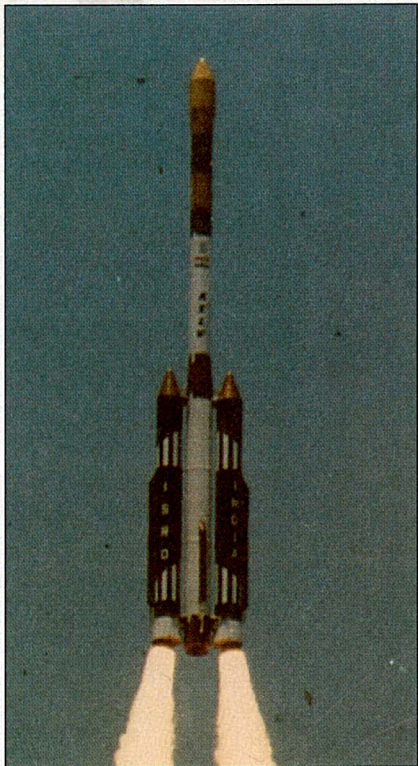
India's space effort began in 1962 with the establishment of INCOSPAR (Indian Committee for Space Research), under the auspices of the Dept. of Atomic Energy. This led a year later to the creation of the Thumba Equatorial Rocket Launching Station, used to launch French, U.S., and Soviet sounding rockets. In 1965, Vikram Sarabhai, considered the father of the Indian space program, created the Space Science and Technology Center. Next came the establishment of the Indian Space Research Organization (ISRO) in 1969, with Sarabhai as its head.

From the outset, the objectives of the national program were to develop and master space technologies and thus achieve independence in this strategic sector. The Indian program has always focused on three main sectors: telecommunications, remote sensing, and launch vehicle development. Mirroring these priorities are ISRO's

main programs: INSAT, for telecommunications and meteorology, the Indian remote sensing (IRS) satellite, and the PSLV and GSLV launchers.

ISRO implemented these objectives under heavy technological and financial constraints. As far as possible, developmental efforts sought to integrate home-grown and foreign technologies. A step-by-step approach was used for satellite and launcher development. This was especially true for development of the SLV-3 and augmented SLV (ASLV), which were essentially technology demonstrators for the PSLV and GSLV launchers.

The 39-tonne ASLV served as a demonstrator for various technologies.



Building a base: SLV-3 and ASLV

Indian launcher development efforts go back to the creation of the TERLS in 1963. Local production of the Centaur sounding rockets and indigenous development and production of Rohini, a family of such rockets, provided experience that was used for the launcher program.

Development of the SLV-3 began in the early 1970s. This four-stage solid propellant launcher, which is very similar to the U.S. Scout and weighs 17 tonnes, can put a 40-kg payload in LEO. In August 1979, the first attempt to launch a satellite with the SLV-3 failed. In the second attempt, on July 18, 1980, the SLV-3 successfully orbited the Rohini RS-1.

After this first success, the SLV-3 was used two more times, launching the Rohini-D1 in May 1981 and the Rohini-D2 in April 1983. The latter flight was only a partial success, because the satellite was put into the wrong orbit and burned up in the atmosphere after only eight days. Following the third successful flight of the SLV-3 in 1983, emphasis shifted to the ASLV.

Fundamentally an SLV-3 with two solid rocket boosters (SRBs), the ASLV was capable of putting 100-150 kg in LEO. The 39-tonne launcher served as a technology demonstrator for stage separation and vehicle guidance technologies. It validated an indigenous closed-loop guidance system as well as Indian-manufactured HTPB (hydroxyl terminated polybutadiene) propellant. The latter replaced the PBAN (polybutadiene-acrylic-acid-acrylonitrile) used by the SLV-3.

ASLV's development was far from trouble free, however. The launch sequence called for the SRBs to ignite on the ground, and for first-stage ignition 44 sec into flight. The first ASLV was lost when the initial stage failed to ignite. A year later, in 1988, the second flight failed because the control system was unable to handle instabilities caused by the transition between the strap-on and the first stage.

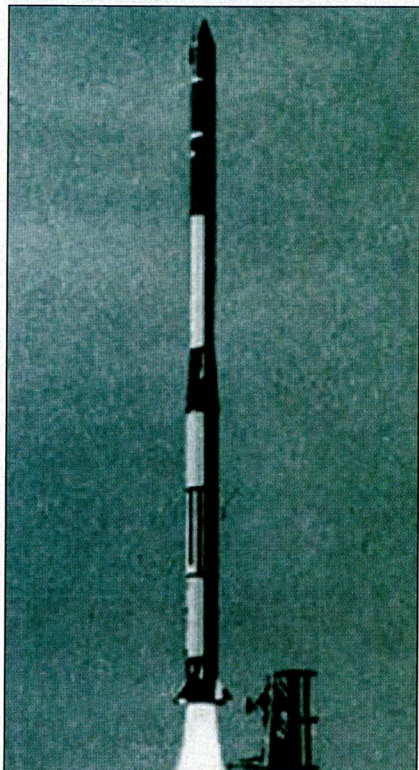
It was only in May 1992 that the ASLV flew successfully. The vehicle was modified with the addition of two passive fins in the pitch plane to improve stability. The digital autopilot also was redesigned for enhanced control margin. Structural strengthening led to a reduced payload of 113 kg for the fourth and last flight in 1994.

PSLV

All of these developmental efforts were directed toward realization of the PSLV, which was capable of putting 1-1.2 tonnes in a 900-km heliosynchronous polar orbit. The PSLV represented a total change of scale for an Indian launcher; it also marked ISRO's first use of liquid propulsion.

Built around what ISRO claims is the world's third largest solid propellant booster, the PSLV stands 44 m tall and weighs 294 tonnes at liftoff. A four-stage rocket, it uses a unique

Development of the SLV-3 began in the early 1970s.



The PSLV sparked development of a ground segment and infrastructure, including a 3,000-tonne mobile service tower for vertical integration of the launcher and payload.

combination of solid and liquid propellant stages. The first is a 20-m-tall solid propellant stage carrying 138 tonnes of HTPB. Flanking it are six SRBs, each providing 66 tonnes of thrust. The SRBs are derived from the ASLV's first stage.

The PSLV's central stage provides 460 tonnes of thrust. The second stage is a liquid propulsion unit burning hydrazine (UDMH) and nitrogen tetroxide. It uses an engine called Vikas, a locally built variant of France's Viking. India bought the license for local production from SEP (Société Européenne de Propulsion) in the early 1980s. The third stage uses solid propellants, and the fourth reverts to liquid propulsion with ISRO-designed engines.

The PSLV also sparked development of a ground segment and infrastructure. A 3,000-tonne mobile service tower allows for vertical integration of the launcher and payload before moving 180 m away prior to launch. A network of radars and ground stations in Sriharikota, Thiruvananthapuram, Bangalore, Lucknow, the Andaman islands, and Mauritius follow the vehicle during its flight.

The first PSLV launch took place in September 1993 with the IRS-1E

satellite as the payload. A software error in the guidance system during second- and third-stage separation led to the failure of the mission. The second launch successfully orbited the IRS-P2 experimental remote sensing satellite. However, at 804 kg, the payload was 20% lower than the original 1-tonne planned capability. By the fourth flight, the payload had been increased to 1.2 tonnes. This resulted from increasing the propellant load of the first and second stages and from a weight reduction program.

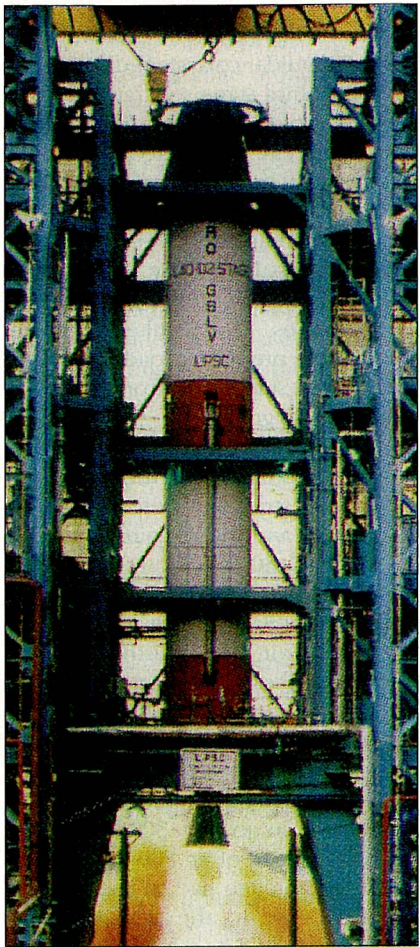
The firing sequence of the SRBs also was modified: For the first three flights, two strap-ons were ignited on the ground and the remaining four in the air at T+30 sec; from the fourth flight on, this was changed to four strap-ons ignited on the ground and two in the air. The fourth flight, although successful in placing the IRS-1D remote sensing satellite in orbit, suffered from a leak of the helium used to pressure-feed the last stage's engines. This meant that the satellite was placed in an 800×300-km elliptical orbit instead of an 800-km circular orbit. The satellite had to use its own engine to get to the desired orbit, thereby reducing its orbital life.

The PSLV's last flight—the second for the upgraded version—took place on May 26 and carried the IRS-P4 (Oceansat-1) as its primary payload. Also on board were two microsatellites from Germany (Tubsat-C) and South Korea (Kitsat-3). This was the first commercial launch for the PSLV; ISRO hopes many will follow.

GSLV

Having achieved independence in the launch of 1-tonne-class payloads, the next step is to attain a geostationary capability for a 2.5-tonne-class telecommunications payload. This is to be done through the GSLV, which builds on the technologies and experience gained from the PSLV program. The GSLV uses the same first and second stages as the PSLV. Replacing the six

The GSLV uses the same first and second stages as the PSLV, followed by a single cryogenic stage.



SRBs are four liquid propellant boosters powered by the same Vikas engine used for the second stage. The third and fourth PSLV stages are replaced by a single cryogenic stage.

Because ISRO has very limited experience with liquid propulsion and almost none with cryogenic propulsion technologies, the organization decided to buy the cryogenic engine and technologies from abroad. In 1991 it reached an agreement with Russia's Glavkosmos, which was to supply engines for the first flights of the GSLV and transfer cryogenic technologies to ISRO. But the U.S., claiming that the deal violated MTCR (Missile Technology Control Regime) rules, imposed sanctions on ISRO and threatened to do the same to Glavkosmos if the deal went ahead. Finally, the agreement was limited in 1993 to the sale of seven KhimMach KVD-1 engines, for a value of \$250 million-\$300 million, without any transfer of technology. The KVD-1 engine produces 7.5 tonnes of thrust; the first flight unit was delivered in September 1998.

India is now obliged to develop a cryogenic engine alone. ISRO's effort to develop cryogenic technologies began with the launching of a study project in 1986. This led to the July 1989 test firing of a 1-tonne-thrust subscale pressure-fed engine using liquid oxygen (LO_x) and gaseous hydrogen.

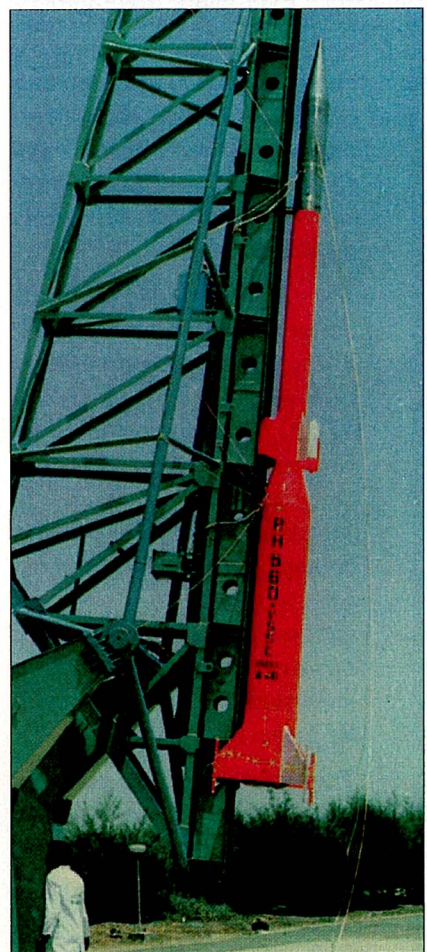
The project's aim was to acquire a basic understanding of cryogenics and of the developmental problems related to making an engine. To respect the GSLV timetable, ISRO decided it could obtain the technology faster from abroad.

ISRO only acquired the capability for making liquid hydrogen (LH_2) in 1992. In 1993, development efforts suffered a setback when a subscale pressure-fed engine exploded after ISRO tried using LO_x and LH_2 . Begun in 1993, the design for a 7.5-tonne-thrust engine was completed in 1996, and design work started on a 12-16-tonne engine for a growth version of the GSLV. It was only in February 1998 that an engine was successfully test fired using LO_x and LH_2 . This was still a pressure-fed version, although the flight version of the engine is to use

turbopumps that seem to be still some way off.

Work is continuing on the GSLV itself for a first launch by mid-2000. The launcher's liquid-fueled boosters successfully underwent qualification tests in March 1998 after developmental firings in July 1995 and May 1997. The strap-on boosters are 19.7 m long and have a 2.1-m diameter. Burning a mixture of UDMH and N_2O_4 , they produce 60 tonnes of thrust for 160 sec. This means the solid-propellant first stage that burns for 107 sec actually burns out before the strap-ons. This reduces the GSLV's payload, as the launcher will carry the dead weight of the central core before the strap-ons burn out. However, this compromise seems to have been considered acceptable, probably because of reduced development risks and

Rohini sounding rockets laid the foundation for India's launch business.



INDIAN LAUNCH VEHICLES AND LAUNCHES

Launcher	Height×diameter, meters	Mass, tonnes	Launch vehicle	Satellites	Payload, kilograms	Date	Remarks
SLV-3	22.7×1.0	17 ¹	SLV-3	Rohini-0	40	8/10/79	Launch vehicle failure
			SLV-3	Rohini-1	40	7/18/80	First successful launch
			SLV-3	Rohini-D1	40	5/31/81	
			SLV-3	Rohini-D2	42	4/17/83	
ASLV	23.8×1.0	41.7 ²	ASLV-D1	SROSS-1	150	3/24/87	Launch vehicle failure
			ASLV-D2	SROSS-2	15	7/13/88	Launch vehicle failure
			ASLV-D3	SROSS-C1	106	5/20/92	
			ASLV-D4	SROSS-C2	113	5/4/94	
PSLV	44.4×2.8	283 ³	PSLV-D1	IRS-1E	870	9/20/93	Launch vehicle failure due to software problems
			PSLV-D2	IRS-P2	804	10/15/94	Successful launch of experimental version of the IRS
			PSLV-D3	IRS-P3	922	3/21/96	
		294 ⁴	PSLV-C1	IRS-1D	1,200	9/29/97	Fourth stage malfunction left satellite in lower orbit
			PSLV-C2	IRS-P4	1,050	5/26/99	First launch of foreign payloads
				Kitsat-3 (S. Korea)	107		
				Tubsat-C (Germany)	45		
			GSLV-D1	GSAT-1A	2,000	2000	Cryogenic third stage with Russian engine

¹Four stages solid propellant. ²Four stages plus two boosters solid propellant. ³Four stages plus six solid boosters mixed liquid and solid propellant.

⁴Four stages plus six solid boosters mixed liquid and solid propellant. ⁵Three stages plus four liquid boosters mixed solid plus liquid and cryogenic.

economies of scale through commonality with the PSLV.

Toward a commercial future?

Over the past 35 years, Indian efforts to achieve an independent launch vehicle capability have been continuous, as has the development of telecommunications and remote sensing satellites. Launcher development accounts for 50% of ISRO's budget, and this is likely to continue, as the GSLV will demand a substantial effort. While ISRO's budget is small compared to those of the major space agencies, it has been growing at an impressive rate: The 1998-1999 budget was up more than 50% over that of the previous year. India is now seeking to capitalize on its investments in the space sector.

In 1992 ISRO created a commercial branch called ANTRIX. Its IRS se-

ries of remote sensing spacecraft has enjoyed some success on world markets. This success and the leasing of transponders on INSAT-2E to Intelsat in a \$100-million deal have prompted ISRO to try and enter the launcher business. So far the PSLV has won three contracts to launch minisatellites as additional payloads. The first two, Tubsat and Kitsat, were launched by the PSLV-C2 for around \$1 million. The third, the Belgian PROBA, is to be launched by a PSLV-C3 in 2000-2001.

To try and get a greater share of the minisatellite market, ISRO and ArianeSpace signed an agreement in April 1998 that allows for the launch of microsatellites on either Ariane or ISRO vehicles. A common users' manual for auxiliary payload clients has been established and is compatible with both Ariane 5 and the PSLV.

India still has some way to go before becoming a major player in the commercial launcher market, despite lower costs. The PSLV has a rather limited payload capacity compared with other launchers, and a lot depends on the GSLV and the successful development of its associated technologies.

ISRO's launchers have been developed specifically for the home market. With a capability of two launches a year, this means that for the immediate future ISRO can offer to launch only additional payloads. But the approaching maturation of the Indian space program means that in the medium-to-long term, the commercial launcher business will see the emergence of a new and serious contender.

**Virendra C. Sharma
Thierry M. Faure**

Université Pierre et Marie Curie

Laser Doppler Anemometry Measurements in an Axial Compressor Stage

Thierry M. Faure,* Guy-Jean Michon,† Hubert Miton,‡ and Nicolas Vassilieff§
Université Pierre et Marie Curie, Paris 6, 91405 Orsay, France

The aim is to provide unsteady experimental data of the flowfield in a benchmark one-stage axial compressor, to improve the understanding of the flow features. The investigation is conducted with a two-component laser Doppler anemometer, and 32 axial locations are surveyed, from the rotor inlet to the stator outlet. Because laser Doppler anemometry is a nonintrusive device, data are obtained from the rotor row, providing information in a region difficult to explore with other techniques. Limitation of blade shadowing is addressed with an adjustment of the laser head orientation, which permits reaching any point inside the rotor. Furthermore, a dual probe orientation gives two sets of measurements yielding three velocity components. The dynamics of the rotor tip clearance vortex is discussed in the interrow gap. There is a strong interaction between this vortex and the rotor blade wake. Phase-averaged results show the unsteady flowfield and the rotor-stator interaction. The rotor wakes are cut up by the stator row and are visible until the exit of the axial zone of measurements. Their interaction with the stator blades boundary layers creates strong time-dependent flow structures resulting in phase lags between the rotor wakes at the stator outlet.

Nomenclature

A_{ij}	= matrix (4×3) of geometrical probe volume position
c_r	= rotor blade axial chord at midspan
D	= determinant
H	= normalized distance between the hub and the casing
N	= parameter of geometrical probe volume position
p_{t_1}	= inlet total pressure
p_{t_2}	= outlet total pressure
r	= radial direction
r_h	= hub radius
r_t	= tip radius
t	= time
V	= absolute velocity
W	= relative velocity
x	= axial direction
α	= absolute angle
β	= relative angle
θ	= tangential direction
ϑ	= laser head pitch angle
φ	= laser head roll angle
ϕ	= phase angle
ψ	= laser head yaw angle

Subscripts

b	= blue laser component
g	= green laser component
i	= index
m	= meridian component
x, r, θ	= axial, radial, and tangential directions
1	= first laser head position
2	= second laser head position

Received 15 November 1999; revision received 30 June 2000; accepted for publication 10 July 2000. Copyright © 2000 by the American Institute of Aeronautics and Astronautics, Inc. All rights reserved.

*Assistant Professor, Laboratoire d'Énergétique et de Mécanique des Fluides Interne. Member AIAA.

†Research Engineer, Laboratoire d'Énergétique et de Mécanique des Fluides Interne.

‡Researcher, Laboratoire d'Énergétique et de Mécanique des Fluides Interne.

§Research Assistant, Laboratoire d'Énergétique et de Mécanique des Fluides Interne.

Superscript

\sim = phase-averaged property

I. Introduction

RECENT improvements in axial turbomachinery lead to a compressor efficiency that tends to an asymptotic value. Nowadays, the need is not only to understand the behavior of the mean flowfield, but also to get information on the time-dependent features. For a better understanding of the unsteady velocity, inside a confined high-velocity rotating channel, it is necessary to use unsteady and nonintrusive measurement systems.

Thus, laser velocimetry is a useful tool for turbomachinery flow investigation, which is able to provide information on the three-dimensional velocity field. Some attempts to use laser two focus (L2F) anemometers have been carried out^{1–3} in this kind of high-loaded, high-speed rotating flow. The extension of these systems for three-dimensional measurements are under development.^{4–8} However, L2F anemometry measurements are difficult to validate for complex and turbulent three-dimensional high-speed flows. That is the reason we preferred using laser Doppler anemometry (LDA) for this study. Furthermore, this technique is still evolving. The miniaturization of hardware, with recent improvements in laser diodes and photodiodes, will lead in the near future to miniature systems at a low cost.⁹ These new systems tend to improve the resolution of the probe volume or to measure the spatial turbulence correlation.¹⁰ Additional improvements are made in the signal processing of the electric output of the photomultiplier. In the past, the common technique was to count the zero crossing of the Doppler signal; however, now, the spectral analysis of Doppler bursts is preferred. This is a much more powerful technique and can operate in high background noise conditions.¹¹

Most of the recent work on unsteady three-dimensional flow in turbomachinery has been conducted in rotor turbines.^{12–15} The first application of a three-component LDA on an axial-flow compressor, was carried out by Chesnakas and Dancey.¹⁶ However, the experiments performed in compressor rigs are usually limited to turbulence measurements within the airfoil rows¹⁷ or tip leakage studies. For instance, Murthy and Lakshminarayana¹⁸ made LDA two-component measurements of the tip region flowfield within and aft of the axial compressor blade passage. Stauffer¹⁹ used a five-beam LDA system to make time-resolved measurements both between compressor blade rows and within the rotating blade passages in an axial compressor, to track the three-dimensional flow in the tip region.

In the present investigation, a two-component, two-color LDA is implemented to explore the flow inside a compressor stage. Measurements are completed inside the rotor and stator, providing flow characteristics in regions difficult to investigate with other techniques. The use of the laser head with two off-axis orientations yields the three components of velocity. Time-dependent averages are processed in phase with rotor position to analyze the unsteady flow behavior.

II. Experimental Facility and Instrumentation

A. Test Rig

The single-stage axial compressor setup (CME2) of the laboratory is shown in Fig. 1. This open-circuit facility consists of an inlet with filters for the atmospheric air, a settling chamber followed by the compressor test rig, a flow adjuster, and an outlet duct discharging in the room. This is an improvement of a testbed used for unsteady hot-wire interrow investigation of a four-stage axial compressor.^{20–23} The compressor stage is fitted with a 30-blade rotor and a 40-blade stator. The axial length of the test section is 180 mm, and the radius of the casing $r_t = 275$ mm. The blade clearance is 0.5 mm in the rotor. The hub radius r_h is increasing from 207 mm in rotor inlet to 212.1 mm in rotor outlet and is constant inside the stator row. A summary of the blade geometry is given in Tables 1 and 2. The origin of the axial coordinate is located near the leading edge of the rotor blade hub.

The rotor is powered by an electrical driving motor that delivers a maximum of 180 kW. It drives a low-speed shaft, so that rotor speed is increased by a multiplier to a high-speed shaft, the high-speed/low-speed ratio being 2.345. At the operating point and for standard conditions (inlet temperature 15°C and pressure 101,325 Pa), the speed of rotation is fixed to 6330 ± 14 rpm, and the flow rate is 10.5 ± 0.1 kg/s, providing a total pressure ratio $p_{t_2}/p_{t_1} = 1.15$. The flow rate can be regulated by axial displacement of the hub wall downstream of the compressor rig outlet. This wall is driven by an electrical dc motor controlled by a personal

computer. Inlet and outlet temperatures are obtained from platinum resistance gauges introduced radially in the compressor, as well as total pressure probes to estimate the compressor pressure ratio. The instantaneous blade position is obtained by an optical shaft encoder that delivers a periodic 0–5 V amplitude signal per revolution. This signal is recorded and used in post-processing to calculate phase-averaged velocities.

B. LDA System

The laser Doppler anemometer is a Dantec two-color, four-beam, two-dimensional measuring system. The source is a 5-W argon-ion laser (Coherent model Innova 305) tuned to the 488 nm (blue) and 514.5 nm (green) wavelengths. A power tracking system ensures time stability of laser light emission, whose intensity is a Gaussian-like profile. Each color beam is split in two, and one of these is passed through a 40-MHz Bragg cell, where it is frequency shifted to reduce fringe bias and to solve the direction ambiguity. The half-angle of the beams is 6.772 deg and the measuring volume is 0.8 mm in length and 0.1 mm in diameter. The laser focal distance is 160 mm. Scattered light from the seeding particles passing through the probe volume is collected off-axis from the test rig, which means the optical axis is not aligned with the radial axis. Such an orientation permits closer approach to the access window with the probe volume. The hub and rotor and stator blades are black anodized to reduce surface light reflexions.

In this experiment, because the compressor stage is included in an open-circuit facility, liquid seeding material is preferred. It is provided by a fog created by a fluid containing glycerol, heated and atomized by a SAFEX 2001 smoke generator. The main advantages of this flow-seeding material are its low cost and its easy use. Furthermore, it provides few deposits on the window and the blades, in comparison with oil or incense. Because many points of measurements are recorded per axial section and a long measurement time is necessary to complete a grid section, deposits can affect the window and drastically decrease or stop the data acquisition rate. A cleaning system that removes periodically any dust on the window, without stopping the compressor and removing the window frame, which is an operation that is time consuming, was developed to address this issue. This cleaning system consists of a water and soap mixture injected at two locations on the window frame, providing cleaning for the complete window surface. The seeding fluid is atomized and introduced in the settling chamber 20 cm before the section contraction. According to the seeding fluid manufacturer, the average particle diameter is $1.068 \mu\text{m}$, and the particle density is 10^3 kg/m^3 .

To explore the blade to blade channel, the laser head, which is used both for the laser light emission and backscattered light collection, is mounted on a manipulation robot. This six-degree-of-freedom arm permits the measurement volume to reach any part inside the compressor. The construction of the three-dimensional field requires two measurements at the same place but with different azimuth angular positions. This assumes more than three degree of freedom. The system enables very accurate positioning: The repeatability for

Table 1 Rotor blade geometry

Span	Chord, mm	Thickness, mm	Stagger angle, deg	Camber angle, deg
Hub	84	7.9	33.5	41.5
Midspan	84	5.6	46	23
Tip	84	2.8	54	20

Table 2 Stator blade geometry

Span	Chord, mm	Thickness, mm	Stagger angle, deg	Camber angle, deg
Hub	77	6.2	17.5	46.5
Midspan	77	6.2	15	41.5
Tip	77	6.2	12.5	36

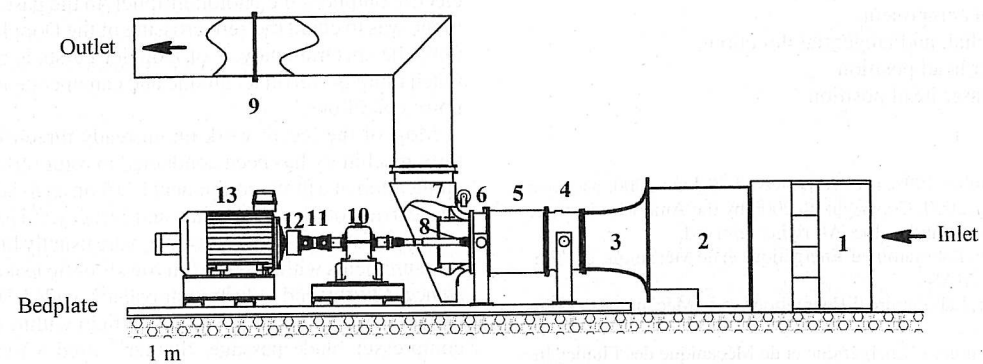


Fig. 1 Experimental setup: 1) inlet filters, 2) settling chamber, 3) convergent, 4) forward bearing, 5) compressor stage, 6) aft bearing, 7) mass flow adjuster, 8) high-speed cardan, 9) diaphragm, 10) low-speed cardan, 11) torque limiter, and 13) driving motor (180 kW).

the measurement volume location is around $20 \mu\text{m}$. Furthermore, the cost of this system is no higher than a high-precision controlled traverse and offers many possibilities for future experiments. No experimental problem was found in conducting measurements, except near the rotor hub inlet and the access window.

The flow in the compressor stage is measured through a curved Plexiglas® rectangular window, which is 200 mm in length and 136 mm wide. It is 2 mm thick, conforming to the cylindrical shape of the casing.

To run the probe displacements, record and process data, a Hewlett Packard workstation is interfaced through an Institute of Electrical and Electronics Engineers connection to the Dantec burst signal analyzers (BSA), which are 14-bit data samplers.²⁴ The analyzers use a hardware fast Fourier transform to measure and to validate the backscattered signal at up to 10,000 bursts per second. The two components are not taken in coincidence filtering, and the number of validated bursts per measurement point is 3000, providing for a confidence level of 95% and error of 0.72% in mean velocity, by the use of the method employed by Strazisar.²⁵ In addition, the laser head displacements are controlled through an RS232 connection. A program has been developed for this study, its main characteristics are as follows.

1) In the first in/first out mode, for each BSA the buffer data are transferred to the workstation during data acquisition.

2) Acquisition is possible with one, two, or three BSA.

3) There is automatic recording of acquisition parameters such as the BSA's setup, position in the robot frame, position in the compressor frame, laser power, etc.

4) There is real-time control with automatic display of data histograms concerning the current measurement point.

To access the phase ϕ (the arrival time of a Doppler burst, related to a blade rotor passage), a top-turn system has been developed. Its principle is to provide a top signal for each rotor rotation; hence, the blade crossing time is deduced. This top-turn signal is recorded with the output of one BSA. Afterward, the phase of a measurement is found with

$$\phi = \frac{t - t_i}{t_{i+1} - t_i}$$

where t_i and t_{i+1} are the crossing times for blades i and $i + 1$ before and after the particle arrival time, respectively. This method is very accurate because the rotation can be assumed constant during a revolution.

C. LDA Data Reduction

In this study, 32 axial sections, spreading from the compressor inlet to the outlet are surveyed. For each plane, 224 measurement points are recorded, covering a blade to blade, hub to tip channel. The problem of the passage of the rotor blades through the incident beams can reduce the investigation zone. It is corrected by the use of an azimuthal position of the laser head axis, which is adapted to the region the probe volume should reach. Thus the limitation of blade shadowing is addressed. Furthermore, the three-dimensional velocity field can be obtained by the implementation of two laser head orientations per point of measurement, leading to two sets of two different velocity components. Because of the high-speed application and the use of BSA, no blade flash problem occurred for particle detection; the light scattered by the blade was detected and rejected by the analyzers. The laser head is mounted on the arm of the manipulation robot (Fig. 2). A frame of reference for the head axis is defined relative to the compressor frame of reference by the angles ϑ , ψ , and φ , respectively, of the pitch, yaw, and roll angle with the head axis direction (Fig. 3). The two positions are defined by two sets of angular parameters, $(\vartheta_1, \psi_1, \varphi_1)$ and $(\vartheta_2, \psi_2, \varphi_2)$, respectively, with $\psi_1 = -10^\circ$ and $\psi_2 = 10^\circ$. If there is no problem of accessibility of the probe volume inside blades and walls, then $\vartheta_1 = \theta_1 = \vartheta_2$ and $\varphi_1 = \varphi_2$; otherwise these values are corrected by a masking program. In the first position, two velocity components V_{b_1} and V_{g_1} relative to the blue and green laser beams are measured, and the second position leads to another set of velocities

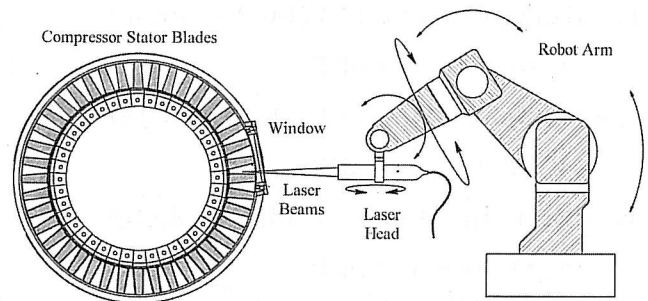


Fig. 2 Robot arm with laser head and optical access to compressor.

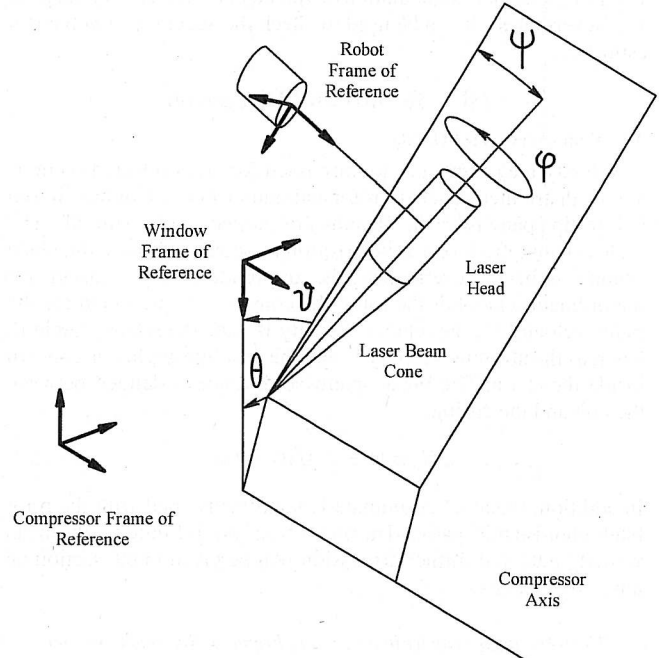


Fig. 3 Laser head angles relative to compressor frame of reference.

V_{b_2} and V_{g_2} . Let us define the parameters of the geometrical laser head position, relative to the compressor coordinates x , r , and θ :

$$N_{b_x} = \cos \psi \cos(\varphi - \pi/4)$$

$$N_{b_r} = \cos \vartheta \sin \psi \cos(\varphi - \pi/4) - \sin \vartheta \sin(\varphi - \pi/4)$$

$$N_{b_\theta} = -\cos \vartheta \sin(\varphi - \pi/4) - \sin \vartheta \sin \psi \cos(\varphi - \pi/4)$$

$$N_{g_x} = \cos \psi \cos(\varphi + \pi/4)$$

$$N_{g_r} = \cos \vartheta \sin \psi \cos(\varphi + \pi/4) - \sin \vartheta \sin(\varphi + \pi/4)$$

$$N_{g_\theta} = -\cos \vartheta \sin(\varphi + \pi/4) - \sin \vartheta \sin \psi \cos(\varphi + \pi/4)$$

These parameters are part of a 4×3 matrix A_{ij} with

$$A_{11} = N_{b_{x_1}}, \quad A_{12} = N_{b_{r_1}}, \quad A_{13} = N_{b_{\theta_1}}$$

$$A_{21} = N_{b_{x_2}}, \quad A_{22} = N_{b_{r_2}}, \quad A_{23} = N_{b_{\theta_2}}$$

$$A_{31} = N_{g_{x_1}}, \quad A_{32} = N_{g_{r_1}}, \quad A_{33} = N_{g_{\theta_1}}$$

$$A_{41} = N_{g_{x_2}}, \quad A_{42} = N_{g_{r_2}}, \quad A_{43} = N_{g_{\theta_2}}$$

The determinant of the three first lines of this matrix is

$$D = A_{11}(A_{22}A_{33} - A_{32}A_{23}) - A_{21}(A_{12}A_{33} - A_{32}A_{13})$$

$$+ A_{31}(A_{12}A_{23} - A_{22}A_{13})$$

Then, the three components of velocity in a cylindrical frame of reference attached to the compressor are calculated:

$$\begin{aligned}
 V_x &= [V_{b_1}(A_{22}A_{33} - A_{32}A_{23}) + V_{b_2}(A_{13}A_{32} - A_{33}A_{12}) \\
 &\quad + V_{g_1}(A_{12}A_{23} - A_{13}A_{22})]/D \\
 V_r &= [V_{b_1}(A_{23}A_{31} - A_{21}A_{33}) + V_{b_2}(A_{11}A_{33} - A_{13}A_{31}) \\
 &\quad + V_{g_1}(A_{13}A_{21} - A_{11}A_{23})]/D \\
 V_\theta &= [V_{b_1}(A_{21}A_{32} - A_{22}A_{31}) + V_{b_2}(A_{12}A_{31} - A_{11}A_{32}) \\
 &\quad + V_{g_1}(A_{11}A_{22} - A_{12}A_{21})]/D
 \end{aligned}$$

Note that in the preceding relationship, the velocity measured from the green laser beam, with the second laser head orientation V_{g_2} , is useless for the calculation of velocity components V_x , V_r , and V_θ . Nevertheless, it can be used to check the accuracy of velocities estimates.

III. Results and Discussion

A. Time-Averaged Velocity

Velocity measurements are discussed for eight selected sections axially distributed inside the rotor and stator rows and for five chosen hub to tip spanwise radii. Results are plotted vs the azimuth: The scales change from one axial position to another because the blade channel is bent. Nevertheless, the amplitude is kept constant for the ordinate scale. For the rotor, the components presented are the radial velocity V_r , the relative velocity W , and the relative angle β , whereas the absolute velocity V and the absolute angle α are shown inside the stator. The blade spanwise distance is defined between the hub and the casing:

$$H = (r - r_h)/(r_t - r_h)$$

In addition, the axial coordinate is nondimensioned with the rotor blade chord at midspan c_r . The present analysis is limited to the mean velocity field and further discussion will be given in the section on unsteady velocity.

1. Time-Averaged Velocity in a Rotating Frame of Reference (Rotor)

The time averaging is performed in the relative frame of reference, rotating with the rotor blades. These averages are carried out to remove any turbulent part in the velocity signal. Figure 4 shows the distribution over a blade to blade azimuth of the averaged radial velocity V_r in a rotating frame of reference, upstream, inside, and immediately downstream of the rotor row. Note that all of the profiles for $H = 22\%$ span are a little jagged because of greater measurement uncertainties due to the difficulty of introducing proper seeding in that zone and the important noise in the scattered light. For these reasons, results for lower spans inside the rotor row are not shown. The V_r velocity component is difficult to obtain, but it is small compared with axial and tangential velocities. However, it is taken into account for the estimates of W or V . The main variations of V_r are observed at the rotor outlet in the blade wakes. The averaged relative velocity distribution is shown in Fig. 5. For the first plane, located at $x/c_r = -0.059$, the potential blockage of the rotor blade causes a smooth depression in the velocity profile for every spanwise location. We also notice the regular velocity increase with span, caused by a greater entrainment velocity at the blade tip. Because of the increase of the stagger angle of the rotor blade from the hub to the tip, this first measurement plane is farther away from the leading edge for the $H = 90\%$ span than for the $H = 22\%$ span. For $x/c_r = 0.12$, a plane inside the rotor channel, the relative velocity distribution increases linearly from the pressure side to the suction side. For the span corresponding to $H = 22\%$, the distribution is not as linear because of lower acquisition data rates. The plane $x/c_r = 0.63$ shows an almost constant distribution from the pressure side to the suction side: This plane of measurement is located slightly before the rotor exit. For the rotor outlet ($x/c_r = 0.80$), the velocity distribution is flat out of the blade wake, which is noticeable as a velocity depression. The wider wake region for the $H = 90\%$ span is certainly due to a tip clearance vortex. This vortex is created on the blade suction side because of the pressure gradient and is convected downstream. After

the blade trailing edge, the vortex is deflected by interaction with the wake and is detected on the wake side corresponding to the blade pressure side.

2. Time-Averaged Velocity in a Fixed Frame of Reference (Stator)

Figure 6 shows the absolute velocity distribution V inside the stator row. The flow is decelerated between the inlet and the outlet of the row, from a 130 m/s maximum value to 100 m/s, as the stator plays its role by converting velocity into pressure. For the inlet location ($x/c_r = 0.93$), the velocity gradient is higher at the suction side, and the blockage due to the leading edge of the blade can be identified as velocity minima. The linear velocity increase from the pressure side to the suction side is clearly observed inside the stator channel for $x/c_r = 1.23$. However this velocity gradient is smoothed by the channel camber as long as the flow goes to the stator outlet, providing an almost constant velocity distribution at $x/c_r = 1.87$ except in the blade wakes. Figure 7 shows the distribution of the absolute angle α inside the stator. We notice that the order in magnitude of this quantity decreases from around 45 deg at the inlet to 0 deg at the outlet; this shows the stator row influence on the axial orientation of the flow. For the plane at $x/c_r = 0.93$, the large variations of α (around 10 deg) are associated with the blockage effect at the blade leading edge. Note the tangential variation of the absolute angle α with radius, which varies from 10 deg for $H = 22\%$ to 20 deg for $H = 90\%$. This can be explained by the rotor blade camber difference between the hub and the tip. For $x/c_r = 1.23$, the absolute flow angle α is quite uniform between the suction and pressure sides and disturbed only near the blade trailing edge ($x/c_r = 1.74$) because of the increase of the boundary layers. At the exit, the stator wake causes a small decrease of absolute angle at the suction side (-5 deg) and, as a consequence, a small increase at the pressure side (5 deg).

B. Unsteady Velocity

The periodic part of the flow motion relative to the compressor rotation is discussed in this section. Phase-averaged data are calculated from the time-dependent velocity signals delivered by the BSA thanks to the synchronization top-turn signal. The period of the top-turn signal is 9.48×10^{-3} s. Because the rotor blade number is 30, this gives a blade to blade passing period of 3.16×10^{-4} s. The interblade rotor channel is divided into 24 time-dependent positions providing a time step $\Delta t = 1.32 \times 10^{-5}$ s and an accuracy of 0.5 deg for the description of flow structures. Although the unsteady phenomena are split into 24 phases, only 6 are shown for an easier understanding of periodic flow motion. Figure 8 is a three-dimensional view of the investigated region covering rotor inlet to stator outlet with the time-dependent blade positions. The axial absolute velocity is shown for three orthogonal sections to visualize the different levels inside the compressor stage: 1) an inlet-outlet, root-tip section, referred to as section A, situated at 25% of the stator blade passage width; 2) a stator blade to blade section (r, θ plane) situated in the rotor-stator gap at $x/c_r = 0.87$ and referred to as section B; and 3) a section at a constant $H = 31\%$ (x, θ plane), referred to as section C.

Note that section A is a rectangular plane inside the rotor row (x, r plane) and is a curved surface conforming to the blade suction side inside the stator row. A large blue region inside the stator in section A, without any periodic change, is associated to flow acceleration on the stator blade. It is visible for every phase. The red stripes at the top of sections A and B are the casing boundary layers that spread from the inlet to the outlet. The blade rotor wake is clearly identified in section B as a time-dependent yellow zone associated to a velocity defect close to 65 m/s. In addition, the red time-dependent region at the tip of the blade corresponds to the low-velocity core of the tip clearance vortex. This vortex is strong for phases 1 and 5 and tends to vanish when it is convected by the mean axial flow. Also, the rotor blade blockage effect resulting in a lower yellow velocity zone immediately at the rotor blade leading edge in section C can be observed in Fig. 8.

In Fig. 9, the axial velocity is detailed for three planes of measurements, situated in the rotor inlet ($x/c_r = -0.059$), rotor-stator gap

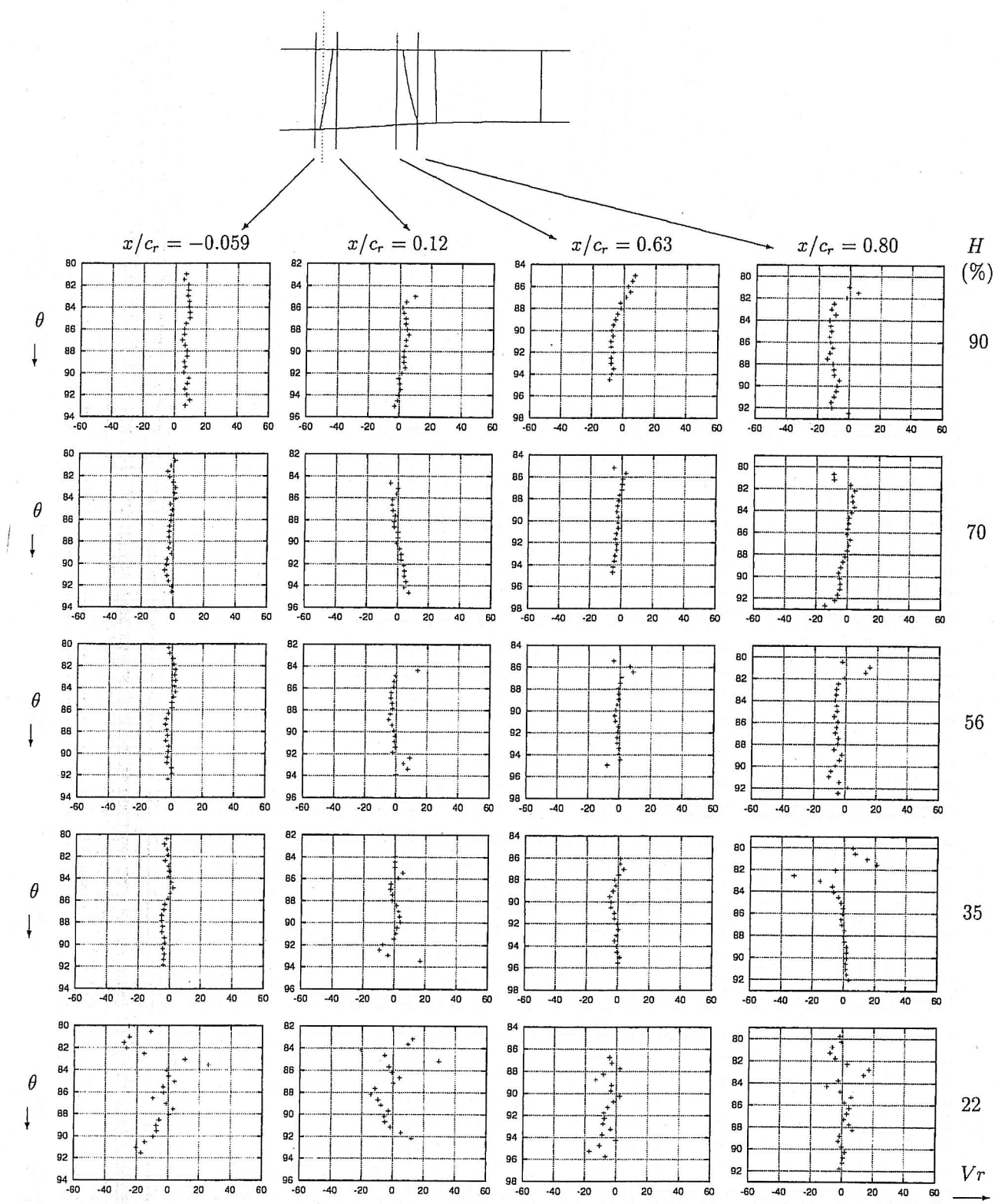


Fig. 4 Tangential distribution (degree) of the radial velocity V_r (m/s) in the rotating frame of reference, for four axial stations inside the rotor and five spanwise positions.

($x/c_r = 0.93$), and stator outlet ($x/c_r = 1.87$). For $x/c_r = -0.059$, the velocity is almost constant in the central part of the channel, except for the boundaries of the investigated zone, where lower velocities are found, associated to the rotor blades blockage effect. Note that for $H < 20\%$ the measurements could not be completed because of high noise in the scattered light and the difficulty in introducing proper seeding, as mentioned earlier. The measurements are not shown. For $x/c_r = 0.93$, the rotor wake is identified in the center of the channel as a green lower velocity (around 70 m/s),

whereas the velocity providing the major part of the flow rate is at 100 m/s. This lower velocity, bent wake structure ends in a tip clearance vortex, identified by a velocity depression. This vortex originates from the pressure gradient between the pressure side and the suction side of the rotor blade, in the beginning of the rotor chord and is convected to the suction side. Downstream from the blade, the vortex interacts with the rotor blade and goes in the wake to the side corresponding to the pressure side of the blade as mentioned in the preceding section. For $H > 80\%$, because of the carter proximity,

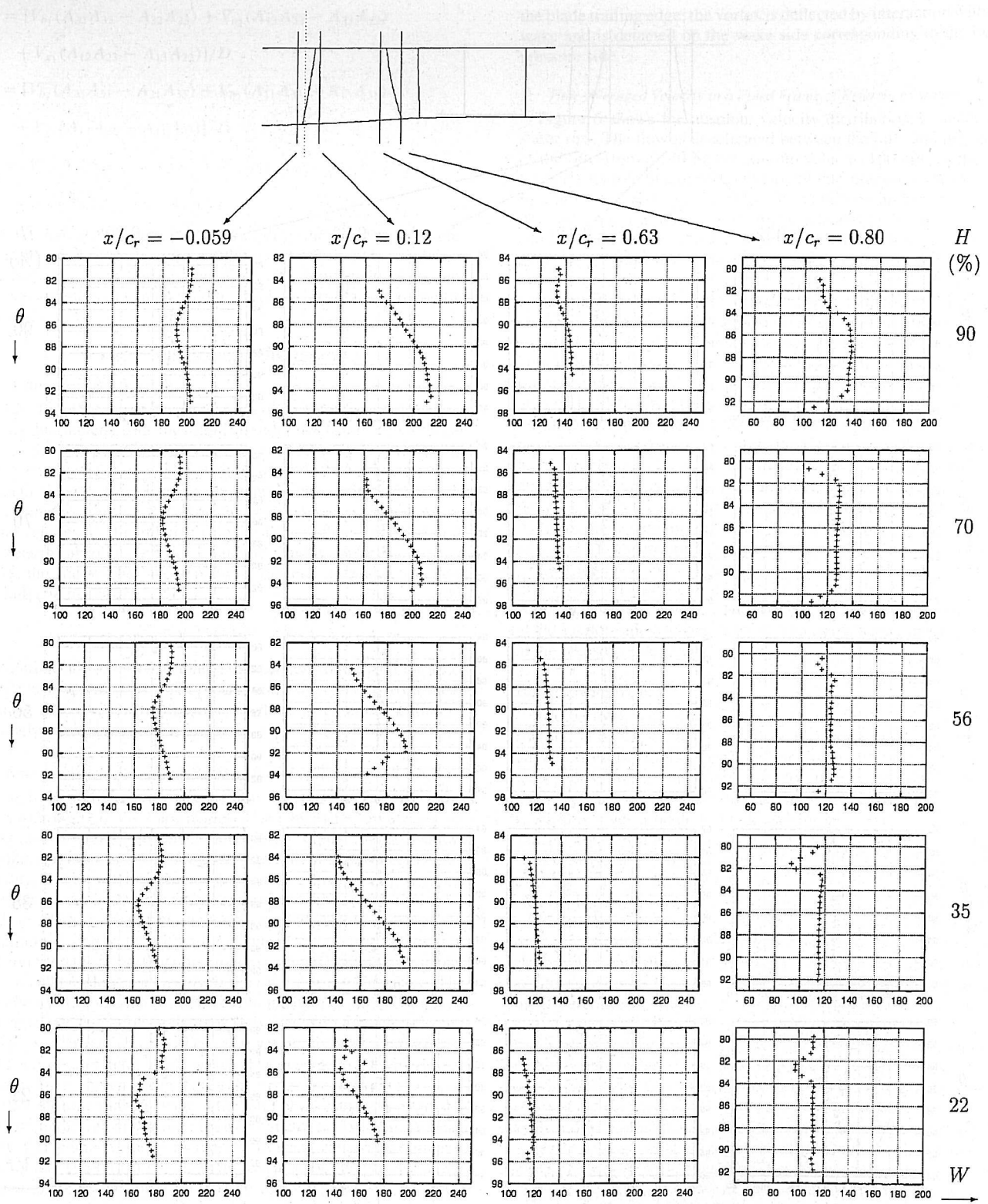


Fig. 5 Tangential distribution (degree) of the relative velocity W (m/s) in a rotating frame of reference, for four axial stations inside the rotor and five spanwise positions.

there is a strong unsteady interaction. It is caused by the main flow and the stator boundary layer on the one hand and the wake and tip clearance vortex on the other hand. Furthermore, the blockages of the stator blades, which are very close of the plane of measurements, are identified as the green stripes at the boundary of the channel. At the stator outlet, $x/c_r = 1.87$, the stator blade wakes can be seen as velocity defects. Inside the channel, the axial velocity is almost uniform, but the rotor wake influence is detected as a bent light blue velocity zone on the right.

The time-dependent tangential velocity is displayed for the same axial measurements planes in Fig. 10. The relative tangential velocity is plotted for the rotor inlet and rotor-stator gap, whereas the absolute velocity is plotted for the stator outlet. For $x/c_r = -0.059$, there is an increase of tangential velocity amplitude from root to tip, with a time-dependent gradient from pressure side to suction side. As for the axial velocity, data below $H = 20\%$ are incorrect and are not given. In the rotor outlet ($x/c_r = 0.93$), the tangential velocity gradient from root to tip is due to a greater amplitude of

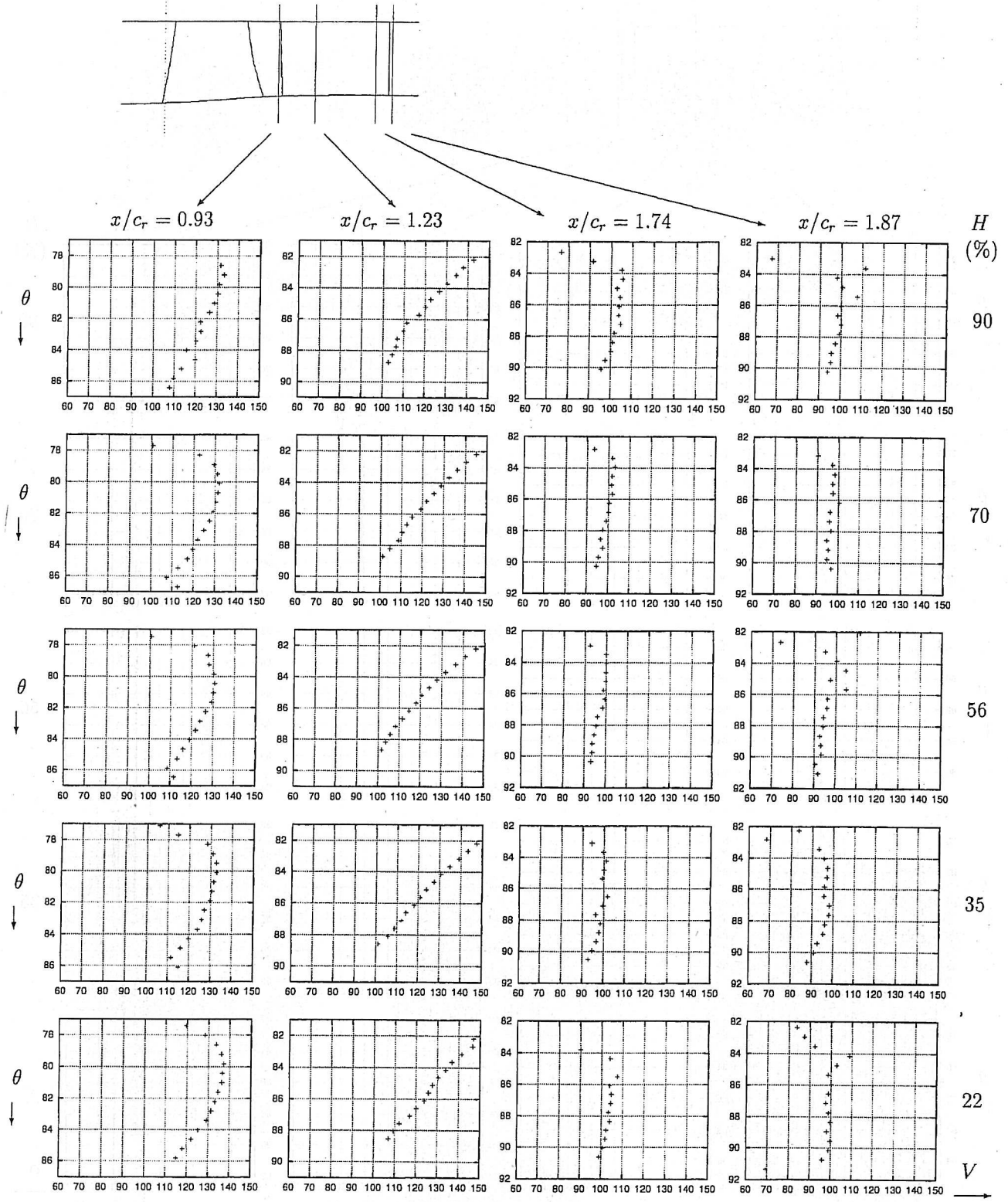


Fig. 6 Tangential distribution (degree) of the absolute velocity V (m/s) in a fixed frame of reference, for four axial stations inside the stator and five spanwise positions.

the entrainment velocity near the casing. In addition, the blade passage creates a time-dependent change in velocity corresponding to the rotor wake. For this phase, it is situated in the middle of the channel. At stator outlet, the absolute tangential velocity is almost zero except in the stator blade wakes, where the flow is deflected. In addition, the rotor wake can be identified as a time-dependent change in the sign of the velocity. For this phase time, it is identified in the upper right corner of the channel.

For a better understanding of the dynamics of the rotor blade wakes, a view in the (x, θ) section for $H = 50\%$ is shown in Fig. 11 for six phases. Three rotor wakes can be identified inside the stator channel; they are pointed out by arrows in their arrival time order for the second time plotted (phase 5). As already mentioned, \bar{V}_θ is higher in the wake, and this structure can be seen as a violet-dark blue region in the stator blade inlet. As the rotor wake is swallowed by the stator, the tangential motion decreases. For a given time (for

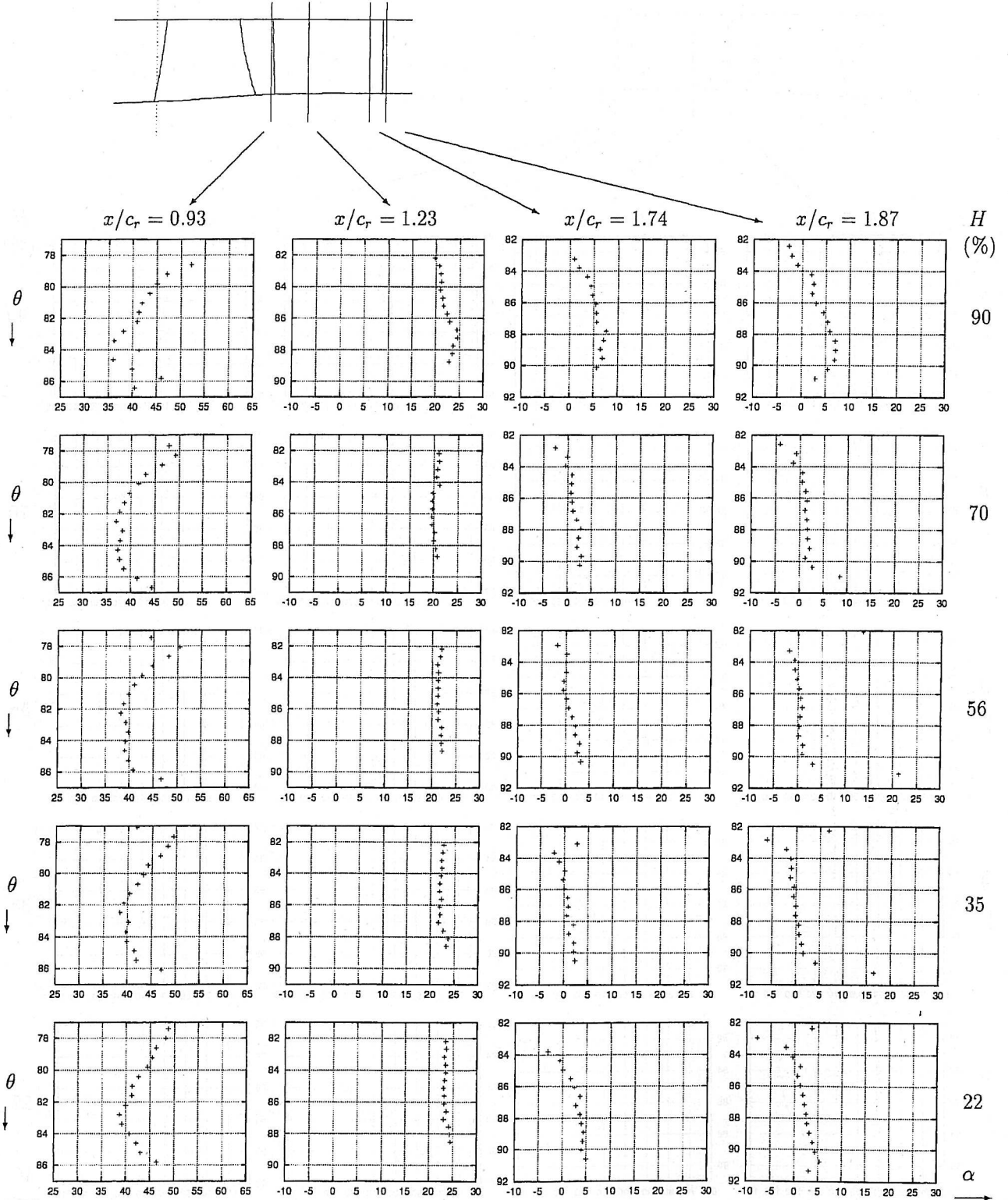


Fig. 7 Tangential distribution (degree) of the absolute radial flow angle α (deg) in a fixed frame of reference, for four axial stations inside the stator and five spanwise positions.

example, phase 9), the three wakes can be identified: The first is upstream from the top blade leading edge, the second is in the middle of the channel, and the third is near the exit. The passing of these wakes induces a periodic variation of the aerodynamic load on the blades. The rotor wakes are cut up by the the stator row, and as a consequence, they interact with the stator blades boundary layers. On the blade pressure side, this interaction is uniform. On the suction side, the wake is interacting with the boundary layer without

distortion for around one-third of the blade chord. Downstream, its structure is modified showing a gap between the wake and the blade boundary layer. The rotor wakes are cut up and convected on the suction side faster than on the pressure side. As a consequence, they interfere with the stator wakes, which results in a time-dependent oscillatory flow structure at the outlet. The small red region, associated with a negative velocity, that is present near the stator blade suction side trailing edge is a boundary-layer separation zone. The

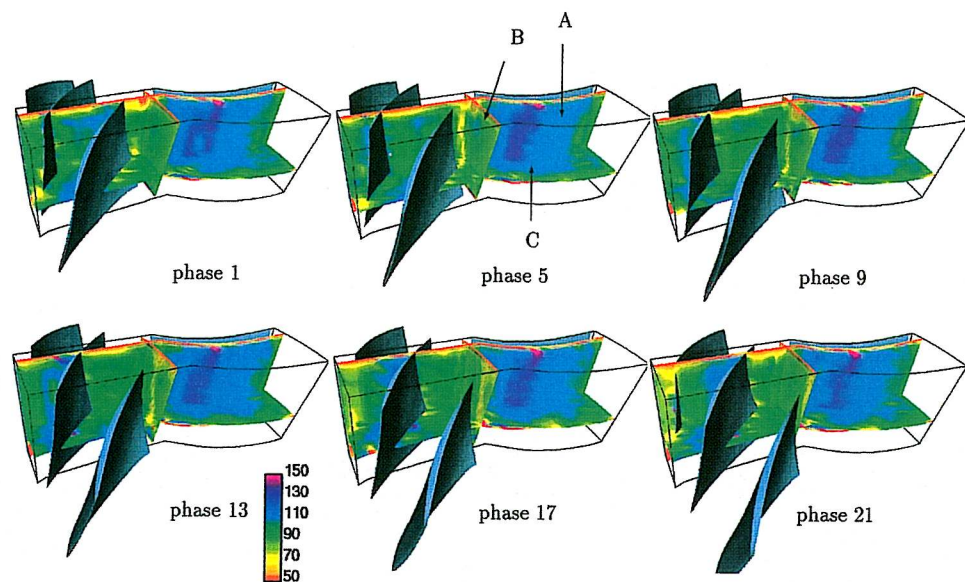


Fig. 8 Distribution of the phase-averaged absolute axial velocity \bar{V}_x (m/s).

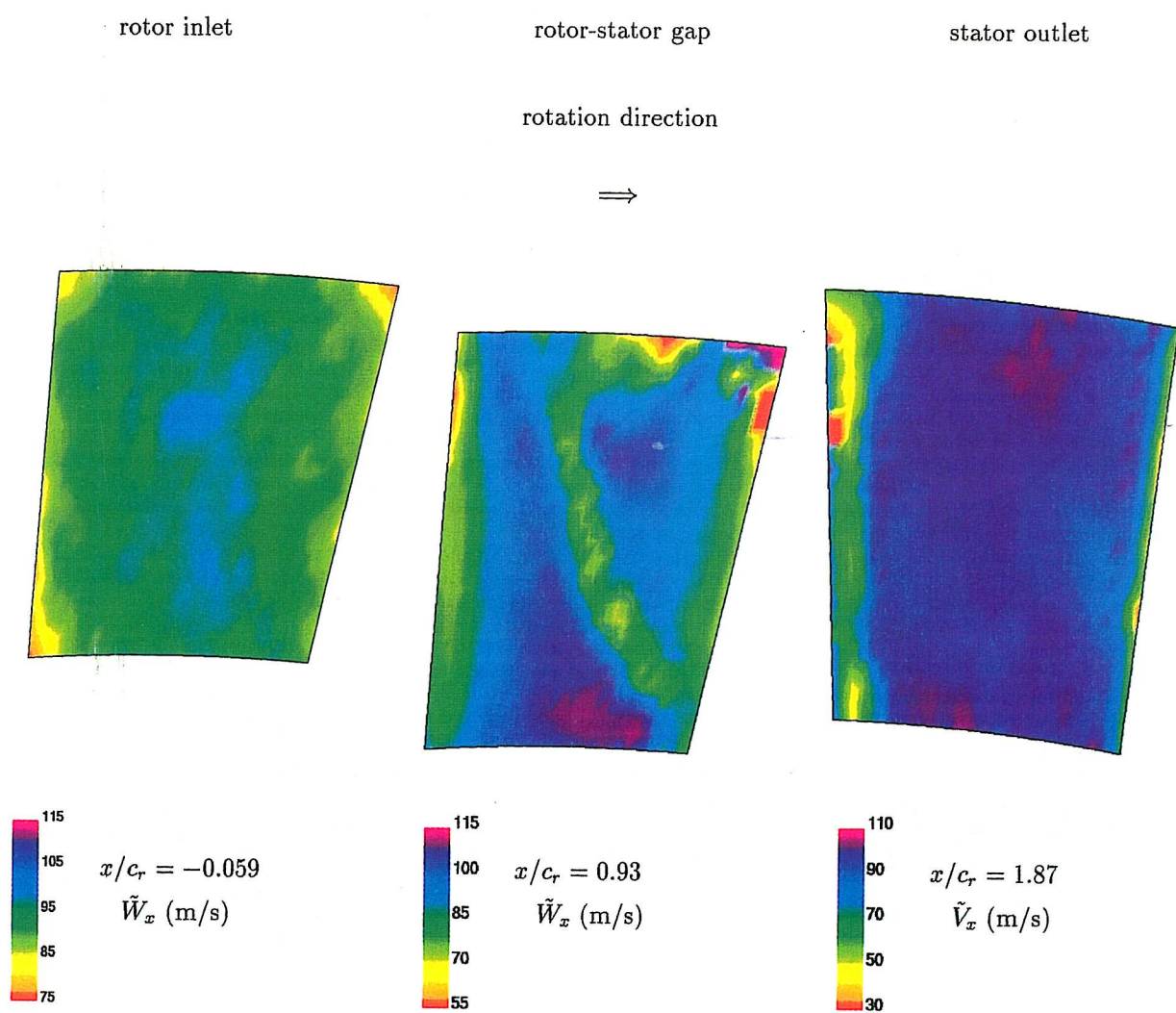


Fig. 9 Distribution of the phase-averaged axial velocity (meter per second) for phase 13.

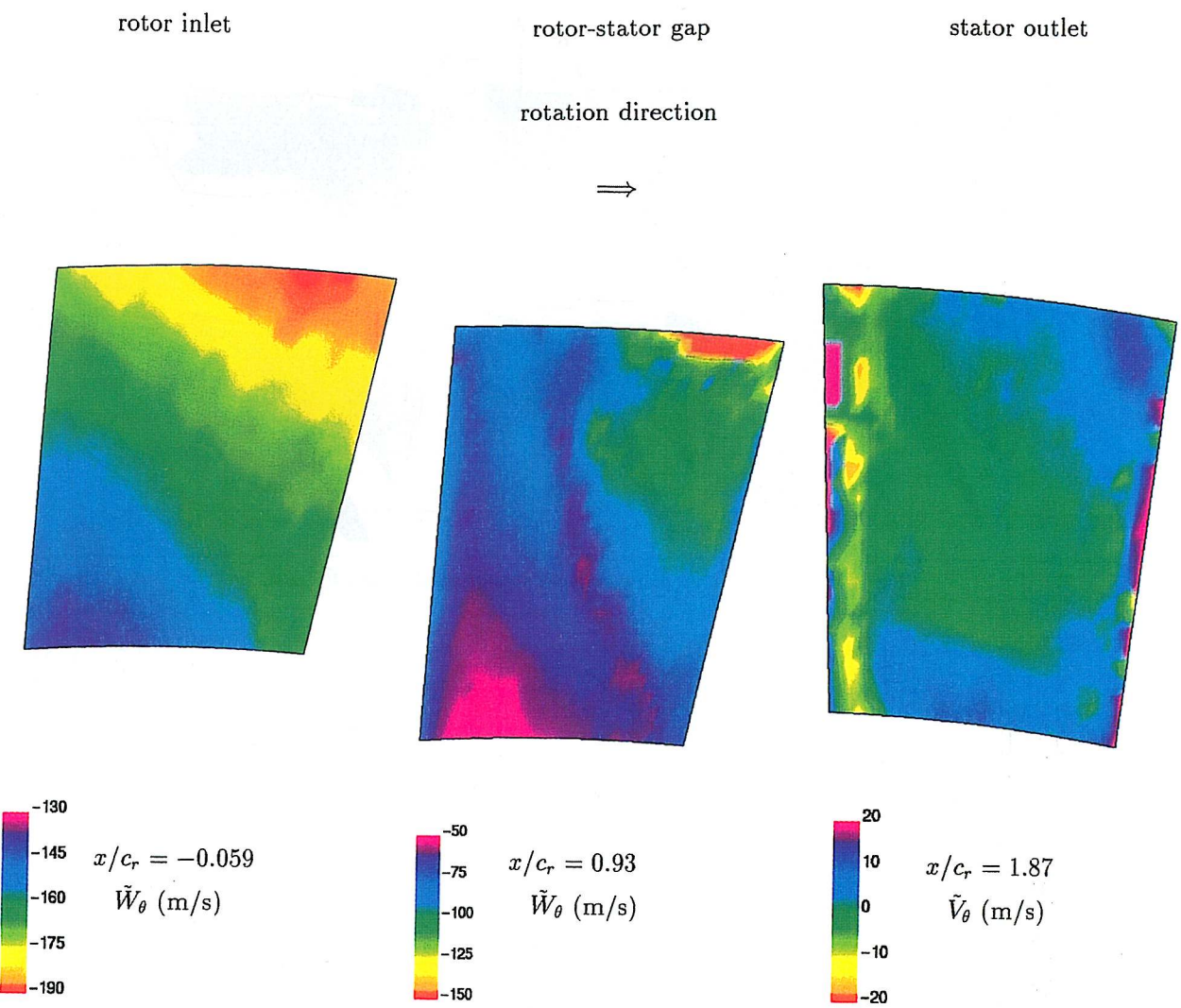


Fig. 10 Distribution of the phase-averaged tangential velocity (meter per second) for phase 13.

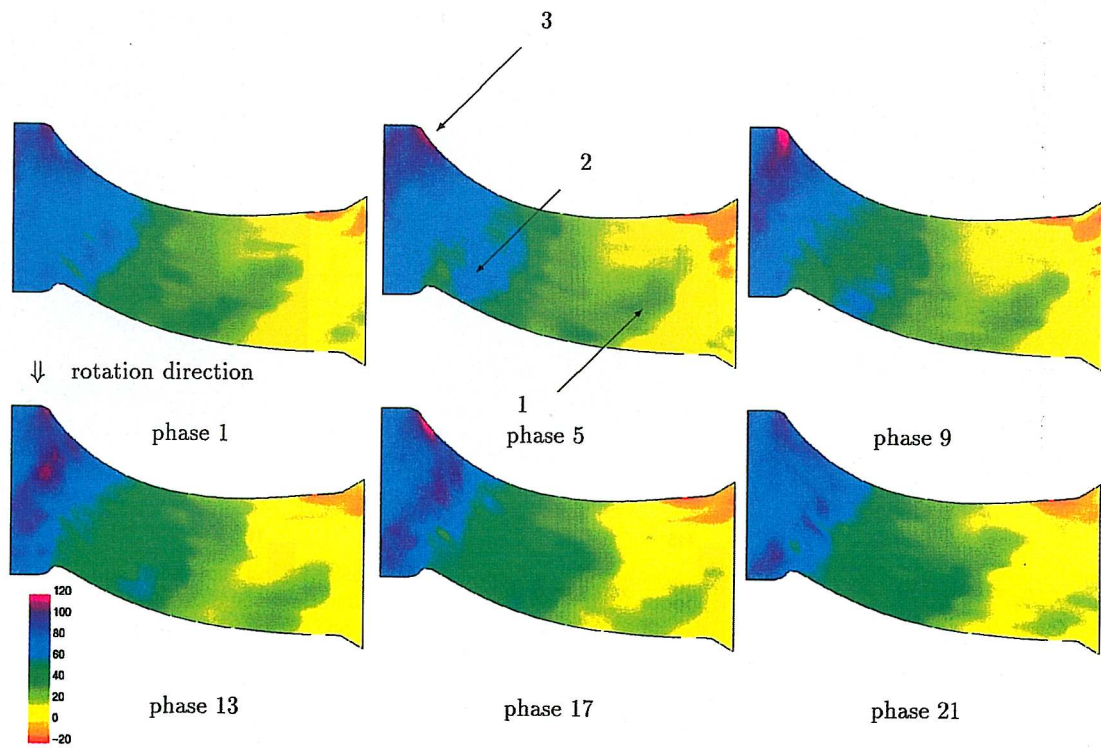


Fig. 11 Distribution of the phase-averaged tangential velocity \tilde{V}_θ (m/s) for $H = 0.5$ inside the stator.

interaction of this steady zone with the rotor wakes passing increases the phase lag of two successive rotor wakes downstream from the stator blade trailing edge.

IV. Conclusions

A two-component LDA system has been implemented on an axial compressor to study the velocity field. The use of two laser head orientations per point of measurement inside the compressor stage allows the global features of the three-dimensional flow to be obtained with only this laser system. A complete flowfield survey was carried out from the rotor inlet to the stator outlet, and data triggered with the rotor rotation provide phase-averaged results of velocity.

Measurements inside the rotor show the blockage effect caused by the blade leading edge at the inlet, velocity deceleration inside the rotor channel, and the rotor wakes at the exit. The use of BSA is valuable because there is no need to cut the laser beam during the passage of the rotor blades. Inside the stator row, the decay of the flow angle α from the inlet to the outlet is measured.

The phase-averaged three-dimensional view of velocity field over a rotor blade channel permits the observation of the main time-dependent flow characteristics. Casing boundary layers and rotor tip clearance vortices are identified at the rotor outlet. The tip clearance vortex created by pressure gradient on the rotor blade sides is deflected by interaction with the wake and detected in the interrow gap. The rotor wake is cut up by the stator and can be identified as far as the outlet. For a given time, the wakes of three successive blades are observed inside the stator blade to blade channel. The interaction of these wakes with the blade boundary layers generates strong three-dimensional unsteady effects, which are associated with time-dependent aerodynamic loads on the stator blade.

Acknowledgments

The support of the Région Ile de France through a SESAME grant is acknowledged. This work is a part of the Turbo-3D project of the Laboratoire d'Énergétique et de Mécanique des Fluides Interne, Université Pierre et Marie Curie, Paris 6, partially supported by the Société Nationale d'Études et de Construction de Moteurs d'Aviation, Turbomeca, Électricité de France and the Centre National de la Recherche Scientifique. The technical assistance of J. P. Dalac and R. Pidoux is gratefully acknowledged. The authors are listed alphabetically.

References

- ¹Schödl, R., "Laser-Two-Focus Velocimetry," *Advanced Instrumentation for Aero Engine Components*, CP-399, AGARD, 1986, pp. 7.1–7.31.
- ²Beversdorff, M., Hein, O., and Schödl, R., "An L2F-Measurement Device with Image Rotator Prism for Flow Velocity Analysis in Rotating Coolant Channels," CP-527, AGARD, 1993, pp. 16.1–16.7.
- ³Ottavy, X., "Mesures par anémométrie laser dans un compresseur axial transsonique—Étude des structures instationnaires périodiques," Ph.D. Thesis, No. 99–25, Laboratoire de Mécanique des Fluides et d'Acoustique, École Centrale de Lyon, Lyon, France, May 1999.
- ⁴Förster, W., Schödl, R., and Rijmenants, E., "Design and Experimental Verification of 3D Velocimeters Based on the L2F Technique," *5th International Symposium on Applications of Laser Techniques to Fluid Mechanics*, Lisbon, Portugal, 1990.
- ⁵Maass, M., Förster, W., and Thiele, P., "Unsteady Flow Experiment at the Exit of a Ducted Propfan Rotor," *30th AIAA/ASME/SAE/ASEE Joint Propulsion Conference*, Indianapolis, IN, 1994.
- ⁶Ardey, S., Fottner, L., Beversdorff, M., and Weyer, H., "Laser Two Focus Measurements on a Turbine Cascade with Leading Edge Film Cooling," *90th Symposium of Propulsion and Energetics Panel on Advanced Non-Intrusive Instrumentation for Propulsive Engines*, AGARD, Brussel, Belgium, 1997.
- ⁷Beversdorff, M., Matziol, L., and Blaha, C., "Application of 3D Laser Two Focus Velocimetry in Turbomachine Investigations," *90th Symposium of Propulsion and Energetics Panel on Advanced Non-Intrusive Instrumentation for Propulsive Engines*, AGARD, Brussel, Belgium, 1997.
- ⁸Charpenel, S., "Caractérisation d'une technique d'anémométrie laser bipoint tridimensionnelle L2F-3D pour l'analyse de l'écoulement dans un compresseur axial basse-vitesse," Ph.D. Thesis, No. 98-17, Laboratoire de Mécanique des Fluides et d'Acoustique, École Centrale de Lyon, Lyon, France, April 1998.
- ⁹McLean, C., and Camci, C., "Analysis and Quantification of a Solid-State Laser Doppler Anemometer," *AIAA Journal*, Vol. 33, No. 10, 1995, pp. 1880–1887.
- ¹⁰Fraser, R., Pack, J., and Santavicca, D. A., "An LDV System for Turbulence Length Scale Measurements," *Experiments in Fluids*, Vol. 4, 1986, pp. 150–152.
- ¹¹Stephanini, J., Menon, R., Elena, M., and Deleuze, J., "Impact du traitement du signal sur les mesures de vélocimétrie laser Doppler," *5ème Congrès Francophone de Vélocimétrie Laser*, Association Francophone de Vélocimétrie Laser, Rouen, France, Sept. 1996, pp. A5.1–A5.3.
- ¹²Gallus, H. E., Zeschky, J., and Hah, C., "Endwall and Unsteady Flow Phenomena in an Axial Turbine Stage," *Journal of Turbomachinery*, Vol. 117, Oct. 1995, pp. 562–570.
- ¹³Walraevens, R. E., Gallus, H. E., Jung, A. R., Mayer, J. F., and Stetter, H., "Experimental and Computational Study of the Unsteady Flow in a 1.5 Stage Axial Turbine with Emphasis on the Secondary Flow in the Second Stator," *International Gas Turbine and Aeroengine Congress and Exhibition*, American Society of Mechanical Engineers, Stockholm, Sweden, June 1998.
- ¹⁴Zaccaria, M., Ristic, D., and Lakshminarayana, B., "Three-Dimensional Flowfield in a Turbine Nozzle Passage," *Journal of Propulsion and Power*, Vol. 12, No. 5, 1996, pp. 974–983.
- ¹⁵Ristic, D., Lakshminarayana, B., and Chu, S., "Three-Dimensional Flowfield Downstream of an Axial-Flow Turbine Rotor," *Journal of Propulsion and Power*, Vol. 15, No. 2, 1999, pp. 334–344.
- ¹⁶Chesnakas, C. J., and Dancey, C. L., "Three-Component Measurements in an Axial-Flow Compressor," *Journal of Propulsion*, Vol. 6, No. 4, 1990, pp. 474–481.
- ¹⁷Camp, T. R., and Shin, H. W., "Turbulence Intensity and Length Scale Measurements in Multistage Compressors," *Journal of Turbomachinery*, Vol. 117, Jan. 1995, pp. 38–46.
- ¹⁸Murthy, K. N. S., and Lakshminarayana, B., "Laser Doppler Velocimeter Measurement in the Tip Region of a Compressor Rotor," *AIAA Journal*, Vol. 24, No. 5, 1986, pp. 474–481.
- ¹⁹Stauter, R. C., "Measurement of the Three-Dimensional Tip Region Flow Field in an Axial Compressor," *Journal of Turbomachinery*, Vol. 115, July 1993, pp. 468–476.
- ²⁰Belhabib, M., and Miton, H., "Experimental Analysis of Unsteady Blade Rows Interaction in a Multistage Turbomachine," *Journal de Physique III*, Vol. 5, Dec. 1995, pp. 2003–2028.
- ²¹Blidi, S., and Miton, H., "Basic Instrumentation of a Low Speed Axial Compressor," *Journal de Physique III*, Vol. 5, July 1995, pp. 919–924.
- ²²Blidi, S., and Miton, H., "Use of the Hot Wire Anemometry for Velocity and Temperature Measurements in a Turbomachine," *Journal de Physique III*, Vol. 5, Oct. 1995, pp. 1513–1535.
- ²³Miton, H., Belhabib, M., and Kus, U., "Experimental and Numerical Investigation of Unsteady Flow Properties in a Stator of Multistage Flow Compressor," *85th Symposium on Loss Mechanisms and Unsteady Flows in Turbomachines*, CP-571, AGARD, 1996, pp. 20.1–20.17.
- ²⁴Pradère, T., "Contribution au développement de la vélocimétrie laser Doppler dans les turbomachines," Ph.D. Thesis, Laboratoire d'Énergétique et de Mécanique des Fluids Interne, Univ. Pierre et Marie Curie, Paris, France, Dec. 1998.
- ²⁵Strazisar, A. J., "Laser Fringe Anemometry for Aero Engine Components," *Advanced Instrumentation for Aero Engine Components*, CP-399, AGARD, 1986, pp. 6.1–6.32.

Analysis of Inducer Recirculating Inlet Flow

François Bario,^{*} Thierry M. Faure,[†] and Emmanuel Jondreau[‡]
École Centrale de Lyon, 69131 Écully Cedex, France
and
Jean-Luc Normand[§] and Jean-Michel Nguyen Duc[§]
SNECMA moteurs, 27207 Vernon, France

The mean and turbulent features of inducer inlet flow covering various operating points of a centrifugal pump are analyzed. Measurements are conducted in an air test facility with a five-hole pressure probe and an X-wire probe. For flow rates lower than the design flow rate, the recirculation located upstream of the inducer is very strong and creates a global rotation of the fluid from the tip to the hub, upstream of the inducer. The axial extent of the separated flow decreases as the flow rate increases. The stagnation pressure in this region is higher than the upstream stagnation pressure and can reach several times the inlet dynamic head. In the inlet channel axis, within the recirculated flow, the stagnation pressure is lower than what is found for upstream stations outside the recirculation. This can be related to upstream fluid motion and mixing with the inverse flow, providing stagnation pressure losses. For the flow rates where the recirculation region is large, the incoming flow is deflected toward the hub. Phase-averaged measurements in the inducer inlet show the main time-dependant flow features and their evolution with the flow rate. The analysis shows that, at design and higher flow rates, the evolution of the meridional velocity is correlated with the evolution of the relative flow angle. Relative velocity is not affected by the blade leading edge and is constant at a given radius. The change in the axial velocity is mainly due to the sudden change of the relative flow angle before the blade leading edge.

Nomenclature

D	= inlet pipe diameter
h	= normalized relative radial position
p	= static pressure
p_t	= stagnation pressure
Q	= flow rate
r	= radial coordinate
r_h	= hub radius
r_t	= tip radius
U	= entrainment velocity
V	= absolute velocity
V_m	= meridional velocity
V_u	= tangential velocity
W	= relative velocity
z	= axial coordinate
α	= absolute flow angle
β	= relative flow angle
θ	= tangential coordinate
ρ	= air density
φ	= mass flow rate coefficient
ψ_s	= static pressure coefficient
Ω	= angular velocity

Subscripts

h	= hub
t	= tip or stagnation
n	= design operating point parameter
1	= inlet parameter
2	= outlet parameter

Introduction

INDUCERS have many applications including water jet propulsion, feed systems for rocket pumps, and centrifugal impellers.¹ They are used in the first part of the pump to protect the high-pressure-ratio stages from unsteadiness due to cavitation. The inducer is used to force the collapse of cavitation bubbles into the first part of the pump.^{2,3} Thus, the long and narrow passages are designed to increase the stagnation pressure gently and gradually and to avoid cavitation before the main pump.⁴ The inducer is also designed to provide a uniform velocity profile to the rotor. Nevertheless, for flow rates lower than the design value, oscillating cavitation can appear and generate shaft vibration,⁵ which must be avoided. Increasing tip clearance was found to be effective in preventing rotating cavitation⁶ but could not extinguish it. A suction ring, used to control the inlet inverse flow, is very effective in suppressing such cavitation.

Experiments conducted with an air test facility permit the understanding of noncavitating flow behavior. Most of the time, the operating point is selected to avoid a recirculated flow inside the inducer; nonetheless, inlet recirculation can be found during the pump start-up. It has been shown that the cavitation regions are strongly correlated with the recirculating flow.⁷ In the past, measurements have underscored the need for a better description of flow patterns in the inducer axial stage inlet.⁸ Pump inducer flow is very complex with strong three-dimensional viscous structures developing in the channel due to the very long chord of the inducer blades compared with the channel height (small aspect ratio of the blades). At low flow rates, a separation appears with negative axial flow generally located at the tip of the blade at the inducer inlet. Extensive studies have been conducted on the dynamics of this flow by Janigro and Ferrini⁹ and Janigro and Schiavello,¹⁰ who showed the inlet inverse flow or prerotation usually starts at the blade tip and affects various cavitation-related phenomena. These authors suggest that the

Received 23 July 2001; revision received 22 April 2002; accepted for publication 20 May 2002. Copyright © 2003 by the authors. Published by the American Institute of Aeronautics and Astronautics, Inc., with permission. Copies of this paper may be made for personal or internal use, on condition that the copier pay the \$10.00 per-copy fee to the Copyright Clearance Center, Inc., 222 Rosewood Drive, Danvers, MA 01923; include the code 0748-4658/03 \$10.00 in correspondence with the CCC.

^{*}Research Engineer, Laboratoire de Mécanique des Fluides et d'Acoustique, Unité Mixte de Recherche 5509, Centre National de la Recherche Scientifique.

[†]Assistant Professor, Laboratoire de Mécanique des Fluides et d'Acoustique, Unité Mixte de Recherche 5509, Centre National de la Recherche Scientifique; currently Assistant Professor, Université Pierre et Marie Curie, Paris, 91405 Orsay Cedex, France.

[‡]Engineer, Laboratoire de Mécanique des Fluides et d'Acoustique, Unité Mixte de Recherche 5509, Centre National de la Recherche Scientifique.

[§]Engineer, Direction Grosse Propulsion à Liquides.

radial flow may not necessarily be the cause for leakage flow in unshrouded inducers. The recirculation region extends far upstream of the inducer, up to 10 times the inlet diameter.⁷ Its induces circumferential and radial velocities in the inlet flow region. Thus, it is important to take recirculation into account for the calculation of the inducer inlet flow. For applications such as rocket pump feed system, where the tank is not far from the inducer, it is possible that this recirculation induces in-block rotation of the fluid in the tank, altering the global behavior of the pump.

Experimental Setup and Apparatus

The experimental setup is an open-circuit facility consisting of an inlet with filters for atmospheric air, a settling chamber followed by the cylindrical inlet duct, the pump that was tested, a vane, a flow meter, and an outlet duct (Fig. 1). The flow is discharged outside the room through the outlet duct. The pump is fitted with a 4-blade inducer, an 8-blade axial-radial shrouded impeller with 8 additional splitters, and an 11-blade diffuser (Figs. 2 and 3). The tip radius r_t is constant from the cylindrical inlet duct to the inducer

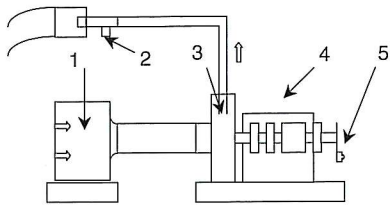


Fig. 1 Schematic view of test rig: 1) inlet settling chamber with dust filter and honeycomb, 2) outlet with venturi and vane, 3) air test pump, 4) electric motor, torque meter, shaft, and bearings, and 5) synchronization device.

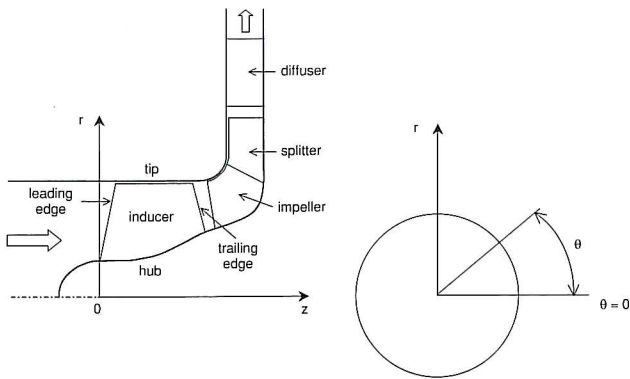


Fig. 2 Schematic of the pump and coordinate system.



Fig. 3 Experimented inducer.

outlet. The rotational speed is fixed to 5000 ± 10 rpm at standard conditions (inlet pressure $101,325$ Pa and temperature 288 K). The origin of the axial direction, $z = 0$, is started at the inducer's tip leading edge. Three flow rates are considered: Q_n (design flow rate), $0.7Q_n$ (reduced flow rate), and $1.3Q_n$ (increased flow rate). The flow rates, corrected for standard conditions, are checked to fall within a 0.6% uncertainty. The Reynolds number for the design condition is 1.78×10^5 and for the investigated flow rates the Reynolds number range varies from 1.24×10^5 to 2.31×10^5 .

Seven probe supports on the inlet duct casing wall allow the investigation of velocity and pressure fields, by a directional five-hole probe. The probe diameter is 1 mm and does not perturb the flow. The probe is driven in translation and rotation around its axis by a traversing system. Pressures are measured with differential pressure transducers, giving an accuracy of 10 Pa.

In addition, an X-hot-wire probe was used for instantaneous velocity measurements at a single station upstream of the inducer inlet (plane located at 0.015 inlet diameter of the leading edge of the inducer blade and parallel to it). This probe is calibrated, both in velocity and angle, using the method described by Browne et al.,¹¹ giving a maximum error of 0.5% for the velocity. Phase averaging of the velocity output was performed with synchronization signal. The instantaneous relative blade position is obtained from the periodic 0–5 V amplitude signal given by the combination of an optical encoder and a toothed wheel placed on the shaft (one pulse per revolution). The probe is aligned with the mean flow obtained from the five-hole pressure probe measurements. The evolution of the tangential and meridional mean and fluctuating velocities over one revolution of the inducer is obtained from the X-hot-wire signals.

Results and Discussion

Overall Performance of the Inducer

The mass flow coefficient is defined as

$$\varphi = Q / \pi \rho \Omega (r_t^2 - r_h^2) r_t$$

and the static pressure coefficient by

$$\psi_s = (p_2 - p_1) / \rho \Omega^2 r_t^2$$

The static pressure performance is shown in Fig. 4. The discontinuity in the curve near $\varphi \sim 0.05$ is due to a higher uncertainty for the lower flow rates. The pump's design value is $\varphi_n = 0.0929$. The curve has a negative slope throughout the flow rates investigated in this study (0.7–1.3 φ_n), and neither surge nor rotating stall occurs.

Upstream Mean Measurements with Five-Hole Pressure Probe

Figure 5 shows the relative radial distribution of the stagnation pressure p_t measured against the atmospheric pressure for several

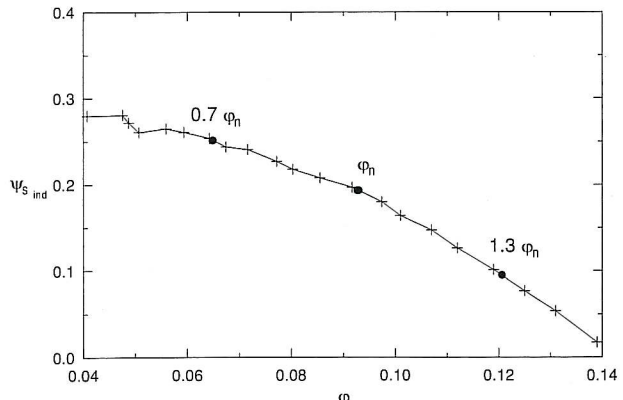


Fig. 4 Static pressure performance of the inducer (ordinate measurement error 10^{-3}).

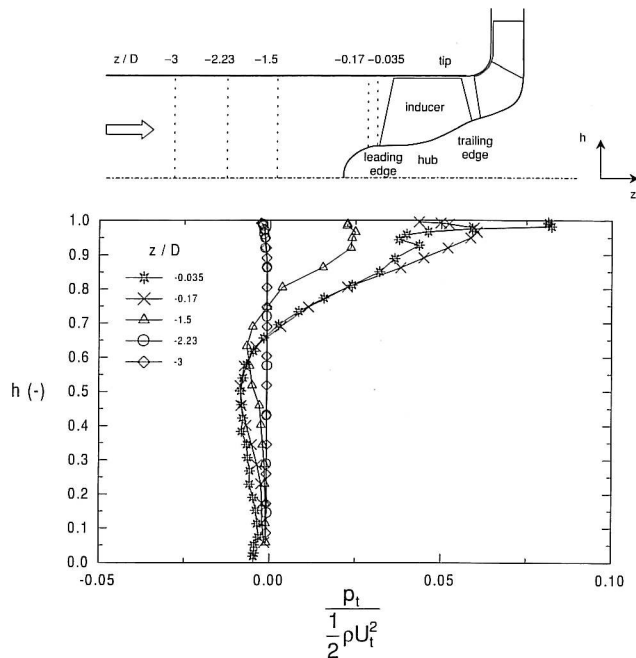


Fig. 5 Relative radial distribution of stagnation pressure upstream from the inducer inlet for $0.7Q_n$ mass flow rate (ordinate measurement error 2×10^{-3}).

axial positions upstream of the inducer and for a flow rate of $0.7Q_n$. The relative radial position is defined as

$$h = (r - r_h) / (r_t - r_h)$$

where r_t and r_h are the tip and hub radius, respectively, with $r_h = 0$ upstream of the pump. The stagnation pressure (measured against the atmospheric pressure) far from the inducer ($z/D = -3$) is constant along the channel height and slightly negative because of stagnation pressure losses in the plenum filter. Near the tip casing, it decreases, showing the viscous effect in the casing boundary layer estimated around 10% of the channel height. Closer to the inducer, the stagnation pressure is negative around $h \sim 0.5$. This negative pressure must be due to losses that are generated upstream of the inducer and can be related to a boundary-layer separation due to the inverse flow with strong energy coming from the inducer. This inverse flow with high tangential and axial velocities in the vicinity of the tip casing acts as a barrier for the incoming axial flow and induces a separation on the casing. This return flow develops radially from the casing into the main flow. Its interaction with the main flow creates important loses through the effect of strong shear forces between the axial main flow and the swirling inverse flow. Figure 5 shows that the negative pressure zone is not attached to the tip casing; nevertheless, its radial development (Fig. 6) occurs over a very short axial distance. The transition region between the low stagnation pressure region ($h < 0.6$) and the inverse flow region where high stagnation pressure is found ($h > 0.9$) corresponds to the flow coming from the inducer and returning toward it through the action of the main incoming flow. According to Yokota et al.,⁷ the vortex created in this shear layer area is directly related to the cavitation vortex. The hypothesis of a barrier effect of the swirling inverse flow against the axial incoming flow is verified by the axial velocity plot in the inlet plane (Fig. 6). Near the tip casing, very high levels of absolute stagnation pressure are achieved. This results from flow coming from the inducer. The absolute flow angle, presented in Fig. 7, shows the strong swirl of the inlet flow. In the recirculating area, the flow angle at the tip (varying between -40 deg immediately before the leading edge and -10 deg for the other measurement stations) associated with a high level of absolute velocity (Fig. 8) results because the tangential and axial velocities are very high (Figs. 6 and 9). The thickness of the affected zone is 15% of the channel height at $z/D = -1.5$. The thickness falls to

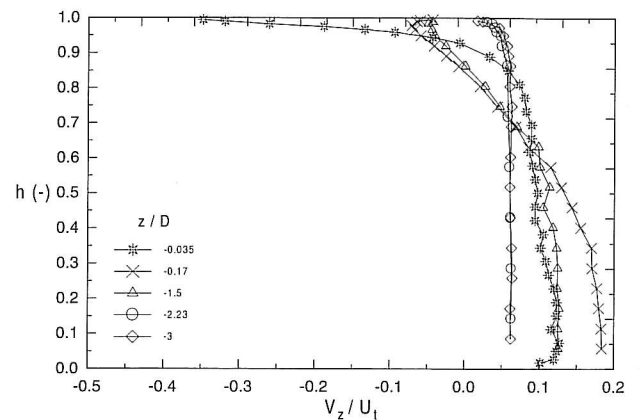


Fig. 6 Relative radial distribution of absolute axial velocity V_z / U_t upstream from the inducer inlet for $0.7Q_n$ mass flow rate (ordinate measurement error 2×10^{-3}).

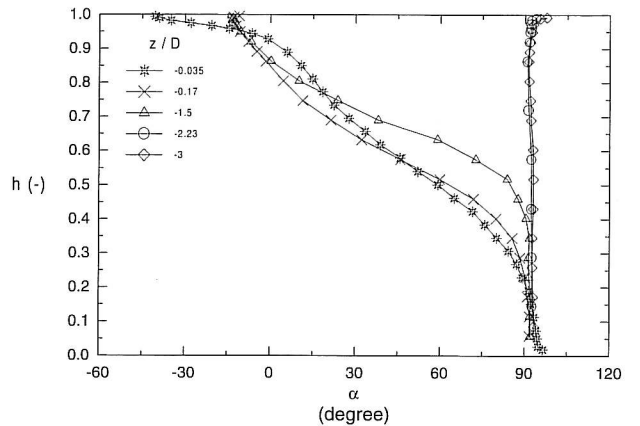


Fig. 7 Relative radial distribution of absolute flow angle α (degree) upstream from the inducer inlet for $0.7Q_n$ mass flow rate (ordinate measurement error 1 deg).

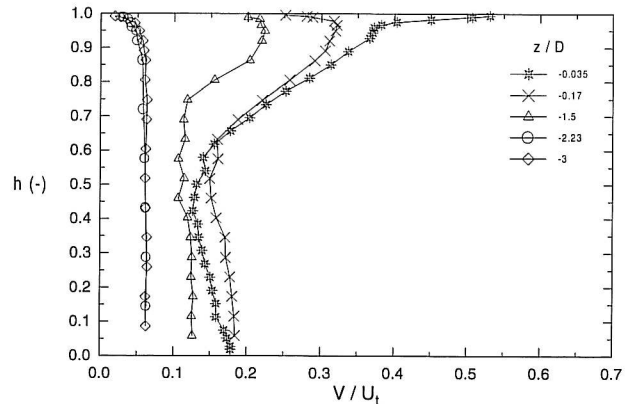


Fig. 8 Relative radial distribution of absolute velocity V / U_t upstream from the inducer inlet for $0.7Q_n$ mass flow rate (ordinate measurement error 2×10^{-3}).

8% immediately before the leading edge ($z/D = -0.035$), but this area is associated with a higher negative axial velocity. Under the momentum balance between the incoming flow and the return flow, there is radial (Fig. 9) and tangential spreading of the inverse flow.

The question that arises is the following: What is the origin of the inverse flow? According to El Ghazzani et al.,¹² the flow exhibits an inviscid vortex coming from the inducer. Near the leading-edge blade tip, because of the camber and shape of the leading edge (from hub to tip), the streamlines on the pressure side are deflected toward

the low-pressure area, that is, toward and upstream the tip. On the suction side, the streamlines are deflected toward and downstream the hub. This purely inviscid explanation of the phenomenon is validated by three-dimensional Euler calculations on the LH2 pump of the Vulcain engine of Ariane V.¹² This vortex is not related to the tip leakage vortex mentioned by Del Valle et al.¹³ or Bhattacharyya et al.¹⁴ because the inviscid calculation of El Ghazzani et al.¹² is done without tip leakage. It is a fully three-dimensional effect, strongly

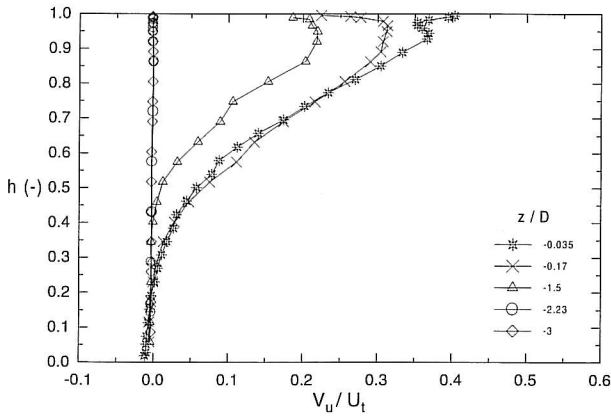


Fig. 9 Relative radial distribution of absolute tangential velocity V_u/U_t upstream from the inducer inlet for $0.7Q_n$ mass flow rate (ordinate measurement error 2×10^{-3}).

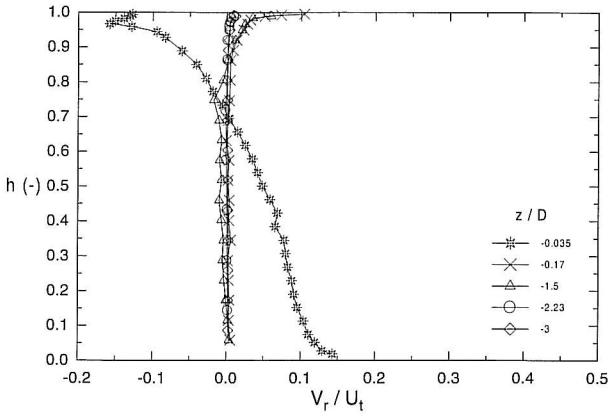


Fig. 10 Relative radial distribution of absolute radial velocity V_r/U_t upstream from the inducer inlet for $0.7Q_n$ mass flow rate (ordinate measurement error 2×10^{-3}).

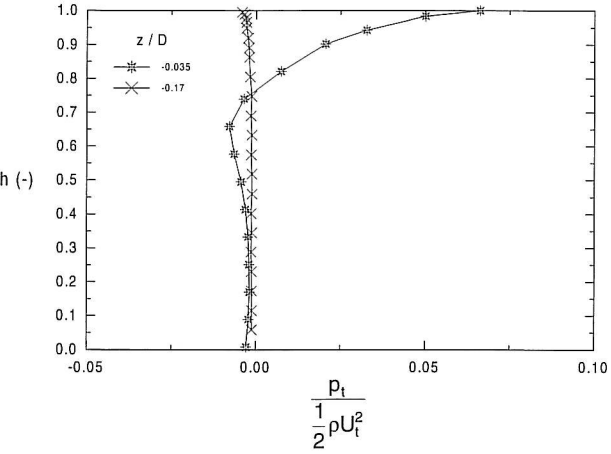


Fig. 11 Relative radial distribution of stagnation pressure upstream from the inducer inlet for $0.9Q_n$ mass flow rate (ordinate measurement error 2×10^{-3}).

coupled with the incidence effect along the leading-edge span. The fact that recirculating flow is not generated in the tip leakage flow is also confirmed by the experimental study of Offtnger et al.¹⁵ They compare the flow of an unshrouded inducer and the flow of the same inducer with a shroud. The difference between the two tangential and axial velocity distributions upstream of the inducers at low mass flow rate is small. The effect of the removal of the shroud is a slight increase of the absolute flow angle; there is no change in the global evolution of the flow. Although this vortex origin maybe inviscid, this high-energy vortex with strong tangential velocity and high resulting absolute stagnation pressure interacts with other vortices, such as the tip leakage vortex and casing boundary-layer vortices, where

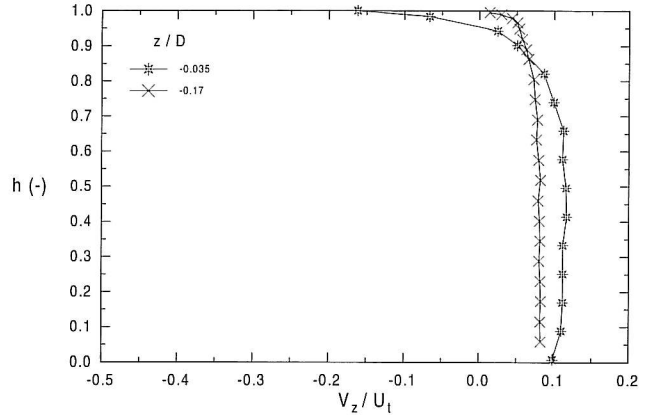


Fig. 12 Relative radial distribution of absolute axial velocity V_z/U_t upstream from the inducer inlet for $0.9Q_n$ mass flow rate (ordinate measurement error 2×10^{-3}).

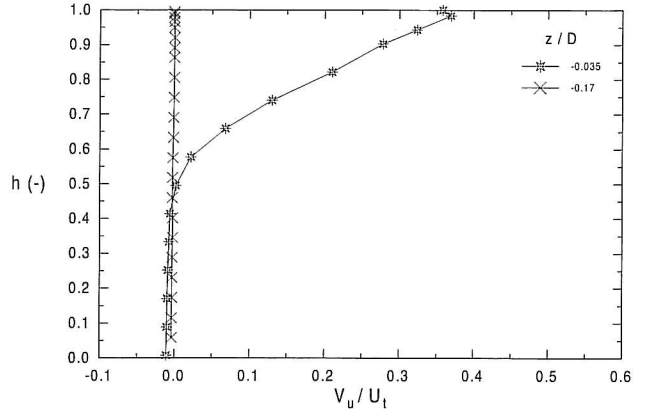


Fig. 13 Relative radial distribution of absolute tangential velocity V_u/U_t upstream from the inducer inlet for $0.9Q_n$ mass flow rate (ordinate measurement error 2×10^{-3}).

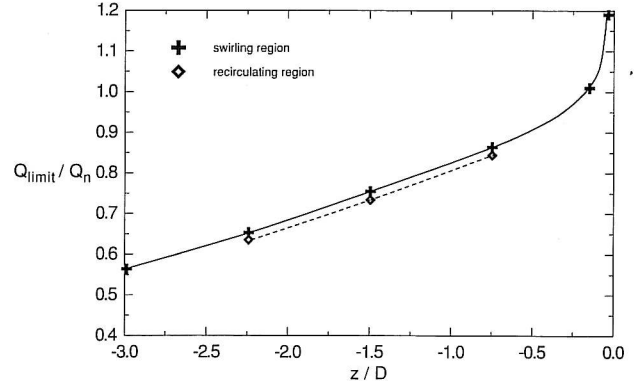


Fig. 14 Evolution of the length of the recirculated flow with the flow rate.

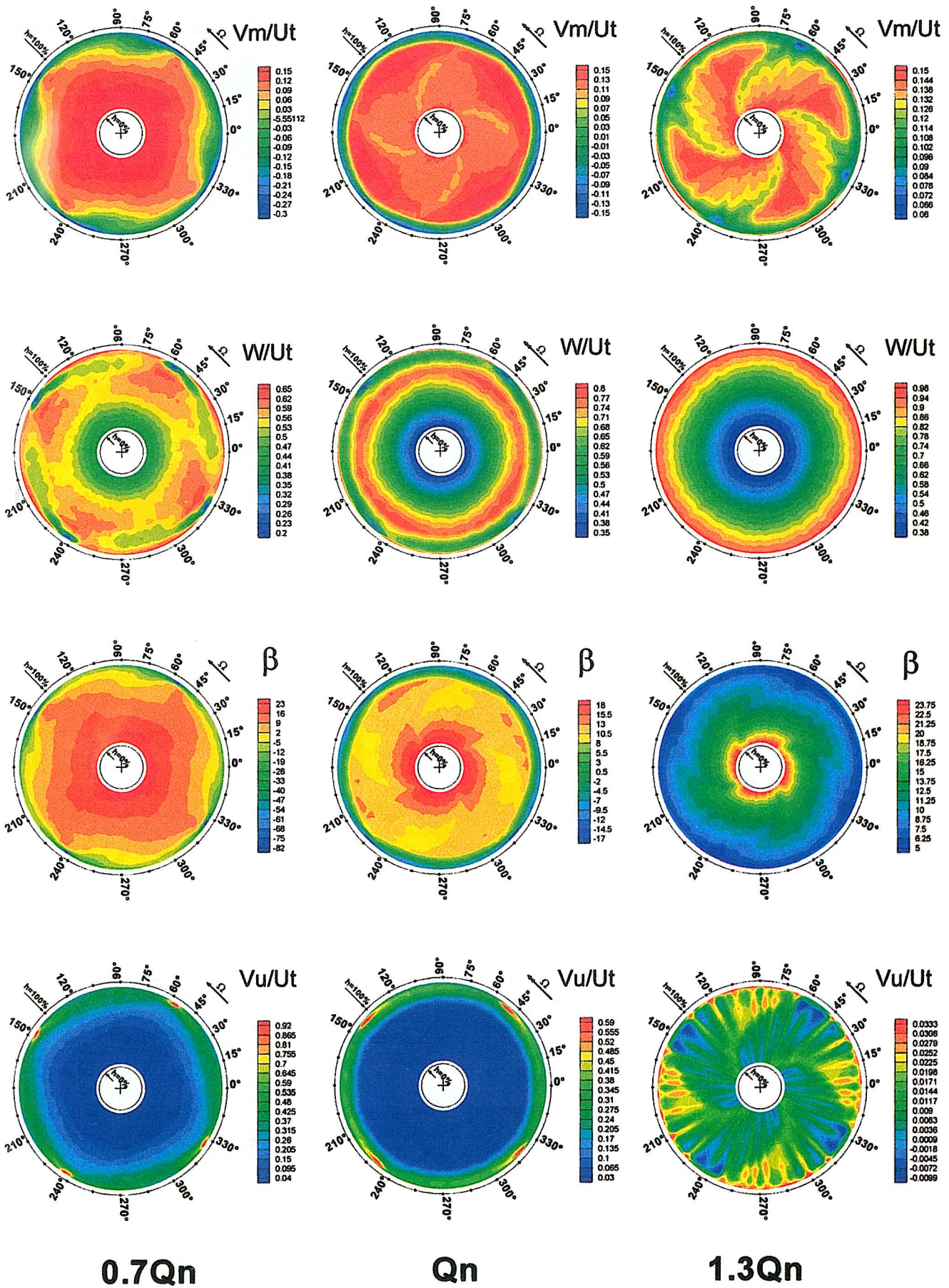


Fig. 15 From top to bottom, meridional and relative velocity, relative flow angle and tangential velocity for three flow rates (from left to right, $0.7Q_n$, Q_n , and $1.3Q_n$).

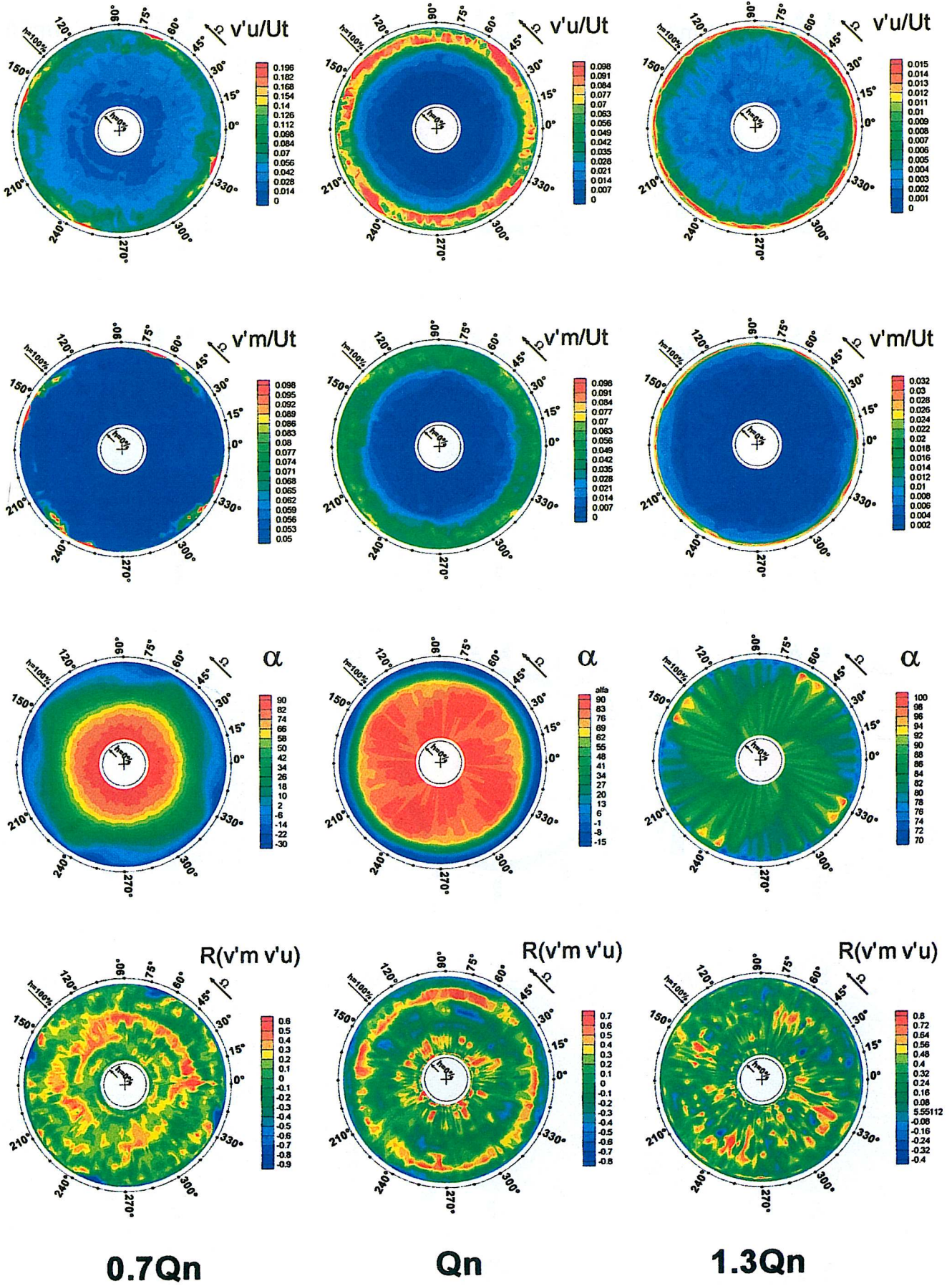


Fig. 16 From top to bottom, standard deviations of tangential and meridional velocity fluctuations, absolute flow angle, and cross-correlation coefficient for three flow rates (from left to right, $0.7Q_n$, Q_n , and $1.3Q_n$).

viscous effects are dominant. For these reasons many authors impute the origin of the recirculating flow to the tip leakage flow.

The velocity distribution (Fig. 8) exhibits a constant value, except in the boundary layers, for stations $z/D = -2.23$ and $z/D = -3$. For $z/D = -1.5$, the increase in the tangential velocity everywhere inside the channel is due to the viscous effect of the inducer's rotation. This rotation increases near the inducer inlet. The radial velocity distribution is almost constant except in the casing vicinity for all of the profiles (Fig. 10) not immediately upstream of the leading edge. A radial gradient from root to tip appears for $z/D = -0.035$ and is caused by the strong vertical motion of the inducer suction. Similar comments are valid for flow rates greater than $0.7Q_n$, the recirculation length decreasing with increasing flow rate. Note that in Figs. 11–13, for $0.9Q_n$, there is no evolution upstream of $z/D = -0.17$.

Extent of Recirculating and Swirling Zones

Figure 14 shows the limit flow rate corresponding to the beginning of the recirculating and swirling regions as a function of the axial position of the measurement. The recirculation limit corresponds to the location where the first zero axial velocity is found near the casing. The swirling limit corresponds to the location where induced tangential velocities are found without negative axial velocity near the casing. For that, a probe is put near the casing and aligned with the axial direction. The flow rate is varied from high values to low values. The probe accuracy is defined to ± 2 deg; thus, if a 2-deg change is found at a given flow rate, then it is considered the limit of an induced tangential velocity. This measurement is repeated for the seven axial locations of the probe. As mentioned earlier, the extent of the swirling region along the radius is greater than the extent of the recirculating region. The difference of the axial extent between these two zones at the tip casing is small. For $0.7Q_n$, the swirling zone extends up to 1.85 inlet diameters upstream of the inducer. Very close to the inducer leading edge, recirculation region exists up to $1.2Q_n$. The extrapolation of Fig. 14 for $0.4Q_n$ yields a swirling zone extending 4–5 inlet diameters upstream of the inducer.

Upstream Measurements with X-Wire Probe

Polar plots of phase-averaged mean velocities, standard deviation of fluctuating velocities, and phase-averaged flow angles are shown in Figs. 15 and 16 for a station immediately upstream of the inducer leading edge. Three operating points are presented: From left to the right, Figs. 15 and 16 show results for the low flow rate $0.7Q_n$, the design flow rate Q_n , and the high flow rate $1.3Q_n$, respectively. To show the different flow features, the scaling is not the same for the three flow rates.

At $1.3Q_n$, the meridional velocity V_m shows that there is no mean or local negative meridional velocity in the measurement plane. The four blades and the shape of the leading edge are clearly identified as a velocity defect. At the tip, four spots of low meridional velocity are found at $\theta = 65, 155, 245, 335$ deg. They are directly connected with four spots of low relative flow angle β . There are no corresponding spots of low relative velocity W . The W velocity plot shows rings of equal level regions, with increasing velocity from root to tip. In the entire flowfield, the tangential gradients of the meridional velocity V_m are not correlated to relative velocity W gradients but to relative flow angle β gradients. In other words, at this station, the relative velocity does not decrease when the relative flow reaches the leading edge of the inducer. There is no blockage effect in terms of relative velocity reduction. The tangential velocity shows the four blades shapes with a modulation probably induced by information coming from downstream. The change of the meridional velocity is only related to the change of direction of the relative velocity. This is also clearly visible for the nominal mass flow rate $Q = Q_n$. At this flow rate, a quasi-circular ring of negative meridional velocity V_m is found at the tip. The width of the recirculating region attached to the casing is 8–10% of the channel height, depending on the azimuthal location considered. The tangential velocity V_u and the absolute flow angle α (Figs. 15 and 16) show that the rotation of the fluid is important and affects the whole flow field, not only the recirculating

region. Four spots of high tangential velocity V_u located at the tip at $\theta = 50, 140, 230, 320$ deg are found. Except for these regions, the tangential velocity distribution is axisymmetric.

At the lower flow rate $0.7Q_n$, the meridional velocity shows a higher gradient in the circumferential plane. The width of the recirculating region is 8–20% of the channel height depending on the azimuthal location and is larger in the vicinity of the blade tip. These regions with high relative velocities can be considered similar to the core at the blade passage vortex described by Lashminarayana.¹ The fluctuations of the tangential velocity are stronger than the fluctuations of the meridional velocity. Near the blade tip, very high fluctuations are observed for the tangential velocity in Fig. 16. The highest value of the tangential fluctuation is found in the zones with the highest tangential velocity corresponding to the lower relative velocity region. This zone is located at the tip at $\theta = 50, 140, 230, 320$ deg for the nominal mass flow rate and at $\theta = 58, 148, 238, 328$ deg at $0.7Q_n$. This difference is due to the larger value of the tangential velocity: At the measurement location, the rotation of the flow in the absolute frame is larger for the lower mass flow, and so this zone is found at a higher azimuthal location. The turbulent shear stress (the ratio of the shear stress to the product of the tangential and axial fluctuating velocity in Fig. 16) is very high at the border of the recirculating flow. This border is the starting point of cavitation in the inducer of a liquid pump.⁷ For the higher mass flow $1.3Q_n$, as mentioned before, there is no inverse flow, particular flow features are observed in the tangential velocity and absolute flow angle plots. A modulation of these quantities is found probably induced by information coming from the impeller.

Conclusions

Measurements have been performed with five-hole pressure probes and hot-wire at the inlet and immediately upstream of the leading edge of a four-blade inducer. Classical results concerning inducer recirculating flows are found.

1) The tip casing shows high stagnation pressures. The stagnation pressure becomes negative at midchannel. This negative pressure is probably due to losses that are generated upstream of the inducer and can be linked to boundary-layer separation due to inverse flow induced by the inducer. This inverse flow with high tangential and axial velocities in the tip casing vicinity acts as a barrier for the axial incoming flow.

2) The axial length of the swirling zone (rotation of the fluid without inverse flow) is greater than the extent of the inverse flow. The zone of high stagnation pressure is greater than the recirculation zone.

3) The recirculating flow is not generated in the tip leakage flow; it is a fully three-dimensional effect strongly coupled with the incidence effect along the leading-edge span and is mainly in the tip region.

4) The tangential gradients of the axial velocity are not correlated to relative velocity gradients but to relative flow angle gradients: The relative velocity does not decrease when the relative flow reaches the leading edge of the inducer.

5) There is no blockage effect in terms of relative velocity reduction. The change of the axial velocity is only related to the change of direction of the relative velocity.

6) Phase-averaged turbulent measurements have been conducted immediately upstream of the inducer to address the questions about time-dependant flow features. The standard deviations of the fluctuations for tangential velocity are stronger than for the meridional velocity, particularly near the casing. Information from the impeller and the downstream diffuser may affect the flow for this section at the $1.3Q_n$ flow rate.

Acknowledgments

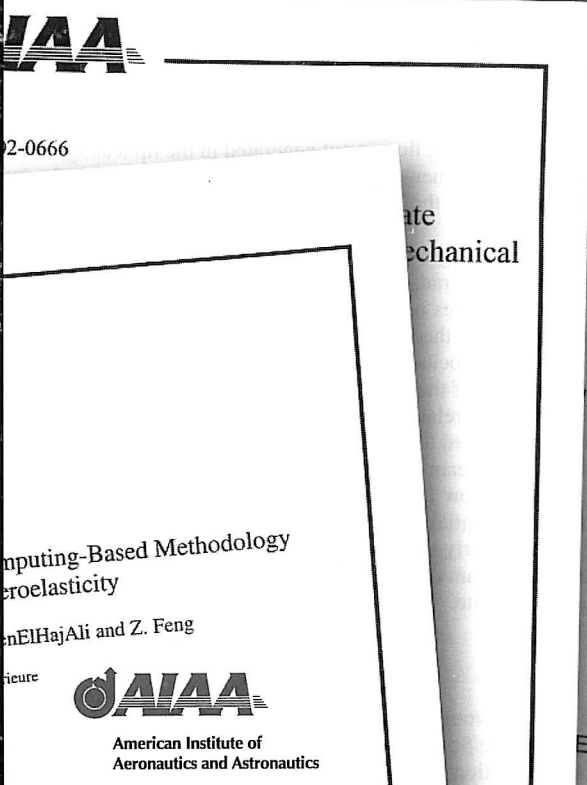
The authors would like to thank the Centre National d'Études Spatiales and the Société Nationale d'Études et de Construction de Moteurs d'Aviation for financial support of this study. The help of V. C. Sharma for the text revision is gratefully acknowledged.

References

- ¹Lakshminarayana, B., "Fluid Dynamics of Inducers—A Review," *Journal of Fluids Engineering*, Vol. 104, No. 4, Dec. 1982, pp. 411–427.
- ²Boccazz, A., Perdichizzi, A., and Schiavello, B., Tabacco, U., "Cavitation Behaviour and Internal Flow Measurements by Laser Doppler Anemometry in a Low Solidity Inducer," XXèmes Journées de l'Hydraulique, Société hydrotechnique de France, Rept. 16, 4–6 April 1989.
- ³Boccazz, A., Perdichizzi, A., and Tabacco, U., "Flow Field Investigation in a Low Solidity Inducer by Laser Doppler Velocimeter," *Journal of Turbomachinery*, Vol. 112, No. 1, Jan. 1990, pp. 91–97.
- ⁴Lakshminarayana, B., *Fluid Dynamics and Heat Transfer of Turbomachinery*, Wiley, New York, 1996, pp. 131–142.
- ⁵Tsujimoto, Y., Yoshida, Y., Maekawa, Y., Watanabe, S., and Hashimoto, T., "Observations of Oscillating Cavitation of an Inducer," *Journal of Fluids Engineering*, Vol. 119, No. 4, Dec. 1997, pp. 775–781.
- ⁶Kamijo, K., Yoshida, M., and Tsujimoto, Y., "Hydraulic and Mechanical Performance of LE-7 LOX Pump Inducer," *Journal of Propulsion and Power*, Vol. 9, No. 6, 1993, pp. 819–826.
- ⁷Yokota, K., Kurahara, K., Kataoka, D., Tsujimoto, Y., and Acosta, A. J., "A Study of Swirling Backflow and Vortex Structure at the Inlet of an Inducer," *Japanese Society of Mechanical Engineers International Journal*, Series B, Vol. 42, No. 3, 1999, pp. 451–459.
- ⁸Bario, F., Barral, L., and Bois, G., "Air Test Flow Analysis of the Hydrogen Pump of Vulcain Rocket Engine," *Journal of Fluids Engineering*, Vol. 113, No. 4, Dec. 1991, pp. 654–659.
- ⁹Janigro, A., and Ferrini, F., "Inducer Pumps," *Recent Progress in Pump Research*, von Kármán Inst. Lecture Series 61, Rhode St. Genèse, Belgium, Vol. 1, 1973, pp. 1–113.
- ¹⁰Janigro, A., and Schiavello, B., "Prerotation in Centrifugal Pumps. Design Criteria," *Off-Design Performance of Pumps*, von Kármán Inst. Lecture Series 1978–3, Rhode St. Genèse, Belgium, 1978.
- ¹¹Browne, L. W. B., Antonia, R. A., and Chua, L. P., "Calibrating of X-probes for Turbulent Flow Measurements," *Experiments in Fluids*, Vol. 7, No. 3, 1989, pp. 201–208.
- ¹²El Ghazzani, M., Bois, G., Geai, P., and Lebœuf, F., "Three-Dimensional Inviscid Flow Computations in a Spatial Turbopump Inducer Using a Distributed Loss Model," American Society of Mechanical Engineers, ASME Paper 92GT65, June 1992.
- ¹³Del Valle, J., Braisted, D. M., and Brennen, C. E., "The Effects of Inlet Flow Modification on Cavitating Inducer Performance," *Journal of Turbomachinery*, Vol. 114, No. 2, April 1992, pp. 360–365.
- ¹⁴Bhattacharyya, A., Acosta, A., Brennen, C., and Caughey, K., "Observations on Off-design Flows in Non-cavitating Axial Flow Inducers," *Pumping machinery*, FED Vol. 154, American Society of Mechanical Engineers, Fairfield, NJ, 1993, pp. 135–141.
- ¹⁵Offtinger, C., Henry, C., Morel, R., and Spettel, F., "Experimental Comparison of Flow Fields at the Inlet and the Outlet of an Inducer With Shrouded and Unshrouded Configurations," *Journal of Fluids Engineering*, Vol. 119, No. 4, Dec. 1997, pp. 954–959.



AIAA MEETING PAPERS ONLINE!



Each year, AIAA publishes more than 4000 technical papers presented at AIAA conferences. These papers contain the most recent discoveries in aerospace and related fields. No other organization offers this depth and breadth in the aerospace field.

You now have immediate access to more than 20,000 technical papers online!

Beginning with 1996 and adding about 4,000 papers every year, AIAA's online archive allows you to search for the latest developments in:

- Astrodynamic
- Aerodynamics
- Guidance
- Structures
- Fluids
- Propulsion
- Controls
- Modeling and Simulation
- Flight Mechanics
- and more...

Search and purchase only those papers that fit your needs. Papers are delivered in pdf format. Search by:

Title • Keyword • Author • AIAA Paper Number
• Conference Title • Publication Year

Click on "Citations Database" from the AIAA Web site at www.aiaa.org

A laser Doppler anemometry technique for Reynolds stresses measurement

Thierry M. Faure, Hubert Miton, Nicolas Vassilieff

Abstract A technique is described for the measurement of all components of mean velocity and Reynolds stresses, in a complex turbulent flow where achieving coincidence data acquisition is difficult. The method is based on data recorded using four orientations of the laser probe. It is shown that the measurement errors are not the same for all the components of the Reynolds tensor, but they are sufficiently small to give a good accuracy. An application to a turbomachinery flow is given to illustrate the method.

1 Introduction

The measurement of Reynolds stresses is an important issue for turbulent flow diagnostics, and this can be achieved with a three-dimensional laser Doppler anemometer in coincidence filtering mode (a same seeding particle is validated through the three probe volumes at the same time). A first problem is that the intersection of the three probe volumes is six or seven times smaller than with a one-dimensional system. Moreover, for applications to internal flows such as turbomachinery, many drawbacks are caused by the presence of a cylindrical window between the flow and the optics (deviation of the beams, smoke deposits on the window) leading to very low data acquisition rates. While coincidence measurements have been successfully achieved in a low-speed axial turbine (Ristic et al. 1999), these drawbacks become important in high-speed compressors (Edmonds et al. 1997). Nevertheless, the measurement of all components of mean velocity and Reynolds stresses in a complex turbulent flow has been described with a single hot-wire (Hoagland 1960) and with a crossed hot-wire (Cutler and Bradshaw 1991). These authors showed a technique that gives the components of the Reynolds tensor with measurements obtained in four roll positions of the hot-wire probe. To achieve this, they used only the two variances of velocity fluctuations along each hot-wire and the cross-correlation between them,

measured for each roll position. Such a technique has been also applied to a single component laser system (Melling and Whitelaw 1976).

The aim of the present study is to develop this idea for applications to internal flows, where laser Doppler anemometry is a non-intrusive technique which has demonstrated great promise, including for multicomponent applications (Chesnaks and Dancey 1990; Stauter 1993; Strazisar 1986). The laser probe uses two laser heads; the first one is a two-dimensional measuring system tuned to the blue (488 nm) and green (514.5 nm) wavelengths. The second one is a one-dimensional measuring system tuned to the green-yellow (532 nm) wavelength. The velocity components relative to these colors are denoted by the subscripts b , g , y hereafter. A technique based on the recording of four different laser probe orientations is developed in order to process the six components of the Reynolds tensor, in addition to the mean velocity field.

2 Analysis

The heads are mounted on a robot arm, with the angle between their optical axes fixed to $2\chi=30^\circ$. This gives sufficient resolution of the radial velocity in turbomachinery applications (Ristic et al. 1999). The laser probe frame of reference is defined relative to the compressor cylindrical frame of reference (e_z, e_r, e_θ) by the angles ϑ, ψ and φ , respectively the pitch, yaw and roll angle to the laser probe axis (Fig. 1). The color axes (e_b, e_g, e_y) are the directions of measurement of the velocity for each laser component; e_g, e_y are in the plane of the laser heads with an angle 2χ between them, e_b is orthogonal to this plane. These axes are written for any laser probe position as functions of $(\vartheta, \psi, \varphi)$. Four laser probe orientations are selected to obtain the alignment of one or two color components with the cylindrical coordinates. Four positions have been selected:

- | | | |
|------------------------------------|------------------|---------------|
| position 1 : $\vartheta = 0$ | $\psi = -\chi$, | $\varphi = 0$ |
| position 2 : $\vartheta = 0$ | $\psi = \chi$, | $\varphi = 0$ |
| position 3 : $\vartheta = -\chi$, | $\psi = -\chi$, | $\varphi = 0$ |
| position 4 : $\vartheta = \chi$, | $\psi = -\chi$, | $\varphi = 0$ |

As (e_b, e_g, e_y) are not orthogonal axes, the successive orientations provide a maximum angular resolution in probe positioning and a minimal error in velocity estimates. The velocity is decomposed in mean velocity \bar{U} and its fluctuation u , the averaging being either stationary or periodic, and the Reynolds tensor components are evaluated from the variances of color fluctuations.

Received: 4 December 2000 / Accepted: 28 February 2004

Published online: 8 April 2004

© Springer-Verlag 2004

T. M. Faure (✉), H. Miton, N. Vassilieff
Université Pierre et Marie Curie, Paris 6, 91405 Orsay, France

The authors are grateful to the Consortium Industrie Recherche en Turbomachines (CIRT) for its funding of the instrumentation and for the financial support of this work.

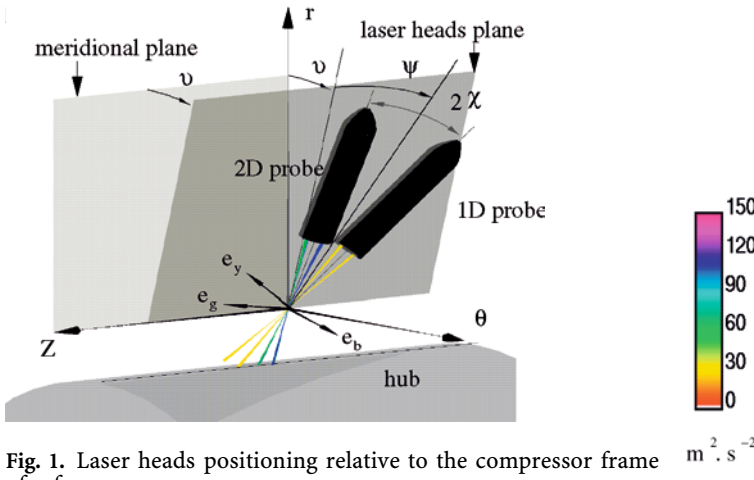


Fig. 1. Laser heads positioning relative to the compressor frame of reference

Any position provides the three components of mean velocity. However, to minimize the error they are calculated using orientations 1 and 2 only:

$$\bar{U}_z = \frac{\bar{U}_{g,1} + \bar{U}_{y,2}}{2}, \quad \bar{U}_\theta = \frac{\bar{U}_{b,1} + \bar{U}_{b,2}}{2}, \quad \bar{U}_r = \frac{\bar{U}_{g,2} + \bar{U}_{y,1}}{2 \sin 2\chi}$$

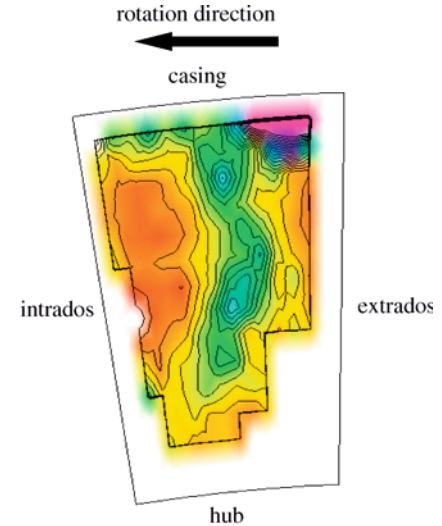
The Reynolds stresses are obtained by:

$$\begin{aligned} \overline{u_z^2} &= \frac{\overline{u_{g,1}^2} + \overline{u_{y,1}^2}}{2}, \quad \overline{u_\theta^2} = \frac{\overline{u_{b,1}^2} + \overline{u_{b,2}^2}}{2} \\ \overline{u_r^2} &= \frac{\overline{u_{y,1}^2} + \overline{u_{g,2}^2} - \cos^2 2\chi (\overline{u_{g,1}^2} + \overline{u_{y,2}^2})}{2 \sin^2 2\chi} \\ \overline{u_z u_r} &= \frac{\overline{u_{g,2}^2} - \overline{u_{y,1}^2}}{4 \sin 2\chi \cos 2\chi}, \quad \overline{u_r u_\theta} = \frac{\overline{u_{b,4}^2} - \overline{u_{b,3}^2}}{4 \sin \chi \cos \chi} \\ \overline{u_\theta u_z} &= \frac{\overline{u_{y,4}^2} - \overline{u_{y,3}^2} + 4 \cos^2 \chi \sin^2 \chi (\overline{u_{b,4}^2} - \overline{u_{b,3}^2})}{8 \cos \chi \sin^2 \chi (\cos^2 \chi - \sin^2 \chi)} \end{aligned}$$

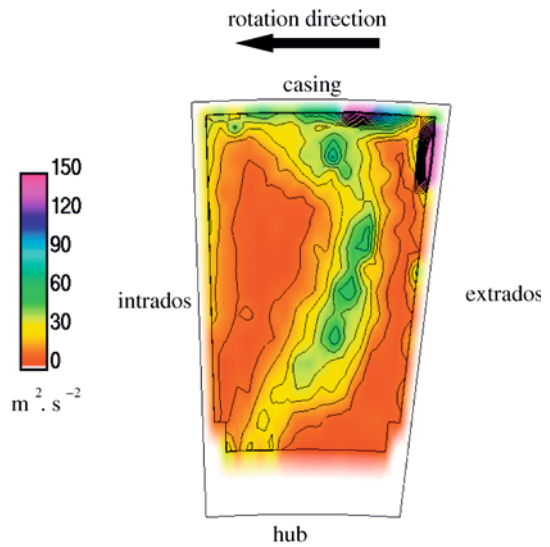
Let us assume a constant absolute measurement error for the mean velocity of the color components η and for the variance of the color velocity fluctuations ϵ^2 . It is then possible to calculate the absolute measurement error resulting in the procedure with four successive positions. The corresponding errors for the mean velocity and Reynolds stresses in cylindrical coordinates are given in Table 1.

Table 1. Measurement errors for mean velocity and Reynolds tensor

Quantity	Absolute error
$\overline{U_z}$	η
$\overline{U_\theta}$	η
$\overline{U_r}$	2η
$\overline{u_z^2}$	ϵ^2
$\overline{u_\theta^2}$	ϵ^2
$\overline{u_r^2}$	$7\epsilon^2$
$\overline{u_z u_r}$	$1.15\epsilon^2$
$\overline{u_z u_\theta}$	$2\epsilon^2$
$\overline{u_\theta u_z}$	$5.58\epsilon^2$



Present technique



3D coincidence filtering

Fig. 2. Axial stress component measured with the present technique (above) and 3D coincidence filtering (below) for an axial distance situated at 66% of the chord inside the stator channel

3 Experiment

Velocities are obtained using a Dantec Burst Spectrum Analyzer processor based on the Fourier transform of the signal for determination of Doppler frequency.

The test rig is a single-stage axial compressor, providing a total pressure ratio of 1.15 for a flow rate of 10.5 kg/s and a nominal speed of rotation fixed at 6330 rpm. An extended description of the facility is available in (Faure et al. 2001).

4 Results

A comparison between the axial stress component measured with the present technique and 3D coincidence fil-

tering mode is presented in Fig. 2. Measurements have been performed inside the stator row of the compressor for a mass flow rate of 10.5 kg/s, in an axial section located at two-thirds of the chord downstream of the stator blade leading edges. The grid of measurement is made up of 16×16 points. These maps are phase-averaged representations of the flow for a given time (each rotor blade passage relative to the stator channel being divided into 24 time intervals). Note for the instant and location chosen, the blade rotor wake is clearly visible in the middle of the stator channel. First, it is clear that the 3D coincidence filtering mode permits exploring a wider region of the channel than the present technique especially near the hub, due to the larger extent of the laser heads positions. Quite similar levels of the axial velocity fluctuations are found with the two methods. Particularly very high levels can be observed in the rotor blade wake and especially in the tip vortex and secondary flow near the casing. However, with the present technique the values observed are slightly higher than with the 3D coincidence filtering mode. It can be thought of as though the combination of two variances introduces a bit of artificial turbulence in the result. Nevertheless, the structures of the flow are practically identical with the two methods.

5

Conclusions

A technique for the measurement of Reynolds stresses in complex turbulent flows has been implemented. The method does not require the acquisition of coincident

Doppler bursts for the three light components and is particularly useful for hard internal flow applications. It gives mean velocity and Reynolds stresses with a reasonable accuracy. The structures usually observed in compressor flows are well described.

References

- Chesnakas CJ, Dancey CL (1990) Three-component LDA measurements in an axial-flow compressor. *J Prop Power* 6:474–481
 Cutler AD, Bradshaw P (1991) A crossed hot-wire technique for complex turbulent flows. *Exp Fluids* 12:17–22
 Edmonds JD, Wiseall SS, Harvey D (1997) Recent developments in the application of laser Doppler anemometry to compressor rigs. In: *Proceedings of the 90th Symposium on Advanced Non-Intrusive Instrumentation for Propulsion Engines*, AGARD. Brussels, Belgium, 20–24 October
 Faure TM, Michon GJ, Miton H, Vassilieff N (2001) Laser Doppler anemometry measurements in an axial compressor stage. *J Prop Power* 17(3):481–491
 Hoagland LC (1960) Fully developed turbulent flow in straight rectangular pipes. Ph.D Thesis, MIT
 Melling A, Whitelaw JH (1976) Turbulent flow in rectangular duct. *J Fluid Mech* 78:289–315
 Ristic D, Lakshminarayana B, Chu S (1999) Three-dimensional flowfield downstream of an axial-flow turbine rotor. *J Prop Power* 15:334–344
 Stauffer RC (1993) Measurement of the three-dimensional tip region flow field in an axial compressor. *J Turbomachinery* 115:468–476
 Strazisar AJ (1986) Laser fringe anemometry for aero engine components. *Advanced Instrumentation for Aero Engine Components*, AGARD CP-399

Thierry M. Faure
e-mail: thierry.faure@limsi.fr

François Lusseyran
e-mail: françois.lusseyran@limsi.fr

Pierre Gouyat
e-mail: gouyat@limsi.fr

Laboratoire d'Informatique pour la Mécanique et les Sciences de l'Ingénieur,
Unité Propre de Recherche 3251,
Centre National de la Recherche Scientifique,
Université Pierre et Marie Curie,
Paris 6,
B.P. 133,
91403 Orsay Cedex, France

François Launay
Institut de Physique Nucléaire d'Orsay,
Unité Mixte de Recherche 8608,
Centre National de la Recherche Scientifique,
15 rue Georges Clémenceau,
91406 Orsay Cedex, France
e-mail: launayf@ipno.in2p3.fr

Experimental Investigation of the Flow Distribution Inside a Tubular Heat Exchanger

The velocity field inside a new concept of heat exchanger, which is a component of a high protons linear accelerator, is investigated experimentally in order to validate the design. A full scale facility with optical accesses is used for the measurements by particle image velocimetry. The choice of the technique is set by the three-dimensional and strongly unsteady structure of the flow. A filtering procedure is applied to the recorded images before processing the velocity field with an optical flow algorithm using dynamical programming. The distribution of the velocity between the different tubes of the heat exchanger shows a large scatter of flow rate between these tubes. In addition, the turbulence characteristics are presented. [DOI: 10.1115/1.2353277]

1 Introduction

Although a flow developing inside a rectilinear duct is well known, the understanding of the behavior of fluid motion inside a system of branching tubes is difficult. One can argue that linear and singular head losses are tabulated [1], but they are not applicable to complex tube branching and cannot give a precise description of the velocity field. However, such geometries are of interest in many applications, but there is a lack of information about them. Investigations have been conducted for Y-shape bifurcations, such as the lung bifurcations flows. This geometry is characterized by a network of repeatedly bifurcating tubes with a diameter decreasing progressively, each bifurcation forming an angle of around 70 deg between the two downstream tubes. The Reynolds number is less than and of the order of 10,000. The first experiments were conducted with intrusive techniques, such as pressure probes and hot-wire anemometry [2,3]. Fractal-like branching channel networks were analyzed numerically with temperature effect [4]. The lung bifurcations flows are oscillatory flows, and visualizations have been carried out [5]. The issue of drops dynamics inside the lung geometry has been studied numerically using a boundary integral formulation [6]. Recent numerical simulations have also been done for a better understanding of the flow structure and particle deposits [7,8]. Extensive investigations have been conducted with laser Doppler velocimetry (LDV) and particle image velocimetry (PIV) oscillatory flows [9–12]. Another type of Y-shape bifurcation flow is the blood flow in arteries, with geometry close to that of the lung bifurcation [13]. Doppler ultrasonic velocimetry measurements and visualizations have been conducted inside the Y-shape bifurcation of a rectangular section channel with different bifurcation angles [14]. A variation of the Y-shape bifurcation is the 45 deg junction investigated for laminar inlet conditions [15]. An industrial domain of application of branching tube flows is flat plate solar energy

collectors [16]. In that geometry, there is a straight-angle bifurcation, and the change in diameter between the upstream and downstream tubes generates strong singularities and recirculation regions. PIV measurements have been conducted in a 90 deg bifurcation under pulsating conditions, within a rectangular section channel [17].

The present work reports the measured flow inside a new heat exchanger design, which is a component of a high-current protons linear accelerator, for inlet flow rates in the operating range 3–15 l/min. The objective is to provide a complete set of data for understanding the fluid dynamics inside the exchanger and for future comparison to numerical simulations for a validation of the design. Its geometry is three-dimensional and combines bifurcations with an angle of 70 deg and orthogonal branching of six tubes with a change of diameter. This geometry is original, and the turbulence characteristics are helpful for understanding heat transfer. Particular attention is devoted to the comparison of the measured velocity distribution between each of the six tubes because the flow rate distribution inside the tubes is the main technological issue.

2 Experimental Setup

2.1 Hydraulic Loop. The hydraulic loop is made of a water circuit to feed the heat exchanger model (Fig. 1). A single stage radial pump rotating at a nominal speed of 2850 rpm permits the water circulation inside the closed-loop circuit. It is fed by a 30 l water tank with a bypass on the pump outlet. Downstream of the pump, there is a regulation valve and two flowmeters for the measurement of the inlet flow rate. The water goes through the heat exchanger model and comes back toward the feeding tank. Flow seeding is provided by 10 μm dia glass spheres coated with a silver film; their density is 1400 kg/m³.

2.2 Heat Exchanger Model. The new concept of the heat exchanger for cooling the high-current protons accelerator is given in Fig. 2. It depicts a complex three-dimensional geometry

Contributed by the Fluids Engineering Division of ASME for publication in the JOURNAL OF FLUIDS ENGINEERING. Manuscript received July 7, 2005; final manuscript received May 15, 2006. Assoc. Editor: Malcolm J. Andrews.

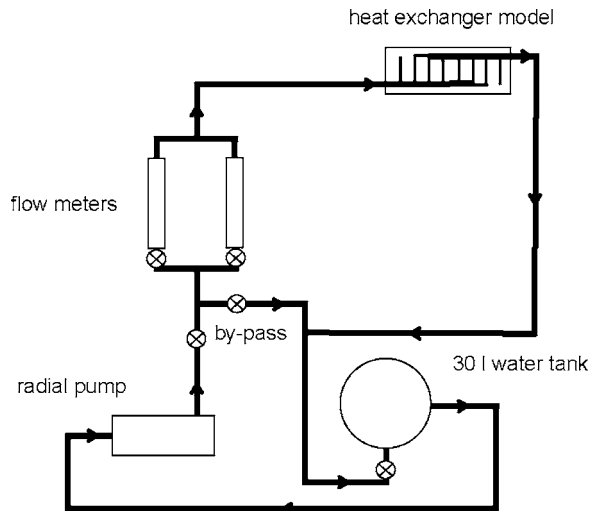


Fig. 1 Hydraulic loop

with changes in the duct diameter.

A full-scale heat exchanger model is made with aluminum and glass, this latter material permitting an easy optical access inside the central part of the tubes (Fig. 3). The heat exchanger consists of, following the flow direction: an inlet duct; an inlet collector feeding six parallel glass tubes, each one with a length of 44 mm; an outlet collector; and an outlet duct. The ducts and collectors are 8 mm dia, whereas the inside diameter of the tubes is 4 mm. The six parallel tubes and the inlet and outlet ducts are in the same plane, but the inlet collector is forming an angle of 25 deg with the parallel tubes plane, whereas the outlet collector is forming an angle of 155 deg with it. The exit of the inlet duct is located in front of tube number 2 and the entry of the outlet duct is in front of tube number 5. A stand-alone tube (on the right side of Fig. 3) with the same dimensions is placed on the model frame and can be fed by the water circuit, allowing the validation of the measurement technique on a well-known flow established inside a rectilinear channel. An additional tube (on the left of Fig. 3) contains a calibration target immersed in water for the measurement of the camera magnification.

2.3 Particle Image Velocimetry Apparatus

2.3.1 Laser Emission Device and Camera. Light emission is achieved with a laser YAG Quantel Twins Ultra, consisting of two sources emitting a 532 nm light flash with an energy of 30 mJ by pulse. Each pulse is 6 ns long. A cylindrical lens placed at the head emission end creates a light plane, which is directed toward the region of measurement by the means of a plane mirror. The image recording system consists of an 8-bit camera with 768 \times 484 pixels, its focal depth is 25 mm. The image magnification

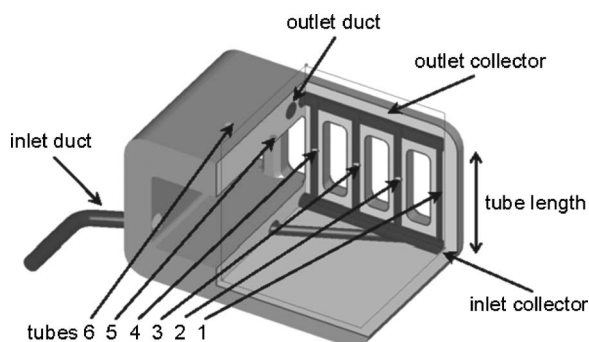


Fig. 2 View of the new heat exchanger model

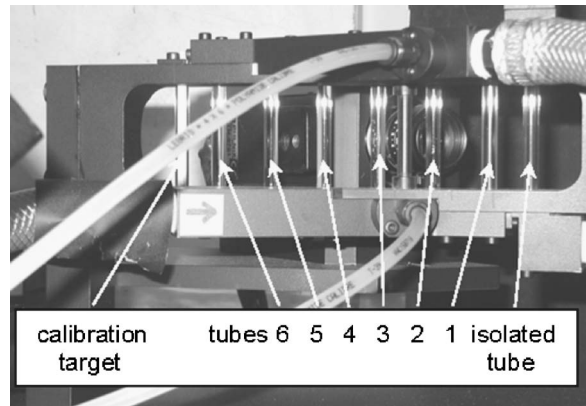


Fig. 3 Heat exchanger model

is 2.4. A Quantel DPS 01 box achieves the synchronization between laser emission and camera recording by the variation of the lag between two pulses. The laser emission head and the camera are placed on a one-axis traversing system to successively explore the flow inside each of the six tubes (Fig. 4). The axial translation accuracy is 1 μ m. The laser sheet thickness is 0.25 mm and passes through the tube diameter without deviation along the tube height, forming an angle of 45 deg with the tube's alignment axis.

2.3.2 Optical Flow With Dynamical Programming. The method used for particle image displacement calculation is the optical flow using dynamical programming [18,19]. It is based on the minimization of the Minkowski L^p norm between two successive images. A division of the image in smaller and smaller slices allows the calculation of a displacement field by orthogonal iterations. The advantage of this method over other PIV methods is its ability to provide a high density field of one vector calculated by pixel, with high accuracy in the regions of strong gradient. Measurements are conducted with a mean ten pixel particle displacement between successive images. Thus, the time delay between two flashes is adjusted for the velocity inside the tube, and is varied from 84 μ s to 422 μ s. With this set of parameters, the measurement accuracy is 1/32 pixel, which corresponds to a relative velocity accuracy of 0.31%.

2.3.3 Image Filtering. A simple image-filtering method was developed in the course of this work and is compared to classical image-filtering techniques [20]. During the experiment setting, particular attention is devoted to laser light positioning and to the suppression of all the undesirable light reflections. However, some reflections remain in the recorded images and can alter the PIV processing (Fig. 5(a)). In order to eliminate these optical noise sources, it seems easy to subtract from an image with flow, an image recorded without flow where only undesirable reflections are present. But such a reference image is impossible to get straightforward because of the presence of the tracers in the flow, which modifies the background scattered light. An alternative to that issue is addressed in the average of all the recorded images with tracer images, statistically equally distributed in the measurement field. That reference image retains the undesired reflections and is well known for image subtraction in PIV measurements [21]. But this process implies a background noise estimate altered by the average of the particle traces. In addition, the average is affected by the light source variation with time. The image filtering obtained with this method is given in Fig. 5(b). Another classical way to obtain a reference image is to erode the initial image, which removes any isolated cluster, followed by a dilatation of the gray level. As a result, the only remaining traces are light reflections. This image can be used to filter the initial image, as it is presented in Fig. 5(c). To get rid of the light variation between the two sources and with time, an original and very simple method

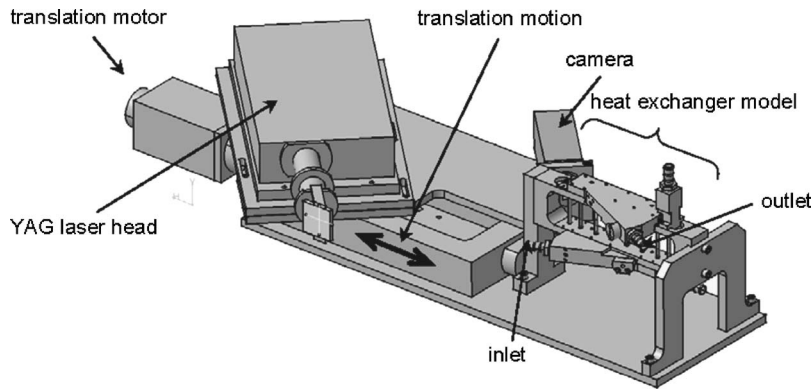


Fig. 4 Laser emission head and its translation system

has been implemented, which is compared to the previous ones. We have chosen to subtract to each image number n , the image recorded with the following flash coming from the same source, that is to say image number $n+2$ (Fig. 5(d)). It is worth noticing that almost no tracer identified on the rough image is rejected by this operation. The filtering residual can be estimated with the autocorrelation of the images. The zero correlation peak is identified on the images with any of the three filtering methods (Figs.

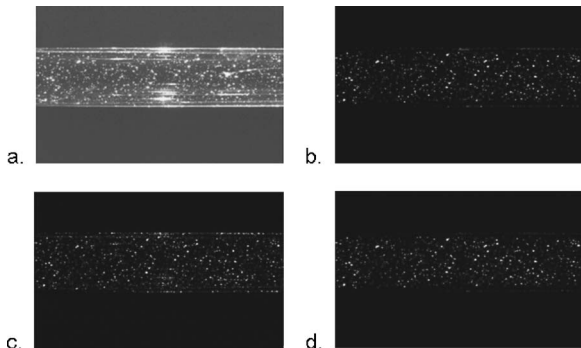


Fig. 5 Comparison between (a) a rough image, (b) an image with mean background noise subtraction, (c) with an eroded-dilated noise image subtraction, and (d) with subtraction of images n and $n+2$

6(b)–6(d)), while the same peak is mixed with noise if no correction is applied (Fig. 6(a)). The cross-correlation of two successive images, without and with filtering, is given in Fig. 7. A correlation peak in zero is remaining with the method based on the erosion-dilatation (Fig. 7(c)). It is worth noting that, with the filtering by the subtraction of image n and $n+2$, as for the filtering with an averaged image, there is no residual zero displacement correlation peak, the only peak identified corresponds to the mean displacement of ten pixels. Figure 8 quantifies the improvement obtained by this processing with the histogram of the x average for the rough and filtered images (on the left) and with the cut of the cross-correlation at $\Delta y=0$ (on the right). One can observe the secondary peak at $\Delta x=0$ for the cross-correlation of the rough image, which vanishes completely on the filtered images. The only noticeable difference between the two filterings is the remaining wall tube reflections (Fig. 8, on the left, circle), which for filtering with an averaged image, is higher by a factor 2 in comparison to the filtering by subtraction of image n and $n+2$. Finally, the method based on the filtering by subtraction of image n and $n+2$ is used for this study.

2.3.4 Optical Deformations Correction. The optical path in the tube radial direction is modified by the presence of three media, air, glass, and water. The solution generally employed to reduce optical distortions with round tubes is to enclose the experimental setup within a rectangular water-filled box. In fact, an alternative solution was used for this study. The interfaces be-

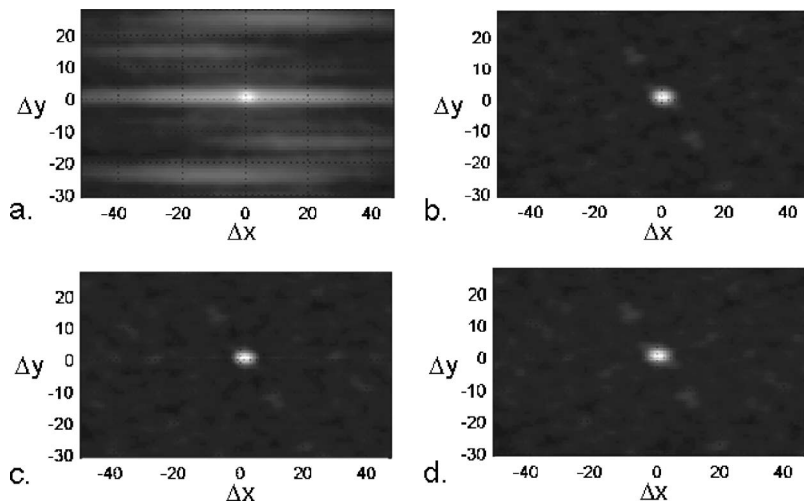


Fig. 6 Comparison between (a) the autocorrelation function of the rough image, (b) with mean background noise subtraction, (c) with an eroded-dilated noise image subtraction, and (d) with subtraction of images n and $n+2$

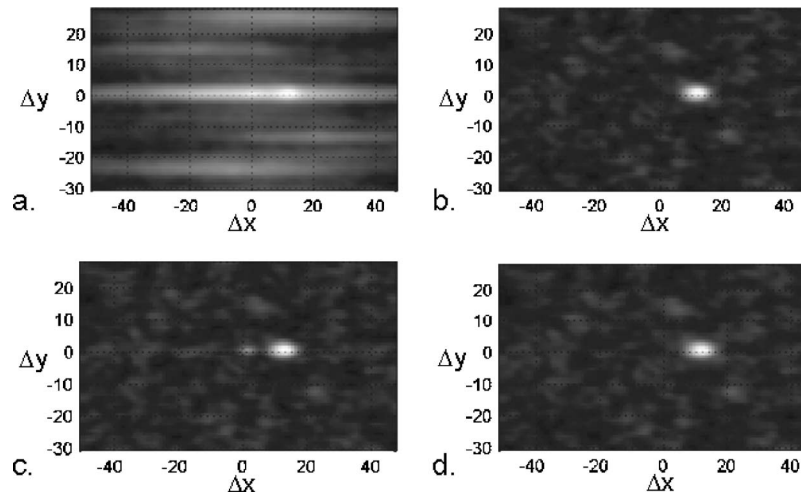


Fig. 7 Comparison between the cross-correlation function of (a) a couple of rough images, (b) with mean background noise subtraction, (c) with an eroded-dilated noise image subtraction, and (d) with subtraction of images n and $n+2$

tween air and glass, and between glass and water, generate light refractions and thus a deformation of the laser sheet image inside the tube and of the tracer image displacements (Fig. 9). A distance r inside the visualization plane will be observed as an apparent distance r_a inside the plane of the image of the camera, as a consequence of the angular deviations $\alpha_2, \alpha_3, \beta_1, \beta_2$.

The relationship between these two positions is obtained by solving

- Snell-Descartes equation for the interface between each medium

$$n_1 \sin \beta_1 = n_2 \sin \beta_2$$

$$n_2 \sin \alpha_2 = n_3 \sin \alpha_3$$

- The relationships of optical geometry provide the expressions for the angles $\alpha_2, \alpha_3, \beta_1, \beta_2$

$$\sin \alpha_2 = \frac{n_1 r_a}{n_2 R_i}$$

$$\sin \alpha_3 = \frac{n_1 r_a}{n_3 R_i}$$

$$\sin \beta_1 = \frac{r_a}{R_i + e}$$

$$\sin \beta_2 = \frac{n_1 r_a}{n_2 R_i + e}$$

with the values of the refraction indices for air $n_1=1$, for glass $n_2=1.5$, for water $n_3=1.33$, and the internal tube radius $R_i=2$ mm and its thickness $e=1$ mm. The solution of this set of equations results in the apparent radial distance r_a as a function of the real radius r given by the expression plotted in Fig. 10

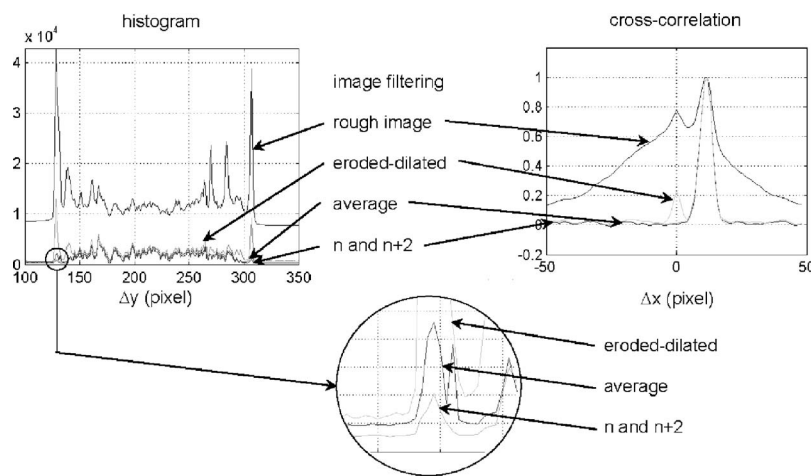


Fig. 8 Histogram of a rough image, with mean background noise subtraction and with subtraction of images n and $n+2$ (left) and cross-correlation at $\Delta y = 0$ for a couple of the same images (right)

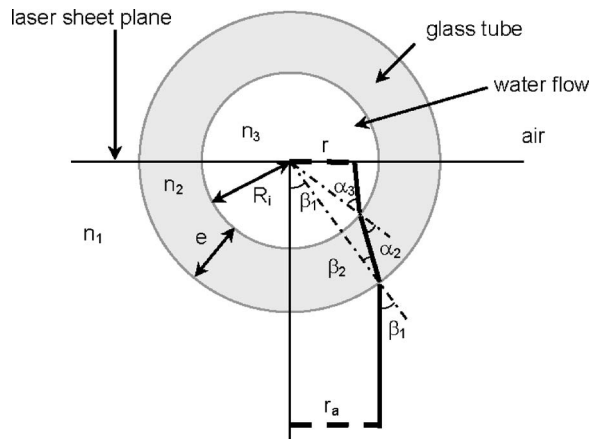


Fig. 9 Light path deformation caused by the different media

$$r_a = \frac{n_3}{n_1} \cos[\alpha_3 - (\beta_1 - \beta_2 + \alpha_2)]$$

This correction is taken into account for the radial positions for the measured displacements before velocity processing.

3 Results and Discussion

The flow inside the heat exchanger is investigated for flow rates between 3 l/min and 15 l/min, which correspond to inlet Reynolds numbers varying from 7960 up to 39,760. As the glass tubes are fixed in the aluminum frame and the camera positioning cannot be changed along the tube height, only the central half of the tubes length is explored in the plane of symmetry passing through the cylinder axes.

3.1 Error Analysis. We recall that PIV measurements are conducted with a mean ten pixel particle displacement between successive images. The time delay between two flashes is adjusted for the velocity inside the tube and is varied from 84 to 422 μ s, according to the flow rate under consideration. With this set of parameters and the use of optical flow with dynamical programming for image displacement calculation, the measurement accuracy is 1/32 pixel, which corresponds to a relative velocity accuracy of 0.31%. The experimental results are obtained with the recording of 600 images providing 300 PIV fields for each tube. The average of these fields gives the mean velocity field inside each of the six heat exchanger tubes, with maximum statistical confidence accuracy on the mean velocity of 0.1 m/s, corresponding to a maximum relative error of 2.5%. For the variances of the axial and radial velocity fluctuations and the shear stress of the axial-radial velocity fluctuations, the maximum statistical confidence accuracy is 0.015 m^2/s^2 corresponding to a maximum relative error of 5%.

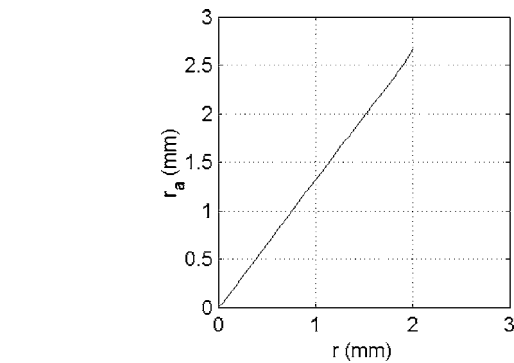


Fig. 10 Apparent radius function of the true radial position

accuracy is 1/32 pixel, which corresponds to a relative velocity accuracy of 0.31%. The experimental results are obtained with the recording of 600 images providing 300 PIV fields for each tube. The average of these fields gives the mean velocity field inside each of the six heat exchanger tubes, with maximum statistical confidence accuracy on the mean velocity of 0.1 m/s, corresponding to a maximum relative error of 2.5%. For the variances of the axial and radial velocity fluctuations and the shear stress of the axial-radial velocity fluctuations, the maximum statistical confidence accuracy is 0.015 m^2/s^2 corresponding to a maximum relative error of 5%.

3.2 Mean Flow. Mean velocity inside the measurement plane is obtained by PIV measurements. In order to analyze the flow behavior inside the six tubes, a grayscale map of the mean velocity field is provided for the central area of the tube, corresponding to the PIV camera field, with the same grayscale for each tube in Fig. 11, for the same inlet flow rate condition. The x -axis origin is located 11 mm downstream of the inlet collector-tube connection. We observe the axial evolution of the velocity profile. The distribution is strongly nonhomogeneous between the tubes, with a maximum velocity inside tube 2 and a minimum velocity inside tube 3. Figures 12 and 13 display the axial and radial velocity profiles inside the tubes for three axial positions of the investigated region. Inside tube 2, a strong axial velocity gradient is

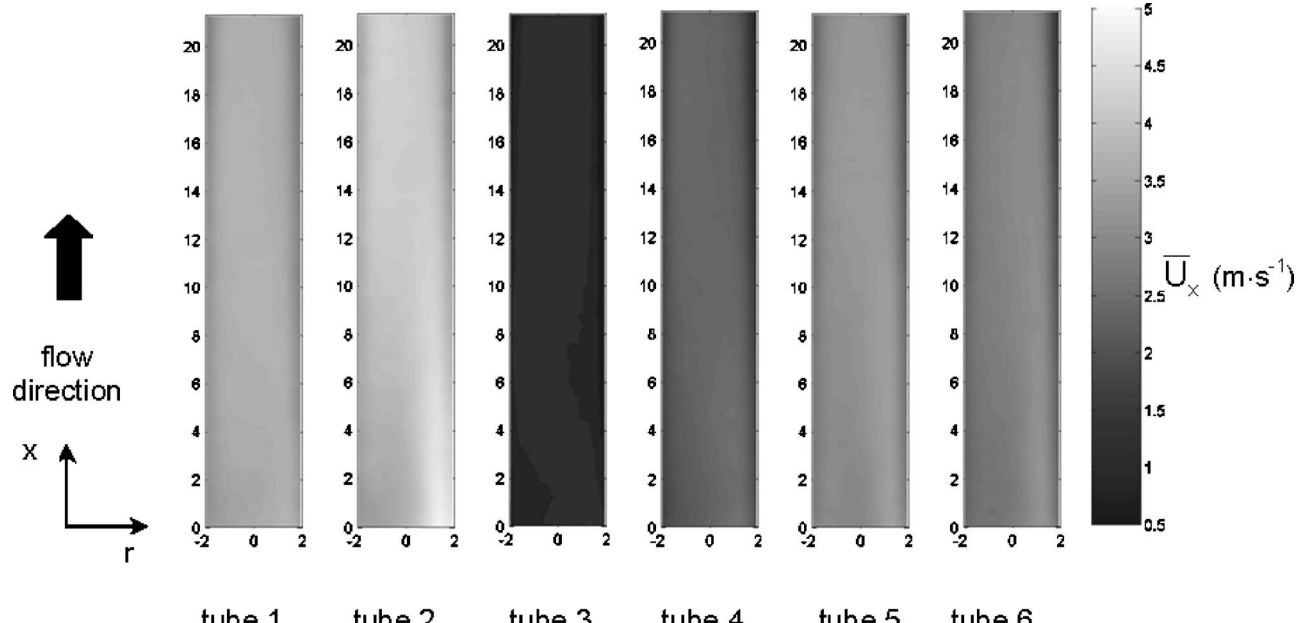


Fig. 11 Mean axial velocity distribution in the tubes for the inlet flow rate 12 l/min

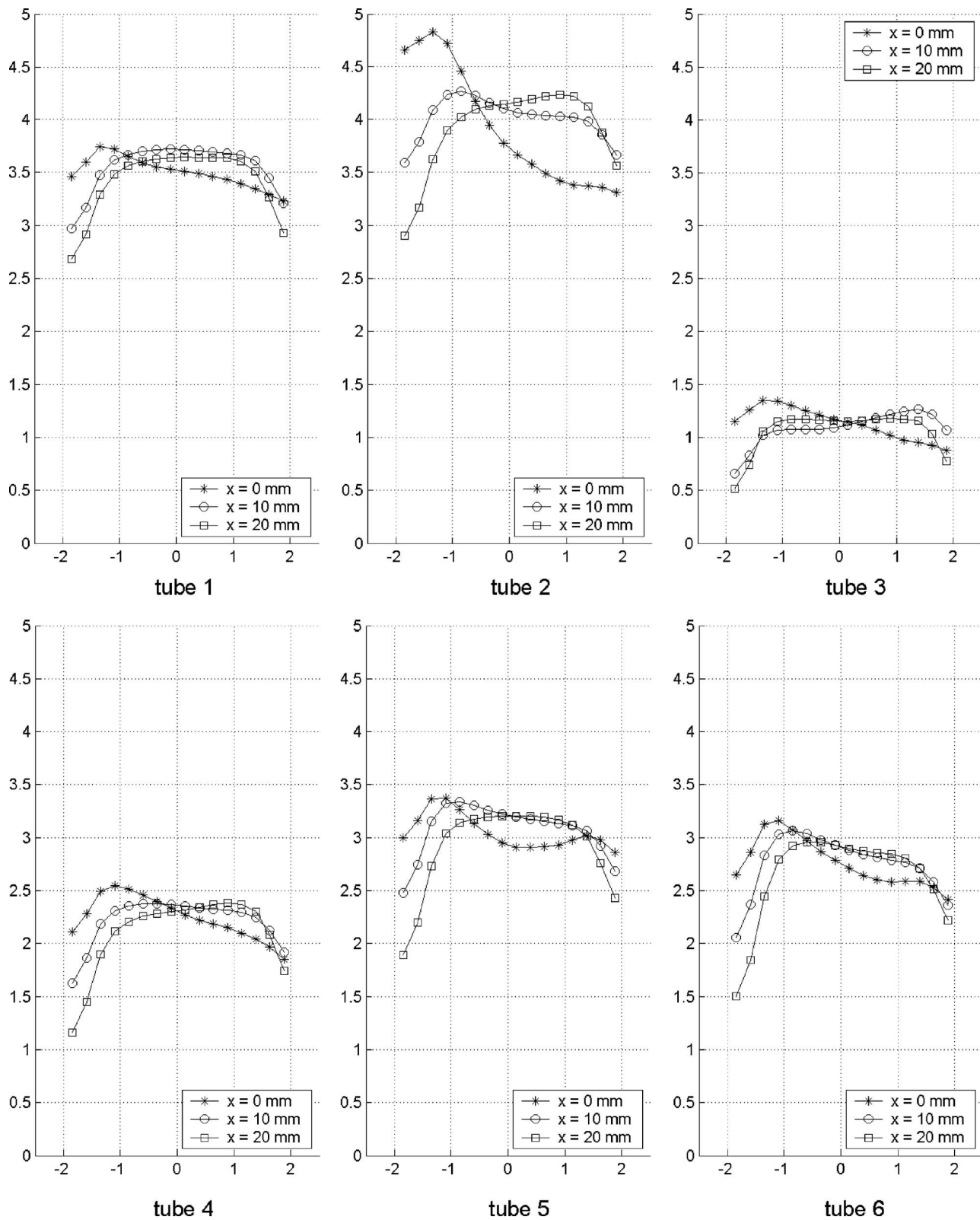


Fig. 12 Radial evolution of the axial velocity for three axial positions inside the tubes and for the inlet flow rate 12 l/min

present along a diameter for the first explored axial distance ($x=0$ mm). The velocity is smooth in the middle of the explored window ($x=10$ mm) and tends toward the inversion of the gradient for $x=20$ mm. This is evidence of the presence of a strongly nonestablished three-dimensional flow. The same behavior is

found inside the other tubes. As the radial velocity and its gradient are small, the continuity equation yields to a strong gradient of the tangential velocity in the direction of the azimuth, which is not measured in the study. Tube 3 displays an axial velocity smaller a factor of 4 from tube 2. The radial gradient has the same shape at

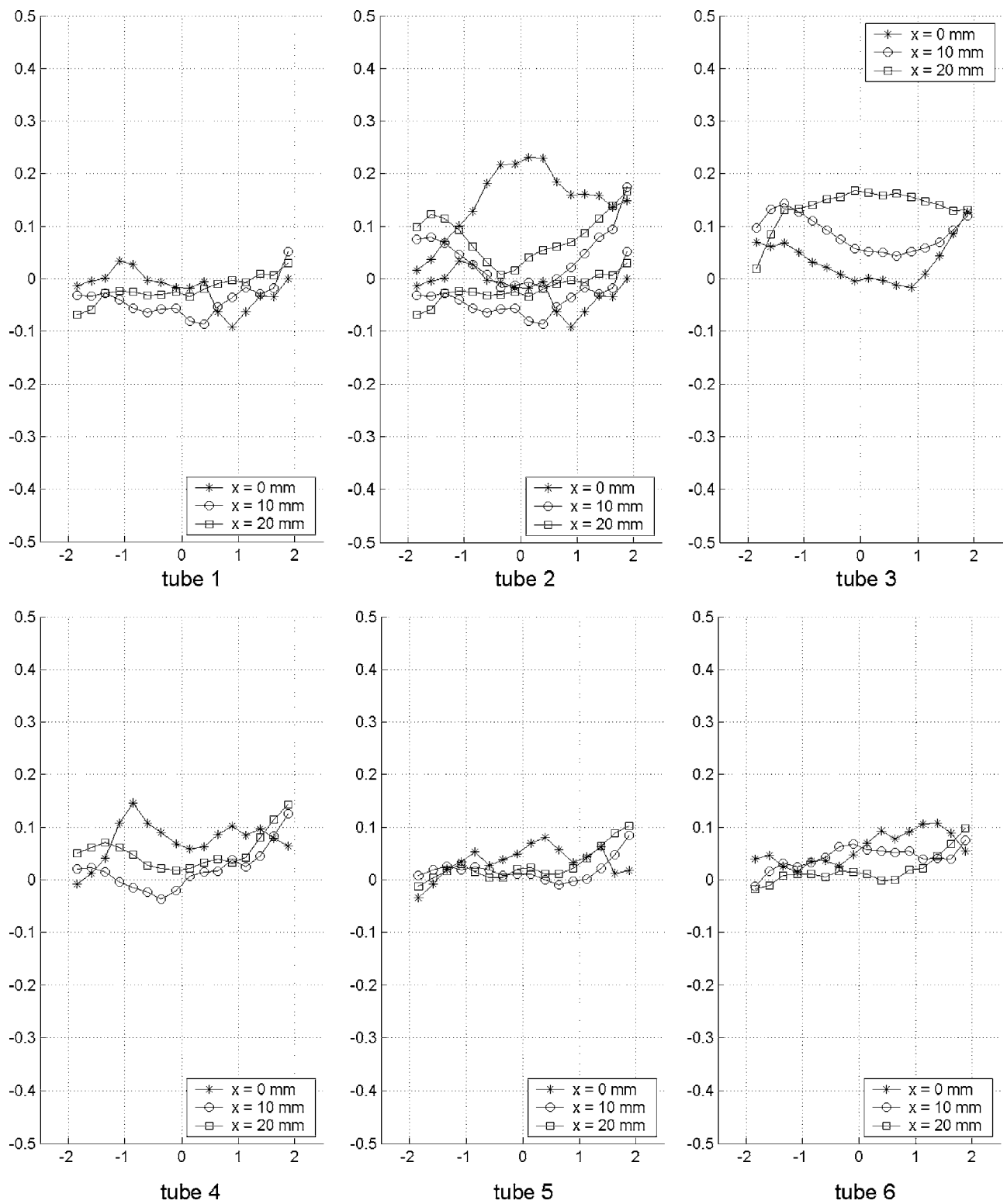


Fig. 13 Radial evolution of the radial velocity for three axial positions inside the tubes and for the inlet flow rate 12 l/min

$x=0$ mm, but is inversed for $x=10$ mm and shows an established profile for $x=20$ mm, which is consistent with the lower Reynolds number inside this tube. The radial velocity component and gradient remain low and are represented with a smaller scale in Fig. 13. The larger amplitude is found in tube 2 where the axial velocity is a maximum value. The heat transfer coefficient is proportional to the axial velocity gradient near the wall. As the axial velocity is zero on the wall, although it is not measured for this

particular position, the greater the velocity inside a tube is, the larger the velocity gradient. The larger heat transfer between the fluid and the exchanger is obtained for tube 2. We observe on the axial velocity (Fig. 12) that the heat transfer is asymmetric inside each tube in the first half of the length and tends to a uniform distribution when the flow reaches an established velocity profile.

3.3 Velocity Distribution Between Tubes.

The velocity is

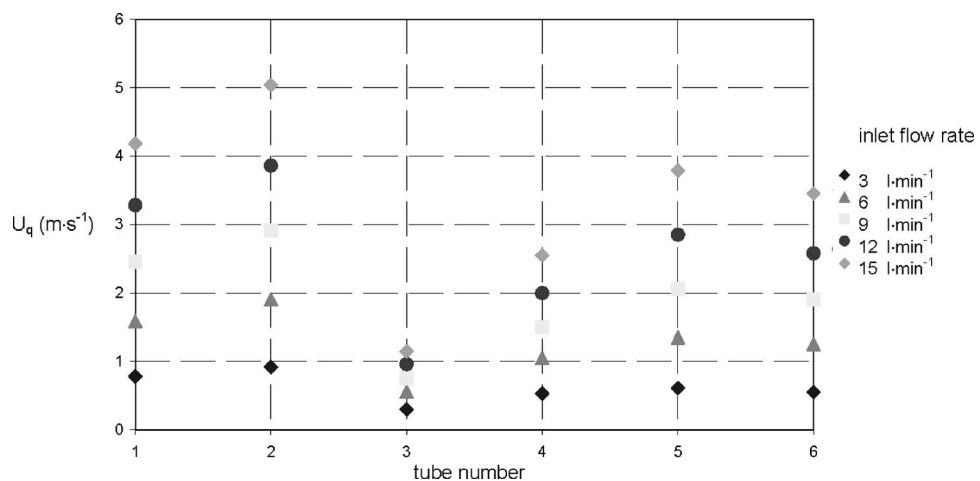


Fig. 14 Averaged reference velocity U_q distribution inside the tubes for five inlet flow rates

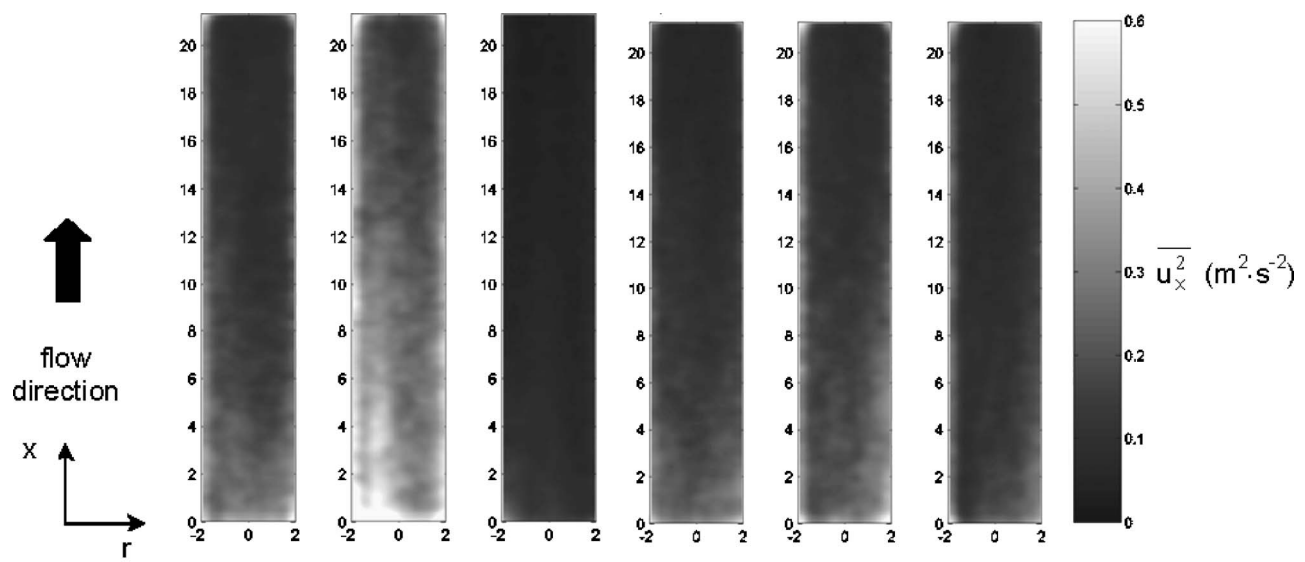


Fig. 15 Variance of the axial velocity fluctuations for the inlet flow rate 12 l/min

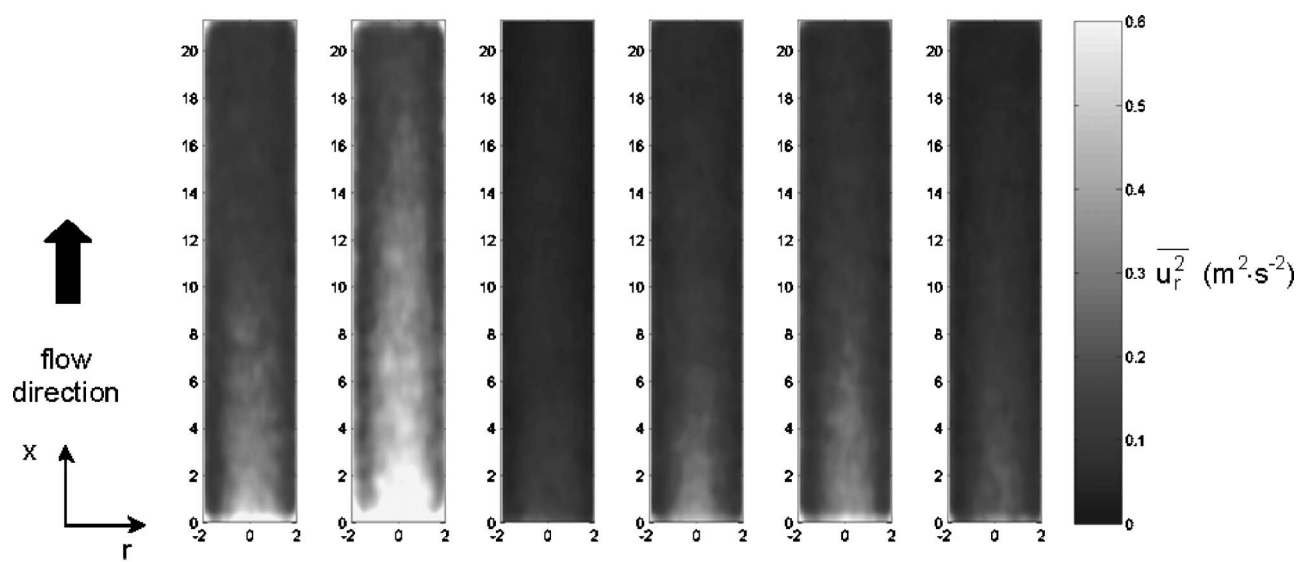


Fig. 16 Variance of the radial velocity fluctuations for the inlet flow rate 12 l/min

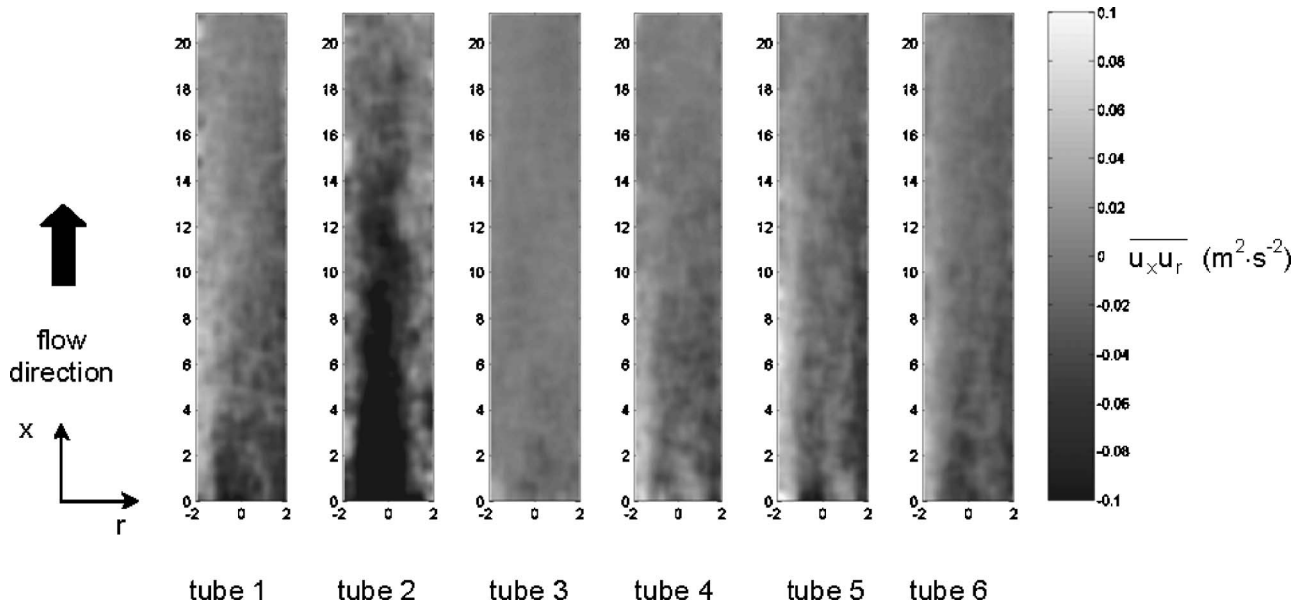


Fig. 17 Shear stress of the axial-radial velocity fluctuations for the inlet flow rate 12 l/min

averaged in the radial and axial directions and the distribution of the reference velocity U_g between the six tubes of the heat exchanger is displayed in Fig. 14, for five inlet flow rates varying from 3 l/min to 15 l/min. It has been checked that this reference velocity U_g is not far from the flow velocity through each one of the tubes by comparing the inlet flow rate measured with the flow meters to the integration of the measured velocities along the six tubes. For every inlet flow rate, the velocity distribution along the tubes shows a minimum value for tube 3 and a maximum value for tube 2, with a second local maximum value for tube 5. In fact, a careful examination of the heat exchanger geometry proves that tube 2 is in front of the junction between the inlet collector and the inlet duct and tube 5 is in front of the junction between the outlet collector and the outlet duct, which makes a traversing flow easier. This must be the reason why higher axial velocities are found inside these tubes for any flow rate.

3.4 Turbulent Flow. The statistical convergence of the second-order moments of velocity fluctuations is obtained with an estimated accuracy of $0.05 \text{ m}^2/\text{s}^2$ or a relative error of 0.3%. The variance of the axial velocity fluctuations (Fig. 15) shows a maximum intensity in the beginning of the investigation region and in the wall neighborhood of tube 2, which is the channel with the maximum flow rate. Note the dissymmetry of the variance of axial fluctuations with higher levels in the left part of the tube. That is the evidence of a recirculating region, which is present after the collector-tube connection and which spreads in the first third of tube 2. The turbulence is lower in the other tubes, especially inside tube 3, where the mean velocity is the lowest. Similar comments can be made for the variance of the radial velocity fluctuations (Fig. 16). The turbulence feature for the radial component is more symmetrical inside tube 2 than it is for the axial component. Figure 17 presents the axial-radial shear with higher amplitude and dissymmetry for tube 2. The large central negative region is typical of the recirculation coming from the connection between the inlet collector and tube 2. This is the evidence that the flow is highly anisotropic inside this tube.

4 Conclusion

The flow inside a heat exchanger, which is a component developed for cooling a high-current protons linear accelerator, has been investigated experimentally. A full-scale water model has been built for the study, and a PIV system has been implemented

on the setup. The noise light refraction and displacement distortions inside the tubes have been corrected. Regarding the fluid dynamics inside the heat exchanger, the study focused on velocity distribution between each one of the small tubes. It is found, for the range of investigated inlet Reynolds numbers, that velocity distribution among the tubes does not depend on the flow rate. The global velocity field shows three-dimensional features. The velocity reaches a maximum value in tube 2 and a minimum value in tube 3, with a second relative maximum value in tube 5. For every inlet flow rate, the velocity ratio between tubes 2 and 3 is 4. The heat transfer coefficient is proportional to the velocity gradient near the wall, and it is asymmetric inside each tube in the first half of the length and tends to a uniform distribution when the flow is established. The larger velocity gradient inside tube 2 provides a larger heat transfer coefficient and a better heat transfer efficiency than the other tubes. The turbulent components measured show higher levels inside tube 2, which will be more efficient in terms of heat transfer.

Acknowledgment

The authors are indebted to A. Chaboche, A. Stephen, and L. Vattrinet, for building the facility, and to V. Bourdin and S. Rieublanc for the improvements brought to the hydraulic loop. They would like to thank D. Rougier, J. Bissirieux, and J. P. Baronick for the conception of the heat exchanger model.

References

- [1] Idel'cik, I. E., 1986, "Memento des Pertes de Charges" (French translation from Russian) Eyrolles, Paris.
- [2] Pedley, T. J., Schroter, R. C., and Sudlow, M. F., 1971, "Flow and Pressure Drop in Systems of Repeatedly Branching Tubes," *J. Fluid Mech.*, **46**(2), pp. 365–383.
- [3] Pedley, T. J., 1977, "Pulmonary Fluid Dynamics," *Annu. Rev. Fluid Mech.*, **9**, pp. 229–274.
- [4] Alharbi, A. Y., Pence, D. V., and Cullion, R. N., 2003, "Fluid Flow Through Microscale Fractal-Like Branching Channel Networks," *ASME J. Fluids Eng.*, **125**, pp. 1051–1057.
- [5] Haselton, F. R., and Scherer, P. W., 1982, "Flow Visualization of Steady Streaming in Oscillatory Flow Through a Bifurcating Tube," *J. Fluid Mech.*, **123**, pp. 315–333.
- [6] Manga, M., 1996, "Dynamics of Drops in Branched Tubes," *J. Fluid Mech.*, **315**, pp. 105–117.
- [7] Comer, J. K., Kleinstreuer, C., and Zhang, Z., 2001, "Flow Structures and Particle Deposition Patterns in Double-Bifurcation Airway Models. Part 1: Air Flow Fields," *J. Fluid Mech.*, **435**, pp. 25–54.
- [8] Zhang, Z., Kleinstreuer, C., and Kim, C. S., 2002, "Gas-Solid Two-Phase Flow

- in a Triple Bifurcation Lung Airway Model," *Int. J. Multiphase Flow*, **28**, pp. 1021–1046.
- [9] Corieri, P., 1994, "Experimental and Numerical Investigation of Flows in Bifurcations Within the Lung Airways," Ph.D. thesis, Université Libre de Bruxelles.
- [10] Ramuzat, A., and Riethmuller, M. L., 2002, "Étude Expérimentale des Écoulements Oscillatoires dans un Modèle de Bifurcations Multiples Tridimensionnel," 8^eme Congrès Francophone de Vélocimétrie Laser, Orsay (France), Sept. 17–20, pp. 125–130.
- [11] Ramuzat, A., 2002, "Techniques de Mesures Non-invasives Appliquées aux Écoulements Biologiques: Étude des Bifurcations Pulmonaires Successives," Ph.D. thesis, von Karman Institute for Fluid Dynamics and Université Paris XII Val de Marne.
- [12] Theunissen, R., Corieri, P., and Riethmuller, M. L., 2004, "Application de la PTV à la Modélisation d'Écoulements d'Aérosols dans les Voies Aériennes Pulmonaires," 9^eme Congrès Francophone de Vélocimétrie Laser, Brussels (Belgium), Sept. 14–17, pp. K.5.1–K.5.9.
- [13] Ku, D. N., 1997, "Blood Flow in Arteries," *Annu. Rev. Fluid Mech.*, **29**, pp. 399–434.
- [14] Rieu, R., Pelissier, R., and Farahifar, D., 1989, "An Experimental Investigation of Flow Characteristics in Bifurcation Models," *Eur. J. Mech. B/Fluids*, **8**(1), pp. 73–101.
- [15] Ethier, C. R., Prakash, S., Steinman, D. A., Leask, R. L., Couch, G. G., and Ojha, M., 2000, "Steady Flow Separation Patterns in a 45 Degree Junction," *J. Fluid Mech.*, **411**, pp. 1–38.
- [16] Kubilay, E., 1982, "Répartition du Débit et Pertes de Charge Singulières d'un Absorbeur Solaire Tubulaire," Ph.D. thesis, Université Pierre et Marie Curie, Paris VI.
- [17] Nikolaidis, N. M., and Mathioulakis, D. S., 2002, "Axial and Secondary Flow Study in a 90 deg Bifurcation Under Pulsating Conditions Using PIV," *ASME J. Fluids Eng.*, **124**, pp. 505–511.
- [18] Quénod, G. M., 1992, "The Orthogonal Algorithm for Optical Flow Detection Using Dynamic Programming," *Proc. IEEE*, **III**, pp. 249–252.
- [19] Quénod, G. M., Pakleza, J., and Kowalewski, T. A., 1998, "Particle Image Velocimetry With Optical Flow," *Exp. Fluids*, **25**(3), pp. 177–189.
- [20] Faure, T. M., Lusseyran, F., Gouyat, P., and Launay, F., 2004, "Exploration de l'Écoulement dans un Échangeur de Chaleur Tubulaire par Vélocimétrie par Images de Particules," 9^eme Congrès Francophone de Vélocimétrie Laser, Brussels (Belgium), Sept. 14–17, pp. K.4.1–K.4.8.
- [21] Rémy, D., and Buisine, D., 2005, "Caractérisation à l'Aide de la Tomographie et de la PIV d'une Structure Spirale Apparaissant dans une Cavité Rotor-Stator Aspirée," Actes du Colloque FLUVISU 11, June 7–9, Ecully (France).

Visualizations of the flow inside an open cavity at medium range Reynolds numbers

Thierry M. Faure · Panayotis Adrianos ·
François Lusseyran · Luc Pastur

Received: 14 February 2006 / Revised: 18 May 2006 / Accepted: 13 July 2006 / Published online: 29 November 2006
© Springer-Verlag 2006

Abstract The interaction between a laminar boundary layer and an open cavity is investigated experimentally for medium range Reynolds numbers. Flow visualizations are carried out for three different observation directions in order to understand the spatial development of dynamical structures. In particular, synchronized visualizations in two parallel planes picture the transverse development of the flow. The study is conducted by changing the cavity aspect ratio, the Reynolds number and therefore the flow patterns inside the cavity. The issue is to emphasize the 3-D development of the flow. In particular, we show that the dynamical structures are not due to secondary shear layer instabilities.

k	wave number
L	cavity length
R	aspect ratio
r_c	curvature radius
Re	Reynolds number
S	wind tunnel span
t	time
U_c	convection velocity inside the cavity
U_e	external velocity
(x, y, z)	Cartesian coordinates
Δ	difference
δ	boundary layer thickness inside the cavity
δ_2	momentum thickness inside the cavity
Λ	dimensionless coefficient
λ	wavelength
ν	kinematics viscosity

Nomenclature

A	plate length upstream of the cavity
B	plate length downstream of the cavity
D	wind tunnel height
$Gö$	Görtler number
H	cavity height

T. M. Faure (✉) · P. Adrianos · F. Lusseyran · L. Pastur
Laboratoire d'Informatique pour la Mécanique et les
Sciences de l'Ingénieur, Unité Propre de Recherche 3251,
Centre National de la Recherche Scientifique,
B.P. 133, 91403 Orsay Cedex, France
e-mail: thierry.faure@limsi.fr

T. M. Faure · P. Adrianos
Université Pierre et Marie Curie, Paris 6,
4 place Jussieu, 75252 Paris Cedex 05, France

L. Pastur
Université Paris-Sud, Paris 11, 91405 Orsay Cedex, France

1 Introduction

A boundary layer interacting with a cavity is a benchmark case for environmental applications (airflow in a canyon street), aeronautics (landing gear cavities, bomb holds), automobile aerodynamics (interaction between the flow and an air inlet or an opening roof...) or industrial applications (structural discontinuities) where the velocity over a rectangular cavity is relatively low. The dynamical behavior of the vortices inside the cavity is unsteady and shows small as well as large vortex structures and it can be thought that it is mainly driven by the boundary shear layer. On the one hand, full information has been provided on the rectangular cavity configuration for high velocities with compressible effect. On the other hand, very low

velocity and Stokes flows in the Reynolds number range 50–1,600 were studied for the removal of a contaminated fluid inside the cavity (Fang et al. 1999). However, the dynamics of the boundary between the external flow and the cavity behaves in a different way for moderate Reynolds numbers (1,150–10,670), and few publications are available in that case. For this Reynolds number range the interaction between a turbulent boundary layer and a cavity was explored with particle image velocimetry measurements in water tunnel (Lin and Rockwell 2001) for a maximum Reynolds number of 11,000, and for a Reynolds number of 10,000 with a horizontal top plate above the end of the cavity (Kuo and Chang 1998). A local periodic excitation was applied at the beginning of the cavity to understand its coupling with the shear layer dynamics (Kuo and Jeng 2003). The flow developing in a series of canyon streets has been investigated recently (Chang and Meroney 2003a, b; Dezsö-Weidinger 2003).

General features of the dynamics can be depicted as follows. Viscous diffusion between the external and cavity flow generates a region with steep gradients of streamwise velocity concentrating most of the vorticity (Huerre and Rossi 1998). This organized vorticity is impinging on the downstream cavity wall, creating an acoustic feedback loop for high velocity configurations (Rockwell 1983). Many studies concerning the sound generation of the interaction between a flow and a cavity have been conducted (Rockwell and Naudascher 1978; Komerath et al. 1987; Howe 2003). The first model of the radiated acoustic waves was established on experimental results for Mach numbers greater than 0.4 (Rossiter 1964). An improved analytical model of the discrete frequency oscillations was established over the Mach number range $0.8 \leq M \leq 3$, without empirical constants (Bilanin and Covert 1973). It was suggested that the simultaneous excitation of two or more discrete frequencies which are not harmonics corresponds to the simultaneous participation of two or more vortex sheet displacement modes. A simple analytical model, where no vortex shedding is observed, describes the features of pressure fluctuations (Heller and Bliss 1975). A mathematical model based on the coupling of the shear layer instabilities with the acoustic feedback was developed considering the shear layer thickness (Tam and Block 1978).

One of the first experimental descriptions devoted to the mixing layer over a deep cavity for a compressible subsonic flow has been investigated by Forestier et al. (2003), where coherent vortices were established in the shear layer. The acoustic tones due to the feedback mechanism were consistent with the Rossiter formulation. A large-eddy simulation was

conducted for the same configuration, with a time-frequency analysis showing a temporal modulation of the Rossiter mode levels, resulting in a special form of intermittency with competitive energy exchanges between modes (Larchevêque et al. 2004). A mode beating phenomenon has been reported for a supersonic flow (Kegerise et al. 2004). In that case, it is known that acoustic waves couple to the hydrodynamic field so as to close the feedback loop. Direct numerical simulations showed a transition from a shear-layer mode for shorter cavities and lower Mach numbers, to a wake mode, for longer cavities and higher Mach numbers (Rowley et al. 2002). Pressure fluctuations were also measured in the transonic regime (Chung 2001). Schlieren images and acoustic pressure measurements have been obtained for a supersonic flow over a cavity with length to height ratio varying in the range 0.25–6.25 (Umesh Chandra and Chakravarthy 2005).

The moderate Reynolds number range was investigated recently with acoustic and velocity measurements (Chatellier et al. 2004). A linearized stability analysis has modelled the interface of the cavity with a vorticity layer. For the same velocity range, the influence of the upstream laminar or turbulent boundary layer was studied (Grace et al. 2004). Flow oscillations on an axisymmetric cavity drag were studied for low velocities inside a water tunnel (Gharib and Roshko 1987). The cavity height is found to have little influence on the oscillations as far as it is not the same order in magnitude as the upstream boundary layer thickness (Sarohia 1977).

For the same Reynolds number range, flow dynamics studies have been achieved on lid-driven cavities: the difference with the present case is the absence of a freely developing shear layer. Ghia et al. (1982) used a multi-grid method to simulate the flow inside a square lid-driven cavity, where a main vortex is developing along the whole length. Visualizations have been conducted by Koseff and Street (1984) with dye emission, with tiny particle seeding (Migeon 2002; Migeon et al. 2003) and comparisons with numerical simulations were carried out for the same measurements (Guermond et al. 2002).

This short analysis of the flow in an open cavity reveals the diversity of the approaches. A synthesis is obviously not yet of topicality. The present study relates to an aspect not well documented in the literature, that of transverse instabilities. The 3-D features of the flow are not responsible for the strong frequency modes, which is the reason why this approach has not been much studied. However, at moderate flow rates, transverse modulation of the swirl, strongly conditions

the exchanges between the cavity and the main flow. The present study focuses on flow visualizations on moderate Reynolds number range varying the length over height ratio of the shear-layer driven cavity. The aim is to address the following issues:

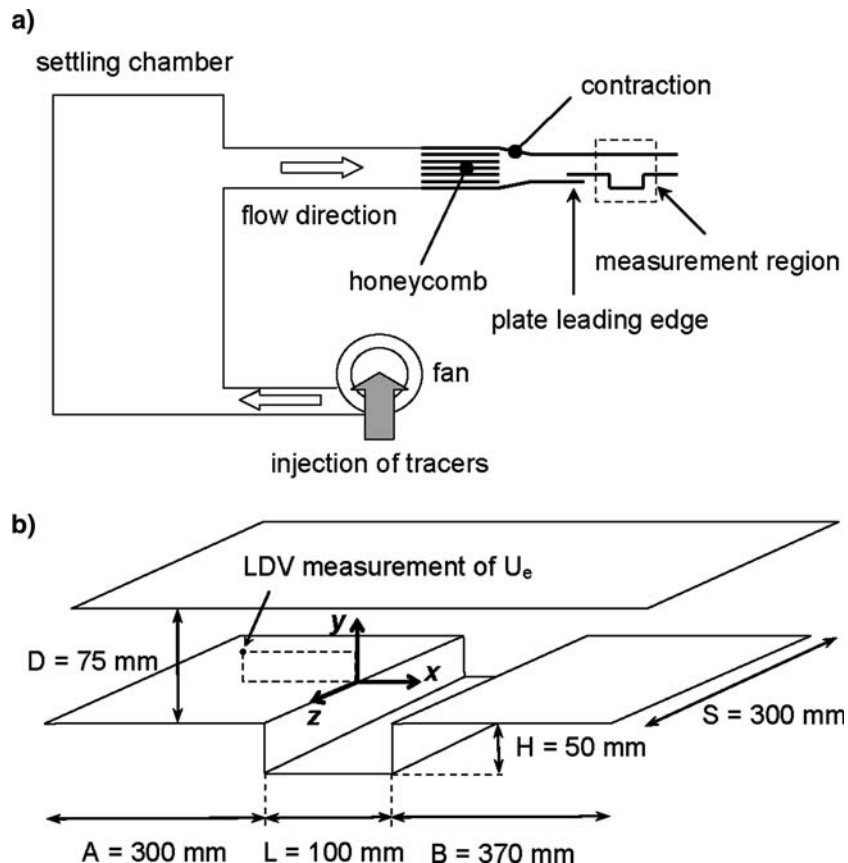
- Give the flow morphology with cavity aspect ratio and Reynolds number.
- Track the 2-D or 3-D spatial nature of the flow.
- Provide the time development of the flow features.
- Analyze whether the 3-D flow development in the cavity is caused by secondary shear layer instabilities.

2 Experimental set-up and apparatus

The airflow is generated by a centrifugal fan placed upstream of a settling chamber (Fig. 1a). The seeding particle injection is achieved by the fan inlet. An axial duct terminated with honeycomb and a contraction drives the flow toward the experimental facility, which consists of a test section containing a flat plate beginning with an elliptical leading edge, in order to fix the boundary layer origin. The length of the plate is $A = 300$ mm providing an established laminar bound-

ary layer. To reduce light wall reflections, the whole test section is made of antireflection glass 2 mm in thickness. The cavity height is fixed to $H = 50$ mm and its span is $S = 300$ mm (Fig. 1b), the cavity ends in the span direction are the wind tunnel vertical walls. The cavity aspect ratio $R = L/H$ (length over height) is studied from 0.5 to 2 by step of 0.5 by moving the glass pieces consisting in the downstream wall of the cavity and the downstream plate which has a length $B = 370$ mm. At the wind tunnel outlet, the flow is rejected inside the experimental room. The Reynolds number, determined with the cavity length L and the upstream boundary layer external velocity U_e , varies from 1,150 to 10,670, corresponding to external velocities from 0.69 to 1.60 m/s. The external velocity is measured with laser Doppler velocimetry 102 mm upstream the cavity and 25.5 mm above the flat plate. This point of measurement is in the external flow sufficiently upstream of the cavity to avoid any perturbation from the instability developing above the cavity. The origin of the coordinate system is set at the upstream edge of the cavity at mid span, the x axis is the flow direction, the y axis is normal to the upstream wall where the boundary layer develops and the z axis is along the cavity span. It has been checked that the test

Fig. 1 Experimental set-up:
a wind tunnel, **b** test section dimensions for $R = 2$ and coordinate system



section wall, located at $D = 75$ mm above the cavity, has no influence on the shear layer developing on the cavity. The thickness of the boundary layer developing on this wall is less than 10 mm and has no influence on the external flow along the longitudinal and spanwise directions. It has been shown for backward facing step flows that the influence of the upper wall affects the flow from 10 cavity heights downstream of the beginning of the step. The cavity under investigation is not a shallow cavity ($L/D > 5$), where the shear layer tends to attach the cavity floor (Geveci et al. 2003). However, in that configuration, the development and propagation of the large-scale vortices appear to be relatively unaffected by confinement effects. In the present study, it will be even more so given the maximum aspect ratio of 2.

Hereafter, the expressions “upstream” and “downstream” will refer to the external velocity direction. As smoke is used, the observed structures are emission lines of fluid injection inside the cavity and not the streamlines themselves. However, the flow injection inside the cavity gives information on the flow dynamics and the developing structures. Flow visualizations are carried out in different observation directions. The first configuration consists of two parallel planes (Fig. 2a). The light source is a 5 W argon-ion laser tuned to the blue (488 nm) and green (514.5 nm) wavelengths. The laser beams provide, by passing through cylindrical lenses, laser sheets which thickness

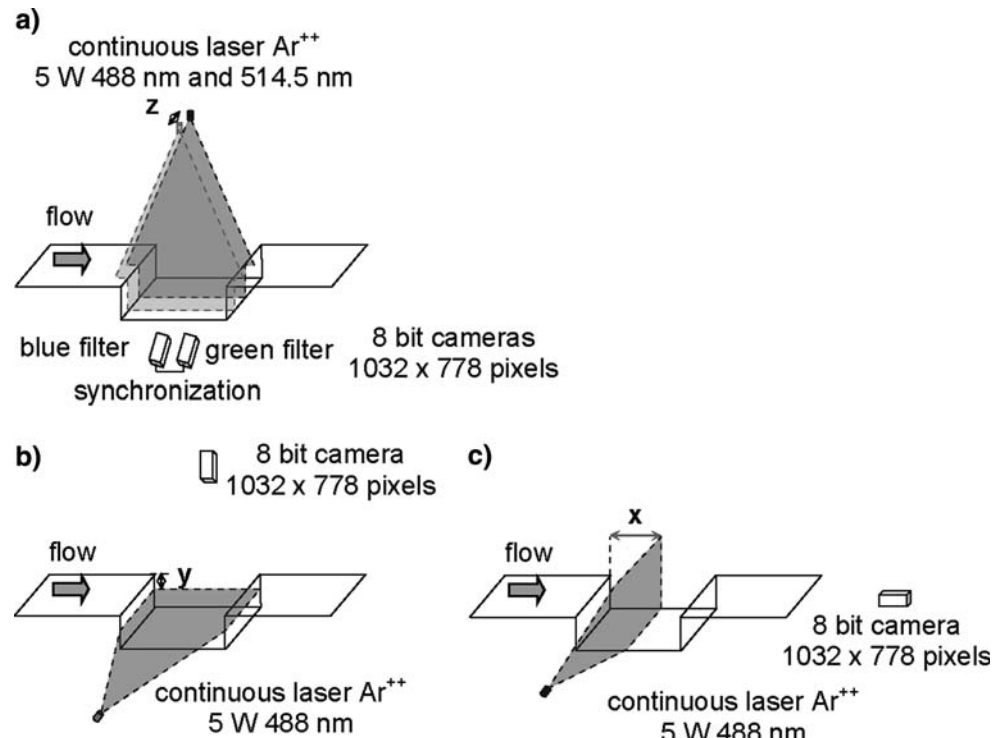
is 0.25 mm. The blue laser sheet is settled in the middle of the span of the cavity ($z = 0$), the green one being moved along the span ($z = 30$ mm). A light trap is placed under the test section to remove any light scattering by the floor. The image recording system consists of two synchronized 8-bit cameras with $1,032 \times 778$ pixels and a frequency of 20 Hz. In order to make out only one wavelength by camera, two pass-band filters of appropriate frequencies are placed in front of the cameras. The magnification is the same for the two cameras, each one having a complete view of inside the cavity. Flow seeding is provided by a fog created with a low density smoke generator Starway Puffer One.

The second configuration visualizes a horizontal plane inside the cavity and uses the same system, with only one camera and the blue laser wavelength (Fig. 2b). The laser sheet position is counted from the upstream flat plate ($y = -15$ mm).

The third configuration provides observation in a transverse plane from downstream (Fig. 2c). The laser position x is taken from the upstream cavity edge, and set to the middle of cavity length ($x = L/2$).

The repeatability of flow visualizations has been checked by recording different image series with different wind tunnel runs, and by testing different smoke injections. The following section will present the flow dynamics in the three observation planes for each cavity aspect ratio considered. The external flow is

Fig. 2 Visualization planes:
a two parallel vertical planes,
b horizontal plane and
c transverse plane



established and uniformly seeded with smoke when the images are recorded. Note that if the observation time is too long, there is a saturation of the cavity with smoke and no dynamical flow structure can be identified anymore.

3 Results

3.1 Aspect ratio $R = 2$

In the following figures, the view observed in the blue laser sheet, which is fixed in the middle span of the cavity ($z = 0$), is always presented on the left while the view observed in the green laser sheet ($z = 30$ mm) is on the right. The external flow direction is from left to right.

The best parameter to compare different flows could be the Reynolds number. However, the two space scales of the cavity (L and H) make the reduction of the flow properties impossible. Therefore, to provide a good understanding of the flow development with the velocity and aspect ratio, we have chosen to set a velocity and to vary the aspect ratio. Hereafter, the external velocity and Reynolds number are both provided in each figure caption.

Figure 3a shows the cavity flow for $U_e = 0.69$ m/s where the development and the oscillations of the shear layer are clearly identified by the boundary between the external flow, with a high smoke density and light levels, and the cavity flow with low smoke density and dark levels. The interaction between the shear layer and the downstream cavity edge leads to seeding injection inside the cavity that is not continuous, because of the shear layer oscillations. Note that the smoke pattern of the shear layer interaction with the downstream edge is similar in the two observation planes, which is evidence that this phenomenon could be 2-D. The seeding is advected inside the cavity as a mushroom like pattern. This pattern comes from the injection of the external flow inside the cavity. It originates from the shear layer oscillation near the downstream edge of the cavity and is similar to a jet pulsed flow. These successive patterns are advected inside a main vortex, which is filling the downstream part of the cavity. This vortex is developing in time and space, as it can be seen comparing its axial dimension between the middle cross-plane at $z = 0$ (Fig. 3a, left) and the plane situated at $z = 30$ mm (Fig. 3a, right) at the same time. The observation of the time records leads to the following comments. The vortex longitudinal modulation induces deformations of the patterns, which keep their coherence inside the vortex motion

on a complete cycle. The interaction of the main vortex with the upstream part of the fluid inside the cavity creates a secondary counter-rotating vortex, which dimension is confined between the main vortex and the upstream cavity edge. This structure is highly time-dependant regarding the main vortex extension. The rotation of the two eddies generates an induced flow between them, confined by the cavity upstream wall and the shear layer. This induced flow has nowhere to develop except in the spanwise direction, leading to a transverse flow. Spanwise flows may exist inside the vortices cores, but are not clearly identified because of the lack of seeding.

Figure 3b is the same view of the flow for $U_e = 1.21$ m/s. The same dynamics is found, but for this time and $z = 30$ mm (Fig. 3b, right), the main vortex extension reaches the upstream edge, while the secondary vortex is limited to the bottom of the upstream edge. However, the seeding patterns are still well defined. A small counter-rotating secondary vortex is also identified at the bottom of the downstream wall corner.

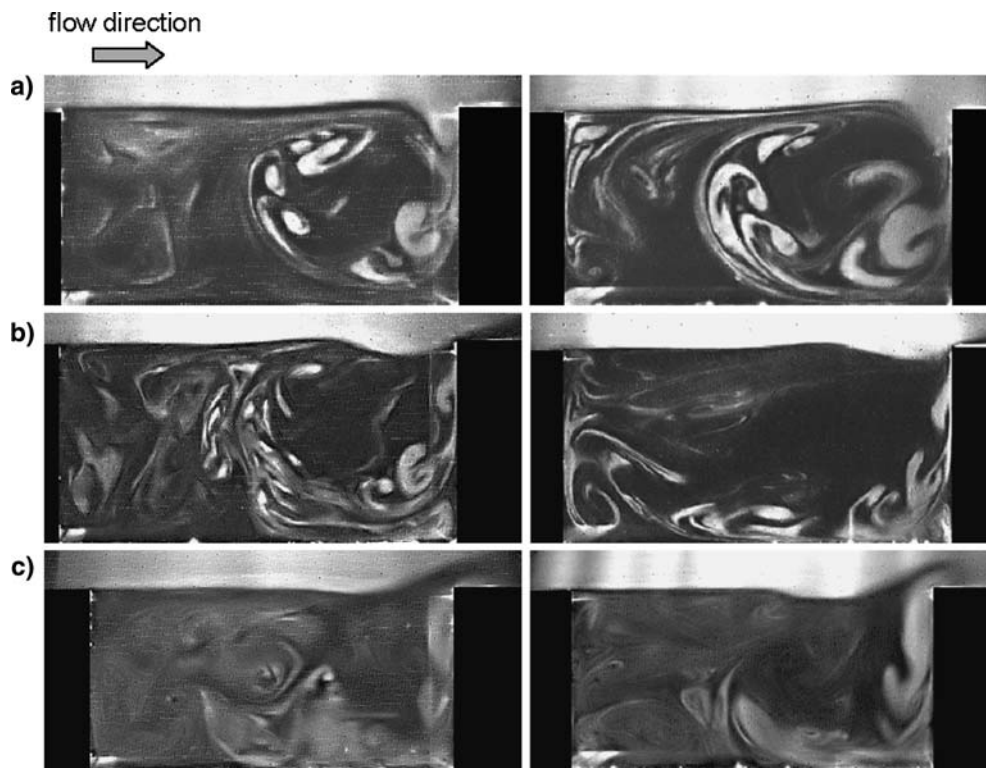
Figure 3c presents the flow for $U_e = 1.60$ m/s with the same dynamics. Comparing this visualization with what is obtained for lower velocities (the right and left image in Fig. 3a, b, taken for the same time), note the fast smoke diffusion inside the cavity, reflected as a fog, caused by a higher turbulence level.

The axial extension of the main vortex fluctuates, leading to an alternated occupation of the upstream half of the cavity by the main or the secondary vortex. The fact that for two values of U_e and $z = 0$ (Fig. 3a, b, left) the main vortex takes up the downstream half of the cavity is fortuitous. Following in time this alternated occupation reveals that the spanwise modulation of these two vortices is not stationary.

In the top view plane shown in Fig. 4, the external flow is coming from the bottom of the figure. Figure 4 depicts the flow for $U_e = 1.21$ m/s and $y = -15$ mm below the flat plate inside the cavity, for four successive times. The image centering shows the whole cavity span. The two vertical white lines are the vertical visualization planes for $z = 0$ and $z = 30$ mm. The almost uniform white smoke strip at the downstream edge existing for time $t_0 + 0.1$ s (Fig. 4) is the smoke injection inside the cavity which confirms that it is mainly 2-D, except maybe near the span edges of the wind tunnel. The seeded parts of the cavity show patterns moving towards the top of the image (in the external flow direction), for the upper two third of the image, corresponding to the motion of the upper part of the main vortex. The spanwise modulation of this vortex is strongly time-dependant providing the presence of an unsteady flow inside the whole cavity. In the

Fig. 3 Visualization in two parallel vertical planes (*left*: $z = 0$, *right*: $z = 30 \text{ mm}$) for the same time and $R = 2$.

- a $U_e = 0.69 \text{ m/s}$ ($Re = 4,600$)
- b $U_e = 1.21 \text{ m/s}$ ($Re = 8,070$)
- c $U_e = 1.60 \text{ m/s}$ ($Re = 10,670$)



lower third of the image, smoke clusters are moving to the bottom, which indicates the motion of the secondary vortex. Destabilized pairs of unsteady counter-rotating vortices are also identified. In addition there is a spanwise flow near the upstream edge, resulting in the interaction of the fluid motion induced by the two vortices which is confined by the cavity edge and the shear layer, and forced to a lateral motion. As a result, the cavity flow looks fully 3-D.

For visualizations in the transverse plane, located in the middle of the cavity length (Fig. 5), the external flow is orthogonal to the figure pointing toward the reader. The view in this transverse plane shows the whole cavity span. The central white strip is a shadow zone where there is a reflection of the inner cavity flow: it is caused by the flow observation through the downstream flat glass plate, and has been removed in the image for clarity. First, we can notice, in the upper part of the image, the uniform smoke density of the laminar external flow, with the pattern of the honeycomb that is placed upstream of the wind tunnel contraction. The top and the bottom of the cavity are seeded while there is little smoke in the center: this corresponds to the main vortex motion. The lace-like pattern of the seeded regions indicates the deformation of the smoke lines injected uniformly along the span, caused by the main vortex motion inside the cavity. It reveals the main vortex motion of the 3-D flow

development. These spanwise structures in the lower part of Fig. 4 might also be thought as Görtler-like vortices, but they are very unsteady and it is difficult to measure a wavelength. Moreover these structures are rapidly and repeatedly destroyed by the relatively high turbulence level inside the cavity.

Figure 6 sketches the flow dynamical structures for $R = 2$, with the external flow, the shear layer boundary which interacts with the downstream edge, the main vortex with a counter-rotating corner vortex, the secondary vortex, the flow induced by the vortices interaction and the resulting spanwise flow. In the central part of the span, the development of the shear layer and its interaction with the downstream wall are mostly 2-D but the flow is destabilized inside the cavity and gets 3-D features.

3.2 Aspect ratio $R = 1.5$

Similar analysis is achieved for aspect ratio $R = 1.5$. Figure 7a depicts, for $U_e = 0.69 \text{ m/s}$ the shear layer injection inside the cavity with smoke volutes advected inside the main vortex. Note for this velocity the very low smoke diffusion inside the cavity resulting in well defined marks for the injection patterns, which is an evidence of a lower turbulence level than for $R = 2$. The 3-D character of the fluid motion is observed by the differences between the two planes. The same flow

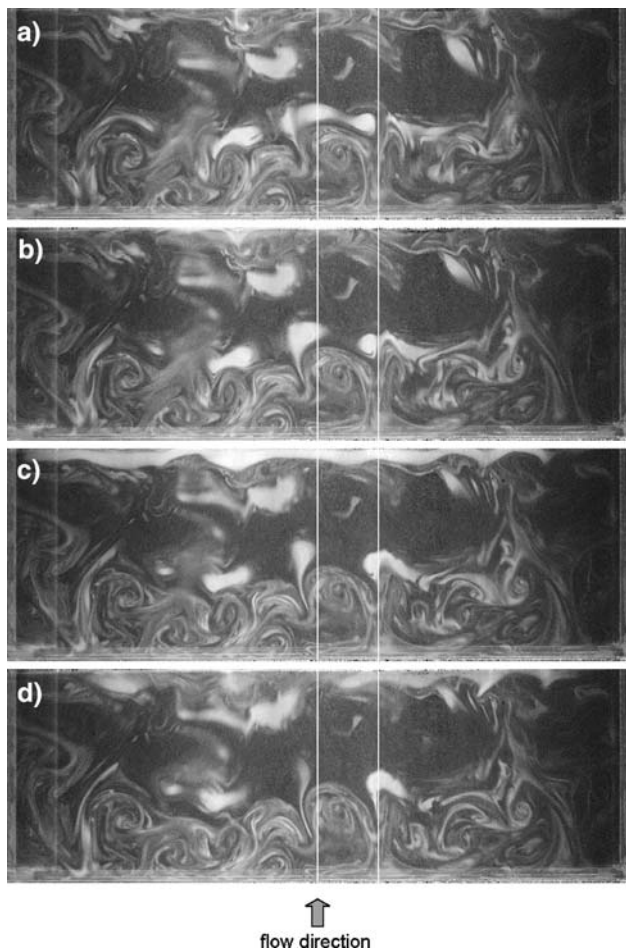


Fig. 4 Visualization in a horizontal plane for $R = 2$, $U_e = 1.21$ m/s ($Re = 8,070$) and $y = -15$ mm. **a** Time t_0 , **b** time $t_0 + 0.05$ s, **c** time $t_0 + 0.1$ s, **d** time $t_0 + 0.15$ s

structure is found as for $R = 2$ with a main downstream vortex and a second counter-rotating upstream vortex. This secondary vortex is smaller than for $R = 2$ and is limited to the lower part of the cavity as it can be seen in the plane of visualization for $z = 30$ mm (Fig. 7, left) while the main vortex extension reaches, in the central plane ($z = 0$ mm), the upstream cavity wall. The mushroom-like patterns are less marked than for $R = 2$, this may be due to a lower momentum of flow injection inside the cavity.

Fig. 5 Visualization in a transverse plane for $R = 2$, $U_e = 1.21$ m/s ($Re = 8,070$) and $x = L/2$

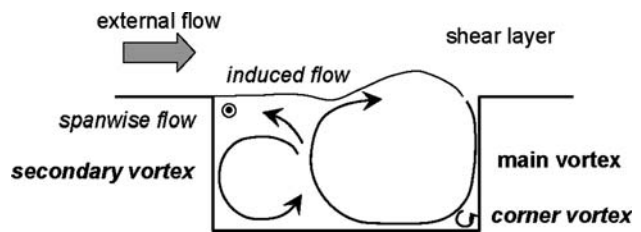
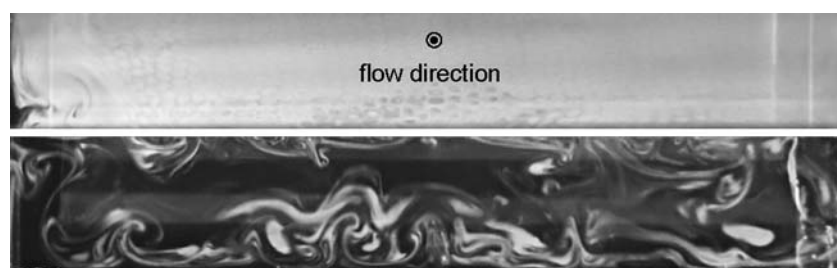


Fig. 6 Sketch of the cavity flow dynamics for $R = 2$

Figure 7b is the same view for $U_e = 1.21$ m/s. The same dynamics is found, but the smoke diffusion inside the main vortex is stronger and the volutes of seeding injection inside the cavity cannot be identified. Note at this particular time the secondary vortex extension limited to a corner in the central plane (Fig. 7b, left), while it is spreading in height in the second plane (Fig. 7b, right).

A similar behavior is observed for $U_e = 1.60$ m/s (Fig. 7c).

The flow visualizations in the horizontal plane are shown in Fig. 8, where the two white lines are the vertical visualization planes for $z = 0$ and $z = 30$ mm. The pairs of counter-rotating vortices are steadier than for $R = 2$ and are aligned along the upstream cavity wall. Flattened features are also present near the downstream cavity wall with the same spanwise periodicity. The central part of the flow is marked by a transverse flow from the span ends toward the centerline. The increase of the external velocity acts only on smoke diffusion and on the stability of the vortices.

Figure 9 is a sketch of the flow for $R = 1.5$, very similar to the vortices morphology found for $R = 2$.

3.3 Aspect ratio $R = 1$

For $R = 1$ the flow is only driven by one main vortex, spreading along the cavity length and height and induced by the shear layer oscillations which are lower than for the aspect ratios previously exposed (Fig. 10a). Two corner vortices are present at the bottom of the cavity as previously observed in a lid-driven cavity for a similar range of Reynolds numbers

Fig. 7 Visualization in two parallel vertical planes (left: $z = 0$, right: $z = 30 \text{ mm}$) for the same time and $R = 1.5$

- a $U_e = 0.69 \text{ m/s} (Re = 3,450)$
- b $U_e = 1.21 \text{ m/s} (Re = 6,050)$
- c $U_e = 1.60 \text{ m/s} (Re = 8,000)$

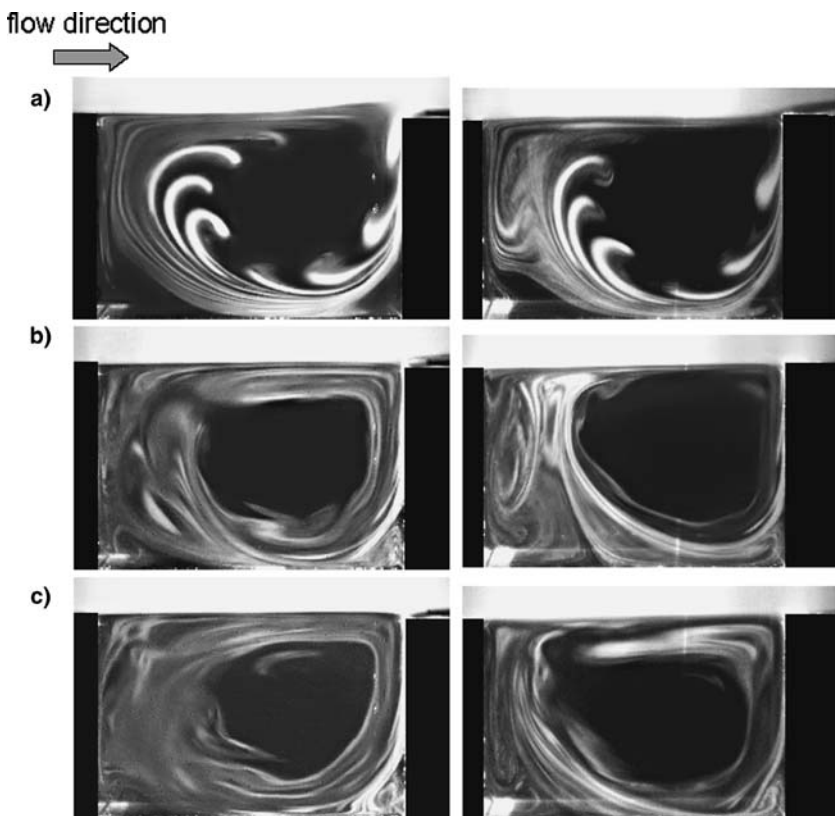
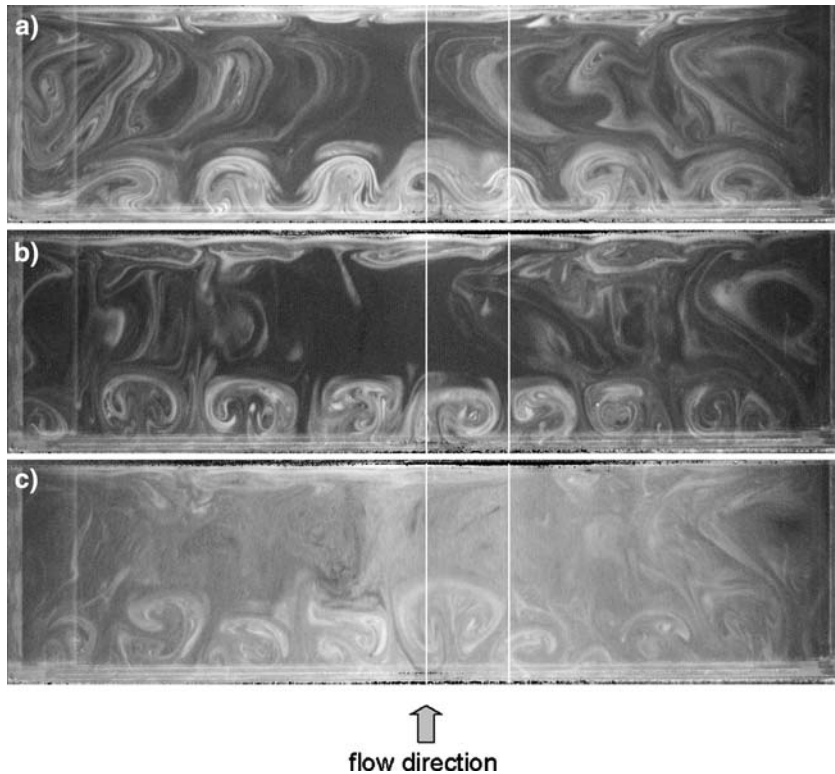


Fig. 8 Visualization in a horizontal plane for $R = 1.5$ and $y = -15 \text{ mm}$.

- a $U_e = 0.69 \text{ m/s} (Re = 3,450)$
- b $U_e = 1.21 \text{ m/s} (Re = 6,050)$
- c $U_e = 1.60 \text{ m/s} (Re = 8,000)$



(Koseff and Street 1984). It appears that the upstream corner vortex is the development, for $R = 1$, of the secondary vortex existing for $R = 2$ and 1.5. As the

main vortex, containing most of the flow energy, occupies the entire cavity length, there is no room for the counter-rotating eddy to develop, except in a

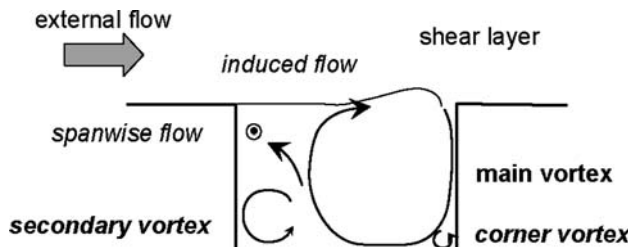


Fig. 9 Sketch of the cavity flow dynamics for $R = 1.5$

corner. Whatever the velocity is, the 3-D seems to be comparable (Fig. 10a–c). Moreover, the spanwise development in those two planes is not observable. The stretching is stronger with higher velocities as it can be seen by the alteration of the injection pattern into a sliced pattern.

Fig. 10 Visualization in two parallel vertical planes (*left*: $z = 0$, *right*: $z = 30$ mm) for the same time and $R = 1$.
a $U_e = 0.69$ m/s ($Re = 2,300$)
b $U_e = 1.21$ m/s ($Re = 4,030$)
c $U_e = 1.60$ m/s ($Re = 5,330$)

The views of the flow inside a horizontal plane are shown in Fig. 11. The white lines are the vertical visualization planes for $z = 0$ and $z = 30$ mm (Fig. 11a–c). Note for $U_e = 0.69$ m/s (Fig. 11) that there is no undulated streamline flow pattern as it was found inside a square lid-driven cavity for almost the same Reynolds number (Migeon 2002). For $U_e \geq 1.21$ m/s, mushroom-like counter-rotating cells are observed at the bottom of the cavity near the upstream wall (Fig. 11b, c). Their transverse positioning in pairs is suggesting a development of Görtler vortices. Their origin can be related to the flow curvature induced by the main cavity vortex, which spreads over the entire cavity length and height. There is another structure, symmetric to each mushroom-like structure, located at the downstream cavity wall which can be understood as the same pattern, structured into a

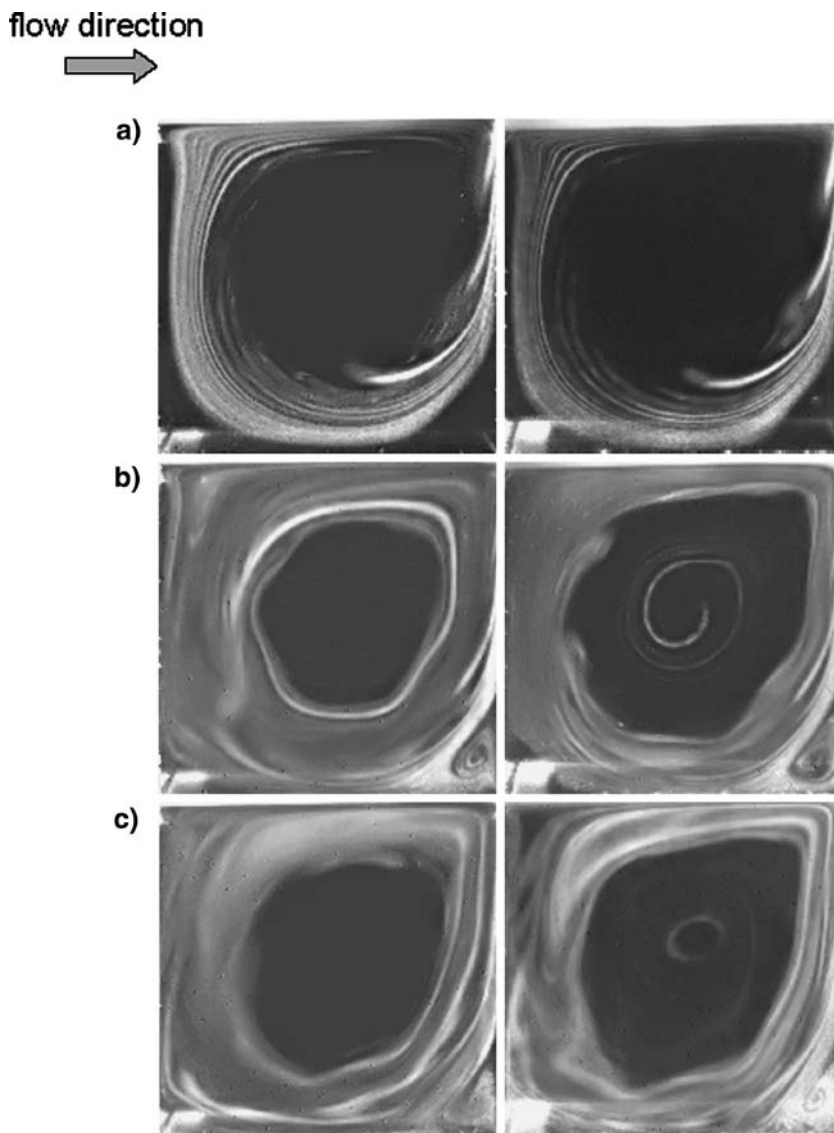
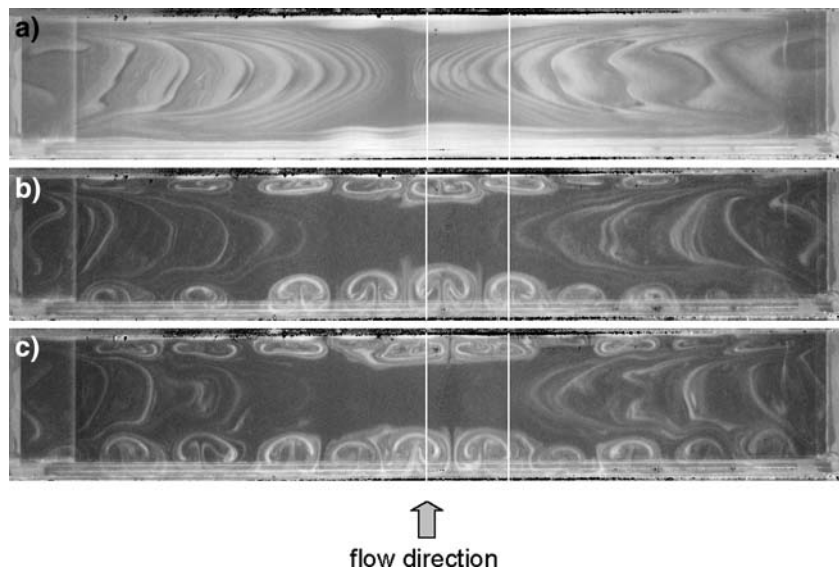


Fig. 11 Visualization in a horizontal plane for $R = 1$ and $y = -15$ mm.
a $U_e = 0.69$ m/s ($Re = 2,300$).
b $U_e = 1.21$ m/s ($Re = 4,030$).
c $U_e = 1.60$ m/s ($Re = 5,330$)



closed loop around the main vortex that would be cut by the laser plane. Note that the downstream part of the structure is much more flattened because of the shear layer injection inside the cavity. These vortices are not identified for velocity below $U_e = 1.21$ m/s. The inner part of the cavity shows a spanwise flow, coming from the cavity sides toward the centerline. The view in a transverse plane (Fig. 12) also exhibits these mushroom-like vortex patterns.

Figure 13 is a sketch of the flow for $R = 1$. The secondary vortex is nothing else but a corner vortex limited to the upstream wall bottom. Görtler-like vortices are present and the turbulence level is similar to what was observed on the tracer lines diffusion for $R = 1.5$. As the shear layer oscillations have little influence, the cavity flow is much similar to a lid-driven cavity flow (Koseff and Street 1984; Migeon 2002). Section 4 will come back to a deeper discussion of the Görtler-like vortices properties.

3.4 Aspect ratio $R = 0.5$

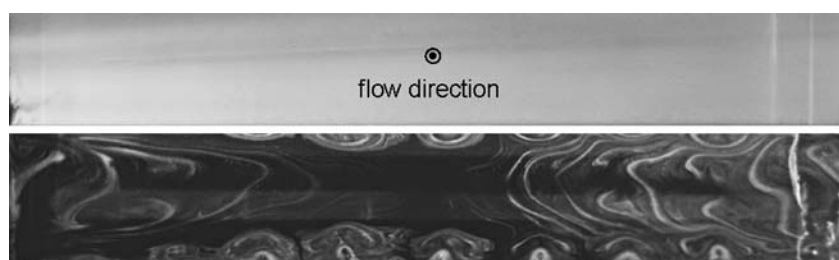
The flow dynamics drastically changes for $R = 0.5$. The seeding of the cavity by the external flow is very low and the injection volutes keep their consistence inside

the cavity. The flow is purely laminar as there is no diffusion of the flow patterns. For $U_e = 0.69$ m/s (Fig. 14a), there is a vortex in the upper half of the cavity and no lower vortex is identified. This may be due to the absence of seeding or to the presence of a spanwise flow developing in the lower cavity half. For higher velocities (Fig. 14b, c), two counter-rotating vortices are developing along the cavity height. In fact, the lower vortex is seeded by the shear layer injection, and develops a spiraling pattern, while the upper vortex seeding is mainly provided by smoke diffusion. A spanwise flow may exist inside the vortices cores but is not clearly identified because of the lack of seeding.

The two white lines are the vertical visualization planes for $z = 0$ and $z = 30$ mm (Fig. 15). There is no more Görtler vortices generation (Figs. 15 and 16) but a slow diffusive-type spanwise motion. In the lower part of the cavity (Fig. 16), the span modulation of the smoke lines shows the transverse oscillation of the lower cavity vortex, and the associated core spanwise flow.

Figure 17 sketches the flow for $R = 0.5$. For the low velocities, there is a vortex limited to the upper half of the height, with no lower vortex or a spanwise flow below. For the higher velocities, there is a stack of two

Fig. 12 Visualization in a transverse plane for $R = 1$, $U_e = 1.21$ m/s ($Re = 4,030$) and $x = L/2$



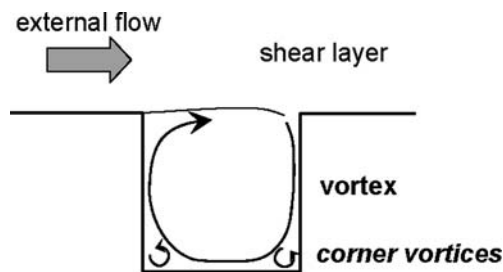


Fig. 13 Sketch of the cavity flow dynamics for $R = 1$

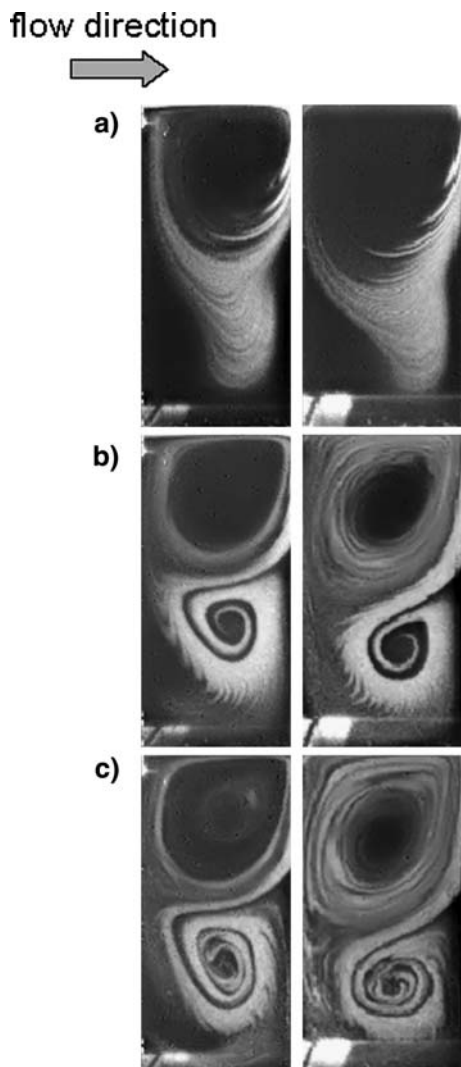


Fig. 14 Visualization in two parallel vertical planes (left: $z = 0$, right: $z = 30 \text{ mm}$) for the same time and $R = 0.5$. **a** $U_e = 0.69 \text{ m/s}$ ($Re = 1,150$). **b** $U_e = 1.21 \text{ m/s}$ ($Re = 2,020$). **c** $U_e = 1.60 \text{ m/s}$ ($Re = 2,670$)

counter-rotating vortices. This behavior is alike the flow inside a lid-driven cavity, with no much influence of the shear layer dynamics.

4 Görtler vortices

The longitudinal vortices developing on a concave wall are subject to a linear stability mechanism as suggested by H. Görtler in Gottingen in 1940. The transverse positioning in pairs of the counter-rotating mushroom-like cells observed at the bottom of the cavity near the upstream wall for $R = 1$ and 1.5 (Figs. 11b, c and 8) is suggesting a development of Görtler-like vortices. In the present case, the flow curvature is caused by the main vortex. That hypothesis is consistent with quantitative results on the spanwise primary instability (Swearingen 1987). The Görtler number, defined from the curvature radius r_c , the kinematics viscosity of the fluid ν and the velocity inside the cavity U_c developing away from the boundary layer of momentum thickness δ_2 is:

$$Gö = \frac{U_c \delta_2}{\nu} \left(\frac{\delta_2}{r_c} \right)^{1/2}.$$

The dimensionless coefficient λ is built from the transverse wavelength λ , measured as the distance between a pair of two vortices:

$$\Lambda = \frac{U_c r_c}{\lambda} \left(\frac{\lambda}{r_c} \right)^{3/2}.$$

The wave number k is defined as:

$$k = \frac{2\pi}{\lambda}.$$

It is associated with the wavelength λ to get a dimensionless wave number $k\delta_2$. This is leading to the Görtler number expression:

$$Gö = \frac{\Lambda}{(2\pi)^{3/2}} (k\delta_2)^{3/2}.$$

For $R = 1$ the orders of magnitude can be estimated from flow visualizations. The wavelength λ is the distance between two pairs of structures measured in Fig. 11b, U_c is an estimate of the main vortex convection velocity inside the cavity and δ is an estimate of the boundary layer thickness inside the cavity determined from the displacement of a smoke mark in two successive images in a vertical plane, and r_c is the radius of curvature of the main vortex. The kinematics viscosity for the air is $\nu = 15 \times 10^{-6} \text{ m}^2/\text{s}$. The flow inside the cavity is laminar, the maximum Reynolds number calculated with the velocity U_c is 370, and, from the Blasius theory, the momentum thickness δ_2 is calculated from the relationship $\delta_2 = \delta/7.4$ with δ the

Fig. 15 Visualization in a horizontal plane for $R = 0.5$, $U_e = 1.21 \text{ m/s}$ ($Re = 2,020$) and $y = -15 \text{ mm}$

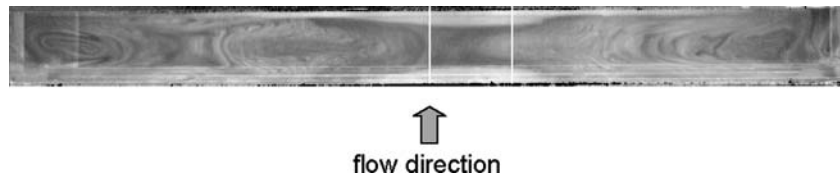
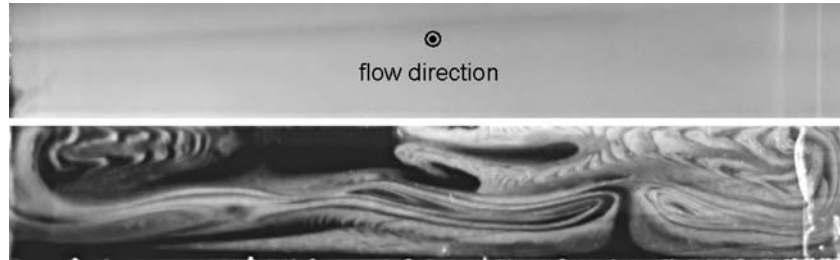


Fig. 16 Visualization in a transverse plane for $R = 0.5$, $U_e = 1.21 \text{ m/s}$ ($Re = 2,020$) and $x = L/2$



boundary layer thickness inside the cavity obtained from views in parallel planes. The measured data are presented in Table 1. Reporting the Görtler number versus the dimensionless wave number $k\delta_2$ on the stability diagram (Fig. 18) we observe a good agreement between our estimates and previous measurements. The experimental points, for a particular measurement, establish lines of constant slope 3/2, along which the non-dimensional wavelength is constant. Comparison is made with the neutral stability curves of Floryan and Saric (1982) and Hall (1983). Note that the present investigation has been obtained for much smaller curvature radii and velocities than the other ones (Tani 1962; Bippes 1972; Winoto and Crane 1980).

Now let us discuss some features of the Görtler-like vortices, postponing a more detailed analysis of their properties to a further work. First of all, it must be noticed that such longitudinal vortices are the most robust when only one main vortex exists within the cavity. Indeed, as soon as the secondary vortex appears, the Görtler-like vortices are stretched and dislocate. This is suggesting that the cavity aspect ratio range of their existence should be narrow around $R = 1$. For $R = 1$, the spanwise structures in the lower

part of Fig. 4 must be thought as Görtler-like vortices, but they are very unsteady and it is difficult to measure a wavelength. Moreover these structures are continuously destroyed by the relatively high turbulence level inside the cavity.

Another interesting feature lays in the fact that the Görtler-like vortices raw, as seen in Figs. 11b, c and 12, is not stationary. To quantify their dynamical properties, we have plotted in Figs. 20 and 21, space–time diagrams of the pattern. Space–time diagrams are made by stacking over each other in Fig. 20b–d (respectively, in Fig. 21b–d) the single white line plotted in Fig. 20a (respectively, in Fig. 21a), at different successive times. These images are recorded in time with the set-up detailed in Fig. 2b. Time delay between two such lines is 50 ms. Total recording time along the vertical axis is 25 s. Time is passing from the bottom to the top, while the horizontal axis is the transverse z direction. The gray level in the diagrams corresponds to intensity variations along the extracted horizontal line. On such diagrams, vertical lines are associated to stationary events, while oblique lines are associated to traveling patterns. If oblique lines are moreover straight lines, it means that the pattern is traveling at a constant velocity $c = \Delta y/\Delta t$. Figure 20

Fig. 17 Sketch of the cavity flow dynamics for $R = 0.5$. **a** for $U_e = 0.69 \text{ m/s}$ ($Re = 1,150$), **b** for $U_e = 1.21 \text{ m/s}$ ($Re = 2,020$) and $U_e = 1.60 \text{ m/s}$ ($Re = 2,670$)

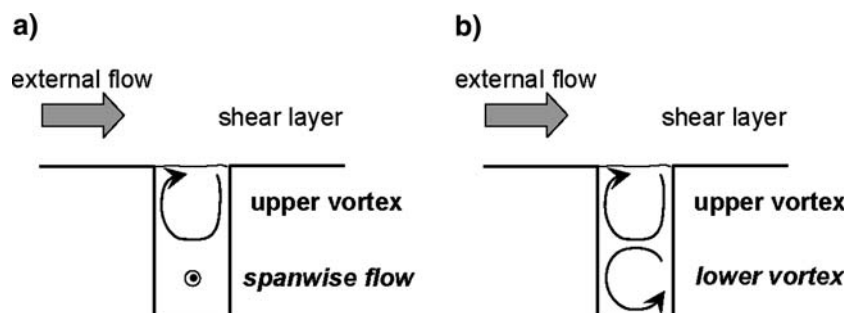


Table 1 Parameters for the calculation of the Görtler number and the dimensionless wave number for $R = 1$

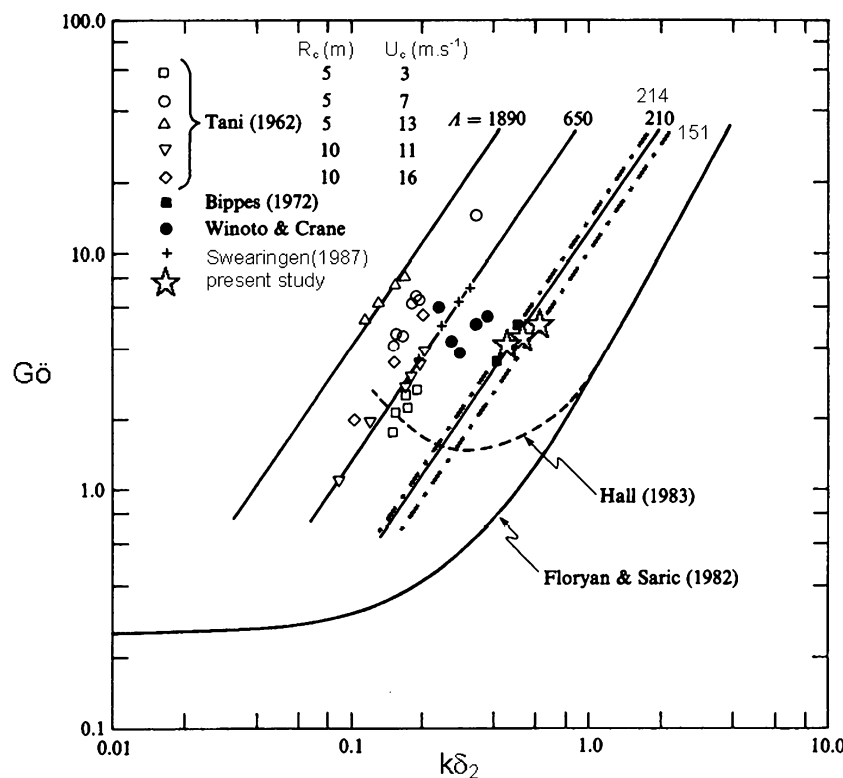
U_e (m/s)	λ (10^{-2} m)	U_c (m/s)	r_c (10^{-2} m)	δ (10^{-2} m)	δ_2 (10^{-3} m)	$Gö$ (-)	Λ (-)	$k \delta_2$ (-)
1.21	2.95	0.1	2.5	1.5	2.03	3.85	214	0.456
1.6	2.6	0.105	2.5	1.5	2.03	4.04	186	0.517
2.09	2.2	0.11	2.5	1.5	2.03	4.23	151	0.611

exhibits the space–time behavior of the Görtler vortices raw located upstream inside the cavity and Fig. 21 the raw located downstream inside the cavity. In each one of these figures, the space–time diagrams are plotted for three different external velocities (b $U_e = 0.89$ m/s, c 1.21 m/s and d 1.595 m/s). The observation of these space–time diagrams leads to the following comments:

1. The Görtler vortices are not stationary as soon as they appear, for $U_e > 0.89$ m/s (Fig. 20b–d). There is a drifting symmetry with respect to the centerline. The left part of the raw is drifting to the left (left side of Fig. 20c), the right part is drifting to the right (right side of Fig. 20c). As a consequence, there appears a source-like singularity in the vortex raw, where there is a collision between a domain of left-traveling vortices to the left, and a domain of right-traveling vortices to the right. There, two adjacent vortices drift into two different directions (left vortex to the left, right vortex to the right) emptying an area in between which a new pair of

vortices can nucleate. Let us remark that although source-like singularities exist with well-defined properties in the frame of non-linear traveling waves (Van Hecke et al. 1999; Pastur et al. 2003), the term “source” should be considered here in a very general context. Indeed, the “source” observed here seems to be induced by a secondary side flow symmetrical with respect to the centerline. This side flow, turned from the centerline toward the sides of the cavity, is expected to be forced by the inner spanwise flow coming from the cavity sides toward the centerline (Fig. 19), as previously reported (Migeon 2002).

2. The vortices drift over space with an increasing velocity with respect to their distance to the centerline. Such an increase of the velocity seems however not to be related to an increasing vortex amplitude, since on the very right side of the picture the vortices are evanescent and still drifting with the highest velocity. Drifting velocities reach a maximum value $c_{\max} \sim 8.5$ mm s⁻¹.

Fig. 18 Görtler number versus the dimensionless wave-number for previous studies and present measurements at $R = 1$ 

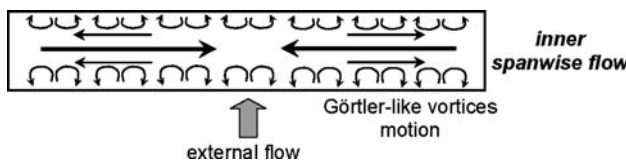


Fig. 19 Sketch of the flow dynamics and Görtler-like vortices motion for $R = 1$

3. Finally, when comparing the space–time diagrams obtained in the upstream (Fig. 20) and the downstream (Fig. 21) parts of the cavity, both patterns appear to be amazingly similar for $U_e > 0.89 \text{ m s}^{-1}$. Such a strong correlation may not be due to chance. It instead confirms the annular shape of the Görtler-like vortices. It moreover indicates how strong and coherent their shape remains over space against any perturbation that the incoming flow may produce, although, from Figs. 20a or 21a, it is obvious that the downstream part of the Görtler vortices is strongly flattened compared with its upstream part.

For $R = 1$, before any increase of U_e the wind tunnel velocity was first brought to very high values so as to blow the smoke out of the cavity. It is strongly believed that such an operation may destroy the Görtler raw. Moreover after varying the aspect ratio ($R = 1.25$, Fig. 22), we recover a very similar space–time pattern of the Görtler raw. Therefore the reproducibility of the raw slowly drifting dynamics strongly suggests the existence of a secondary flow, symmetrical with respect to the centerline. In particular, a fruitful comparison

could be done with the flow characteristics of Görtler-like vortices observed behind a backward facing step (Beaudoin et al. 2004).

5 Conclusion

Visualizations of the flow inside a rectangular cavity with aspect ratio varying between 0.5 and 2 have been conducted for $1,150 \leq Re \leq 10,670$. Three-dimensional spanwise structures are developing. The analysis of visualization time course of the flow shows that 3-D developments are not caused by shear layer secondary instabilities, as the latter remains rather a 2-D phenomenon. The study of the cavity flow with aspect ratio and Reynolds number has shown three morphological behaviors. For this range, the Reynolds number has little influence on that global flow morphology.

For $R = 2$, the flow is driven by the interaction between the shear-layer and the downstream wall. The injection inside the cavity is a rather 2-D phenomenon, creating a strongly unsteady main vortex in the downstream half of the cavity. A counter-rotating secondary vortex is size-modulated near the bottom upstream wall, and an induced flow is due to the motion of the two vortices, which is evolving in a spanwise flow. The presence of a secondary vortex in the upstream part of the cavity, linked with the unsteadiness of the main vortex, is opposing to the birth of the Görtler instabilities or is perturbing them.

The same global features are found for $R = 1.5$ with a lower turbulence level.

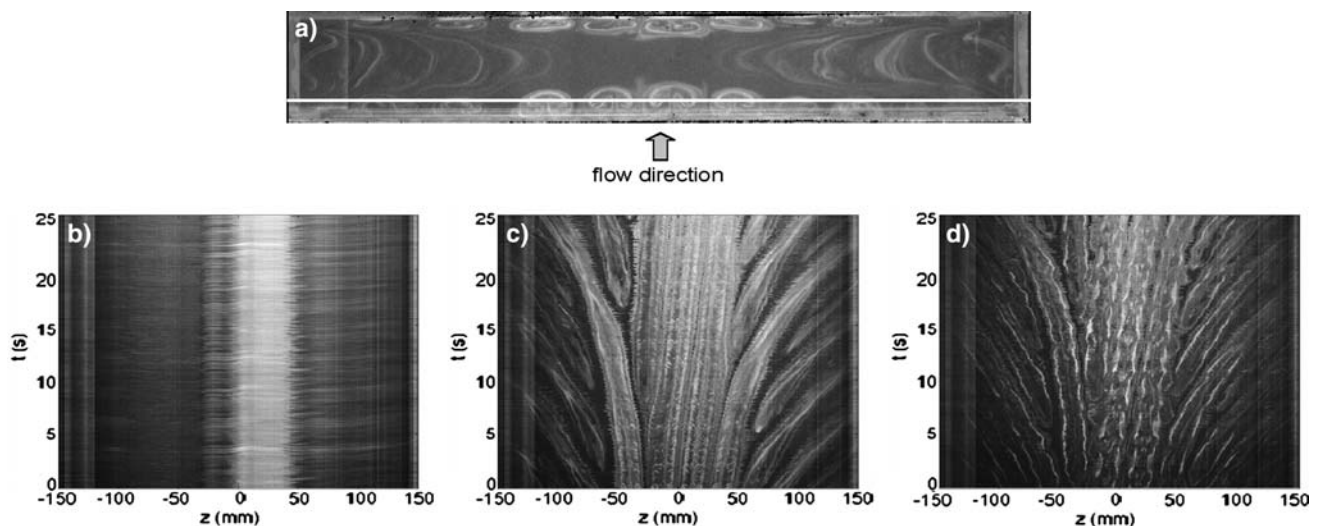


Fig. 20 **a** Visualization for $R = 1$, $U_e = 1.21 \text{ m/s}$ and $y = -15 \text{ mm}$ with the upstream white line used for the making of space–time diagrams. **b** Space–time diagram for $U_e = 0.89 \text{ m/s}$ ($Re = 2,970$).

c Space–time diagram for $U_e = 1.21 \text{ m/s}$ ($Re = 4,030$). **d** Space–time diagram for $U_e = 1.6 \text{ m/s}$ ($Re = 5,330$)

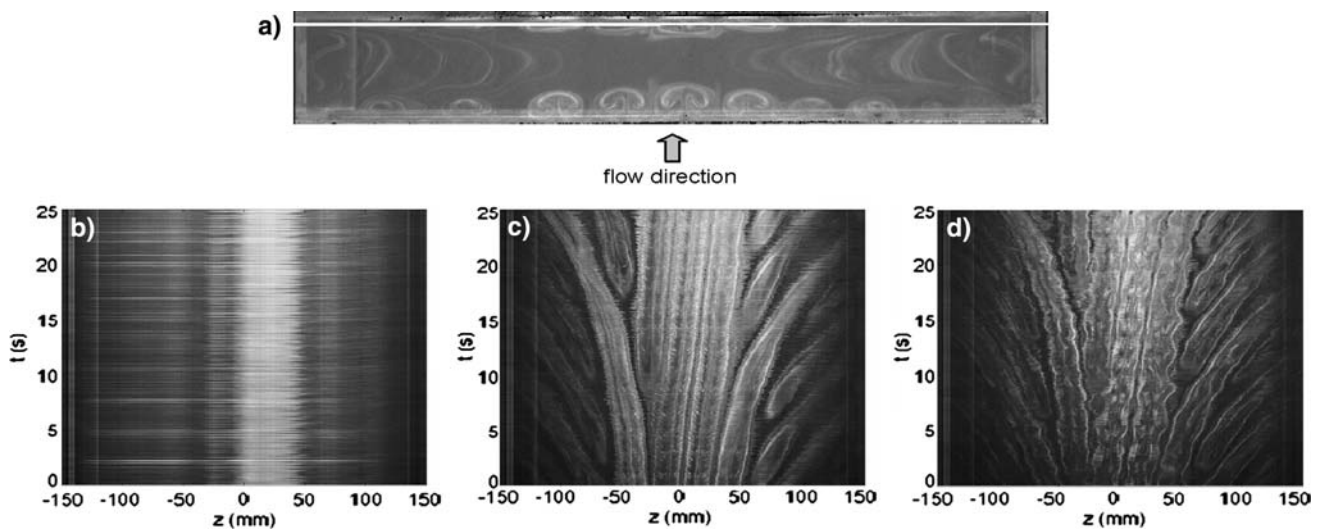


Fig. 21 **a** Visualization for $R = 1$, $U_e = 1.21 \text{ m/s}$ and $y = -15 \text{ mm}$ with the downstream white line used for the making of space-time diagrams. **b** Space-time diagram for $U_e = 0.89 \text{ m/s}$

($Re = 2,970$). **c** Space–time diagram for $U_e = 1.21 \text{ m/s}$ ($Re = 4,030$). **d** Space–time diagram for $U_e = 1.6 \text{ m/s}$ ($Re = 5,330$)

For $R = 1$, the main vortex occupies the entire length of the cavity, and the secondary upstream vortex is reduced to a corner vortex. The main vortex boundary is time-evolving, as one can see in Fig. 10b with a small core associated with a large periphery for $z = 0$ and a larger core associated with a smaller periphery for $z = 30 \text{ mm}$. There is also counter-flow acting in the core of the main vortex, from the cavity sides toward the symmetry plane, providing a seeding inside the cavity. The Görtler-like vortices migrate from the flow center of symmetry toward the cavity

span sides. This motion is likely due to the spanwise flow acting in the periphery of the main vortex, from the center to the cavity sides (Migeon 2002).

For $R = 0.5$, there are two superimposed vortices, with a very low velocity and a purely laminar flow inside the cavity.

The Görtler-like vortices range of existence and dynamics will be further discussed in a forthcoming paper.

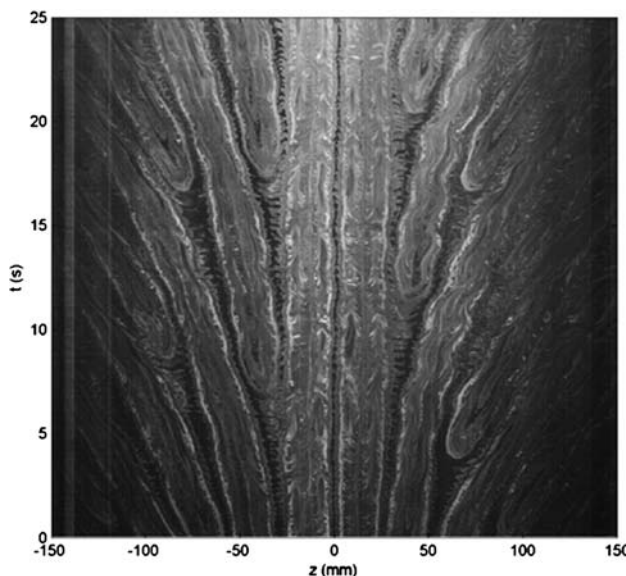


Fig. 22 Space–time diagram for $R = 1.25$ and $U_e = 1.21 \text{ m/s}$ ($Re = 5,042$)

- Beaudoin JF, Cadot O, Aider JL, Weisfreid JE (2004) Three-dimensional stationary flow over a backward-facing step. *Eur J Mech B Fluids* 23:147–155
- Bilanin AJ, Covert EE (1973) Estimation of possible excitation frequencies for shallow rectangular cavities. *AIAA J* 11(3):347–351
- Bippes H (1972) Experimentelle Untersuchung des laminar-turbulenten Umschlags an einer parallel angestromten konkaven Wand. Heidel. Akad. Wiss. Naturwiss. Kl. 3:103 (also NASA TM-75243, 1978)
- Chang CH, Meroney RN (2003a) The effect of surroundings with different separation distances on surface pressures on low-rise buildings. *J Wind Eng Ind Aerodyn* 91:1039–1050
- Chang CH, Meroney RN (2003b) Concentration and flow distributions in urban street canyons: wind tunnel and computational data. *J Wind Eng Ind Aerodyn* 91:1141–1154
- Chatellier L, Laumonier J, Gervais Y (2004) Theoretical and experimental investigations of low Mach number turbulent cavity flows. *Exp Fluids* 36:728–740
- Chung KM (2001) Three-dimensional effect on transonic rectangular cavity flows. *Exp Fluids* 30:531–536
- Dezsö-Weidinger G, Stitou A, Van Beeck J, Riethmüller ML (2003) Measurements of the turbulent mass flux with PTV in a street canyon. *J Wind Eng Ind Aerodyn* 91:1117–1131

- Fang LC, Nicolaou D, Cleaver JW (1999) Transient removal of a contaminated fluid from a cavity. *Int J Heat Fluid Flow* 20:605–613
- Floryan JM, Saric WC (1982) Stability of Görtler vortices in boundary layers. *AIAA J* 20(3):316–324
- Forestier N, Jacquin L, Geffroy P (2003) The mixing layer over a deep cavity at high-subsonic speed. *J Fluid Mech* 475:101–145
- Geveci M, Oshkai P, Rockwell D, Lin JC, Pollack M (2003) Imaging of the self excited oscillation of flow past a cavity during generation of a flow tone. *J Fluids Struct* 18:665–694
- Gharib M, Roshko A. (1987) The effect of flow oscillations on cavity drag. *J Fluid Mech* 177:501–530
- Ghia U, Ghia KN, Shin CT (1982) High-re solutions for incompressible flow using the Navier-Stokes equations and a multigrid method. *J Comput Phys* 48:387–411
- Grace SM, Dewar WG, Wroblewski DE (2004) Experimental investigation of the flow characteristics within a shallow wall cavity for both laminar and turbulent upstream boundary layers. *Exp Fluids* 36:791–804
- Guermond JL, Migeon C, Pineau G, Quartapelle L (2002) Start-up flows in a three-dimensional rectangular driven cavity of aspect ratio 1:1:2 at $Re = 1000$. *J Fluid Mech* 450:169–199
- Hall P (1983) The linear development of Görtler vortices in growing boundary layers. *J Fluid Mech* 130:41–58
- Heller HH, Bliss B (1975) The physical mechanism of flow-induced pressure fluctuations in cavities and concepts for their suppression. *AIAA Paper 75–491*, 2nd Aeroacoustics Conference, Hampton
- Howe MS (2003) Mechanism of sound generation by low Mach number flow over a wall cavity. *J Sound Vib* 273:103–123
- Huerre P, Rossi M (1998) Hydrodynamic instabilities in open flows. In: Godrèche C, Manneville P (eds) *Hydrodynamics and nonlinear instabilities*. Cambridge University Press, pp 81–294
- Kegerise MA, Spina EF, Garg GS, Cattafesta LN III (2004) Mode-switching and nonlinear effects in compressible flow over a cavity. *Phys Fluids* 16(3):678–687
- Komerath NM, Ahuja KK, Chambers FW (1987) Prediction and measurement of flows over cavities—a survey. *AIAA Paper 87–0166*
- Koseff JR, Street RL (1984) Visualization studies of a shear driven three-dimensional recirculating flow. *J Fluids Eng* 106:21–29
- Kuo CH, Chang CW (1998) Shear-layer characteristics across a cavity with a horizontal top plate. *Fluid Dyn Res* 22:89–104
- Kuo CH, Jeng WI (2003) Lock-on characteristics of a cavity shear layer. *J Fluids Struct* 18:715–728
- Larchevêque L, Sagaut P, Lê TH, Comte P (2004) Large-eddy simulation of a compressible flow in a three-dimensional open cavity at high Reynolds number. *J Fluid Mech* 516:265–301
- Lin JC, Rockwell D (2001) Organized oscillations of initially turbulent flow past a cavity. *AIAA J* 39(6):1139–1151
- Mendoza JM, Ahuja KK (1995) The effect of width on cavity noise. *J Aircr* 14(9):833–837
- Migeon C (2002) Details on the start-up development of the Taylor-Görtler-like vortices inside a square-section lid-driven cavity for $1,000 \leq Re \leq 3,200$. *Exp Fluids* 33:594–602
- Migeon C, Pineau G, Texier A (2003) Three-dimensionality development inside standard parallelepipedic lid-driven cavities at $Re = 1000$. *J Fluids Struct* 17:717–738
- Pastur L, Westra MT, Van de Water W (2003) Sources and sinks in 1D travelling waves. *Physica D* 174:71–83
- Rockwell D (1983) Oscillations of impinging shear layers. *AIAA J* 21(5):645–664
- Rockwell D, Naudascher E (1978) Review self-sustained oscillations of flow past cavities. *J Fluids Eng* 100:152–165
- Rossiter JE (1964) Wind-tunnel experiments on the flow over rectangular cavities at subsonic and transonic speeds. *Aeronautical Research Council Reports and Memoranda* 3438
- Rowley CW, Colonius T, Basu AJ (2002) On self-sustained oscillations in two-dimensional compressible flow over rectangular cavities. *J Fluid Mech* 455:315–346
- Sarohia V (1977) Experimental investigation of oscillations in flows over shallow cavities. *AIAA J* 15(7):984–991
- Swearingen JD, Blackwelder RF (1987) The growth and breakdown of streamwise vortices in the presence of a wall. *J Fluid Mech* 182:255–290
- Tam CKW, Block PJW (1978) On the tones and pressure oscillations induced by flow over rectangular cavities. *J Fluid Mech* 89:373–399
- Tani I (1962) Production of longitudinal vortices in the boundary layer along a concave wall. *J Geophys Res* 67:3075–3080
- Umesh Chandra B, Chakravarthy SR (2005) Experimental investigation of cavity-induced acoustic oscillations in confined supersonic flow. *J Fluids Eng* 127:761–769
- Van Hecke M, Storm C, Van Saarloos W (1999) Sources, sinks and wavenumber selection in coupled CGL equations and implications for counterpropagating wave systems. *Physica D* 134:1–47
- Winoto SH, Crane RI (1980) Vortex structure in laminar boundary layers on a concave wall. *Int J Heat Fluid Flow* 2:221–231

Quantifying the nonlinear mode competition in the flow over an open cavity at medium Reynolds number

L. R. Pastur · F. Lusseyran · T. M. Faure ·

Y. Fraigneau · R. Pethieu · P. Debesse

Received: 29 August 2006 / Revised: 8 October 2007 / Accepted: 16 October 2007 / Published online: 4 November 2007
© Springer-Verlag 2007

Abstract Our purpose is to quantify the rate of intermittency of nonlinearly competing modes, in a dominantly mode-switching scenario. What is the rate of presence of each mode? Can they simultaneously appear in, or disappear from the signal? The study is done in the context of open flows, exhibiting self-sustained oscillations, where air is here flowing over an open cavity. Reynolds numbers are of the order of 14,000. Velocity measurements downstream of the cavity are based on a laser Doppler velocimetry technique. We propose two methods to estimate the rate of presence of each mode: one based on a complex demodulation technique, the other on the distribution of the state vectors in the phase portrait of the signal.

1 Introduction

It is a remarkable fact that open flows such as jets, cavity flows, etc., may present spontaneous self-sustained oscillations. This is typical of an unstable configuration in which a preferred mode is selected and amplified (Rockwell and Naudascher 1979). In the case of flows past an open cavity, it has been observed, for medium and large Reynolds

numbers, some nonlinear competition between a few spectral components (usually two) (Rockwell 1983; Kegerise et al. 2004). The competition reveals to be dominated by a mode switching scenario, where one mode tends to prevent the rise of the other one, and reciprocally. Up to now, the physical mechanisms responsible for such a nonlinear competition has not been understood yet. In this article, we propose to focus on a quantitative analysis of the mode-switching phenomenon observed in the experimental flow over an open cavity at a moderate Reynolds number. The experimental setup and the mode-switching phenomenon are introduced in Sects. 2 and 3. Section 4 points out the fact that no mode-switching phenomenon is observed in a numerical flow, whose working parameters are similar to the experimental ones. To quantify the rate of existence of each competing mode, we introduce two different techniques. The first method is based on the complex demodulation of the time-signal, using the Hilbert transform (Sect. 5). In Sect. 6, existence rates are discussed with respect to three different threshold values. The second method is based on the dynamics phase portrait (Sect. 7). Both methods require to band-pass filter the signal around the spectral components under interest. A statistical analysis is conducted on the competing mode lifetimes in Sect. 8. Finally, a phase space first characterization is performed in Sect. 9, wondering about an underlying deterministic mechanism of the mode-switching phenomenon, before concluding in Sect. 10.

L. R. Pastur (✉) · F. Lusseyran · T. M. Faure · Y. Fraigneau ·
R. Pethieu · P. Debesse
LIMSI-CNRS, BP 133, 91403 Orsay Cedex, France
e-mail: luc.pastur@limsi.fr

L. R. Pastur · R. Pethieu
Université Paris Sud XI, 91405 Orsay Cedex, France

T. M. Faure · P. Debesse
Université Pierre et Marie Curie, Paris VI,
75252 Paris Cedex 05, France

2 Experimental configuration

The system under study is a cavity of length $L = 10$ cm along the longitudinal x direction of the incoming air flow, height $H = 5$ cm along the vertical y direction (aspect ratio $R = L/H = 2$), and width $S = 30$ cm along the transverse z

direction (Fig. 1b). The cavity is enclosed into a vein ($D + H$) = 12.5 cm high. The origin of the axes in the (x, y) plane is taken at the upstream edge of the cavity, and midspan along the transverse z direction. The air flow is generated by a centrifugal fan placed upstream of a settling chamber (Fig. 1a). The incoming air flow is laminar and stationary, and the flow rate is kept constant during the experiment. The external velocity U_e is measured using laser Doppler velocimetry (LDV), 102 mm upstream of the cavity and 25.5 mm above the flat plate. This point of measurement is in the external flow sufficiently upstream of the cavity to avoid any perturbation from the instability developing above the cavity. At the wind tunnel outlet, the flow is rejected inside the experimental room. The reference flow velocity is $U_e = 2.09$ m/s (Reynolds number $Re_L = U_e L / \nu \approx 14,000$). The measurement is performed over the x -component of the velocity downstream of the cavity, at point $x/L = 1.15$, $y/h = 0.33$, $z/\ell = 0$, using a LDV measurement. The time-series are acquired over 9 min, at a mean frequency rate of $f_e = 1,530$ Hz. The signal is re-sampled using a linear interpolation between the actual points of measurement, so as to provide regular time intervals of $\delta t = 1/f_e = 0.650$ ms. The time series is therefore constituted of about $N = 840,000$ points.

3 About the power spectral density

The power spectral density (psd) of the LDV signal exhibits two main components, that are not in an harmonic ratio (Fig. 2), the first spectral component (mode 1) at

$f_1 = 23.2$ Hz, the second (mode 2) at $f_2 = 31.0$ Hz. Their peak to peak ratio is $W_1/W_2 = 1.66$ (W_i being the power density in mode i). Other peaks appear as combinations of f_1 and f_2 , and harmonics. By construction, the psd only provides a statistical information on the spectral weight of each spectral component, composing the overall signal. It does not teach anything about the actual mode coexistence or exclusion in time. Indeed, the spectral density sensitively depends on the instantaneous mode amplitude, but also on its rate of presence over time. It may therefore happen that the most energetic modes in the psd only occur very episodically in time, in the LDV signal, but with an amplitude much larger than the amplitude of the other mode, so as to significantly contribute to the power spectrum.

To illustrate this point, a time-frequency representation of the signal has been plotted in the spectrogram of Fig. 3. There, the switching phenomenon between one spectral band, centred on f_1 , and a second spectral band centred on f_2 , clearly appears. Such a spectrogram should however be considered with some care, both axes t and f being reciprocally constrained by the uncertainty relation $\Delta t \cdot \Delta f = 1/2$, which means that the precision over one axis is inversely proportional to the precision over the second axis. Henceforth, the time localization of the switching events is directly related to the temporal sliding window width Δt used to perform the “instantaneous” Fourier transform at time t . In our case, $\Delta t \sim 10/f_1$ s, with a time step $\delta t = 112$ ms. Theoretically, it might be possible to extract the amplitude evolution of modes f_1 and f_2 by simply picking up the horizontal lines centred on f_1 and f_2 in the spectrogram. In practice, we will not use this technique, the

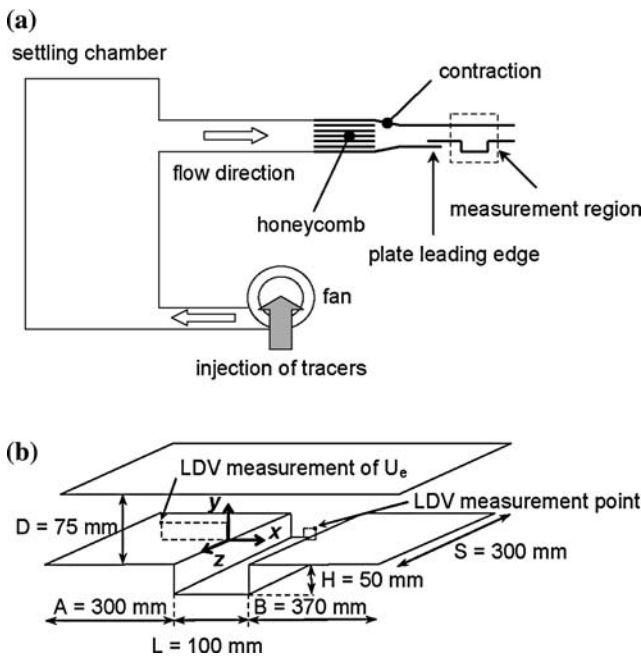


Fig. 1 Experimental setup. **a** Wind-tunnel principle; **b** cavity scheme

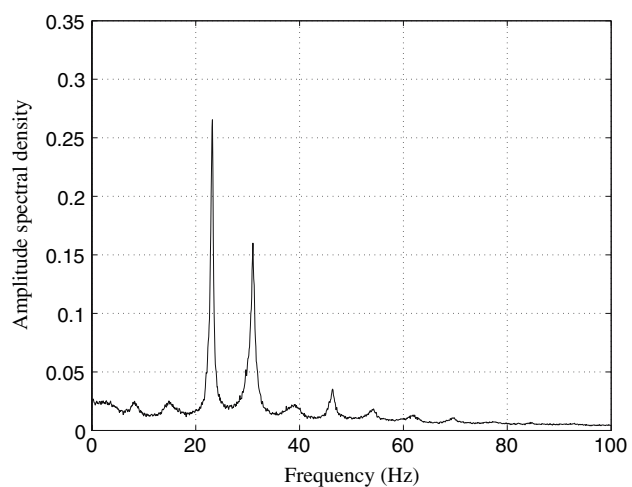
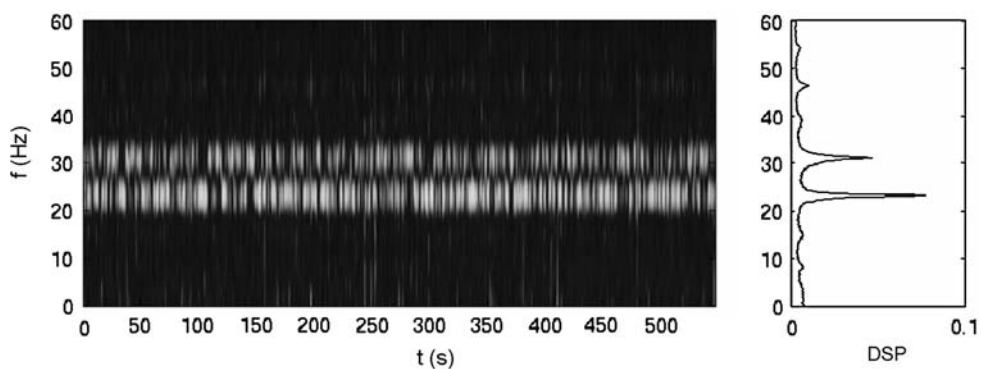


Fig. 2 Square root of the power spectral density, normalized to 1, of the LDV time series $s(t)$. Incoming flow velocity $U_e = 2.09$ m/s, aspect ratio $R = 2$. Two main modes emerge at $f_1 = 23.2$ Hz and $f_2 = 31.0$ Hz. The other peaks are nonlinear combinations of f_1 and f_2

Fig. 3 Spectrogram of the signal. The horizontal axis is the flowing time, the vertical axis is the frequency space. Power spectral density is plotted as grey levels, from dark for small amplitude values to bright for larger amplitude values. The right inset is the time-integrated spectrogram



temporal resolution being three times larger than the slowest period $T_1 = 1/f_1$.

4 Mode-switching phenomenon in numerical simulation

Experimentally, the origin of such a mode switching phenomenon is not clearly understood yet. However, a 3D direct numerical simulation, carried out in our group, may bring some insights. The flow is assumed incompressible ($\nabla \cdot \mathbf{v} = 0$) and described by the Navier–Stokes equation

$$\frac{\partial \mathbf{v}}{\partial t} + \nabla \cdot (\mathbf{v}' \mathbf{v}) = -\frac{1}{\rho_0} \nabla P + \nabla \cdot (\nu \nabla \mathbf{v}),$$

where t is the time, ρ_0 the uniform and constant density, P the pressure and ν the constant kinematic viscosity (isothermal flow). The numerical method is similar to the one proposed in the framework of natural convection flow instability by Le Quéré et al. (1992) and Gadouïn et al. (2001), and further applied to our open cavity flow (Podvin et al. 2006). Momentum equations are discretized following a finite volume approach on staggered structured grid with a second-order approximation in time and space. Scalar variables are defined at cell centres whereas vectorial variables are defined at cells boundaries. Advection fluxes are calculated with a QUICK scheme (Leonard 1979) and the viscous terms are defined with an usual second-order centred scheme. For stability reasons, the viscous fluxes are discretized using an implicit method. The incompressibility constraint ($\nabla \cdot \mathbf{v} = 0$) is guaranteed by a prediction/projection method, implying the resolution of a Poisson equation for the pressure updating.

The domain of simulation is similar to the experimental configuration shown in Fig. 1b. However, the spanwise direction is considered periodic and the length of the upstream cavity channel is reduced in order to save CPU time. The length of the domain is 400 mm, the width 200 mm and the height 125 mm. The inlet is located at the specific coordinate $x_0 = -110$ mm, the x -origin being located on the upstream edge of cavity. The inlet

conditions for the longitudinal velocity component are fixed such that the flow rate $U_q = 2.0$ m/s. It corresponds to the velocity profile of a laminar growing channel flow at the specific coordinate x_0 , calculated in a 2D channel flow simulation, which is in good agreement with the experiment. The other velocity component gradients are equal to zero. Usual nonsliding conditions are applied at the top and bottom walls. The domain is covered with 256 cells in the longitudinal direction, and 128 in the spanwise and normal directions. The mesh is particularly refined close to the walls and over the cavity, to well resolve upstream laminar boundary and stress layers and the eddy structures generated in the shear layer.

The numerical simulation is carried out over a time duration of 24.5 s, after the statistically converged flow has been reached out. The power spectral density of the signal picked up downstream of the cavity, at the same point of measurement as the experimental one, with a sampling frequency of $f_s = 454.5$ Hz, is shown in Fig. 4. The shear layer instability frequency is measured at $f_0 = 31.9$ Hz, close to $f_2 = 31.0$ Hz. No other mode of oscillation is

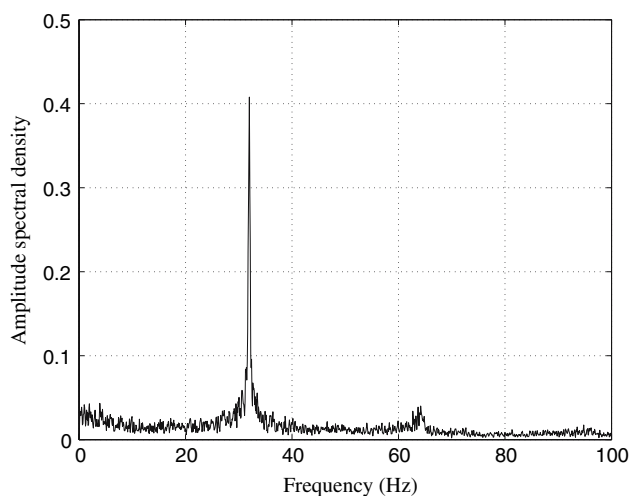


Fig. 4 Power spectral density in the 3D direct numerical simulations of the flow over an open cavity at the flow rate $U_q = 2$ m/s. Only one spectral component is present in the spectrum

however detected, meaning that the mode switching phenomenon is absent from the simulation. The reason for the discrepancy may teach us about the physical mechanism involved. First of all, note that although the numerical flow could be much more robust (with respect to environmental noise) than the experimental flow, which could let no chance to the other mode to develop, it remains that the cavity recirculation flow should be able to initiate, in the experimental flow as well as in the numerical one, strong enough perturbations in the upstream corner of the cavity to allow, at some time, the rise of the other mode. This is however not what happens. We may also wonder about the refinement of the mesh grid. But it appears that the highest frequency f_2 , which should be the less well-resolved one (since it is associated to smaller spatial structures), actually is resolved by the code, while the missing frequency is the lowest one f_1 . Henceforth, it is doubtful that the mesh grid may be responsible for the lack of mode switching phenomenon. Another possibility may lay in the numerical QUICK scheme under use, that could overdamp one of the two modes. In this respect, it may be useful to test a centred scheme. A last possibility for the discrepancy may lay in the transverse boundary conditions. They are rigid in the experiment, while they are periodic in the simulations. As a consequence, the recirculating secondary flows, in the transverse direction, symmetrically to the medium plane, as observed in the experiment, are absent in the simulations. How such secondary flows could induce the mode switching phenomenon is not obvious, but the possibility cannot be a priori excluded. A forthcoming campaign of simulations will be held with rigid boundary conditions, so as to mimic the experimental conditions, and should therefore bring more insights about the relevance of the boundaries in the mode switching phenomenon.

5 Complex demodulation

In this section, we propose to analyse more quantitatively the mode-switching phenomenon. It is necessary to

determine the instantaneous amplitude of each mode, at any time in the experimental time series. This is done using a complex demodulation technique on the basis of Hilbert transform. The method first requires to band-pass filter the signal around the spectral component under interest. This is done using a (noncausal) Butterworth filter of order 4. Mathematically, the Hilbert transform of a time-signal $s(t)$ is defined by the integral transform:

$$\mathcal{H}\{s(t)\} = \frac{1}{\pi t} * s(t), \quad (1)$$

where $*$ is the convolution product. In the Fourier space, it can equivalently write

$$\mathcal{F}\{\mathcal{H}\{s\}\} = -i, \operatorname{sgn}(\omega) \cdot \mathcal{F}\{s\}(\omega), \quad (2)$$

where \mathcal{F} is the Fourier transform operator, and $\operatorname{sgn}(\cdot)$ the sign function. The Hilbert transform therefore simply consists in rotating by $-\pi/2$ the positive part of the signal spectrum (multiplication by $-i = e^{-i\pi/2}$), by $+\pi/2$ its negative part (multiplication by $i = e^{i\pi/2}$). The Hilbert transform will therefore transform a cosine into a sine. As a consequence, it is possible to define an analytical signal $w(t)$ by

$$w(t) = s(t) + i\mathcal{H}\{s\}(t) \equiv A(t) \cdot e^{i\phi(t)}, \quad (3)$$

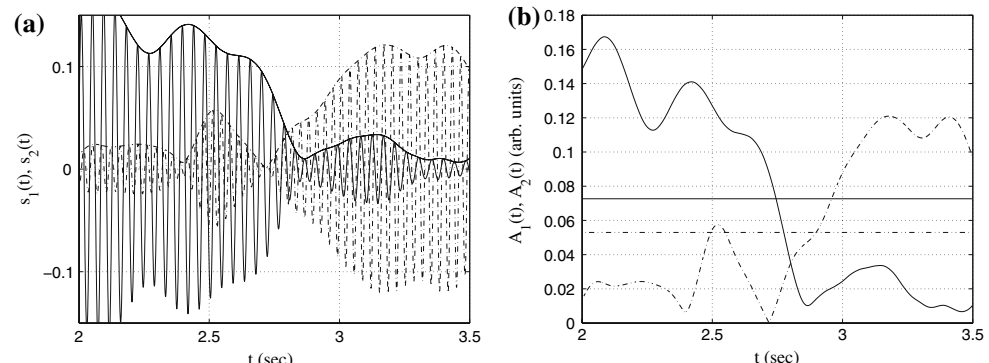
from which an amplitude $A(t)$ and a phase $\phi(t)$ can be derived, as

$$\begin{cases} A(t) &= |w(t)| \\ \tan \phi(t) &= \frac{\mathcal{I}m\{w\}}{\mathcal{R}e\{w\}} \end{cases} \quad (4)$$

The Hilbert transform is applied to the signals $s_1(t)$ and $s_2(t)$, obtained by band-pass filtering the LDV signal $s(t)$ around f_1 and f_2 , respectively. The resulting amplitudes $A_1(t)$ and $A_2(t)$, associated with $s_1(t)$ and $s_2(t)$, are plotted in Fig. 5 for an arbitrary time interval, where the mode switching phenomenon can be observed.

The mode-switching nature of the phenomenon is again confirmed by plotting A_2 with respect to A_1 (Fig. 6). It exhibits two compact clouds of points, one corresponding to A_1 saturating, A_2 vanishing, the other to A_2 saturating,

Fig. 5 Amplitudes $A_1(t)$ (solid line) and $A_2(t)$ (broken line) of modes f_1 and f_2 in signals $s_1(t)$ and $s_2(t)$, **a** with, or **b** without, the carrier. The threshold amplitudes \bar{A}_1 and \bar{A}_2 are plotted as horizontal solid and broken lines, respectively, in **b**



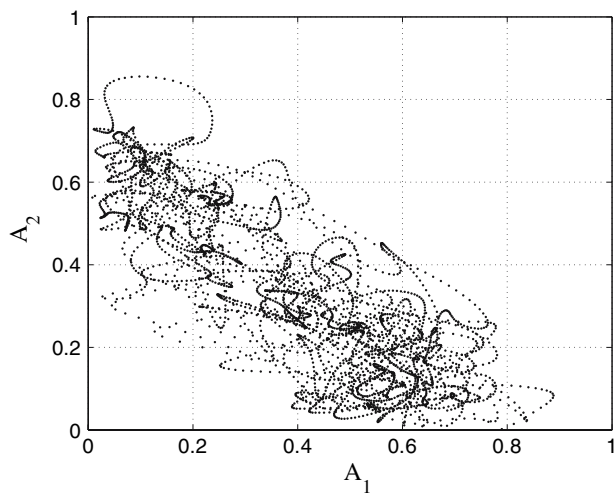


Fig. 6 Amplitude of mode 2 versus amplitude of mode 1, at any time

A_1 vanishing, with a more scattered cloud of points around the anti-diagonal when modes f_1 and f_2 are exchanging their stability, typical of an anti-correlated behaviour.

6 Criterion of existence

Now, we would like to determine the existence ranges of each mode f_1 and f_2 . For that, it is necessary to define a threshold value for the amplitude. A natural criterion is to compare the instantaneous mode amplitude $A_i(t)$ to the time averaged mode amplitude \bar{A}_i . For mode f_1 , $\bar{A}_1 = 0.073$, for mode f_2 , $\bar{A}_2 = 0.053$. At a given time t , the mode is considered present if $A_i(t) > \bar{A}_i$, absent unless. Defining t_i as the integrated time over which the mode f_i is present in the signal $s_i(t)$, we define the rate of

presence of the mode f_i as $\eta_i = t_i/T$, where T is the overall time of the signal. Following the criterion, it is found $\eta_1 = 0.524$, and $\eta_2 = 0.479$.

Noting that $\eta_1 + \eta_2 \approx 1.00$, one may conclude that the mode switching scenario is perfect, one mode being strictly present when the other is absent—and reciprocally. In fact, it appears that f_1 and f_2 are simultaneously present over $\eta_{\text{together}} = 6.8\%$ of the overall signal. It therefore follows that both modes must also be simultaneously absent from the LDV signal over a significant fraction of time, found to be $\eta_{\text{none}} = 6.5\%$. Henceforth, η_1 and η_2 also count common events. In Fig. 7 is shown an example in which both modes are seen simultaneously present in the signal (event of stability exchange, f_2 disappearing to the benefit of f_1).

Another natural threshold value can be defined, based on the mid-value A_{ic} between the largest and the smallest amplitude values:

$$A_{ic} = \frac{1}{2} \left(\max_t(A_i) + \min_t(A_i) \right). \quad (5)$$

This criterion has the benefit to well distinguish the existence range of a mode that would predominantly be present in the signal, with some rare events where it disappears. In this case, the mean amplitude \bar{A}_i would be close to the saturated value A_{is} , and even small instantaneous fluctuations around A_{is} would enhance artificial transitions from present to absent. Threshold values are increased by +29% for mode f_1 , by +47% for mode f_2 . It follows $\eta_1 = 0.376$ (−29%) and $\eta_2 = 0.283$ (−41%), $\eta_{\text{together}} = 0.15\%$, $\eta_{\text{none}} = 34.2\%$. The disproportion between η_{together} and η_{none} is dubious. Actually, in Fig. 8 is plotted the longest time interval, over which no mode should be present in the signal, following this criterion. This confirms that the criterion tends to overestimate the rate of common absence, which therefore appears rather irrelevant here.

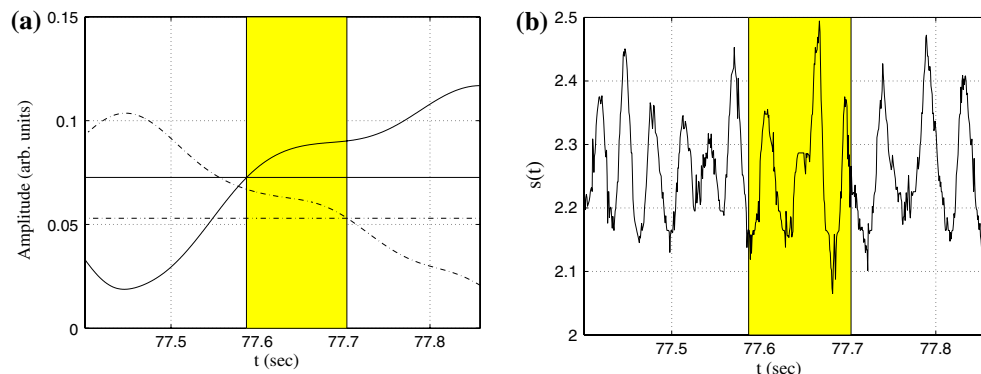


Fig. 7 Time range over which both modes are simultaneously present in the signal $s(t)$, following the criterion based on the mean amplitudes \bar{A}_1 and \bar{A}_2 . Mean amplitudes are plotted as horizontal solid

line for \bar{A}_1 and broken line for \bar{A}_2 . The common range is grey filled. **a** Amplitudes $A_1(t)$ and $A_2(t)$ are shown; **b** signal $s(t)$ is shown

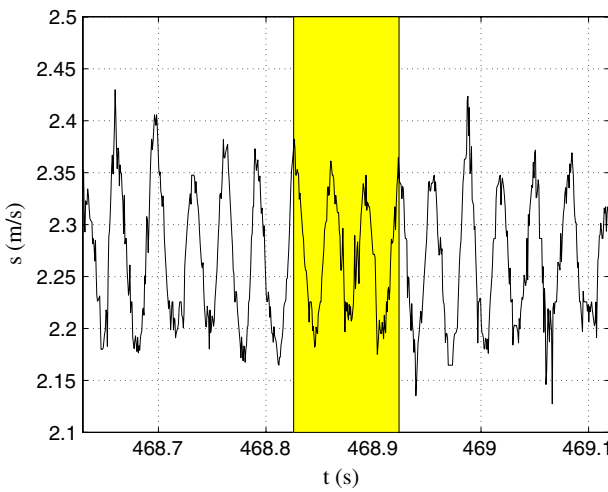


Fig. 8 In between solid lines, longest time range over which neither mode f_1 nor mode f_2 are detected within the signal, following the threshold value defined by Eq. 5

Another threshold value can be defined, when considering the amplitude distributions of modes f_1 and f_2 in Fig. 9. Two maxima are separated by a local minimum. The first maximum is the vanishing amplitude A_{iv} of mode f_i . The second maximum is the saturated amplitude A_{is} . The transition between the vanishing and the saturated amplitudes occurs when the amplitude passes through the local minimum A_{im} , which can provide a new threshold amplitude:

$$A_{im} = \min_{A_i \in [A_{iv}, A_{is}]} A_i. \quad (6)$$

If so, $A_{1m} = 0.060$ (-18%), $A_{2m} = 0.050$ (-6%). It follows $\eta_1 = 0.598$, $\eta_2 = 0.501$, $\eta_{\text{together}} = 13.0\%$, $\eta_{\text{none}} = 3.1\%$. Figure 10 shows the longest event for which both modes are simultaneously seen present in the signal. We will see in Sect. 7 that a similar criterion can be used, based on the system phase portrait.

Whatever criterion is used, η_1 is always greater than η_2 , already suggested by the PSD ratio between f_1 and f_2 , and the constraint $\eta_1 + \eta_2 + \eta_{\text{none}} - \eta_{\text{together}} = 1$ is always satisfied (see Table 1). The mean and maximum mode

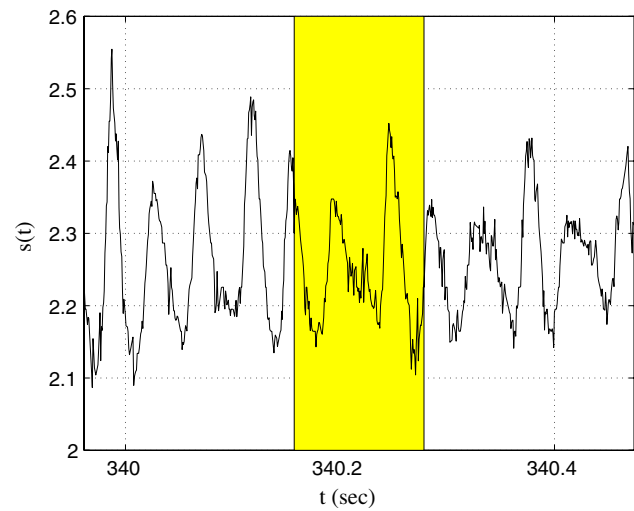


Fig. 10 Longest time range over which both modes f_1 and f_2 are detected in the signal $s(t)$, following the threshold value defined by Eq. 6

Table 1 Rate of existence η_1 (mode 1) and η_2 (mode 2), rate of coexistence of both modes η_{tgh} (η_{together}), rate of absence of both modes η_{none} (η_{none}), depending on the chosen threshold value (in %)

	η_1	η_2	η_{tgh}	η_{none}
Mean value \bar{A}_i	52.4	47.9	6.8	6.5
Mid-value A_{ic}	37.6	28.3	0.1	34.2
Local minimum A_{im}	59.8	50.1	13.0	3.1

Table 2 Mean lifetimes for modes f_1 and f_2 , depending on the chosen threshold value

	\bar{A}_i	A_{ic}	A_{im}
Δt_1 (T_1 units)	19.6	12.0	24.7
Δt_2 (T_2 units)	18.3	11.1	20.0

lifetimes are given in Tables 2 and 3, respectively. Short lifetimes are collected in Tables 4 and 5 for modes f_1 and f_2 . Lifetimes of common absence or presence are reported

Fig. 9 Amplitude distribution for (a) mode f_1 , (b) mode f_2 , using the Hilbert transform filter

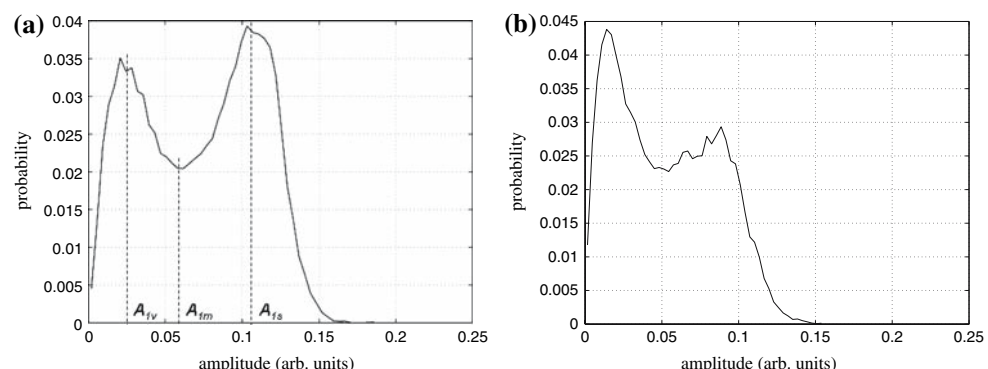


Table 3 Longest lifetimes for modes f_1 and f_2 , depending on the chosen threshold value

	\bar{A}_i	A_{ic}	A_{im}
Max Δt_1 (T_1 units)	408	238	454
Max Δt_2 (T_2 units)	509	211	511

Table 4 Nonrelevant lifetimes Δt_1 for mode f_1 depending on the chosen threshold value

	\bar{A}_1	A_{1c}	A_{1m}
Min Δt_1 (T_1 units)	0.27	0.31	0.23
Fraction of $\Delta t_1 < 2T_1$	6.3%	8.3%	9.7%

Table 5 Nonrelevant lifetimes Δt_2 for mode f_2 depending on the chosen threshold value

	\bar{A}_2	A_{2c}	A_{2m}
Min Δt_2 (T_2 units)	0.16	0.55	0.14
Fraction of $\Delta t_2 < 2T_2$	7.9%	12.5%	10.1%

Table 6 Time ranges over which both modes are either simultaneously present or absent from the signal

	\bar{A}_i	A_{ic}	A_{im}
Max $\Delta t_{\text{together}}$ (T_1 units)	12.3	2.5	17.1
Max Δt_{none} (T_1 units)	10.5	29.9	7.2
$\bar{\Delta t}_{\text{together}}$ (T_1 units)	1.9	0.8	2.7
$\bar{\Delta t}_{\text{none}}$ (T_1 units)	2.1	4.9	1.8
Fraction of $\Delta t_{\text{together}} < 2T_1$	62.2%	96.0%	46.9%
Fraction of $\Delta t_{\text{none}} < 2T_1$	56.9%	24.7%	64.3%

in Table 6. Time intervals whose duration are less than two basic oscillations may be considered as signal processing artifacts. Whatever threshold value is used, such events however represent less than 10% of the overall lifetimes for mode f_1 (Table 4), and not more than 13% for mode f_2 (Table 5). From Tables 4, 5, and 6, the mean amplitude seems to be the well adapted criterion here.

Depending on the criterion used, rates of existence sensibly vary. This is a consequence of the fact that the chosen threshold amplitude is to some extent arbitrarily defined. Moreover, we are facing the intrinsic limitation of any Fourier-based technique, where there exists a fundamental uncertainty over the time precision and where windowing usually introduce oscillations. The Hilbert transform, here based on band-pass filtered signals, extracts amplitudes that never vanish completely, even when one mode seems to be absent from the LDV signal. One may therefore ask whether this could result from

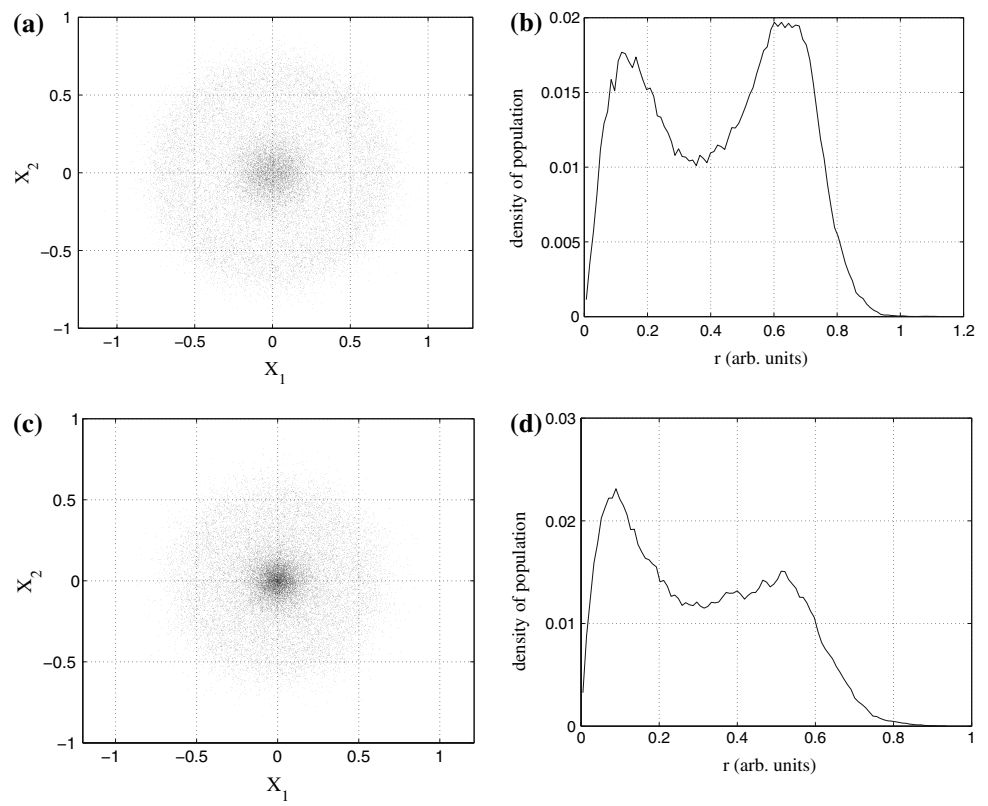
some processing artifact. However, a similar behaviour is observed in coupled complex Ginzburg–Landau equations, where two modes are similarly competing, and none never totally disappears. We have shown that none of the criterions introduced here, although justified by some aspects, looks fully satisfying, all being in some way arbitrary. Each of them however tells us that the coexistence or simultaneously absence of the two modes cannot be excluded, not only during events where both modes are exchanging stability, but also on reasonably long time durations (a few periods of oscillations for instance in Fig. 14a).

7 Phase space-based criterion

The phase space reconstruction is based on the singular value decomposition (SVD) of the delayed data matrix S , as proposed in Broomhead and King (1986). The SVD technique is described in Appendix. Derivative-based techniques would also generate an equivalent embedding phase space (Gouesbet and Letellier 1994).

Another threshold amplitude for the mode existence, similar to the one defined by Eq. 6, can be defined in the reconstructed phase spaces of the band-pass filtered signals $s_1(t)$ and $s_2(t)$. Let X be the matrix whose columns X_i are the phase space dynamical variables (see Appendix for the definition of X). Suppose that two columns of X , say X_1 and X_2 , are phase-quadratically correlated, as it is expected in an oscillating phenomenon. Then, X_1 is related to X_2 as would $s_1(t)$ be with respect to its first time-derivative $\dot{s}_1(t)$. For the sake of simplicity, consider the sub-phase space spanned by (s_1, \dot{s}_1) . Time ranges where both the amplitude and its time-variations are small will correspond to states close to the origin of the phase space (zero amplitude, zero derivative). On the contrary, time ranges over which the mode f_1 is present produce, in the signal $s_1(t)$, high amplitude levels (with a carrier time-varying at a frequency close to f_1), that generate orbits of finite radius $r(t) = \sqrt{s_1(t)^2 + \dot{s}_1(t)^2}$, with a significant dispersion if the amplitude modulations are large (Fig. 11a, c), further increased by the presence of noise. Between those two very distinct clouds of points should stand a “switching” area, associated with sharp amplitude falls (resp. rising) from the saturated (resp. vanishing) amplitude to the vanishing (resp. saturated) amplitude. Such front-like shaping in $A_1(t)$ occurs over time intervals where f_1 passes from being present (amplitude close to its saturated value), to absent (amplitude close to zero) in the signal (resp. from absent to present). Plotting the fraction of points as a function of their distance to the origin (Fig. 11b, d), it is observed two maxima, one at $r_{\text{inf},1} \simeq 0.14$, the other at $r_{\text{sup},1} \simeq 0.63$ for f_1 .

Fig. 11 **a** Phase portrait of the filtered signal $s_1(t)$, generated by applying the SVD to $s_1(t)$, as defined by Eq. 9. The two axes are the first two columns X_1 and X_2 of the matrix X , as defined by Eq. 10. **b** Radius distribution in the phase space. Each class of radius covers a $\Delta r = 0.01$; **c** idem to **a**, and **d** idem to **b**, for mode f_2



The first maximum is associated with the *vanishing* radius [when f_1 is absent from $s_1(t)$], the second maximum to the *saturated* radius. In between stands a relative minimum at $r_{0,1} \simeq 0.37$, which may be considered as the core of the transitory area, and may provide a new threshold amplitude. Next, the phase portrait distance $r(t) = \sqrt{(X_1(t) - \bar{X}_1)^2 + (X_2(t) - \bar{X}_2)^2}$, of a point at time t with respect to the phase portrait centre, has to be compared with $r_{0,1}$. If $r(t) > r_{0,1}$, the mode is present in the signal, at time t , and absent otherwise. Noting n_1 the number of points in the phase space that fulfil the criterion, one can define the rate of presence of mode f_1 in the signal $s(t)$ as $\eta_1 = n_1/N$, N being the overall number of points. The same is done for f_2 , defining its rate of presence η_2 . One finds, in its associated phase portrait, $r_{\text{inf},2} \simeq 0.09$, $r_{\text{sup},2} \simeq 0.51$, and $r_{0,2} \simeq 0.30$. Applying the criterion, it comes $\eta_1 = 0.56$ and $\eta_2 = 0.46$. It is also found that both modes are simultaneously present in the LDV signal over 7.3% of T , while they are simultaneously absent from the signal over 6.0% of T . Rather surprisingly, the criterion gives results closer to those obtained when using the mean amplitude criterion, although it was expected to be more similar to the threshold value defined by Eq. 6. Note that the procedure may also introduce oscillations at $2\omega_1$ in $r(t)$, at least when $X_1(t) = \rho_1(t)\cos(\omega_1 t)$ and $X_2(t) = \rho_2(t)\sin(\omega_1 t)$, with $\rho_1 \neq \rho_2$, which might usually be the case (see Fig. 12).

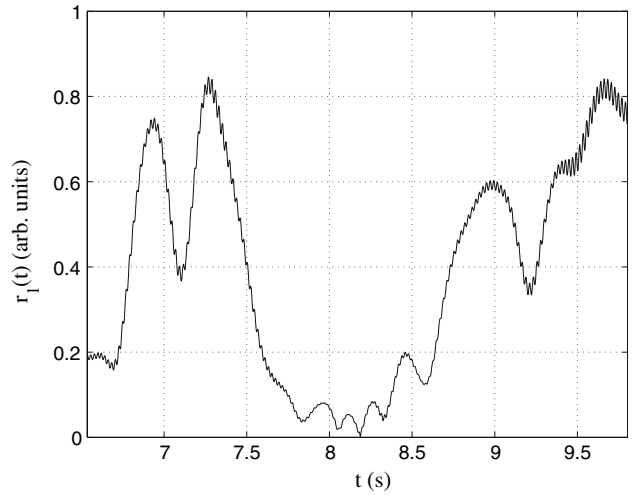


Fig. 12 Radius in the phase space, defined as $r(t) = \sqrt{(X_1(t) - \bar{X}_1)^2 + (X_2(t) - \bar{X}_2)^2}$, versus time, here for the mode f_1 . Small amplitude, high frequency oscillations at $2f_1$, can be seen on the slowly varying radius dynamics

8 Burst lifetime statistics

In what follows, the analysis is based on the threshold value defined by the time averaged amplitude. A sequence of events where both modes become simultaneously present or absent from the signal $s(t)$ is shown in Fig. 13 (grey

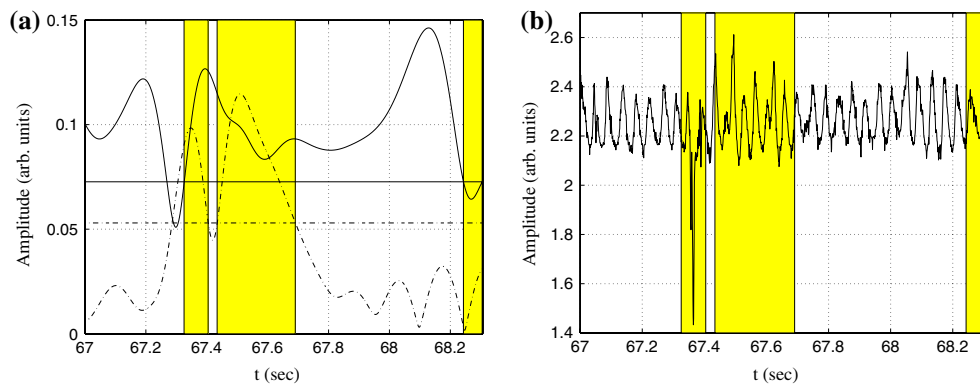


Fig. 13 Sequence of events where both modes become either simultaneously present or absent from the signal, (a) for the amplitudes, (b) for the signal $s(t)$. Such events are coloured in grey filled bands. The longest durations of simultaneous absence or presence are shown in Fig. 14.

Both mode lifetime distributions exhibit an exponential-like decay (Fig. 15), with a characteristic time duration $\tau_1 = 650$ ms for f_1 , $\tau_2 = 615$ ms for f_2 . The mean lifetimes are found to be $\bar{\Delta}t_1 = 795$ ms for mode f_1 (corresponding to about 20 cycles of basic oscillations at f_1), and $\bar{\Delta}t_2 = 545$ ms for mode f_2 (corresponding to about 18 cycles of basic oscillations at f_2). The longest lifetimes of each mode is found to be of the order of 5 s.

Similarly, the common time of presence or absence distributions are plotted in Fig. 16.

The successive n lifetimes $\{\Delta t_i^{(n)}, n = 1, 2, \dots\}$ of mode f_i , $i = 1, 2$, are plotted with respect to the $(n - 1)$ th lifetime in Fig. 17. In Fig. 18 is plotted the recurrence time of a mode, *i.e.* the elapsed time $\Delta\tau_{(k+1)}$ between two risings of the mode f_i in the signal with respect to $\Delta\tau_k$. From Figs. 17, 18, a deterministic law underlying the mode-switching phenomenon does not clearly appear, and a phase space analysis might help.

bands. Left-hand and middle bands: both modes are present; right-hand band: both modes are absent. The threshold mean amplitude is shown as horizontal line in (a); solid for \bar{A}_1 , broken for \bar{A}_2

9 Phase space analysis

We now come back to the phase space reconstruction introduced in Sect. 7. The SVD is now applied to the original signal $s(t)$. It provides the matrix X defined in Appendix. Using a Grassberger Procaccia algorithm to estimate the phase space dimension (Grassberger and Procaccia 1983), it is found that the correlation dimension dynamics of the LDV signal $s(t)$ is of the order of 4.2, which means that the actual phase space dimension would at most be 10. Consequently, the number of coordinates required out of X is at most ten. The 2D projections of the phase portrait, in the planes (X_1, X_2) and (X_2, X_3) , are shown in Fig. 19a, b, respectively. The phase portrait is composed of a torus-like trajectory in a plane (almost) coplanar to the plane (X_2, X_3) , and exhibits transverse excursions in the X_1 direction.

To gain insights, a Poincaré section (Π) is defined by

$$\Pi = \{X_1, X_3 \in \mathbb{R}^2 | X_3 = 0, X_2 < 0\}. \quad (7)$$

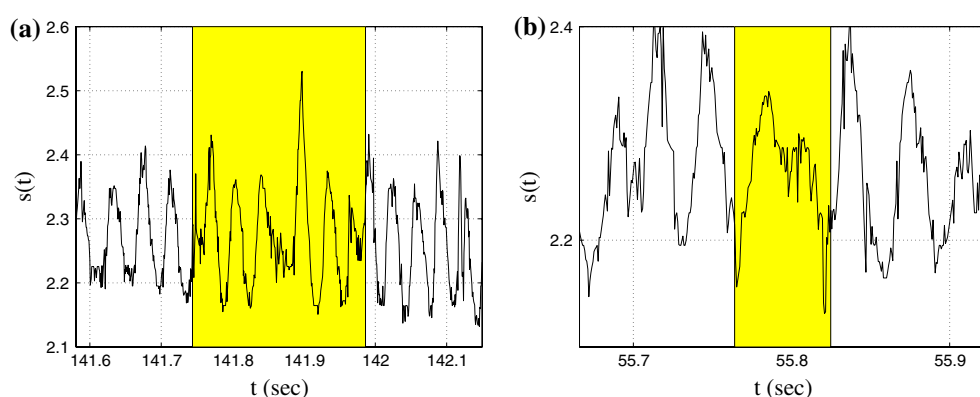


Fig. 14 Longest time of simultaneous (a) presence, (b) absence, of modes f_1 and f_2 in the signal, following the criterion based on the time averaged amplitude

Fig. 15 Life time distribution
(a), (b) for mode f_1 , (c), (d) for mode f_2

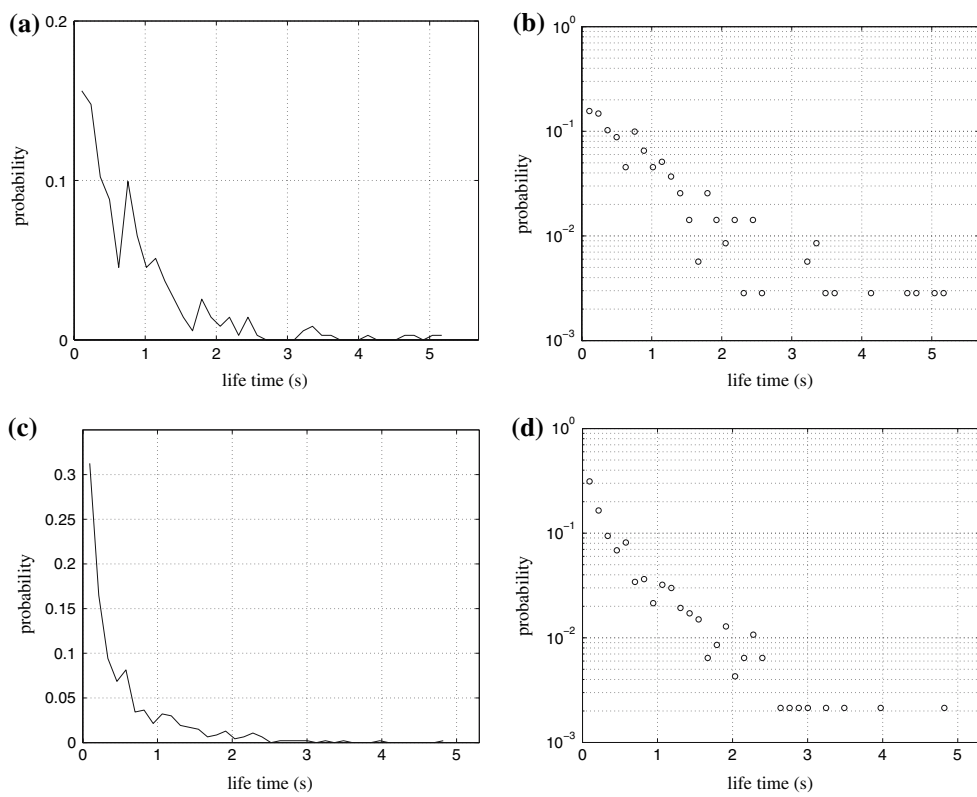


Fig. 16 Common time range distributions of (a) presence or (b) absence of both modes in the signal. The threshold amplitude is defined by the time-averaged amplitude

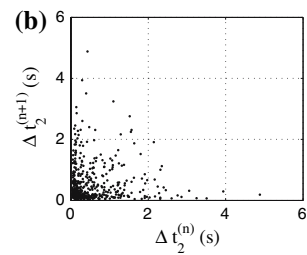
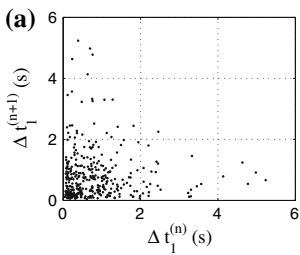
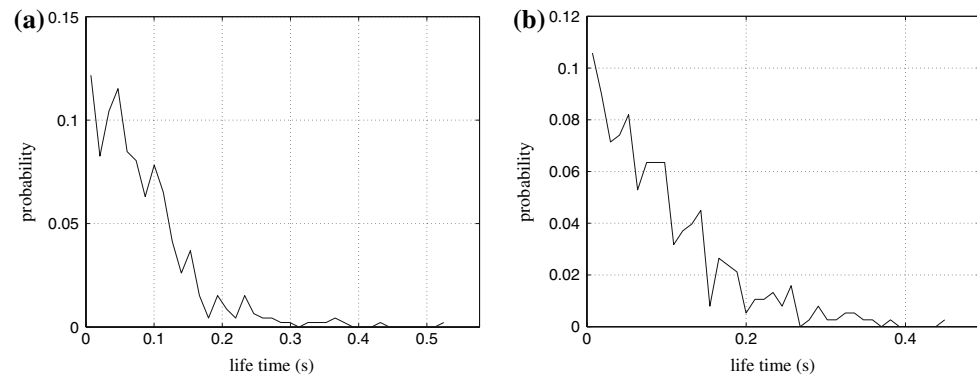


Fig. 17 ($n + 1$)th lifetime of mode (a) f_1 , (b) f_2 with respect to the n th one

The resulting Poincaré section is shown in Fig. 20. It exhibits two intricated clouds of points, each corresponding to the intersections of the (Π) plane with either the orbits at f_1 or f_2 (represented in two different colours). Points P_1 and

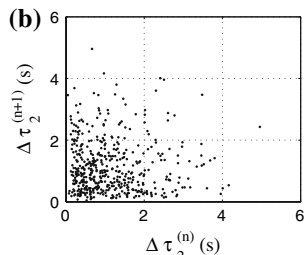
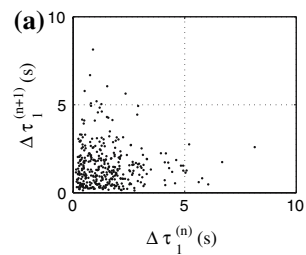


Fig. 18 ($n + 1$)th cycle of rising/disappearance of mode (a) f_1 , (b) f_2 in the signal with respect to the n th one

P_2 are the barycenters of the set of orbits associated with the modes f_1 and f_2 , respectively. Their coordinates, in the 10D reconstructed phase space, are:

Fig. 19 Phase portrait of $s(t)$, **(a)** in the (X_1, X_2) projection of the phase space (see Appendix for a description of matrix X), **(b)** in the (X_2, X_3) projection of the phase space

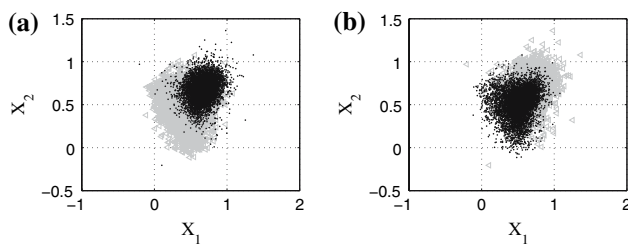
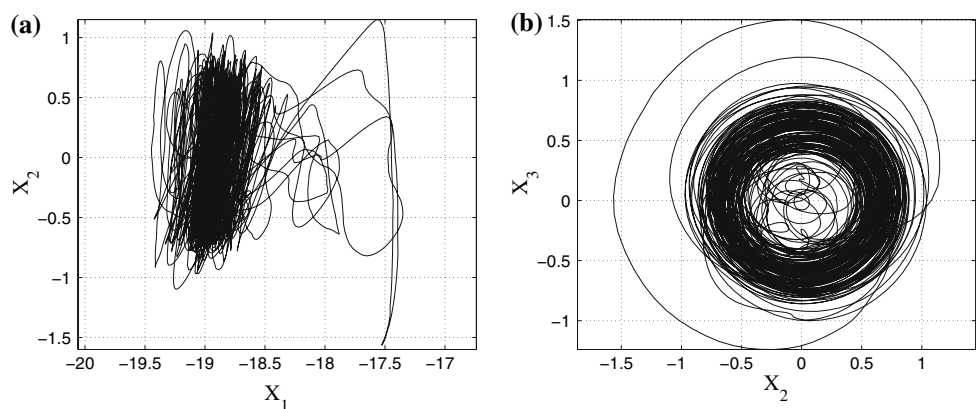


Fig. 20 Poincaré section (Π), as defined by Eq. 7. **a** Dark points are the (Π) intersections with mode f_1 , grey points are the (Π) intersections with mode f_2 , **b** colours are inverted with respect to the previous case

$$P_1(-18866, 673, -31, -64, -13, 74, 37, -21, 24, 7.3) \times 10^{-3}$$

$$P_2(-18780, 509, -28, -15, -156, 39, 10, -22, -4, 6) \times 10^{-3}$$

Both barycenters are very close, which is coherent with the fact that orbits corresponding to modes f_1 and f_2 are closely intricate. In case there would exist two different attractors, each associated with each mode of oscillations, then the transition from one attractor to the other might be very easy, their basin of attraction presumably being intricate as well. In another case, the dynamics could evolve over one unique attractor. From the Hilbert analysis (see Fig. 7) and the power spectrum of Fig. 2, none mode never completely disappears from the signal (background level), since it can be seen from Fig. 15 that amplitudes $A_{1,2} = 0$ are very unlikely. Therefore, the dynamics should essentially evolve over a torus, whose section would most of the time be pretty elliptic, since one of the two amplitudes is usually small when the other is saturated. The phase space trajectories would essentially be orbits cycling along the torus, at the frequency of the strongest mode. At some time, mode predominance is exchanging, and the torus main extension would become the saturated amplitude of the other mode, while orbits would now evolve at the new frequency.

10 Conclusion

The self-sustained oscillations observed in open flows may present a very rich phenomenology. In the case of a fluid flowing above an open cavity, here at a moderate Reynolds number ($Re_L \simeq 14,000$), for an aspect ratio $R = 2$, the nonlinear competition between noncommensurable modes of oscillations reveals to be essentially dominated by a mode-switching scenario. It is however shown, following any criterion introduced in this paper, that a non-negligible fraction of time can be found, where both modes may simultaneously be present in, or absent from the flow oscillations.

Working in the phase space, it might be possible to introduce another criterion based on a first-return map built on the Poincaré section. Would the resulting symbolic dynamics have any sense with respect to the mode-switching phenomenon, it would be possible to define an absolute criterion, whose time-precision would be at the scale of the orbit duration (impact through the Poincaré section). A deeper study of the symbolic dynamics, though out of the scope of this paper, would therefore be interesting to investigate, possibly revealing the mechanisms responsible for the exchange of stability between the two modes.

The spatial flow structure is controlled by the length and height of the cavity, and by the lateral (rigid) boundary conditions (Faure et al. 2007). The later are suspected to play a key role in the nonlinear mode competition observed in the shear layer oscillations. Further investigations are necessary. Hopefully, 3D direct numerical simulations of the flow, in the condition of the experiment, should advantageously help understanding the fine interaction between the spatial structure dynamics, and the shear layer time dynamics. It is known that modifying Re_L will also modify the excited mode frequencies in the shear layer, their relative amplitude in the spectrum, and modifies their rates of existence as well as the fraction of common times (Faure et al. 2005).

11 Appendix: Phase portrait based on a singular value decomposition

The method for reconstructing an embedding phase space is based on the singular value decomposition (SVD) of the matrix S of the delayed data, built from the LDV signal $s(t)$ as

$$S = \begin{pmatrix} s(t_1) & s(t_2) & \dots & s(t_m) \\ s(t_2) & s(t_3) & \dots & s(t_{m+1}) \\ \vdots & & & \\ s(t_{N-m+1}) & s(t_{N-m+2}) & \dots & s(t_N) \end{pmatrix}. \quad (8)$$

Matrix S is of size $m \times N$. Times $t_k = t_{1+k} \delta t$, $k \in \mathbb{N}$, are defined with respect to the initial acquisition time t_1 , with $\delta t = 0.65$ ms. Henceforth, one period of the basic cycle contains about $m = 70$ points. The SVD procedure then identifies the singular vectors of the matrix S (and its associated singular values), which correspond to the proper “deterministic” axes of the matrix. The singular vectors are ranked as columns of a matrix V_S such that

$$S = U_S \cdot D_S \cdot V_S^T, \quad (9)$$

where D_S is the $m \times N$ matrix of the singular values (ranked from the largest to the smallest one). Note that S is most usually not a square matrix, and therefore most of its singular values vanish. In fact, $N \gg m$, and therefore $(N - m) \gg 1$ singular values are equal to zero. Consequently, it has no sense to compute all the singular values and singular vectors of S , since only m of them are dynamically relevant. The time-delayed system S is then projected onto its singular basis, namely, V_S , through the matrix product $S \cdot V_S$. The matrix V_S being orthogonal, it follows that $V_S^T \cdot V_S$ is the identity matrix, and therefore $S \cdot V_S = U_S \cdot D_S$. Henceforth, the searched out phase space may be spanned by the columns of the matrix X , defined as

$$X = U_S \cdot D_S. \quad (10)$$

References

- Broomhead D, King G (1986) Extracting qualitative dynamics from experimental data. *Physica D* 20:217–236
- Faure TM, Debesse P, Lusseyran F, Gougam P (2005) Structures tourbillonnaires engendrées par l’interaction entre une couche limite laminaire et une cavité. In: 11ème Colloque de Visualisation et de Traitement d’Images en Mécanique des Fluides, IUTAM, Lyon, France, pp 6–9
- Faure T, Adrianos P, Lusseyran F, Pastur L (2007) Visualizations of the flow inside an open cavity at medium range reynolds numbers. *Exp Fluids* 42:169–184
- Gadoin E, Quéré PL, Daube O (2001) A general methodology for investigating flow instability in complex geometries: application to natural convection in enclosures. *Int J Numer Methods Fluids* 37:175–208
- Gouesbet G, Letellier C (1994) Global vector-field reconstruction by using a multivariate polynomial l_2 approximation on nets. *Phys Rev E* 49:4955–4972
- Grassberger P, Procaccia I (1983) Characterization of strange attractors. *Phys Rev Lett* 50:346–349
- Kegerise M, Spina E, Garg S, Cattafesta L (2004) Mode-switching and nonlinear effects in compressible flow over a cavity. *Phys Fluids* 16:678–687
- Le Quéré P, Masson R, Perrot P (1992) A Chebyshev collocation algorithm for 2D non-Boussinesq convection. *J Comput Phys* 103(2):320–335
- Leonard BP (1979) A stable and accurate convective modelling procedure based on quadratic upstream interpolation. *Comput Methods Appl Mech Eng* 19:59–98
- Podvin B, Fraigneau Y, Lusseyran F, Gougam P (2006) A reconstruction method for the flow past an open cavity. *J Fluids Eng* 128:531–540. doi:[10.1115/1.2175159](https://doi.org/10.1115/1.2175159)
- Rockwell D (1983) Oscillations of impinging shear layers. *AIAA J* 21(5):645–664
- Rockwell D, Naudascher E (1979) Self-sustained oscillations of impinging free shear layers. *Annu Rev Fluid Mech* 11:67–94

Three-dimensional centrifugal instabilities development inside a parallelepipedic open cavity of various shape

Thierry M. Faure · Luc Pastur · François Lusseyran · Yann Fraigneau · Danièle Bisch

Received: 23 July 2008 / Revised: 27 April 2009 / Accepted: 29 April 2009 / Published online: 16 May 2009
© Springer-Verlag 2009

Abstract This experimental study reports flow developments inside a parallelepipedic cavity of variable shape and dimensions. That flow is generated by the interaction between a laminar boundary layer and the cavity, which creates shear-layer oscillations. The aim is to understand the three-dimensional flow morphology varying the Reynolds number and the cavity shape. Flow visualizations are obtained in a plane situated inside the cavity in order to get the dynamical structures. Dimensional analysis of the cavity flow teaches that three dimensionless numbers are necessary for the flow reduction. This is confirmed by experimental results pointing thresholds of appearance of instabilities identified for some combinations of Reynolds number and geometric parameters. The key mechanisms for their existence are centrifugal effects induced by a vortex of spanwise axis with sufficient intensity, and viscous effects due to the wall confinement of the cavity. Their destruction is linked to flow transition to turbulence above a limiting convective velocity generated by the vortex of spanwise axis. These

instabilities are generally present in a spanwise row of counter-rotating pairs of vortices, but for some cases, isolated pairs are also identified. Secondary modulations of primary instabilities are also present for particular parameters. Results permit to discriminate the relevant scales associated with the shear layer and the inner cavity flow.

List of symbols

A	Plate length upstream of the cavity
B	Plate length downstream of the cavity
D	Wind tunnel height
F	Span ratio
H	Cavity height
\mathcal{H}	Helicity
L	Cavity length
N	Number of pairs of spanwise vortices
R	Aspect ratio
Re	Reynolds number
S	Cavity span
t	Time
U_e	External velocity
U_c	Maximum advection velocity inside the cavity
\vec{V}	Velocity vector
W_s	Spanwise drift velocity
(x, y, z)	Cartesian coordinates
δ_2	Momentum thickness of the upstream boundary layer
λ	Spanwise wavelength of the instabilities
μ	Dynamics viscosity
ν	Kinematics viscosity
ρ	Density
$\bar{\omega}$	Vorticity

T. M. Faure (✉) · L. Pastur · F. Lusseyran · Y. Fraigneau · D. Bisch
Laboratoire d’Informatique pour la Mécanique et les Sciences de l’Ingénieur, Unité Propre de Recherche 3251, Centre National de la Recherche Scientifique, B.P. 133, 91403 Orsay Cedex, France
e-mail: thierry.faure@limsi.fr

T. M. Faure
Université Pierre et Marie Curie, Paris 6, 4 Place Jussieu,
75252 Paris Cedex 05, France

L. Pastur
Université Paris-Sud, Paris 11, 91405 Orsay Cedex, France

1 Introduction

The interaction between a boundary layer and a cavity results in a complex coupling of shear layer and recirculating flow (Pereira and Sousa 1995). That wall-bounded three-dimensional flow is the place for the development of primary instabilities whose dynamics is strongly led by the vortical flow motion inside the cavity. Such instabilities are found for different configurations.

The Görtler instability is a boundary layer instability induced by concave curvature. When the boundary layer is very small in comparison with the wall curvature radius, the centrifugal effects can be neglected in the basic state, which is considered as a quasi-parallel flow. However, centrifugal effects actually act in destabilizing the basic flow. The Görtler instability is the origin of transition to turbulence in bounded shear flow within low disturbance environment (Saric 1994). It is found from the range of low velocities (Cui 2004), to hypersonic flows (Aymer de la Chevalerie et al. 1997; Navarro-Martinez and Tutty 2005).

The Taylor-Couette instability is a centrifugal instability in a viscous flow confined by two rotating cylinders of radii R_1 and R_2 . The basic state is the sum of a linear and a hyperbolic function of the radius. This instability has been widely studied for a narrow gap $d = R_2 - R_1$ with a stability transfer, above a critical threshold, between the basic state and stationary toroidal vortices. Similarly, Dean instability occurs for the same configuration with the presence of an azimuthal pressure gradient. Instability thresholds from the basic state to stationary vortex rings have also been established. An alternative approach of the shear-layer cavity flow has been conducted by its identification with the Taylor-Couette problem: the solid-body rotation of a central vortex is similar to the inner rotating cylinder and the cavity walls are the outer fixed cylinder (Brès and Colonius 2008). Then, it is possible to unify the previous types of instabilities into a single type coupling centrifugal effects and wall effects.

Flow dynamics studies have been achieved on lid-driven cavities for the same Reynolds number range as the present case: the difference is the absence of a developing unstable shear layer. Ghia et al. (1982) used a multi-grid method to simulate the flow inside a square lid-driven cavity, where a main vortex is developing along the whole length. Visualizations have been conducted by Koseff and Street (1984a, b, c) with dye emission, with tiny particle seeding by Migeon (2002) and Migeon et al. (2003) and comparisons with numerical simulations were carried out for the same measurements (Guermond et al. 2002). In these studies, a row of vortices was identified along the span.

This work considers centrifugal instabilities generated by the combination of wall curvature and a recirculating vortical flow inside a parallelepipedic cavity. A numerical

simulation of the three-dimensional development of the cavity flow has been conducted for compressible flow conditions (Brès and Colonius 2008). The nature of the upstream boundary layer is important for the cavity flow developments (Chatellier et al. 2004; Chang et al. 2006). Visualizations in different planes have been reported previously (Faure et al. 2007) showing the main cavity flow morphology, for Reynolds numbers built on the cavity length, between 860 and 27,700. The driving mechanisms of the flow are the shear layer that is developing above the cavity, and at least one vortex of spanwise axis, developing inside the cavity.

The present study focuses on flow visualizations in a spanwise plane inside the cavity at very low Mach number, varying the length and the height of the shear-layer-driven cavity. The aim is to address the following issues:

- analyze whether the flow dynamics can be reduced to dimensionless numbers,
- give the flow morphology with cavity geometry and Reynolds number,
- track threshold parameters for which centrifugal vortices are present,
- provide features of centrifugal instability vortices.

2 Experimental setup and apparatus

The airflow is generated by a centrifugal fan placed upstream of a settling chamber (Fig. 1a). The seeding particle injection is achieved at the fan inlet. An axial duct

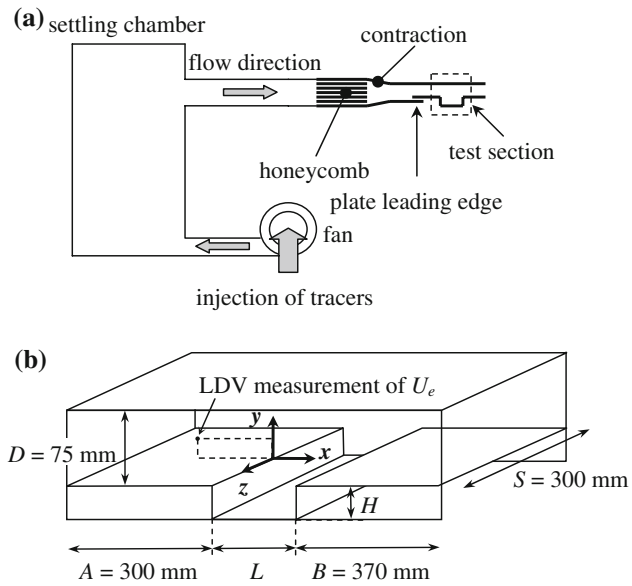


Fig. 1 Experimental setup: **a** wind tunnel, **b** test section dimensions and coordinates system

terminated with honeycomb and a contraction drives the flow toward the experimental facility, which consists of a test section containing a flat plate beginning with an elliptical leading edge, in order to fix the boundary layer origin. The length of the plate is $A = 300$ mm providing an established laminar boundary layer at the cavity upstream edge. To reduce light wall reflections, the whole test section is made of antireflection glass 2 mm in thickness. The cavity height is varied between $H = 25$ and 150 mm. Its span $S = 300$ mm is constant because the cavity ends in this direction are the wind tunnel vertical walls (Fig. 1b). In addition to the Reynolds number, two other dimensionless numbers are defined: the span ratio, $F = S/H$ (span over height) studied from 2 to 12, and the cavity aspect ratio, $R = L/H$ (length over height) from 0.25 to 2.5. This latter ratio can be changed continuously by moving the glass pieces consisting in the downstream wall of the cavity and the downstream plate, which has a length $B = 370$ mm. The flow is incompressible since the maximum Mach number is lower than 0.01. At the wind tunnel outlet, the flow is rejected inside the experimental room.

The choice of a relevant length scale to build a Reynolds number is of first importance. Many authors working with compressible conditions (Forestier et al. 2003) chose a Reynolds number built on the momentum thickness δ_2 of the laminar boundary layer upstream of the cavity, which is the length scale for the shear layer initial development, and the upstream external velocity U_e . In the present work, that Reynolds number $Re_{\delta,2}$ is between 71 and 180, corresponding to external velocities from 0.57 to 2.77 m s⁻¹. If we consider the development of the shear layer above the cavity, the amplitude of its oscillations increases with the distance from the upstream edge of the cavity. Then, the cavity length L is pertinent for selection of linearly unstable modes in the shear layer. As a consequence, the relevant Reynolds number is Re_L . In the present study, it varies from 860 to 36,900. If we focus on the flow development inside the cavity, the confinement between the upstream and downstream walls, distant of L , and the confinement between the bottom of the cavity and the shear layer, distant of H , lead to define an additional Reynolds number Re_H , here from 1,150 to 36,800. As it has been shown (Brès and Colonius 2008), the development of an unstable three-dimensional unsteady mode inside the cavity with an oscillation frequency based on the cavity height H is comparable in all configurations, suggesting that H is the most appropriate scale to characterize the three-dimensional flow development. Then, that latter Reynolds number will be chosen and its relevance for the development of instabilities will be confirmed hereafter. Three independent dimensionless numbers are thereafter necessary for the cavity flow description, respectively, the Reynolds number

based on cavity height $Re_H = \rho U_e H / \mu$, the aspect ratio $R = L/H$, and the span ratio $F = S/H$.

The external velocity is measured with laser Doppler velocimetry 102 mm upstream of the cavity and 25.5 mm above the flat plate. This point of measurement is in the external flow sufficiently upstream of the cavity to avoid any perturbation from the instability developing above the cavity. The origin of the coordinate system is set at the upstream edge of the cavity at mid-span, the x -axis is the flow direction, the y -axis is normal to the upstream wall where the boundary layer develops, and the z -axis is along the cavity span. It has been checked that the test section upper wall, located at $D = 75$ mm above the cavity, has no influence on the shear layer developing on the cavity and, as a consequence, no influence on the flow. The thickness of the boundary layer developing on this wall has no influence on the external flow along the longitudinal and spanwise directions. It has been shown for backward facing step flows that the influence of the upper wall affects the flow from 10 cavity heights downstream of the beginning of the step. The cavity under investigation is not a shallow cavity (for $L/H > 5$), where the shear layer tends to attach the cavity floor. However, in that configuration, the development and propagation of large-scale vortices appear to be relatively unaffected by confinement effects. In the present study, it will be even more so given the maximum aspect ratio of 2.5.

Hereafter, the expressions “upstream” and “downstream” will refer to the external velocity direction. Flow visualizations by tracer injection are carried out with fog obtained with a low density smoke generator. As a result, the observed structures are streaklines of fluid injection inside the cavity and not the streamlines themselves. The identity between streaklines and streamlines is valid only for stationary flows, which is not strictly the case for present measurements. However, the Reynolds number is sufficiently low and the velocity inside the cavity is small enough to ascertain that visualizations show flow structures in well-seeded regions. This has been confirmed by comparisons with PIV measurements (Faure et al. 2008). Finally, the flow injection inside the cavity gives information on the flow dynamics and the developing structures.

The light source is a 5 W argon-ion laser tuned to the blue wavelength (488 nm). The laser beam provides, by passing through a cylindrical lens, a sheet whose thickness is 0.25 mm. The image recording system consists of a 10-bit camera with $1,032 \times 778$ pixels and a frequency of 20 Hz. The camera has a complete view of the cavity span. For each cavity geometry, the position of the (x, z) visualization plane is set to a relative vertical position $y^* = y/H = -0.3$ (Fig. 2). An exploration of the cavity along the y -axis points out the overall annular flow pattern. That particular value of y^* is retained, for comparison of

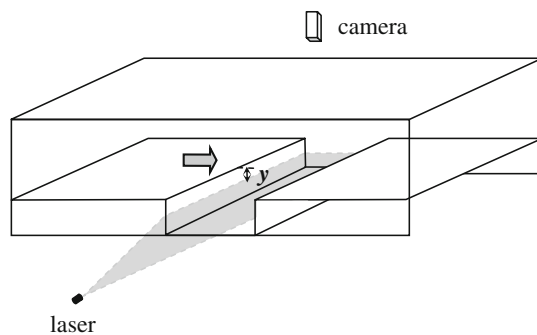


Fig. 2 Visualization in a (x, z) plane inside the cavity

different cases, because a vortex of spanwise axis is always present in the upper part of the cavity. The recording time is 25 s, which is sufficient to capture the flow dynamics unsteadiness. The repeatability of flow visualizations has been checked by recording different image series with different wind tunnel runs, and by testing different smoke injections. The external flow is established and uniformly seeded with smoke when the images are recorded. Note that if the observation time is too long, there is a saturation of the cavity with smoke and no dynamical flow pattern can be identified anymore.

3 Flow morphology

The three-dimensional character of the cavity flow has been recognized in previous studies (Faure et al. 2007; Brès and Colonius 2008). The shear-layer oscillations present amplification along the cavity length and interact with the downstream edge of the cavity (Fig. 3b). It results in a periodic injection of the external flow inside the cavity, carried along a primary vortex of spanwise axis. A secondary counter-rotating vortex of spanwise axis is also identified for long ($R > 1.25$ Fig. 3a) or short ($R < 0.75$ Fig. 3c) cavities. In that latter case, the vortex is placed in the lower half of the cavity while in the former case it forms in the upstream half of the cavity. These primary and secondary vortices are unsteady for most configurations. In the following part, the existence and properties of additional spanwise instabilities are discussed in relation with the Reynolds number, aspect ratio and span ratio. Three behaviors are identified: the absence of any spanwise row of vortices (Fig. 3d), spanwise instability vortices aligned in rows in the upper and lower cavity edges (Fig. 3e) or the presence of an isolated pair of vortices near the upstream edge (Fig. 3f). These instability vortices are carried off toward the lateral sides of the cavity by a spanwise flow, coming from the cavity sides toward the centerline and forming four recirculation cells (Fig. 3d–f). The development of these three-dimensional instabilities is caused by

perturbations on the basic flow. It has been shown that these instabilities are essentially independent of the Mach number (Brès and Colonius 2008).

3.1 Absence of spanwise row of vortices

Let us consider first cases where no spanwise row of vortices is present, that is the case when the advection flow velocity inside the cavity is not strong enough to destabilize the wall boundary layers. That advection velocity comes from the primary vortex, developing along the cavity span, which places in the downstream part of the cavity. Figure 4 shows the dynamical structures for $Re_H = 2,967$ and $R = 1$ in the visualization plane; the external flow, passing above the cavity, is from the bottom to the top of the figure. We note the downstream cavity shear-layer interaction with the cavity, producing seeding injection. The tracer is advected inside a main vortex, developing in the (x, y) plane, that is identified as the upstream cavity wall white line. The inner part of the cavity points out a flow coming from the sides to the centerline. Thus, there is a coupling between the left and right sides and the central part of the flow, leading to four low velocity recirculation cells inside the cavity (Faure et al. 2007).

Another type of flow without row of vortices shows two corner spiral vortices near the cavity spanwise sides, the left one being in a shadow zone (Figs. 5, 6). This type of flow has been reported and studied extensively in lid-driven cavities (Chiang et al. 1997; Migeon et al. 2003), for a Reynolds number of 1,000. The corner vortices are the consequence of a fluid transport from the sides into the primary vortex core, due to an Ekman layer. Note that in the present investigation, they have been identified only for the span ratio $F = 3$ and small aspect ratios $R < 1$. They may be present for other cases, but the laser plane, located at $y^* = -0.3$, is not necessarily perpendicular to the spiral vortex axis, preventing their visualization. In some cases, the effect of a limited flow seeding near the cavity span sides can also affect their observation.

3.2 Presence of spanwise instabilities

Figure 7 shows the cavity flow for a configuration with a row of mushroom-like patterns near the upstream cavity edge. Note that views in three different planes are not taken at the same time. The mushroom-like seeded patterns are visualizations of pairs of counter-rotating vortices whose axes are orthogonal to the observation plane (Fig. 7a, b). These vortices are also observed near the downstream cavity edge, and, for that case with a single vortex of spanwise axis spreading over the cavity section, this pattern is found for different relative position y^* inside the cavity,

Fig. 3 Sketch of the cavity flow dynamics in a (x, y) plane for: **a** $R > 1.25$, **b** $1.25 \geq R \geq 0.75$, **c** $R < 0.75$ and in a (x, z) plane with: **d** the absence of any spanwise row of vortices, **e** spanwise instability vortices aligned in rows and **f** the presence of an isolated pair of vortices

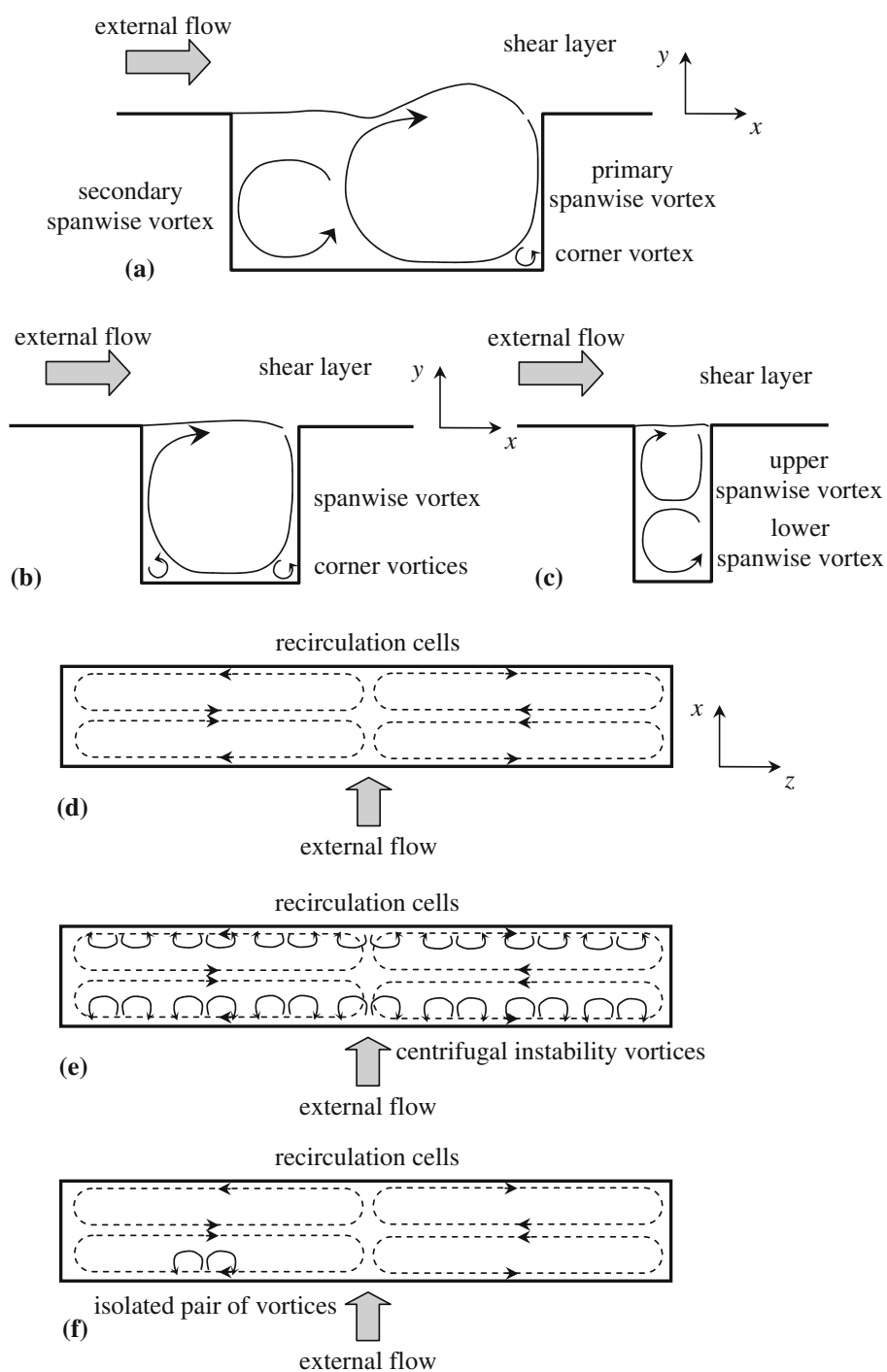


Fig. 4 Visualization for $F = 6$, $R = 1$ and $Re_H = 2,967$

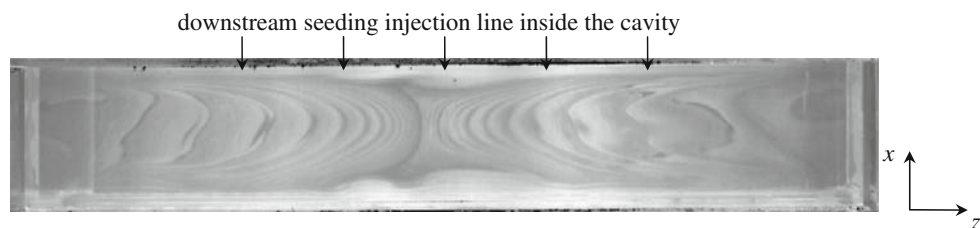


Fig. 5 Visualization for $F = 3$, $R = 0.25$ and $Re_H = 10,632$



Fig. 6 Visualization for $F = 3$, $R = 0.5$ and $Re_H = 4,120$

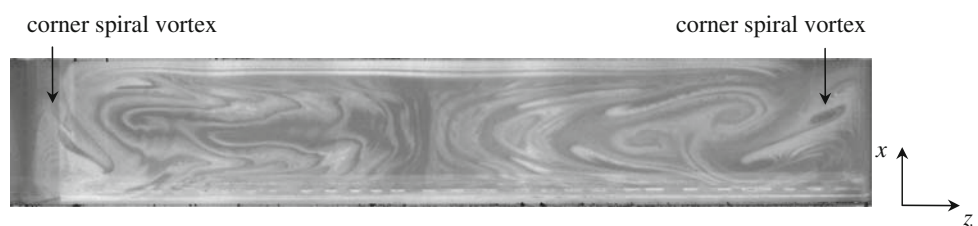
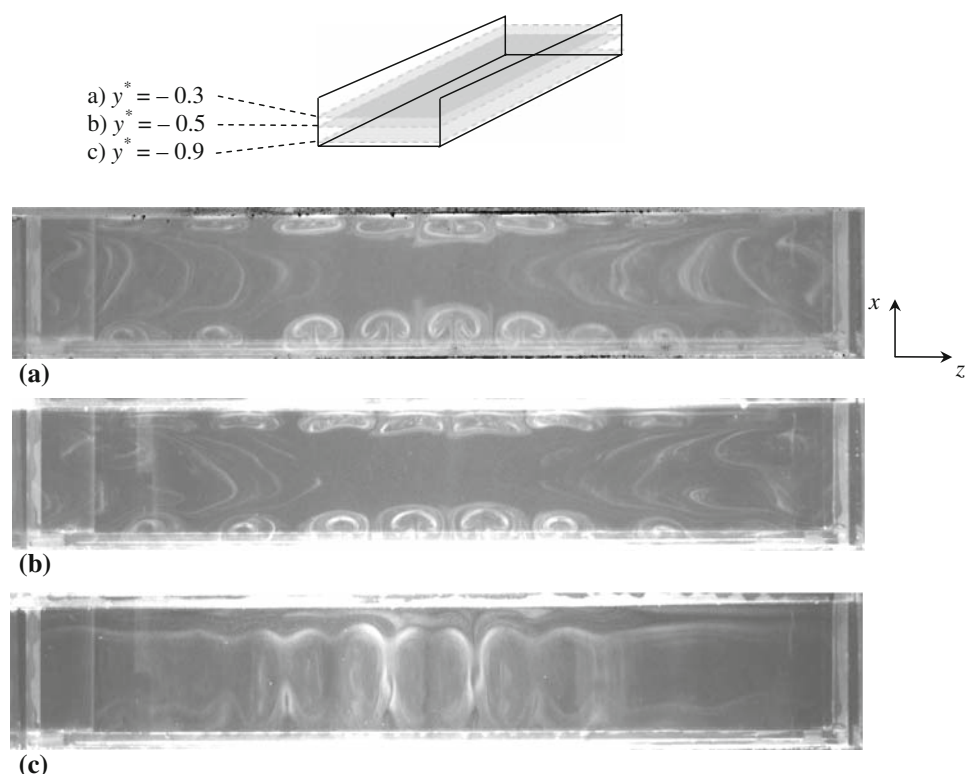


Fig. 7 Visualization for $F = 6$, $R = 1$ and $Re_H = 4,230$ for **a** $y^* = -0.3$, **b** $y^* = -0.5$ and **c** $y^* = -0.9$



evidence that they are forming a loop inside the cavity. Particularly for $y^* = -0.9$, near the cavity bottom, the row of vertical oval patterns is the intersection of tire-like instabilities with the laser plane (Fig. 7c). For that Reynolds number, between 9 and 11 pairs of vortices are observed. Note that the spacing between pairs is not constant, as mentioned by Finnis and Brown (1997). The vortices are smaller near the cavity sides (left and right part in Fig. 7a), where the spanwise flow is dominant, which evidences that the spanwise flow tends to stabilize the cavity boundary layer, preventing the development of instabilities.

For a larger Reynolds number (Fig. 8), the upstream row is still present, but is a little more deformed, while the downstream row tends to flatten on the wall. For that

configuration, between seven and nine pairs of vortices are observed near the upstream edge. They are also identified near the downstream cavity edge, evidence of their annular shape (Fig. 8).

The issue of the flow properties description previously addressed with a dimensional analysis can be raised if one observes the cavity flow for the same aspect ratio and the same Reynolds number, but for two different span ratios (Figs. 9, 10). For $F = 6$, there is a well organized row of mushroom-like patterns around the center span of the cavity (Fig. 9) while there is no more row of instabilities for $F = 2$ (Fig. 10).

An incompressible, isothermal, unsteady three-dimensional direct numerical simulation (DNS) has been realized for the particular case $F = 6$, $R = 1$ and $Re_H = 4,230$ with

Fig. 8 Visualization for $F = 6$, $R = 1.5$ and $Re_H = 4,230$

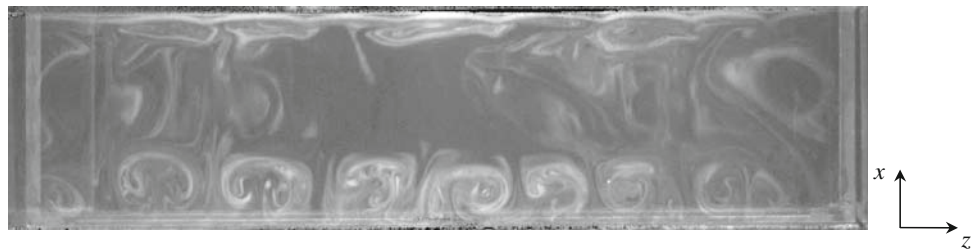


Fig. 9 Visualization for $F = 6$, $R = 0.75$ and $Re_H = 9,070$

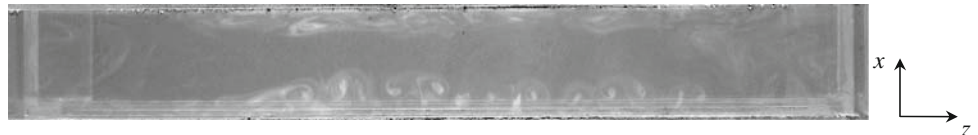
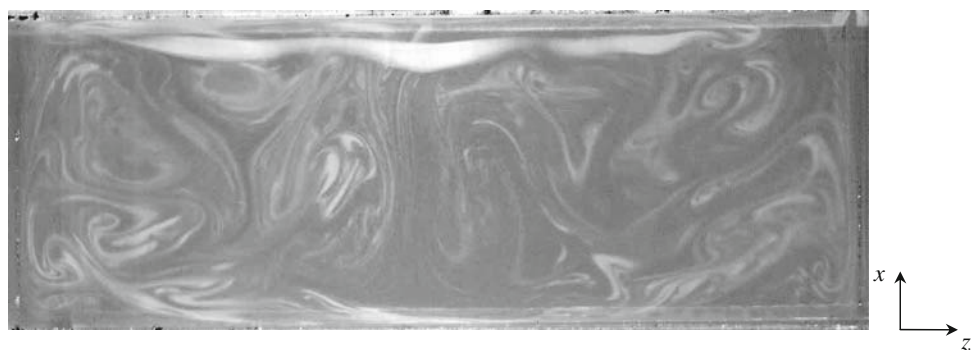


Fig. 10 Visualization for $F = 2$, $R = 0.75$ and $Re_H = 9,070$



the Olorin code developed in LIMSI. Navier-Stokes equations are discretized following a finite volume approach on a staggered structured grid with a second order approximation in time and space. Advection fluxes are calculated with a quadratic upstream interpolation for convective kinematics scheme (Leonard 1979). The discretized Navier-Stokes equations are implicitized on viscous terms leading to the set of Helmholtz equations resolved by an incremental alternating direction implicit method (Hirsch 1987). The incompressibility is realized with a usual prediction/projection method. The projection step leads to resolve a Poisson equation for the pressure with a relaxed Gauss-Seidel method, coupled with a multigrid method to accelerate the time convergence of calculation (Gadoïn et al. 2001). The grid is $256 \times 128 \times 128$ nodes with clustering of points spacing near the walls in the cavity and shear layer. The computational domain extends several cavity heights upstream and downstream. Top, bottom and lateral boundaries of the domain are rigid and a laminar boundary layer develops upstream of the cavity. The simulated velocity field is carried out over 40 s after the flow is converged in a statistical sense. The recording frequency is 30 Hz. It is representative of the dynamical

scales inside the cavity. Figure 11 shows the three-dimensional view of the cavity with the helicity of the velocity field defined as:

$$\mathcal{H} = \vec{V} \cdot \vec{\omega}$$

with \vec{V} the velocity vector, $\vec{\omega} = \overrightarrow{\text{curl}} \vec{V}$ the vorticity vector.

If one compares this result (Fig. 11) with the flow visualization (Fig. 7a), a very good agreement is found, which confirms the accuracy of the visualizations. The pair of positive and negative helicity contours corresponds to pairs of centrifugal instability vortices. A comparison in the (x, z) plane located at $y^* = -0.3$ is provided in Fig. 12. Note that the number of centrifugal instability vortices is a little more important in the simulation (between 12 and 14) than in the experiment (between 9 and 11), but their sizes are comparable. This difference is probably due to the comparison of two instantaneous fields at a different time. In addition, the lateral parts of the cavity along the span might be not correctly seeded in the visualization and we could miss some pair of instabilities. This simulation is also in good agreement with the calculation of Brès and Colonius (2008) obtained for a similar configuration with a compressible code with a linear stability analysis to search

Fig. 11 Helicity obtained by DNS for $F = 6$, $R = 1$ and $Re_H = 4,230$

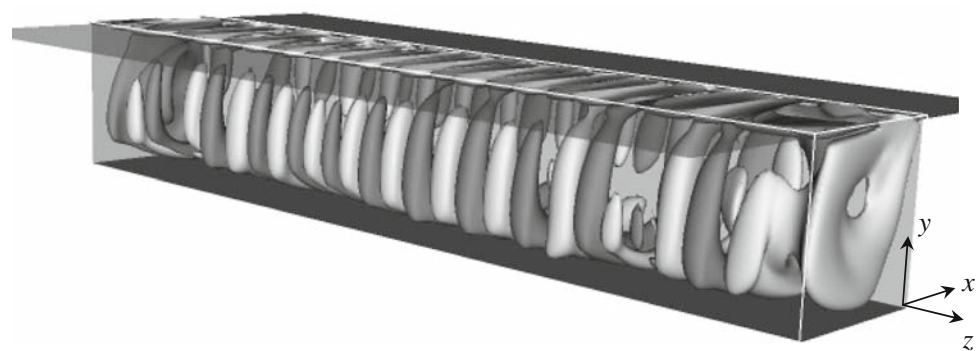
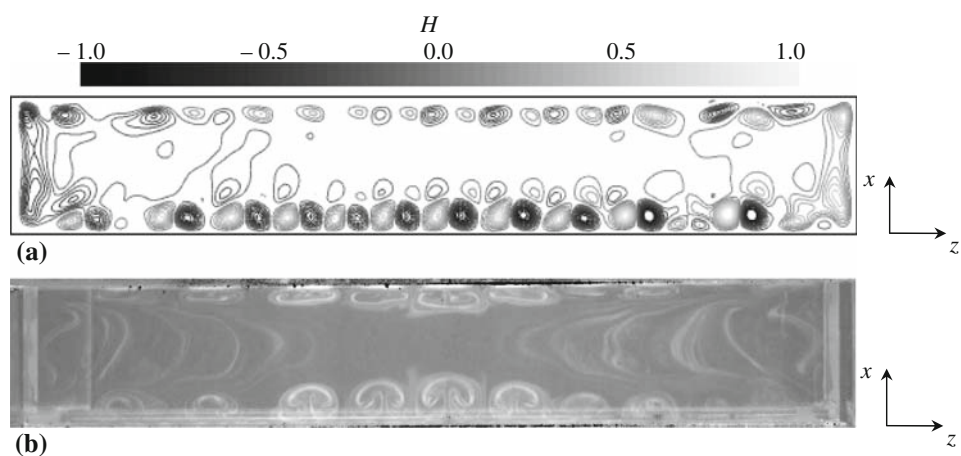


Fig. 12 Spanwise instabilities development for $F = 6$, $R = 1$ and $Re_H = 4,230$; **a** helicity of the numerical simulation and **b** flow visualization



for three-dimensional global instabilities of the two-dimensional mean flow, with lateral periodic boundary conditions. For that latter computation, the comparison with the visualization is realized in the central part of the cavity and does not take into account the effects of the lateral sides.

3.3 Secondary spanwise instabilities modulation

The row of instabilities is also subject, for some parameters, to present a second order time-dependent modulation of its amplitude (Fig. 13). The mechanism involves two adjacent pairs of mushroom-like structures. When one of these pairs is well developed in the z extension, its neighbor shows a narrow and elongated shape along the x -axis. Then the first one is crushed and ejected in the central part of the cavity, while the latter is increasing in z and decreasing in x extension, down to the upstream edge of the cavity. The mechanism of stability exchange is then repeated periodically in time with a given period of around 1 s. This time-dependent secondary instability is observed only for $F = 12$, for any aspect ratio where a row of instability is present and $R > 1$. To the authors' knowledge, this result

has never been mentioned in previous studies on open cavity flows or lid-driven cavity flows.

3.4 Isolated unsteady instabilities

Figure 14 points out a case where the pairs of vortices are not organized into a row, but rather form unsteady isolated pairs. In this figure, only one pair of vortices is present on the left side of the image near the upstream wall with no counterpart close to the downstream wall. This suggests that the annular shape of the centrifugal instability is lost.

3.5 Transitional flow

For high Reynolds numbers, no row of identified flow patterns is observable because the flow is transitioning toward turbulence (Fig. 15). Centrifugal instability vortices are, however, still present but their patterns are no more stable structures. They evolve in coherent large-scale structures, which cannot be identified with flow visualization because of tracer diffusion. As it can be thought, the Reynolds number is not the only parameter to define the

Fig. 13 Visualization for $F = 12$, $R = 1.75$ and $Re_H = 2,660$, with time interval $\delta t = 0.2$ s (the arrows note two neighboring pairs of vortices to point out their amplitude modulation with time)

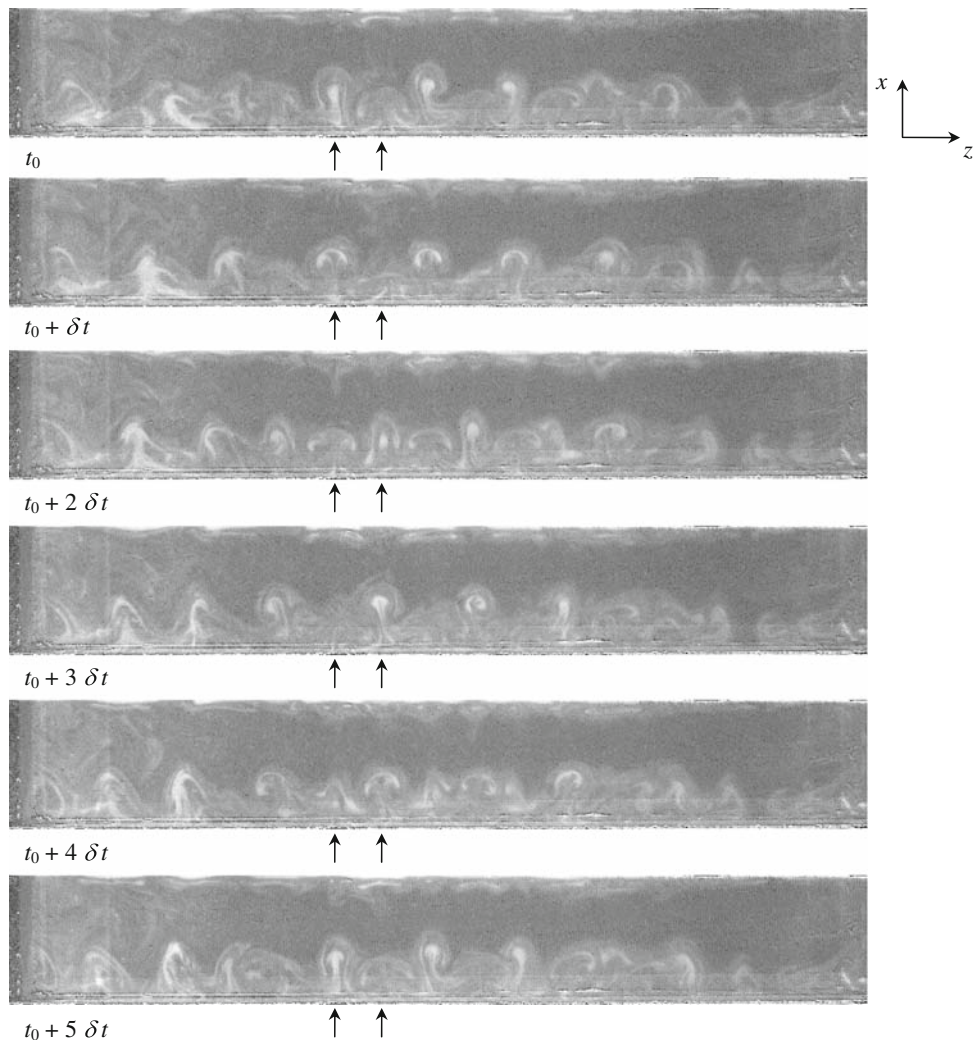


Fig. 14 Visualization for $F = 3$, $R = 0.5$ and $Re_H = 15,000$

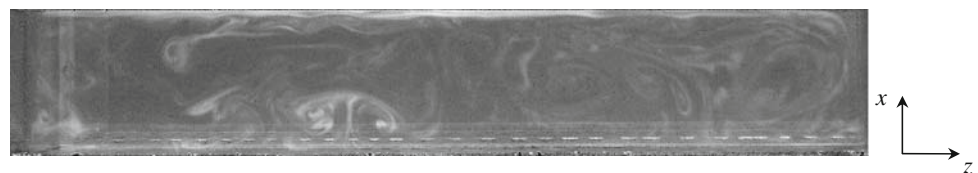


Fig. 15 Visualization for $F = 6$, $R = 1.5$ and $Re_H = 7,500$



presence or absence of these vortices, since the cavity geometry plays an important role.

The existence domain of structured spanwise vortices is thus limited by a domain with no spanwise row of vortices,

for lower Reynolds numbers, and a domain of transition of these vortices toward a turbulent flow, for much higher Reynolds numbers. The limiting thresholds are established and discussed in the following section.

4 Properties and data reduction

4.1 Influence of the span ratio

Figure 16 ascertains the domain of existence of centrifugal instability vortices, as functions of Reynolds number Re_H and aspect ratio R , for different span ratios F . For $F = 12$ –3 (Fig. 16a–c), the region where instabilities are present in the plane (R, Re_H) is forming a compact domain, which is not the case for $F = 2$ (Fig. 16d), where there are two distinct regions with the presence of spanwise instabilities linked by a zone with isolated pairs instead of rows of instabilities. For this case, this particular behavior may be caused by the influence of lateral confinement on the generation mechanism of the centrifugal instability vortices. The centrifugal instability vortices development can be understood as a three-dimensional perturbation of a two-dimensional mean flow. The secondary spanwise instability is only present for $F = 12$ and for every aspect ratio $R > 1$ (Fig. 16a). It might be thought that the time-dependent secondary instability of the row is due to a balance between the spanwise recirculation and the primary cavity vortex expansion, since a secondary vortex exists for $R > 1$.

Another interesting result, under the limitation of the investigation domain, is that the lower threshold of existence of instabilities is independent of Re_H for $R \geq 1.5$ (Fig. 16a–c). This suggests that the number of vortices of spanwise axis inside the cavity strongly modifies the instability process. Previous studies of lid-driven cavities, available for $F = 3$ and $R = 1$, show the development of centrifugal instability vortices for $Re_H > 1,300$ (Chiang et al. 1997, 1998) or $Re_H > 1,000$ (Koseff and Street 1984a, b, c), which is consistent with the present study since the centrifugal instability vortices are identified for the first Reynolds number measured, which is 4,120 (Fig. 16c). Studies for $F = 2$, $R = 1$ and $Re_H = 1,000$ and $F = 4$, $R = 2$ and $Re_H = 500$ (Migeon et al. 2003) do not show any development of centrifugal instability vortices, which is also consistent with the present measurements. We can say that the confinement effects, resulting in a division of the existence domain of instabilities, are limited to span ratios $F < 2$. If we get rid of the span ratio $F = 2$, a unique domain of existence of centrifugal instability vortices is found, also considering isolated vortices, with the same thresholds for any span ratio (Fig. 17). Thus, the analysis of the flow dynamical properties inside the cavity

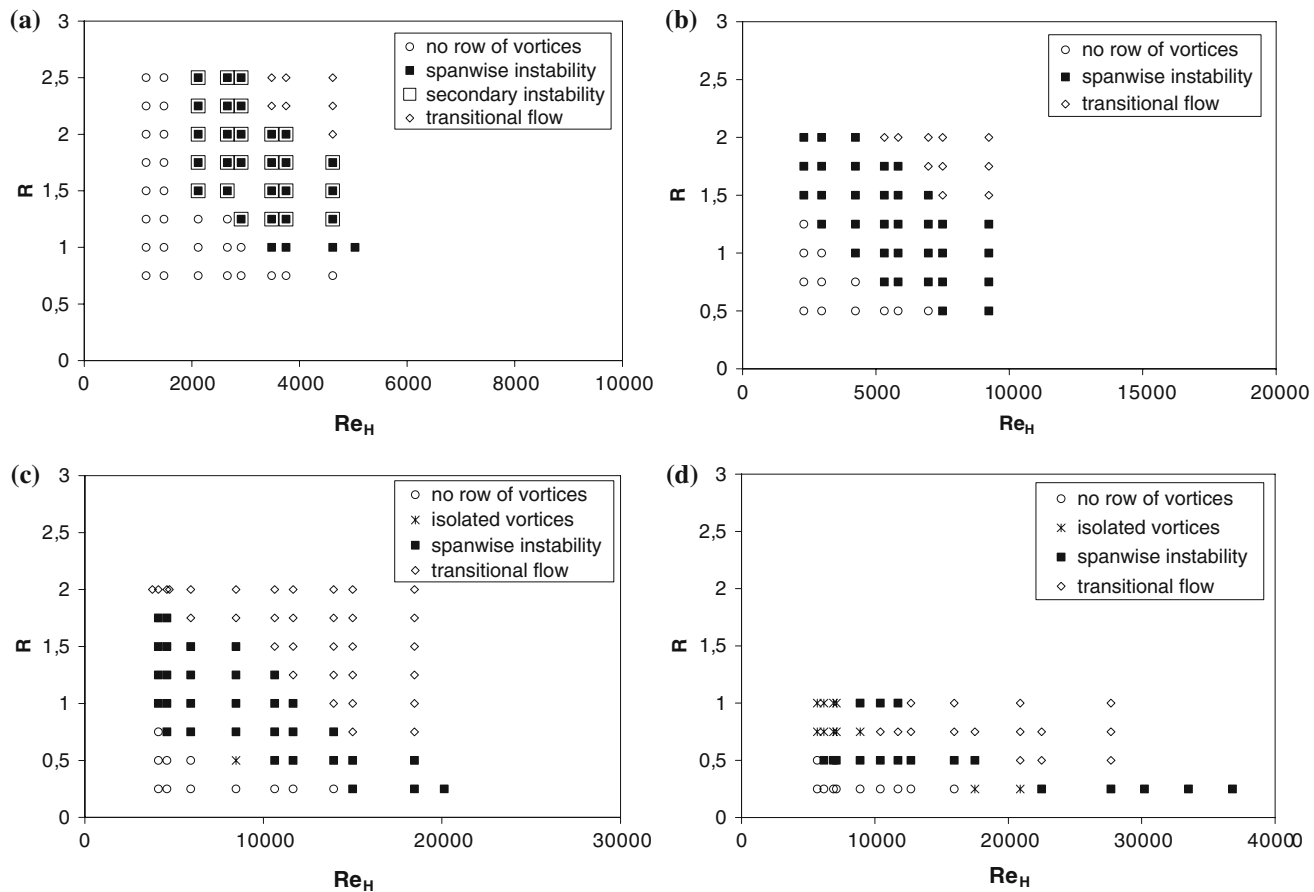


Fig. 16 Existence diagram of centrifugal instability vortices versus Re_H for **a** $F = 12$, **b** $F = 6$, **c** $F = 3$ and **d** $F = 2$

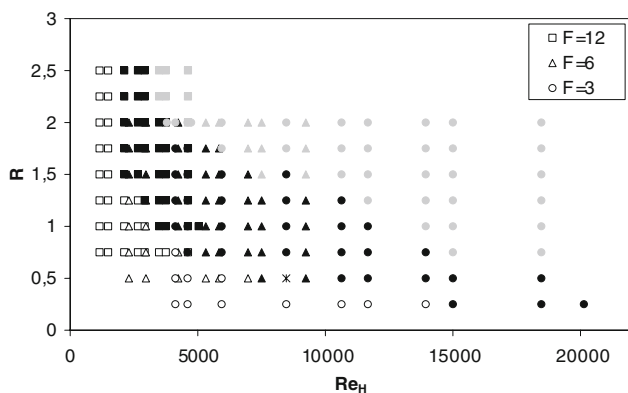


Fig. 17 Existence diagram of centrifugal instability vortices versus Re_H for $F = 12$ (squares), $F = 6$ (triangles), $F = 3$ (circles) with the following notation conventions: *hollow symbol* no row of vortices, *full symbol* spanwise instability, *cross isolated vortices for $F = 3$* , *gray symbol* transitional flow

can be reduced to two dimensionless numbers, say Re_H and R , for large span ratio cavities ($F \geq 3$), not considering the secondary instability. In some regions of the stability diagram (Fig. 17), near the upper limit of stability, there is a superposition of hollow and full symbols, for instance, for $R = 2$ and $Re_H = 3,790$, where hollow circles are mixed with full squares. It must be due to the uncertainty in the parameters setting. Notice that the cavity height H is the appropriate scale to describe the cavity flow instability development, while the cavity length L is the appropriate scale for the shear-layer development.

4.2 Number of centrifugal instability vortices

Figure 18 shows the number of pairs of centrifugal instability vortices present simultaneously inside the visualization plane versus Re_H . Cases with vortices rows as well as cases with isolated pairs of vortices are considered (then, $N = 1$). Limiting cases where vortices are not present are also marked (then, $N = 0$). As the vortices are evolving with time, the uncertainty on their number is estimated to ± 1 and the figures plotted are averaged values on the recorded sequences. For each span ratio where a complete cycle of appearance, presence and vanish of instabilities is investigated experimentally, we note an increase followed by a decrease of the number of pairs of vortices. This is the proof that the appearance-vanish cycle is a continuous phenomenon driven by the external velocity U_e . The geometry is also important since there is an aspect ratio for which the vortices number reaches a maximum. We can notice in Fig. 18a and b that this maximum number of spanwise pairs of vortices is found for $R = 1$. This must be connected to the presence of a main round vortex of spanwise axis inside the cavity, which provides a best radius of curvature with respect to wall confinement. There

is a drop of the number of vortices for $F = 3$ (Fig. 18c), the maximum being get for $R = 1.25$. The same comment is done for $F = 2$ with a lower number of vortices (Fig. 18d). That decrease of the number of vortices inside the cavity with span ratio increase points that the three-dimensional flow is a phenomenon preventing the formation of centrifugal instability vortices.

As very few data concerning the number of centrifugal instabilities are available, these measurements deserve comparison with the results of Koseff and Street (1984a) for a lid-driven cavity. They found 8 pairs of centrifugal instability vortices for $F \leq 3$, $R = 1$, $Re_H = 3,000$ and 11 pairs for $Re_H = 6,000$. The present measurements give four pairs of instability vortices, respectively, for $F = 3$, $R = 1$, $Re_H = 4,120$ and 5,930. If we can draw a conclusion from the comparison between these two Reynolds numbers, it can be said that oscillations of the shear layer affect the flow organization inside the open cavity, which is different from a lid-driven cavity. However, we note here 8 pairs for $F = 6$, $R = 1$ and $Re_H = 4,230$ and 10 pairs for $F = 6$, $R = 1$ and $Re_H = 5,830$, results close to Koseff and Street's observation. The comparison of our measurements with the development of a shear-layer-driven cavity flow, for $R = 1$ and $Re_H = 6,970$, presents a good agreement (Brès and Colonius 2008). As there is a span periodicity in their simulation, these authors found five pairs of centrifugal instability vortices, to compare with the five pairs obtained in the central third of the span in present measurements (Fig. 12). The difference in the number of vortices between lid-driven and shear-layer cavity flow could suggest that the latter, with the development of a shear layer, is more affected by the span ratio than the lid-driven cavity.

The viscous effects on the stability development inside the cavity are stronger for small aspect ratios R and small span ratios F . This could explain the peculiar existence diagram for $F = 2$ (Fig. 16d) with two distinct regions and cases where isolated vortices are present. Similarly, viscous effects get stronger for small aspect ratios R , which could explain the absence of secondary instability for $F = 12$ and $R = 1$ (Fig. 16a). An attempt of description of the instability generation process could be observed as follow, increasing the cavity dimensions (span ratio F). The viscous effects tends to limit the development and number of spanwise instabilities for $F = 2$ (Fig. 18d), there is a development of spanwise instabilities as a row of pairs of vortices for $3 \leq F \leq 6$ and for $F = 12$ the secondary spanwise instability modulation appears.

4.3 Wavelength

As the centrifugal instability vortices are developing along the cavity span, their number is strongly tied to their

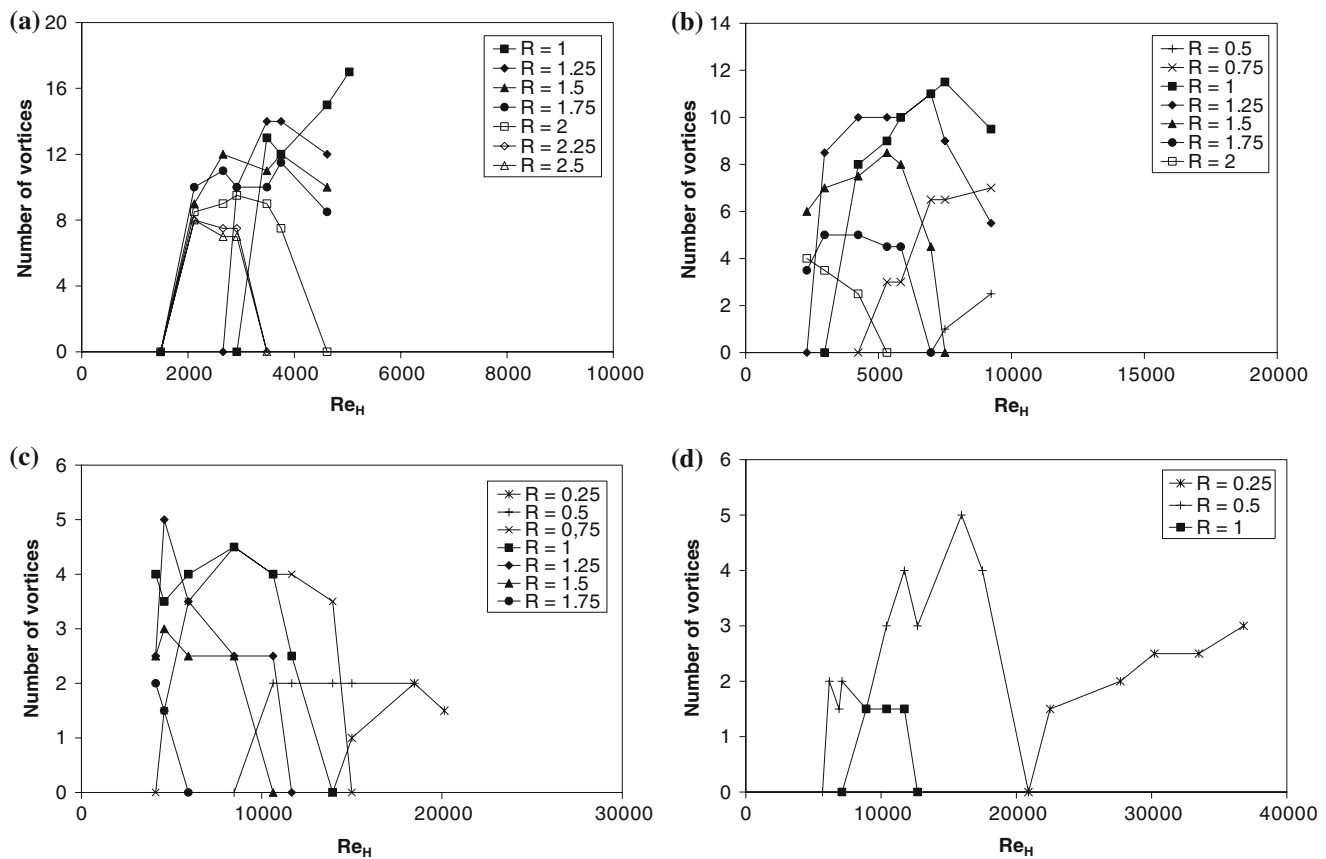


Fig. 18 Number of centrifugal instability vortices versus Re_H for **a** $F = 12$, **b** $F = 6$, **c** $F = 3$ and **d** $F = 2$

wavelength. However, the pairs of vortices are not always adjoined, so the measurement of an averaged wavelength from flow visualizations seems relevant. Its uncertainty is ± 2 mm. Figure 19 presents the development of the spanwise wavelength λ , corresponding to the distance between two pairs of vortices, versus the Reynolds number Re_H . Note that the wavelength is plotted only when a row of instabilities is present, thus cases with isolated unsteady instabilities are not considered. As we noted previously, the spacing between vortices is not always constant, and the estimated wavelengths must be understood as maximum averaged values. The wavelengths have been measured on the images recorded for each geometrical and wind tunnel parameter. An automatic research of the wavelength can be achieved, for example, with a Fourier transform of the image of flow visualization to get the more significant wave number. However, this is difficult to realize because small scale structures appear as the most powerful components in a rather broadband spectrum, and finally the search is conducted by visual analysis. The general trend observed in Fig. 19 is an increase of the wavelength with the aspect ratio R except for $F = 2$ where three-dimensional effects on the mean flow are very strong. It means that larger instabilities, along the z -axis, are present for

long cavities. The instability generation is driven by a three-dimensional coupling between the axial and span directions. Note that for large span ratios ($F = 12, 6$) the wavelength can be greater than the cavity height. The wavelength tends also to increase slowly with the Reynolds number Re_H , for most of the cases, confirming an influence of the external flow on the instabilities generation.

An estimate of the wavelength measured by Koseff and Street (1984a) gives $\lambda/H = 0.38$ for $F \leq 3$, $R = 1$ and $Re_H = 3,000$ and $\lambda/H = 0.27$ for $Re_H = 6,000$. Similarly, Freitas and Street (1988) provide $\lambda/H = 0.2 – 0.3$ for $F = 3$, $R = 1$ and $Re_H = 3,200$. In the present study, $\lambda/H = 0.78$ for $F = 3$, $R = 1$ and $Re_H = 4,120$ and $\lambda/H = 0.68$ for $F = 3$, $R = 1$ and $Re_H = 5,930$. As mentioned in the discussion on the number of instabilities vortices, the oscillations of the shear layer above an open cavity may affect the flow organization inside the cavity in a different way from a lid-driven cavity.

4.4 Spanwise drift velocity

It has been shown by Faure et al. (2007) that the spanwise instabilities are migrating from the cavity centerline outward the cavity sides. This drift motion is due to the

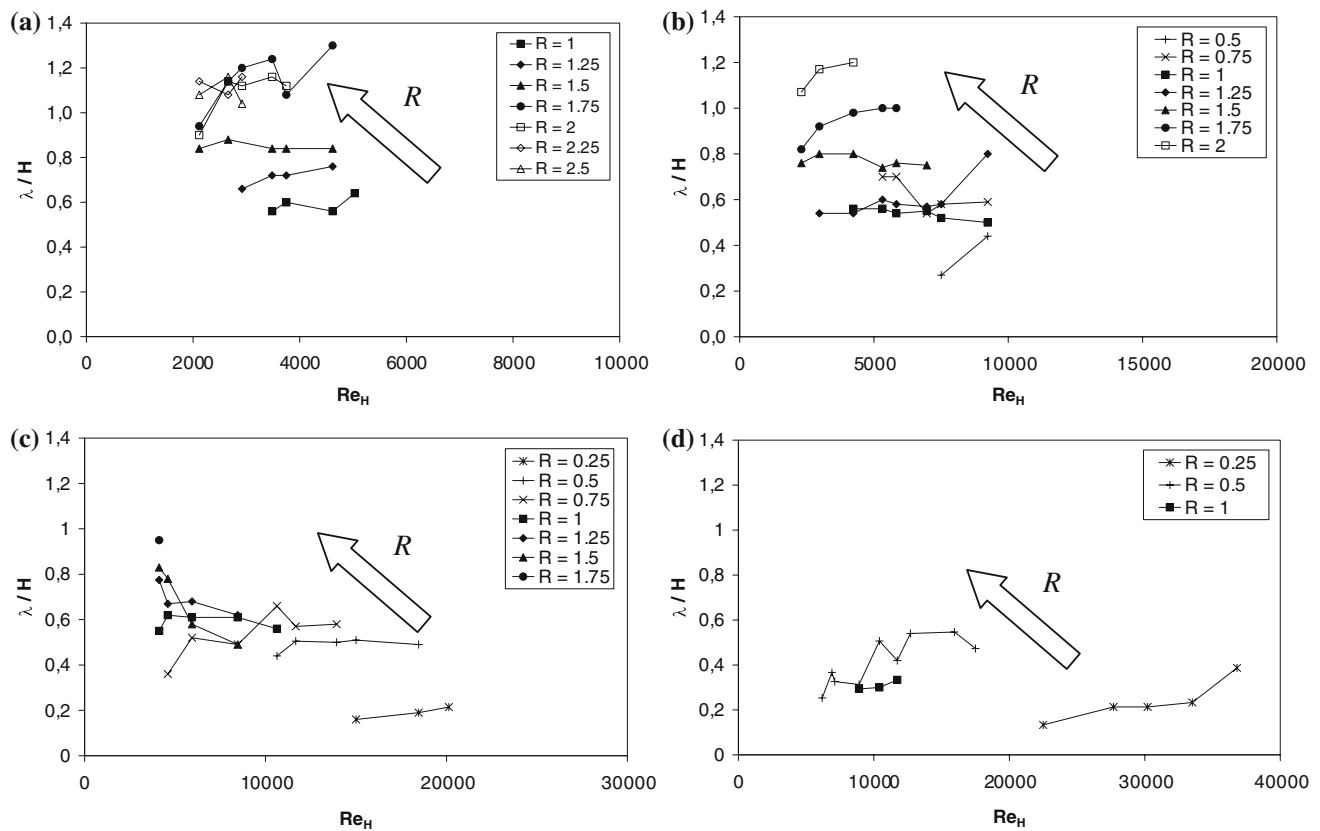


Fig. 19 Wavelength of the centrifugal vortices row versus Re_H for **a** $F = 12$, **b** $F = 6$, **c** $F = 3$ and **d** $F = 2$

spanwise flow in the inner part of the cavity from the sides toward the centerline. The spanwise drift velocity W_s is measured from space-time diagrams. They are built stacking, over each other, a horizontal line of the visualization chosen in a region where spanwise instabilities are present, at different successive times (dashed white line in Fig. 20a). On such diagrams, vertical lines are associated to stationary events, while oblique lines are associated to traveling patterns (Fig. 20b). If oblique lines are, moreover, straight lines, it means that the pattern is traveling at a constant velocity. As these lines have a slope between zero and a maximum value, we choose to characterize each configuration with a maximum spanwise drifting velocity W_s . That velocity can also be measured from a Fourier transform of the space-time diagram (Fig. 20c), where the spanwise drift velocities consist in a set of maxima around zero, limited by a maximum value (dashed white line, Fig. 20c). The measurement of W_s brings to 7.3 mm s^{-1} with both of these methods.

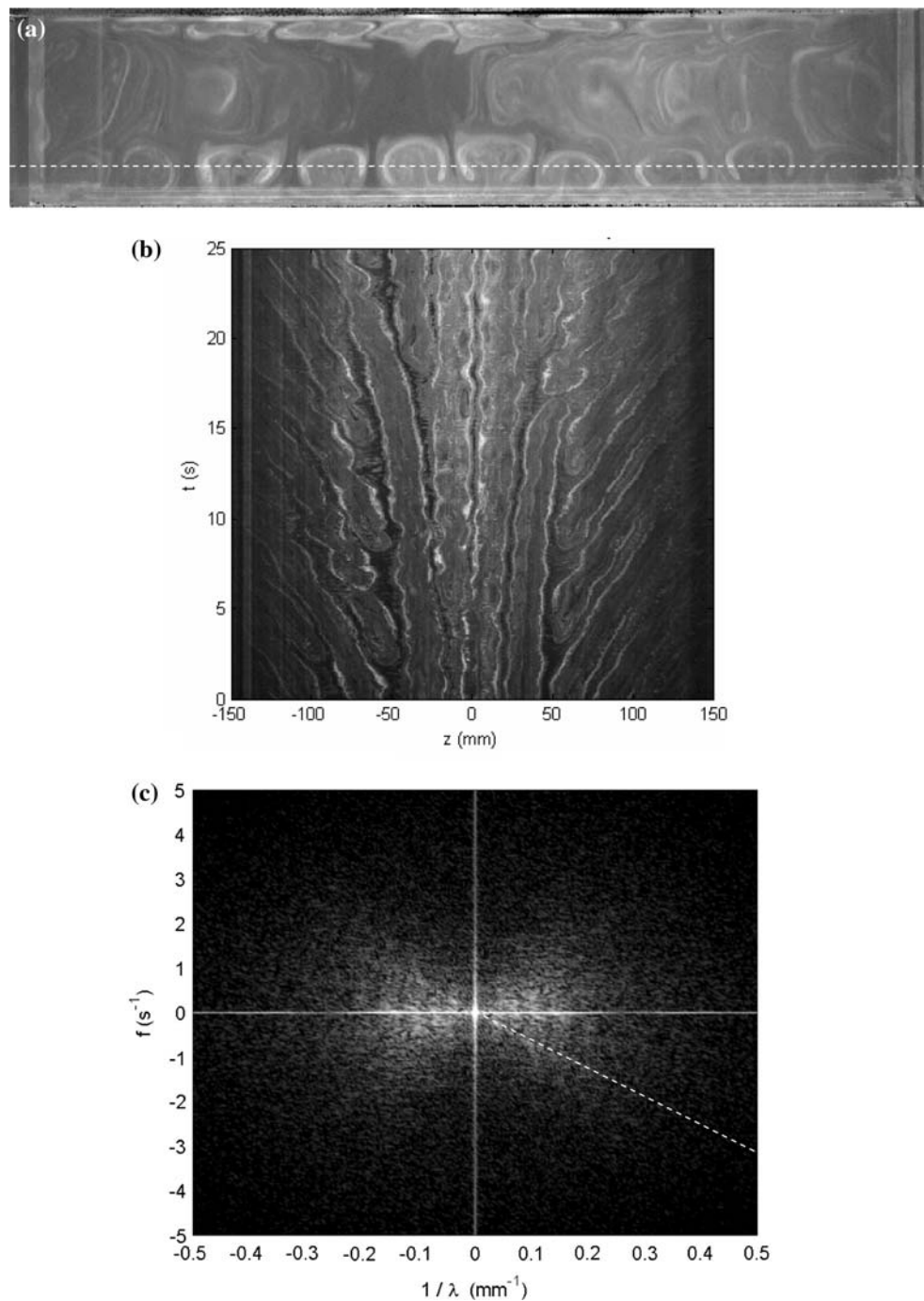
Another reason to choose the maximum spanwise drift velocity to characterize the span flow motion is that the drift motion is not symmetrical for all configurations. There is a shift of the symmetry axis from the centerline of the cavity. This shift is not an experimental artifact since it can

be found for different successive wind tunnel runs and is reproduced in the numerical simulations. Note that the spanwise drift velocity W_s is very low in comparison with the external velocity, reaching a maximum value of 2% of U_e . This velocity W_s is also lower than the maximum advection velocity inside the cavity U_c which is generally 5% of U_e (Fig. 21):

$$\frac{U_c}{U_e} \leq 0.05 \quad \frac{W_s}{U_e} \leq 0.02$$

Let us now consider the variation of that drift velocity with Re_H , R and F . The general behavior is a global decrease of W_s/U_e with R , showing that short cavities help the drift flow. For $F = 12$ (Fig. 22a), the drift velocity tends to decrease when the Reynolds number increases except for $R \geq 2$. The drift velocity is generally greater for the lower Reynolds number Re_H where spanwise instabilities are present than for higher Reynolds numbers. For $F = 6$ (Fig. 22b), the drift velocity is almost constant versus Reynolds number. For $F = 3$ (Fig. 22c), the drift velocity decreases as Reynolds number increases. There is no spanwise drift velocity for $F = 2$ because of the very low number of spanwise instabilities. Notice that in numerical simulations with periodic boundary conditions, there is no more drift of the pairs of vortices. This would

Fig. 20 **a** Visualization for $F = 6$, $R = 1.25$ and $Re_H = 5,320$, **b** corresponding space-time diagram and **c** Fourier transform of the space-time diagram



confirm that the mechanism of the drift originates in the lateral sides of the cavity, where an Ekman layer is present.

5 Conclusion

The flow inside a parallelepipedic cavity shows the development of different morphologies discussed in terms of the presence or the absence of centrifugal instability vortices. These flow instabilities are induced by the

advection velocity and the flow curvature radius induced by a main vortex whose axis is the cavity span, and they are known as independent of the Mach number. For a squared section cavity and $Re_H = 4,230$, features of these instabilities present a good agreement with results obtained by a DNS of the flow. The pairs of vortices are not always present and the thresholds for their appearance and disappearance are identified. For low Reynolds numbers, they are not observed. This can be caused by an advection velocity that is not strong enough to destabilize the

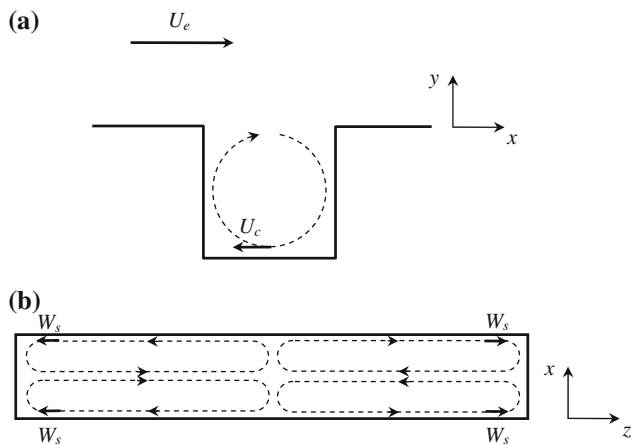


Fig. 21 Velocity scales **a** in a (x, y) plane and **b** in a (x, z) plane

boundary layer on the cavity walls. The spanwise flow coming from the cavity sides toward the centerline may also act as a stabilizing process preventing the formation of instabilities. For much higher Reynolds numbers, the flow is transitioning to a fully developed turbulent flow, and there are no more patterns resulting in spanwise instabilities. The geometry is also an important parameter in terms

of existence of these instabilities. It has been pointed out that three dimensionless numbers are necessary to describe the flow, the Reynolds number and two geometrical ratios in order to take into account the three-dimensional flow features. However, the flow description can be reduced to two dimensionless numbers for $F \geq 3$.

The centrifugal instability vortices are generally developing in a spanwise row, but for some configurations, isolated pairs of vortices are observed particularly for low span ratios ($R = 2, 3$). The properties of the instabilities are also discussed in terms of drifting velocity toward the sides, wavelength and number. The spanwise drifting velocity is decreasing with aspect ratio. The wavelength of the row of instabilities mainly increases with aspect ratio. For cases with an established row ($F = 12, 6$), a maximum number is reached when $R = 1$. For lower span ratios, the number of pairs decreases rapidly since there is no more stable row but isolated pairs of vortices. It seems that the spanwise flow may prevent the centrifugal instability vortices generation.

The existence diagrams of instabilities point, for span ratios larger than 2, that the investigated zone where centrifugal instability vortices are present is forming a

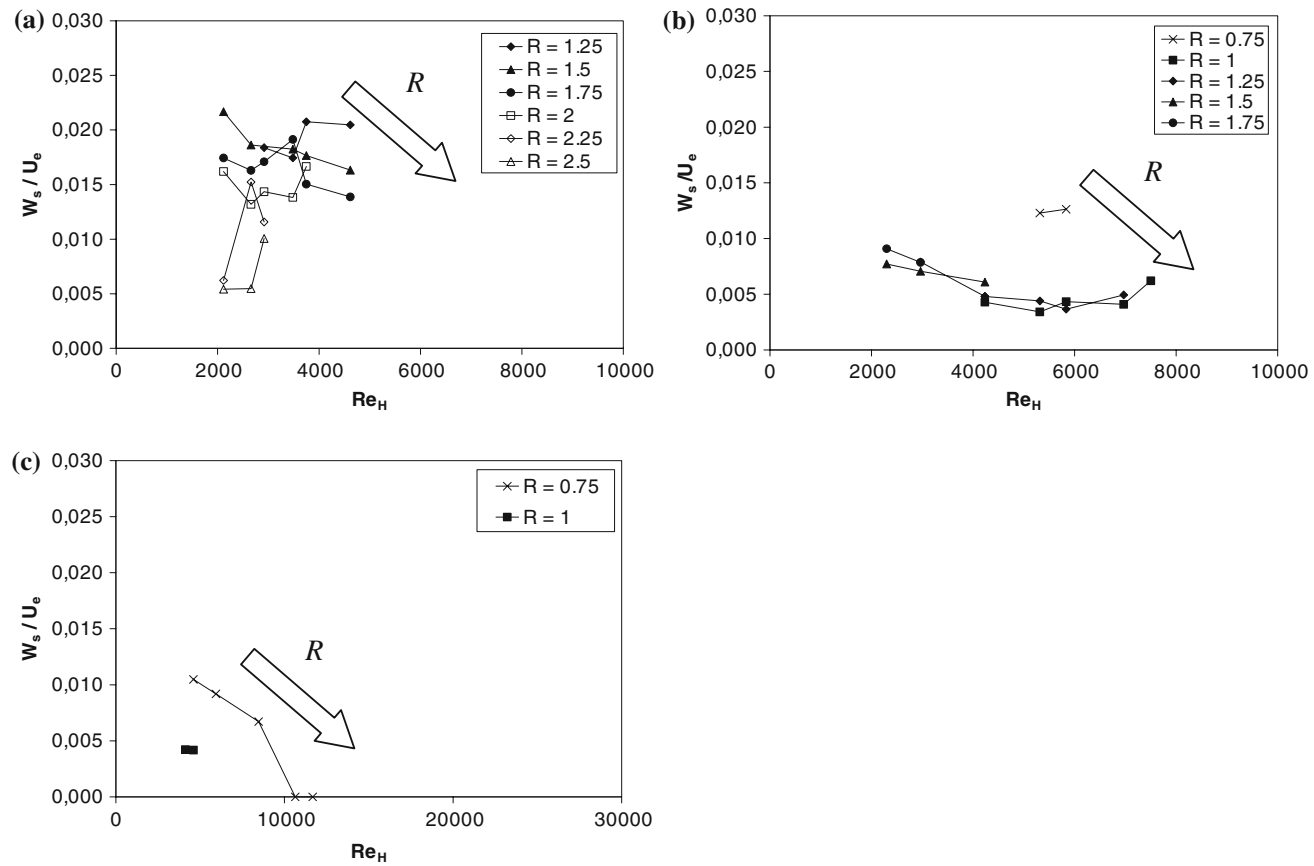


Fig. 22 Spanwise drift velocity W_s/U_e versus Re_H for **a** $F = 12$, **b** $F = 6$ and **c** $F = 3$

compact domain. This is not true for $F = 2$, where the existence domain is divided between two regions separated by a line where isolated pairs are observed. A similar division into two existence domains may also be relevant for higher span ratios, but for aspect ratios larger than 2.5, which have not been investigated. The lower threshold of existence of instabilities is independent of Re_H for $R \geq 1.5$, which suggests that the number of vortices of spanwise axis inside the cavity strongly conditions the instability process. The similarity behavior of the existence region of instabilities for different values of $F \geq 3$ is obtained with the Reynolds number built on cavity height. It seems that this dimension is the driving parameter for the cavity flow dynamics.

References

- Aymer de la Chevalerie D, Fonteneau A, De Luca L, Cardone G (1997) Görtler-type vortices in hypersonic flows: the ramp problem. *Exp Thermal Fluid Sci* 15:69–81
- Brès GA, Colonius T (2008) Three-dimensional instabilities in compressible flow over open cavities. *J Fluid Mech* 599:309–339
- Chang K, Constantinescu G, Park SO (2006) Analysis of the flow and mass transfer processes for the incompressible flow past an open cavity with a laminar and a fully turbulent incoming boundary layer. *J Fluid Mech* 561:113–145
- Chatellier L, Laumonier J, Gervais Y (2004) Theoretical and experimental investigations of low Mach number turbulent cavity flows. *Exp Fluids* 36:728–740
- Chiang TP, Hwang RR, Sheu WH (1997) On end-wall corner vortices in a lid-driven cavity. *J Fluids Eng* 119:201–204
- Chiang TP, Sheu WH, Hwang RR (1998) Effects of the Reynolds number on the eddy structure in a lid-driven cavity. *Int J Numer Methods Fluids* 26:557–579
- Cui X (2004) Numerical simulations of the generation of Taylor-Görtler vortices during spin-down to rest in finite-length cylinders. *Comput Fluids* 33:603–621
- Faure TM, Adrianos P, Lusseyran F, Pastur L (2007) Visualizations of the flow inside an open cavity at medium range Reynolds numbers. *Exp Fluids* 42:169–184
- Faure TM, Defrasne A, Lusseyran F, Pastur LR (2008) Flow instabilities development inside an open cavity. 13th international symposium on flow visualization, Nice (France), 1–4 July 2008, paper ID 81
- Finnis MV, Brown A (1997) The linear growth of Görtler vortices. *Int J Heat Fluid Flow* 18:389–399
- Forestier N, Jacquin L, Geffroy P (2003) The mixing layer over a deep cavity at high-subsonic speed. *J Fluid Mech* 475:101–145
- Freitas CJ, Street RL (1988) Non-linear transport phenomena in a complex recirculating flow: a numerical investigation. *Int J Numer Methods Fluids* 8:769–802
- Gadoïn E, Le Quéré P, Daube O (2001) A general methodology for investigating flow instability in complex geometries: application to natural convection in enclosures. *Int J Numer Methods Fluids* 37:175–208
- Ghia U, Ghia KN, Shin CT (1982) High-Re solutions for incompressible flow using the Navier-Stokes equations and a multigrid method. *J Comput Phys* 48:387–411
- Guermond JL, Migeon C, Pineau G, Quartapelle L (2002) Start-up flows in a three-dimensional rectangular driven cavity of aspect ratio 1:1:2 at $Re = 1000$. *J Fluid Mech* 450:169–199
- Hirsch C (1987) Numerical computation of internal and external flows. Wiley, New York
- Koseff JR, Street RL (1984a) Visualization studies of a shear driven three-dimensional recirculating flow. *J Fluids Eng* 106:21–29
- Koseff JR, Street RL (1984b) On end wall effects in a lid-driven cavity flow. *J Fluids Eng* 106:385–389
- Koseff JR, Street RL (1984c) The lid-driven cavity flow: a synthesis of qualitative and quantitative observations. *J Fluids Eng* 106:390–398
- Leonard BP (1979) A stable and accurate convective modeling procedure based on quadratic upstream interpolation. *Comput Methods Appl Mech Eng* 19:59–98
- Migeon C (2002) Details on the start-up development of the Taylor-Görtler-like vortices inside a square-section lid-driven cavity for $1,000 \leq Re \leq 3,200$. *Exp Fluids* 33:594–602
- Migeon C, Pineau G, Texier A (2003) Three-dimensionality development inside standard parallelepipedic lid-driven cavities at $Re = 1000$. *J Fluids Struct* 17:717–738
- Navarro-Martinez S, Tutty OR (2005) Numerical simulation of Görtler vortices in hypersonic compression ramps. *Comput Fluids* 34:225–247
- Pereira JCF, Sousa JMM (1995) Experimental and numerical investigation of flow oscillations in a rectangular cavity. *J Fluids Eng* 117:68–74
- Saric WS (1994) Görtler vortices. *Annu Rev Fluid Mech* 26:379–409